

D-A 198 015

245 95.2-MS-CF

DTIC FILE COPY

①

Proceedings of the 10th Annual Meeting of the Adhesion Society, Inc.

Edited by
LOUIS H. SHARPE

DISTRIBUTION STATEMENT A

Approved for public release

Distribution unlimited

GORDON AND BREACH

DTIC
ELECTE
AUG 10 1988
S H D

UNCLASSIFIED

SECURITY CLASSIFICATION OF THIS PAGE (When Data Entered)

REPORT DOCUMENTATION PAGE		READ INSTRUCTIONS BEFORE COMPLETING FORM
1. REPORT NUMBER ARO 24595.2-MS-CF	2. GOVT ACCESSION NO. N/A	3. RECIPIENT'S CATALOG NUMBER N/A
4. TITLE (and Subtitle) Adhesion International 1987 Proceedings of the 10th Annual Meeting of the Adhesion Society, Inc.		5. TYPE OF REPORT & PERIOD COVERED Book
		6. PERFORMING ORG. REPORT NUMBER N/A
7. AUTHOR(s) Louis H. Sharpe (editor) Lawrence T. Drzal (principal Investigator)		8. CONTRACT OR GRANT NUMBER(s) DAAL03-87-G-0094
9. PERFORMING ORGANIZATION NAME AND ADDRESS Michigan State University East Lansing, MI 48823		10. PROGRAM ELEMENT, PROJECT, TASK AREA & WORK UNIT NUMBERS N/A
11. CONTROLLING OFFICE NAME AND ADDRESS U. S. Army Research Office P. O. Box 12211 Research Triangle Park, NC 27709		12. REPORT DATE
14. MONITORING AGENCY NAME & ADDRESS (if different from Controlling Office)		13. NUMBER OF PAGES
		15. SECURITY CLASS. (of this report) Unclassified
15a. DECLASSIFICATION/DOWNGRADING SCHEDULE		
16. DISTRIBUTION STATEMENT (of this Report) Submitted for announcement only.		
17. DISTRIBUTION STATEMENT (of the abstract entered in Block 20, if different from Report)		
18. SUPPLEMENTARY NOTES The view, opinions, and/or findings contained in this report are those of the author(s) and should not be construed as an official Department of the Army position, policy, or decision, unless so designated by other documentation.		
19. KEY WORDS (Continue on reverse side if necessary and identify by block number) Adhesion, Composites, Elastomers, Resins, Bonding, Structures, Polymers, Symposia. (7 pages)		
20. ABSTRACT (Continue on reverse side if necessary and identify by block number) This volume is a compilation of more than half of the papers presented at the 10th Annual Meeting of The Adhesion Society, Inc., in Williamsburg, Virginia, U.S.A., February 23-27, 1987. The proceedings were originally published in regular issues of The Journal of Adhesion. The meeting was a highly successful international one, attended by some 350 people. Nine countries were represented on the technical program and at least three Societies. The Plastics and Rubber Institute of Great Britain, The Adhe- sion Society of Japan and the Adhesive and Sealant Council, sent delegates.		

DD FORM 1 JAN 73 1473 EDITION OF 1 NOV 65 IS OBSOLETE

UNCLASSIFIED

SECURITY CLASSIFICATION OF THIS PAGE (When Data Entered)

Adhesion International 1987

\$ 94.00

Adhesion International 1987
Proceedings of the 10th Annual Meeting
of the Adhesion Society Inc.
Williamsburg, Virginia, USA
February 23-27, 1987

Edited by
Louis H. Sharpe

GORDON AND BREACH SCIENCE PUBLISHERS
New York London Paris Montreux Tokyo Melbourne



© 1988 by Gordon and Breach Science Publishers S.A., Post Office Box 161, 1820
Montreux 2, Switzerland. All rights reserved.

Gordon and Breach Science Publishers

Post Office Box 786
Cooper Station
New York, New York 10276
United States of America

Post Office Box 197
London WC2E 9PX
England

58, rue Lhomond
75005 Paris
France

3-14-9, Okubo
Shinjuku-ku, Tokyo
Japan

Private Bag 8
Camberwell, Victoria 3124
Australia

Library of Congress Cataloging in Publication Data

Adhesion Society. Meeting (10th : 1987 : Williamsburg, Va.)
Adhesion international : proceedings of the 10th Annual Meeting of
the Adhesion Society Inc., Williamsburg, Virginia, USA, February
23-27, 1987 / edited by Louis H. Sharpe.
p. cm.
Bibliography: p.
Includes index.
ISBN 0-677-21930-X
1. Adhesives—Congresses. 2. Adhesion—Congresses. I. Sharpe,
Louis H. II. Title.
TP967.A483 1987 668'.3—dc19 88-7321

No part of this book may be reproduced or utilized in any form or by any means, elec-
tronic or mechanical, including photocopying and recording, or by any information
storage or retrieval system, without permission in writing from the publishers. Printed in
the United States of America.

Sold by:
Gordon and Breach Science Publishers
Post Office Box 786
New York, NY 10276
Price: \$94.00

Accession For	
NTIS GRA&I	<input checked="" type="checkbox"/>
DTIC TAB	<input type="checkbox"/>
Unannounced	<input type="checkbox"/>
Justification	
<i>Price \$94.00</i>	
<i>Available from</i>	
<i>By per telcom</i>	
Distribution/	
Availability Codes	
Dist	Avail and/or Special
<i>A-1</i>	<i>21</i>

CONTENTS



Preface

xiii

SESSION OF JAPAN

Estimation of the Surface Energy of Polymer Solids

Toshio Hata, Yasuaki Kitazaki and Takanori Saito

1

Stress Distribution and Strength of T-type Adhesive Joint with Reinforcement for Bending Moment

Yukisaburo Yamaguchi, Susumu Amano and Sadao Sato

19

A Method of Estimating the Strength of Adhesive Bonded Joints of Metals

Kozo Ikegami and Toshio Sugibayashi

35

Effect of a Side Chain Length of Polymer on Both the Adhesion and Dispersibility of $\gamma\text{-Fe}_2\text{O}_3$

Katsuhiko Nakamae, Satoshi Tanigawa, Naoto Hirayama, Katsuya Yamaguchi and Tsunetaka Matsumoto

53

Viscoelastic Analysis of Shear Adhesion Test for Pressure-Sensitive Adhesive Tape

Zenichi Miyagi and Kentaro Yamamoto

67

**Rheological Study on Tack of Pressure-Sensitive
Adhesives**

Hiroshi Mizumachi and Yasunori Hatano 75

SESSION OF THE UNITED KINGDOM

**A Review of Contemporary Views of Theories of
Adhesion**

K. W. Allen 85

**Non-destructive Inspection of Adhesively-bonded
Joints**

R. D. Adams, P. Cawley and C. C. H. Guyott 103

The Adhesive Bonding of Thermoplastic Composites

A. J. Kinloch and C. M. Taig 115

**Durability and Surface Analytical Studies of Adhesive
Bonding to Wood**

D. M. Brewis, J. Comyn and C. Phanopoulos 127

**The Effect of Electrochemical Potentials on the
Durability of Rubber/Metal Bonds in Sea Water**

A. Stevenson 137

**The Effect of Water on Matrix/Filler Adhesion in a
Polyurethane Elastomer**

M. R. Bowditch and K. J. Stannard 153

**Application of Secondary Ion Mass Spectrometry to
Adhesion Studies**

D. Briggs 167

SESSION OF WEST GERMANY

Adhesion on Carbon-Fibre-Reinforced Plastics

Ch. W. Matz 177

CONTENTS

vii

Adhesion Between Metals and Polymers as a Three-Dimensional System

O.-D. Hennemann

183

Chemical Aspects of Adhesion Between Metals and Polymers

H. Brockmann

187

Organically Modified Silicates (Ormosils) as Adhesives for Siliceous Surfaces

H. Schmidt

193

Adhesion Effects of Intermediate Layers on the Densification of Ceramic Powders

B. Frisch and W.-R. Thiele

197

SESSION OF SWITZERLAND

Quantitative Measurement of the Energy of Fracture of an Adhesive Joint Using the Wedge-Test

J. Cognard

213

Reactive Hot Melts on the Basis of Polyester and Polyamide

F. Annighöfer

225

The Repair of Concrete Structures by Injection With Epoxide Resin

A. C. Roulin-Moloney and A. R. Berchten

241

Thermoset Matrices for Structural Adhesives: Imidazole-Catalysed Curing of Epoxy Resins

Jürgen Vogt

255

New Developments in Structural Adhesives for the Automotive Industry

U. T. Kreibich and A. F. Marcantonio

269

SESSION OF AUSTRALIA**The Interaction Parameter and the Strength of Adhesive Joints**

B. W. Cherry and P. B. Evelyn 283

A Thermodynamic Model of the Adhesive Bond

W. S. Gutowski 295

Silane Coupling Agents as Adhesion Promoters for Aerospace Structural Film Adhesives

W. Thiedman, F. C. Tolan, P. J. Pearce and C. E. M. Morris 309

SESSION OF ISRAEL**Correlation Between the Total Morphology of an Epoxy System and Some of its Properties**

Dov Katz and Eli Alon 323

Room Temperature Curing Epoxy Adhesives for Elevated Temperature Service

H. Dodiuk, S. Kenig and I. Liran 339

SESSION OF CANADA**Polymer Mixing and the Thermodynamics of Cell Adhesion at Fluid Interfaces**

Donald J. L. McIver and Samuel Schürch 365

Surface Characteristics of Hydroxyapatite and Adhesive Bonding.1. Surface Characterization

D. C. Smith, D. G. Murray, J. D. Zuccolin and N. D. Ruse 403

Component Interaction and Properties of Pigmented Epoxy Systems

Sylvia Ponce, R. Bazinet and H. P. Schreiber 425

CONTENTS

ix

Adhesion of Hydrophilic Particles to Polymer Substrates Immersed in Aqueous Media

Darryl R. Absolom and A. Wilhelm Neumann 441

SESSION OF FRANCE

Recent Developments in the Spectroscopic Characterization of Modified Surfaces for Adhesive Bonding or Painting

M. Romand, F. Gaillard, M. Charbonnier and A. Roche 469

Elementary Mechanisms in the Interaction of Organic Molecules with Mineral Surfaces

C. Boiziau, S. Leroy, C. Reynaud, G. Lecayon, C. LeGressus
and P. Viel 489

The Role of the Interface in Carbon Fibre-Epoxy Composites

J. Schultz, L. Lavielle and C. Martin 513

Adherence of Elastomers: Fracture Mechanics Aspects

D. Maugis 529

SESSION OF THE UNITED STATES. I

Synthesis and Characteristics of Novel Poly(Imide Siloxane) Segmented Copolymers

R. H. Bott, J. D. Summers, C. A. Arnold, L. T. Taylor,
T. C. Ward and J. E. McGrath 535

Adhesion Tensile Testing of Environmentally Exposed Ti-6Al-4V Adherends

H. M. Clearfield, D. K. Shaffer, J. S. Ahearn and
J. D. Venables 551

Cathodic Debonding of Neoprene from Steel

F. J. Boerio, S. J. Hudak, M. A. Miller and S.G. Hong 567

New and Improved Tests for Adhesion	
A. N. Gent	583

A Comparison Between Measurements and Finite Element Predictions of Crack Opening Displacements Near the Front of an Interface Crack	
K. M. Liechti, D. Ginsburg and E. C. Hanson	591

SESSION OF THE UNITED STATES. II

Anisotropic Wetting of Liquids on Finely Grooved Surfaces	
H. Schonhorn	615

The Study of Reactive Functional Groups in Adhesive Bonding at the Aramid-Epoxy Interface	
L. S. Penn, T. J. Byerley and T. K. Liao	631

Poster Session

Thermodynamic Criteria for the Maximum and Minimum Strength of Fibre-Reinforced Composite Materials	
W. Gutowski	655

A Study on the Properties and Structure of Polyether- Sulfone-Modified Epoxy Adhesives	
Wang Zhi-Lu, Chen Dao-Yi and Liu Xiao-Hui	669

SESSION OF THE UNITED STATES. III

Effect of Adhesive Ductility on Cyclic Debond Mechanism in Composite-to-Composite Bonded Joints	
S. Mall and K. T. Yun	677

Elastoplastic Fracture Behavior of Structural Adhesives Under Monotonic Loading	
Erol Sancaktar, Hooshang Jozavi, Joseph Baldwin and Jing Tang	695

CONTENTS

xi

**Effect of Adherend Thickness and Mixed Mode Loading
on Debond Growth in Adhesively Bonded Composite
Joints**

P. D. Mangalgi, W. S. Johnson and R. A. Everett, Jr. 725

Predicting Bond Strength

G. P. Anderson and K. L. Devries 751

Author Index

765

Subject Index

767

PREFACE

This volume is a compilation of more than half of the papers presented at the 10th Annual Meeting of The Adhesion Society, Inc., in Williamsburg, Virginia, U.S.A., February 23-27, 1987. The proceedings were originally published in regular issues of *The Journal of Adhesion*. The meeting was a highly successful international one, attended by some 350 people. Nine countries were represented on the technical program and at least three Societies, The Plastics and Rubber Institute of Great Britain, The Adhesion Society of Japan and the Adhesive and Sealant Council, sent delegates. This Editor, as President of The Adhesion Society, had the pleasure of presiding over the Meeting.

The presence of the logo of the 10th Meeting of The Adhesion Society on the cover marks this volume as something much more special than the usual proceedings of a technical meeting. This is a *Souvenir Volume*, a memento of a very special occasion for The Adhesion Society and for the attendees at its 10th Annual Meeting. It is a tribute to the international cooperation between the many individuals and groups which resulted in the excellent technical program as evidenced by the contents of this volume; to the spirit of international friendship and fellowship which was apparent in all of the technical and social activities of this meeting; to the many individuals and groups who not only made the meeting possible but who integrated all of its elements and made them work so well together. Few will forget the "unplanned" contribution of the British delegation to the entertainment at the Banquet and the initially reluctant but ultimately enthusiastic participation of many of our overseas colleagues when they were drawn into the Banquet's planned entertainment; the thoughtful gift presented to

The Society by the representatives of the PRI; the mark which the British delegation left on the good inn-keepers and burghers of the Town of Williamsburg; the Swiss delegation's presentation of a huge Swiss watch to keep future meetings of The Society running on time and, of course, the Canadian delegation who, in the abovementioned spirit of international friendship, caused so many meeting attendees to wear a miniature Canadian flag in their lapels when the Canadians were in session.

This preface would not be complete without mention of the many people who contributed to the planning, the organization and the smooth operation of the meeting which produced the papers in this volume. The General Chairman, Prof. L. T. Drzal; the Arrangements Chairman, Dr. D. B. Rahrig, ably assisted by Prof. J. P. Wightman and Dr. D. D. Wheeler; the Fund Raising Chairman, Dr. D. R. Speth; the Session Chairmen: from France, Prof. J. Schultz; from Japan, Profs. H. Mizumachi and K. Nakamae; from the U.K., Messrs. S. G. Abbott and G. W. Stockdale and Dr. A. J. Kinloch; from W. Germany, Dr. W. Brockmann; from Switzerland, Dr. J. Cognard; from Australia, Dr. C. E. M. Morris; from Israel, Dr. H. Dodiuk; from Canada, Profs. H. Schreiber and A. W. Neumann; from the U.S.A., Prof. J. A. Koutsky and Dr. D. L. Hunston; the Poster Session Chairmen, Drs. D. J. Zalucha and H. R. Anderson. In addition, our able Treasurer, Dr. G. F. Hardy, was in charge of Finances; Dr. M. Lattimer put together the Meeting Brochure; Dr. R. E. Hartz was in charge of Registration, ably assisted by Ms. A. Klingbeil and Mrs. Betty Hardy who was also in charge of the Guest Program. We owe all of these people a great debt of gratitude for their countless hours of work.

Our thanks must also go to the Cosponsors of the Meeting: Office of Naval Research; Army Research Office; NASA; NSF; also to our many Corporate and Individual Sponsors whose financial contributions, particularly in support of the attendance of many of our overseas colleagues, made a Meeting of this size and scope possible.

Finally, I would like to thank my wife, Diane, for her help and counsel in the general planning and with the details of the social events and entertainment for the meeting and for her forbearance of my preoccupation of many months with, and the great amount of time which I spent on, matters related to this meeting.

LOUIS H. SHARPE, Editor
Hilton Head Island, SC
U.S.A.

SESSION OF JAPAN

Estimation of the Surface Energy of Polymer Solids†

TOSHIO HATA

*Emeritus Professor of Tokyo Institute of Technology and Gunma University.
8-1-7-103, Shakujii-machi, Nerima-ku, Tokyo 177, Japan*

YASUAKI KITAZAKI

Technical Department, Nichiban Co., Ltd. 100, Nishihara Ohyazawa, Hidaka-cho, Iruma-gun, Saitama 350-12, Japan

TAKANORI SAITO

Research Laboratory of FSK Corporation. 5-14-42, Nishiki-cho, Warabi-shi, Saitama 335, Japan

(Received August 26, 1986)

The methods to estimate the surface tension of polymer solids using contact angles have been reviewed in the first part. They are classified into the following three groups depending on the theories or the equations applied: (1) the methods using the Young's equation alone, (2) the methods using the combined equation of Young and Good-Girifalco, and (3) the methods using the equations of work of adhesion. Some notes and comments are given for each method and results are compared with each other. The two-liquids method for rather high energy surface is also introduced.

Next, some new possibilities to evaluate the surface tension of polymer solids are presented by our new contact angle theory in consideration of the friction between a liquid drop and a solid surface. The advancing and receding angles of contact (θ_a and θ_r) are explained by the frictional tension γ_F and accordingly two kinds of the critical surface tension γ_C (γ_{Ca} and γ_{Cr}) are given.

This work has shown that one of the recommendable ways to evaluate γ_S is either the maximum $\gamma_{LV} \cos \theta_a$ or the maximum γ_C using the advancing contact angle θ_a alone, and another way is the arithmetic or the harmonic mean of the γ_{Ca} and γ_{Cr} . A

† Presented at the Tenth Annual Meeting of The Adhesion Society, Inc., Williamsburg, Virginia, U.S.A., February 22-27, 1987.

depiction to determine the γ_c such as $\ln(1 + \cos \theta_0)$ vs. γ_{LV} with $\cos \theta_0 = (\cos \theta_a + \cos \theta_r)/2$ has also been proposed.

KEY WORDS Critical surface tension; contact angle; friction; methods; polymers; surface energy; surface tension; work of adhesion.

1 INTRODUCTION

The surface energy of polymer solids cannot directly be measured, but there recently appeared some indirect methods which include the extrapolating methods from liquid state using the temperature dependence or the molecular weight dependence of surface tension.

Another series of the method using the contact angle of liquids on a solid polymer surface has also been developed. There are varieties of this method depending on the theories or the equations applied, which will be reviewed in the first part of this paper. Next, we will present some possibilities to evaluate the surface tension of polymer solids from a new theory of the contact angle proposed by us.

2 THE REVIEW OF THE CONTACT ANGLE METHODS

Most of the contact angle methods are based on the Young's equation (1) concerning a liquid drop on an ideally smooth, undeformable, homogeneous and planar surface of a solid.

$$\gamma_{SV} = \gamma_{SL} + \gamma_{LV} \cos \theta \quad (1)$$

where γ_{SV} and γ_{LV} are surface tensions of the solid and the liquid respectively in equilibrium with the saturated vapor of the liquid, γ_{SL} the interfacial tension between the solid and the liquid and θ the contact angle. Equation (1) is rewritten as

$$\gamma_S = \gamma_{SL} + \gamma_{LV} \cos \theta + \pi_e \quad (2)$$

$$(\text{with } \pi_e = \gamma_S - \gamma_{SV})$$

$$\approx \gamma_{SL} + \gamma_{LV} \cos \theta \quad (3)$$

$$(\text{for negligible } \pi_e)$$

where γ_s is the surface tension of the solid in vacuum and π_e is the surface pressure. For a polymer of low surface energy, π_e can usually be neglected and Eq. (2) is approximated to the Eq. (3). Depending on the usage of the Young's equation whether alone or combined with the other surface-chemical equations the methods can be classified into following three groups.

2.1 The methods using Young's equation

(a) The maximum $\gamma_{LV} \cos \theta$ (T. Hata and Y. Kitazaki¹)

In Eq. (2), if both γ_{SL} and π_e tend to zero, $\gamma_{LV} \cos \theta$ will get to the maximum and nearly be equal to γ_s . When liquids 1 and 2 have the equal polarity and chemical structure, the interfacial tension γ_{12} is experimentally known to be very small and close to zero. Similarly in the case of γ_{SL} between a solid and liquids, if one carefully chooses the testing liquids, one can find the condition that γ_{SL} is almost zero and π_e is so small that $\gamma_{LV} \cos \theta$ reaches the maximum giving γ_s . Figure 1 shows an example for polytrifluoroethylene.

The most important matter in this method is that one should use at least three kinds of testing liquids such as nonpolar, polar and hydrogen bonding liquids for a solid of unknown polarity. (More strictly speaking, acidic and basic liquid should be distinguished).

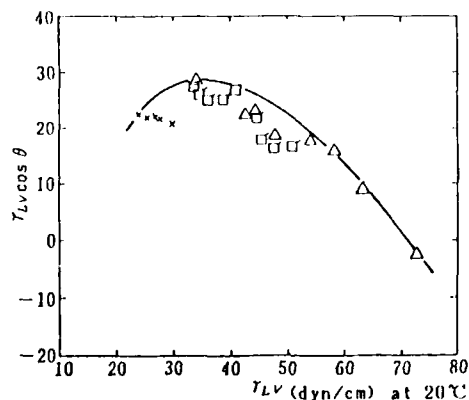


FIGURE 1 $\gamma_{LV} \cos \theta$ plotted against γ_{LV} at 20°C for Polytrifluoroethylene. (x) nonpolar liquids (n-alkanes), (Δ) polar liquids, (\square) hydrogen-bonding liquids.

(b) *The maximum γ_C (Y. Kitazaki and T. Hata²)*

Equation (2) also shows that the extrapolated value of γ_{LV} at $\cos \theta = 1$ is equal to γ_S in case $\gamma_{SL} = 0$ and π_e is negligible. The critical surface tension γ_C of W. A. Zisman is defined as the γ_{LV} at $\cos \theta = 1$. Therefore, using the Eq. (2), γ_C is given by

$$\gamma_C = \gamma_S - \gamma_{SL}^\circ - \pi_e^\circ \quad (4)$$

where γ_{SL}° and π_e° are γ_{SL} and π_e at $\cos \theta = 1$, respectively. Since γ_{SL}° and π_e° depend on the combination of solid and liquid, γ_C may be diverse. Figure 2 shows the three different lines of $\cos \theta$ vs. γ_{LV} obtained by using liquid series of nonpolar (A), polar (B) and hydrogen bonding (C) for polytrifluoroethylene.

Zisman himself was interested in the minimum γ_C as a measure of the wetting property of the solid. However, we take an interest in the maximum γ_C , which is almost equal to γ_S because it corresponds to the minimum of $(\gamma_{SL}^\circ + \pi_e^\circ)$.

In this method it is also necessary to use at least three kinds of testing liquids as above mentioned for an unknown specimen. If one does not like the discrete spectra as shown in Figure 2, one can use the band spectrum (assembly of plots) obtained from many liquids

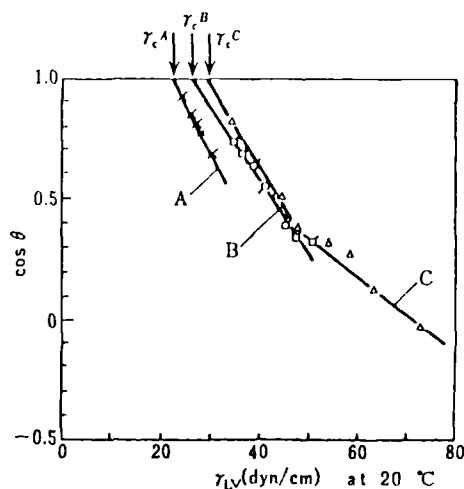


FIGURE 2 Zisman's plots using liquid series of different polarities for Polytrifluoroethylene. A: nonpolar liquids, B: polar liquids, C: hydrogen-bonding liquids.

having various polarities. The extremely right-hand line of the band give $\gamma_C(\max)$.

2.2 The methods using the combined equation of Young and Good-Girifalco

The interfacial tension γ_{12} has been expressed by the equations involving surface tension of each phase γ_1 and γ_2 . One of them is the following equation of Good and Girifalco³.

$$\gamma_{12} = \gamma_1 + \gamma_2 - 2\Phi(\gamma_1\gamma_2)^{1/2} \quad (5)$$

where Φ is the parameter of molecular interaction. Combining this with the Young's equation gives

$$\gamma_s = \frac{\{\gamma_{LV}(1 + \cos \theta) + \pi_e\}^2}{4\Phi^2\gamma_{LV}} \quad (6)$$

$$\approx \frac{\gamma_{LV}(1 + \cos \theta)^2}{4\Phi^2} \quad (7)$$

or

$$\cos \theta = 2\Phi \left(\frac{\gamma_s}{\gamma_{LV}} \right)^{1/2} - 1 - \frac{\pi_e}{\gamma_{LV}} \quad (8)$$

$$\approx 2\Phi \left(\frac{\gamma_s}{\gamma_{LV}} \right)^{1/2} - 1 \quad (9)$$

If the value of Φ is found for a pair of the testing specimen and liquid, we can evaluate the approximate γ_s from the contact angle data using Eq. (7). Good and Girifalco⁴ evaluated γ_s of a glassy fluorocarbon in this way, where they obtained Φ from the experimental values of γ_1 , γ_2 and γ_{12} using Eq. (5) for a liquid homolog of the solid specimen and the testing liquid. However, this method is not general and the following methods using only the contact angle have instead been developed.

(a) *The method of S. Wu*⁵

According to the definition of γ_C , that is $\gamma_C = \lim_{\theta \rightarrow 0} \gamma_{LV}$, Wu derived the following relation from the Eq. (6)

$$\gamma_C = \Phi^2\gamma_s - \pi_e \quad (10)$$

where the higher terms are truncated in the series expansion.

Equation (10) shows that γ_C is a function of Φ , therefore Wu has used $\gamma_{C\Phi}$ in place of γ_C . Combining the Eqs. (10) and (6), and neglecting the smaller terms gives

$$\gamma_{C\Phi} = \frac{\gamma_{LV}(1 + \cos \theta)^2}{4} \quad (11)$$

The maximum value of $\gamma_{C\Phi}$ on the plot of $\gamma_{C\Phi}$ vs. γ_{LV} is regarded as γ_S , because it corresponds to $\Phi_{\max} = 1$ in Eq. (10), when π_e can be neglected (Figure 3).

The criterion of $\gamma_C(\max) \approx \gamma_S$ has been proposed by us as mentioned in the Section 2.1(b).

If, otherwise, $\Phi_{\max} = 1$ could be considered to the condition of determining γ_S , then Wu may have gone a roundabout way through γ_C , because Eq. (6) directly gives

$$\gamma_S \Phi^2 = \frac{\gamma_{LV}(1 + \cos \theta)^2}{4} + \pi_e \left(\frac{1 + \cos \theta}{2} + \frac{\pi_e}{4\gamma_{LV}} \right) \quad (12)$$

$$\approx \frac{\gamma_{LV}(1 + \cos \theta)^2}{4} + \pi_e \quad (13)$$

or the Eq. (7) gives

$$\gamma_S \Phi^2 \approx \frac{\gamma_{LV}(1 + \cos \theta)^2}{4} \quad (14)$$

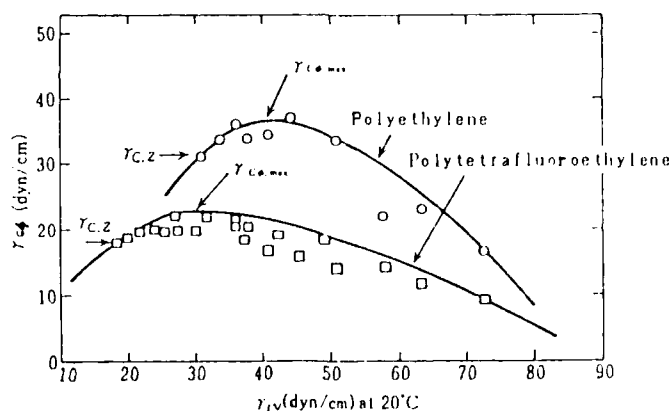


FIGURE 3 $\gamma_{C\Phi} = ((1/4)\gamma_{LV}(1 + \cos \theta)^2)$ plotted against γ_{LV} for polyethylene and polytetrafluoroethylene (after S. Wu, Ref. 5). $\gamma_{C,Z}$ is the Zisman's γ_C .

Equation (13) is quite the same as the combined Eqs. (10) and (11). Neglecting π_e , the maximum value of $(1/4)\gamma_{LV}(1 + \cos \theta)^2$ is here again corresponding to $\Phi_{\max} = 1$ and gives γ_s .

(b) *The method of T. Hata and Y. Kitazaki*¹

As Wu pointed out, Φ_{\max} may be 1 for a pair of equal polarity. This fact can be shown by the Good-Girifalco equation itself. Putting $\gamma_{12} = 0$ as the condition of equal polarity, Eq. (5) gives $\Phi = (\gamma_1 + \gamma_2)/2(\gamma_1\gamma_2)^{1/2}$. This is the ratio of the arithmetic mean to the geometric mean of γ_1 and γ_2 , then if γ_1 does not differ too much from γ_2 , Φ is nearly equal to unity. For example Φ is equal to 1.04 for even such different surface tensions as $\gamma_1 = 36$ and $\gamma_2 = 64$. Among many combinations of a solid with testing liquids, a certain one will satisfy the condition of $\Phi_{\max} = 1$. To find this point there are two ways. The one is the same plot as made by Wu, but on the different basis of Eq. (13) or (14). The other is the plot of $\cos \theta$ against $1/(\gamma_{LV})^{1/2}$ according to Eq. (8). An example is shown in Figure 4 for polytetrafluoroethylene (PTFE) using Zisman's data.⁶ The largest slope of the line through $(-1, 0)$ approximately corresponds to $\Phi_{\max} = 1$ and gives $2(\gamma_s)^{1/2}$. Otherwise, the intercept of the horizontal line at $\cos \theta = 1$ by this largest slope gives $1/(\gamma_{LV})^{1/2} \approx 1/(\gamma_s)^{1/2}$. We obtained from this method $\gamma_s = 22.0$ dyn/cm for PTFE, the value being in good agreement with the value by other methods.

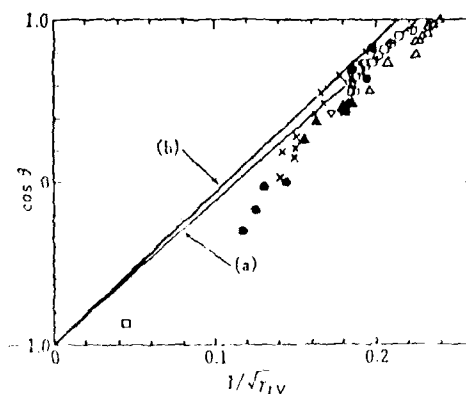


FIGURE 4 Plots of $\cos \theta$ vs. $1/(\gamma_{LV})^{1/2}$ for polytetrafluoroethylene after Zisman's data (Ref. 7). (a) The slope by Good and Girifalco. (b) The largest slope by Hata and Kitazaki.

2.3 The methods using the equations for the work of adhesion

This method starts from the fact that the surface tension γ can be divided into its components, γ^d , γ^p and if necessary γ^h , that is $\gamma = \gamma^d + \gamma^p (+\gamma^h)$, where the superscripts d , p and h refer to dispersion (nonpolar), polar and hydrogen bonding components. If these components are determined independently, we can obtain γ_s by summing them up. On the other hand, the work of adhesion W_a has been expressed by these components of two phases, which originated in the work of F. M. Fowkes⁷ for non-polar liquids as

$$W_a = 2(\gamma_1^d \gamma_2^d)^{1/2} \quad (15)$$

This has been extended to a pair of polar liquids as follows;

Y. Kitazaki and T. Hata⁸

$$W_a = 2(\gamma_1^d \gamma_2^d)^{1/2} + 2(\gamma_1^p \gamma_2^p)^{1/2} + 2(\gamma_1^h \gamma_2^h)^{1/2} \quad (16)$$

D. K. Owens, *et al.*⁹ D. H. Kaelble, *et al.*¹⁰

$$W_a = 2(\gamma_1^d \gamma_2^d)^{1/2} + 2(\gamma_1^p \gamma_2^p)^{1/2} \quad (17)$$

Instead of these equations of geometric mean, the harmonic mean equation has been proposed by S. Wu,¹¹ that is

$$W_a = \frac{4\gamma_1^d \gamma_2^d}{\gamma_1^d + \gamma_2^d} + \frac{4\gamma_1^p \gamma_2^p}{\gamma_1^p + \gamma_2^p} \quad (18)$$

Combining any of these equations with the Young-Duprè equation,

$$W_a = \gamma_1 + \gamma_2 - \gamma_{12} = \gamma_{LV}(1 + \cos \theta) \quad (19)$$

the following equation is reached from, for example, the equation (17)

$$\gamma_{LV}(1 + \cos \theta) = 2(\gamma_s^d \gamma_L^d)^{1/2} + 2(\gamma_s^p \gamma_L^p)^{1/2} \quad (20)$$

Using at least two kinds of liquids with known γ_L^d and γ_L^p , γ_s^d and γ_s^p are determined from the contact angle measurements and then γ_s .

2.4 The two-liquids method¹²

The contact angle method above described cannot be applied to a solid of such high energy surface that most of liquids never form

beads but spontaneously spread out. Even in such cases, a liquid drop can be formed on the surface immersed in the second liquid which is incompatible with the first. For instance if a drop of *n*-alkane (*H*) is introduced on the surface of a solid (*S*) immersed in water (*W*), we have the following equations using the geometric mean for the work of adhesion.

$$\gamma_{SW} = \gamma_{SH} + \gamma_{HW} \cos \theta \quad (21)$$

$$\gamma_{SH} = \gamma_S + \gamma_H - 2(\gamma_S^d \gamma_H^d)^{1/2} \quad (22)$$

$$\gamma_{SW} = \gamma_S + \gamma_W - 2(\gamma_S^d \gamma_W^d)^{1/2} - 2(\gamma_S^p \gamma_W^p)^{1/2} \quad (23)$$

TABLE 1
The surface tension of polymer solids by various methods (dyn/cm) at 20°C

Polymer solids	γ_c (max) *1	$\gamma_{LV} \cos \theta$ (max)	γ_s (Φ_{max}) *2	$\gamma_{c\phi}$ (max)	γ_L (20°C) *3	G.M. (2) *4	G.M. (3) *5	H.M. *6
Polytetrafluoroethylene	21.5(B)	21.6	22.0	22.7	22.6 ^d	19.1	21.5	22.5
Polytrifluoroethylene	29.0(C)	28.4	28.7	28.7	—	23.9	31.2	27.3
Poly(vinylidene fluoride)	40.0(C)	37.1	37.0	37.2	—	30.3	40.2	33.2
Poly(vinyl fluoride)	44.2(C)	42.7	42.7	42.7	—	36.7	43.5	38.4
Polyethylene (air)*7	38.3(B)	36.1	36.5	36.5	35.6	33.2	35.6	36.1
Polyethylene (glycerine)*7	43.9(B)	43.1	43.1	43.1	(35.6)	—	43.3	—
Polyethylene (Hg)*7	41.3(B)	39.4	39.5	39.5	(35.6)	—	41.6	—
Polyethylene (PTFE)*7	29.2(B)	26.8	28.6	28.6	(35.6)	—	26.8	—
Polyethylene (treated by chromic acid)	52.0(B)	49.9	50.3	50.2	(35.6)	—	—	—
Polypropylene	29.8(B)	27.5	29.1	29.1	29.8	—	29.8	—
<i>n</i> -C ₃₆ H ₇₄ (cleavage surface) ^Z	20.6(A)	21.5	21.8	22.0	35.0 ^W	19.1	20.6	23.6
Polystyrene ^Z	43.0(B)	43.1	43.1	43.1	40.6	42.0	40.6	42.6
Poly(methyl methacrylate)	43.5(BC)	44.9	45.0	44.9	41.4 ^W	40.2	43.5	41.2
Poly(vinyl chloride) ^Z	43.9(B)	43.8	43.9	43.8	—	41.5	44.0	41.9
Poly(vinylidene chloride) ^Z	44.0(B)	44.4	44.4	44.6	—	45.0	45.8	45.4
Nylon 66 ^Z	46.0(C)	42.9	43.0	43.2	46.5 ^W	47.0	46.5	44.7
KEL-F ^Z	31.5(B)	32.1	31.9	32.1	30.9 ^S	27.5	31.5	30.1
Polyoxymethylene	46.5(C)	44.6	44.5	44.7	—	—	44.6	—
Poly(ethylene terephthalate)	43.9(B)	43.8	43.9	43.8	44.6 ^W	41.3	—	42.1
PET(corona discharged)	51.1(C)	51.9	51.9	52.0	—	—	—	—
Poly(γ -methyl-L-glutamate)(α) ^{Z,*8}	50.0(C)	—	—	—	—	—	48.0	—
Poly(γ -methyl-L-glutamate)(β) ^{Z,*8}	37.0(BC)	—	—	—	—	—	37.8	—
Polyglycine ^Z	48.5(C)	50.4	50.4	50.7	—	—	—	—
Bakelite	38.0(BC)	36.9	37.3	37.5	—	—	38.5	—

Notes: *1, A, B and C in the parenthesis mean that the nonpolar (A), polar (B) and hydrogen-bonding (C) liquid series each gave the maximum γ_c . *2, The calculated values from the largest slope of $\cos \theta$ vs. $1/(\gamma_{LV})^{1/2}$. *3, The extrapolated values of surface tension at 20°C from molten state. *4, The geometric mean equation of two components. *5, The geometric mean equation of three components. *6, The harmonic mean equation. *7, Surfaces produced by the contact with materials in parenthesis. *8, α and β mean the surface of α -helix conformation and β -structure, respectively. *Others Z, J, W and S mean that γ_s are calculated from the data of Zisman, Johnson, Wu and Schonhorn, respectively.

where γ_s , γ_H and γ_w are the surface tensions of solid, hydrocarbon and water and γ_{sw} , γ_{sh} and γ_{hw} are the interfacial tensions between S/W , S/H and H/W respectively. Combining the equations (21) ~ (23) we have

$$\underbrace{\gamma_H - \gamma_w - \gamma_{HW} \cos \theta}_Y = 2(\gamma_s^d)^{1/2} \{ \underbrace{(\gamma_H^d)^{1/2} - (\gamma_w^d)^{1/2}}_X \} - 2(\gamma_s^p \gamma_w^p)^{1/2} \quad (24)$$

By using a series of *n*-alkanes, a linear relationship is obtained by plotting the quantity Y as a function of X , and accordingly γ_s^d is given by the slope and γ_s^p by the intercept. L. Lavielle and J. Schultz¹³ recently adopted this two-liquids method for the estimation of γ_s of acrylic acid grafted polyethylene.

This method has an advantage over the single liquid method in that the surface pressure π_e does not appear in the equations. However the adsorption of the second liquid may be a new problem.

Now, γ_s obtained by the various methods are summarized in Table I and especially γ_s of the fluorine substituted polyethylenes obtained by the two ways are shown in Figure 5 together with

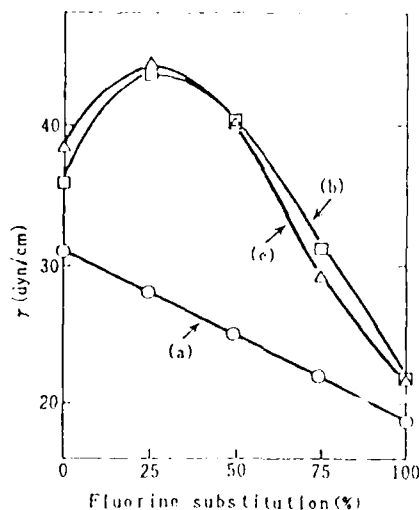


FIGURE 5 γ_s and Zisman's γ_c of fluorine substituted polyethylene, (a) Zisman's γ_c , (b) γ_s by the extended Fowkes Eq. (16), (c) $\gamma_c(\max)$.

Zisman's γ_C . The maximum γ_S of poly(vinylfluoride) is reasonable when taking its polarity into consideration.

In conclusion, we recommend the methods of the maximum $\gamma_{LV} \cos \theta$ and the maximum γ_C as described in the section 2.1, because they are simply based on the Young's equation, while the others are all combined with equations which are not thoroughly proved.

3 A NEW METHOD OF THE ESTIMATION OF γ_S USING CONTACT ANGLES

3.1 The contact angle in consideration of the friction between liquid drop and solid surface

The angle (θ) of contact between a liquid drop and a solid surface has been derived by us as follows,¹⁴

$$\cos \theta = \frac{r}{\gamma_{LV}} \{ \gamma_S - \gamma_{SL} - \pi_e \pm \gamma_F \} \quad (25)$$

where r is the roughness factor and γ_F the frictional tension defined by

$$\gamma_F = \left(\frac{\tau}{\sigma_Y} + \tan \alpha \right) \left(\frac{mg \sigma_Y \cos \theta}{\pi} \right)^{1/2} \quad (26)$$

with τ as the shear stress at liquid-solid interface, σ_Y the yield stress of the liquid, α the base angle of isosceles triangle expressing surface roughness, r the roughness factor being equal to $1/\cos \alpha$, and mg the weight of the liquid drop.

The plus and minus signs before γ_F correspond to the receding angle θ_r and the advancing angle θ_a of contact, respectively. Our theoretical Eq. (25) is in result the form of the equation of Adam and Jessop¹⁵ who *a priori* introduced the friction force. According to our previous work¹⁶ the reversible and the irreversible work of adhesion, W_a and W_A , for a partially miscible interface can be expressed by and related with each other as,

$$W_a = \gamma_S + \gamma_{LV} - \gamma_{SL} = 2(\gamma_S)^{\psi_S} (\gamma_L)^{\psi_L} \quad (27)$$

$$W_A = \frac{\pi}{2} (\tan \delta_S)^{\psi_S} (\tan \delta_L)^{\psi_L} W_a \quad (28)$$

where $\tan \delta_s$ and $\tan \delta_L$ are the loss tangent of the solid and the liquid, $\psi_s = (1 - \psi_L)$ and ψ_L are the mean mole fraction of the molecule or the segment of the solid and the liquid in the interfacial layer.

Taking the irreversibility of the friction into account,¹⁴ W_A can be equated to γ_F for the flat surface ($r = 1$). By substituting the Eq. (28) for the γ_F in the Eq. (25), we obtain the following equation for the flat surface

$$\cos \theta = \frac{\gamma_s - \gamma_{SL} - \pi_e}{\gamma_{LV}} \pm \pi \left(\frac{\gamma_s}{\gamma_{LV}} \right)^{\psi_s} (\tan \delta_s)^{\psi_s} (\tan \delta_L)^{\psi_L} \quad (29)$$

Eliminating $(\gamma_s - \gamma_{SL})$ in the equation (29) by the Eq. (27) gives

$$\cos \theta = \left\{ 2 \left(\frac{\gamma_s}{\gamma_{LV}} \right)^{\psi_s} \left[1 \pm \frac{\pi}{2} (\tan \delta_s)^{\psi_s} (\tan \delta_L)^{\psi_L} \right] - 1 \right\} - \frac{\pi_e}{\gamma_{LV}} \quad (30)$$

Incidentally, the equations (29) and (30) prove the positive correlation of the advancing contact angle and $\tan \delta_s$ which was experimentally shown by Neumann and Tanner¹⁷.

3.2 The critical surface tension γ_c and the surface tension of solid

3.2.1 Relationship of γ_c with the advancing angle θ_a or the receding angle θ_r of contact

As the Eq. (25) shows, the critical surface tension γ_c depends on whether the contact angle is advancing or receding, then two kinds of the γ_c , i.e., γ_{ca} for θ_a and γ_{cr} for θ_r can be obtained by making θ be zero in the Eq. (25),

$$\gamma_{ca} = r(\gamma_s - \gamma_{SL}^\circ - \pi_e^\circ - \gamma_F^\circ) = r(\gamma_{SV}^\circ - \gamma_{SL}^\circ - \gamma_F^\circ) \quad (31)$$

$$\gamma_{cr} = r(\gamma_s - \gamma_{SL}^\circ - \pi_e^\circ + \gamma_F^\circ) = r(\gamma_{SV}^\circ - \gamma_{SL}^\circ + \gamma_F^\circ) \quad (32)$$

where the superscript ($^\circ$) stands for the corresponding quantity at the zero contact angle. The equations (31) and (32) indicate the following.

a) The difference between γ_{ca} and γ_{cr} arises from the frictional tension, and the inequality or the difference of them can be written

as

$$\gamma_{Ca} < r(\gamma_S - \gamma_{SL}^\circ - \pi_e^\circ) < \gamma_{Cr} \quad (33)$$

$$\gamma_{Cr} - \gamma_{Ca} = 2r\gamma_F^\circ \quad (34)$$

b) Since the $\gamma_C(\gamma_{Ca}, \gamma_{Cr})$ is a function of such factors as π_e° , γ_{SL}° and γ_F° along with γ_S and r , the γ_C of the solid has diversity due to those factors depending on the liquids used for measuring the contact angle.

c) According to the reason above mentioned, experimental values and/or the information on π_e° , γ_{SL}° , γ_F and r as well as γ_{Ca} and γ_{Cr} are needed in order to estimate the γ_S from the γ_C .

3.2.2 Estimation of γ_S from γ_{Ca} and γ_{Cr}

When estimating γ_S from γ_C , the γ_F can be eliminated by adding the Eqs. (31) to (32) as follows.

$$\gamma_S = \frac{\gamma_{Cr} + \gamma_{Ca}}{2r} + \gamma_{SL}^\circ + \pi_e^\circ \quad (35)$$

$$\approx \frac{\gamma_{Cr} + \gamma_{Ca}}{2} \quad \left(\text{for } r = 1, \gamma_{SL}^\circ + \pi_e^\circ \ll \frac{\gamma_{Cr} + \gamma_{Ca}}{2} \right) \quad (36)$$

If we assume here that γ_{SL}° , γ_{Ca} and γ_{Cr} are compatible with the Eq. (27), γ_{SL} can be expressed by

$$\gamma_{SL}^\circ = \gamma_S - \gamma_S^{\psi_S}(\gamma_{Cr}^{\psi_L} + \gamma_{Ca}^{\psi_L}) + \frac{\gamma_{Cr} + \gamma_{Ca}}{2} \quad (37)$$

Equation (35) can then be rearranged in case $\psi_S \neq 0$ as

$$\gamma_S = \left\{ \frac{1}{\gamma_{Cr}^{\psi_L} + \gamma_{Ca}^{\psi_L}} \left[\frac{1}{2} \left(1 + \frac{1}{r} \right) (\gamma_{Cr} + \gamma_{Ca}) + \pi_e^\circ \right] \right\}^{1/\psi_S} \quad (38)$$

$$= \left(\frac{\gamma_{Cr} + \gamma_{Ca} + \pi_e^\circ}{\gamma_{Cr}^{\psi_L} + \gamma_{Ca}^{\psi_L}} \right)^{1/\psi_S} \quad \text{for } r = 1 \quad (39)$$

$$= \left(\frac{\gamma_{Cr} + \gamma_{Ca}}{\gamma_{Cr}^{\psi_L} + \gamma_{Ca}^{\psi_L}} \right)^{1/\psi_S} \quad \text{for } \pi_e/(\gamma_{Cr} + \gamma_{Ca}) \ll 1 \quad (40)$$

In case $\psi_S = 1$, Eq. (38) is reduced to

$$\gamma_S \approx \frac{\gamma_{Cr} + \gamma_{Ca}}{2} \quad \text{for } r = 1, \quad \pi_e/(\gamma_{Cr} + \gamma_{Ca}) \ll 1 \quad (41)$$

For the macroscopically flat surface, we can estimate γ_S from Eq.

(30) under the condition of $\psi_s \neq 0$ as

$$\gamma_s = \left\{ \frac{2 + \frac{\pi_e^\circ}{2} \left(\frac{1}{\gamma_{Cr}} + \frac{1}{\gamma_{Ca}} \right)}{\left(\frac{1}{\gamma_{Cr}} \right)^{\psi_s} + \left(\frac{1}{\gamma_{Ca}} \right)^{\psi_s}} \right\}^{1/\psi_s} \quad (42)$$

$$\approx \left\{ \frac{2}{\left(\frac{1}{\gamma_{Cr}} \right)^{\psi_s} + \left(\frac{1}{\gamma_{Ca}} \right)^{\psi_s}} \right\}^{1/\psi_s} \quad \text{for } \frac{\pi_e^\circ}{4} \left(\frac{1}{\gamma_{Cr}} + \frac{1}{\gamma_{Ca}} \right) \ll 1 \quad (43)$$

When ψ_s is unity, the Eq. (42) can be reduced to

$$\gamma_s = \frac{2\gamma_{Cr}\gamma_{Ca}}{\gamma_{Cr} + \gamma_{Ca}} + \frac{\pi_e^\circ}{2} \quad (44)$$

While the Eq. (30) provides us with the following equations for $\psi_s \neq 0$

$$\gamma_s = \gamma_{Ca} \left\{ \frac{1 + \frac{\pi_e^\circ}{2\gamma_{Ca}}}{1 - \frac{\pi}{2} (\tan \delta_s)^{\psi_s} (\tan \delta_L)^{\psi_L}} \right\}^{1/\psi_s} \quad (45)$$

$$\gamma_s = \gamma_{Cr} \left\{ \frac{1 + \frac{\pi_e^\circ}{2\gamma_{Cr}}}{1 + \frac{\pi}{2} (\tan \delta_s)^{\psi_s} (\tan \delta_L)^{\psi_L}} \right\}^{1/\psi_s} \quad (46)$$

If the γ_F is small enough compared to the reversible work of adhesion W_a i.e.,

$$\frac{\gamma_F}{W_a} = \frac{\pi}{2} (\tan \delta_s)^{\psi_s} (\tan \delta_L)^{\psi_L} \ll 1 \quad (47)$$

and π_e is negligible, i.e.,

$$\frac{\pi_e^\circ}{2\gamma_C} \ll 1 \quad (48)$$

Equations (45) and (46) can be reduced as

$$\gamma_s = \gamma_{Ca} \left(1 + \frac{\pi_e^\circ}{2\psi_s \gamma_{Ca}} \right) \left\{ 1 + \frac{\pi}{2\psi_s} (\tan \delta_s)^{\psi_s} (\tan \delta_L)^{\psi_L} \right\} \quad (49)$$

$$\gamma_s = \gamma_{Cr} \left(1 + \frac{\pi_e^\circ}{2\psi_s \gamma_{Cr}} \right) \left\{ 1 - \frac{\pi}{2\psi_s} (\tan \delta_s)^{\psi_s} (\tan \delta_L)^{\psi_L} \right\} \quad (50)$$

In the case of $\psi_s = 0$, we obtain the following from Eq. (29).

$$\gamma_s = \gamma_{Ca} \left(1 + \frac{\pi_e^\circ}{\gamma_{Ca}} + \tan \delta_L \right) + \gamma_{sL}^\circ \quad (51)$$

$$\gamma_s = \gamma_{Cr} \left(1 + \frac{\pi_e^\circ}{\gamma_{Cr}} - \tan \delta_L \right) + \gamma_{sL}^\circ \quad (52)$$

Equations (51) and (52) can be rewritten as

$$\gamma_s = \gamma_C + \gamma_{sL}^\circ \quad \text{for} \quad \frac{\pi_e^\circ}{\gamma_C} \pm \tan \delta_L \ll 1 \quad (53)$$

where the γ_C is the γ_{Ca} or the γ_{Cr} . Equation (53) is identical to Eq. (4) derived by the Young's relationship.

3.2.3 Estimation of the mean mole fraction ψ_s

In the case that γ_F is small enough as shown in the Eq. (47), and π_e/γ_{LV} is negligibly small, Eq. (30) can be reduced to

$$\cos \theta \approx 2 \left(\frac{\gamma_s}{\gamma_{LV}} \right)^{\psi_s} - 1 \quad (54)$$

We then obtain the following equation.

$$\ln(1 + \cos \theta) \approx \ln 2 (\gamma_s)^{\psi_s} - \psi_s \ln \gamma_{LV} \quad (55)$$

which shows an approximate ψ_s is able to be determined by the slope in the plot of $\ln(1 + \cos \theta)$ vs. $\ln \gamma_{LV}$, and the γ_C can also be determined by the γ_{LV} corresponding to the intersection of $\ln 2$ and $\ln \gamma_{LV}$.

3.3. Comparison of γ_s determined by various methods

Using the data on γ_{Cr} and γ_{Ca} by Petke and Ray¹⁸, we can estimate the γ_s of some polymers. Besides, Zisman's⁶ and our

TABLE II
Estimation of γ_s of polymers from γ_{Ca} and γ_{Cr} reported.

Polymers	*1 γ_{Cr}	*1 γ_{Ca}	*2 γ_s Eq. (36)	*2 γ_s Eq. (44)	γ_s $\gamma_{LV} \cos \theta$ (max)	*3 ψ_s Eq. (55)	*3 γ_s Eq. (55)	*4 γ_s Eq. (40)	*4 γ_s Eq. (43)
PE	42.8 ^a	36.3 ^a	39.6	39.3	36.1	0.844	39.4	39.6	39.3
PS	40.7 ^a	33.3 ^a	37.0	36.6	43.1	0.577	42.7	37.1	36.7
POM	43.3 ^a	38.2 ^a	40.8	40.6	44.6	0.847	43.7	40.8	40.6
PC	43.5 ^a	34.7 ^a	39.1	38.6	32.0	0.683	35.3	39.2	38.7
PET	45.5 ^a	40.3 ^a	42.9	42.7	43.8	0.914	44.1	42.9	42.7
FEP	24.0 ^a	19.8 ^a	21.9	21.7					
PTFE	20.0 ^b	7.6 ^b	14.0	11.1	21.6	0.679	23.1	14.5	11.5
PMMA	45.6 ^b	44.0 ^b	44.8	44.8	45.0	1.02	43.4	44.7	44.7

*1. At 20°C after Petke and Ray¹⁸; b) at 25.5 ± 1.5°C after Shimi and Goddard¹⁹.

*2. After the data*1.

*3. Estimated by Eq. (55) with our data of θ_a at 20 ± 2°C.

*4. γ_{Ca} , γ_{Cr} , and ψ_s at 20°C after Petke and Ray¹⁸, and at 25.5 ± 1.5°C after Shimi and Goddard¹⁹ using Eq. (55).

works allow us to estimate the ψ_s and the γ_{Ca} from the Eq. (55). Results are summarized in Table II, which indicates that each method using γ_{Ca} and γ_{Cr} is able to give reasonable γ_s being almost equal to, for example, the maximum $\gamma_{LV} \cos \theta$. So we consequently recommend rather the simplified Eqs. (36) and (44) than equations involving the ψ_s and ψ_L .

4 CONCLUDING REMARKS

In this article we have reviewed and proposed various methods to evaluate γ_s of polymers, above all using contact angles. The following methods are eventually recommended as mentioned in the text.

1) Either the maximum $\gamma_{LV} \cos \theta$ or the maximum γ_C using the advancing contact angle is appropriate to estimate the γ_s .

2) Allowing for the frictional tension at the liquid-solid interface, both the critical surface tension γ_{Ca} and γ_{Cr} should be determined by advancing angle (θ_a) and receding angle (θ_r) of contact, respectively. The γ_s can then be obtained from the arithmetic mean (Eq. (36)) or the harmonic mean (Eq. (44)) of γ_{Ca} and γ_{Cr} .

3) Another recommendable method is based on the contact angle (θ_0) being independent of the frictional tension γ_F . An equation

about $\cos \theta_0$ can readily be derived by the equation (25) as follows.

$$\cos \theta_0 = \frac{\cos \theta_a + \cos \theta_r}{2} \quad (56)$$

Therefore γ_s can also be evaluated from a plot such as $\gamma_{LV} \cos \theta_0$ vs. γ_{LV} (e.g., Fig. 1), $\cos \theta_0$ vs. γ_{LV} (the Zisman's plot) or $\ln(1 + \cos \theta_0)$ vs. $\ln \gamma_{LV}$ (Eq. (55)).

Finally, we just touch on the mean mole fraction ψ_s and ψ_L at the liquid-solid interface. The estimated values of $\psi_s = (1 - \psi_L)$ is diverse and not necessarily equal to 0.5 as shown in the Table 2. This result shows that the Berthelot's approximation ($\psi_s = \psi_L = 0.5$) is not appropriate for evaluating the work of adhesion, the critical surface tension and other quantities affected by the interaction in the intermixing interface. The divergence of ψ_s from 0.5 has also been confirmed by the Eq. (27) using directly measured γ_1 , γ_2 , and γ_{12} of liquids. This is an important fact in surface-chemical problems.

References

1. T. Hata and Y. Kitazaki, *Preprints of the Annual Meeting of the Society of Fiber Science and Technology, Japan*, P. 147 (1981); *Kobunshi* **32**, 648 (1983).
2. Y. Kitazaki and T. Hata, *J. Adhesion Soc. of Japan* **8**, 123 (1972); *J. Adhesion* **4**, 123 (1972).
3. L. A. Girifalco and R. J. Good, *J. Phys. Chem.* **61**, 904 (1957); R. J. Good, L. A. Girifalco and G. Kraus, *ibid.* **62**, 1418 (1958).
4. R. J. Good and L. A. Girifalco, *J. Phys. Chem.*, **64**, 561 (1960).
5. S. Wu, *Adhesion and Adsorption of Polymers*, L. H. Lee ed., (Plenum Pub Co., New York, 1980), Part A, P. 53; *Polymer Interface and Adhesion*, (Marcel Dekker, Inc., New York, 1982), P. 172.
6. H. W. Fox and W. A. Zisman, *J. Colloid Sci.* **5**, 520 (1950); *ibid.* **7**, 109 (1952).
7. F. M. Fowkes, *Contact Angle, Wettability and Adhesion*, Advances in Chemistry Series, No. 43, (Am. Chem. Soc., Washington D.C. 1964), P. 99.
8. T. Hata, *Kobunshi* **17**, 594 (1968), Y. Kitazaki and T. Hata, *J. Adhesion Soc. of Japan* **8**, 131 (1972).
9. D. K. Owens and R. C. Wendt, *J. Appl. Polym. Sci.* **13**, 1741 (1969); *ibid.* **14**, 1725 (1970).
10. D. H. Kaelble and K. C. Uy, *J. Adhesion* **2**, 50 (1970).
11. S. Wu, *J. Polym. Sci.* **C34**, 19 (1971); *J. Adhesion* **5**, 39 (1973).
12. Y. Tamai, M. Makuuchi and M. Suzuki, *J. Phys. Chem.* **71**, 4176 (1967).
13. a) J. Schultz, K. Tsutsumi and J. B. Donnet, *J. Colloid Interface Sci.* **59**, 272 (1977), b) L. Lavielle and J. Schultz, *J. Colloid Interface Sci.* **106**, 438 (1985).

14. T. Saito, Y. Kitazaki and T. Hata, *J. Adhesion Soc. of Japan*, in press.
15. N. K. Adam and G. Jessop, *J. Chem. Soc.* **127**, 1863 (1925).
16. T. Saito, *J. Adhesion Soc. of Japan* **22**, 9 (1986).
17. A. W. Neumann and W. H. Tanner, *J. Colloid Interface Sci.* **34**, 1 (1970).
18. F. D. Petke and B. R. Ray, *J. Colloid Interface Sci.* **31**, 216 (1969).
19. A. E. Shimi and E. D. Goddard, *J. Colloid Interface Sci.* **48**, 242 (1974).

Stress Distribution and Strength of T-type Adhesive Joint with Reinforcement for Bending Moment†

YUKISABURO YAMAGUCHI‡, SUSUMU AMANO, and SADA O SATO

Kogakuin University

(Received August 26, 1986)

The stress distribution in the adhesive layer of T-type adhesive-bonded butt joint between rigid adherends has been measured experimentally, and the equation relating the maximum stress in the adhesive layer to the bending moment applied to the joint and to the joint dimensions was derived. The equation is used to calculate the adhesive strength of a T-type joint from the measured breaking load. These strengths show reasonable agreement with experimental values.

The distribution in the adhesive layer of a T-type adhesive joint with the reinforcement having the section of a right-angled isosceles triangle has been measured experimentally. The strength efficiency of the reinforcement η and the strengthening magnification of the reinforcement μ are discussed geometrically comparing with the equation. The values of η and μ measured by the experiments showed good agreement with the values obtained geometrically.

KEY WORDS Bending moment; reinforced adhesive joints; rigid adherends; strength; stress distribution; T-type adhesive joints.

1 INTRODUCTION

In the first part of this paper, the equation relating the maximum stress in the adhesive layer to the applied bending moment Pl in

† Presented at the Tenth Annual Meeting of The Adhesion Society, Inc., Williamsburg, Virginia, U.S.A., February 22–27, 1987.

‡ Author to whom all correspondence should be addressed at: Hongo 4–9–8, Bunkyo- Tokyo 113, Japan.

2 DERIVATION OF EQUATION RELATING MAXIMUM STRESS TO BENDING MOMENT IN T-TYPE ADHESIVE JOINT

The diagram illustrates the stress distribution in a beam of length ℓ under a point load P applied at the right end. The beam is divided into two regions: (A) the elastic region and (B) the plastic region. The transition point is labeled E . The stress distribution in region (A) is shown as a linear profile, while in region (B) it is shown as a constant value σ_2 . The diagram also indicates the location of the neutral axis and the plastic layer.

FIGURE 1 T-type adhesive joint with applied bending moment Pl and its schematic stress distribution.

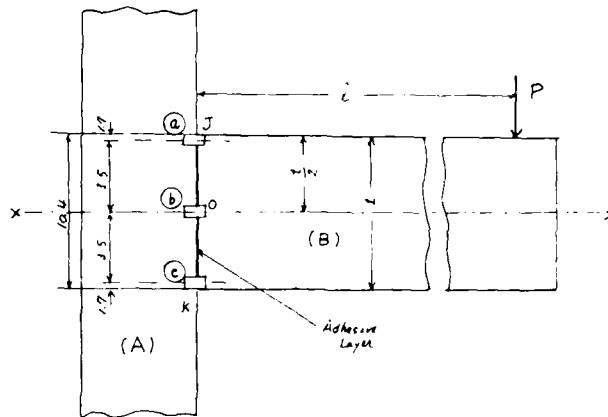


FIGURE 2 Positions of strain gauges to measure strain under applied bending moment for T-type adhesive joint.

Before the maximum stress/bending moment relationship can be derived, it is necessary to know the stress distribution induced in the adhesive as the result of the bending moment. This was determined by placing three strain gauges across the adhesive layer of the T-type joint, as indicated by (a), (b) and (c) in Figure 2. The strains at these points under different bending forces P applied at $l = 80$ mm are shown in Figure 3. It is clear from this figure that a tensile strain is induced at (a) and compression strain at (c), with almost zero strain at (b). As the stress is directly proportional to the strain, the stress σ_x at the distance x from the mid-point is given by;

$$\sigma_x = \sigma_1 \frac{x^n}{t/2} \quad (1)$$

where σ_1 is the stress at (a) or the distance $t/2$ from the mid-point O , t is the vertical length of the adhesive surface and n is almost equal to one. If $n = 1$ in Eq. (1), then the tensile stress distribution across OJ and the compressive stress distribution across OK is shown by the arrows in Figure 1, and σ_1 is the maximum tensile stress. If the area dA at a distance x from O is the product of the breadth b and a small vertical length of adhesive dt , then the

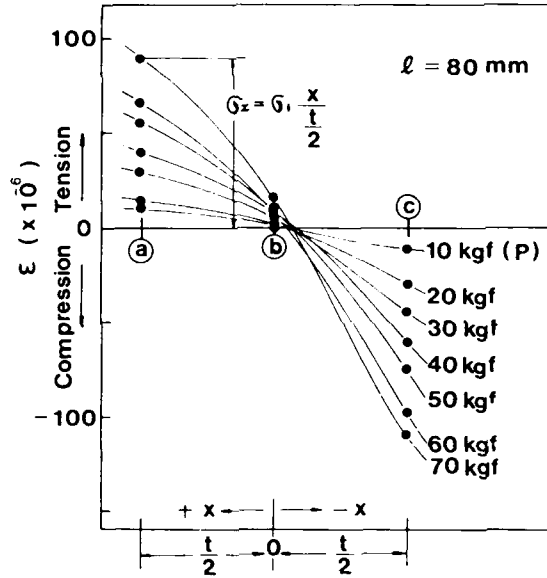


FIGURE 3 Strains detected at (a), (b) and (c) in T-type adhesive joint under each applied bending force P .

bending moment dM reacting against Pl at dA is given by;

$$dM = \sigma_x dAx \quad (2)$$

From Eq. (1)

$$\begin{aligned} dM &= \sigma_1 \frac{x}{t/2} b dx \\ &= 2b \frac{\sigma_1}{t} x^{(n+1)} dx \end{aligned}$$

The integral value of dM from O to J must be half of the bending moment Pl . Hence;

$$\begin{aligned} \frac{Pl}{2} &= \int_{x=0}^{x=t/2} dM \\ &= \frac{2b\sigma_1}{t} \int_{x=0}^{x=t/2} x^{(n+1)} dx \end{aligned}$$

$$\begin{aligned}
&= \frac{2b\sigma_1}{t} \frac{1}{n+2} (x^{n+1})_{x=0}^{x=t/2} \\
&= \frac{2b\sigma_1}{(n+2)t} \left(\frac{t}{2}\right)^{n+2} \\
\therefore \sigma_1 &= \frac{2^n(n+2)Pl}{bt^{(n+1)}} \quad (3)
\end{aligned}$$

When $n = 1$

$$\sigma_1 = \frac{6Pl}{bt^2} \quad (3a)$$

As shown in Figure 1, the average shear stress τ_{av} or the maximum shear stress τ_{max} induced at the adhesive surface JK by the shearing force P' is;

$$\tau_{av} = \frac{P'}{bt} = \frac{P}{bt} \quad (4)$$

$$\tau_{max} = \alpha \tau_{av} = \frac{P}{bt} \alpha \quad (5)$$

where α is the shear stress concentration factor^{1,2} the maximum combined stress or the equivalent tensile stress σ_{e1} (comprising σ_1 and τ_{max}) is derived from the equation $\sigma_e = (\sigma^2 + \tau^2)^{1/2}$

$$\begin{aligned}
\sigma_{e1} &= \left[\left(\frac{2^n(n+2)Pl}{bt^{(n+1)}} \right)^2 + \left(\frac{P}{bt} \alpha \right)^2 \right]^{1/2} \\
&= \frac{P}{bt} \left[\left(\frac{2^n(n+2)}{t^n} \right)^2 + \alpha^2 \right]^{1/2} \quad (6)
\end{aligned}$$

when $n = 1$

$$\sigma_{e1} = \frac{P}{bt} \left[\left(\frac{6l}{t} \right)^2 + \alpha^2 \right]^{1/2} \quad (6a)$$

when l/t is greater than 2, $\sigma_1 \gg \tau_{max}$. Thus τ_{max} becomes negligible compared with σ_1 , so that Eq. (3) or (3a) is applicable.

3 EXPERIMENTAL VERIFICATION OF THE EQUATION

T-type adhesive-bonded butt joints were prepared between stainless steel adherends (A and B) with an epoxy-polyamide adhesive at JK .

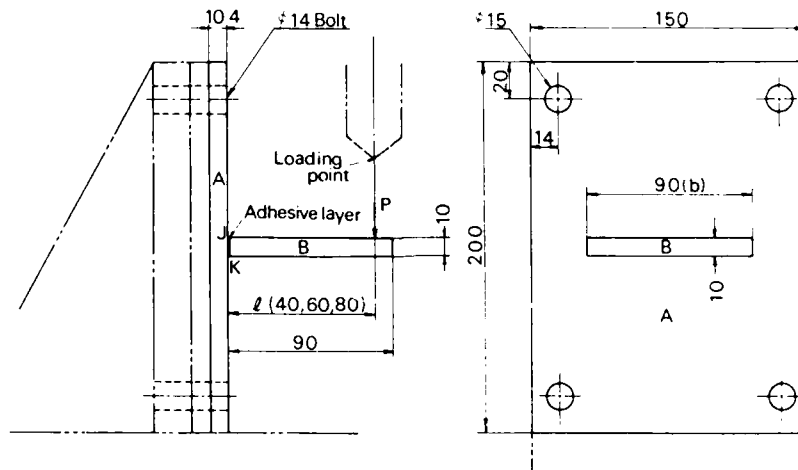


FIGURE 4 Experimental apparatus for breaking the adhesive joint by bending moment Pl .

The joint were mounted in the apparatus shown in Figure 4, and the breaking load P_{\max} was measured by increasing the load at distance l of 40, 60 or 80 mm from the adhesive surface. The average value of P_{\max} obtained are presented in Table I.

The tensile adhesive strength σ_{j1} of the joint was calculated by substituting the value of P_{\max} into Eq. (3a) or (6a) that is,

TABLE I
Bending (or tensile) adhesive strength σ_{j1} for each bending moment $P_{\max}l$. For T-type joint

Distance l (mm)	No.	Breaking load P_{\max} (kgf)	Mean breaking load $P_{\max \text{ av}}$ (kgf)	Bending adhesive strength σ_{j1} (kgf/mm ²)
40	1	196	195.5	5.2
	2	195		
	3	—		
60	1	172	169.7	6.8
	2	167.5		
	3	—		
80	1	102	104	5.5
	2	106		
	3	104		

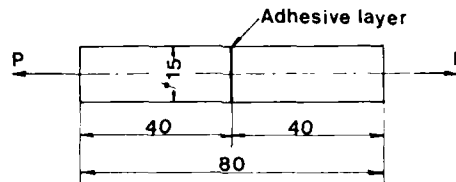
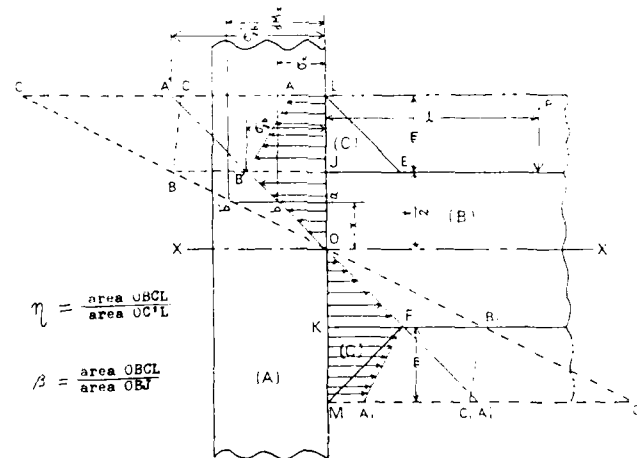


FIGURE 5 Test specimen to measure the tensile adhesive strength.

$\sigma_{j1} = 6P_{\max}l/bt^2$. These values of σ_{j1} are shown in the right-hand column of Table I: they range from 5.2 to 6.8 kgf/mm², with the average value being 5.8 kgf/mm². Since in these tests the value of l/t is 4 to 8, then $\sigma_1 \gg \tau_1$ and $\sigma_1 = \sigma_{e1}$.

The tensile adhesive strength σ_{jt} obtained using the specimen shown in Figure 5 was 5.2 kgf/mm². The reasonable agreement obtained between the theoretical adhesive strength σ_{j1} under bending moment Pl and the tensile experimental value σ_{jt} verifies the use of Eq. (3a) and (6a) to estimate the strength of T-type adhesive bonded butt joint under an applied bending load moment.

FIGURE 6 T-type adhesive joint with the reinforcement C having the section of a right-angled isosceles triangle and its schematic distributions of stress and reacting bending moment under applied bending moment Pl .

4 T-TYPE ADHESIVE JOINT WITH REINFORCEMENT

a) Distributions of stress and reacting moment in adhesive layer

To know the stress or strain distribution at the adhesive layers between steel adherends (*A*) and (*B*), (*C*), eleven strain gauges ① ~ ⑪ were placed across the adhesive layer *LM* in Figure 7(a), and also six strain gauges ⑫ ~ ⑰ were placed across the adhesive layers *JE* and *KF* between the steel adherend (*B*) and the reinforcement (*C*). Strains detected by the strain gauges at the adhesive layer *LM* are shown as Figure 8. It is clear from this figure that the stress distribution at the adhesive layer *JK* is similar to that of T-type adhesive joint shown by Figure 1, and that the strain amounts at the layers *LJ* and *KM* between adherend (*A*) and

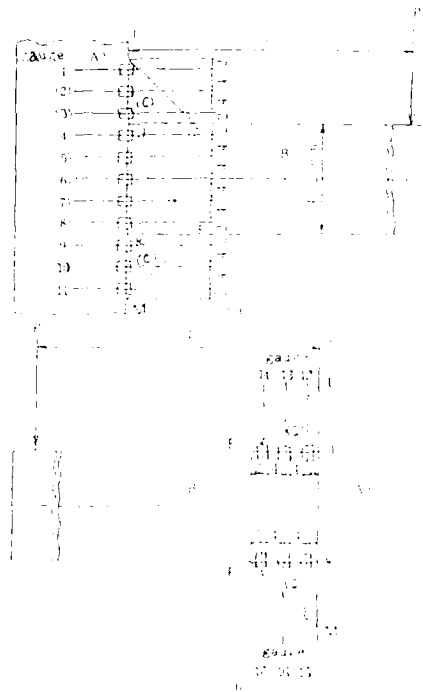


FIGURE 7 Positions of strain gauges attached across the adhesive layer of T-type adhesive joint with the reinforcement *C*.

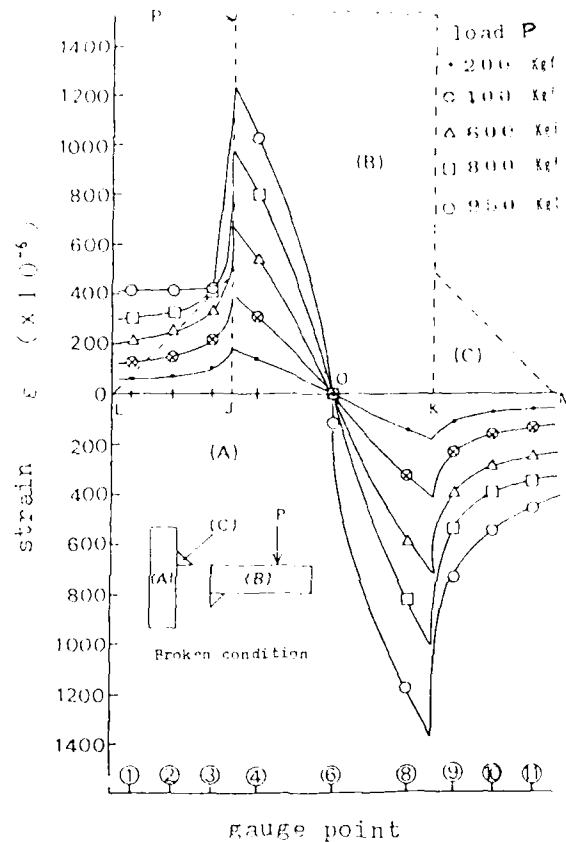
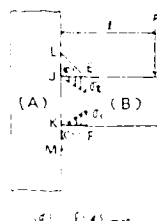


FIGURE 8 Strains detected by strain gauges ①~⑪ of T-type adhesive joint with the reinforcement under each applied bending load P .

reinforcement (C) are smaller than that at JK . The stress distributions at the adhesive layers JE and KF under bending load are also shown by Figure 9, where σ_t is tensile stress and σ_c is compressive stress. The reason for those phenomenons is assumed to be that there are some relaxations of bonding between adherends (B) and (C) due to the much lower elastic modulus of the adhesive layers.

We would consider now the distribution of reacting bending moment at adhesive layer LM to be balanced to the bending moment Pl for a T-type adhesive joint with or without reinforce-

FIGURE 9 Strain distribution at the adhesive layer of JE and KF .

ment. In the upper half side of the adhesive joint in Figure 6, the reacting bending moment dM_x at minute adhesive area dA having length of dx and width of $b = dx \cdot b$ and x far from mid-point O to be balanced to applied bending moment $Pl/2$ is given by:

$$dM_x = \sigma_x dx b x \quad (7)$$

where σ_x is the tensile stress at the points x far from O . Along the adhesive layer JO , the following relation is obtained;

$$\begin{aligned} \frac{Pl}{2} &= \int_{x=0}^{x=l/2} dM_x \\ &= \int_{x=0}^{x=l/2} \sigma_x \cdot b \cdot x \cdot dx \end{aligned} \quad (8)$$

The value of σ_x is shown geometrically by the distance from OJ to the line OB in Figure 6, and the maximum amount of σ_x is given by BJ . As dM_x is the product of σ_x , dA and x , the value of dM_x is shown geometrically by the length parallel to axis xx of triangle OBJ , and the maximum value is presented by BJ . And then the area of triangle OBJ is equivalent to $\int_{x=0}^{x=l/2} dM_x$. When the thickness of a adherend (B) becomes $(t + 2m)$ and the length of adhesive layer is LM . The value of σ_x is shown by the length parallel to the axis xx of triangle OAL , and the maximum value is presented geometrically by $A'L$. Accordingly, the value of dM_x is shown geometrically by the length parallel to the axis xx of triangle $OC'L$ and then $\int_{x=0}^{x=l/2} dM_x$ is shown by the area of triangle $OC'L$.

The value of σ_x along the adhesive layer OL of the joint with reinforcement (C) is shown by the length parallel to the axis xx of quadrilateral $OB'AL$ which is similar to that in Figure 8. As there

are some relaxations at adhesive layer and some deformation of the reinforcement (C), it being an elastic the solid, the amount of dM_x of this case is shown geometrically by the length parallel to the axis xx of the quadrilateral $OBCL$, and $\int_{x=0}^{x=1/2+m} dM_x$ is shown by the area of the quadrilateral $OBCL$. The larger the area presented by the integral of dM_x the larger the adhesive strength against the applied bending moment. If $P_{\max}l$ is the applied bending moment to break the T-type adhesive joint with thickness of $(t + 2m)$ of adherend (B) and $P'_{\max}l$ is that to break T-type adhesive joint with the reinforcement (C) with adhesive length of m , then their ratio, designated the strength efficiency of reinforcement, η , is given by:

$$\eta = \frac{P'_{\max}l}{P_{\max}l} = \frac{\text{area } OBCL}{\text{area } OC'L} \quad (9)$$

When σ'_{jb} is the stress at L of T-type adhesive joint with adhesive length of $(t + 2m)$, the area of triangle $OC'L$ is given by:

$$\frac{F_{\max}l}{2} = \frac{\sigma'_{jb}b \cdot (t + 2m)^2}{12} \quad (10)$$

When $P_{0\max}l$ is the maximum bending moment for T-type adhesive joint with adhesive layer of JK and thickness of adherend (B) of t and $P'_{\max}l$ is the maximum bending moment for T-type adhesive joint with the reinforcement (C) with adhesive length of m , their ratio μ is designated the strengthening magnification of reinforcement and is given by:

$$\mu = \frac{P'_{\max}l}{P_{0\max}l} = \frac{\text{area } OBCL}{\text{area } OBJ} \quad (11)$$

b) Experimental

When a bending moment Pl was applied to a T-type adhesive joint with 20 or 44 mm thickness and 40 mm width of adherend (B), the breaking loads $P_{0\max}(t = 20 \text{ mm})$ and $P_{\max}(t = 44 \text{ mm})$ for each arm length l of 110, 70 and 45 mm were obtained experimentally as shown in Table II. In these cases, the adherends were stainless steel and the adhesive was an epoxy-polyamide.

The tensile or bending adhesive strength σ_{jb} obtained from equation (3a) or (6a) for those T-type adhesive joints were 5.0 to

TABLE II
Experimental results

Type of adhesive bonded joint	Arm length l (mm)	Breaking load $P_{0\max}$ or P'_{\max} (kgf)	Strength efficiency of reinforcement η (%)	Strengthening magnification μ	Adhesive strength σ_{jb}
Without reinforcement	110	$P_{0\max}$ 129	100	1.0	5.0
	70	$P_{0\max}$ 238	100	1.0	6.3
T type	45	$P_{0\max}$ 323	100	1.0	5.5
$t = 20$ mm					
With reinforcement	m 4 mm	110 P'_{\max} 217	86	1.68	4.6
		70 P'_{\max} 374	80	1.57	5.1
		45 P'_{\max} 459	77	1.42	4.0
	m 8 mm	110 P'_{\max} 372	90	2.88	4.8
		70 P'_{\max} 571	74	2.39	4.7
		45 P'_{\max} 776	76	2.40	4.2
	m 12 mm	110 P'_{\max} 451	73	3.49	3.9
		70 P'_{\max} 754	65	3.16	4.2
		45 P'_{\max} 1,084	72	3.34	4.0
Without reinforcement	70	P_{\max} 1,061	100		5.6
T type					
$t = 44$ mm					

 $P_{0\max}$ without reinforcement, P'_{\max} with reinforcement

6.3 kgf/mm² as shown in Table II. The tensile adhesive strength σ_{jt} , obtained by the test pieces shown in Figure 5, was 4.8 kgf/mm² and their bending adhesive strengths, σ_{jb} , were 5.3 to 6.3 kgf/mm². The values of σ_{jb} , σ_{jt} and σ_{jf} show good agreement.

For T-type epoxy-polamide adhesive joints between steel adherends (A) and (B) with breadth 40 mm and thickness 20 mm attached adhesively the steel reinforcement (C) with equilateral length m of 4, 8 or 12 mm, the breaking bending load P'_{\max} for each arm length l of 110, 70 or 45 mm were obtained as shown in Table II, using the apparatus presenting in Figure 4. The strength efficiencies of reinforcement η were obtained from those values as follows:

$$\eta = \frac{P'_{\max} l}{P_{\max} l} = \frac{P'_{\max}}{P_{\max}} \quad (\text{for same } l \text{ and } t) \quad (12)$$

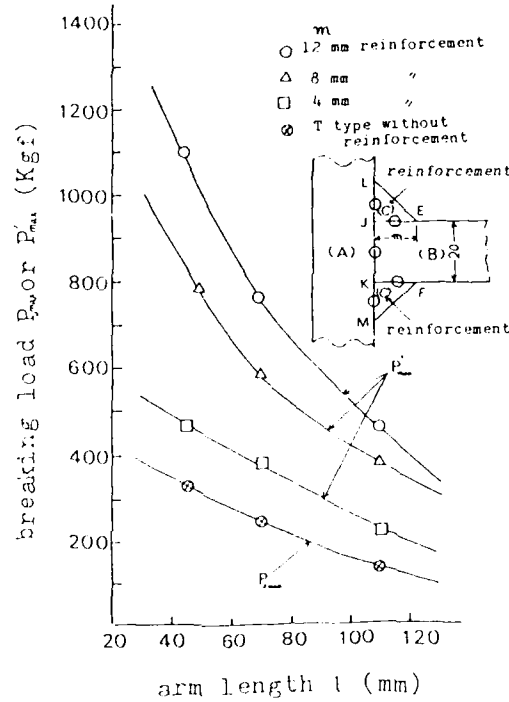


FIGURE 10 Relation between breaking load P'_{\max} or $P_{0\max}$ and arm length l of bending moment for T-type adhesive joint with each reinforcement C .

The values of η are shown in Table II. Figure 10 shows the relations between the breaking load $P_{0\max}$ for 20 mm of t without reinforcement or P'_{\max} for each equilateral length m of reinforcement and arm length l of bending moment. Figure 11 shows the relations between adhesive strength of each adhesive joint σ_{jb} obtained from Eq. (3a) assuming that t is $(20 + 2m)$ or strength efficiency of reinforcement η and arm length l . It seems from this figure that the value of η increases slightly with increase in l .

The strengthening magnifications of reinforcement μ were obtained by the following:

$$\mu = \frac{P'_{\max} l}{P_{0\max} l} = \frac{P'_{\max}}{P_{0\max}} \quad (13)$$

where $P_{0\max}$ is the breaking bending load of T-type adhesive joint

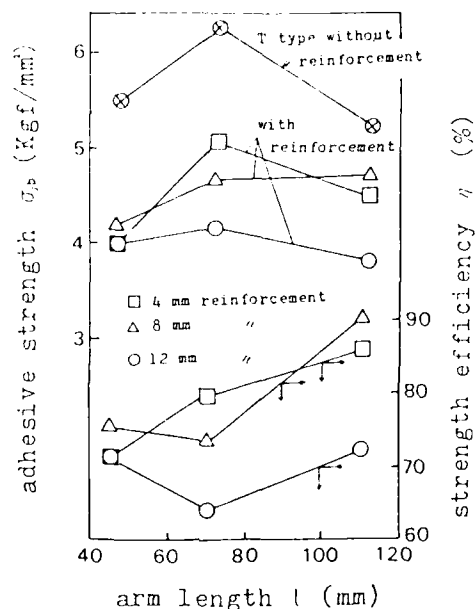


FIGURE 11 Relation between adhesive strength σ_b or strength efficiency of reinforcement η and arm length l of bending moment.

with 20 mm thickness of adherend (B) and P'_{\max} is that with 20 mm thickness of (B) and the reinforcement of 4, 8 and 12 mm of equilateral length m . The values of μ for various cases are shown in Table II. It is clear from the Table that the values of μ are 1.5 for 4 mm of m , 2.55 for 5 mm of m and 3.26 for 12 mm of m . Those values of η or μ are nearly equal to the values obtained from the area ratio given by Eq. (9) or (11) and Figure 6. It seems that there is good agreement between the value of η or μ obtained experimentally and that obtained from the area ratio geometrically.

5 CONCLUSIONS

When a bending force P is applied parallel to and at a distance l from the adhesive surface of a T-type adhesive-bonded butt joint between two steel adherends of thickness t and width b , the maximum tensile stress σ_1 , and the maximum equivalent tensile

stress σ_{e1} induced at the adhesive layer are given by the equation;

$$\sigma_1 = \frac{2^n(n+2)Pl}{bt^{(n+1)}}$$

$$\sigma_{e1} = \frac{P}{bt} \left[\left(\frac{2^n(n+2)P}{t^2} \right)^2 + \alpha^2 \right]^{1/2}$$

where the value of n is 1 when t is less than 10 mm, but becomes greater than 1 when t is greater than 10 mm; α is the shear stress concentration factor and is generally greater than 1 and σ_1 is almost equal to σ_{e1} when l/t is greater than 2.

When a similar bending force is applied to a T-type adhesive joint with a reinforcement having the section of a right-angled isosceles triangle of length m of equilateral, the distributions of stress and reacting bending moment could be presented geometrically. The strength efficiency of reinforcement η and the strengthening magnification of reinforcement μ are given by following:

$$\eta = \frac{P'_{\max}}{P_{\max}}$$

$$\mu = \frac{P'_{\max}}{P_{0\max}}$$

where P'_{\max} is the breaking bending load of the joint with reinforcement of equilateral length m and vertical adhesive length of $(t+2m)$, P_{\max} is that of T-type joint in which the thickness of adherend (B) equals to $(t+2m)$ and $P_{0\max}$ is that of T-type joint with thickness t of adherend (B). The values of η obtained experimentally were 65 to 90% and those of μ were from 1.5 to 3.2, and those values showed reasonable agreement with the values obtained geometrically as the area ratio.

References

1. F. Szépe, *Exptl. Mech.* **6**, 282 (1965/6).
2. J. J. Bikerman, *The Science of Adhesive Joints* (Academic Press, NY, 1968), pp. 215-234.

A Method of Estimating the Strength of Adhesive Bonded Joints of Metals†

KOZO IKEGAMI and TOSHIO SUGIBAYASHI

Research Laboratory of Precision Machinery and Electronics, Tokyo Institute of Technology, Nagatsuta, Midori-ku, Yokohama 227, Japan

(Received August 26, 1986)

The strength of adhesive bonded joints is investigated both analytically and experimentally. The deformed states of lap joints under tensile shear loading are analysed by the finite element method on the assumption of elastic deformation. A method of using the adhesive strength law is proposed to estimate the joint strength. The adhesive strength law is experimentally determined by subjecting butt joints of two thin-walled tubes to combined axial load and torsion. The strength of lap joints is determined by adopting the adhesive strength law to the adhering interface as well as the strength law of adherend and adhesive resin. The calculated strain distribution and strength of the joints are compared with the experimental results. The effects of the joint configurations on the deformation and strength are discussed. It is shown that the proposed method is useful to predict the joint strength.

KEY WORDS Adhesive joint strength; adhesive strength laws; lap-shear joints; metal adherends; strength prediction; stress distribution.

1 INTRODUCTION

Adhesive bonded joints have many advantages for structural usages compared with mechanical fastenings such as bolts, nuts and rivets. However, they do not always have enough reliability as to joint strength. This is caused by the fact that the strength of adhesive

† Presented at the Tenth Annual Meeting of The Adhesion Society, Inc., Williamsburg, Virginia, U.S.A., February 22-27, 1987.

joints is difficult to evaluate. A rational method is necessary for the estimation of the joint strength.

Adhesive joints deform under loading conditions in a complicated manner, as they are composite structures consisting of different materials in the adherends and in the adhesive layer. Such joint deformation has been investigated by many researchers within the framework of the theory of elasticity and plasticity and by numerical methods such as the finite element method. Some of the research results are found in a recently published book.¹ The prediction of the joint strength is more complicated than the stress analysis. The fracture of the joints is related to the interfacial strength as well as the strength of the adherend and adhesive layer. To evaluate the joint strength, it is necessary to correlate the stress distribution with the interfacial strength. In this paper, the adhesive strength law, which is determined by subjecting butt joints of thin-walled tubes to combined axial load and torsion, is proposed as the reference value for the correlation of the interfacial strength and stress distribution. The proposed method is applied to the stress distribution of various lap joints of metal. The predicted strength is compared with the experimental value.

2 STRAIN ANALYSIS

2.1 Lap joints under tensile shear load

(1) *Analytical model* The coordinates, dimensions and boundary conditions are given in Fig. 1(a, b). The joint length, the length of upper and lower adherends and the adhesive length are represented by notations l , l_1 and l_2 , respectively. The thickness of both adherend and adhesive are represented by notations t_1 and t_2 , respectively. The position in the x -direction and the adhesive length are shown by non-dimensional notations \bar{X} ($\bar{X} = x/l_2$) and \bar{L}_0 ($\bar{L}_0 = l_2/l$), respectively. The boundary conditions are assumed that all nodal points on the left edge of the upper adherend are fixed in x and z directions, and the uppermost nodal point on the right edge of the lower adherend is free in the x direction and fixed in the z direction. The load per unit width, f , is applied to all nodal points on the right edge of the lower adherend. The material constants of adherends (carbon steel) and adhesive resin (epoxy resin) used in this research are given in Table I.

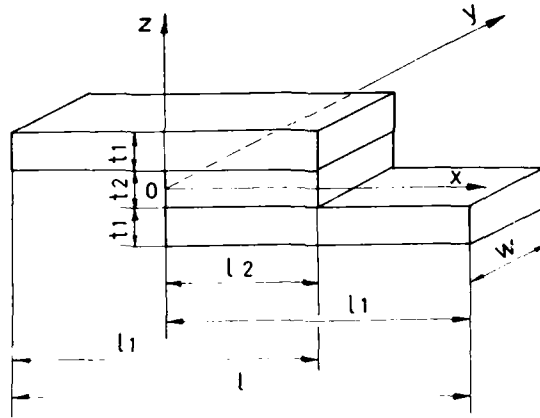


FIGURE 1(a) Coordinate system and dimensions of single lap joint.

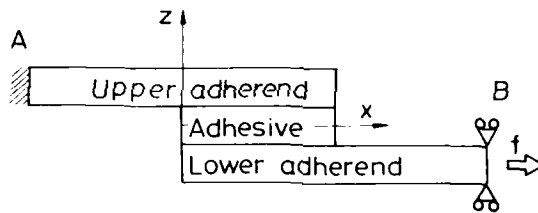


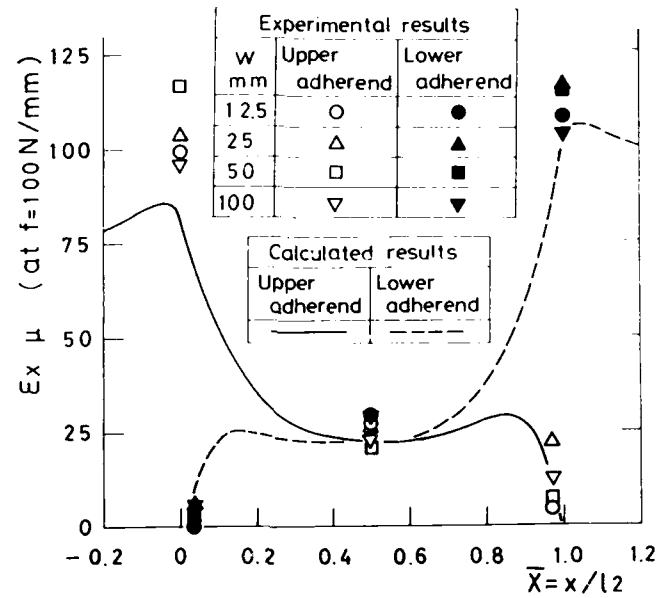
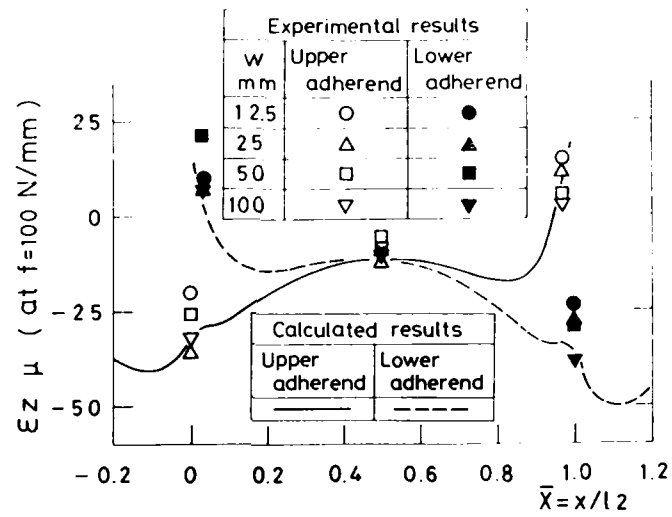
FIGURE 1(b) Boundary conditions of single lap joint.

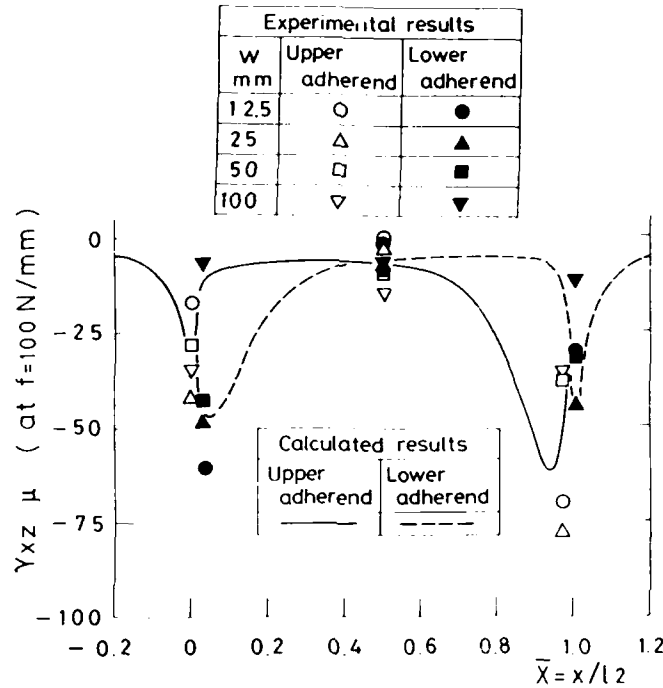
(2) *Strain distributions* The strain and stress distributions were computed by the elastic finite element method under the assumption of the plane strain condition. The finite element mesh divided the joint triangularly into 89 layers of elements in the x direction and into 12 layers of elements in the z direction and they formed 8 layers in the adherends and 4 layers in the adhesive layer.

The joint for strain analysis is 178 mm in length and 0.05 mm in

TABLE I
Material constants for the joint

	Adherend (carbon steel)	Adhesive (epoxy resin)
Young's modulus GPa	206	3.33
Poisson's ratio	0.33	0.34

FIGURE 2 Distributions of the strain ϵ_x in adherends of single lap joint.FIGURE 3 Distributions of the strain ϵ_z in adherends of single lap joint.

FIGURE 4 Distributions of the strain γ_{xz} in adherends of single lap joint.

adhesive thickness. The results in Figures 2 to 4 correspond to the case of $l_1 = 114$ mm, $l_2 = 50$ mm, $t_1 = 10$ mm, $t_2 = 0.05$ mm and $\bar{L}_0 = 0.281$. These figures show the strain distributions ϵ_x , ϵ_z and γ_{xz} of the adherends in the x direction at $z = t_1/8 + t_2/2$ ($z = 1.275$ mm) in the upper adherend and $z = -t_1/8 - t_2/2$ ($z = -1.275$ mm) in the lower adherend. The range of \bar{X} from zero to unity corresponds to the overlapping length of the joint. The strains ϵ_x , ϵ_z and γ_{xz} vary significantly in the vicinity of $\bar{X} = 0$ and 1.0 , i.e. on the edges of adhesive layer, while they are approximately constant in the region near to $\bar{X} = 0.5$. Figure 5 shows the strain distributions ϵ_z of adherends in z direction at $\bar{X} = 0.01$, $\bar{X} = 0.05$ and $\bar{X} = 0.99$. The range of \bar{Z} from zero to unity corresponds to the adherend thickness. The strains ϵ_z on $\bar{X} = 0.01$ and $\bar{X} = 0.99$ increase in the vicinity of $\bar{Z} = 0$, i.e. on both layers of the adhesive

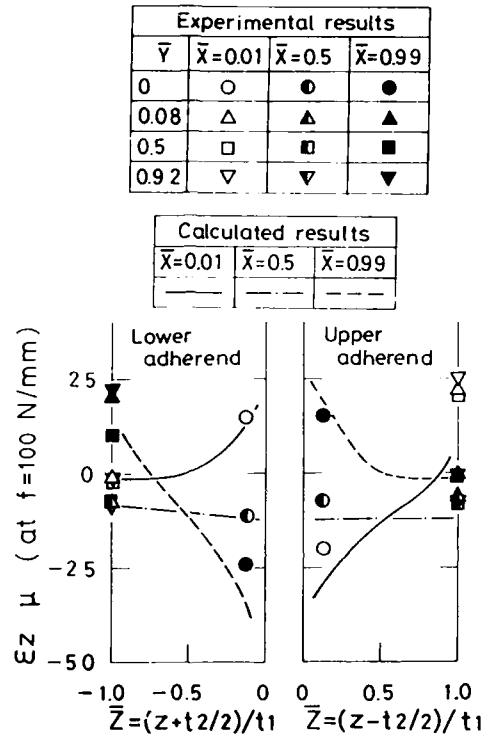


FIGURE 5 Distributions of the strain ϵ_z in adherends of single lap joint along the thickness.

interface; while the value at $\bar{X} = 0.5$ is approximately constant in the ranges of \bar{Z} from 0 to 1.0 and from 0 to -1.0.

The strain distributions of joints under tensile shear loading were measured by the use of the tensile loading equipment.² The experimental results for a load $f = 100 \text{ N/mm}$ are also shown in Figures 2 to 5. The experimental strain distributions coincide with the analytical ones.

2.2 Tapered lap joints under tensile shear load

(1) *Analytical model* The coordinates, dimensions and boundary conditions of the tapered lap joint are given in Figure 6. The length

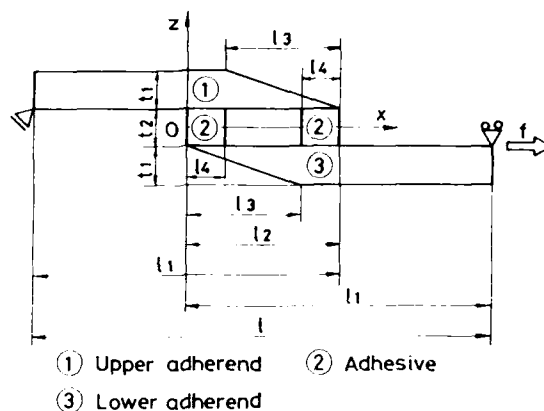


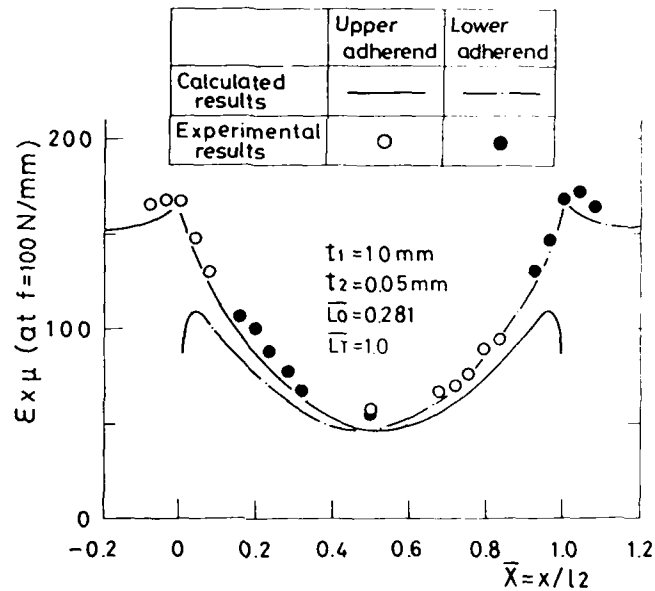
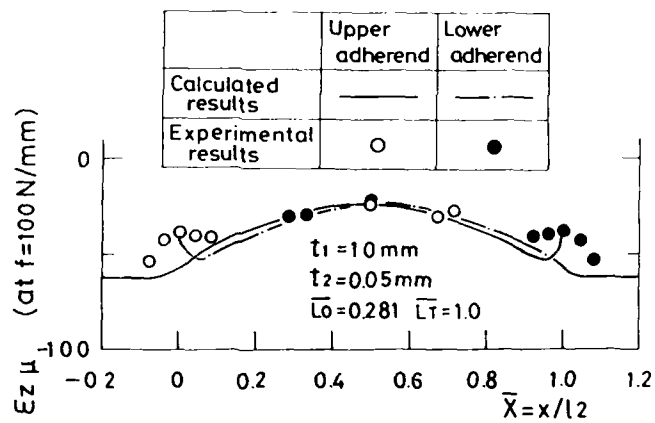
FIGURE 6 Coordinate system, dimensions and boundary conditions of tapered lap joint.

of the joint, adherend overlap, taper and adhesive layer are represented by notations l , l_1 , l_2 , l_3 and l_4 , respectively. The thickness of adherends and adhesive layer are shown by notations t_1 , and t_2 , respectively. The non-dimensional length of the overlap, the adhesive and the taper are given in Table II.

The assumed boundary conditions are that the lowermost nodal point on the left edge of upper adherend is fixed in the x and z directions and that the uppermost nodal point on the right edge of the lower adherend is free in the x direction and fixed in the z direction. The load per unit width, f , is applied to the uppermost nodal point on the right edge of the lower adherend. The analytical method and the material constants are the same as the previous section.

TABLE II
Non-dimensional length of tapered lap joint

Overlap length	\overline{L}_O	l_2/l
Adhesive band length to joint length	\overline{L}_A	$2 \times l_4/l$
Adhesive band length to overlap length	\overline{L}_B	$2 \times l_4/l_2$
Tapered length	\overline{L}_T	l_3/l_2

FIGURE 7 Distributions of strain ϵ_x in adherends of tapered lap joint.FIGURE 8 Distributions of strain ϵ_z in adherends of tapered lap joint.

(2) *Strain distributions* The analysed joint was 178 mm in length, $t_2 = 0.05$ mm in adhesive thickness, $t_1 = 10$ mm in thickness of adherends and $l_3 = 50$ mm in tapered length.

Figures 6 to 8 show the strain distributions ϵ_x , ϵ_z and γ_{xz} , respectively. The joint dimensions are $l_1 = 114$ mm, $l_2 = 50$ mm and $l_3 = 50$ mm and $\bar{L}_B = 1.0$. The strain ϵ_x changes remarkably in the vicinity of $\bar{X} = 0$ and 1.0 , i.e. near both edges of adhesive layer, and it varies parabolically in the range of \bar{X} from zero to unity. The strain ϵ_z becomes maximum near the center in the overlapped length. The strain γ_{xz} increases in the vicinity of $\bar{X} = 0$ and $\bar{X} = 1.0$.

Comparing the single lap joints with the tapered lap joints, the strain distributions in the single lap joint vary uniformly in a wide range of the overlap length, while the distributions in the tapered lap joint change parabolically in the overlap region. The maxima of the ϵ_x , ϵ_z and γ_{xz} in the tapered lap joint are reduced to about one-half of the values for the lap joint without tapering. This suggests that the tapering of the adherends improves the joint strength.

Tensile shear loading tests were carried out by a method similar to that in the previous section. The measured strain distributions for the load $f = 100$ N/mm are shown in Figs. 7 to 9. The experimental

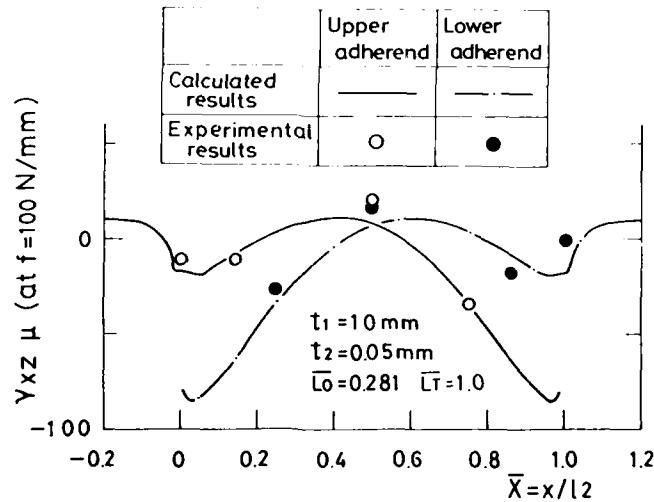


FIGURE 9 Distributions of strain γ_{xz} in adherends of tapered lap joint.

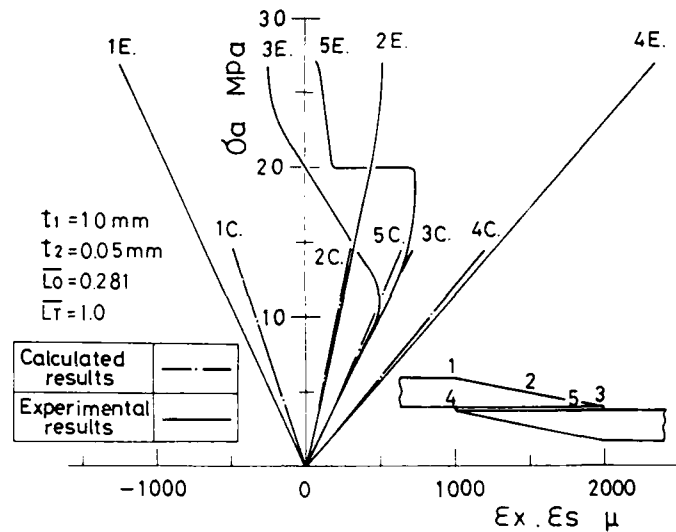


FIGURE 10 Variations of the strains ϵ_x and ϵ_s in the tapered lap joint.

results are in good agreement with the computed distributions. The variations of ϵ_x and ϵ_s (the strain on the adherend surface in the direction x) under the tensile load are illustrated in Fig. 10. The measured points are shown in the inserted figure. The ordinate indicates the average stress σ_a which is defined as the applied load divided by the whole cross section of adhesive. The strain ϵ_s at the position 3 decreases abruptly in the vicinity of $\sigma_a = 10$ MPa, and then it approaches nearly to zero due to cracking on the edge of the adherend. With the increase of the applied stress, the strain ϵ_x at the position 5 varies greatly according to the crack propagation.

3 STRENGTH EVALUATION BY USE OF AN ADHESIVE STRENGTH LAW

To evaluate the strength of structures or machine elements, the strength laws of their constituted materials are adopted to the stress distributions and the critical loads are estimated. A similar method may be applied to predict the strength of adhesive joints. The strength of a joint can be obtained by using the strength laws of the

adherend and adhesive resin. But the thus-obtained strength is higher than the actual strength. This is due to the lack of consideration of the strength of the adhering interface which is generally weaker than the adherend and adhesive resin. To include the strength of the interface in the estimation of joint strength, what kind of strength law is used for the interface becomes a subject of discussion. The authors proposed³ that the adhesive strength law determined by subjecting a butt joint of two thin-walled tubes to combined loads is useful as the reference value in the strength design of the adhesive joints, as the strength is obtained under combined uniform stress states. The adhesive strength law, as well as the strength laws of the adherend and adhesive resin, are used to evaluate the joint strength. Those three strength laws are adopted to the adhering interface, adherends and adhesive layer. The critical loads of each part of the joint are calculated. The joint strength is decided by using the minimum value among the calculated critical loads.⁴

4 STRENGTH OF LAP JOINTS

4.1 Strength laws

Von Mises criteria were applied to the adherends and adhesive layer. They were represented as follows.

For the adherend,

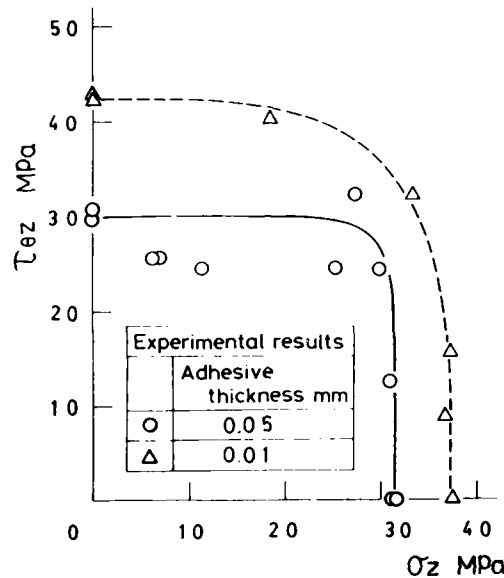
$$F_1 = (\sigma_x^2 - \sigma_x \sigma_z + \sigma_z^2 + 3\tau_{xz}^2)^{1/2} / \sigma_{01} = 1 \quad (1)$$

For the adhesive layer,

$$F_2 = (\sigma_x^2 - \sigma_x \sigma_z + \sigma_z^2 + 3\tau_{xz}^2)^{1/2} / \sigma_{02} = 1 \quad (2)$$

where σ_{01} and σ_{02} correspond to the yield stresses of adherend and adhesive resin, respectively. For the material in this research, $\sigma_{01} = 343$ MPa and $\sigma_{02} = 64$ MPa. Figure 11 are adhesive strength laws which were determined by using butt joints of thin-walled tubes subjected to combined axial load and torsion. The adhesive strength law is represented in the form of the expression,

$$F_3 = |\sigma_z / \sigma_{04}|^m + |\tau_{xz} / \tau_{01}|^m = 1 \quad (3)$$

FIGURE 11 Adhesive strength law in $\sigma_z - \tau_z$ stress state.

In Eq. (3), the stress component along the adhesive layer (σ_x) can be neglected because of the small effect on the adhesive strength.² From Figure 11 the constants σ_{04} , τ_{01} and m in Eq. (3) are obtained as follows; for the adhesive thickness 0.05 mm, $\sigma_{04} = 31.5$ MPa, $\tau_{01} = 30.8$ MPa, $m = 8.66$, and for adhesive thickness 0.01 mm, $\sigma_{04} = 37.2$ MPa, $\tau_{01} = 42.4$ MPa, $m = 3.54$.

4.2 Strength prediction and comparison with experimental results

The joint strength is calculated by applying strength laws of Eqs. (1), (2) and (3) to the stress distributions of corresponding parts in the joint. Figure 12 shows the strength distributions in the joint for which strain distributions are given in Figure 2 to 4. The notation f indicates the force per unit width for the initial failure of the part. The values f are small at both edges of adhesive layer and adhesive interfaces. This suggests that the initial failure occurs at those points in the joint.

The effect of the tapered length on the joint strength is shown in

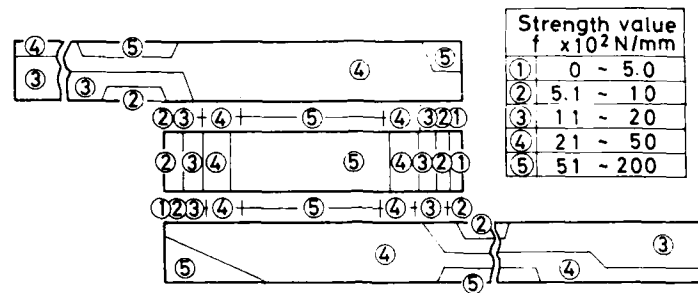


FIGURE 12 Strength distributions in the single lap joint.

Figure 13. The ordinate shows the average failure stress σ_b which is given by the failure load divided by the whole adhesive area of the joint. The abscissa shows the non-dimensional tapered length \bar{L}_O , which is given by the overlap length l_2 divided by the joint length l . In this figure, the average failure strength σ_b saturates above $\bar{L}_T 1.0$. The calculated results for the tapered lap joint ($\bar{L}_T = 1.0$) are about twice as large as those for the single lap joint ($\bar{L}_T = 0$). The predicted results for the single lap joint are illustrated in Figure 14. The strength of the tapered lap joint ($\bar{L}_T 1.0$) coincides approximately with that of the single lap joint ($\bar{L}_T = 0$) below $\bar{L}_O = 0.2$. But

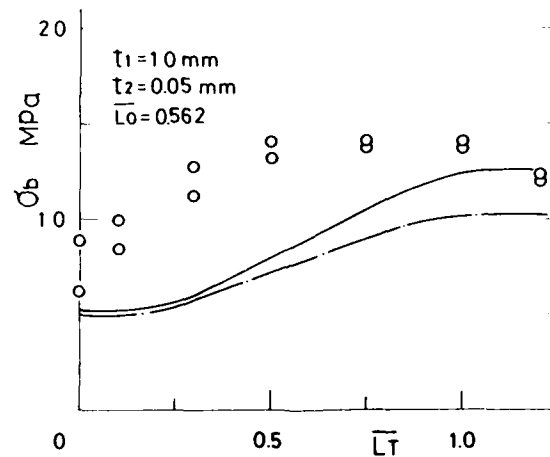


FIGURE 13 Effect of tapered length on the joint strength.

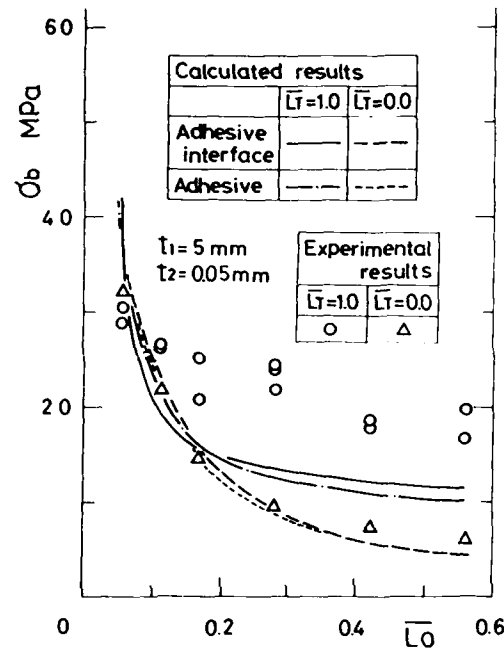


FIGURE 14 Effect of adhesive length on the joint strength.

the strength with tapering is about twice as large as the strength without tapering above $\bar{L}_0 = 0.2$. In the single lap joint, as shown by the two broken lines in Fig. 14, the strength of the adhesive interface is approximately consistent with that of the adhesive layer above $\bar{L}_0 = 0.2$. In the case of the tapered lap joint, the strength of the adhesive interface is greater than that of the adhesive. Therefore, the strength of the tapered lap joint above $\bar{L}_0 = 0.2$ is dominated by the strength of the adhesive layer.

The effects of the band adhesive length on the joint strength are shown in Figure 15. The overlap length and the tapered length of the tapered lap joints are constant. The left and right ordinates show the average failure stress σ_b and the load for unit width, f , respectively. The abscissa shows the non-dimensional adhesive band length \bar{L}_B . The joint strength f saturates above $\bar{L}_B = 0.5$. This means that the tapered lap joint, which is bonded for half of the whole overlap length ($\bar{L}_B = 0.5$) from both adhesive edges, has the

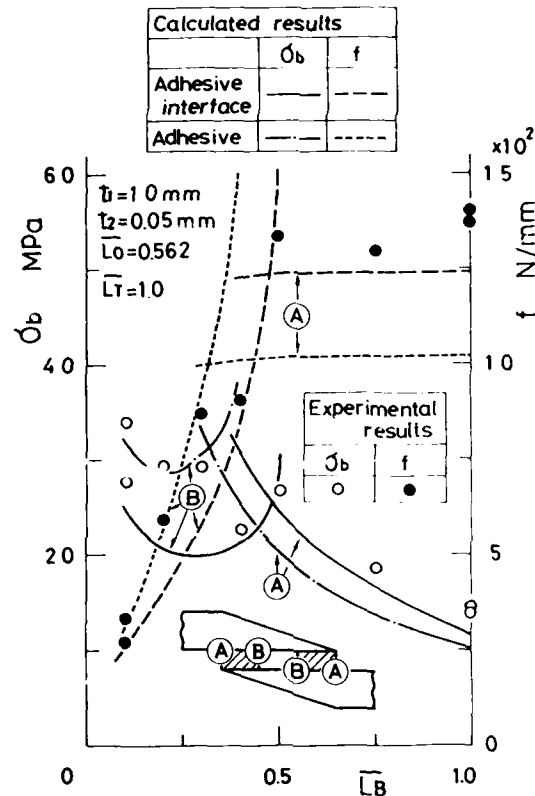


FIGURE 15 Effect of adhesive band length on the joint strength for tapered lap joint.

same strength as the tapered lap joint bonded with the whole overlap length $\bar{L}_B = 1.0$.

Figure 16 shows the effect of the band adhesive length on the strength of the single lap joints. The joint strength f saturates above $\bar{L}_B = 0.25$ with the adherend thickness $t_1 = 10 \text{ mm}$. This shows that a quarter of the bonding length of the whole overlap ($\bar{L}_B = 0.25$) is enough to obtain the strength of the single lap joint.

The experimental results of the joint strength are indicated in Figs. 13 to 16. The experimental values coincide approximately with the analytical results for the small values of L_0 , L_T and \bar{L}_B , but

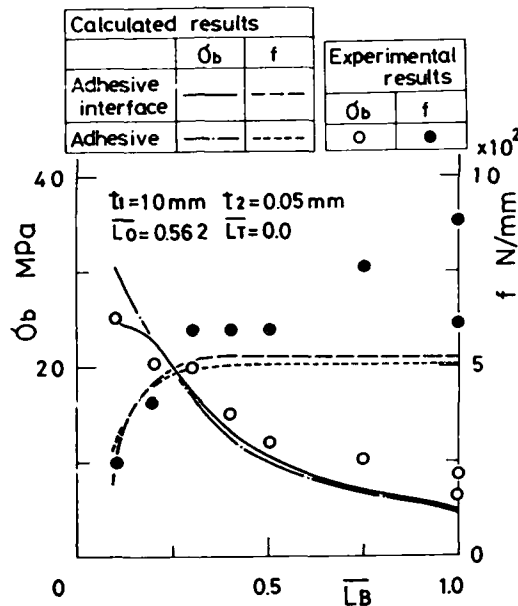


FIGURE 16 Effect of adhesive band length on the joint strength for single lap joint.

they are larger than the analytical results for the large values of \overline{L}_0 , \overline{L}_T and L_B . The experimental strength is obtained by the final fracture load, while the analytical strength corresponds to the initial fracture load. As shown in Figure 10, the joint does not fracture after the initial failure and the joint can bear the increasing load. This is one reason for the discrepancy between experimental strength and predicted strength. The process to the final fracture from the initial cracking should be investigated in future.

5 CONCLUSIONS

A method of estimating the strength of adhesive bonded joints was proposed. The adhesive strength law which was determined under combined stress states was used to decide the joint strength as well as the strength law of adherends and of the adhesive resin. Those

three strength laws were adopted to the stress distributions in the adhering interface, adherends and adhesive layer, and the critical loads in each part of the joint were calculated. The minimum load among them was taken as the joint strength. The proposed method was applied to predict the strength of lap joints.

The lap joints used in this research consisted of carbon-steel adherends bonded with epoxy resin. The deformed states under tensile shear loading were analysed by the elastic finite element method. The calculated strain distributions were compared with the experimental results. The joint geometry influenced the strain distributions remarkably. The adhesive strength law was experimentally determined by subjecting a butt joint of carbon-steel cylinders to combined axial load and torsion. The strength of lap joints with various configurations was predicted by the proposed method. The effects of overlap length, tapering length and adhering length on the strength were obtained. The predicted strength was compared with the experimental value. It was shown that the method of using the adhesive strength law was useful for the prediction of joint strength.

References

1. R. D. Adams and W. C. Wake, *Structural Adhesive Joints in Engineering* (Elsevier Applied Science Publishers, London, 1984).
2. T. Sugibayashi and K. Ikegami, *Trans. The Japan Society of Mech. Engrs. Ser. C*, 50-449, (1984).
3. K. Ikegami, M. Kajiyama, S. Kamiko and E. Shiratori, *J. Adhesion* **10**, 25 (1979).
4. K. Ikegami, *Preprint of the Adhesion Society of Japan*, No. 19, 1 (1981).

Effect of a Side Chain Length of Polymer on Both the Adhesion and Dispersibility of $\gamma\text{-Fe}_2\text{O}_3$ [†]

KATSUHIKO NAKAMAE, SATOSHI TANIGAWA,
NAOTO HIRAYAMA, KATSUYA YAMAGUCHI
and TSUNETAKA MATSUMOTO

*Department of Industrial Chemistry, Faculty of Engineering, Kobe University,
Rokko, Nada, Kobe, 657 Japan*

(Received August 26, 1986)

Acrylic ester-acrylic acid copolymers were synthesized as model binder of magnetic paints. The dispersibility of $\gamma\text{-Fe}_2\text{O}_3$ was investigated as a function of the content of —COOH groups and the aliphatic side chain length. The following results were obtained. The saturated absorbance of copolymers on $\gamma\text{-Fe}_2\text{O}_3$ increased with the increase in content of —COOH groups, and then the dispersibility of $\gamma\text{-Fe}_2\text{O}_3$ was improved. However, when the content of —COOH group was over the 2 mol%, the saturated adsorbance of polymers was constant and the dispersibility of $\gamma\text{-Fe}_2\text{O}_3$ decreased with increasing number of carbon atoms in the acrylic ester side groups. However, the dispersibility of $\gamma\text{-Fe}_2\text{O}_3$ was explained by the difference in conformation of adsorbed polymers.

KEY WORDS Dispersibility; acrylic ester-acrylic acid copolymer; adsorption; interfacial tension; $\gamma\text{-Fe}_2\text{O}_3$; magnetic paint.

1 INTRODUCTION

The interaction between a polymer and an inorganic powder is one of the most important factors which controls the properties of composite materials, e.g., magnetic recording tape, paints, inks.

[†] Presented at the Tenth Annual Meeting of The Adhesion Society, Inc., Williamsburg, Virginia, U.S.A., February 22–27, 1987.

etc. The need for high-density recording has grown along with the development of recording methods. Knowledge of magnetic materials such as co-containing $\gamma\text{-Fe}_2\text{O}_3$ ^{1,2} and alloy powder^{3,4} for high-density recording is far advanced. However, fundamental studies on the binder polymers which give high performance have clarified the interaction between $\gamma\text{-Fe}_2\text{O}_3$ particles and vinyl polymers by measuring the adsorption, the phase separation ability for particles in the concentrated solution, and the interfacial tension ($\gamma_{w/o}$) of polymer solution-water interface.⁵⁻⁸

The surface of $\gamma\text{-Fe}_2\text{O}_3$ was covered with a number of water molecules adsorbed both chemically and physically. Therefore, it was proved that the interface of $\gamma\text{-Fe}_2\text{O}_3$ surface-polymer solution can be substituted by the water-polymer solution interface.^{5,7,8}

From these results, it was clarified that the polymer giving a lower interfacial tension of water-polymer solution interface ($\gamma_{w/o}$) has a higher interaction with $\gamma\text{-Fe}_2\text{O}_3$ surface.

Interaction between poly(acrylic ester-acrylic acid) copolymer and magnetic particles and the dispersibility of particles in magnetic paints were investigated as a function of the number of carbon atoms in the acrylic ester groups by using the adsorption, an interfacial tension ($\gamma_{w/o}$), and the magnetic properties measured by a Vibrating Sample Magnetometer (VSM).

2 EXPERIMENTAL

2.1 Materials

The $\gamma\text{-Fe}_2\text{O}_3$ particles have an average length of $0.25\ \mu\text{m}$, an average acicular ratio of 1/7, and a nitrogen surface area of $53.2\ \text{m}^2/\text{g}$.

Acrylic ester-acrylic acid copolymers were synthesized as model binders. Samples were twice purified by the solution-precipitation method. Acrylic acid content was measured by titration, and molecular weight was measured by GPC. Table I shows characterization of the polymers.

2.2 The Measurements of adsorption

The adsorption of polymers on the $\gamma\text{-Fe}_2\text{O}_3$ surface was obtained by determining the change of concentration of the supernatant solutions. Glass tubes ($25\ \text{cm}^3$ capacity) containing $20\ \text{cm}^3$ polymer

TABLE I
Characterization of the polymers used

Polymers	Molecular weight ^a	Carboxyl group mol%
Poly methyl acrylate (PMA)	33000	0
P(MA-AA) ^b	34000	5.30
Poly ethyl acrylate (PEA)	100000	0
P(EA-AA)	31000	5.26
Poly buthyl acrylate (PBA)	30000	0
P(BA-AA)	62000	5.18
Poly 2-ethyl-hexyl acrylate (PEHA)	42000	0
P(EHA-AA)	118000	5.41
Poly lauryl acrylate (PLA)	200000	0
P(LA-AA)	170000	5.36
Poly stearyl acrylate (PSA)	29000	0
P(SA-AA)	98000	5.27

^a Peak molecular weight obtained by GPC.

^b AA: Acrylic acid.

solution and 2.0 g γ -Fe₂O₃ were subjected to 29 KHz ultrasonic waves for 30 min. After samples were shaken 24 hours and were allowed to stand for another 24 hours, the adsorbance were determined by the measurement of the concentration difference of the supernatant solutions.

2.3 The interfacial tension of the water-polymer solution interface

The interfacial tension $\gamma_{w/o}$ was measured by the du Nouy ring method. The adsorption of polymers at an interface between water and a polymer solution was achieved by placing 50 cm³ of water into each of several du Nouy dishes and cautiously adding a similar volume of the polymer solution of the desired concentration. All measurements were carried out at 25°C. Since the interfacial tension of the water-polymer solution interface is slightly time dependent, $\gamma_{w/o}$ was measured after 3 hours of standing.

2.4 Measurements of magnetic properties and dispersibility of γ -Fe₂O₃ particles

The magnetic paint was prepared by a ball-milling process for 100 hours. The glass vessel (450 cm³ capacity) contained 21.4 g polymer, 107.1 g solvent and stainless-steel balls.

The magnetic properties were measured by a Toei Kogyo Vibrating Sample Magnetometer (VSM) specially designed for this study.

An attempt was made to evaluate the quality of dispersion of the particles in the magnetic paint under a low magnetic field. The rotation of particles in the paint can be traced by measuring the initial magnetization (M_i) to the saturated magnetization (M_s) and the holding time for the applied field of +50 Oe.⁹ Figure 1 shows that the M_i/M_s of paint A increased with time; however, that of paint B remained constant and was equivalent to that of cobalt-containing $\gamma\text{-Fe}_2\text{O}_3$ powder itself. This means that particles in paint B were not well dispersed. In the case of paint A the M_i is given by

$$M_i = M_{im} + M_{io}$$

where M_{im} is the magnetization associated with removing the magnetic moment from the easy axis (=long axis of particles) and is

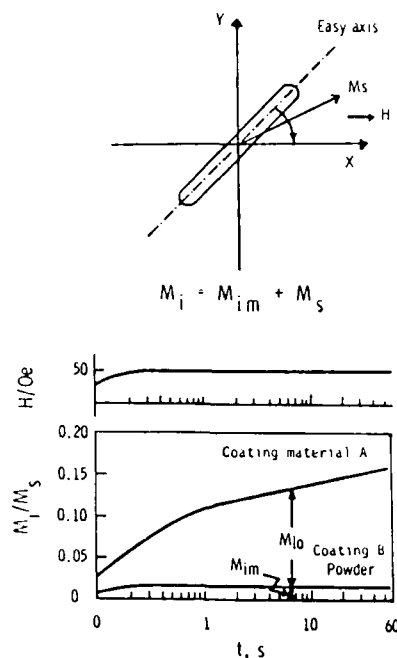


FIGURE 1 Relation between M_i/M_s and time of applied field of 50 Oe.

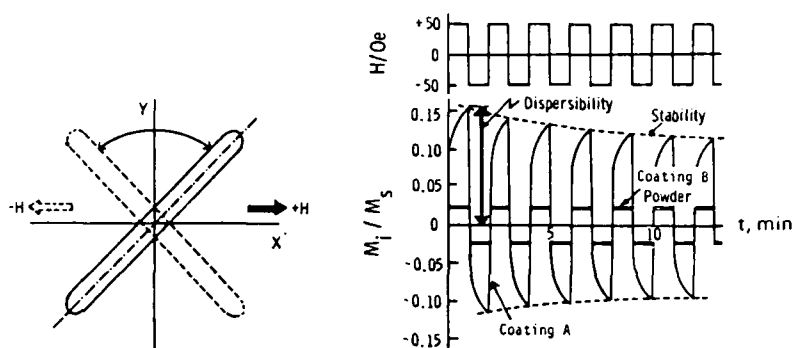


FIGURE 2 Vibration curve of M_i/M_s with a field of ± 50 Oe at 1 minute intervals.

the quickly responding component. M_{io} is the magnetization associated with the orientation of particles and the slowly responding component. The particles should orient in the viscous magnetic paint.

Figure 2 shows the vibration curve of M_i/M_s for A, B, and powder over a 1 minute interval. The curve of B did not involve the component M_{io} and coincide with that of the $\gamma\text{-Fe}_2\text{O}_3$ itself. The curve of A shows the large M_{io} component and the slower decay vibration (dotted line). The degree of decay was related to the stability of the paint. Since the amplitude of vibration of M_i/M_s for A increased with the dispersing time in the ball mill, the value at 1 minute can be used as a monitor of dispersion of magnetic particles in paint.

3 RESULTS AND DISCUSSION

3.1 Adsorption behavior of poly(acrylic ester-acrylic acid) copolymer on $\gamma\text{-Fe}_2\text{O}_3$

Figure 3 shows the adsorption of poly(acrylic ester-acrylic acid) copolymer which contains 5 mol% of acrylic acid. The adsorbance increases in the order of P(MA-AA), P(EA-AA) and P(BA-AA).

Figure 4 shows the effect of acrylic acid (AA) content of copolymer on the adsorbance. The adsorbance of copolymers saturated over 4 mol% of AA. Therefore, the following results were

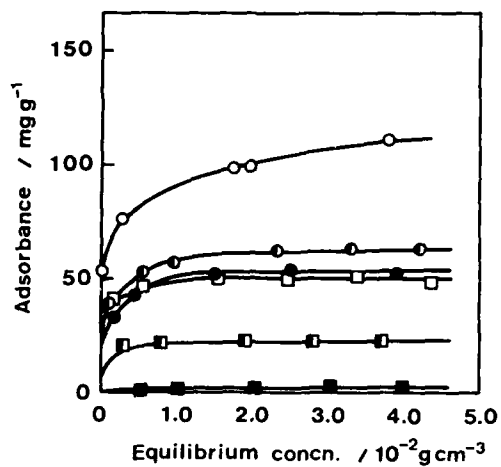


FIGURE 3 Adsorption isotherms of polymers on $\gamma\text{-Fe}_2\text{O}_3$ at 30°C: \circ , P(MA-AA); \bullet , P(EA-AA); \bullet , P(BA-AA); \square , PMA; \blacksquare , PEA; \blacksquare , PBA; AA content, 5 mol%.

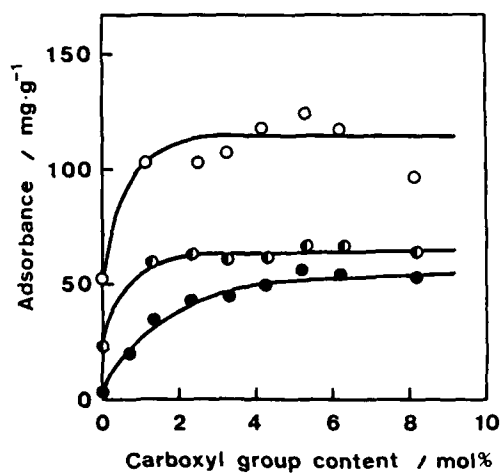


FIGURE 4 Effect of the carboxyl group content of alkylacrylate-acrylic acid copolymer on the saturated adsorbance of $\gamma\text{-Fe}_2\text{O}_3$: \circ , P(MA-AA); \bullet , P(EA-AA); \bullet , P(BA-AA).

obtained for the poly(acrylic ester-acrylic acid) copolymer containing 5 mol% acrylic acid.

Figure 5 shows the effect of the number of carbon atoms in the acrylic ester side group on the saturated adsorbance of polymer on the γ -Fe₂O₃ surface. The saturated adsorbance decreases significantly with increase in the number of carbon atoms in the acrylic ester side group, *i.e.* aliphatic side chain length. This means that the side chain bulkiness of the polymer affects the adsorbance of the polymers, and should affect the dispersibility of γ -Fe₂O₃ particles because of the difference in the conformation and solution properties at the γ -Fe₂O₃ surface-solution interface.

3.2 The dispersibility of γ -Fe₂O₃ particles in magnetic paint

Figure 6 shows the M_i/M_s curves for various paints. As mentioned in the experimental part, the dispersibility of γ -Fe₂O₃ particles ($D = M_i/M_s$) increases in the order P(MA-AA), P(EA-AA) and P(BA-AA), *i.e.* the same order of side chain length.

Figure 7 shows the effect of the carboxylic acid content of poly(acrylic ester-acrylic acid) copolymer on the dispersibility. Each

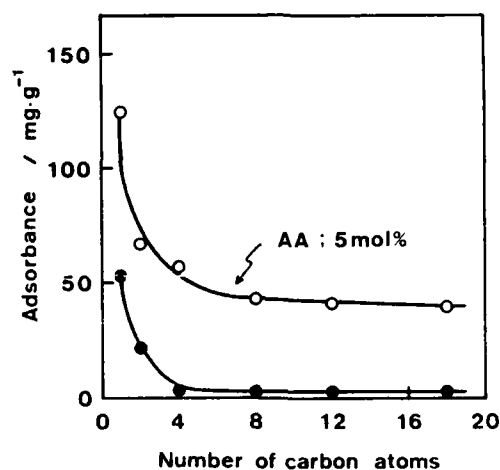


FIGURE 5 Effect of the number of carbon atoms of a side chain on the saturated adsorbance of polymers: ○, copolymer; ●, homopolymer.

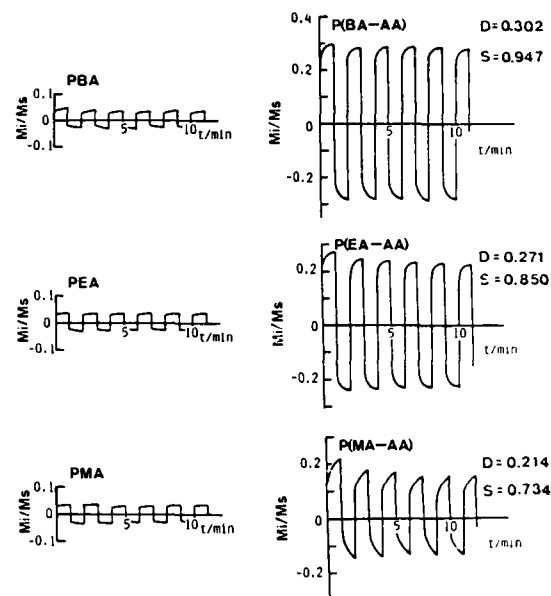
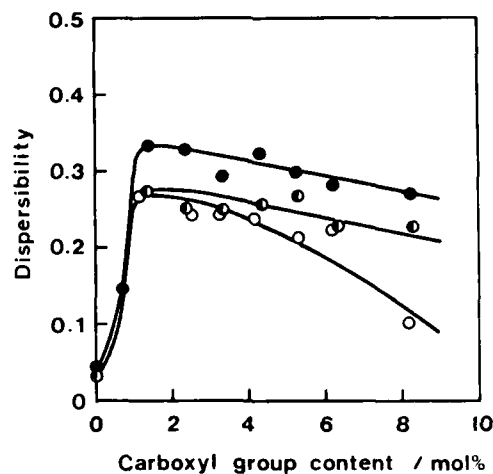
FIGURE 6 The M_i/M_s curves for various paints.

FIGURE 7 Effect of the carboxyl group content of alkylacrylate-acrylic acid copolymer on the dispersibility of a paint: ○, P(MA-AA); ◐, P(EA-AA); ●, P(BA-AA).

polymer has a maximum of dispersibility of $\gamma\text{-Fe}_2\text{O}_3$ in these polymer systems.

Figure 8 shows the effect of the aliphatic side chain length of acrylic ester side group on the dispersibility of $\gamma\text{-Fe}_2\text{O}_3$ as a function of carbon atoms in the acrylic ester side group. From these results, the homopolymer of acrylic ester with a different side chain length does not have high dispersibility. However, the dispersibility of $\gamma\text{-Fe}_2\text{O}_3$ using the poly(acrylic ester) with 5 mol% AA increases with increasing the number of carbon atoms *i.e.* the aliphatic side chain length.

In the previous paper, we have investigated the dispersibility of $\gamma\text{-Fe}_2\text{O}_3$ by means of interfacial tension ($\gamma_{w/o}$), and a surface pressure-area method of the Langmuir type. We proposed that the polymer having a stronger interaction with an $\gamma\text{-Fe}_2\text{O}_3$ surface gives a large adsorbance and a lower interfacial tension ($\gamma_{w/o}$). On the basis of these results, the relationship between the adsorbance and the dispersibility of $\gamma\text{-Fe}_2\text{O}_3$ in this study is a little different from previous results. That is, the polymer having a long aliphatic side chain in acrylic ester with 5 mol% AA has a high dispersibility of $\gamma\text{-Fe}_2\text{O}_3$ in spite of a lower adsorbance.

Figure 9 shows the effect of content of AA in poly(acrylic

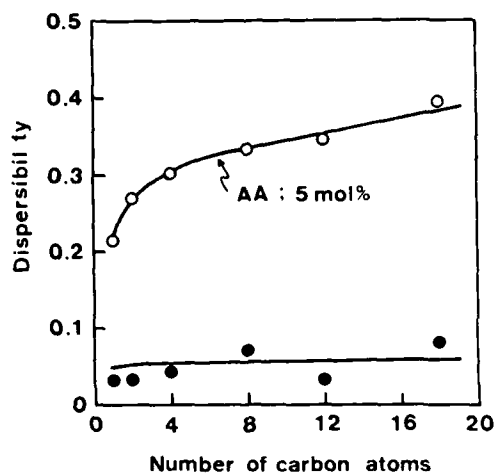


FIGURE 8 Effect of the number of carbon atoms of a side chain on the dispersibility of a paint: \circ , copolymer; \bullet , homopolymer.

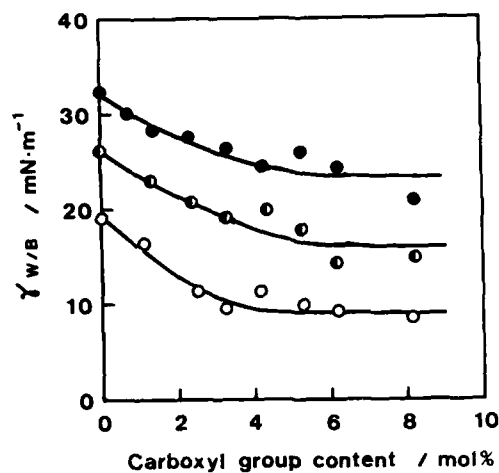


FIGURE 9 Effect of the carboxyl group content of alkylacrylate-acrylic acid copolymer on the interfacial tension at the water/benzene interface: ○, P(MA-AA); ◐, P(EA-AA); ●, P(BA-AA).

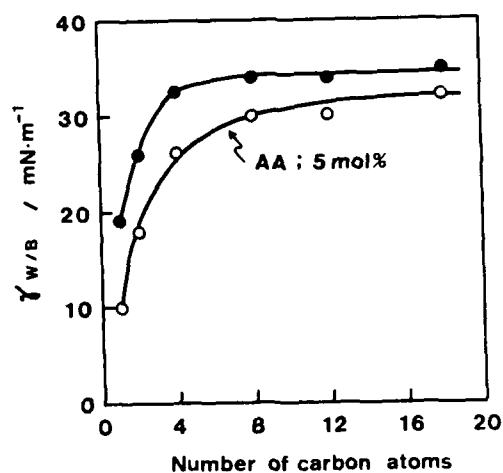


FIGURE 10 Effect of the number of carbon atoms of a side chain on the interfacial tension of polymers at the water-benzene interface: ○, copolymer; ●, homopolymer.

ester-acrylic acid) copolymer on the interfacial tension at the water-polymer solution interface. $\gamma_{w/o}$ decreases with increasing AA content. This agreed with the behavior of partially-sulfonated polystyrene.¹⁰

The $\gamma_{w/o}$ of a longer side chain, *e.g.* P(BA-AA), is lower than that of a shorter side chain (P(MA-AA)). This means that the interaction of P(BA-AA) at the water-benzene interface is weaker than that of P(MA-AA), and the adsorbance of P(BA-AA) on the γ -Fe₂O₃ surface is smaller than that of P(MA-AA). This behavior agreed the results shown in Figure 3.

Figure 10 shows the effect of the number of carbon atoms in the acrylic ester side group on the interfacial tension. The interfacial tension ($\gamma_{w/o}$) increases with increasing number of carbon atoms in the acrylic ester. This means that the content of polymer segments at the water-benzene interface with increasing side chain length in acrylic ester group decreased owing to its high bulkiness. The dispersibility of γ -Fe₂O₃ by adsorbed polymer increased with increasing side chain length of the ester group as shown in Figures 7 and 8. On the basis of the previous paper, the properties and structure of the γ -Fe₂O₃-polymer solution interface were the most important factor for the dispersibility of γ -Fe₂O₃.

Figure 11 shows the schematic representation of the conformation of poly(acrylic ester-acrylic acid) adsorbed at the γ -Fe₂O₃-polymer solution interface. From the previous results,^{7,8} we concluded that the loop-anchor type adsorption of polymer at the γ -Fe₂O₃ surface is the most important factor, because a certain length of the loop segment solvates the solvent strongly and then the solvation layer at the γ -Fe₂O₃ surface acts as a protecting layer for the aggregation of γ -Fe₂O₃ particles owing to its entropy effect. On the basis of this concept, in the case of the shorter side chain length the polymer strongly adsorbed due to the acrylic acid group and the carbonyl group in the ester group because the C=O group has an interaction to the γ -Fe₂O₃ surface. On the other hand, in the case of the long side chain length, *e.g.* acrylic stearate, the adsorption of polymer is prevented by the long aliphatic side chain, which is solvated with hydrophobic solvent. Therefore, in the case of the long side chain, the adsorbed long aliphatic side chain acts as an excellent protecting layer owing to the solvation layers, despite its small adsorbance.

Consequently, it is reasonable to conclude that the adsorption of

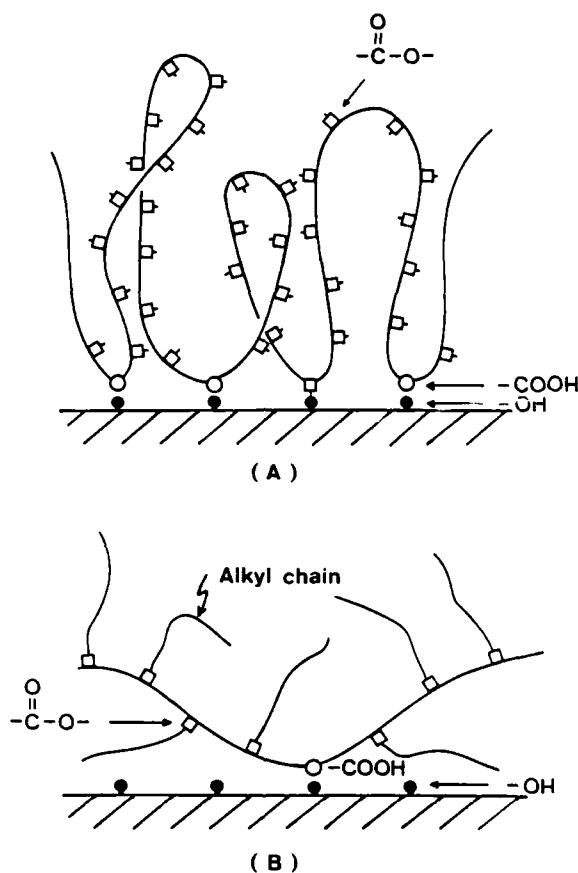


FIGURE 11 Schematic representation of alkylacrylate-acrylic acid copolymer adsorbed at the solvent/ $\gamma\text{-Fe}_2\text{O}_3$ interface.

polymer which has a long aliphatic side chain solvated with a hydrophobic solvent provides a protection layer for aggregation of $\gamma\text{-Fe}_2\text{O}_3$ and the binder.

References

1. K. Sumiya, S. Watatani, F. Hayama, H. Naono and T. Matsumoto, *Nippon Kagaku kaishi*, 1033 (1979).
2. M. Kishimoto, *IEEE Trans. Magn.* **MAG-15**, 906 (1979).
3. A. L. Oppegard, F. J. Darnell and H. C. Milliee, *J. Appl. Phys.* **32**, 184s (1961).

4. T. Uehori, A. Hosaka, I. Izumi and Y. Imaoka, *IEEE Trans. Magn.* **MAG-14**, 852 (1978).
5. T. Matsumoto and K. Nakamae, *Adhesion and Adsorption of Polymers Part B*, L. H. Lee, Ed. (Plenum Press, New York, 1980), p. 707.
6. K. Sumiya, *et al.*, *Kobunshi Ronbunshu* **37**, 49 (1980).
7. K. Nakamae, K. Sumiya and T. Matsumoto, *Prog. Org. Coat.* **12**, 143 (1984).
8. K. Nakamae, K. Sumiya, T. Taii and T. Matsumoto, *J. Polym. Sci., Polym. Sympos.* **71**, 109 (1984).
9. K. Sumiya, *et al.*, in *Ferrites*, H. Watanabe, Ed. (Proc. 3rd Int. Conf., Kyoto, Japan, 1980), p. 566.
10. K. Sumiya, *et al.*, *Kobunshi Ronbunshu* **41**, 273 (1984).

Viscoelastic Analysis of Shear Adhesion Test for Pressure-Sensitive Adhesive Tape†

ZENICHI MIYAGI and KENTARO YAMAMOTO

Laboratory of Applied Metrology, Dept. of Precision Engineering, Meiji University, 1-1-1 Higashi-mita, Tama-ku, Kawasaki-shi, 214, Japan.

(Received August 26, 1986)

A new shear adhesion tester of a pressure-sensitive adhesive tape is developed, by which the slippage of the tape under shearing force can be measured as accurately as $1\text{ }\mu\text{m}$ or $0.1\text{ }\mu\text{m}$ per digit by the aid of a linear variable differential transformer. When shearing force is exerted on a tape applied on an adherend, two kinds of slippages are expected, that is, the one between the surface of the adhesive and the adherend and the other of the shearing strain of the adhesive. In order to separate the two kinds of slippages, slippage under shearing force and the recovery displacement after removing the force are measured. Analysing the results of measurements it becomes clear that viscoelastic models of Voigt units connected in series are suitable for both of the slippages.

KEY WORDS Boundary and cohesive slippage; pressure-sensitive adhesive tape; shear adhesion test; test apparatus; Voigt model.

1 INTRODUCTION

In order to analyse viscoelastically shear adhesion tests of a pressure-sensitive adhesive tape (PSA tape), a new testing apparatus has been developed. The shear slippage can then be measured as accurately as 1.0 or $0.1\text{ }\mu\text{m}$ per digit. A viscoelastic model of slippage is consequently proposed.

† Presented at the Tenth Annual Meeting of The Adhesion Society, Inc., Williamsburg, Virginia, U.S.A., February 22–27, 1987.

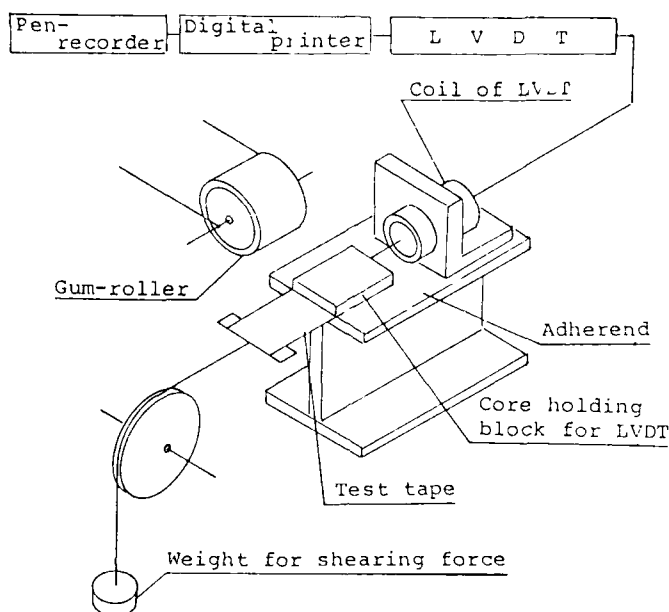


FIGURE 1 Schematic diagram of a device developed for shear adhesion.

2 TESTING APPARATUS

A schematic diagram of the apparatus is shown in Figure 1. The specimen is applied on an adherend made of stainless steel plate in the way prescribed by JIS (Japanese Industrial Standard). Shearing force is applied by a dead weight. A block with a core of a LVDT (Linear Variable Differential Transformer) is put on the specimen. The core is inserted into a detector of the LVDT, so that the slippage of the specimen is detected and recorded by a digital printer or a pen recorder.

3 VISCOELASTIC MODEL OF THE SHEAR ADHESION TEST

When shearing force is applied to the tape, there arise two kinds of displacement of the tape, that is, the cohesive slippage inside the adhesive and the boundary slippage between the adhesive and the

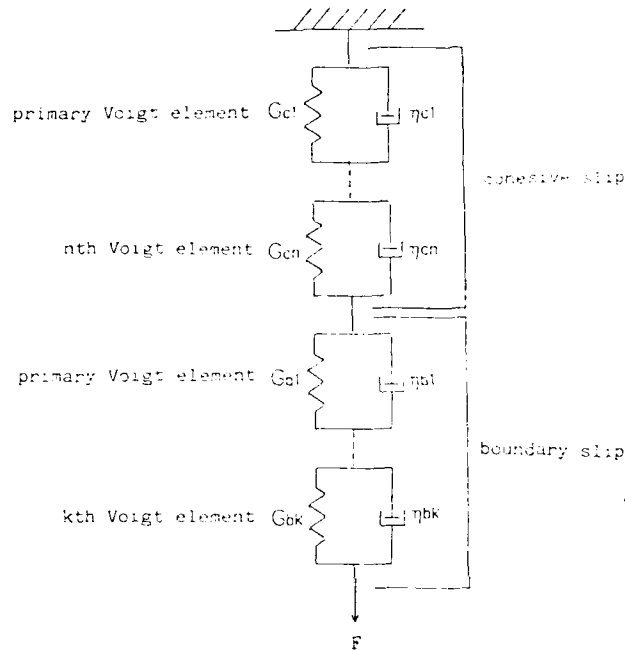


FIGURE 2 Generalized visco-elastic model of shear adhesion.

adherend. Therefore, a viscoelastic model is expressed by a series of Voigt units in both kinds of slippage, as shown in Figure 2, where the model of boundary slippage has unrecoverable elements of springs and dampers, because the boundary slippage does not recover practically. As is shown in Figure 2 the model of cohesive slippage has n Voigt units, the elements of which are denoted by G_{ci} and η_{ci} of the springs and dampers respectively, and that of the boundary slippage has k Voigt units in which the elements of the units are denoted by G_{bi} and η_{bi} in a way similar to the cohesive slippage.

4 THEORETICAL ANALYSIS OF THE MODEL

When the shearing force F (gf) is applied to the specimen, both cohesive and boundary slippage ϵ_c and ϵ_b (mm) take place and the

two kinds of slippages are given by the following equations:

$$\epsilon_c = F \sum_i^n (1/G_{ci}) \{1 - \exp(-t/\tau_{ci})\} \quad (1)$$

$$\epsilon_b = F \sum_j^k (1/G_{bj}) \{1 - \exp(-t/\tau_{bj})\} \quad (2)$$

where $\tau_{ci} : (\eta_{ci}/G_{ci})$ and $\tau_{bj} : (\eta_{bj}/G_{bj})$ are the relaxation time of i th and j th unit of the Voigt model shown in Figure 2. The total slippage is thus given by the following equation;

$$\epsilon = \epsilon_c + \epsilon_b \quad (3)$$

If the shearing load is removed after a lapse of time t_1 from its application, the boundary slippage stops, for no shearing force for the boundary slippage exists but, on the other hand, the cohesive slippage begins to recover owing to the elongation of springs in the Voigt units. The recovering displacement ϵ_r is given by the following equation;

$$\epsilon_r = \sum_i^n A_i \exp\{(t - t_1)/\tau_{ci}\} + F \sum_j^k (1/G_{bj}) \{1 - \exp(-t_1/\tau_{bj})\} \quad (4)$$

where A_i is the initial condition of recovering displacement at time t_1 of the Voigt unit, and the second term means the boundary slippage during the application of the shearing load. The boundary slippage can be obtained through the recovering displacement at sufficiently long time after removal of the load.

When the slippage of the tape under the shearing load and the recovering displacement free from the shearing load are measured, the viscoelastic constants of the Voigt elements shown in Figure 2 can be determined by the aid of the least squares method.

5 MEASUREMENT OF THE SLIPPAGE

The experimental results for a polyester tape coated with polyacrylate adhesive are shown in Figure 3 for 30 min in loading time and 30 min in recovering time. The measuring conditions are as follows: 25 × 25 mm in adhesion area, 100 gf in shearing load, 0, 20, 40 and

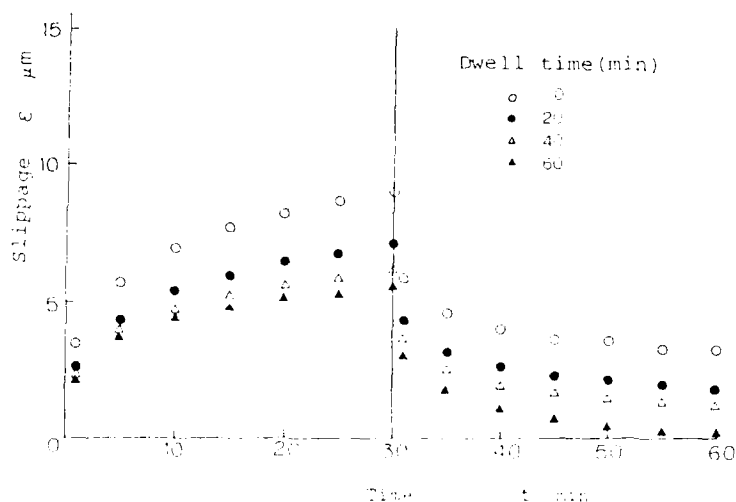


FIGURE 3 Slippage under shear adhesion test and viscoelastic recovery after unloading.

60 min in dwell time and $23 \pm 0.5^\circ\text{C}$ and $65 \pm 5\%$ RH as the atmospheric condition.

6 RESULTS OF EXPERIMENTS

From the recovering displacement the model of cohesive slippage can be determined. The number of Voigt units is determined by increasing the number from 1 to 3 and the variance of residuals is successively tested by the *F*-test. The number of 2 is confirmed to be sufficient. The constants of the units are proved to be independent of dwell time by the aid of the analysis of variance. Relaxation time of the units is shown in Table I.

As the slippage under shearing force includes cohesive slippage, the effect of cohesive slippage is eliminated by substituting the constants of the cohesive units and the pure boundary slippage is obtained as shown in Figure 4. In a similar way to the case of the cohesive recovery, the number of the Voigt units of 2 and its constants are determined, which are shown in Table II.

TABLE I
Constants of Voigt units of cohesive slippage

Coefficient	
G_{c1} 10^6 Pa·m	0.413
G_{c2}	0.326
η_{c1} 10^6 Pa·s·m	4.878
η_{c2}	133.8
τ_{c1} s	11.32
τ_{c2}	410.4

In Figure 4 the pure boundary slippage, experimentally determined, is shown and it is observed that the boundary slippage decreases as the dwell time increases. At a dwell time of 60 min no boundary slippage is recognized and the velocity of slippage is higher at the beginning of slippage, becoming slower until it is constant. The initial transient phenomena disappear when the dwell

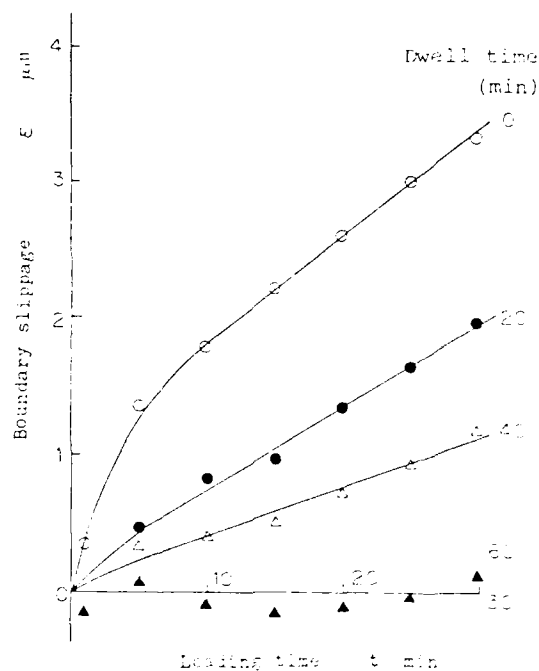


FIGURE 4 Relationship between loading time and boundary slippage.

TABLE II
Constants of Voigt units of boundary slippage

Coefficient	Dwell time T min		
	0	20	40
G_{b1} 10^6 Pa·m	0.938	7.175	16.76
G_{b2}	0.102	0.056	0.046
η_{b1} 10^6 Pa·s·m	189.8	234.8	643.5
η_{b2}	672.8	919.1	1630
τ_{b1} s	202.3	32.72	38.40
τ_{b2}	6596	16413	35200

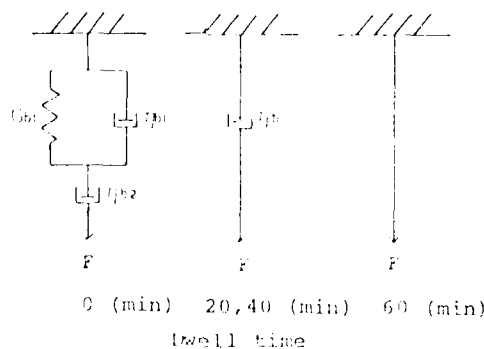


FIGURE 5 Simplified models of boundary slippage.

time is longer. Determining the constants of the Voigt elements by the aid of the least squares method, the model of a boundary slippage can be simplified as is shown in Figure 5 with respect to dwell time.

7. CONCLUSIONS

A new shear adhesion tester of high accuracy and precision was developed. A polyester tape coated with a polyacrylate adhesive was tested using this tester. Viscoelastic models of boundary slippage and the cohesive slippage of the adhesive were analysed by introducing a combination of Voigt units in series. The results are

briefly summarized as follows:

- 1) Two kinds of slippages in the shear adhesion test are separated by measuring the slippage under shearing force and the recovering displacement after removing the force.
- 2) Viscoelastic characteristics of the adhesive can be determined by introducing a model of two Voigt units in series and the constants of the units are determined. They are not influenced by dwell time.
- 3) Two Voigt units connected in series are also successfully applied in the analysis of boundary slippage. The models of the slippage are greatly influenced by the dwell time.

Rheological Study on Tack of Pressure-Sensitive Adhesives†

HIROSHI MIZUMACHI and YASUNORI HATANO

Laboratory of Chemistry of Polymeric Materials, Department of Forest Products, Faculty of Agriculture, The University of Tokyo, Bunkyo-ku, Tokyo 113, Japan

(Received August 26, 1986)

It is pointed out that the tack of pressure-sensitive adhesives should be expressed in terms of rolling friction coefficient f of the adhesives. Values of f were determined by both rolling ball and pulling cylinder experiments, and the dependence of f upon viscoelastic properties and thickness of the adhesives was studied. The experimental results were interpreted by the model theory previously proposed. It is also shown that the tack of pressure-sensitive adhesives by the conventional ball tack tests corresponds to f measured at the velocity ranging from $v \sim 10$ to $v \sim 10^2$ cm/sec.

KEY WORDS Pressure-sensitive adhesives; rolling ball; pulling cylinder; rolling friction coefficient; viscoelastic properties; tack.

INTRODUCTION

The tack of pressure sensitive adhesives is often measured by rolling ball methods.¹ It is reasonable to express the tack in terms of rolling friction coefficient f , because it depends upon the physical properties of the material, and not upon such experimental conditions as the leading distance or the angle of inclination of a surface. It has been shown that f of a pressure-sensitive adhesive can be evaluated by analysing the rolling motion of a ball on it.² If we assume that f is

† Presented at the Tenth Annual Meeting of The Adhesion Society, Inc., Williamsburg, Virginia, U.S.A., February 22-27, 1987.

a linear function of velocity v , namely $f = \varphi_0 + \varphi_1 v$, with φ_0 and φ_1 being constants, both the rolling process and rollout distance of a ball on a pressure-sensitive adhesive can satisfactorily be analysed according to a unified theory.³ However, it has also been pointed out that f of a pressure sensitive adhesive can more easily be determined by a pulling cylinder method, without any assumption about the dependence of f on v .^{4,5}

H. Mizumachi⁶ proposed a model theory where f is expressed in terms of viscoelastic parameters of the material, by which the dependence of f on v can be calculated in a wide range. In this study, the influence of the viscoelastic properties of several pressure-sensitive adhesives upon f are experimentally examined and the rheological discussions are made on the results.

EXPERIMENTAL

Samples used in this study are shown in Table I which also gives the temperature of the viscoelastic adsorption peak $T(E''_{\max})$ at 110 Hz and thickness of the adhesives.

TABLE I
Pressure sensitive adhesives

Sample	$T(E''_{\max})$ at 110 Hz (°C)	Thickness (cm)
A1†	-50	4.0×10^{-3}
A2†	-45	4.0×10^{-3}
A3†	-30	4.0×10^{-3}
A4†	0	4.0×10^{-3}
B1‡	-35	2.6×10^{-2}
B2‡	-38	1.8×10^{-3}

† The pressure-sensitive adhesive is mounted directly on a glass plate.

‡ A double-faced pressure-sensitive adhesive tape is adhered on a glass plate, upon which a sample tape is placed with the adhesive surface facing up.

(A) Measurement of f by the rolling ball method

The Nichiban tester¹ was employed to measure the rollout distance $(x - x_0)_{st}$ as a function of initial height H of a ball. Measurements

were repeated ten times (10 runs) for one condition, and a new specimen was set in the tester at each run. Values of φ_0 and φ_1 were determined by the least squares method, using the following equation;³

$$(x - x_0)_{st} = \frac{7R}{5g\varphi_1} \left\{ \left(\frac{10}{7} gH \right)^{1/2} - \frac{\varphi_1}{\varphi_1} \log \left(1 + \frac{\varphi_1}{\varphi_0} \left(\frac{10}{7} gH \right)^{1/2} \right) \right\}$$

and then f is given by

$$f = \varphi_0 + \varphi_1 v$$

(B) Measurement of f by the pulling cylinder method

A cylinder was pulled at a constant velocity on a horizontal surface of pressure-sensitive adhesives, and the resistance P was measured. Actually, the plate carrying the specimen is driven at various speeds, while the cylinder is placed on the specimen and connected to a load cell. Velocity can be varied from 0.001 to 100 cm/sec. A new specimen was set in the tester at each run. Values of f can be calculated by the following equation⁶ without any elaborate analysis;

$$f = \frac{PR}{Mg}$$

RESULTS AND DISCUSSIONS

(A) Dependence of f upon viscoelastic properties of a pressure-sensitive adhesive

Figure 1 shows some of the typical examples of a plot of rollout distance $(x - x_0)_{st}$ at 20°C vs. initial height H of a ball for a few pressure-sensitive adhesives with different $T(E''_{max})$. $T(E''_{max})$ at 110 Hz is higher than T_g by about twenty degrees. The average relaxation time τ at room temperature increases with the increase of $T(E''_{max})$. The shape of the curve in Figure 1 changes systematically with the change of the average relaxation time of the pressure-sensitive adhesives. Values of φ_0 and φ_1 , obtained by the least squares method, for each adhesive are given in Table II.

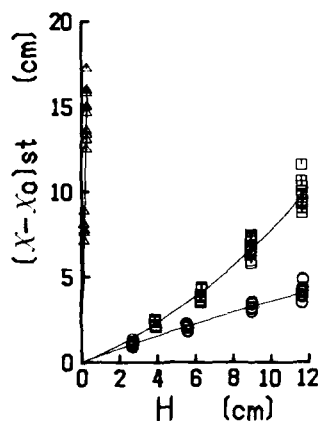


FIGURE 1 Typical examples of a plot of rollout distance $(a - x_0)_{st}$ at 20°C vs. initial height H of a ball for some pressure-sensitive adhesives.

○: A2, $R = 0.64$ cm, $\varphi_0 = 1.32$, $\varphi_1 = 0.006$

□: A3, $R = 0.96$ cm, $\varphi_0 = 2.258$, $\varphi_1 = -0.012$

△: A4, $R = 0.159$ cm, $\varphi_0 = 0.00465$, $\varphi_1 = -0.000115$

Theoretical curves are illustrated by the solid lines.

It is interesting that f at room temperature changes from a decreasing function of v (i.e., $\varphi_1 < 0$) to an increasing function (i.e., $\varphi_1 > 0$) as $T(E''_{max})$ decreases.

Then, f of the same pressure-sensitive adhesives were also measured by the pulling cylinder method at various velocities, and the results are illustrated in Figure 2. It is evident that f of a viscoelastic material has a peak at some velocity and that the peak

TABLE II
Values of φ_0 and φ_1 obtained by the least squares method

Sample	R (cm)	φ_0 (cm)	φ_1 (sec)	DEV† (cm ²)
A2	0.96	0.696	0.00066	6.96×10^1
	0.80	0.859	0.00116	3.52×10^1
	0.64	1.32	0.0060	3.14×10^0
A3	0.96	2.26	-0.0120	1.15×10^1
	0.80	2.76	-0.0141	7.31×10^0
	0.64	3.60	-0.0166	1.71×10^0
A4	0.159	0.00465	-0.000115	2.69×10^1

† DEV = $\sum (y - y_i)^2$

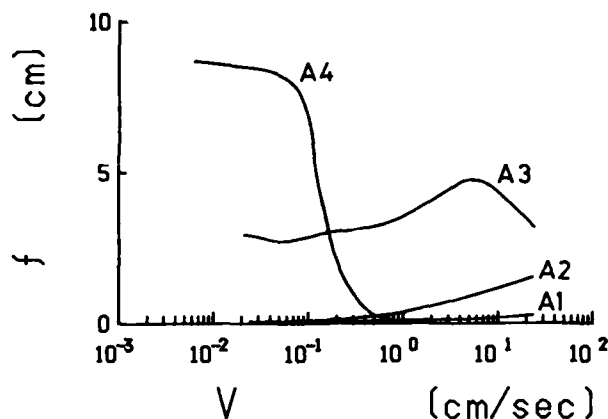


FIGURE 2 Values of f obtained from the pulling cylinder experiments at 20°C plotted against $\log v$ for A1, A2, A3 and A4. $R = 0.5$ cm, $b = 2.5$ cm, $M = 50$ g.

shifts toward the higher velocity region as the average relaxation time τ or T_g decreases, as schematically shown in Figure 7. This is in agreement with the trends of the theoretical curves of f vs. $\log v$, calculated according to the model theory.⁶ In the previous report,³ the rolling motion of a ball on some pressure-sensitive adhesives was traced by means of stroboscopic photography, and data on time/position of a ball were analysed according to equations of motion. In every case, all the experimentally observed data fell in the velocity range between approximately 10 and 10² cm/sec. Values of ϕ_0 and ϕ_1 could be determined from the data, and rollout distance calculated using those values agreed very well with the experimentally measured one. This means that the tack of pressure-sensitive adhesives which is measured by the conventional rolling ball tack tests must be related to f of a relatively narrow range of velocity, namely from $\log v \sim 1$ to $\log v \sim 2$. At room temperature, f of A1 and A2 is an increasing function of v in the above-mentioned velocity range and, on the other hand, f of A3 and A4 is a decreasing function of v in the same range.

It has been made clear that f in the velocity range 10 – 10² cm/sec corresponds well to the rolling motion of a ball in the conventional ball tack tests, and that f of pressure-sensitive adhesives can easily

be measured by the pulling cylinder method in a wide range of velocity.

(B) Dependence of f upon temperature and thickness of a pressure-sensitive adhesive

Figure 3 and Figure 4 show some examples of $(x - x_0)_{st}$ vs. H plots for the two pressure-sensitive adhesives, B1 and B2, at different temperatures. In the case of B1, the curve is almost straight or somewhat convex at 4°C, but it becomes concave at 20°C, while in case of B2, the curve is concave at both temperatures. This means that φ_1 changes from negative to positive as the temperature is raised from 4°C to 20°C in case of B1, but φ_1 is always negative in the same temperature range in case of B2. Values of φ_0 and φ_1 obtained by the least squares method is given in Table III.

Again, f of the same pressure-sensitive adhesives were measured at 4°C and 20°C by the pulling cylinder method. Figure 5 and Figure 6 show f of these adhesives at 4°C and 20°C as a function of velocity. A broad peak is generally observed. In the case of B1, f is a decreasing function of v at 4°C in the velocity range from 10 to

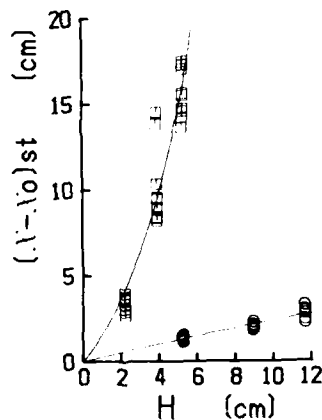


FIGURE 3 Examples of a plot of $(x - x_0)_{st}$ vs. H for B1 at different temperatures.

□: 4°C, $R = 0.96$ cm, $\varphi_0 = 0.799$, $\varphi_1 = -0.00746$

○: 20°C, $R = 0.96$ cm, $\varphi_0 = 3.13$, $\varphi_1 = 0.0115$

Theoretical curves are illustrated by the solid lines.

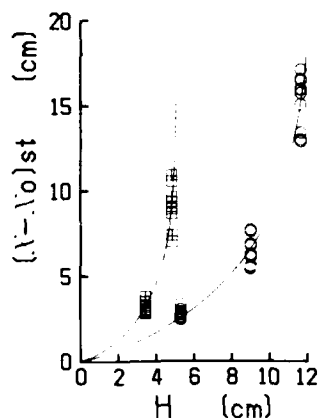


FIGURE 4 Examples of a plot of $(x - x_0)_{st}$ vs. H for B2 at different temperatures.

□: 4°C, $R = 0.159$ cm, $\varphi_0 = 0.4488$, $\varphi_1 = -0.005288$

○: 20°C, $R = 0.96$ cm, $\varphi_0 = 3.701$, $\varphi_1 = -0.0279$

Theoretical curves are illustrated by the solid lines.

10^2 cm/sec, but it is almost a constant or a somewhat increasing function at 20°C in the same range, while in the case of B2, f is a decreasing function of v between $v = 10$ and 10^2 cm/sec at both temperatures, which is consistent with the trends observed in the rolling ball experiments.

TABLE III
Values of φ_0 and φ_1 obtained by the least squares method

Sample	Temperature (°C)	R (cm)	φ_0 (cm)	φ_1 (sec)	DEV† (cm ²)
B1	20	0.96	3.13	0.0115	2.20×10^0
		0.80	4.05	0.0002	7.28×10^{-1}
		0.64	0.378	0.0719	7.73×10^{-1}
	4	0.96	0.799	-0.00746	7.78×10^1
		0.80	1.042	-0.00975	5.04×10^1
		0.64	1.152	-0.0100	2.73×10^1
B2	20	0.96	3.701	-0.0279	3.05×10^1
		0.80	3.989	-0.0304	3.67×10^1
		0.64	3.67	-0.0268	1.37×10^1
	4	0.159	0.4488	-0.00529	1.42×10^1

† DEV = $\sum (y - y_i)^2$

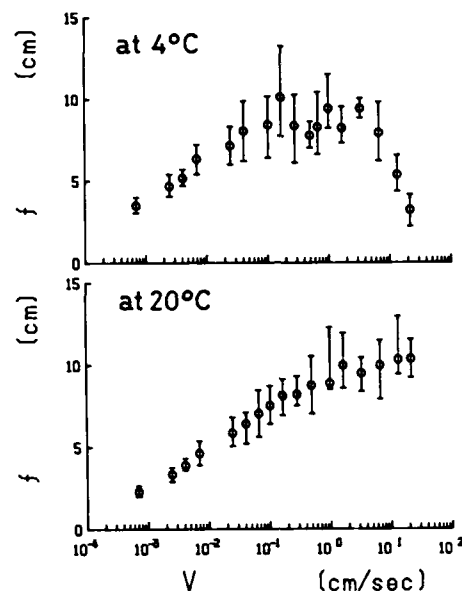


FIGURE 5 Values of f obtained from the pulling cylinder experiments at 4°C and 20°C plotted against $\log v$ for B1, $R = 0.5$ cm, $B = 2.5$ cm, $M = 50$ g.

Now, we have to discuss the reason why these differences appear in the two pressure-sensitive adhesives. Viscoelastic properties of the two adhesives are quite similar, but B1 is much thicker than B2. If thickness of the adhesive is different, rate of strain of the adhesive is different at the same velocity of movement of a ball or a cylinder.

It is easily shown by the model theory⁶ that a peak of f shifts toward higher velocity region as the adhesive becomes thicker. (Figure 7).

In the case of B1, which is very thick, a peak is then located at very high velocity, and the velocity range of our concern corresponds to the increasing part of the curve of f vs. v at 20°C, which corresponds to $\varphi_1 > 0$. But when the temperature is lowered to 4°C, the peak shifts toward the lower velocity region, and then f will become a decreasing function within the above-mentioned velocity range, which corresponds to $\varphi_1 < 0$. On the other hand, the adhesive layer of B2 tape is very thin and in this case a peak of the curve of f vs. v is located at very low velocity, and then f is

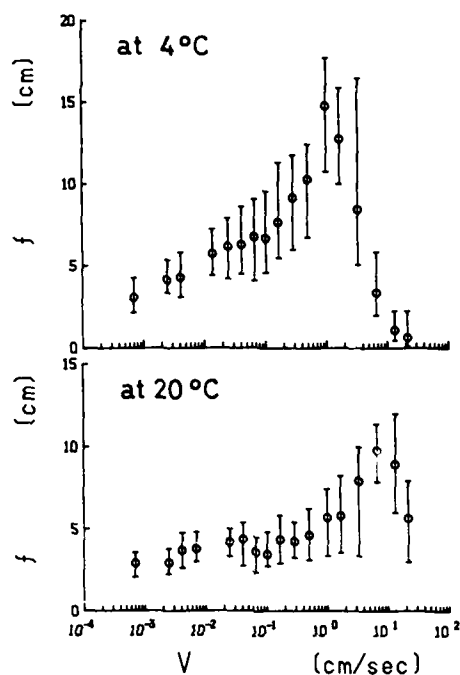


FIGURE 6 Values of f obtained from the pulling cylinder experiments at 4°C and 20°C plotted against $\log v$ for B2. $R = 0.5$ cm, $b = 2.5$ cm, $M = 50$ g.

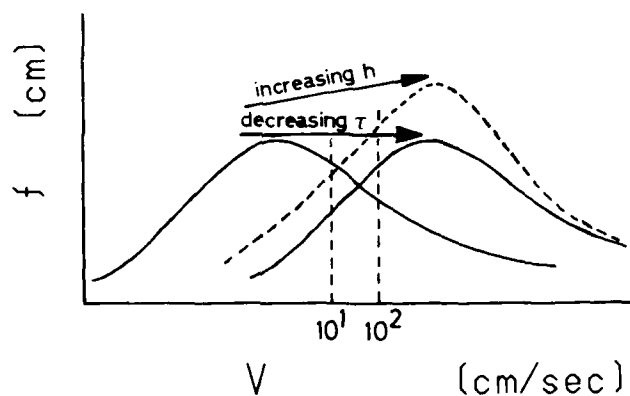


FIGURE 7 Schematic representation of f vs. $\log v$ curve. Direction of shifts of the curve due to the change of some parameters are shown by the arrows. The curve shifts toward the higher velocity region when the average relaxation time τ decreases (*i.e.*, when temperature is raised for a pressure-sensitive adhesive, or when T_g 's of the adhesives are lowered in case the temperature of tests is fixed), or when thickness h of the adhesive layer increases.

decreasing during $10 - 10^2$ cm/sec at 20°C . When the temperature is lowered, the peak shifts further toward the lower velocity region, and the effective velocity range in the conventional ball tack tests still corresponds to a decreasing part of f , which means that φ_1 is always negative.

CONCLUSIONS

The tack of pressure-sensitive adhesives should be expressed by the rolling friction coefficient f of the adhesives, and it can be estimated by analysing the rolling motion of a ball. By employing the pulling cylinder method, f can be measured more easily.

It has been indicated that f is closely related to the viscoelastic properties of the material. If we plot f of a viscoelastic material against $\log v$ over a very wide range of velocity, a curve having a peak is generally observed, and the curve shifts toward the higher velocity region when the average relaxation time τ is lowered (*i.e.*, when temperature is raised for a pressure-sensitive adhesive, or when T_g 's of the adhesives are lowered in case the temperature of measurement is fixed), or when thickness of the adhesive becomes larger.

It was pointed out that f obtained from rolling ball experiments corresponds to that from pulling cylinder experiments in the velocity range of $10 - 10^2$ cm/sec. The pulling cylinder method is a good way to measure f of pressure-sensitive adhesives over a very wide range of velocity under a well-defined condition.

Acknowledgement

Part of the work was supported by a Grant-in-Aid for Co-operative Research of The Ministry of Education, Science and Culture of Japan. The authors wish to thank Dr. T. Saito of Nichiban Co. Ltd. for providing samples.

References

1. J. Johnston, *Adhesives Age* **26**, 34 (1983).
2. F. Urushizaki, H. Yamaguchi and H. Mizumachi, *J. Adhesion Soc. Japan* **20**, 295 (1984).
3. H. Mizumachi and T. Saito, *J. Adhesion*, **20**, 83 (1986).
4. H. Mizumachi, *Material Technology (Japan)* **2**, 6 (1984).
5. H. Mizumachi, *J. Adhesion Soc. Japan* **20**, 522 (1984).
6. H. Mizumachi, *J. Appl. Polym. Sci.* **30**, 2675 (1985).

SESSION OF
THE UNITED KINGDOM

A Review of Contemporary Views of Theories of Adhesion†

K. W. ALLEN

Adhesion Science Group, The City University, London EC1V 0HB, U.K.

(Received October 3, 1986)

The once distinct and independent theories of adhesion have been losing their isolation and converging. Ideas of the effects of surface roughness, once dismissed as irrelevant except in the case of textiles, have been revised; albeit on a smaller scale as details of surfaces have been revealed by sophisticated techniques. Electrostatic interactions across an interface have been more deeply explored and their significance recognised and expounded. Diffusion of groupings and chain segments within a polymer have been related to the possibilities of interaction with a variety of surfaces. Perhaps most important, theories of adsorption have been extended in depth. The precise nature of the molecular interactions have been recognised and quantified. In doing this the contribution of diffusion and elastoplastic phenomena have been integrated. These developments are collated and analysed to present the present understanding of the concepts.

KEY WORDS Adsorption interactions; diffusion mechanisms; electrostatic interactions; mechanical interlocking; review, theories of adhesion.

INTRODUCTION

The need for a deep understanding of the basis of adhesion was recognised over sixty years ago when, in 1922, the First Report of the Adhesives Research Committee¹ stated, "Finally it may be added, there is still no generally acceptable explanation of the action by which glues etc. cause surfaces to stick together. It is

† Presented at the Tenth Annual Meeting of The Adhesion Society, Inc., Williamsburg, Virginia, U.S.A., February 22-27, 1987.

obviously necessary to investigate the nature of adhesion, be it physical or chemical. This problem which has such an important bearing upon many branches of industry, is constantly before the Committee".

The first stages along the path towards understanding were taken by McBain² who, in the Second Report of that Committee, first drew a distinction between joints of two categories; one involving a mechanical type of mere embedding and the other with a specific type of true adhesion.

Over the intervening years, a number of theories have been advanced to account for and explain the observed phenomena. These have been of varying depths of sophistication and development. Frequently particular theories have suffered from the enthusiasm of their protagonists who have been inclined to promote their own view as a universal panacea. Although the shortcoming of this misconception were recognised at quite an early date^{3,4} it has only quite slowly been eroded. Only in comparatively recent years has it been freely possible to consider which theories and mechanisms are appropriate for each particular example of adhesion and to begin to resolve the way in which the contribution of different mechanisms might be combined to provide a further understanding of observed phenomena.

So, in this paper I shall review some of the areas where deeper understanding has been achieved and finally try to bring these together into a coherent whole.

Mechanical interlocking

This concept, which suggests that the interlocking of the adhesive with the irregularities of the adherend surface is the basis of adhesion, has immediate and intuitive appeal. However, the fact that strong adhesive bonds can and are achieved between surfaces as smooth as optical glass flats demonstrates that it cannot be of general application. The results for the bond strengths of maple wood samples of different roughness were clear evidence for its apparent fallacy.⁵

Nevertheless, the classic work of Wake and Borroff⁶ on the adhesion of rubber to textiles for material woven from spun staple of natural origin proved that the most important factor governing

TABLE I
Maplewood samples, bonded,
side grain, with unreaformal-
dehyde resin at 5 lb f in^{-2} pres-
sure and tested in shear

Surface	Shear strength
Planed	$3120 \text{ lb f in}^{-2}$
Sanded	$2360 \text{ lb f in}^{-2}$
Sawn	$2690 \text{ lb f in}^{-2}$
Combed	$2400 \text{ lb f in}^{-2}$

the bond strength was the penetration of fibre ends from the spun yarn into the rubber. These fibre ends are broken off when the textile and the rubber are separated and the strength of the bond depends upon the number of them originally present. The specific interaction between the rubber and the surface of the fibre is only of indirect importance, as it will determine the length of fibre end which must be embedded before the interfacial shear strength exceeds the tensile strength of the fibre. Moreover, if the spun staple natural fibre was replaced by continuous filament of synthetic origin then the bond strength was very considerably reduced. Various special treatments and finishes had to be introduced to enhance the specific interaction between the surface of the textile and the fibre in order to achieve a satisfactory bond.

Another well established example where mechanical interlocking makes a significant contribution towards the bond strength is in the electroless plating of certain plastics with metal. The most commonly used base is either high impact polystyrene or ABS, both of which consist of a continuous phase of glassy polymer with an elastomer dispersed within it. The process of plating involves an etching step which results in the oxidation and removal of the rubbery material to leave a highly reticulate and porous surface following which the metal (usually copper) is deposited. Electron micrographs of sections show quite clearly the penetration and interlocking of the metal within the plastic to a depth of up to $10 \mu\text{m}$. A similar procedure is used for plating polyalkenes but here the etching produces less well defined attack at grain boundaries and various surface defects. Here a very extensive study by Perrers and Pettett⁷ showed that there were two mechanisms involved and

interacting; a mechanical interlocking and an interaction depending upon the surface chemistry of the polymer.

These were all special cases and out of the main stream of structural adhesion technology and for this reason it was, at one stage, fashionable to dismiss mechanical interlocking as insignificant and irrelevant. The change began with Packham's⁸ work on the adhesion of polyethylene to aluminium. He studied the behaviour of polyethylene which was sintered on to the surface of aluminium which had been treated in various way but particularly which had been anodised in acid electrolytes. It was already well known that the oxide film produced comprised a dense barrier layer of compact oxide immediately adjacent to the metal, surmounted by a layer of hexagonal oxide cells each with a circular pore at its centre. The size and relative number of these pores could be controlled by the conditions and duration of anodising. The diameters ranged from 120 Å to 330 Å. Measurements of bond strength showed a direct correlation with the size and concentration of these pores in the oxide. Electron micrographs of polymer surfaces which had been separated from the metal oxide revealed clusters of tufts. These clusters were about 1 μm deep and 500–2000 Å in diameter and corresponded to groups of tufts. Thus a mechanical component was clearly indicated as contributing to this adhesion.

More recently, Venables⁹ and his team have studied the detailed morphology of the surfaces of aluminium and titanium which have been treated for adhesive bonding by the established etching processes. Sophisticated surface analytical techniques have revealed that these surfaces are both extremely rough and porous on a microscopic scale. Their evidence indicates that there is mechanical interlocking of the polymer of the adhesive which gives much stronger bonds than if the surface had been smooth. Indeed the bond only fails when the polymer itself fails by visco-elastic deformation. In contrast, when the oxide lacks the roughness and porosity and the bond depends for its strength solely on chemical forces across the interface, then separation will occur quite cleanly at the boundary at much lower levels of stress. They have gone on to show that when bond strengths deteriorate as they are exposed to a hostile environment, the cause is a change in the chemistry and morphology of the oxide layer. Aluminium oxide is converted to

hydroxide which is itself weaker and is only poorly bonded to the underlying metal. Similar results have been indicated for titanium.

Thus clear and conclusive evidence has been provided for a mechanical component in the adhesion mechanism for structural adhesives as used in the aerospace industries.

The fundamental explanation for this mechanical contribution to the total strength of adhesive bonds lies in the existence of a zone between the two materials—adherend and adhesive—wherein both are present. This zone depends upon the interpenetration of the one material into the roughness of the other. Its depth will be governed by the extent of this roughness and the completeness of penetration. In order to separate the two, energy will have to be expended and work done in order to deform and draw the material of lower compliance. This is always provided that the surface features of the roughness of the more rigid material are strong enough to withstand the force and do not themselves fracture. It is this energy which is reflected as extra bond strength.

Adsorption interactions

Any ideal solid material has a mechanical strength of cohesion which depends upon the various forces of attraction between the fundamental particles of which it comprises. The nature of these forces of attraction are varied but include ionic attractions, covalent bonds, hydrogen bonds and van der Waals' forces of several types. Which are the most important in any particular case depends upon the chemistry of the material but the van der Waals' forces are universally present, whichever of the others may also be involved. This strength will be modified and reduced in all real structures (except in a very specialised instances) by various flaws and imperfections in the structure and especially in the immediate surface layers.

It has been recognised for a long time that all the forces which provide cohesive strength in a uniform solid may also be available to provide adhesive strength across the interface in a joint between two materials.¹⁰ The common feature of these forces is that all of them are only effective over distances which are comparatively short on an atomic scale, at most a few tens of angstrom units. So if they

are to be invoked across an interface between two materials, it is a necessary first requirement that they must be in the closest and most intimate contact.

It is from this requirement that all the concern for wetting and spreading springs.

This concept of the origin of forces of adhesion also links the whole of this science with the main stream of physical chemistry in two ways. First of all, there are all the classical studies of the adsorption of gases and, to a lesser extent, liquids on solids. While the detailed mathematics and theories associated with the names *inter alia* of Langmuir and Brunauer may have little immediate correlation with, for instance, the interaction of an epoxy adhesive system with a prepared metal surface, yet the fundamental ideas of interaction between two sets of different molecules are common to both. The considerations of physical and chemical adsorption have direct parallels in our exposition of the fundamentals of adhesion. Secondly, all that part of surface science which considers the energy relationships of interfaces and the origins of surface tension and energy is of direct and immediate relevance.

The magnitude of the attraction arising from the entirely universal dispersion forces is, at first sight, unexpectedly high. For two perfectly plane parallel plates when the centres of molecules comprising the surface layers in each plate are separated by 10 Å, the attractive force is about 10^8 – 10^{10} dynes cm^{-2} and if the separation is increased to 100 Å the force is reduced to 10^5 – 10^7 dynes cm^{-2} .¹¹ The magnitude of these forces depends upon the material and is greater between two metals and is about an order of magnitude less between two dielectrics. So there is a potential source of strength here considerably greater than is normally achieved in real adhesive joints and their involvement in adhesion has been extensively considered.

The relationships involved can be seen to originate in Dupré's equation¹² for the reversible thermodynamic work of adhesion W_A to separate two phases which are originally in intimate contact to give two clean surfaces. This gives the relationship:

$$W_A = \gamma_1 + \gamma_2 - \gamma_{12}$$

when γ_1 , γ_2 are the surface free energies of the two phases and γ_{12} is the interfacial free energy between them.

Good and Girifalco¹³ estimated this interfacial free energy by considering the ratio of this free energy of adhesion to the geometric mean of the free energies of cohesion of the two pure phases:

$$(\gamma_1 + \gamma_2 - \gamma_{12})/2(\gamma_1\gamma_2)^{1/2} = \Phi$$

They showed that in the simplest cases Φ is approximately unity. So

$$\gamma_{12} = \gamma_1 + \gamma_2 - 2(\gamma_1\gamma_2)^{1/2}$$

and

$$W_A = 2(\gamma_1\gamma_2)^{1/2}$$

Fowkes¹⁴ proposed that this work of adhesion was the result of contributions from a variety of interactions across the interface. These may include dispersion forces, hydrogen bonds, dipole/dipole and dipole/induced forces, acid/base interactions and in addition perhaps covalent bonds. Further he suggested that these contributions might be combined by a simple addition, thus

$$W_A = W_A^d + W_A^h + W_A^x + W_A^i + W_A^{ab}$$

and similarly the surface free energy (and the work of cohesion) could be expressed in terms of contributions from the various interactions

$$\gamma = \gamma^d + \gamma^h + \gamma^x + \gamma^i + \gamma^{ab}$$

where the superscripts represent *d*—dispersion forces, *h*—hydrogen bonding, *x*—dipole/dipole interactions, *i*—induced dipole/dipole interactions, *ab*—acid/base interactions.

These relationships were often contracted to

$$W_A^d = W_A^d + W_A^p$$

where the superscript *p* represented all the polar, non-dispersion forces involved.

Considerable success was achieved by correlations where only dispersion forces were relevant by using the Good and Girifalco relationship. However, this success led to the introduction of similar proposals to write

$$W_A^p = 2(\gamma_1^p\gamma_2^p)^{1/2}$$

which are not justified in terms of the original derivation and the

terms of the approximation which put $\Phi = 1$, although they led to useful results in some cases.

More recently, as the fallacies of this type of extension have become recognised, considerable attention has been directed towards the nature and relative significance of the other, non-dispersion interactions.

The first discussion of this was due to Bolger and Michaels¹⁵ who, considering the case of (acidic) polar polymers and (basic) metallic oxides, suggested that the only forces other than dispersion forces which needed to be invoked were hydrogen bonds. These could best be treated using the Bronstead proton definition and theories of acid/base relationships, which gave satisfactory results for these particular examples of adhesion.

Then it was recognised¹⁶ that this sort of treatment might be extended to a wider field by use of the Lewis acid/base definitions and theories which consider electron donor/acceptor interactions.

This most recent consideration¹⁷ was based on the work of Drago¹⁸ on the enthalpies (heats of reaction, ΔH) of acid/base pair reactions. He correlated experimental values with theoretical ones calculated on the basis of four constants, two for the acid and two for the base. The results demonstrated that the dipole interactions did not contribute measurably to the enthalpies of molecular interaction. This conclusion initially appeared to conflict with earlier work on intermolecular forces due to Keesom¹⁹ and Debye²⁰, until the differences are recognised between the situation in gases, with which the latter worked, where intermolecular distances are considerable and interactions principally involve only two molecules, and the situation in condensed phases where molecules are close and dipole interactions are minimised by multiple nearest neighbours.

Thus the work of adhesion is now to be considered as effectively arising from two components; the dispersion forces and the polar forces to be considered as acid/base interactions. Fowkes and his co-workers²¹ have prepared series of polymers of controlled acidity or basicity by copolymerisation of ethylene with either acrylic acid or vinyl acetate. For each of these series of solids they have estimated the acid-base contribution to the work of adhesion for a series of liquids of known basicity or acidity by measurement of contact angles. In each case a set of smooth curves was obtained

relating the acid/base contribution to the work of adhesion with the degree of acidity or basicity. In addition, for an acidic liquid there was nothing but dispersion force interaction with the acidic polymers and similarly for a basic liquid with the basic polymers.

Adsorption studies of the interaction of polymers in solution in different solvents with inorganic solids confirmed this to be a triangular competition. It involved the dispersion force and acid/base interactions between polymer and solid, between polymer and solvent and between solvent and solid. The differences in dispersion forces cancel out and it is the acid/base competition which controls the adsorption behaviour.²²

Direct effects upon adhesion can be illustrated by comparison of the adhesion of cast films of basic polymethyl methacrylate on an acidic glass (less than 0.1% alkali metal oxides) and on a basic glass (20% alkali metal oxide). It was difficult to remove the film from the acidic glass but it was quite easy to peel it away from the basic glass.¹⁷

A survey of the practical use of adhesives indicates that acid/base (electron donor/acceptor) interactions have been utilised largely by empirical, trial and error methods. There is some hope that, for the future, these results may be more directly achieved by consideration of the acid/base characteristics of the substrates and of the polymers used in the adhesives.

So far this discussion has involved only the secondary interaction (van der Waals) forces in the form of dispersion forces, electron pair interactions and dipole interactions (even if these last have been shown to be generally negligible). While, as was shown at the beginning, these secondary interactions are more than adequate to provide high bond strengths, yet there are instances where primary covalent bonding is believed to be involved. This is particularly the case where techniques have been developed to increase the durability of bonds and their resistance to deterioration in hostile environments.

Direct and positive evidence for this mechanism is somewhat sparse but there is considerable indirect evidence. The use of primers or coupling agents, particularly silane compounds, is now extensive especially for the manufacture of glass-fibre reinforced composites. The film of silane is itself polymerised and there is now clear evidence from Laser-Raman²³ spectroscopy and Secondary

Ion Mass Spectroscopy²⁴ that there are —Si—O—X— groups in the surface (where X represents the surface material) held by covalent bonds. It is believed that it is these covalent bonds which confer upon the interface the resistance to hydrolytic attack under wet conditions which is the particular object of the use of these primers. Indirect evidence also arises from studies where it has been shown by thermodynamic techniques that secondary interactions are insufficient to account for the observed properties of strength and durability.²⁵

Direct evidence also arises from introducing quite small amounts (0.001–0.1 mole fraction) of reactive functional groups into the adhesive which often greatly increases the adhesive bond strength.²⁶ For a number of cases a relationship of the form

$$\sigma_c = \sigma_0 + kC^n$$

applies where σ_c is the adhesive strength when the concentration of functional group in the adhesive is C , and k and n are constants, and usually n is in the range 0.6–1.0.

Moreover, the effectiveness of functional groups in increasing adhesion shows considerable specificity with the adherend. Thus particular functional groups may be selected for particular adherends where they may give rise to chemical bonding across the interface. For example, carboxyl groups (introduced by copolymerisation with acrylic, methacrylic or maleic acid) will promote adhesion to metals.

Electrostatic forces in adhesion

Derjaguin and his co-workers²⁷ developed an explanation for the observed behaviour of pressure-sensitive tapes based upon the development of an electric double layer in the interface. The separation of the adherends and breaking of the bond was accompanied by the drawing apart of the two components of the double layer and the work of adhesion was identified with the electrical energy stored in the capacitor system. The agreement which they reported between theoretical and experimental results appears to ignore the energy which, particularly in peeling tests, is dissipated in the viscous and visco-elastic deformation of the adherents.

The only attempt made in the West directly to develop this

approach used direct tension tests rather than peeling and reported great difficulty in measuring the charge densities and obtained considerably lower values.²⁸

The adhesion of thin, vacuum-deposited metal films on polymer substrates has been considered in terms of electrostatic interactions. The experimental facts are that²⁹ the force needed to remove, by scratching, a thin film of metal from a polymer surface increased with the elapsed time. Suggestions that this might be due to slow oxidation processes leading to the formation of chemical bonds between the metal and the insulator were discounted by the observation that this phenomenon occurred in the case of gold as well as with base metals. Moreover, if a metal film was deposited on a polymer, allowed to age to develop strength and was then exposed to a "glow" discharge, the bond strength dropped almost to zero. It was inferred, reasonably, that this demonstrated clearly the electrostatic origin of the adhesion.

The Russian workers had argued that electron transfer had occurred from the metal to the polymer to equalise their Fermi energy levels. Weaver suggests²⁹ that this is improbable since it would require an excess energy of about 3 eV to overcome the potential energy barrier at the interface. Instead he postulated positive hole injection with the electron moving from polymer to metal. The nature of the charge-carrying bodies in the polymer is not clear. In any case, the process would be expected to be slow because of the relatively small number of conduction electrons in an insulator like the polymer, and they are likely to be in situations where their mobility is low. Thus a quite slow development of adhesion would be expected—just as is observed. Moreover, the final charge concentration might well depend upon the number of available electrons rather than their energy levels and no relationship would exist between the work function of the metal and the adhesive forces developed.

If one turns from the consideration of adhesion between plane surfaces to the adhesion of fine particles then there is clear evidence that electrostatic forces are significant. This has been demonstrated particularly by experiments³⁰ with gold particles and has been suggested as important in the retention of pollen on the stamen in flowers and its removal by bees.³¹

More recently, Derjaguin³² has continued the discussion of the

relative importance of electrostatic forces as compared with the forces of molecular attraction. The particular point which arises is that so long as the distance between the plates of a condenser is small compared with their area then the mechanical force of attraction between them is independent of their distance apart, while the forces of molecular interaction are inversely proportional to the cube of the distance. Thus, while at close distances the electrostatic forces may be small compared to the molecular interactions, as the separation is increased so the relative significance of the forces changes and the electrostatic become more important. So, when the process of breaking adhesive bonds is considered, the electrostatic forces contribute a not insignificant proportion to the total energy involved.

Diffusion mechanisms in adhesion

The classical work suggesting that diffusion is an important phenomenon in some instances of adhesion is due to Voyutskii.³³ Fundamentally, it involves the simple concept that if two polymers are in close contact at temperatures above their glass transition temperatures, then the long chain molecules, or at least segments of them, will interdiffuse. This is undoubtedly true in the examples of the adhesion of a polymer to itself. So when adhesives in solution are applied to two surfaces and the solvent is allowed to evaporate before the two are brought together, it is a diffusion process which is responsible for the combination and eventual disappearance of the interface between the adhesive surfaces.

From this original concept Vasenin³⁴ developed a series of theoretical relationships derived initially from the theories of mixing and inter-diffusion of liquids. For the autohesion of a polymer to itself, he gave an expression for the force required for peeling separation which was directly proportional to the rate of separation and to the one quarter root of the time of contact, as well as inversely proportional to the two-thirds root of the molecular weight. A number of series of experimental results have been shown to be in accord with these relationships.^{35,36} All this approach was criticised by Anand³⁷ who suggested that the change with time was due to a slow increase in the true area of contact by

rheological processes not involving diffusion. To this Voyutskii³⁸ replied with qualitative evidence and interpretation.

Much of the evidence in this area is indirect and deductive and only part is direct. However, a number of workers have now studied the interfacial structure by methods which include optical and electron microscopy, radiothermoluminescence, UV luminescence, paramagnetic probe and Fourier Transform, internal reflection IR spectroscopy.³⁹ Microscopy shows, in some instances, the interface as a band in which the density varies gradually from one phase to the other over a zone which ranges from 10 Å to 1000 Å thick.

The variations of peeling strength with the temperature of bonding of pairs of polymers shows quite sharp increases at temperatures which correspond with changes of the mode of failure from interfacial to cohesive. These changes can reasonably be attributed to the incidence of effective interdiffusion between the adherends.³³

An alternative approach to this is by consideration of free volume within the polymer systems. Campion⁴⁰ developed this for the case of rubbers and particularly considered the free spaces which inevitably occur close to the chains because of their geometry. He was able to correlate the autohesive properties of rubbers with the cross sectional area of holes available for diffusion.

The usual technique for joining polycarbonates or polysulphones is that known as "solvent bonding".⁴¹ One or both surfaces are treated with a suitable solvent and after a short time the two surfaces are brought together under pressure. This produces a good bond and the original interface cannot be detected, although there is a zone in which the polymer has undergone some structural alteration. Here it appears that inter-diffusion has occurred within this bond zone but that is only possible when the solvent has loosened the chains and allowed some mobility. Thus it appears certain that for mutually compatible polymers of similar solubility parameter and at temperatures above their glass transition points then mutual interdiffusion is a prime mechanism of adhesive bonding.

A similar mechanism is involved when a coherent film is formed from a polymer latex. As the dispersing agent is lost there is a phase inversion and the polymer particles which were originally the disperse phase now become the continuous phase. At this stage the

long chain polymer molecules begin a process of interdiffusion which entirely eliminates the particle boundaries.

It has been suggested that the mechanism whereby an adhesive penetrates into the fine structure of a metal oxide is one of diffusion of the polymer into the interstices of the oxide.

CONCLUSION

It is now quite clear that none of the accounts of the mechanism of adhesion has any reasonable claim to covering all the situations; none is a panacea. It is necessary to make this assertion because, certainly in the past, protagonists have been over-enthusiastic in their support of, and claims for, their particular theory to the exclusion of alternative explanations. Also, more recently, it has been suggested that there is not an accepted explanation of adhesion because people have not recognised the multi-component nature of the problem.

Undoubtedly, in every case where two phases are brought together there will be dispersion forces acting between them tending to hold them together. How far these ubiquitous forces will be sufficient for practical bonding will depend upon the extent and intimacy of the contact, but they will inevitably contribute to the total interactions.

Supplementary to these there are the specific interactions which have been considered under the adsorption headings. It now appears that the dipole interactions which had been postulated are insignificant compared with those arising from electron donor/acceptor interactions. These interactions are primarily considered in the Lewis view of acid/base behaviour and encompass hydrogen bonds. Clearly these are electrostatic forces and there is a convergence of this approach with that of Derjaguin and his co-workers in the strictly electrostatic theory of adhesion. There appears to be a need for a fuller exploration of this relationship between the two methods of consideration.

If we turn to the mechanical component of adhesion it is evident that, other things being equal, a surface which is rough and porous on a sufficiently small scale will result in stronger bonds than one which is relatively smooth. There is even some indication that the

precise morphology of the structure of the roughness has some effect upon the bonding behaviour. It is necessary that the surface, rough or smooth, is properly wetted by the adhesive, probably for two reasons. First of all there must be proper intimate contact between the surfaces of the two phases so that the dispersion and electron interaction forces can be effective. Secondly, the interstices of the roughness must be penetrated so that advantage may be taken of the mechanical effect. At the extreme, the mechanism whereby this penetration is achieved is one of diffusion, so there is a relationship here with the fundamental concepts originated by Voyutskii even in circumstances remote from the areas which he was considering.

So we begin to see that an adhesive bond achieves its strength from the combination of a variety of sources; the adsorption interactions including dispersion forces, acid/base electron donor/acceptor forces and chemical bonds, all of which may be described as electrostatic; mechanical interpenetrations which depend upon topography and flow and diffusion and, in the case of two polymers, interdiffusion of polymer segments. For these various mechanisms, the relative importance and the proper way in which they should be combined will vary from one example to another, but none should be excluded without very careful consideration and exploration. The whole is, usually, greater than the sum of the parts.

References

1. *First Report of the Adhesives Research Committee HMSO*, London 1922.
2. J. W. McBain and D. G. Hopkins (i) *Second Report of the Adhesives Research Committee HMSO*, London 1926; (ii) *J. Phys. Chem.* **29**, 88 (1925).
3. R. M. Vasenin, *Adhesives Age* **8** (5), 21 and (6), 30 (1965).
4. K. W. Allen in *Aspects of Adhesion* **5**, D. J. Alner Ed. (Univ. of London Press Ltd., London, 1969), Chap. 1, p. 23.
5. J. W. Maxwell, *Trans. Am. Soc. Mech. Engs.* **67**, 104 (1945).
6. E. M. Borroff and W. C. Wake, *Trans. Inst. Rubber Industry* **25**, 199 and 210 (1949).
7. L. E. Perrins and K. Pettett, *Plastics and Polymers* **39**, 391 (1971).
8. D. E. Packham in *Aspects of Adhesion* **7**, D. J. Alner and K. W. Allen, Eds. (Transcripta Books, London, 1973), p. 51.
9. J. D. Venables (i) in *Adhesion* **7**, K. W. Allen, Ed. (Applied Science Publishers, London, 1983), Chap. 4; (ii) *J. Materials Sci.* **19**, 2431 (1984).
10. W. C. Wake, *Adhesion and the Formulation of Adhesives 2nd Ed.* (Applied Science Publishers, London, 1982), p. 9.

11. J. R. Huntsberger in *Treatise on Adhesion and Adhesives* Vol. 1, R. L. Patrick, Ed. (Edward Arnold Ltd., London, 1966), Chap. 4, p. 121.
12. A. Dupré, *Theorie mechanique de la chaleur* (Paris 1869).
13. (i) L. A. Girifalco and R. J. Good, *J. Phys. Chem.* **61**, 904 (1957); (ii) R. J. Good in *Aspects of Adhesion* 7, D. J. Alner and K. W. Allen, Eds. (Transcripta Books, London, 1973), p. 182.
14. F. M. Fowkes, (i) in *Contact Angle, Wettability and Adhesion*, *Advances in Chemistry* **43**, (Am. Chem. Soc., Washington, D. C., 1964), p. 99; (ii) *J. Adhesion* **4**, 155 (1972).
15. J. C. Bolger and A. S. Michaels in *Interface Conversion for Polymer Coatings*, P. Weiss and G. D. Cheevers Eds. (Elsevier, New York, 1968), Chap. 1.
16. K. L. Mittal, *Pure and Applied Chem.* **52**, 1295 (1980).
17. F. M. Fowkes, *Physicochemical Aspects of Polymer Surfaces*, Vol. 2 K. L. Mittal, Ed. (Plenum, New York and London, 1985), p. 583.
18. (i) R. S. Drago, G. C. Vogel and T. E. Needham, *J. Am. Chem. Soc.* **93**, 6014 (1971); (ii) R. S. Drago, L. B. Parr and C. S. Chamberlain, *J. Am. Chem. Soc.* **99**, 3203, (1977).
19. W. H. Keesom, *Physik Zeit.* **22**, 129 and 643 (1921).
20. P. Debye, *ibid* **21**, 178 (1920); **22**, 302 (1921).
21. F. M. Fowkes and S. Maruchi in *Organic Coatings and Plastics Chemistry Preprints*, **37**, 65 (1977) (Am. Chem. Soc.)
22. F. M. Fowkes and M. A. Mostafa, *Ind. Eng. Chem. Prod. Res. & D.* **17**, 3 (1978).
23. J. L. Koenig and P. T. K. Shih, *J. Colloid & Interface Sci.* **36**, 247 (1971).
24. M. Gettings and A. J. Kinloch, (i) *J. Material Sci.* **12**, 2511, (1977); (ii) *Surface Interf. Analysis* **1**, 189, (1980).
25. K. W. Allen, L. Greenwood and W. C. Wake, *J. Adhesion* **16**, 127, (1983).
26. S. Wu, *Polymer Interface and Adhesion* (Dekker, New York, 1982), p. 420.
27. (i) B. V. Derjaguin, *et al.*, *Proc. 2nd Int. Congr. Surface Activity Div. VI(c)*, BP 595 (1957). (ii) B. V. Derjaguin and V. P. Smilga in *Adhesion: Fundamentals and Practice* (McLaren, London, 1969), p. 152. (iii) B. V. Derjaguin *Research* **8**, 70 and 365 (1955).
28. S. M. Skinner, R. L. Savage and J. E. Rutzler, *J. App. Phys.* **24**, 438, (1953).
29. C. Weaver (i) in *Adhesion: Fundamentals and Practice* (McLaren, London, 1969), p. 46. (ii) in *Aspects of Adhesion* **5**, D. J. Alner, Ed. (Univ. of London Press Ltd., 1969), p. 262.
30. H. Krupp (i) *J. Adhesion* **4**, 83 (1972) and **5**, 269, (1973). (ii) in *Aspects of Adhesion* **8**, K. W. Allen, Ed. (Transcripta Books, London, 1975), p. 187.
31. Sir James Beaumont, Private communication.
32. B. V. Derjaguin and Yu P. Toporov in *Physicochemical Aspects of Polymer Surfaces*, K. L. Mittal, Ed. (Plenum, New York and London, 1983), p. 605.
33. S. S. Voyutskii, *Autohesion and Adhesion of High Polymers*, translated by S. Kaganoff and edited by V. Vakula (Interscience, New York, 1963).
34. R. M. Vasenin (i) *RAPRA Translations* 1005, 1006, 1010, 1075, R. J. Moseley (1960-63), (ii) *Adhesives Age* **8**, (5) 21 and (6) 30 (1965).
35. J. D. Skewis, *Rubber Chem. Tech.* **39**, (2), 217 (1966).
36. W. G. Forbes and L. A. McLeod, *Trans. Inst. Rubber Ind.* **34**, 154, (1958).
37. J. N. Anand, *J. Adhesion* **1**, 31 (1969); **2**, 23 (1970); **5**, 265 (1973).
38. S. S. Voyutskii, *ibid.* **3**, 69 (1971).
39. N. H. Sung, *Polymer Eng. Sci.* **19**, 810, (1979).
40. R. P. Campion (i) *J. Adhesion* **7**, 1 (1975); (ii) in *Adhesion* **1**, K. W. Allen, Ed., (Applied Science Publishers, London, 1977), Chap. 5.

41. W. V. Titow in *Adhesion* **2**, K. W. Allen, Ed. (Applied Science Publishers, London, 1978), Chap. 12.

In addition to the above particular references four general sources have been used considerably:

A. J. Kinloch, *J. Materials Science* **15**, 2141 (1980) and **17**, 617 (1982).

W. C. Wake (i) *Adhesion and the Formulation of Adhesives*, 2nd Ed. (Applied Science Publishers, London, 1982) (ii) *Polymer* **19**, 291, (1978).

Souheng Wu, *Polymer Interface and Adhesion* (Dekker, New York and Basel, 1982).

Non-destructive Inspection of Adhesively-bonded Joints†

R. D. ADAMS

Department of Mechanical Engineering, University of Bristol, Bristol BS8 1TR, U.K.

P. CAWLEY and C. C. H. GUYOTT

Department of Mechanical Engineering, Imperial College, London SW7 2BX, U.K.

(Received September 2, 1986)

The objective of any system of non-destructively examining an adhesive joint must be to obtain a direct correlation between the strength of the joint and some mechanical, physical or chemical parameter which can readily be measured without causing damage. Faults or defects are defined as anything which adversely affect the short or long term strength of a joint. There are two basic areas for examination, the cohesive strength of the polymeric adhesive, and the adhesive strength of the bond between polymer and substrate.

Adhesive strength is very difficult to measure since it is an interfacial phenomenon involving a very thin layer of material, thin even in comparison with bond-line dimensions. Effectively, it would be necessary to assess intermolecular forces and this is not readily possible with existing techniques. This aspect of quality control is usually reduced to assessing the nature of the adherend surfaces prior to bonding.

The cohesive strength of the adhesive is really the only parameter which can be estimated with any degree of confidence, and it is this which features most on destructive tests of bonded joints.

In this paper, defects including porosity, surface un-bonds, zero-volume unbonds, poor cure and so on are discussed, together with the various methods currently used (and some new methods) for physical non-destructive testing.

KEY WORDS Non-destructive inspection; Defects; Ultrasonics; Coin tapping; Cohesive strength; Adhesive strength.

† Presented at the Tenth Annual Meeting of The Adhesion Society, Inc., Williamsburg, Virginia, U.S.A., February 22-27, 1987.

1 INTRODUCTION

The strength of an adhesively-bonded joint depends on the nature of the materials being joined and the loading. The loads may be steady or alternating, of long or short duration, and may be associated with aggressive environments. At the same time, the designer must bear in mind the manufacturing process which will lead to the production of his joint. As to whether the joint is satisfactory is a question that can be answered in part by experience of making similar joints, by building and testing a series of prototypes, and by over-design where ignorance and uncertainty cannot be eliminated. But there is a further possibility, that of non-destructively examining the joint prior to (or even during) its use.

Non-destructive testing (NDT) is well-established in engineering practice in fields as widely ranging as welds in nuclear reactors to printed circuit boards in electronics. The objective of any system of non-destructive testing is to correlate the strength of the component (however defined) with some mechanical, physical or chemical parameter which can readily be measured without causing damage.

2 THE NATURE OF THE DEFECTS

Several types of defect may occur in bonded structures.

Porosity is caused by volatiles and entrained air in the adhesive. It is therefore present in most bond-lines to some extent. *Adhesive cracks* are due to problems with curing (cure and/or thermal shrinkage) or to large applied stresses, either one-off or repeated (fatigue).

Voids in the adhesive are similar to porosity, except that the individual defect volume can be much greater. It is caused by air or gases becoming trapped by the pattern of laying the adhesive, or to insufficient adhesive being applied. Large voids cannot be caused by volatiles, unless something is very wrong with the adhesive system. *Surface unbonds* are an alternative form of void, often caused when adhesive is applied to one adherend only and unevenly.

Disbonds or *zero-volume unbonds* can occur during manufacture due to the presence of a contaminant, such as grease, on an

adherend. The surfaces of a disbond are generally in close proximity, or are touching, but are incapable of transferring load from the adherend to the adhesive. Disbonds also occur as a result of impact or environmental degradation after manufacture.

Less obvious, but potentially very serious, defects, such as a weak adhesive layer and a poor bond between the adhesive and adherend, can also occur. A weak adhesive layer, giving poor cohesive properties, can result from either incomplete mixing, incorrect formulation, or from insufficient cure of the adhesive. *Adhesion failure* or failure of a weak bond between the adherend and adhesive often results from poor surface preparation or the presence of a contaminant on an adherend.

Detecting defects is not the same as knowing whether they are critical as this depends on their extent, position, and the nature of the applied stresses. Their presence is more likely to be indicative of poor joint manufacture than of an impending failure site, especially for short-term loading. For example, Wang *et al.*¹ used epoxy-bonded aluminium alloy single lap joints with a disbonded area achieved by inserting a polypropylene disc in the central region of the joint. Even though there was a large 'defect' present, the joint strength was essentially unchanged.

The other major form of joint used with structural adhesives is that used in bonding a honeycomb core to skins to form a sandwich construction. The structure is held together by a mesh of fine joints which have to take both shear and direct (tensile or compressive) loading.

Figure 1 illustrates some of the possible forms the skin/honeycomb bond may take. In Figure 1a, we have a well-filled joint in which there is a generous adhesive fillet. In Figure 1b, the moulding pressure, or even gravity, has extruded the adhesive from between the skin and core, but has left a generous fillet which will still carry the loads and is probably as strong if not stronger than the joint in Figure 1a. But in Figure 1c, we see two other possibilities: in one case, the adhesive has formed a thin layer between the skin and core (this is weak and will easily break) but has run down the honeycomb cell wall and has not formed a fillet. In the other case, the adhesive layer on the facing skin has not run to wet the cell wall and again gives a weak bond. Defects of this type shown in Figure 1c may be found by monitoring bond area. There are other forms of

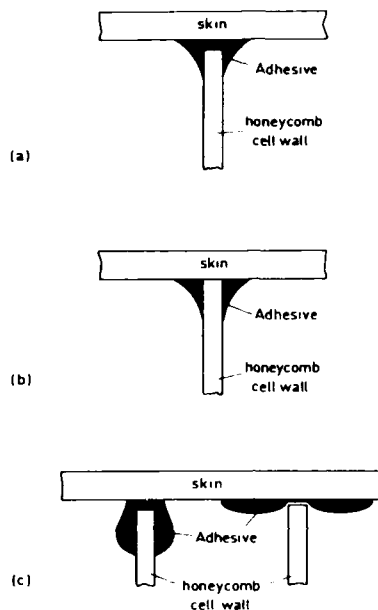


FIGURE 1 Adhesive bonds between the honeycomb cell wall and the facing skin.

defect in honeycomb sandwich construction which are due to lack of attachment between the core and the skin. This may be due to several causes such as locally crushed honeycomb, skin defects, or lack of adhesive. These defects all effectively produce skin-core disbonds. In themselves, none of these defects may prove deleterious to the short-term strength. However, as for the lap joint, they may show poor preparation and may provide sites for fatigue crack propagation.

In addition to monitoring bond area, there are three basic types of defect in adhesive joints which need to be monitored:

- i) complete voids, disbonds or porosity;
- ii) poor adhesion, *i.e.*, a weak bond between the adhesive and adherend;
- iii) poor cohesive strength, *i.e.*, a weak adhesive layer.

3 TESTS PRIOR TO BONDING

Before the adhesive is applied to the joint, the adherend surfaces will have been prepared by washing, abrasion, chemical etching and so on (Adams and Wake²). The state of this surface is crucial in making a good bond. The adhesive properties of the surface may be poor if there are present excessive amounts of water vapour, hydrocarbons or other contaminants.

A simple test involves the wettability of the surface, which is a subjective measurement of the contact angle. If the surface is clean, it is readily wetted and a drop of water will spread over a large area. A simple but quantifiable test involves measuring the spread of a liquid drop of constant volume through a transparent gauge placed over the drop.

The Fokker Contamination Tester, described by Bijlmer,³ uses an oscillating probe to measure the electron emission energy. This varies greatly with the degree of surface contamination, and can even be used to detect residues from alkaline cleaning operations.

Unfortunately, none of these methods is totally satisfactory and the best means of ensuring that a 'good' surface exists prior to bonding is carefully to control the processes leading to its preparation.

4 TESTS AFTER BONDING

4.1 Ultrasonics

Time-domain ultrasonics is one of the most widely used methods of non-destructive examination. It can be used readily to detect voids and disbonds and has the potential for locating very small defects such as porosity. As the pulse of ultrasound propagates through the joint, part of its energy is reflected at each boundary. The amount of energy reflected at a boundary is dependent on the acoustic impedance of the materials on either side of it. Acoustic impedance, Z , can be defined as

$$Z = c\rho \quad (1)$$

where

c = velocity of sound in the material

ρ = material density.

If there is a large difference in the acoustic impedance of the materials, a large proportion of the energy is reflected. Since a defect containing air or any other low density substance will have a very low acoustic impedance relative to the adhesive or adherend, the ultrasonic pulse will be almost totally reflected.

The magnitude of the reflected echoes is displayed with respect to time and is used to indicate the presence of defects. A display of this type is commonly called an A-scan. Figure 2a shows an A-scan from a good single-lap adhesive joint and Figure 2b shows an A-scan from a similar joint but with a disbond at the top adhesive/adherend interface. The reflections from the lower adhesive/adherend interface are no longer present in the defective joint. Also the reflections from the top adhesive/disbond interface decay more slowly than those from the top adhesive/adherend interface of the sound joint, since more energy is reflected at the disbond.

As there is a large difference in acoustic impedance between air and solid materials, it is difficult to propagate ultrasonic energy from the transducer to the structure to be tested. The transducer is therefore coupled at the structure *via* a medium which has a similar acoustic impedance to the structure. Commonly, the structure and transducer are immersed in a water bath. The ultrasound then propagates across the water filled gap (typically 25–100 mm depending on the transducer) into the test piece. An alternative is to use a water jet transducer in which the ultrasound propagates along a moving column of water (jet).

Serious problems can arise, however, if the couplant or some other liquid such as water or fuel is allowed to penetrate the defect. The presence of the liquid reduces the reflection coefficient and the defect becomes much more difficult to detect.

In addition to an A-scan presentation of the ultrasonic echoes, which only gives information at a single point, a map of defects can be produced by scanning the surface of the structure. The amplitude of a particular echo, such as from the bottom adherend-adhesive interface, is measured as the probe traverses the structure. Since the

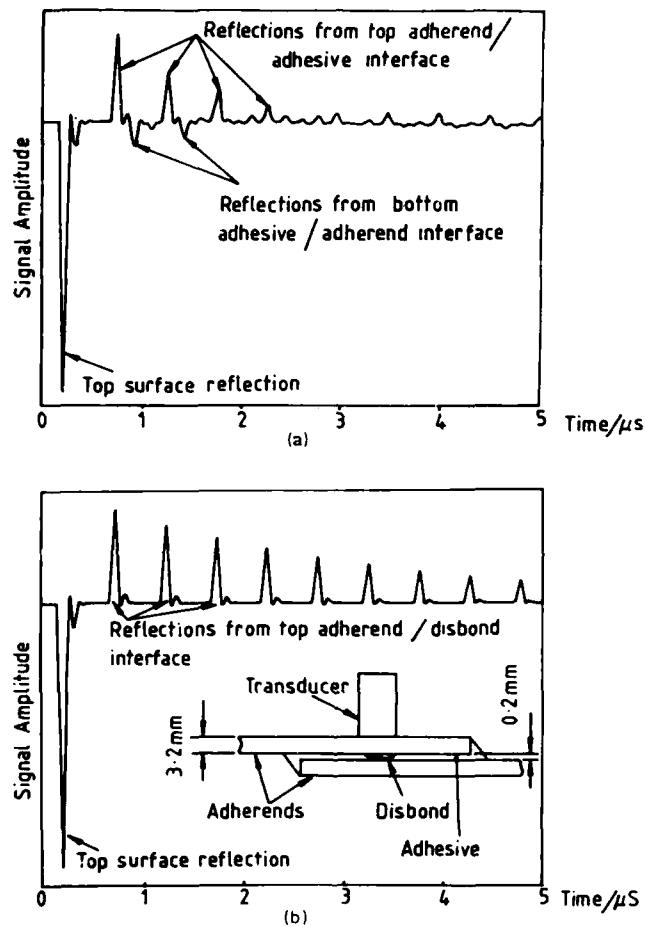


FIGURE 2 A-scan from single lap joints. (a) Well bonded, (b) with defects.

echo amplitude will change in the presence of a defect, a record of defect location is obtained by plotting amplitude against position, see Figure 3. This is usually called the C-scan method. The resolution of small defects, such as porosity, is improved by decreasing the distance between the scan lines, but this also increases the inspection time.

Two transducers can be used in this mode, in which separate

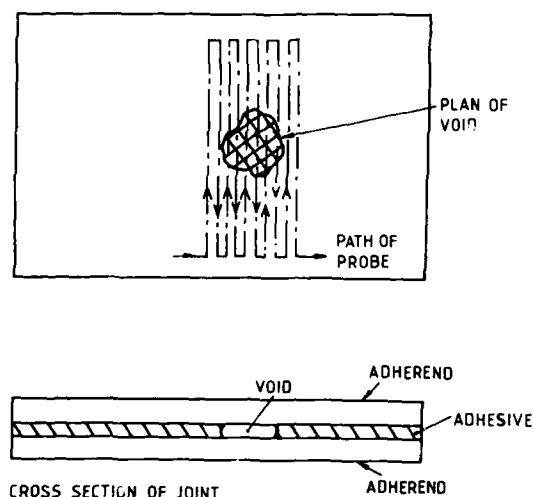


FIGURE 3 C-scan of joint with a void.

transmitting and receiving transducers are positioned either side of the structure and the magnitude of the transmitted signal is used to detect defects. The signal at the receiving transducer either reduces or disappears when a defect is present. Through-transmission is often used for inspecting the bond between the top and bottom skins and the core of a honeycomb structure.

Ultrasonic impedance and resonance tests⁴ can also be used to detect small voids and disbonds. However, they will not generally detect such small defects as porosity, unlike time domain ultrasonic techniques.

4.2 Sonic vibrations

A number of sonic vibration techniques, which effectively measure the local stiffness of the structure, are used for the non-destructive testing of adhesive joints. A defect such as a disbond reduces the local stiffness of a structure, measured perpendicular to the surface. The defect can be modelled as a spring, below which is the rest of the structure whose properties are unaltered. The spring stiffness is given by the stiffness of the layer(s) above the defect.

Instruments of this type typically operate at frequencies between 1 and 30 kHz, which is substantially lower than those for the ultrasonic techniques (usually 0.1–25 MHz). They will generally only detect disbonds or voids, the minimum detectable size depending on the depth and hence the thickness of the adherends. Although the minimum detectable size is larger than for the ultrasonic techniques, the tests are often more convenient since they do not require a couplant between the transducer and test structure.

4.2.1 *Mechanical impedance*

Mechanical impedance measurements can be used to give an indication of the stiffness perpendicular to the surface of a structure. Commercially available instruments generally take measurements at a single pre-set frequency, typically between 1 and 10 kHz. As the probe is moved from a good to a disbonded or more compliant area, the impedance decreases. Unfortunately, as the base structure becomes more flexible, the impedance of a defective zone can be higher or lower than that of a good zone, depending on the frequency, and the test becomes unreliable.⁵

Instead of using a couplant, a dry point contact is used between the transducer and structure. This contact has a finite stiffness⁶ which must be kept as high as possible, otherwise the sensitivity of the technique will be reduced.

4.2.2 *Coin tap test*

The coin tap test is one of the oldest methods of non-destructive inspection. Until recently, however, the technique has remained largely subjective and there has been considerable uncertainty about the physical principles behind it.

When a structure is struck with a hammer or coin, the characteristics of the impact are dependent on the local impedance of the structure and the hammer used. The local change in structural stiffness produced by a defect changes the nature of the impact. The time history of the force applied by the hammer during the impact may be measured by incorporating a force transducer in the hammer. Typical force-time histories from taps on sound and disbonded areas of an adhesively bonded structure are shown in Figure 4. The impact on the sound structure is more intense and of a shorter duration than that on the damaged area, the impact

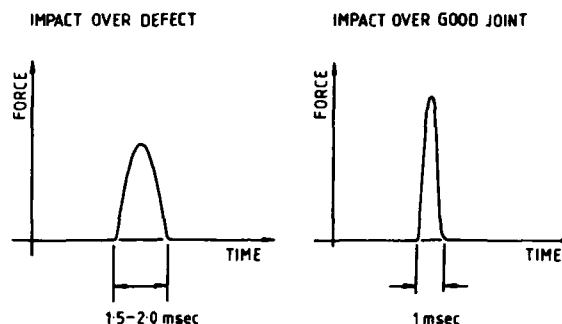


FIGURE 4 Force/time histories.

duration on the sound structure being approximately 1 ms compared with 1.7 ms on the defective zone.

Either the peak force or the duration of the impact can be used to locate defects. Since the method only uses measurements of impact force, no transducers need be attached to the structure, thus avoiding the coupling and alignment problems which arise with, for example, ultrasonic techniques. The sensitivity of the method is increased by further processing of the force time histories and is detailed by Adams *et al.*⁷

5 TECHNIQUES TO LOCATE POOR COHESIVE PROPERTIES

The Fokker Bond Tester Mk II⁸ is the only commercially available instrument which attempts to measure the cohesive properties of the adhesive in a joint. It measures frequency and amplitude changes in the first two modes of through thickness vibration of a system comprising of the transducer and the joint. The measured parameters are dependent on both adherend and bond line thickness and the material properties, *i.e.*, adhesive and adherend moduli and damping. The range of frequencies over which the instrument operates depends on the transducer, but it is typically between 0.3–1.0 MHz.

The instrument will reliably detect small voids and disbonds at different depths in a multilayer joint. However, it is more difficult to predict cohesive properties and strengths⁹ since the frequency shifts,

resulting from a change in cohesive properties or bond line thickness, are small and of a similar magnitude to each other. Consequently, to obtain a true measure of the cohesive properties with this instrument the bond line thickness must be kept constant (or be measured separately).

The technique of ultrasonic spectroscopy¹⁰ is currently being evaluated for measuring the cohesive properties of an adhesive joint. It gives the frequency response over a wide frequency range, typically 1-20 MHz, but difficulties have been experienced in correlating features of the spectrum with adhesive properties and thickness.

6 TECHNIQUES TO LOCATE POOR ADHESION STRENGTH

There is no commercial instrument available that can give an indication of the adhesion strength of a joint after it has been manufactured.

Although acoustic emission has been shown¹¹ to be able to detect adhesion failure prior to fracture, the joint has to be loaded to approximately 50% of its failure load. While such a technique is partially destructive, there are currently few alternatives if adhesion strength is to be monitored.

7 CONCLUSIONS

A variety of methods is available for the detection of complete disbonds in adhesive joints. However, techniques which attempt to predict cohesive strength, such as ultrasonic spectroscopy and the Fokker Bond Tester Type II, are not yet generally regarded as reliable. Research is continuing in this area and shows considerable promise. The non-destructive measurement of adhesion strength is currently not possible.

In practice, adhesion failure and poor cohesive properties are generally prevented by careful surface preparation and process control. This leaves the bond inspector to monitor the presence of voids and disbonds in the glue line. Of the many techniques used for void and disbond detection, some are more suitable for use in particular circumstances than others.

Since the cost and time spent finding voids and disbonds will generally decrease as defect size increases, it is important to decide on the minimum size of defect to be detected. Other factors, such as the type of testing environment, will also influence the choice of method used for void and disbond location. However, the number of suitable techniques decreases as the defect size decreases.

Small defects, such as porosity, will only be located reliably by time domain ultrasonics combined with a scanning mechanism to give a C-scan presentation. For larger defects, a scanning mechanism will be unnecessary unless a C-scan record is required.

Sonic vibration techniques are particularly suited to the inspection of honeycomb structures and do not require the use of a couplant which is essential with the ultrasonic techniques.

References

1. T. T. Wang, F. W. Ryan and H. Schonhorn, *J. Appl. Polymer Sci.* **16**, 1901 (1971).
2. R. D. Adams and W. C. Wake, *Structural Adhesive Joints in Engineering*, (Elsevier Applied Science, London, 1984).
3. P. F. A. Bijlmmmer, in *Adhesion 2*, K. W. Allen, Ed. (Applied Science Publ., London, 1978).
4. M. X. Li, W. Z. Ding and J. M. Chen, *N. D. T. Int.* **15**, 137 (1982).
5. P. Cawley, *N. D. T. Int.* **17**, 59 (1984).
6. Yu. V. Lange and I. I. Teumin, *Soviet J. N.D.T.* **7**, 157 (1971).
7. R. D. Adams, A. M. Allen and P. Cawley, *Proc. 11 WCNDT*, Las Vegas, U.S.A. (1985).
8. R. J. Schliekelmann, *Non-Destructive Testing*, p. 100 (April 1975).
9. G. J. Curtis, in *Ultrasonic Testing-non conventional testing techniques* (Wiley, Chichester, 1982).
10. E. P. Lloyd and A. F. Brown, in *Adhesion 2*, K. W. Allen, Ed. (Applied Science Publishers Ltd., London 1978), p. 133.
11. G. J. Curtis, *Non-destructive Testing*, p. 249, (Oct. 1975).

The Adhesive Bonding of Thermoplastic Composites†

A. J. KINLOCH and C. M. TAIG

*Imperial College of Science and Technology, University of London,
Department of Mechanical Engineering, Exhibition Rd., London, SW7 2BX,
England*

(Received 12 June, 1986; in final form August 12, 1986)

The present paper reports some initial results on the adhesive bonding of thermoplastic composites, based upon carbon-fibre in a matrix of poly(aryl ether-ether ketone). Both single- and double-overlap joints have been employed and the mechanisms of failure studied using scanning electron microscopy. Further, a theoretical model, based upon a shear-lag analysis, has been used to predict the strength of the double-lap joints as a function of the overlap length and the theoretical results are compared to the experimental data.

INTRODUCTION

Thermoplastic fibre-composites appear to offer certain major advantages compared to those based upon thermosetting resin matrices.¹ For example, they possess greater toughness, and therefore a higher damage tolerance, and offer the potential of easy and rapid fabrication, *via* thermoforming processes. However, in any component using thermoplastic composites it is likely that adhesive bonding, employing conventional structural adhesives, will be necessary in order to utilise fully the good strength-to-weight ratio of the fibre-composite.

In the case of fibre-composites based upon thermosetting resins, typically epoxy resins, the previous work²⁻⁶ has clearly shown that

† Presented at the Tenth Annual Meeting of the Adhesion Society, Inc., Williamsburg, Virginia, U.S.A., February 22-27, 1987.

adequate intrinsic adhesion of a structural epoxy adhesive to the surface of the composite may be attained by a surface pretreatment which consists of a simple grit-blast followed by a solvent-wipe to remove any remaining debris, assuming the composite is initially dry and free from excessive release agent.

In the present paper some initial work will be described on the adhesive bonding of a thermoplastic composite based upon carbon fibres in a matrix of the thermoplastic polymer, poly(aryl ether-ether ketone). The aims of this initial study were to determine the strengths of lap joints, identify the mechanisms of failure and compare the measured strengths of the double-lap joints, when the out-of-plane tensile stresses (also termed "peel stresses") are relatively low, to theoretical predictions of the failure load based upon a shear-lag analysis.

EXPERIMENTAL

The materials

The thermoplastic composite was APC-2 ("aromatic polymer composite 2", supplied by Imperial Chemical Industries, UK) which is a carbon-fibre composite containing a volume fraction of fibres of about 60% based upon a matrix of the thermoplastic polymer, poly(aryl ether-ether ketone). The composite substrate was prepared by laying unidirectional tape into a twelve-ply stack. The ply direction was $[0^\circ, 90^\circ, 90^\circ, 0^\circ, 0^\circ, 90^\circ]_2$; giving a balanced laminate to avoid warping during the moulding process which was carried out in a heated press at 380°C and 1 MPa.

The two commercial adhesives examined were (a) a two-part rubber-toughened epoxy-paste and (b) a one-part modified epoxy-film adhesive.

Joint preparation and testing

Both single- and double-lap joints were prepared with overlap lengths which varied from 12.7 to 101.6 mm. The composite sheet, 1.44 mm thick, was cut into strips 25.9 mm wide and the surfaces to be bonded were subjected to a light grit-blast and then wiped using a clean cotton cloth dipped in methyl-ethyl ketone. The adhesives

were then applied in accordance with the manufacturer's instructions and the adhesive cured. In the case of the two-part epoxy this consisted of subjecting the joints to a temperature of 65°C for sixty minutes under a pressure of 100 kPa, and for the epoxy film adhesive to a temperature of 120°C for thirty minutes, also under 100 kPa. Prior to testing, the thickness of the adhesive layer was measured using a travelling microscope. For the former adhesive the average thickness was 0.09 mm whilst for the latter it was 0.11 mm, with a coefficient of variation of about 10%.

The joints were fractured by loading in tension in an "Instron" tensile testing machine at a crosshead speed of 5 mm/min. When testing the double-lap joints a piece of aluminium, approximately the same thickness as the composite substrate, was inserted between the parallel substrates to avoid distortion of the joint. Five replicates for each type of joint were tested.

Electron microscopy

The surface of the APC-2 composite prior to bonding and the fracture surfaces of the joints were examined both visually and using the scanning electron microscope. Before observation in the scanning electron microscope the specimens were sputter-coated with gold to improve the conductivity of the surfaces and reduce charging.

Bulk properties of the adhesive

To ascertain the bulk properties of the adhesive in a state nominally of pure shear, "thick-adherend" shear tests were conducted.^{5,7} Aluminium-alloy substrates, 12 mm thick, were employed and were subjected to a chromic-sulphuric etch⁸ prior to bonding. Application and curing of the adhesives was conducted as described previously for the composite joints. The thickness of the adhesive layer was carefully measured and a transducer attached to the specimen so as to measure accurately the displacements across the central region of the overlap, which was 12.3 mm long. Joints were tested at a rate of 5 mm/min. So that any deformation in the substrates could be compensated for, a solid aluminium-alloy specimen was also machined and tested and the loads and displacements recorded. Four replicate tests were conducted.

RESULTS AND DISCUSSIONS

Single- and double-lap joint fracture studies

The results for the failure loads, expressed as force per unit width of joint, for the single- and double-lap joints as a function of overlap length are shown in Table I. Also recorded are the coefficients of variation and the visually assessed locus of joint failure. Several noteworthy features are apparent.

Firstly, for all the joints the failure load increases as the length of the overlap is increased, generally up to a plateau value. This is, of course, a well established observation^{4-6,9} and arises from the maximum shear stress concentrations in lap joints being located at the ends of the overlap and being proportional to the overlap length. So once a certain overlap length is attained there is no further gain in failure load as the overlap length is increased.

Secondly, for the shorter overlaps the failure load for the double-lap joint is more than twice that of the single-lap joint with

TABLE I
Failure loads for epoxy/thermoplastic composite joints

Type of joint	Overlap (mm)	Failure load (MN/m)	C of V	Locus of failure
<i>Two-part epoxy-paste adhesive:</i>				
Single-lap	12.7	0.143	12%	I
	38.1	0.128	22%	I
	63.5	0.179	23%	I
	102.7	0.320	11%	I
Double-lap	12.7	0.368	20%	I
	38.1	0.429	30%	I
	63.5	0.415	23%	I
	102.7	0.436	11%	I
<i>One-part epoxy-film adhesive:</i>				
Single-lap	12.7	0.199	36%	I
	38.1	0.297	29%	I
	63.5	0.435	21%	I
	102.7	0.365	22%	I
Double-lap	12.7	0.400	34%	I; 1 joint some IL
	38.1	0.712	32%	I; 1 joint some IL
	63.5	0.678	34%	I
	102.7	0.651	18%	

Notes: I = interfacial failure from visual assessment; IL = interlaminar failure in composite substrate.

the same overlap length. This arises from the comparatively high out-of-plane tensile stress concentrations at the ends of the overlap in the single-lap joint and the fact that they decrease in intensity as the overlap lap is increased, *i.e.* as the eccentricity of the loading path and the associated bending moments are reduced.^{6,9}

Thirdly, the coefficient of variation in all the sets of joints is relatively high. The joints were carefully made in the laboratory and certainly for the double-lap joints, a coefficient of variation of about 5% to 8%, or so, would be considered more typical of joints with a thermosetting-based carbon-fibre reinforced-plastic.

Fourthly, the locus of joint failure from a visual assessment is that fracture almost exclusively occurred at the adhesive/composite interface, although two joints prepared using the epoxy-film adhesive failed with some degree of interlaminar fracture in the composite substrate. This interfacial locus of failure is most unwelcome to the adhesives technologist and is frequently associated with relatively low joint strengths and a high scatter. Indeed, it is general practice to select pretreatments and design joints to avoid interfacial failure, since it is easier to predict the strength and control the reproducibility when fracture occurs in the adhesive or substrates. In fact, an interfacial locus of failure is especially uncommon when bonding fibre-composites based upon thermosetting resins. Typically, joint fracture either occurs in the adhesive layer or by interlaminar fracture of the composite substrate; although when bonding very thin composite sheets joint fracture may occur *via* tensile failure in the substrates, often well away from the overlap.

Finally, although of interest, it is difficult to compare directly the strength expected if similar joints were prepared from fibre-composites based upon thermosetting resins. However, for the double-lap joints with long overlap lengths, the plateau strength might be expected to be of the order of about 1 MN/m. But since such joints often fail by interlaminar fracture of the composite this may be increased to about 3 MN/m by redesigning the joint at the ends of the overlap to alleviate the out-of-plane tensile stresses that are, of course, present even in a double-lap joint and are responsible for this mode of failure. Typical redesign methods involve tapering the outer substrates, using an angled adhesive spew fillet, etc.^{4,6,9} Obviously, since the joints with the thermoplastic compos-

ites are apparently failing mainly *via* interfacial fracture, it is doubtful whether such design methods would assist in increasing the joint strength, but this approach is currently being examined.

Fractography studies

The scanning electron micrograph of the untreated APC-2 thermoplastic composite is shown in Figure 1 and the grit blasted and solvent cleaned composite in Figure 2. As may be seen, the surface pretreatment has roughened the surface considerably and exposed areas of the underlying fibres. Micrographs of the "adhesive" and "composite substrate" from opposite sides of the fracture plane from double-lap joints bonded with the two-part paste epoxy adhesive are shown in Figures 3a and 3b respectively. The composite side of the joint appears to resemble strongly the abraded surface prior to bonding, see Figure 2. There is no sign of any substrate transfer to the adhesive, either from the visual or electron microscopy observations. Thus, the locus of failure does indeed appear to be along the adhesive/thermoplastic-composite interface. Micrographs of the "adhesive" and "composite substrate" from opposite sides of the fracture plane from double-lap joints bonded with the one-part film epoxy adhesive are shown in Figures 4a and 4b, respectively. However, whilst these micrographs suggest that a considerable degree of interfacing failure occurs there is also evidence that some of the outermost layer of thermoplastic matrix

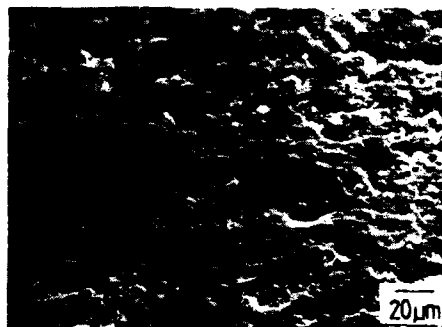


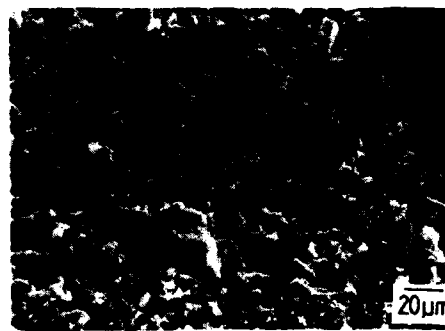
FIGURE 1 Scanning electron micrograph of as-received APC-2 thermoplastic composite.



FIGURE 2 Scanning electron micrograph of abraded/solvent-cleaned APC-2 thermoplastic composite.



(a)



(b)

FIGURE 3 Scanning electron micrograph of fracture surfaces from APC-2/two-part epoxy-paste adhesive joint. (a) "adhesive" side, (b) "composite" side.

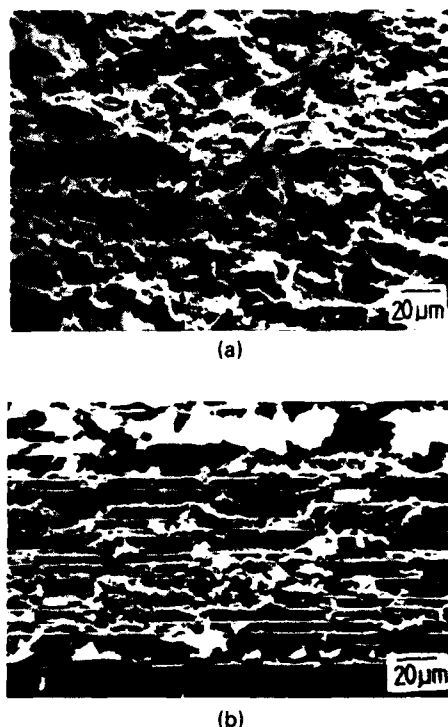


FIGURE 4 Scanning electron micrograph of fracture surfaces from APC-2/one-part epoxy-film adhesive joint. (a) "adhesive" side, (b) "composite" side.

has failed from the fibres. The adhesive side of the fracture plane (Figure 4a) appears to contain some highly-drawn fibrous structure which is not typical of crosslinked epoxy adhesives but might be the thermoplastic matrix of the composite. Also, the composite side (Figure 4b) shows far more exposed fibres compared to the original abraded surface (Figure 2), confirming transfer of some of the outer layer of matrix. Thus, for the joints bonded with the epoxy-film adhesive there is a mixture of failure modes, namely: interfacial, matrix/fibre and interlaminar, the last being observed visually on two joints, as recorded in Table I. The lesser extent of interfacial failure with this adhesive may obviously well be responsible for the higher joint strengths which were observed (Table I).

Comparison of theoretical and experimental joint strengths

One aim of the present initial work was to try and predict the failure loads of the joints using various theoretical analyses. However, all the analyses are based upon the assumption that the adhesive or substrate will be the weakest part of the joint and one cannot predict accurately the joint strength when interfacial failure occurs. The types of joint where least interfacial failure is observed are the double-lap joints employing the epoxy-film adhesive. It is therefore of interest to compare the theoretical and experimental data for this type of joint.

The three failure modes that may be considered theoretically are (a) tensile fracture in the adhesive or "bulk" interlaminar fracture in the composite substrate, (b) shear failure of the adhesive and (c) tensile fracture in the composite substrate, well away from the bonded overlap. The data used in the various analyses are shown in Table II.

Considering firstly the possibility of tensile fracture in the adhesive or "bulk" interlaminar fracture in the composite substrate, then these failure modes arise from the presence of the out-of-plane tensile stresses, σ_{11} . For an elastic adhesive they may be calculated from the equation.⁶

$$\frac{\sigma_{11}(\max)}{\tau_{af}} = \left[\frac{3(1 - \nu_s^2)E_a}{E_s} \right]^{1/4} \left(\frac{d_0}{h_a} \right)^{1/4} \quad (1)$$

where many of the parameters are defined in Table II, d_0 and h_a are the thickness of the outer substrate and adhesive layer respectively and ν_s is the Poisson's ratio of the substrate. Equation (1) yields a

TABLE II
Properties of the epoxy-film adhesive and the substrates used in the theoretical analysis

<i>Adhesive properties:</i>	
Shear modulus	0.80 GPa
Young's (or tensile modulus), E_a	2.16 GPa
Maximum elastic shear stress	31.5 MPa
Plastic shear stress at fracture, τ_{af}	38.8 MPa
Plastic shear strain at fracture	23 %
<i>Thermoplastic-composite substrate properties:</i>	
Young's (tensile) modulus, E_s	64.1 GPa

value of $\sigma_{11}(\text{max})$ of about 40 MPa. This is well below the expected tensile fracture stress of the adhesive (about^{9,10} 55 to 75 MPa) and the "bulk" transverse fracture stress of the thermoplastic (about¹¹ 60 MPa). Hence, the theoretical predictions suggest that tensile fracture in the adhesive or "bulk" interlaminar fracture in the composite substrate is unlikely.

Secondly, considering the fracture strength when the joint fails *via* a shear failure in the adhesive, then the theoretical analysis used was based upon a shear-lag analysis¹² and a computer program, to run on an Apple Macintosh, was written to solve numerically the equations relating the loads to the induced displacements in the joint. The substrates are treated as elastic materials but the adhesive is modelled as an elastic-plastic material. The failure criterion assumed is that joint failure occurs when the shear strain in the adhesive layer, at the ends of the overlap length, attains the value of the maximum shear strain capability of the adhesive. This latter property, along with other engineering shear-properties of the adhesive, was measured using the "thick adherend" test. This test

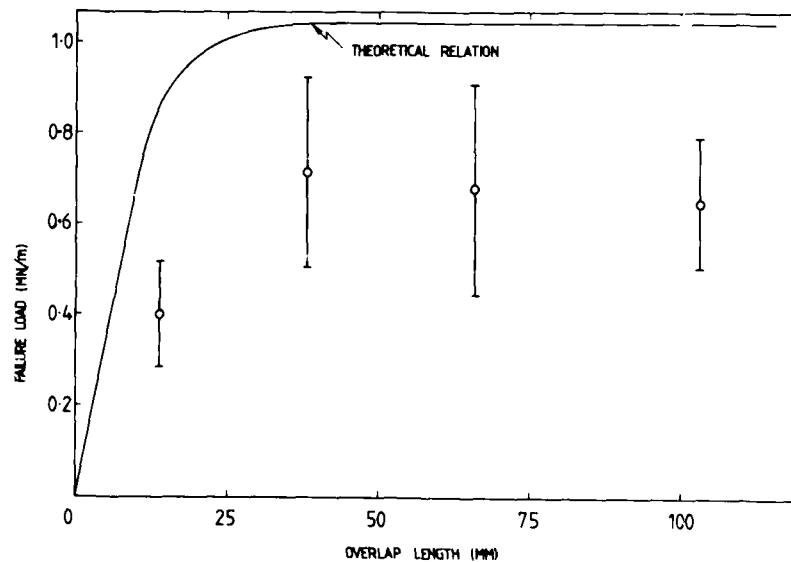


FIGURE 5 Experimental and theoretical relationships between failure loads and overlap length for double-lap joints consisting of APC-2 bonded with an epoxy adhesive.

method was found to give very reproducible results and the data used in the analysis are shown in Table II.

The results of the theoretical analysis are shown in Figure 5, where they are also compared to the experimental results. Both have the same form of relationship between the failure load of the joint and the overlap length. However, the theoretical curve is well above the experimentally measured strengths, again possibly reflecting the considerable amount of interfacial failure observed in these joints.

Thirdly, it is of interest to note that if the joint failed in the composite substrate, well away from the bonded overlap, then the joint strength would be about 1.2 MN/m. This obviously represents the maximum value that may be achieved and values of this order should be obtainable if adequate intrinsic adhesion at the interface(s) is established and attention is given to the details of the joint design.

CONCLUSIONS

The adhesive bonding of a carbon-fibre thermoplastic composite (APC-2) using conventional structural adhesives appears to present some new problems compared to bonding composites based upon thermosetting resin matrices.

The main difference is that joints using the thermoplastic composites exhibit a high degree of interfacial failure. Further, in the case of the better adhesive there is evidence that the joint also fails by the outermost region of the thermoplastic matrix becoming debonded from the fibres. On the other hand, for thermosetting-composite joints a similar abrasion pretreatment to that used on the thermoplastic composites substrates is extremely effective and interfacial failure is rarely observed.

The observed failure mode resulted in the thermoplastic-composite joints possessing relatively low joint strengths and the associated coefficient of variation being high. Further, with such an interfacial failure mode it is difficult to design and predict the failure behaviour of joints. Indeed, whilst a theoretical shear-lag analysis resulted in the correct form for the strength *versus* overlap relation, the predicted strengths, assuming fracture in the elastic-plastic adhesive layer, were significantly higher than the best of the experimentally measured strengths.

Obviously more work is needed to completely identify the mechanisms of failure in thermoplastic-composite joints but it appears that interest should be focussed upon the level of intrinsic adhesion at the adhesive/composite and matrix/composite interfaces. Such studies are currently in progress.

Acknowledgements

The authors are grateful to Westland Helicopters plc for supplying materials and general support for this work.

References

1. F. N. Cogswell, *28th SAMPE, National Sympos. Anaheim, CA.*, 528 (1983).
2. L. W. Crane, C. L. Hammermesh and L. Maus, *SAMPE J.* **12**, (2), 6 (1976).
3. A. V. Pocius and R. P. Wenz, *SAMPE J.* **50**, (Sept./Oct.), 50 (1985).
4. R. D. Adams, R. W. Atkins, J. A. Harris and A. J. Kinloch, *J. Adhesion* **20**, 29 (1986).
5. L. J. Hart-Smith, *Developments in Adhesives 2*, A. J. Kinloch Ed. (Applied Sci. Publ., London, 1981), p. 1.
6. L. J. Hart-Smith, *ASTM, STP 876*, 238 (1985).
7. R. B. Krieger, *Adhesives Age* **28**, (11), 26 (1985).
8. Ministry of Defence (UK), *Defence Standard 03-2/1, Method 0* (1970).
9. A. J. Kinloch, *J. Materials Sci.* **17**, 617 (1982).
10. H. C. Schjelderup and W. B. Jones, *Adhesives Age*, **21**, 35 (1978).
11. Imperial Chemical Industries, *Manufacturer's Data Sheet*.
12. P. J. Grant, *Joining in Fibre Reinforced Plastics* (IPC, Guildford, UK, 1978) p. 41.

Durability and Surface Analytical Studies of Adhesive Bonding to Wood†

D. M. BREWIS, J. COMYN and C. PHANOPOULOS

School of Chemistry, Leicester Polytechnic, P.O. Box 143, Leicester, LE1 9BH U.K.

(Received August 16, 1986)

The effects of aging on adhesively bonded wood joints were examined using non-extracted, water-extracted and solvent-extracted wood. Surface analysis by XPS and SIMS were used to examine the various wood surfaces. The level of surface extractives is seen to be a major influence on the quality of the joints, both in terms of durability and strength.

KEY WORDS Wood, Urea formaldehyde; Phenol resorcinol formaldehyde; durability; XPS; SIMS.

INTRODUCTION

This paper summarises some of our investigations on the interactions between formaldehyde-containing adhesives and soft woods, the work being sponsored by The Building Research Establishment.

Two areas of the work will be considered here. Firstly, durability studies of joints constructed with woods extracted to different levels and secondly some surface analysis, by X-ray photoelectron spectroscopy (XPS) and secondary ion mass spectroscopy (SIMS).

The adhesives used were urea-formaldehyde (UF), and phenol-resorcinol-formaldehyde (PRF) which were kindly supplied by Ciba-Geigy Ltd; they were free from any fillers or extenders. It has long been known that PRF adhesives are superior to UF's in both

† Presented at the Tenth Annual Meeting of The Adhesion Society, Inc., Williamsburg, Virginia, U.S.A., February 22-27, 1987.

durability and strength.¹ Our principal interest, however, has been to discern the mechanism of adhesion to wood and to determine if possible which groups in wood may be involved in bonding.

DURABILITY

Scots pine (*Pinus sylvestris*) was cut and planed to a British Standard² single lap dimensions and subsequently prepared in one of the following ways.

- a) Non-extracted;
- b) Water-extracted. This was achieved by immersing the substrates in boiling water for 7 hours.
- c) Solvent-extracted. This was achieved by extraction in a Soxhlet apparatus with each of the following solvents in sequence for more than 12 hours each³: dichloromethane, benzene/ethanol (2:1 by vol.), acetone, methanol. This procedure is responsible for the removal of extractives. Only a small amount of lignin is removed.

Single lap joints (25 mm × 25 mm overlap) of Scots pine wood were constructed with UF or PRF and left to cure. After two weeks, the bonded joints were placed in a glove box at >95% relative humidity and 30°C, and left for various lengths of time up to 1800 hours. The aged joints were then tested to destruction on a Monsanto Tensometer with a crosshead speed of 5 mm min⁻¹. Strengths of aged joints are shown in Figures 1 and 2.

X-RAY PHOTOELECTRON SPECTROSCOPY

This work was carried out on a VG ESCALAB Instrument using X-ray energy (AlK_{α}) = 1486.6 eV. The analysis area was approximately 5 mm × 5 mm and the beam diameter 6 mm. The samples were 100 μm sections of spruce (*Picea abies*) cut with a microtome. Some samples were aged at >95% RH at 30°C for six weeks. The results of these analyses are shown in Table I. XPS has a sampling depth of 5–10 nm.⁴

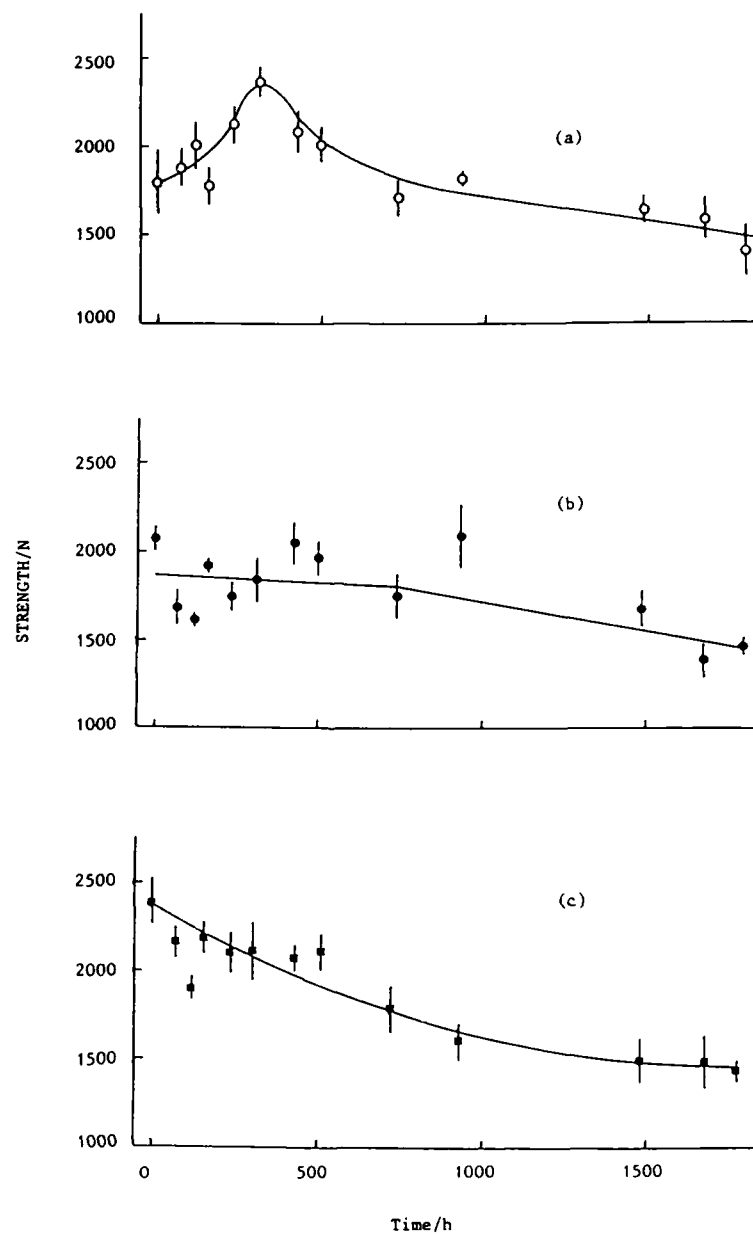


FIGURE 1 Strengths of UF bonded Scots pinewood joints on exposure to moist air at 30°C. (a) non-extracted, (b) water-extracted, (c) solvent-extracted.

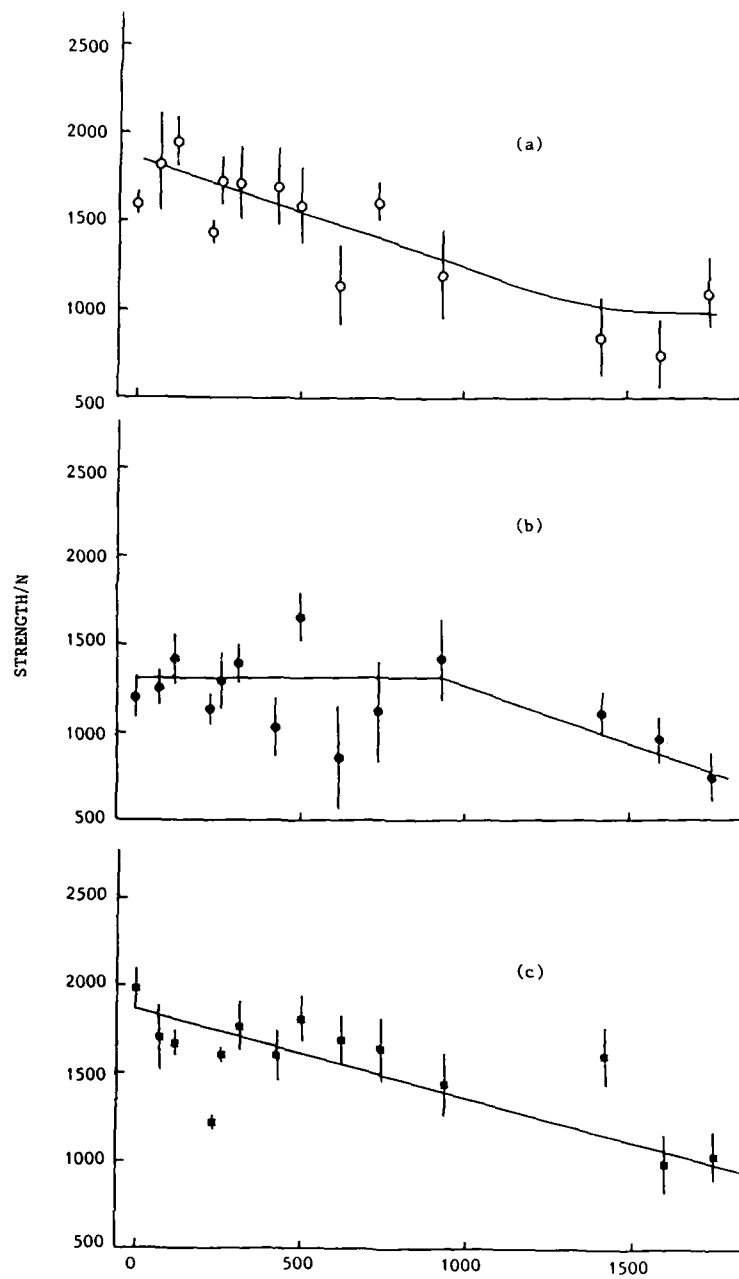


FIGURE 2 Strengths of PRF bonded Scots pinewood joints on exposure to moist air at 30°C. (a) non-extracted, (b) water-extracted, (c) solvent-extracted.

TABLE I
XPS analysis of non-extracted, water-extracted and solvent-extracted sprucewood,
before and after aging

Sample	% Atom composition				
	C	N	O	Contaminants	O/C Ratio
Non-extracted	80.9	0.0	18.3	0.9 (Si)	0.23
Water-extracted	84.3	0.0	14.6	1.1 (Si)	0.17
Solvent-extracted	70.9	0.0	25.6	2.6 (Si)	0.36
Aged non-extracted	83.3	0.0	16.7	0.0	0.20
Aged water-extracted	69.5	1.7	27.1	1.7 (Fe)	0.39
Aged solvent-extracted	63.5	0.0	36.5	0.0	0.57

SECONDARY ION MASS SPECTROSCOPY

This work was undertaken on a VG instrument with a MM 12-12 quadrupole mass spectrometer. The analysis area was 6×6 mm, primary beam current 0.4×10^{-9} A and the primary ion was Xe^+ (2 keV). Secondary ions are ejected from the surface and analysed in a mass spectrometer. SIMS spectra of wood contain a large number of fragments and Figures 3 and 4 are given as examples.

Table II lists the samples that were studied by SIMS. In order to investigate the mechanism by which adhesives bond to wood, some samples were treated with the adhesive components, intermediates or model compounds which are listed in Table II. By comparing spectra of treated and untreated woods we were able to attribute changes to interactions between the adhesives and wood.

DISCUSSION

The results of tensile strength tests of aged joints (Figures 1 and 2) show a number of features common to both adhesives. Firstly, for the first 800 hours of aging, solvent-extracted wood provides stronger joints than non-extracted wood, and these in turn are stronger than water-extracted wood joints. Secondly, for approximately the first 1100 hours of aging, the water-extracted wood joints show no weakening. Finally, after approximately 1000 hours aging, joints with the three types of wood converge to approximately the same strengths.

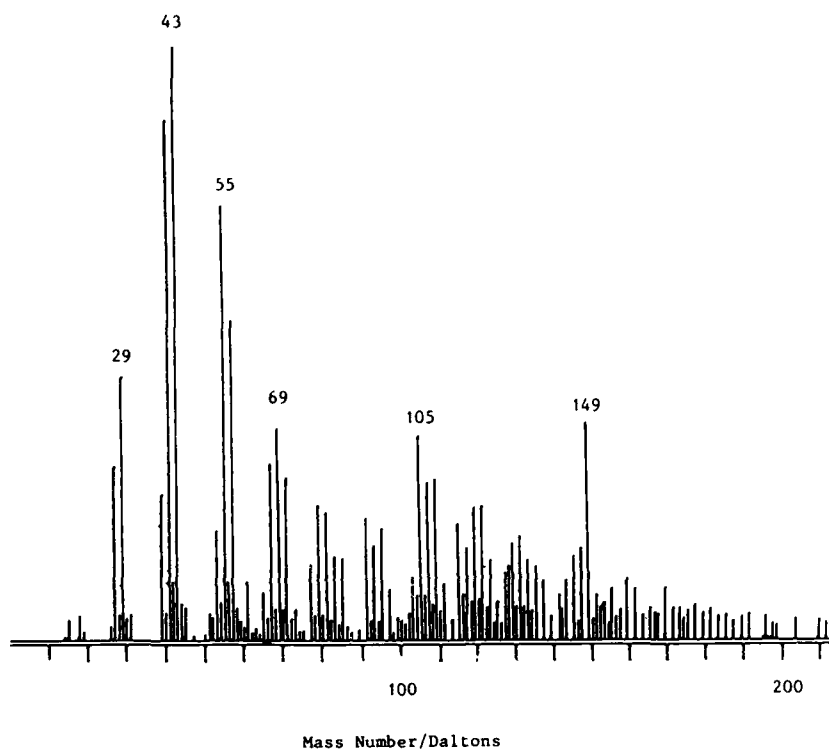


FIGURE 3 Positive ion SIMS spectrum of urea-doped, non-extracted spruce.

How can these changes be explained? It seems that the extractives content at the surface influences bond strengths. This is indicated by the XPS data which shows the oxygen to carbon ratio varying with level of extraction. However, the amounts of extractives are also related to the availability of cellulose; high levels of extractives may restrict adhesives entering the wood pores.

For water-extracted wood, resin penetration is reduced and some of the resin-extractive bonds will form to the detriment of the resin-cellulose bonds. Indeed, strengths of the water-extracted wood joints are initially stable and do not decrease. This suggests a certain amount of hydrolytic stability of these interactions.

The solvent-extracted and non-extracted woods allow increased adhesive penetration and have more cellulose available for bonding

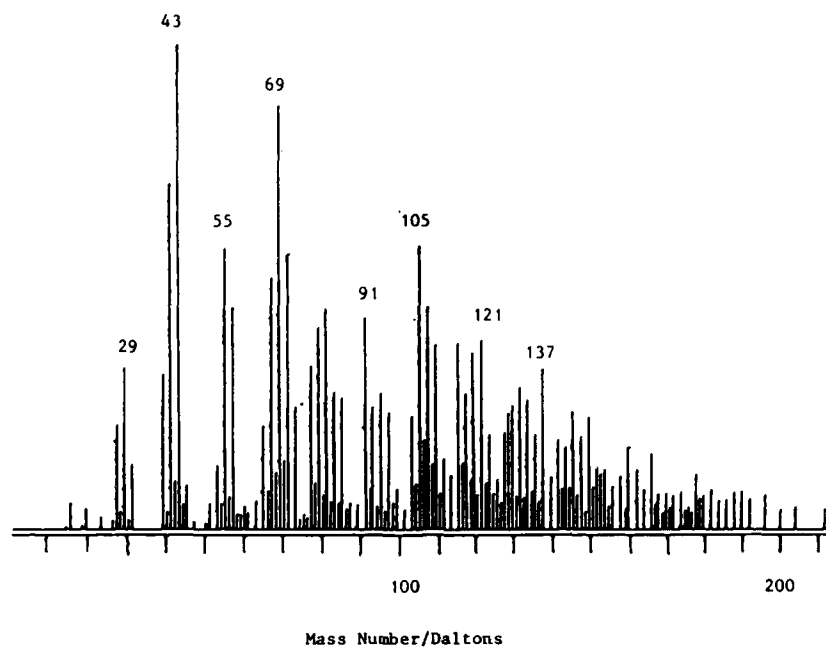


FIGURE 4 Positive ion SIMS spectrum of non-extracted spruce.

TABLE II
Samples analysed by SIMS

1. Solvent-extracted and non-extracted spruce.
2. Solvent-extracted and non-extracted Scots pine.
3. Softwood lignin.
4. Urea-treated, non-extracted spruce and urea.
5. Dimethylol urea-treated, non-extracted spruce and dimethylol urea.
6. Methylene diurea-treated, non-extracted spruce and methylene diurea.
7. Phenol-treated, non-extracted spruce.
8. 2-hydroxybenzyl alcohol (2-HBA)-treated, non-extracted spruce and 2-HBA.
9. Bis(2-hydroxyphenyl)methane (B2-HBM)-treated, non-extracted spruce and B2-HPM.
10. Paraformaldehyde-treated, non-extracted spruce and paraformaldehyde.
11. Cured detached films of UF, PRF and melamine-formaldehyde (MF) adhesives.

TABLE III
Number of SIMS spectral changes observed on
doping non-extracted spruce

Dopant	Cellulose- lignin	Extractive
Urea	77	48
Phenol	9	20
Formaldehyde	41	47
Methylene diurea	23	33
Dimethylol urea	15	23
B2-HPM	14	32
2-HBA	47	51

compared to water-extracted wood. These two factors could account for the superior strengths of joints with these types of wood.

SIMS may provide information on the manner in which molecules are attached to wood and, as an example, spectra of non-extracted spruce both before and after treatment with urea are shown in Figures 3 and 4. These reveal the formation of new fragments (*e.g.* $M = 64$) and the loss of others (*e.g.* $M = 148$). Further, there are numerous changes in relative intensities (counts) of other fragments. By comparing non-extracted and extracted spruce spectra, we were able to identify whether the fragments originated from cellulose plus lignin or from the extractives. Thus, spectral changes on doping can be related to dopant-wood component interactions. In this way, Table III shows the number of spectral changes observed for urea and other dopants which indicate interactions with either cellulose-lignin or extractive components. We have regarded a spectral change as worthy of counting only when its intensity changes by more than 20%. Most of the intensity changes were in fact much greater than 20%. Also, for the doped wood, several new peaks appeared while others were lost when compared to the spectra of the dopant and the treated wood. These results indicate strong chemical interactions between the dopant and wood.

XPS has shown that, during aging, the remaining extractives migrate to the wood surface. Hence, the surfaces of the three types of wood come to resemble each other. This would account for the convergence of the strengths of joints constructed with the three types of wood.

References

1. J. M. Dinwoodie, in *'Wood Adhesives, Chemistry and Technology'*, A. Pizzi, Ed. (Marcel Dekker Inc., New York and Basel, 1983). Chap. 1.
2. BS1204: Part 2: 1979 Synthetic Resin Adhesives (Phenolic and Amino-plastic) for Wood Specifications for Close Contact Adhesives.
3. D. Rodwell, Private Communication, (1983).
4. D. Briggs and M. P. Seah, *Practical Surface Analysis by Auger and X-ray Photoelectron Spectroscopy* (John Wiley and Sons, New York, 1983).

The Effect of Electrochemical Potentials on the Durability of Rubber/Metal Bonds in Sea Water†

A. STEVENSON

Materials Engineering Research Laboratory, Ltd, Tamworth Rd., Hertford SG13 7DG, U.K.

(Received October 3, 1986)

A study of the role of electrochemical potentials on the durability of rubber/metal bonds in seawater is described. In electrochemically inert conditions, these adhesive bonds are shown to be extremely stable—even after more than 3 years immersion in seawater. However, some bond failure is shown to be possible within days—when the rubber is bonded to the more noble of a pair of metals in electrical and electrolytic contact. Resistance to bond failure increased as the cathodic potential was decreased. Mechanical strain in the elastomer layer was shown to have no effect on bond durability.

INTRODUCTION

The difference in electrochemical potential between dissimilar metals in electrical and electrolytic contact causes electron flow between them which usually increases the corrosion attack of the more active metal and reduces that of the more noble metal. While corrosion attack of the more noble metal is decreased, it has been shown¹ that the rate of adhesive bond failure between it and rubber

† Presented at the Tenth Annual Meeting of The Adhesion Society, Inc., Williamsburg, Virginia, U.S.A., February 22–27, 1987.

can be strongly increased. This phenomenon is of potential importance for a number of applications in the Offshore Oil and Gas industry,² where rubber/metal composite bearings or rubber coated pipework are used in close proximity to steelwork protected from corrosion by means of sacrificial anodes or impressed currents. The usual assumption that the rubber coated regions will be unaffected by such cathodic protection are not always true since the latter can cause bond failure between the rubber and the metal.

Previous work¹ reported a study of this effect for rubber/carbon steel, Inconel and titanium. Electrochemical potentials were provided by the natural differences arising from their combination with carbon steel. In addition to the laboratory tests, the results of steel, Inconel and titanium. Electrochemical potentials were provided by the natural differences arising from their combination with carbon steel. In addition to the laboratory tests, the results of parallel deep sea trials at a water depth of 450 ft are also discussed. Finally, the results of some model experiments with testpieces immersed with a positive compressive stress applied to retard the progress of bond failure and with testpieces immersed in a very high pH solution are presented. The results of all these experiments are discussed in terms of the evidence they provide for the likely physical mechanisms involved.

EXPERIMENTAL DETAILS

The testpieces were of the double shear type, consisting of 2 rubber and 3 metal discs of 25 mm diameter alternately bonded in the configuration shown in Figure 1(a). Each testpiece thus has 4

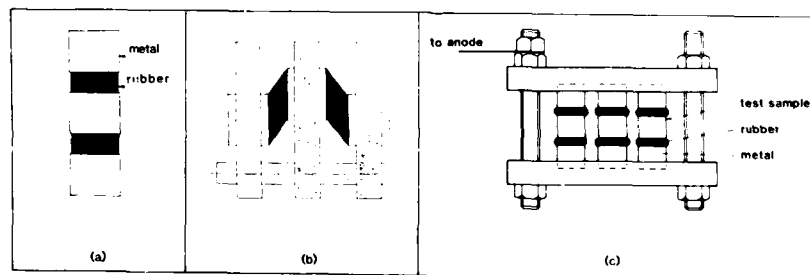


FIGURE 1 Testpiece geometry (a) unstrained (b) simple shear (α 100%). (c) compression @ 25%.

TABLE I
Metal surface preparation and bonding technique

All adhesive bonds were formed in accord with the procedure below:

1. Metal surface degreased with trichloroethane
2. Metal surface grit blasted to white/grey finish with grade 60/80 Aluminium Oxide
3. Cleaned with trichloroethane
4. Within 30 minutes of drying—primer coat (Chemlock 205) applied
5. Within 30 minutes of drying—bonding agent (Chemlock 220) applied
6. Within 30 minutes of drying—metal parts placed in rubber mould
7. Cured *in situ* with rubber—2 hrs @ 125°C

rubber/metal bonded surfaces. The 2 rubber layers were each of 10 mm thickness. The different types of metal used were: (A) carbon steel, (B) Inconel, (C) stainless steel, (D) pure titanium and (E) titanium alloy. The composition of the rubber used was the same for all testpieces. This was a sulphur cured Natural Rubber filled with carbon black.

All metal endpieces of all types underwent the same procedure for forming the adhesive bonds. This is described in Table I. During the test program about 500 testpieces were produced in this way in several batches. Quality control checks were performed on about 25 testpieces removed at random before commencement of the main body of tests. Of these, some were pulled to failure dry, in shear, on a Zwick test machine and some were immersed in sea water for 3 days and then pulled to failure. Such a quality control testpiece was considered to be a failure if there was any sign whatsoever of failure at the metal surface (i.e. 100% rubber failure was required). If a single quality control failure was discovered, then the whole batch was rejected. In addition, the shear modulus of each testpiece produced was measured over the strain range 0–25%. This was required to be within 5% of 0.8 MPa. For some batches, the shear modulus was within 2% of the mean value. This checked the cure and quality of the rubber. Standard tensile, tear and fatigue tests were also performed for each batch of mixed rubber.

At an early stage of the program it was found that the surface roughness of the metal could have a strongly detrimental effect on bond durability after 3 days in sea water—although dry control tests showed no difference. Too fine or inadequate grit blasting could lead to premature failures and one batch of testpieces was rejected for this reason. However, when the procedure in Table I was

TABLE II
Summary of bond failure penetration depths at different
imposed cathodic potentials during sea water exposure at
23°C

Cathodic potential	Induction period (days)	Rate of bond failure {mm/(day) ^{1/2} }	Maximum penetration depth (mm)
1050 mV	1	1.0	15
950 mV	5	1.0	9
850 mV	5	1.0	9
750 mV	20	1.0	7
610 mV	30	1.0	4
0 mV	>1000	—	0

followed carefully there were no failures of this quality control test and no rejects at all.

After the quality control checks, most testpieces were mounted in jigs to hold the rubber layers at 100% shear strain, (see Figure 1(b)), and immersed in sea water. These holding jigs were fabricated from the same grade carbon steel as the carbon steel testpieces. All parts of the jigs were coated in Chemlock 220 to inhibit gross corrosion. However, on fitting the testpieces, metal at the inner faces of the holes was bared so that the metal of the testpiece and the carbon steel jig may be considered to have been in electrical contact from the outset. In this way, when carbon steel was not used in the testpiece there would be a local electrical potential derived from the relative positions of the two dissimilar metals in the galvanic series.

All testpieces were immersed in a large excess (35 litres) of synthetic sea water, prepared in accordance with the ASTM standard.³ All trace heavy elements were included as provided for in the standard. The water pH was measured initially as 8.2. The initial oxygen content was 8 (± 1) mg/l.

After various exposure times, testpieces were removed from the sea water tanks and evaluated for the extent of any bond failure. This evaluation consisted in removing the testpiece from its restraining jig and pulling to failure on a Zwick 1740 universal test machine. The shear modulus, stress and strain at break was recorded, and then all bond surfaces were mapped to provide an accurate record of the area of bond failure. These measurements enable the results to be plotted in terms of failure penetration

depth, % area of bond failure, and stored elastic energy required to cause failure. In this paper, the results are discussed primarily in terms of the failure penetration depth. This was taken as the average of the maximum penetration depths of bond failure over each of the four bonded surfaces.

RESULTS

The effect of high cathodic potentials

The highest potential was provided by means of the system illustrated in Figure 2, namely using a Zinc sacrificial anode in combination with carbon steel/rubber testpieces. This produced a measured cathodic potential of 1040–1070 mV at the testpiece surface (with reference to a Ag/AgCl reference electrode). There then resulted fairly rapid bond failure at all temperatures tested but no corrosion of the carbon steel. Figure 3 shows typical failure surfaces from these tests. Each failure surface consists of three regions. There is a lower black region where failure occurred through the rubber. This region was asymmetrically located because in simple shear bond failure was always observed to initiate at the leading edge. This is the point where local shear or surface tensile strains in the elastomer are a maximum. Adjacent to the region of

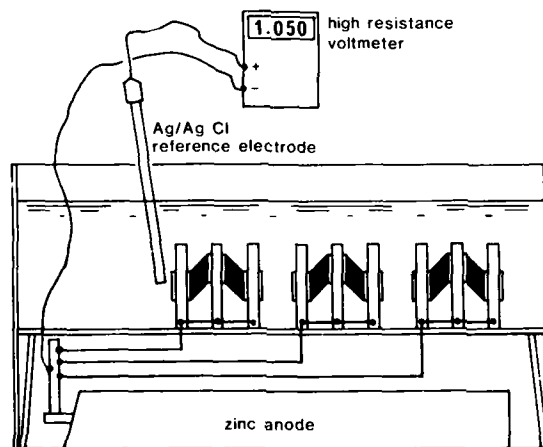


FIGURE 2 Test arrangement for tests at high cathodic potentials.

(a) 45° C



(b) 3° C

FIGURE 3 Typical bond failure surfaces (a) sea water exposure at 3°C (b) sea water exposure at 45°C.

rubber failure is a grey region where the failure locus was predominantly at the bond between the metal and the primer coating. Small rubber particles were, however, left adhering to the steel in places in this region. The bond failure seen here occurred only as a result of the pull to failure test. The uppermost failure region in the photographs of Figure 3 shows a powder deposit. This was a bluish colour for tests at 3°C and a cream white colour for tests at 45°C. The colour was intermediate at 23°C. Chemical analysis showed the blue-white deposit to contain predominantly magnesium (Mg) with lesser amounts of S, Cl, Ca, Fe and Zn while

the cream-white deposit was predominantly Zinc (Zn) with lesser amounts of S, Ca, Mg, S and Cl. All of these elements were constituents of the sea water used in the experiments. These deposits formed on the steel surface after bond failure had occurred. The deposits were observed to increase in thickness until, after about 200 days of sea water exposure, they filled the gap opened between rubber and metal by bond failure. Similar deposits also occurred on all other exposed electrically connected steel surfaces and were, of course, an indication that the cathodic protection provided by the sacrificial zinc anodes was working correctly.

When determining any change in adhesive bond strength (interfacial failure energy), it is important to know if there was any change in the cohesive strength of the rubber. Clearly, if the rubber strength decreased during a test then the area of bond failure could be anomalously lower than would be the case if the rubber strength remained constant. To investigate this point, the energy required to cause fracture was measured by integrating the force/deflection curve from the shear pull to failure test. This energy was then divided by the total rubber volume to derive a characteristic stored energy density, W , at fracture. In the absence of bond failure, W can be used to characterise the critical tearing energy of the rubber—and indeed then yields a value comparable with results from standard tear tests. With an area of bond failure, however, the fracture geometry is more complicated, although the same approach can be used. It is sufficient for present purposes to describe the results empirically. Figure 4 shows the stored energy density plotted against sea water exposure time for each testpiece with a cathodic potential of 1050 mV (the largest areas of bond failure). The root exposure time, in fact, correlated with area of bond failure—the latter acting as a starter crack for subsequent cohesive fracture through the rubber. As a control experiment, a set of new dry testpieces were cut at the bond to various depths—simulating the full range of bond failure depths observed. The geometry of bond failure was also simulated. These testpieces failed at identical failure energies, W , to the testpieces that had exhibited bond failure, following sea water exposure for up to 2 years. This shows clearly that there was *no* significant change in rubber strength during the tests. The failure penetration depths are thus entirely representative of changes in adhesive bond strength.

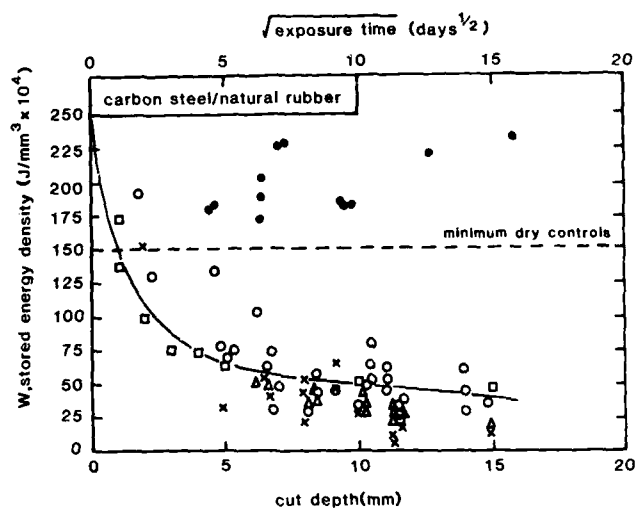


FIGURE 4 Stored elastic energy at failure vs bond exposure time @ 1050 mV Δ 3°C, \circ 23°C, \times 45°C; vs bond exposure time—zero potential \bullet all temps; vs cut depth—dry control testpieces \square .

The characteristic stages of the bond failure process are illustrated in Figure 5, where bond failure penetration depth has been plotted against the square root of seawater exposure time. If diffusion processes are involved, then a linear relation between penetration depth and $(\text{time})^{1/2}$ would be expected from classical theory.

The first stage was a time lag observed before any bond failure could be measured (*i.e.* less than 0.5 mm failure penetration depth). This "induction period" increased with decreasing potential and decreasing temperature. The second stage was a period of increasing penetration of bond failure into the testpiece as an approximately linear function of the square root of exposure time. This enabled a failure penetration rate to be defined for each test condition. Finally, there was an approach to an "equilibrium" depth of bond failure. For the testpiece design used, the maximum possible depth was 15 mm (assuming some asymmetry). In a number of cases the equilibrium failure penetration depth was found to be considerably less than 15 mm.

Additional tests were performed to investigate the effect of lower

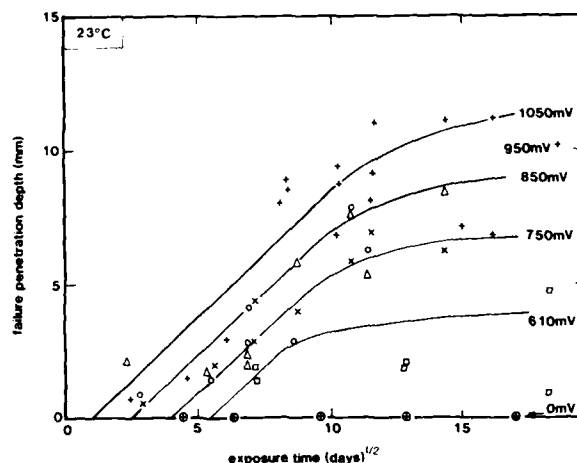


FIGURE 5 Penetration depth of bond failure vs root seawater exposure time 1050 mV, Δ 950 mV, \circ 850 mV, \times 750 mV, \oplus 0 mV. All tests at 23°C. All NR/carbon steel testpieces.

potential differences on carbon steel testpieces than was possible using zinc anodes. For this purpose, a potentiostatic arrangement was installed which supplied a constant impressed current at a chosen potential difference. A series of platinum electrodes were installed and connected to a current source to provide constant cathodic potentials of 0.95 V, 0.85 V, 0.75 V and 0.61 V at the bond edge of the carbon steel testpieces. The same general test method was used as described for the experiments with zinc anodes. Separate sea water tanks were used for each different cathodic potential. All test with impressed currents were performed at 23°C. The results are shown in Figure 5.

Substantial delamination was observed after long sea water exposure periods in all cases. No steel corrosion was observed with cathodic potentials of 950 mV or 850 mV, although some was observed after long periods with 750 mV and more with 610 mV. There were now no thick powder deposits on exposed steel surfaces. There were again no changes in modulus or energy at break that could not be attributed to the geometrical changes caused by bond failure—*i.e.* no changes in the rubber itself.

There was a progressive increase in induction period as the level

of imposed cathodic potential was reduced—from 1 day at 1050 mV to 30 days at 610 mV. After the induction period was completed and bond failure began to be observed, the failure penetration rates were, however, the same for all potentials as far as could be ascertained within the limits of experimental error. This rate was $1.0 (\pm 2) \text{ mm}/(\text{day})^{1/2}$. After very long exposure periods (up to 3 years), the penetration depth approached an equilibrium value which increased from 4 mm at 610 mV to the maximum possible ($\geq 12.5 \text{ mm}$) at 1050 mV. These results are summarised in Table II. Identical testpieces exposed to sea water in the same restraining jigs (Figure 1(b)) but without electrical connection to a potentiostat or to a dissimilar metal (*i.e.* 0 mV) showed no bond failure whatsoever—even after more than 3 years sea water exposure.

The effect of dissimilar metals in contact

Testpieces using metal parts of Inconel, two types of titanium and stainless steel were exposed to seawater at 3°C, 23°C, and 45°C in separate tanks. The testpieces were strained to 100% shear in the holding jigs shown in Figure 1(b). These holding jigs were all fabricated from carbon steel. The system was not electrochemically inert for the Inconel, stainless steel or titanium testpieces, and the possibility existed of electrochemical interactions between the dissimilar metals in contact—throughout the seawater exposure period. The outer surfaces of the holding jigs were initially painted with a chlorinated rubber coating to prevent gross corrosion of the carbon steel. However, this only lasted about 1 year and after this some corrosion of the holding jigs could be observed with a layer of corrosion product over the floor of the test tank. Carbon steel testpieces were also mounted in the carbon steel holding jigs and electrically connected to a large block of zinc to create a known cathodic potential of 1050 mV.

The full set of results are shown in Figure 6, where the failure penetration depth has been plotted against the root seawater exposure period for all electrochemical conditions and all temperatures. Again (*cf* Figure 5) there was a definite time lag or induction period before any bond failure could be observed. This time lag increased with decreasing temperature and decreasing cathodic potential. The dissimilar metal combination showing the largest

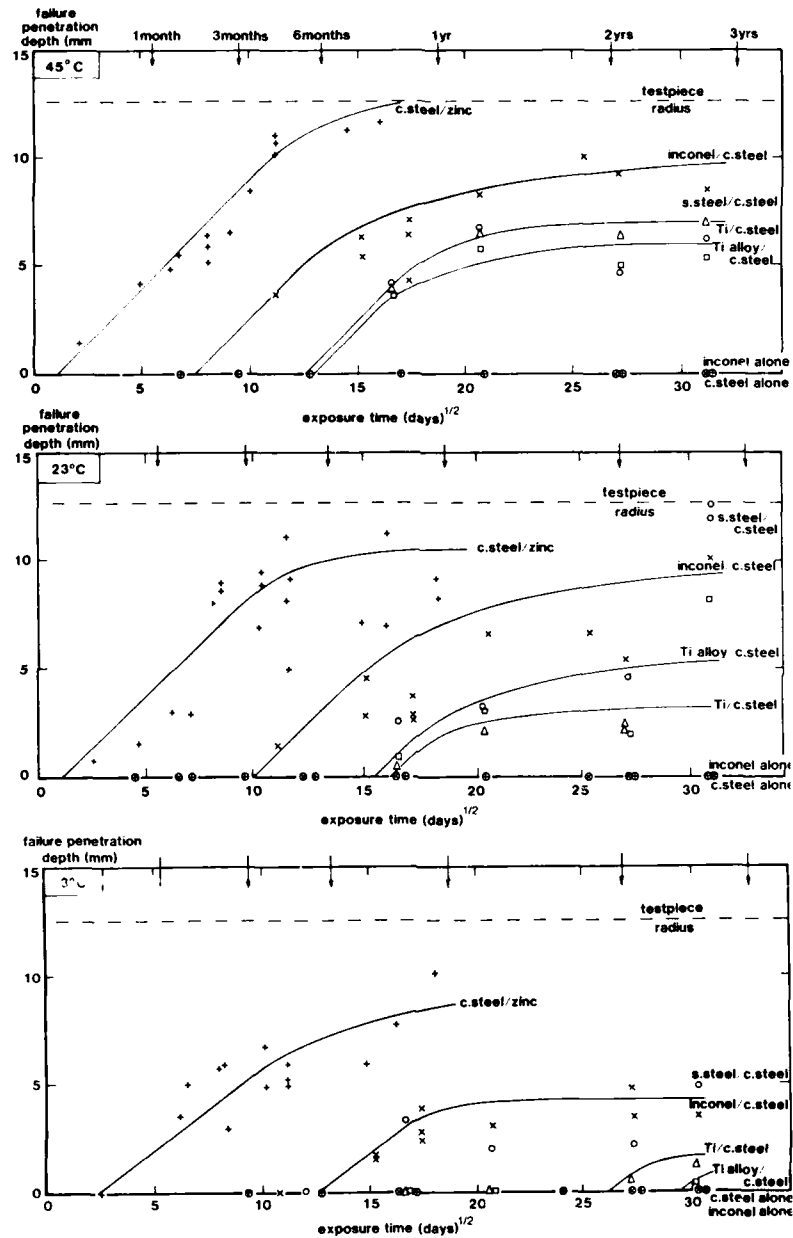


FIGURE 6 Penetration depth of bond failure vs root seawater exposure time (a) 3°C (b) 23°C (c) 45°C. + carbon steel/zinc; ○ stainless steel/carbon steel; × inconel/carbon steel; Δ pure titanium/carbon steel; U titanium alloy/carbon steel; ⊕ carbon steel alone; ⊗ inconel alone.

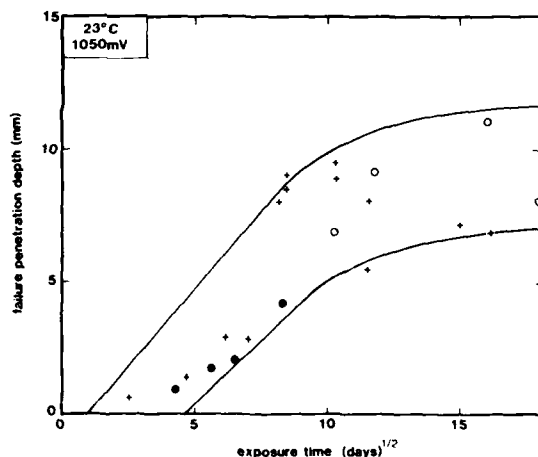
cathodic potential was carbon steel/zinc, at 1050 mV. The exact values of the local potentials caused by the other metallic combinations were not known, but would be considerably less than 1 V. The measured rates of failure penetration were all $1.0 (\pm 0.2) \text{ mm}/(\text{day})^{1/2}$ within experimental error—for all temperatures and all electrochemical conditions. It is possible that there were small differences in rate with temperature, but experimental precision does not permit this to be stated. There appeared to be an approach to a final "equilibrium" depth of bond failure in all cases. This increased with increasing temperature and increasing cathodic potential. These results are summarised in Table III below. It is interesting that the most striking differences are all in induction period—which increased with decreasing temperature or decreasing potential.

Effect of elastomer strain

The asymmetric appearance of the region of bond failure in Figure 3 suggested that elastomer strain may influence the bond failure penetration depth. To investigate this possibility, a series of experiments was performed using different elastomer strains. Twelve carbon steel testpieces were exposed to seawater with a cathodic potential of 1050 mV but zero elastomer strain. A further set of similar testpieces was subjected to 25% compression strain in the holding jigs shown in Figure 1(c). The results of these tests, which were all performed at 23°C are shown in Figure 7.

TABLE III
Summary of bond failure penetration depths for different combinations of dissimilar metals during seawater exposure at 3°C, 23°C, and 45°C

Condition	Induction period (days)			Maximum penetration depth (mm)		
	3°C	23°C	45°C	3°C	23°C	45°C
C. steel/Zn	5.8	1.1	0.8	10	11	15
Inconel/c. steel	151	96	53	5	11	10
S. steel/c. steel	151	96	53	5	10	7
Ti/c. steel	676	262	154	>2	6	7
Ti alloy/c. steel	864	237	164	>1	4	6
Inconel alone	>1000	>1000	>1000	0	0	0
C. steel alone	>1000	>1000	>1000	0	0	0



possibility of, for example, pitting corrosion on stainless steels in seawater. In the present case, it is possible that some change occurs to the metal oxide surface during the induction period before any bond failure is observed. Thereafter, the rate of failure may be determined simply by a reaction rate—possibly influenced by the rate of diffusion of electrolyte through the metal primer layer.

When two dissimilar metals are in electrical and electrolytic contact, the difference in electrochemical potential between them will cause electron flow. Corrosion of the more noble metal is usually decreased and that of the more active metal is increased. It is normally considered⁴ that any electrochemical reaction can be divided into oxidation and reduction reactions and that there can be no net accumulation of electric charge during such reaction. From this, the evolution of hydrogen at the cathode (more noble metal) is likely. It is possible that this evolution of molecular hydrogen enters into an adverse reaction with the primer coating on the metal, such that the bond integrity is destroyed.

There was no evidence of the evolution of hydrogen gas during the tests. The physics of the adhesive bond formed between the interfaces metal/primer/bonding agent/rubber is not well understood at any of these interfaces. The extremely strong and durable nature of the bonds even after prolonged exposure to moisture (in the absence of electrochemical reactions) makes it unlikely that they simply involve secondary intermolecular forces. On the other hand they do possess some features (*e.g.* rapid dissolution in the presence of certain selected solvents) that make it unlikely that they are all primary chemical bonds. It is possible that some form of ionic bonding contributes to perhaps the normal secondary intermolecular bonding thought to occur for other adhesive systems. Such bonds may be relatively more susceptible to disruption by electron flow and electrochemical activity.

These experiments lead to the conclusion that it is *only* in the presence of electrochemical activity that these rubber/metal bonds fail. In electrochemically inert conditions rubber/metal bonds have been found to be completely stable, even after 3 years seawater exposure and significant water absorption by the rubber.

Acknowledgements

The author would like to thank C. G. Doris, Paris, for permission to publish that

part of this work which formed a part of their Deep Water Gravity Tower development program. This program has been supported technically and financially by Chevron, Phillips Petroleum, Britoil, Texaco, Elf Aquitaine, Total CFP, Arco, Shell Oil (US) and the EEC.

References

1. A. Stevenson, *Int. J. Adhesion & Adhesives* **5**, 81-91 (1985).
2. F. Sedillot, R. Monier, and A. Stevenson, *Proc. 18th Offshore Technology Conference, OTC 5232*, Houston, May 1986.
3. ASTM *Standard Specification for Synthetic Ocean Water*, ASTM D1141-75 (Am. Socy. for Testing & Matls., Philadelphia, 1975).
4. R. Baboian and G. S. Haynes, *Corrosion in Natural Environments*, ASTM STP 558 (Am. Socy. for Testing & Matls., Philadelphia, 1974), pp. 171-184.

The Effect of Water on Matrix/Filler Adhesion in a Polyurethane Elastomer†

M. R. BOWDITCH and K. J. STANNARD

Admiralty Research Establishment, Holton Heath, Poole, Dorset BH16 6JU, U.K.

(Received July 24, 1986)

The static "moduli," failure stresses and dynamic moduli of both filled and unfilled polyurethanes were measured over a range of equilibrium water contents and these results are compared with those obtained from dry controls. Where barium sulphate was employed as the major filler component, it is shown that the presence of as little as ~0.7% water results in a profound degradation of mechanical properties with the loss of most of the contribution attributable to the presence of fillers as a result of hydrolytic disruption of filler/matrix adhesion. A quantitative relationship between water content and mechanical properties is established and the mechanics of the water/polymer/filler interaction are considered. Less dramatic effects were observed when barium sulphate was replaced by iron oxide and these were apparently further reduced by the use of a silane coupling agent.

KEY WORDS Failure stress; matrix/filler adhesion; mechanical properties; polyurethane elastomer; silane coupling agent, water absorption.

INTRODUCTION

The rubber investigated was a polyether-based polyurethane system, cured with a polymeric 4,4'-diisocyanatodiphenylmethane cross-linked with trimethylol propane and filled with barytes (and small amounts of fumed silica and carbon black) or iron oxide.

† Presented at the Tenth Annual Meeting of The Adhesion Society, Inc., Williamsburg, Virginia, U.S.A., February 22-27, 1987.

This material was of interest because of its acoustical properties. In certain applications such materials are required to possess a high attenuation and to match closely the sound propagating medium; in this case water. The impedance (z) of a material is a function of density (ρ) and velocity of sound within the material (c) as follows:

$$z = \rho \cdot c$$

It is often necessary to incorporate air in such materials to facilitate the shear deformations associated with high energy absorption. However, the inclusion of air leads to the reduction of c from typically 1500 m s^{-1} to lower values and, in order to re-establish matching, high density fillers, such as barytes or iron oxide are commonly used. In this work only air-free material has been investigated.

EXPERIMENTAL

Dumbbells and other test pieces were cut from material sliced to about 1 mm thickness from cast sheet.

Low equilibrium water contents, up to about 1% w/w, were obtained by exposing material to environments of known relative humidity over saturated salt solutions. Higher values were achieved by immersing specimens in salt solutions and in distilled water. Equilibrium conditions were assumed to be established when specimens, equal in thickness to the prepared test pieces, failed to increase in mass after further exposure to the experimental environment.

Static "moduli" (at 20% extension) and failure stresses were measured using an Instron 1185 tensometer linked to a Hewlett Packard 85 computer. Six replicates were evaluated in each case and mean values are reported. Dynamic moduli were measured using a Polymer Labs Dynamic Mechanical Thermal Analyser (DMTA) machine, generally at 10 Hz. Surface area determinations were carried out using a Micromeritics 2200 high speed surface area analyser. Chemical analyses were undertaken with the use of a Varian AA 775 atomic absorption spectrometer and by classical qualitative methods.

Diffusion coefficients were measured on thin films, typically

0.5 mm thick. These films were immersed in distilled water at 20°C from which they were removed at intervals, mopped superficially dry and weighed before being returned to the water. Plots of percentage mass increase against root time in hours were prepared and diffusion coefficients were calculated¹ from the relationship:

$$D = \left(\frac{\text{slope} \times l}{m_{\infty}} \right)^2 \times 5.45 \times 10^{-11} \text{ m}^2 \text{ s}^{-1}$$

where D is the diffusion coefficient, slope is the initial linear slope of the water uptake *vs* root time plot, l is the thickness of the specimen in mm and m_{∞} is the solubility of water in the material expressed as a percentage.

RESULTS AND DISCUSSION

"Modulus" values for both barytes-filled and unfilled material were obtained at various equilibrium water concentrations and plots of these results against water content are given in Figure 1. At the same time, failure stress results were also generated and these are presented in Figure 2. These figures show clearly the dramatic effect

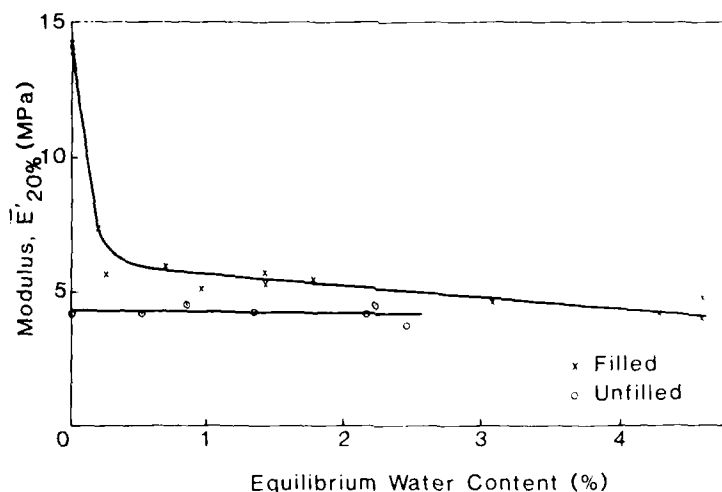


FIGURE 1 The effect of water on "modulus" of both filled and unfilled polyurethane.

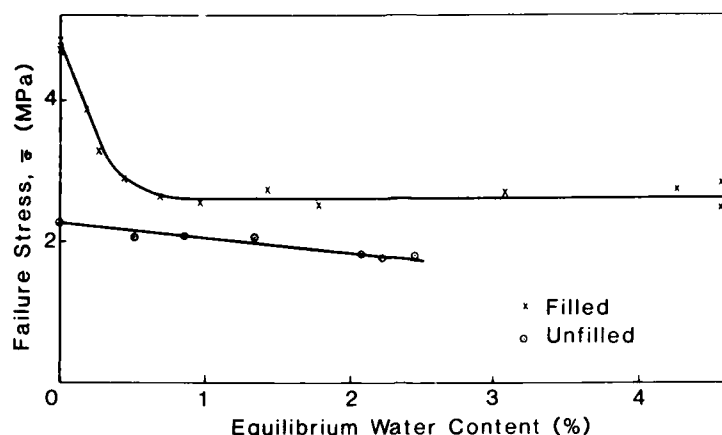


FIGURE 2 The effect of water on the failure stress of both filled and unfilled polyurethane.

on the mechanical properties of the filled material which result from the presence of quite low water contents. The presence of an equilibrium water content of about 0.7% leads to the almost total loss of the reinforcing effect of the filler.

Specific surface area determinations on the fillers used indicated that the silica was by far the most finely divided material with a value of $113.7 \text{ m}^2 \text{ g}^{-1}$ whilst the relatively coarse lampblack had a surface area of $\sim 20 \text{ m}^2 \text{ g}^{-1}$. Barytes, had a surface area of only $0.31 \text{ m}^2 \text{ g}^{-1}$. On the assumption² that each water molecule occupies $1.56 \times 10^{-18} \text{ m}^2$ it was calculated that as little as 230 ppm water would be sufficient for a monomolecular layer over the entire surface of the fillers. In fact some twenty-six times this concentration appears to be necessary to destroy the fillers' contribution to modulus and to failure stress.

However, tests thus far had been conducted on specimens as soon as equilibrium conditions had been achieved and therefore, in case this had allowed insufficient time, at lower water concentrations, for degradation to occur, specimens containing 0.28% equilibrium water concentration were withdrawn and tested at intervals with the results given in Figure 3. These results suggest that the degradation rate-determining stage is complete by the time equilibrium is established. The 0.28% equilibrium water content was chosen

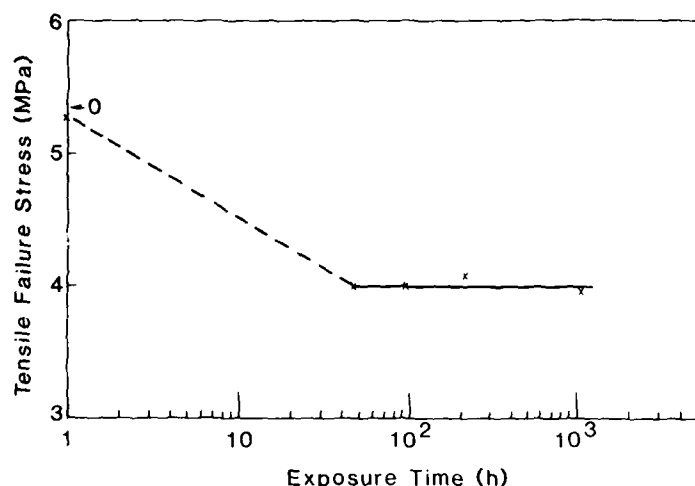


FIGURE 3 The effect of time on the degradative influence of moisture (0.28%) on a barytes-filled polyurethane.

because, although it had been shown to be insufficient to cause a complete loss of properties under the initial conditions of test, there was nevertheless more than enough to provide the few molecular layers which would presumably be sufficient to cause total disruption of polymer/filler adhesion.

In an attempt to clarify further the ultimate destination of absorbed water, water take-up experiments were carried out at two water activity levels with rubbers containing a range of barytes concentrations from 0 to ~65% w/w. The results are shown in Figure 4 where equilibrium water concentration is plotted against the polymer content of the various mixes. Values for equilibrium water contents for these formulations were also calculated on the assumption that the amount of water absorbed was a function of the polymer content only and was quite independent of the filler component. The theoretical curves are drawn on the figure and it can be seen that the experimentally determined points fall quite close to them. It is inferred from these results that, at these lower levels, water concentrates in the polymer, presumably at hydrogen bondable sites, rather than at the polymer/filler interface.

Samples of polyurethane rubber containing barytes filler alone

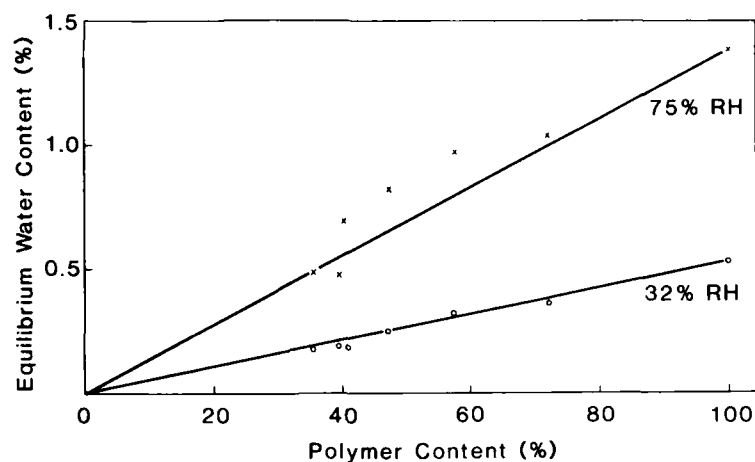


FIGURE 4 Equilibrium water content versus polymer content in a series of filled polyurethanes at two water vapour concentrations.

were made up, as were samples containing carbon black only and fumed silica alone. Initial, control static modulus values for these three formulations were obtained and similar modulus values were measured on specimens which had reached equilibrium in various humid environments. All these results, together with those obtained for the complete formulation, appear in Figure 5 where it can be seen that, of the three fillers, the barytes, which is present in the greatest abundance, contributes most to the superior properties of the original, filled composition. It can also be seen that it is this barytes-containing mix which is most seriously affected by the presence of absorbed water. At an equilibrium water content of about 0.6% it is evident that all those properties attributable to the presence of the barytes have been lost.

A curve obtained for the determination of the diffusion coefficient for the unfilled urethane is given as Figure 6 where it may be seen that the limit of solubility for water in the polymer is $\sim 2.16\%$. This value is equivalent to the presence of $\sim 0.9\%$ in the filled product and so, by reference to Figure 5, it can be seen that the loss of properties attributable to the presence of fillers occurs well before the polymer itself is saturated with water. The diffusion coefficient of $1.51 \times 10^{-11} \text{ m}^2 \text{ s}^{-1}$ is typical for such polyurethane formulations.

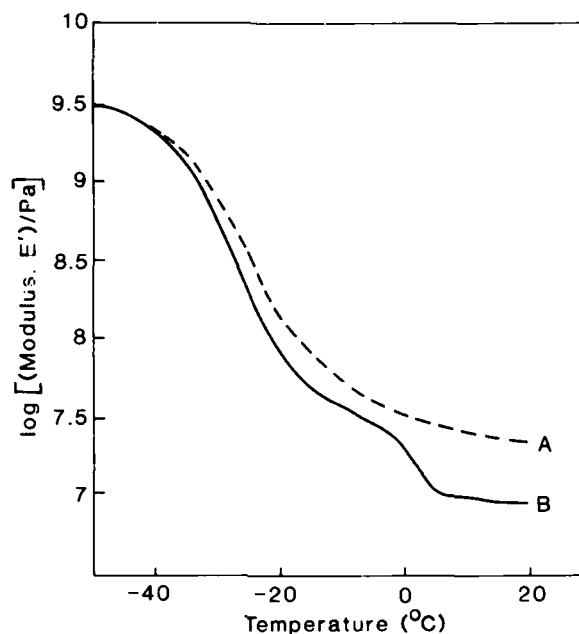


FIGURE 7 Log modulus versus temperature for filled polyurethane showing a transition at 0°C.

equilibrium water contents of <1.8% although this may merely reflect the relative insensitivity of the detection method.

The absorption of water to levels in excess of the solubility limit in the unfilled polymer was clearly attributable to the presence of the fillers and in particular with the barytes which was found to contain small quantities of water soluble material. Analysis showed these materials to be mainly chlorides, the most important being calcium chloride (~590 ppm), sodium chloride (~70 ppm) and magnesium chloride (~40 ppm). It was inferred that once the solution activity level for the soluble salts had been attained in the region of the fillers then osmotic processes commenced and these were responsible for the higher water absorption levels.

At water content levels of up to ~1.8% depression of peak damping temperature was proportional to water concentration and a plot of these results (Figure 8) closely follows the depression of

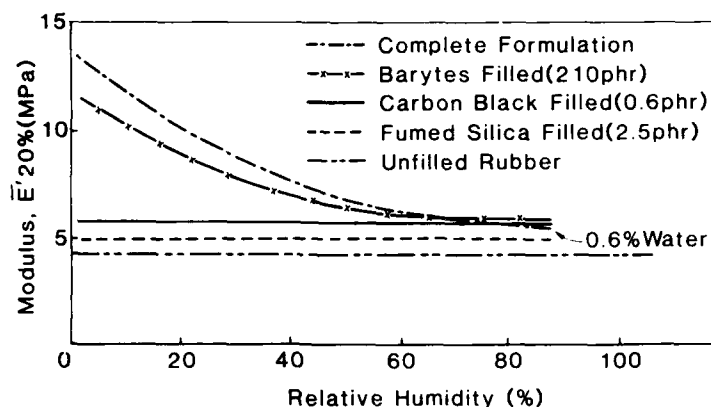


FIGURE 5 Illustrating the dominant influence of the barytes filler on the modulus of polyurethane rubber and the variation of this property with equilibrium water content.

Figure 7 compares the effect of a 4.3% water content (case B) on the dynamic modulus of the filled material by comparison with a dry control specimen (case A). The transition at 0°C was confirmed as being due to the freezing of liquid water when it was found to remain unchanged at this temperature over two decades of frequency. No evidence of such a discontinuity was observed at

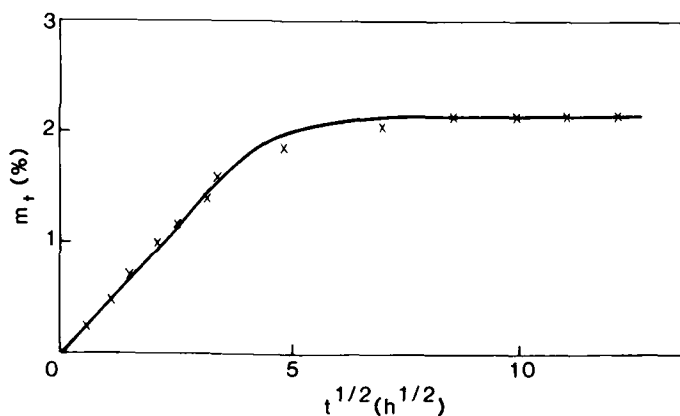


FIGURE 6 Water take-up for the unfilled polyurethane versus root time.

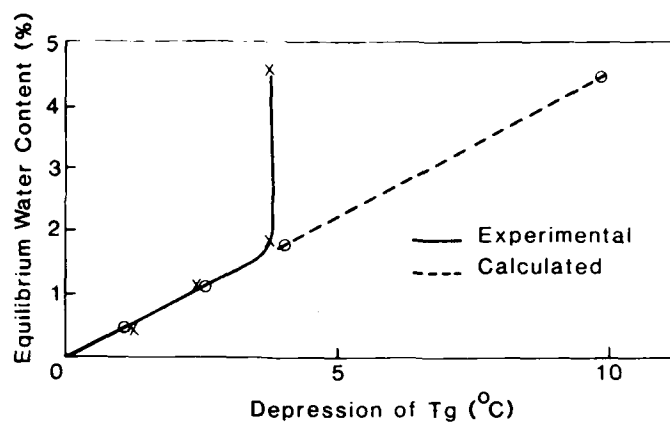


FIGURE 8 Depression of peak damping temperature by sorbed water and corresponding T_g depression calculated from the Fox Equation.

the T_g , as predicted by the Fox equation:³

$$\frac{1}{T_g} = \frac{W_A}{T_{gA}} + \frac{W_B}{T_{gB}}$$

where T_g is the glass transition temperature of the mixture and T_{gA} and T_{gB} are the respective T_g 's of the two miscible components.

For the purposes of this calculation the peak damping temperature of the dry material at 10 Hz was taken to be the T_g . The T_g for water was assumed to be 135° K⁴ and experimental values for peak damping temperature were obtained from DMTA. At higher water contents no further depression of peak damping temperature was observed, perhaps because of the commencement of clustering. On redrying from 4.3% water content, original properties were recovered, indicating that the effect of water was reversible.

It was thought possible that the dissolution of the water-soluble material associated with the barytes filler could have lead to the generation of gross mechanical discontinuities which could have been responsible for some of the observed property degradation, especially if these soluble salts were distributed over the surface of the reinforcing filler. A specially purified barium sulphate, believed to be relatively free of water-soluble material, was therefore investigated as an alternative. Because of its higher specific surface

area this alternative filler was used at the lower level of 150 phr to fill a polyurethane rubber. This rubber was different from that used earlier only in that a purer form of the isocyanate was employed.

Both unfilled and filled specimens were allowed to equilibrate with water at laboratory temperatures after which modulus ($E'_{20\%}$) values were determined. Although the unfilled material was virtually unaffected, the modulus of the filled product was reduced by $\sim 54\%$. By comparison, although the modulus of the earlier version of the unfilled rubber using the less pure isocyanate was also apparently unaffected after exposure to similar conditions, the material filled with soluble salt-containing barytes lost $\sim 69\%$ of its static modulus.

As an alternative to barium sulphate, ferric oxide was also considered as a filler for this polyurethane system. The use of such a filler was attractive partly because silane adhesion promoters could also be incorporated with the hope that the effects of attack by water could be reduced.

The investigation of the performance of iron oxide as the filler was preceded by an examination of the effects of the presence of the silane which was to be employed as the adhesion promoter in the urethane/iron oxide composite. The silane used was γ -aminopropyltriethoxysilane and five unfilled rubber formulations containing from 0 to 3.0 phr of the silane were prepared. In order to maintain stoichiometry, isocyanate content was increased to compensate for amine-terminated silane additions.

The modulus values for these materials, obtained after equilibration with water under conditions of 100% relative humidity, are compared with control values obtained from dry specimens in Figure 9. It can be seen that the modulus of the dry material falls with increasing silane content. This trend is probably the consequence of internal plasticisation of the rubber by bulky pendant silane groups. The rather lower modulus values found for the wet specimens reflect the additional plasticising effects of the $\sim 1.83\%$ equilibrium water content.

Iron oxide-filled versions (51.2% w/w) of each of these formulations were then prepared and modulus values for the dry controls are plotted against silane content in Figure 10. Here it can be seen that there is a significant increase in modulus with increasing silane content which is in sharp contrast with the results obtained with the

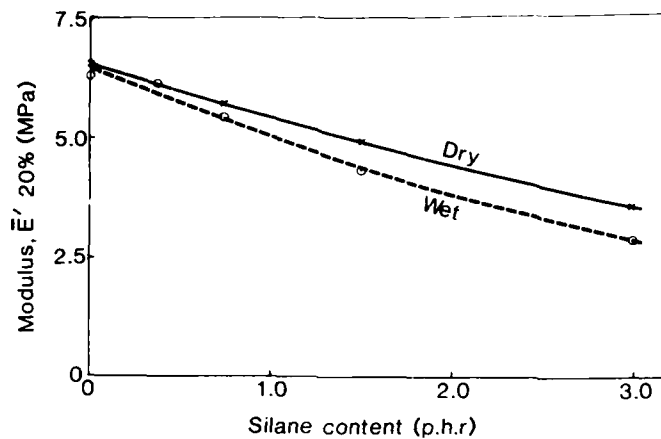


FIGURE 9 The static modulus versus silane content for an unfilled polyurethane comparing wet results with dry control values.

unfilled materials. The implication is that the progressively increasing potential for chemical coupling across the polymer matrix/filler interface is associated with progressively improving mechanical coupling and increasing modulus.

Specimens of iron oxide-filled material containing 0 phr and

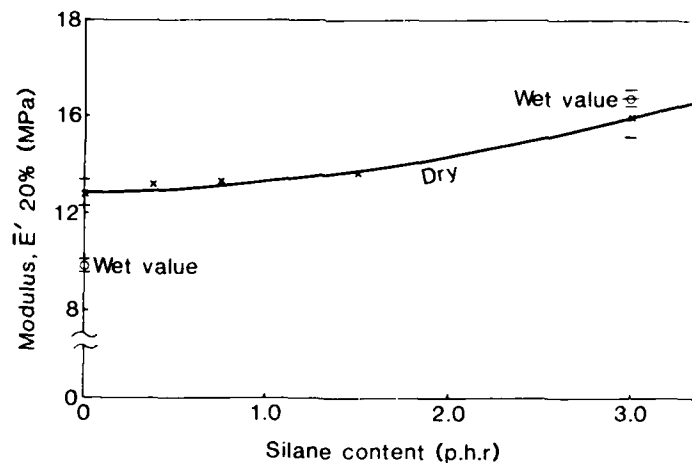


FIGURE 10 Static modulus versus silane content for an iron oxide-filled polyurethane.

3.0 phr of γ -aminopropyltriethoxysilane were immersed in water and, after a period of 240 days, it as noted that, although the composition without silane had suffered a modulus reduction of some 23%, the silane-containing specimens had remained unaffected. These results are also presented in Figure 10. Ninety-five percent confidence limits are also indicated for certain results.

Material was also prepared in which the iron oxide filler was pre-treated with the silane prior to incorporation in the urethane mix. This approach also leads to the production of specimens which were hydrolytically stable under similar conditions of test.

CONCLUSIONS

The presence of small equilibrium water content levels ($\sim 0.7\%$) causes the loss of most of the mechanical properties attributable to the presence of barytes filler in a polyurethane rubber, apparently as the result of the reversible disruption by water of polymer/filler adhesion. This water content is significantly less than the $\sim 1.1\%$ which results from seawater immersion.

This water concentration is approximately twenty-six times that required to provide a monomolecular layer over the entire filler surface and results show that the bulk of this water is associated with the polymer content rather than with the filler. Assuming that not more than two or three molecular layers would be required to cause loss of adhesion between adhesive and adherends it is concluded that, at lower equilibrium levels, water concentrates at hydrogen bondable sites perhaps within the polymer rather than at the polymer/filler interface.

At water activities equivalent to 98% relative humidity and less, water take up is limited in this way by the polymer content of the filled composite to a value of $\sim 0.9\%$ (equivalent to $\sim 2.2\%$ on the unfilled material which is close to the water solubility limit). When immersed in liquid water, however, water activity within the composite appears to be sufficiently high to lead to the solution of soluble species associated with the fillers and higher water contents are achieved as a consequence of the operation of osmotic processes. At these higher water content levels the additional water concentrates around the filler particles and behaves in a liquid-like manner.

Iron oxide-filled polyurethanes appear to be less sensitive than are barytes-filled systems to attack by water and when a silane coupling agent is used, either as an addition to the resin mix or as a pre-coat on the filler particles, an even greater hydrolytic stability is demonstrated.

Acknowledgements

The assistance of Mrs. H. J. Jordan and Mrs. T. S. Pratt in the production and evaluation of materials is gratefully acknowledged as is the contribution of Mr. J. R. Trayler who carried out the inorganic analyses. Surface area determinations were undertaken by Coulter Electronics Ltd. © Controller, HMSO, London, UK, 1986.

References

1. J. Crank, *Mathematics of Diffusion*—2nd edition (Oxford University Press, UK, 1975).
2. A. L. McClellan, and H. F. Harnsberger, *J. Colloid Interface Sci.* **23**, 577 (1967).
3. T. G. Fox, *Bull. Amer. Phys. Soc.* **1**, 123 (1956).
4. M. Sugisaki, H. Suga and S. Seki, *J. Chem. Soc. Japan* **41**, 2591 (1968).

Application of Secondary Ion Mass Spectrometry to Adhesion Studies†

D. BRIGGS

*ICI PLC, Petrochemicals and Plastics Division, PO Box 90, Wilton,
Middlesbrough, Cleveland TS6 8JE, UK*

(Received October 3, 1986)

The present paper firstly describes developments in the technique of static secondary ion mass spectrometry. Secondly, the power of this advanced surface analytical technique is illustrated by discussing the locus of failure of epoxide/polyethylene substrate joints.

KEY WORDS Adhesion studies; epoxide/polyethylene adhesion; instrumentation; locus of failure; static SIMS; weak boundary layer.

1 GENERAL INTRODUCTION

There is no doubt that, over the last ten years or so, surface analytical techniques have had a major impact on the study of adhesion.¹⁻⁴ In particular, two techniques have achieved prominence. X-ray photoelectron spectroscopy (XPS or ESCA) has been used almost exclusively to study polymer surfaces and organic layers because of the lack of problems with sample charging and radiation damage. In the case of non-organic systems, *e.g.* studies of metal oxide structures, Auger electron spectroscopy (AES) has also been applied, especially in combination with argon-ion etching to construct composition depth profiles. AES also has the facility for

† Presented at the Tenth Annual Meeting of The Adhesion Society, Inc., Williamsburg, Virginia, U.S.A., February 22-27, 1987.

microanalysis and surface composition imaging (production of element distribution maps). Unfortunately AES cannot be applied to organic systems because of beam damage and charging problems, whereas XPS lacks spatial resolution. For adhesion studies in general, but for polymer related studies in particular, the requirement is for a technique which combines, or even exceeds, the attributes of both XPS and AES. Static SIMS has the potential to fulfil this demanding role. This technique has been developed rapidly for polymer surface analysis⁵ since about 1981 and the instrumentation is currently undergoing a major revolution with significant implications for adhesion science.⁶

1.1 Static SIMS for polymer surface analysis

1.1.1 General considerations The experiment, in essence, consists of sample irradiation by a beam of low energy (typically 2–4 keV) noble gas ions (Ar^+ , Xe^+) with simultaneous irradiation by relatively low energy electrons (several hundred eV) to provide charge neutralisation of the insulator surface. Ejected secondary ions are mass analysed to provide, sequentially, the positive and negative ion mass spectra. "Static" SIMS means that the primary ion dose acquired during spectral acquisition is so low that the spectra are characteristic of the unperturbed surface. Above a threshold dose (material dependent but for many polymers as low as 10^{13} ions cm^{-2})⁷ the spectra change with dose and represent beam damaged surfaces. Good signal/noise spectra can routinely be obtained for doses $< 2 \times 10^{12}$ ions cm^{-2} . Surface potential control is a key experimental issue and requires significantly different parameters for optimisation of positive and negative SIMS.^{8–10} The spectra are typical of organic mass spectra in general with high mass cluster ions representative of major structural units of polymers (*i.e.* multiple repeat unit fragments, intact side chain fragments) and their daughter fragments. Small molecules, *e.g.* additives, often give quasi-molecular ions (*e.g.* MH^+ where M is the molecular weight) and fragmentation patterns similar to those encountered in conventional mass spectrometry. Many fingerprint spectra of polymers have been reported.^{3,5,11–15} Quantification of SIMS intensity data has been demonstrated for methacrylate¹⁴ and

nylon¹⁵ copolymers and has been used to investigate the surface composition of segmented polyurethanes.¹⁶ The sampling depth in typical static SIMS appears to be $\leq 10\text{\AA}$.¹⁶

1.1.2 Imaging The obvious application for molecular imaging in adhesion studies is the investigation of failure surfaces. Static SIMS imaging of molecular species in all-polymeric systems has been demonstrated with a spatial resolution of $\sim 50\text{ }\mu\text{m}$.^{13,17} In this experiment the focussed ion beam is rastered over the surface with the mass spectrometer tuned to detect a chosen ion (m/z) and the intensity of the signal fed to an oscilloscope scanning synchronously (entirely equivalent to SEM). As the probe diameter decreases (increased spatial resolution) and the irradiated area decreases (higher magnification), two problems occur. Firstly, charge neutralisation becomes more difficult and secondly, the static SIMS threshold is rapidly exceeded producing unacceptable sample damage. To overcome these problems requires more sensitive instrumentation.³

1.1.3 Instrumentation developments A new generation of instrumentation is approaching introduction based on very high spatial resolution liquid-metal ion sources (500A probe) and time-of-flight mass spectrometry (ToF SIMS).⁶ The ToF promises several orders of magnitude improvement in sensitivity over the conventional quadrupole mass spectrometer as well as a vastly increased mass range (>5000 compared with several hundred).¹⁸ The ion source needs to be pulsed which should help overcome charging problems.

1.2 Applications of SIMS to adhesion studies

The twin-aspects of increased molecular specificity and decreased sampling depth, relative to XPS, are of enormous benefit in the study of organic contamination/potential weak boundary layers and failure planes. The importance of small molecules at surfaces and interfaces, arising from *in situ* additives, contamination *via* the atmosphere or by contact (*e.g.* of film surfaces with each other or

with machinery) on adhesion and durability, is becoming increasingly recognised as a result of SIMS information.⁵ In the case of poly(ethylene terephthalate) surface oligomers have even been analysed.¹⁹ The classic case of poor adhesion between polyethylenes and epoxide adhesives has recently been reinvestigated and the results are now discussed as an illustrative case.

2 FAILURE OF POLYETHYLENE/EPOXIDE ADHESIVE JOINTS

2.1 Introduction

In 1976, in the first paper which used XPS to study adhesion to polyolefins,²⁰ Briggs, Brewis and Konieczko briefly reported the results of LDPE/epoxide adhesive failure surface analysis. The apparent lack of LDPE transfer to the adhesive (deduced from a comparison of the adhesive surfaces from a broken joint and from a film cured in air) has subsequently been quoted²¹ as evidence against the weak boundary layer theory for the poor adhesion properties of untreated polyolefins. Because of uncertainties about the XPS sampling depth (at that time) the authors included a caveat in their conclusions to the effect that a very thin layer of LDPE may go undetected. Today caution for this reason can reasonably be dismissed. However, SIMS has since emerged as a more powerful tool than XPS for this type of analysis on account of its greater surface sensitivity and molecular specificity.⁵ Several aspects of the early data and the fact that the experiment has never been repeated, led us to reinvestigate using both XPS and SIMS.

2.2 Experimental

Films, 0.15 mm thick, of Akathene 11 LDPE (ICI), an additive-free blown film, and Rigidex 002-55 HDPE (BP), pressed from additive-free powder between sheets of poly(ethylene terephthalate) previously Soxhlet extracted in carbon tetrachloride, were used. The LDPE was freshly cut from a reel prior to use, the HDPE film was briefly extracted with THF and diethylether.

The "Araldite" (Ceiba Geigy) adhesive used was a 1:1 mixture

of the resin AV100 (a standard bisphenol-A diglycidyl ether) and hardener HV100 (believed to be a polyamide containing a tertiary amine accelerator). Lap shear joints were prepared as described previously.²⁰ Adhesion was very poor ($\leq 0.7 \text{ MN m}^{-2}$), but it should be noted that the same adhesive gives joint strengths with the same polyethylenes, which have received a standard pretreatment, which are greater by an order of magnitude.

XPS measurements were carried out on a Kratos ES200B instrument under control of a DS800 data system which also allowed complex curve synthesis to be carried out. Surface atomic compositions were computed from peak areas using sensitivity factors appropriate to the FRR analyser mode.²² Variable "take-off" angle experiments could be performed and quoted values of θ refer to the electron exit angle with respect to the surface.

SIMS measurements were carried out on a system described previously,⁸ based on an ESCALAB Mk 1 XPS/SIMS instrument (VG Scientific). A primary ion beam of 4 keV Xe^+ (1 nA cm^{-2}) was used with a 700 eV flood of electrons for charge neutralisation.

2.3 Results

The XPS results are collected in Table I. The "deconvolution" of the complex C1s envelope is illustrated in Figure 1, in which four components of similar width are used. For present purposes it is not important to discuss the possible interpretation of the component peaks except to note that: (a) C_1 corresponds to C atoms bound only to C or H (e.g. the position of $(-\text{CH}_2-)_n$ from polyethylene) whereas C_2 – C_4 represent C atoms in functional groups involving O and N; (b) all C1s spectra were fitted identically except for the intensities of the four components and (c) in each case an extremely

TABLE I
XPS data from epoxide adhesive surfaces

Sample (θ)	Relative intensity				atomic %		
	C_1	C_2	C_3	C_4	C	O	N
Epoxide scraped (80°)	69.9	22.0	5.7	2.4	73.4	20.7	5.8
Epoxide/LDPE (80°)	75.5	19.6	4.2	0.7	82.2	13.1	4.7
Epoxide/LDPE (15°)	80.2	14.0	4.4	1.4	82.8	14.5	2.6

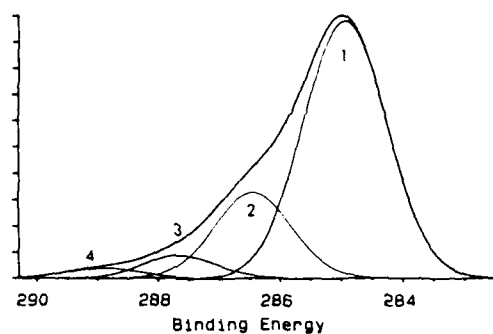


FIGURE 1 Position of components (C_1 - C_4) used to fit the experimental $C1s$ envelope (in this case for the scraped epoxide adhesive surface).

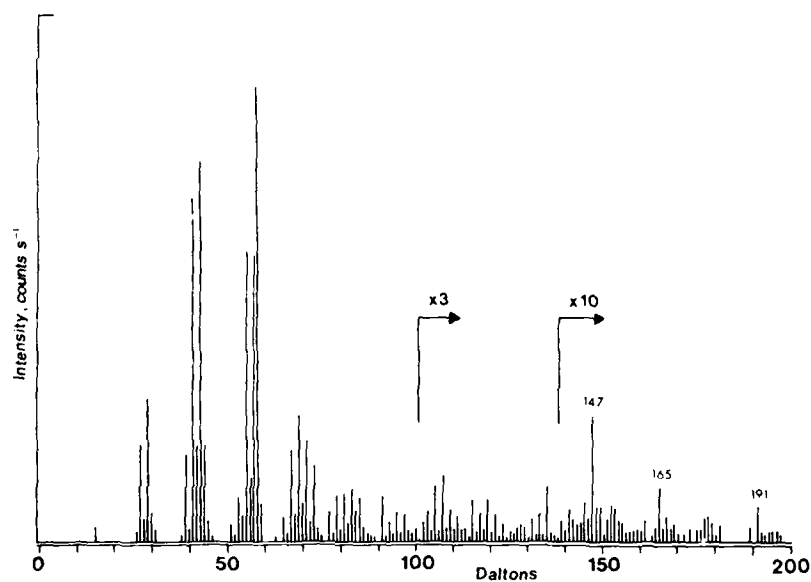


FIGURE 2(a) Positive SIMS of the epoxide adhesive surface resulting from failure of the LDPE/epoxide joint. Annotated peaks are characteristic of dimethyl silicone.

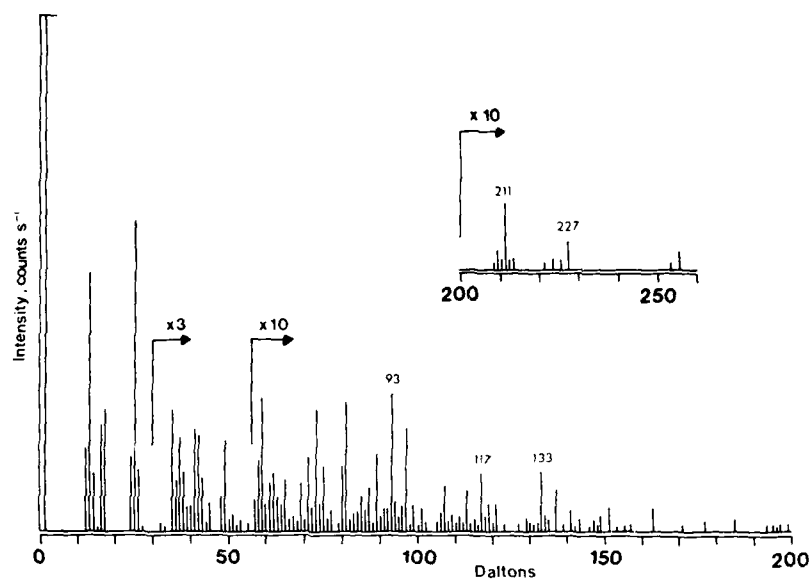


FIGURE 2(b) Negative SIMS of the epoxide adhesive surface resulting from failure of the LDPE/epoxide joint. Annotated peaks are characteristic of the bisphenol-A part of the structure (see Ref. 3 for an interpretation of the polycarbonate spectrum, also derived from bisphenol A).

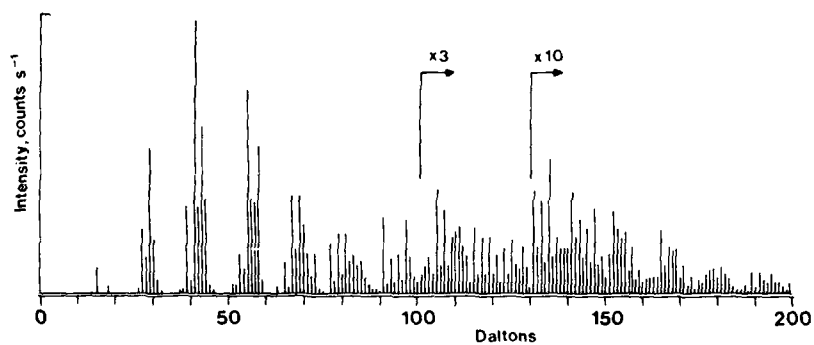


FIGURE 3 Positive SIMS of the epoxide adhesive surface resulting from failure of the HDPE/epoxide joint.

good match between the experimental and synthetic envelope was achieved.

SIMS spectra from the polyethylene film surfaces which had been in contact with the adhesive were identical to those from the original film surfaces (previously reported^{5,23}). Figure 2 shows the spectra from the adhesive surface of the failed LDPE/epoxide joint. The equivalent positive ion spectrum from the HDPE/epoxide joint is shown in Figure 3, the negative ion spectrum being very similar to Figure 2(b). Spectra from the epoxide adhesive after curing in air (with precautions to avoid contamination from the atmosphere) and after scraping this surface with a razor blade are qualitatively similar to Figures 3 and 2(b) (positive and negative ions respectively).

2.4 Discussion

It is quite clear from the SIMS data that failure of the HDPE/epoxide joint is purely interfacial; this can be asserted simply on the basis of the fingerprint nature of the spectra of all the materials involved. In the case of LDPE/epoxide, comparison of Figure 2(a) and Figure 3 reveals a significant contribution from hydrocarbon species ($C_xH_y^+$, e.g. 27, 29, 41, 43, 55, 57D etc) with a relative intensity pattern characteristic of the polyolefin, thus indicating some transfer of LDPE to the adhesive surface. However, the negative ion spectrum (Figure 2(b)) is still characteristic of the adhesive which strongly suggests that the LDPE is very patchy (the negative ion spectrum of LDPE is featureless beyond 30D). The positive ion spectrum also reveals a trace of silicone contamination (peaks at 147, 165, 191D).⁵ The origin of this material is unknown. It is not seen on the original film surfaces, nor is it present in the adhesive. It may have migrated from the aluminium used to make the lap shear joint or have been picked up from the atmosphere during joint preparation. Its presence is not material to the discussion, but its detection reveals another facet of SIMS analytical capability.

The XPS data from the Table are entirely consistent with this conclusion and also with the previously reported results.²⁰ Taking the scraped epoxide data as representative of the bulk adhesive composition (80° giving the maximum sampling depth for our

instrument), comparison with the data from the failed joint reveals a little hydrocarbon transfer (greater % of carbon, but particularly of type C_1). However, the enhancement of this component at $\theta = 15^\circ$ (minimum sampling depth) is very small and definitely not consistent with there being a continuous overlayer of polyolefin, even of only monolayer thickness; *i.e.* transfer is patchy and sub-monolayer.

The variation in composition of the epoxide adhesive surface between the air-cured sample and the failed joint noted previously²⁰ is seen more clearly from the Table, the angular variation data suggesting a significant composition gradient below the surface. This is mirrored by the SIMS data. Relative intensity differences between peaks representing the epoxide resin and others characteristic of the cross-linked (nitrogen-containing) polymer can be observed when comparing air-cured adhesive before and after scraping and the failed joint surfaces. A detailed interpretation of the adhesive spectra is not appropriate in this note, but will be given in a future paper which follows the curing process.

In a recent paper²⁴ concerned with adhesion to polyethylenes we demonstrated that lack of chemical functionality was the key reason for the poor adhesive properties. The presence of mobile low molecular weight material, in the case of LDPE, complicated the situation relative to HDPE, but there could be no doubt that arguments based purely on weak boundary layers are entirely inadequate.

The present results from direct interrogation of the interfacial situation in polyethylene/epoxide joints bears this out. Adhesion is negligible for both HDPE and LDPE. In the former case there is no evidence for cohesive failure whereas in the latter case, where no attempt was made to minimise weak boundary layer effects, only sub-monolayer transfer to the adhesive was observed.

References

1. D. M. Brewis, Ed., *Surface Analysis and Pretreatments of Plastics and Metals* (Applied Science Publishers, London, 1982).
2. D. M. Brewis and D. Briggs, Eds., *Industrial Adhesion Problems* (Orbital Press, Oxford, 1985).
3. D. M. Brewis and D. Briggs, *Polymer* **22**, 7 (1981).

4. D. M. Brewis, *Prog. Rubber Plast. Tech.* **1** (4), 1 (1985).
5. D. Briggs, *Surf. Interface Anal.* **9**, 391 (1986).
6. VG Scientific Ltd, East Grinstead, UK have recently constructed a ToF SIMS microprobe for high resolution (1000 Å) imaging and high mass secondary ion detection.
7. D. Briggs and M. J. Hearn, *Vacuum*, in press.
8. D. Briggs and A. B. Wootton, *Surf. Interface Anal.* **4**, 109 (1982).
9. A. Brown and J. C. Vickerman, *ibid.* **8**, 75 (1986).
10. D. Briggs and M. J. Hearn, in preparation.
11. D. Briggs, *Polymer* **25**, 1379 (1984).
12. D. Briggs, *Surf. Interface Anal.* **4**, 151 (1982).
13. D. Briggs, *ibid.* **5**, 113 (1983).
14. D. Briggs, M. J. Hearn and B. D. Ratner, *ibid.* **6**, 184 (1984).
15. D. Briggs, *Org. Mass Spec.*, in press.
16. M. J. Hearn, D. Briggs, S. C. Yoon and B. D. Ratner, in preparation.
17. D. Briggs and M. J. Hearn, *Spectrochim. Acta* **40B**, 707 (1985).
18. D. M. Hercules and I. V. Bletsos, *Polym. Mat. Sci. Eng.* **54**, 302 (1986).
19. D. Briggs, *Surf. Interface Anal.* **8**, 133 (1986).
20. D. Briggs, D. M. Brewis and M. B. Konieczko, *J. Mater. Sci.* **11**, 1270 (1976).
21. See, for example, A. J. Kinloch, *ibid.* **15**, 2141 (1980).
22. D. T. Clark and H. R. Thomas, *J. Polym. Sci., Polym. Chem. Ed.* **16**, 791 (1978).
23. D. Briggs and M. J. Hearn, *Int. J. Mass Spec. Ion Processes* **67**, 47 (1985).
24. A. Chew, *et al.*, *J. Coll. Interface Sci.* **110**, 88 (1986).

SESSION OF WEST GERMANY

Long Abstract

Adhesion on Carbon-Fibre-Reinforced Plastics†

Ch. W. MATZ

MBB Transport Aircraft, D-2800 Bremen, WEST GERMANY

(Received November 12, 1986)

KEY WORDS Adhesion to CFRP; boundary zone; carbon fibre reinforced plastics; durability; epoxy matrix; prebonding treatments.

INTRODUCTION

The adhesion on CRFP-laminates is technically often used but the microscopic mechanisms are not yet completely understood. Besides the task to characterize the surfaces closely enough, the principal problem to predict the mechanical, physical and chemical properties of the boundary zone remains unsolved. More or less only the "try and error" method leads to the development of adhesive bonding processes, which satisfy the demands of aircraft structures concerning quality, reproducibility and durability. Experiments with varying substrates, surface pretreatments and adhesives show that all these parameters have a distinct influence on the mechanical performance of the bonds.

† This is the long abstract of a paper presented orally at the Tenth Annual Meeting of The Adhesion Society, Inc., Williamsburg, Virginia, U.S.A., February 22-27, 1986.

EXPERIMENTAL

i) Material: The CFRP-laminates were made out of two different unidirectional epoxy matrix resin prepregs from CIBA-Geigy LTD. (Duxford, GB). Both the conventional 125°C curing Fibredux 913C-TS-5-35 and the toughened 180°C curing Fibredux 6376C-T400-5-35 were processed to 1 mm thick sheets with a $(0^\circ/+45^\circ/0^\circ/-45^\circ)_{\text{sym}}$ structure, the 0° layer being the bonding surface.

Two RT-curing paste adhesives from Hysol, Dexter Division (Pittsburg, CA, U.S.A.) were used. These were the EA 934 NA as a proven standard metal bonding material and the EA 9321, which showed the best performance in screening tests. For a minor number of experiments also the 120°C curing film adhesive AF163-2K from the 3M-Company (St. Paul, MN, U.S.A.) was applied.

ii) Bonding Procedures: The curing cycles were performed in accordance with the manufacturers' data sheets.

The surface treatment varied mechanical, physical and chemical methods. Basis for comparisons was the peel-ply technique, which means that just before the application of the adhesive the peel ply was removed from the bonding surfaces.

Mechanical pretreatments were executed with different abrasives ranging from Scotchbrite 7558, type S (3M) to heavy sanding with SiC and Corundum grinding papers.

Physical pretreatments covered the usage of corona discharge. Chemically the surfaces were treated with different solvents and etching agents.

iii) Testing Procedures: As a mechanical property only the tensile shear strength was tested at different temperatures by using single overlap shear specimens.

Besides the initial reference values additional tests were performed after exposure in a hot/wet environment (70°C/70% r.h.) or 70°C warm water for 14 to 30 days until saturation. The completion of the absorption of water was indicated by extra traveller specimens. The bonding surfaces were characterized by optical microscopy and/or DRIFT spectra (Infrared spectroscopy).

RESULTS (SUMMARY)

Most decisive were the mechanical tests after a wet exposure. Depending on the substrate, the standard peel ply technique leads to rather different results (Figure 1), which indicate the easier to bond properties of the 913 material.

The performance of bonds with 6376 laminates can be significantly increased by a mechanical surface pretreatment. Most successful was a medium heavy sanding procedure using a "Scotch-brighting" process with the addition of extra abrasive powder containing quartz and tensides (Figure 2). With this procedure about 40% of the bonding surface area consists of resin free fibers. Very convincing, especially on such optimized surfaces, is the performance of the EA9321 adhesive.

Not so successful were the physical and chemical pretreatments. Although we obtained extremely high values by etching the surface

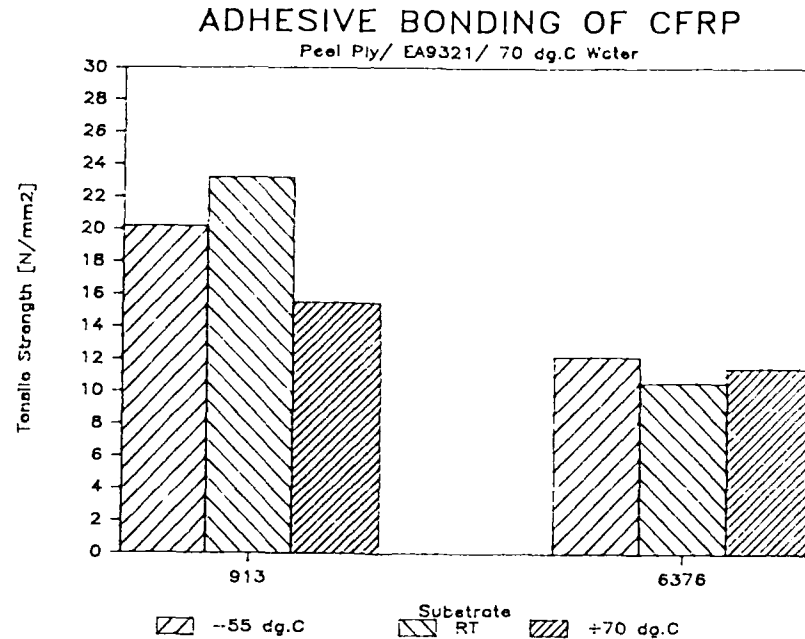


FIGURE 1.

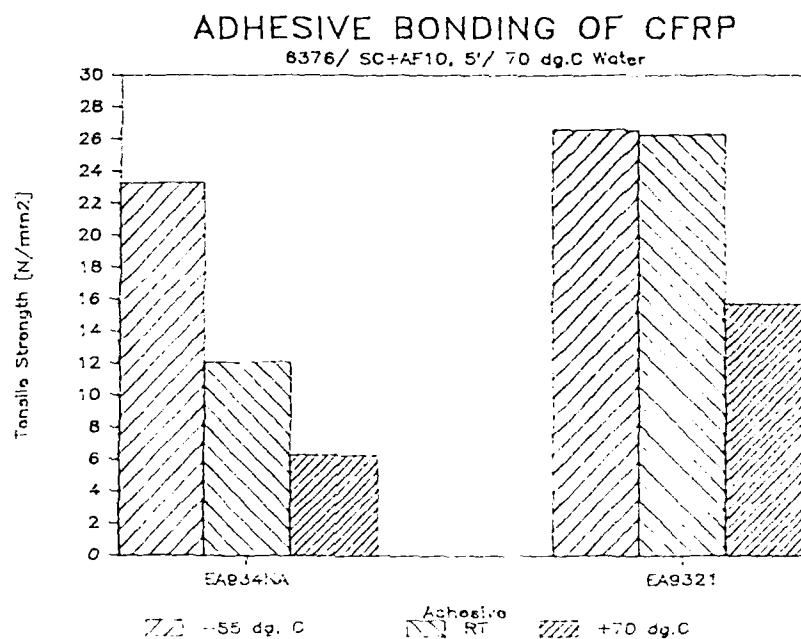


FIGURE 2.

with nitric acid (Figure 3) such bonds behave very poorly with a catastrophic adhesive failure mode after hot/wet exposure. Not so extreme, but similar, were the experiences with other etching chemicals and the corona discharge treatment, even when application parameters like temperature, time, concentration or energy were optimized in screening tests.

The pretreated surfaces could be distinguished from each other by optical microscopy and DRIFT spectroscopy. This gives one the ability to develop a test procedure in order to confirm a correct pretreatment process. On the other hand no criteria were found, which predict generally a successful bonding result.

CONCLUSIONS

An optimized bonding process for CFRP still needs the experimental optimization of the combination of substrate, surface pretreatment and adhesive.

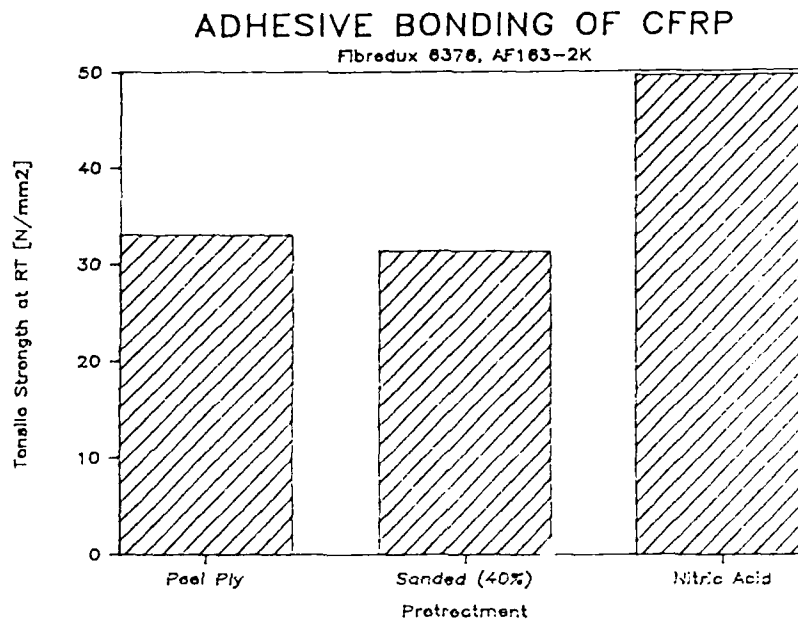


FIGURE 3.

Some of the obtained results indicate that even with RT-curing adhesives it may be possible to bond CRFP structurally, but a full qualification needs further durability testing.

Acknowledgements

Most of the results were obtained in cooperation with Prof. Dr. F. Vohwinkel from the "Fachhochschule Osnabrück". The investigation of the surfaces by DRIFT spectra was performed by Dr. H. Kollek, IFAM Bremen.

Long Abstract

Adhesion Between Metals and Polymers as a Three-Dimensional System[†]

O.-D. HENNEMANN

*Fraunhofer-Institut für angewandte Materialforschung, Lesumer Heerstrasse
36, D-2820 Bremen 77, WEST GERMANY*

(Received November 12, 1986)

KEY WORDS Adhesion; boundary layers; discontinuous phases; interface zones; interphases; oxide layers.

Adhesion science in a technical sense is the study of reactions in boundary layers. From a macroscopic point of view the result is the adhesive joint strength dependent on the magnitude of the adhesion forces without hints on the nature of these forces. So the question of the nature of adhesion has at least to be answered for technical applications by using other measurement techniques. From the microscopic point of view adhesion is of interdisciplinary nature, where molecules or atoms act with each other across the interface. Mainly adhesive bonds are based on these interactions of different bodies like metals and polymers or other material discontinuities. So far we can speak about a "chemical adhesion". But in practice there we realize a "technical adhesion" with more or less sharp discontinuities.

[†] This is the long abstract of a paper presented orally at the Tenth Annual Meeting of The Adhesion Society, Inc., Williamsburg, Virginia, U.S.A., February 22-27, 1986.



FIGURE 1 PAA-oxide layer with the Al-cladding, barrier layer and primer. Magnification 51,000 \times .

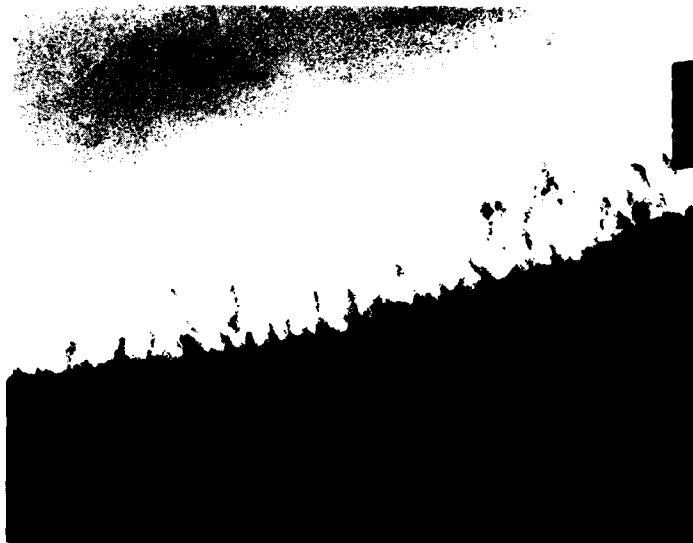


FIGURE 2 Ti-oxide layer with the Ti-surface and primer. Magnification 175,000 \times .

3F

This aspect shall be described in terms of adhesive bonding in the aircraft industry, which in general means the joining of aluminium.

There we realize a composite containing the metal sheet with a rather ductile and deformable cladding of 99.5% pure Al. After a pretreatment process, *e.g.* Phosphoric Acid Anodizing (PAA), there is a dense barrier layer of aluminium oxide. Furthermore, there is the main oxide layer with a split top area Figure 1. The whole oxide layer is penetrated by a polymer, a primer or an adhesive. The oxide layer becomes a composite, a reinforced oxide. The properties of the resin in the oxide are still unknown, but the reactivity of the resin in the aluminium oxide is different from that of the bulk material. The interactions of the resin with the oxide can lead to a weak boundary layer above the oxide. The primer is filled with pigments which make the primer brittle, because it has to promote the adhesion and to reduce aging mechanisms and does not have to fulfil the mechanical aspects of the adhesive. At least there is the discontinuity between the primer and the adhesive.

All the different zones of adhesive Al-bonds are of different



FIGURE 3 Steel-polymer-bond, no oxide is detectable. Magnification 82,000 \times .

elasticity and thickness—all together about $60\text{ }\mu\text{m}$. It is a zone of different material discontinuities and all together they are adhesion in a technical sense. In other words, technical adhesion is the integral property of many single interfaces. This seems to be true not only for aluminium but also for many other metals, *e.g.* titanium and steel in perhaps a more limited fashion.

In titanium we commonly have bare material. By an etching process there results an oxide layer of about 3 nm , by an anodizing process about 60 nm , Figure 2. As a consequence there we have a technical adhesion zone of about $5\text{ }\mu\text{m}$ with less numbers of discontinuities. All mechanical conditioning factors have to be translated during this zone.

Much more critical is the situation in the case of steel bonds. Especially in C-steel there is nearly no oxide layer detectable, Figure 3. If no primer is used, we have a direct transition of mechanical requirements from joined part to the adhesive. In this case there is the highest stress concentration at a very sharp discontinuity.

The question arising from these facts is: Is it necessary to produce a rather large zone and many discontinuity phases between metal and polymer for a good bond?

Long Abstract

Chemical Aspects of Adhesion Between Metals and Polymers†

H. BROCKMANN

*Fakultät für Chemie, Universität Bielefeld, Postfach 8640, D-4800 Bielefeld 1,
GERMANY.*

(Received November 12, 1986)

The present paper considers the binding forces between organic molecules and metal surfaces, especially those covered with an oxide layer. Furthermore, the adherence of low molecular weight organic compounds onto polymers is discussed by comparison with textile dyeing procedures. The results of this analysis allows the molecular design of new adhesion promoters and proposes some modified techniques of metal surface pretreatment.

KEY WORDS Adhesion; adhesion promoters; adsorption; chemical bond; molecular design; textile dyeing.

INTRODUCTION

On exposure to air the surface of most metals will be coated by an oxide layer. The structure of an adhesive joint between two of these metals in a first approximation can then be described as a sequence of five layers, *i.e.* metal 1, oxide 1, adhesive, oxide 2, metal 2 (Figure 1). Typical adhesives for the joining of metals are organic polymers which in many cases—as with phenolic and epoxy

† This is the long abstract of a paper presented orally at the Tenth Annual Meeting of The Adhesion Society, Inc., Williamsburg, Virginia, U.S.A., February 22–27, 1986.

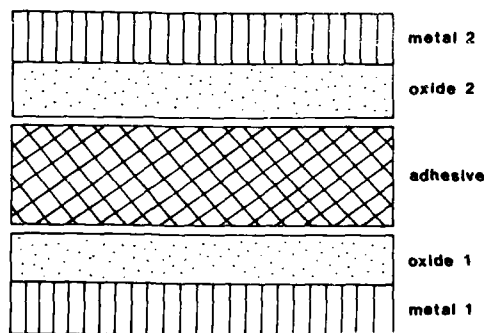


FIGURE 1 Schematic of an adhesive joint between two metals.

resins—are produced only during the joining procedure. The strength and the mechanical properties of an adhesive joint as depicted in Figure 1 will depend on the strength and mechanical properties of the polymer, the mechanical properties of the oxide layer and the adhesive forces between metal and oxide as well as those between oxide and polymer. In the following it will be assumed that the polymer meets the mechanical qualifications, and the mechanical properties of the oxide layer are supposed to be tolerable because of its small depth.

DISCUSSION

Chemical aspects of adhesion between metals and polymers can only be discussed in the dimensions of atoms, molecules, or crystal lattice spacings and, furthermore, the different binding forces between atoms, ions and molecules should be considered. In comparison to these dimensions (0.1–1 nm) glue lines in adhesive joints between metals usually have dimensions of 0.1–5 mm.

i) Chemical Structures: The chemical structure of solids like metals or oxides is described as a three-dimensional lattice structure of either positively charged ions and freely mobile electrons or of oppositely charged ions. In comparison to these the chemical building blocks of polymers are molecules which stick together in the solid state only by intermolecular forces. Although the strength of

intermolecular forces is lower than that of metallic, ionic or covalent bonds by one or two orders of magnitude, cooperative effects of a great number of intermolecular bonds give rise to the high cohesion of polymers.

ii) Adhesion Between Metals and Oxides: If the lattice spacings of the oxide formed on exposure of the metal to air are similar to those of the metal, the oxide will strongly adhere to the metal protecting it from further oxidation, provided the oxide is stable under environmental conditions. This is the case with copper, lead, tin, nickel and also with the less noble metals chromium, zinc and aluminum. The chemical bonds between the oxide and the metal in these examples can be described as a small boundary layer of oxide with increasing amounts of metal followed by metal with decreasing amounts of oxide (Figure 2). On the other hand, iron on exposure to air and humidity forms the well-known rust which does not adhere to the metal surface. Hence, for joining iron by adhesives the pretreatment of the metal surface should be in such a way as to avoid the formation of rust.

iii) Adhesion Between Organic Molecules and Metal Oxides: The fact that the chemical structure of organic molecules differs fundamentally from that of solids like oxides raises the question about possible binding forces between molecules and oxides. From the experience with adsorption chromatography for the separation and purification of organic compounds it can be

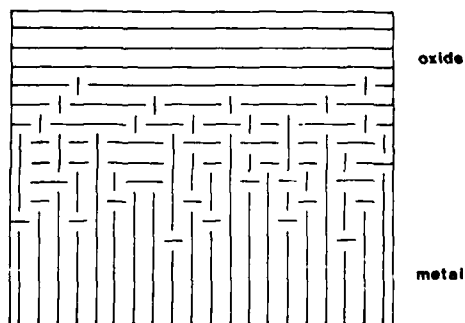


FIGURE 2 Schematic of a bond between metal and oxide.

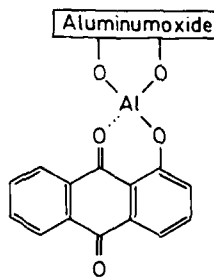


FIGURE 3 Irreversible complex formation of alizarin on aluminum oxide.

concluded that the adherence between oxides and molecules depends on the nature and the 'activity' of the oxide and highly on the structure and the functional groups of the molecules. Thus, compounds with hydroxy and amino groups with the ability to form hydrogen bonds are adsorbed much better than, for example, esters, ethers or hydrocarbons. Some compounds, especially those with chelating properties like hydroxy anthraquinones, even form irreversible adsorbates on aluminum oxide (Figure 3).

Aluminum oxides which are produced on the metal surface by phosphoric acid anodization (PAA) or chromic acid anodization (CAA) were found to be of rather low adsorption activity¹ as compared to aluminum oxide used in adsorption chromatography. Thus, further efforts should be made to enhance the adsorption activity of oxides on metal surfaces. As preliminary investigations indicate, this seems to be possible in the case of aluminum by precipitation of aluminum hydroxide on to the oxide surface.

iv) Adhesion Between Organic Molecules and Polymers: Only a limited number of polymers used as adhesives meets the requirement for good adsorption on oxides and, in practice, adhesion promoters and primers are applied. They are expected to bind just as well to the metal (oxide) as to the polymer. For that reason and as a result of investigations of joint failures which frequently show that the failure occurs in the adhesive very near to the interface,² the 'adhesion' and possible binding forces between molecules and polymers have to be considered. Information on this problem can be best received from textile dyeing procedures.

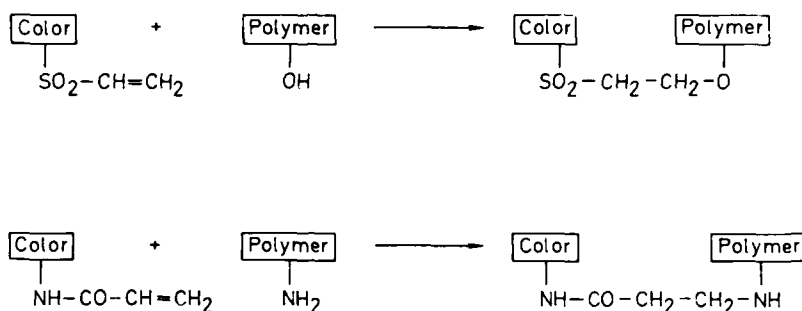


FIGURE 4 Formation of covalent bonds between reactive dyes and polymers.

The chemical diversity of fibrous polymers from synthetic or natural sources used in the manufacture of fabrics has led to the development of a variety of dyes and a variety of dyeing methods. In virtually all dyeing processes a water resistant 'adhesion' between dye and polymer is achieved. The chemical bonds between dyes and polymers formed in these processes range from van der Waals forces (disperse dyes for polyesters) to covalent bonds (reactive dyes for cotton and polyamides) including hydrogen bonds (substantive dyes), ionic bonds (ion exchange dyes for wool and silk) and complex formation (mordant dyes). The formation of covalent bonds between reactive dyes and polymers (Figure 4) suggests the applicability of a similar reaction principle also to adhesion promoters, provided that the polymer contains hydroxy or amino groups which is the case with phenolic and epoxy resins.

CONCLUSION

High adhesive forces between organic molecules and metal oxides as well as between organic molecules and polymers are well known. For the molecular design of bifunctional compounds with high affinity to metal oxides on the one hand and with the ability to form strong bonds to polymers on the other, structural requirements can be deduced from results in adsorption chromatography and from textile dyeing techniques. Compounds of this type, however, can

only serve as adhesion promoters and still call for a joining polymer to fill the glue line in adhesive joints.

References

1. H. Kollek, *Int. J. Adhesion and Adhesives* **5**, 75 (1985).
2. W. Brockmann, O.-D. Hennemann and H. Kollek, in *Adhesive Joints*, K. L. Mittal, Ed. (Plenum, NY, 1984), pp. 469-484.

Long Abstract

Organically Modified Silicates (Ormosils) as Adhesives for Siliceous Surfaces†

H. SCHMIDT

Fraunhofer-Institut für Silicatiforschung, Würzburg, WEST GERMANY

(Received November 12, 1986)

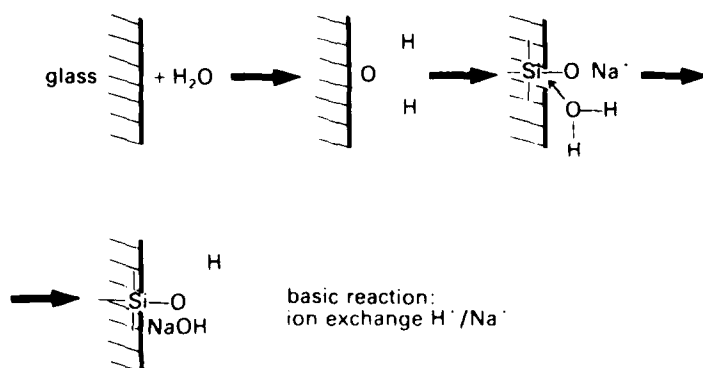
KEY WORDS Adhesion promoters; adhesion to glass; organically modified silicates; coupling agents; durability; silanes.

1 INTRODUCTION

Adhesion to glass surfaces still may be a problem under "heavy duty" conditions such as temperature and moisture or both. In many cases the problem may be overcome by use of adhesion promoters such as reactive silanes. These silanes remove water films from the glass surface by chemical reaction, are able to form chemical bonds to the glass surface and, in addition to this, can have an affinity to the sealing material to be used. A decay of adhesion strength between glass and a seal under wet conditions is

† This is the long abstract of a paper presented orally at the Tenth Annual Meeting of The Adhesion Society, Inc., Williamsburg, Virginia, U.S.A., February 22-27, 1986.

caused by the following effect:



The formation of NaOH leads to an alkaline media interface between seal and glass surface which causes a network degradation of the glass and a subsequent loss of adhesion. The magnitude of the effect depends strongly on the chemical durability of the glass substrate used. Especially, if hot sealing procedures have to be used, serious difficulties due to wetting problems during the sealing procedure and due to a water film remaining on the glass surface can appear.

A special hot sealing material was developed which was proved to be able to overcome most of the described problems:

- a) The material should be "glass-like". Therefore, a silica based polymer with a $\equiv\text{Si}-\text{O}-\text{Si}\equiv$ backbone was chosen.
- b) The material should be thermoplastic. That means the network connectivity of a pure inorganic (non-thermoplastic) polymer had to be reduced. Therefore, $\text{C}_6\text{H}_5-\text{Si}-\text{C}_6\text{H}_5$ groups were introduced. It was well known that these groups can cause thermoplasticity.
- c) Residual groups like $\equiv\text{Si}-\text{OR}$ or $\equiv\text{Si}-\text{OH}$ should remain in the polymer in order to form reactive bonds to the glass surface.
- d) Flexibility and photocurability should be obtained for reasons of application improvement. Therefore, a second type of

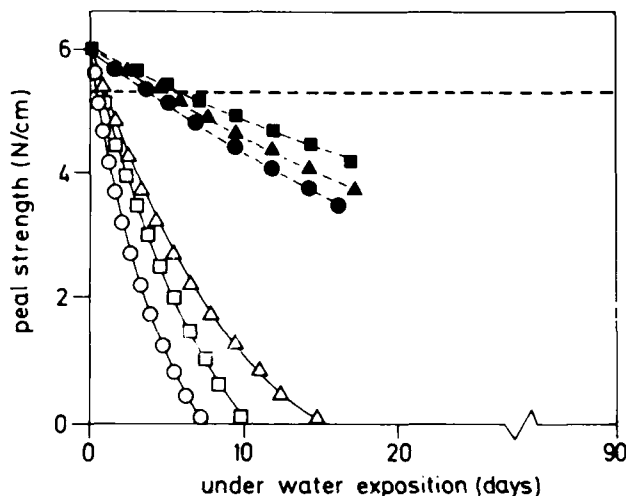


FIGURE 1 Peel strength decay curves of 1 cm Al-strips sealed on glass
 polyamide: untreated: $\triangle \triangle \triangle$
 treated: $\blacktriangle \blacktriangle \blacktriangle$
 vinylacetate/vinylchloride copolymer:
 untreated: $\circ \circ \circ$
 treated: $\bullet \bullet \bullet$
 Surlyn: untreated: $\square \square \square$
 treated: $\blacksquare \blacksquare \blacksquare$
 $(C_6H_5)_2SiO/TiO_2/CH_2=CH(CH_3)SiO$ based copolymer:---
 Treatment: Glass surfaces treated with an epoxy silane as adhesion promoter.

network by vinyl polymerization was introduced into the polymer by use of $CH_3-Si-CH=CH_2$ groupings.

As a result, a three-component system using sol-gel techniques was synthesized from $Si(OC_2H_5)_4$, $(C_2H_5O)_2Si(CH_3)CH=CH_2$ and $(C_6H_5)_2Si(OH)_2$ or $Ti(OC_2H_5)_4$ as starting compounds.^{1,2,3} By proper choice of composition, hydrolysis and condensation and thermal or photocuring, hot melts can be obtained with sealing temperatures between 80 and 160°C as desired. Figure 1 shows the sealing strength (peel strength) of aluminum strips sealed to a glass surface in comparison to other polymers with and without using an adhesion promoter. Figure 2 shows the IR-controlled thermal curing. The OH-group content has to be adjusted for an optimal sealing strength.

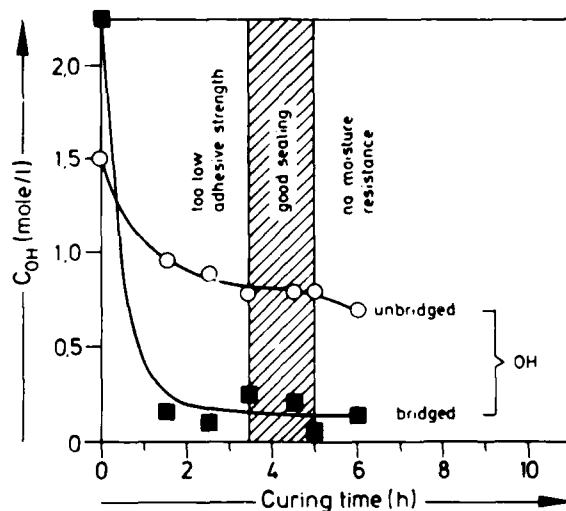


FIGURE 2 SiOH group concentrations for the system based on $(C_6H_5)_2SiO/SiO_2/CH_2=CH(CH_3)SiO$ as received from IR measure units; the hatched area represents the range of high peel strength and high moisture resistance according to Figure 1.

References

1. H. Schmidt, G. Tünker and H. Scholze, DP 30 11 761, 26.03.80 (EP 36 648, 20.03.81, US-Patent 4,374,696, 20.03.81).
2. H. Schmidt, H. Scholze and G. Tünker, *J. Non-Cryst. Solids* **80**, 557-563 (1986).
3. H. Schmidt, G. Philipp, H. Patzelt and H. Scholze, "Glass sealings by sol-gel derived organically modified silicates." Collected papers, XIV Intl. Congr. on Glass, New Delhi (1986), pp. 429-436.

Adhesion Effects of Intermediate Layers on the Densification of Ceramic Powders†

B. FRISCH und W.-R. THIELE

Universität des Saarlandes, Saarbrücken, W. GERMANY

(Received November 12, 1986)

In the ceramic technology the first step to produce sintered bodies is the manufacturing of powders which then are densified. The adhesion mechanisms between the single particles and the agglomerates produced from them determine the densification process. Starting from theoretical considerations adhesion mechanisms, such as solid bridge formation, adhesive bonding and glide-promoting effects, are discussed in principle. Subsequently, the effects of surface-active substances on the densification behaviour of clay-ceramics and oxide-ceramic bodies are discussed. Further, the evaluation of the action of additives to the powder mixtures on the microstructure of the compacts, such as porosity and texture, leads to a compaction equation which describes the transition from the powder pile to a densified green body.

KEY WORDS Adhesion of layers; adhesion mechanisms; ceramic powders; densification; effect of surfactants; structure of compacts.

1 INTRODUCTION

In the clay-ceramic technology the workability of the starting mixtures, containing quartz, feldspar and clay, is determined significantly by the plasticity of the clays. This is particularly valid for the more and more used dry-pressing-technique, which starts in

† Presented at the Tenth Annual Meeting of The Adhesion Society, Inc., Williamsburg, Virginia, U.S.A., February 22-27, 1987.

contrast to the slip-casting from spray-dried or granulated powders with low moisture contents. The deposits of high-plastic clays are decreasing worldwide, so that the application of so-called poor clays in the process engineering causes some difficulties attributed to very low adhesion in the compacts.

In principle, the initial substances for the production of engineering-ceramic products without exception are very brittle materials as alumina or silicon carbide. They are produced either by slip-casting or, increasingly, by the dry-pressing technique. The absence of plastic portions leads to a restricted adhesion ability in the compact and thereby to a very small stability of the green body.

Thus, in clay-ceramics and engineering-ceramic products, higher values for the strength of powder agglomerates are reached by increasing the adhesion between the individual particles, with the result that the rejection of unfired green bodies is essentially decreased in the process line.

2 ADHESIVE LAYERS AND ADHESION MECHANISMS

Investigations by Rumpf¹ on the dependence of the transferable tensile strength on the particle size in agglomerates resulted in an increasing of the strength of the compacts by addition of additives (Figure 1). However, in the technology it must be considered that, on the one hand, the application of large quantities of additives can be expensive. On the other hand, the quantitative removal of the added substances, for example by burning out, leads to problems because of changes in the properties of the sintered bodies.

According to the diagram of Rumpf the highest strength for small grain sizes is reached by building up characteristic solid bridges between the primary particles. In Figure 2 the reaction scheme of the system silicates-trichloromethylsilane (TCMS) is given as an example for the formation of a characteristic adhesive layer between powder particles.² After mixed sorption of silane and water molecules, the silanol groups of the silicate surfaces are integrated into a stabile network between the single particles by spalling hydrochloric acid. Thus, a high specific strength of the single contacts is reached, yet leading to a blocking of gliding processes during the compaction of a powder bed. What follows is a

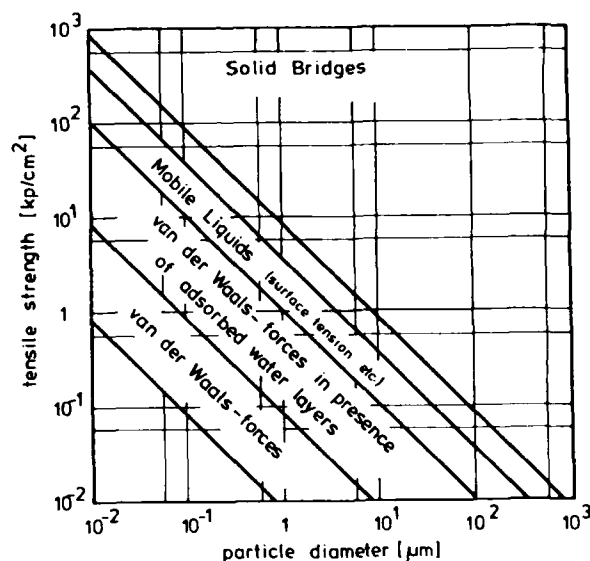


FIGURE 1 Dependence of theoretical tensile strength of agglomerates on the primary particle size for different bond types.

pressing with high strength but with an apparent density insufficient for optimal sintering. Consequently, there results the claim for the dry-pressing technique, that during compacting of powders a sufficient green density is reached by particle gliding simultaneously with an as high-as-possible adhesion between the particles.

In principle, this claim is fulfilled by the use of polar surface-active molecules. After the theory of Fowkes³ the interaction potentials, which determine the total surface energy, are superimposed additively, so that the following equation is valid:

$$\gamma = \gamma_D + \gamma_P$$

with γ_D = the non-polar part, determined by the dispersion forces
 γ_P = the polar part determined by the dipole forces

Within the meaning of adhesion an efficient substance is characterized by a very high polar energy term. According to the results of Fowkes, Michel⁴ gives a systematic listing of the adhesion mechanisms for sticking processes on polymers for different adhesive material combinations.

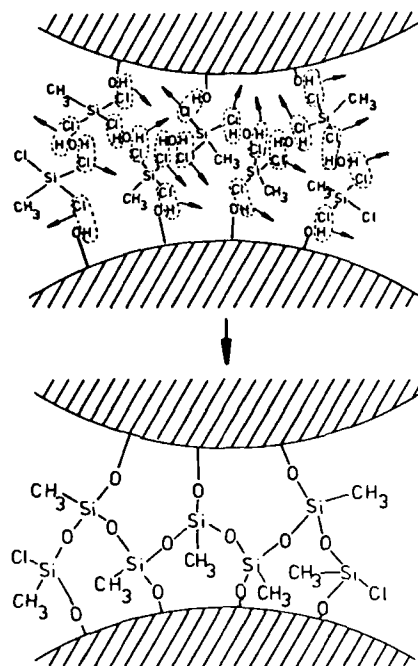


FIGURE 2 Formation of solid bridges on powder surfaces with hydroxylic ions.

The application of polar molecules as adhesion- and glide-promoting substances for compaction of powder piles is determined by the strength of the dipole forces and the number of the active dipoles per molecule. For monopolar substances like water the adsorption causes a saturation of the surface potentials as shown in Figure 3. From this, density-promoting glide processes with a lubrication effect result, whereas the adhesion forces are small. Hereby, the number and the size of the adhesive surfaces increase with simultaneous increase of the total strength and, furthermore, of the compacts' apparent density.

For the adsorption of bipolar molecules, according to their structure, two principally different orientations are possible. In the case of a limited mobility of the molecule, for instance by reason of a double linking, bridges between the particles are formed, caused by polar interaction at the opposite contacting areas (Figure 4a).

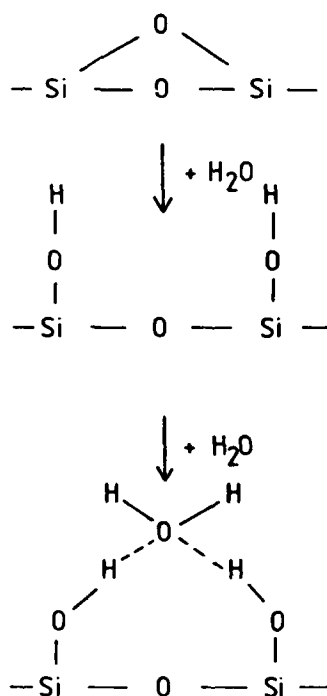


FIGURE 3 Screening of the surface potentials of silicate surfaces by water (Ref. 12).

Against that, if a molecule is able, due to his structure, to carry out turning or bending movements, the adsorption produces only a shielding of the surface forces similar to the monopolar case (Figure 4b). The first process leads to a "strutting" of the powder frame by the adhesive and, therefore, to a glide-hindering effect. In comparison with this, gliding processes between the particles are favored by turning and bending movements.

3 EXPERIMENTAL PROOF OF ADHESIVE LAYERS

In the following, the principal applicability of the different adhesion mechanisms on the compacting of powders are discussed using examples from the ceramic technology.

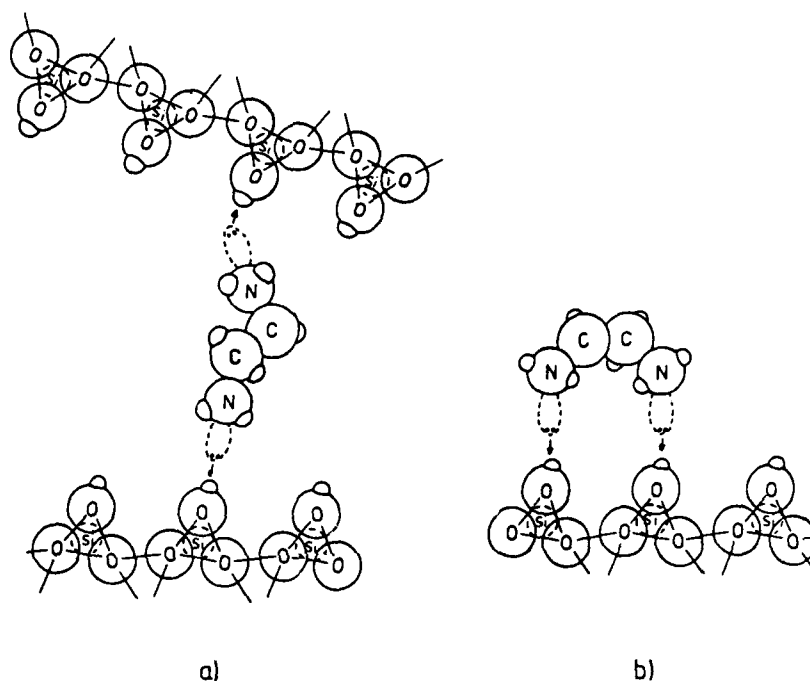


FIGURE 4 Adsorption of bipolar amines on kaolinite.

If spray-dried clay-ceramic batches are pressed without additives, an increasing compacting pressure increases the apparent density. According to Figure 5, the number of contacts raised thereby results in an increasing compression strength of the green bodies.⁵ The adsorption of trichloromethylsilane on the hydroxylic surfaces and the resulting reaction producing hydrochloric acid, after Figure 2, enables the construction of characteristic ideal solid bridges as the sturdiest constellation of the adhesion between the particles. It is possible to reach values for the compression strength, which are more than twice as high as those for powders with equal apparent density but no surface-active additives.

An example for the glide-promoting and the adhesive effect of molecules, is given in Figure 6, for clay-ceramic sprayed grains with a constant apparent density and, therefore, with a constant number of particles in the sample volume.² With increasing water content

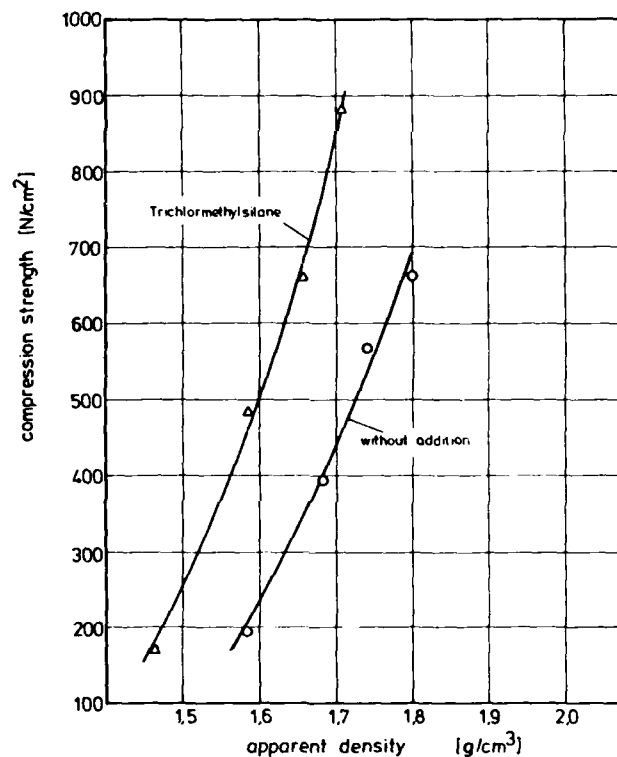


FIGURE 5 Influence of the apparent density on the compression pressure of clay-ceramic spary-dried batches caused by surface-active substances.

the compression pressure of the green bodies drops to a constant value. This trend is typical for the glide-promoting effect of adsorbed molecules, which diminish the surface forces.

In contrast to this, a surface-specific addition of di-iso-propanol-amine (DIPA) strengthens the powder frame into the compact, resulting in a doubling of the strength, an effect opposite to that of water addition. (The measured decrease of the apparent density of the stabilized pressing should be compensated by using a higher compacting pressure.) The competing effect of water (gliding) and DIPA (adhesive) is verified in Figure 6 by the middle curve for the addition of a 1:1 mixing of both substances.

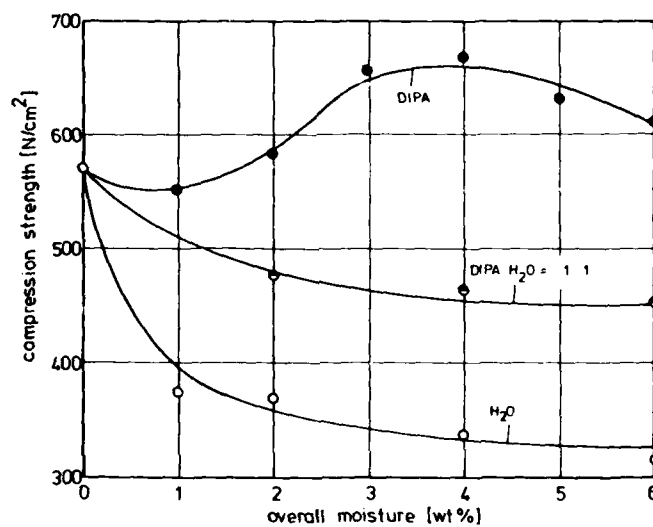


FIGURE 6 Dependence of the compression pressure and the total moisture for clay-ceramic batches.

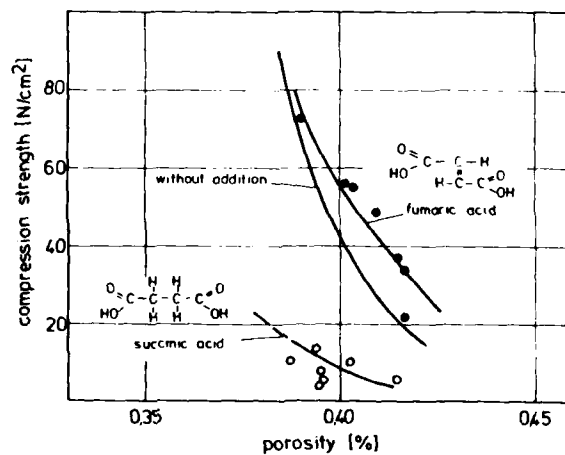


FIGURE 7 Influence of the surface coverage on the compression pressure and the porosity of compacted alumina powders.

The respective stabilizing or destabilizing character of dicarboxylic acids with different molecular mobility was proved for alumina compacts.⁶ According to Figure 7, the stability of a compact produced from dry powder, containing no neck-water but adsorbed water, is guaranteed by the action of the surface adhesive forces between the particles. If a freely revolving molecule such as succinic acid is adsorbed on alumina particles, a continued screening of the adhesion forces gives rise to a drastic decrease in strength. On the other hand, the fumaric acid (isomeric to the succinic acid) causes a distinct strengthening of the frame by adhesion mechanisms. This adhesion is made possible by reason of the central double bond.

4 ADHESION JUNCTION BETWEEN POWDER PARTICLES AND THE STRUCTURE OF COMPACTS

The different adhesion mechanisms between single particles in a ceramic powder are followed by qualitative and quantitative effects on the microstructure of the compacts produced.

The following results are valid for clay-ceramic batches, which were produced from well-defined spray-dried powders as initial material.⁷ Their particles shape is shown in Figure 8.

During compaction with a pressure of 62 N/mm^2 , the microstructure of a spray-dried granulate with addition of water is destroyed (Figure 9a). On the contrary, it was observed, that the adhesive-stabilizing effect of DIPA causes a molding of the agglomerates without destruction of their inner coherence (Figure 9b). The stabilization effect of TCMS is so strong that the spray-dried agglomerates are partially undeformed after compaction, this being caused by the characteristic solid bridges between the primary particles (Figure 9c).

We shall now discuss the quantitative, measurable properties for the characterization of the adhesive effects of additives on the microstructure of compacts. A measure for the arrangement of the powder particles in the compact is given by the X-ray texture, using the (001) and (020) interferences of the kaolinite.⁸ In accordance with Figure 10, the texture index *I* for spray-dried, water-containing batches is increased with the compaction pressure. This indicates a



FIGURE 8 SEM-micrograph of clay-ceramic spray grains.

gliding of the kaolinite particles into a new space-saving configuration. After passing over the maximum of the curve the index decreases, indicating fracture or bending of the individual particles.

The maintenance of the inner microstructure of the secondary grains by adding adhesive substances like DIPA causes a smaller texture index at low compaction pressures. This demonstrates that an orthogonal orientation of the flat kaolinite particles relative to the compaction pressure is hindered by the adhesion between them. The higher index level after the turning point is attributed to a destruction of small agglomerates in the necks of the greater grains, which are polygonized by the compaction pressure.

A further quantitative microstructural parameter for the compaction process is the mean pore width caused by the particle orientation. This so-called mean hydraulic pore width is defined as:

$$d_{\text{hydr.}} = 2 \frac{V_{\text{green body}} - V_{\text{theoret.}}}{A_{\text{spec.}}}$$

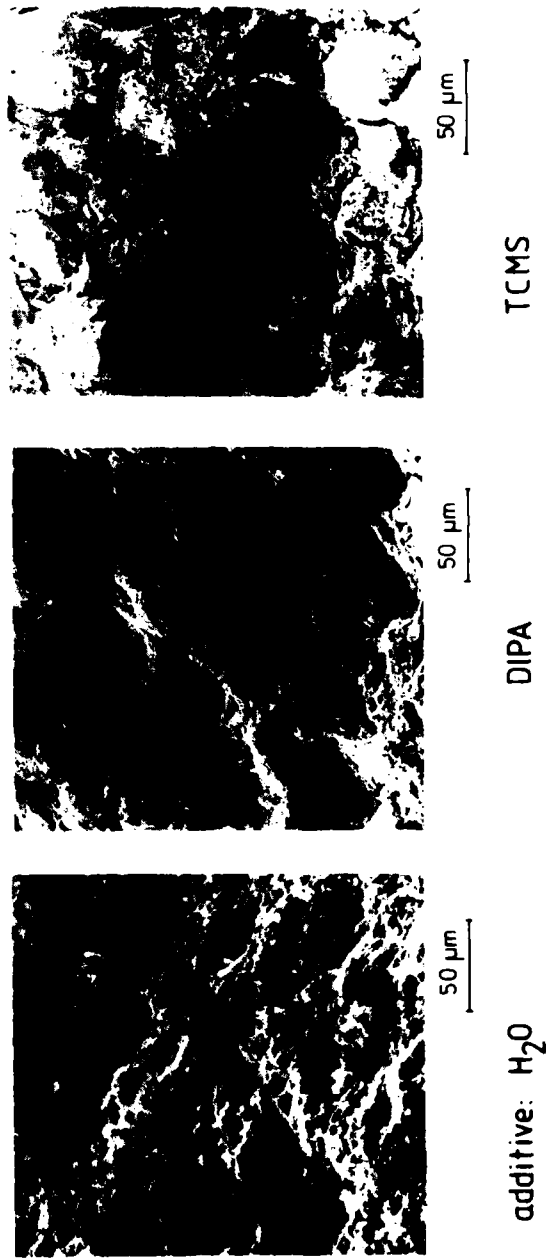


FIGURE 9 SEM-micrographs of the stabilizing effect of surface active substances in the compaction of clay-ceramics (compaction pressure: 62 N/mm²).

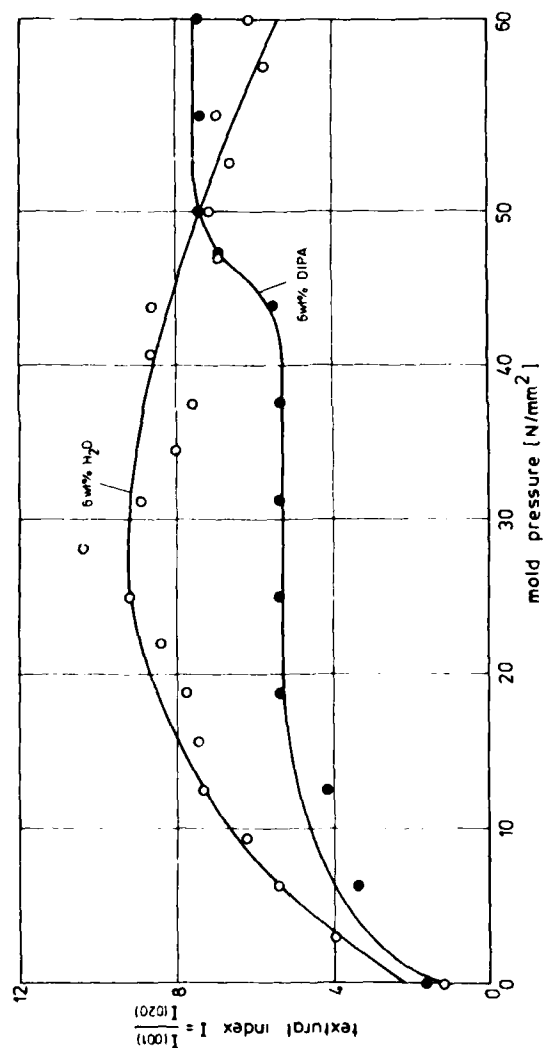


FIGURE 10 Influence of the compaction pressure on the texture index of clay-ceramic compacts.

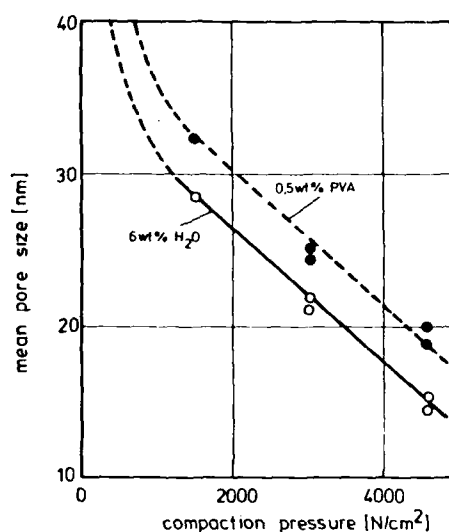


FIGURE 11 Mean hydraulic pore width dependence on the compaction pressure of clay-ceramics.

with

$$V_{\text{green body}} - V_{\text{theoret.}} = \text{pore volume}$$

$$A_{\text{spec.}} = \text{specific surface area}$$

The hydraulic pore width for compacts from clay-ceramic batches depends linearly on the compaction pressure as shown in Figure 11, independent of the pressing aid used.⁹ However, the addition of 0.5 wt% polyvinylalcohol (PVA) causes, over the entire compaction pressure range, a mean pore width which is, in comparison with water addition, more than 10 percent higher. The pore structure is stabilized by the adhesive effect of PVA.

In ceramic technology for producing green bodies, a strength of the compacts as high as possible is demanded for good handling of the products. On the other hand, the sintering process is accelerated by a minimal porosity of the compact. New investigations¹⁰ have demonstrated, that a hyperbolic dependence exists for the compression pressure and the pore volume independent of the kind of compaction process (e.g. simple compaction with high pressure or multiple compaction with low pressure). The dependence is given

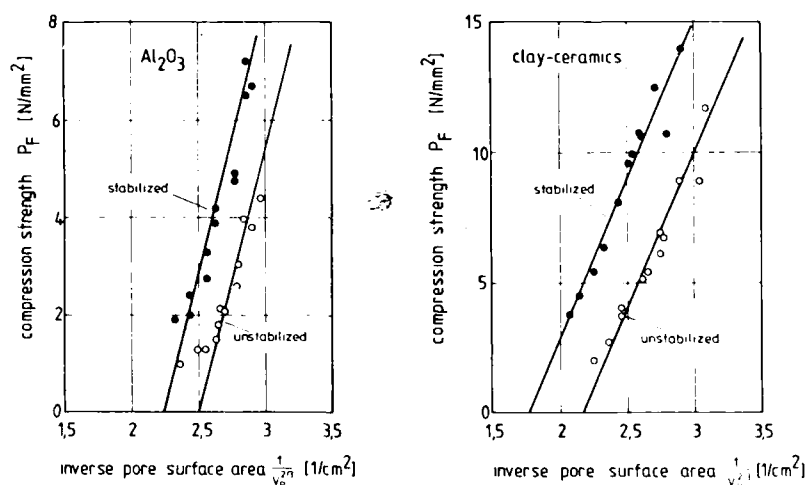


FIGURE 12 Dependence of the compression pressure on the reciprocal pore surface for clay-ceramics and alumina compacts.

by the relation:

$$P_F = \frac{C_i}{V_p^{2/3}} + d_i$$

with

$$\begin{aligned} P_F &= \text{compression pressure} \\ V_p &= \text{pore volume} \\ C_i, d_i &= \text{mass specific constants.} \end{aligned}$$

Figure 12 shows this relation for oxide- and clay-ceramic pressings. On the one hand, the compression pressure for both of these, relative to their plastic quantities extremely different materials, is proportional to $V_p^{-2/3}$. This indicates the increasing transition of inactive free pore surface to active adhesive area. On the other hand, the covering of the contact area by multipolar adhesive molecules leads to an increased strength. The adhesion of thin, probably monomolecular layers, results in an increase of 4.4 N/mm^2 for clay-ceramics and 2.7 N/mm^2 for alumina compacts with respect to water addition. Similar effects may also be expected for other surface-active and adhesive pressing aids.¹¹

The discussed results of the influence of intermediate layers on the densification of ceramic powders do not correspond to the diagram of Rumpf without contradiction. However, it must be considered that the entire number of particles in the specimen volume and, therefore, the number of contacts, is specific for the adhesion mechanisms including the typical effects of additives at the solid surfaces. But this is not included in the diagram of Rumpf.

References

1. H. Rumpf in *Agglomeration*, W. A. Kneper, Ed. (Interscience, New York, 1962), pp. 379-414.
2. R. Kirsch, dissertation (Universität des Saarlandes).
3. C. Bischoff and W. Possart, *Adhäsion* (Akademie Verlag, Berlin, 1983), pp. 83-88.
4. M. Michel, *Schweizer Maschinenmarkt* **28**, 36-39 (1984).
5. B. Frisch, W. R. Thiele, H. Peter and R. Kirsch, *Ber. Dtsch. Keram. Ges.* **54**, 259-263 (1977).
6. B. Frisch and K. Smidoda, *Ber. Dtsch. Keram. Ges.* **53**, 428-432 (1976).
7. B. Frisch, W. R. Thiele and H. Peter, *Ber. Dtsch. Keram. Ges.* **54**, 224-229 (1977).
8. B. Frisch, W. R. Thiele and R. Kirsch, *cfi/Ber. DKG* **58**, 251-262 (1981).
9. B. Frisch, W. R. Thiele, *cfi/Ber. DKG* **59**, 359-364 (1982).
10. B. Frisch, W. R. Thiele and W. Berwanger, *cfi/Ber. DKG* **63**, 263-271 (1986).
11. B. Frisch and E. Bakes-Miller, "Theory of Dust Pressing", in *Handbook of Ceramics, Suppl. to Interceram* **35** (Verlag Schmid, Friburg, 1986), pp 1-7.
12. S. R. Morrison, *The Chemical Physics of Surfaces* (Plenum Press, New York, London, 1977), p. 164.

SESSION OF SWITZERLAND

Quantitative Measurement of the Energy of Fracture of an Adhesive Joint Using the Wedge-Test†

J. COGNARD

ASULAB S.A., Passage Max-Meuron 6, 2001 Neuchâtel, Switzerland

(Received November 24, 1986)

The cleavage of adhesive joints upon the introduction of a wedge allows a measurement of the energy of fracture. Careful attention to the design of the joint leads to quantitative results. We show the relationship between the length of fracture and the geometrical parameters of the joint, the variation of the resistance of fracture with humidity; we also show that the fracture length follows a Weibull statistics, allowing for quality control.

KEY WORDS Cleavage of adhesive joints; durability; energy of fracture; resistance to fracture; wedge test; Weibull statistics.

INTRODUCTION

The cleavage of an adhesive bonded joint by a wedge is not usually used for quantitative determination of the adhesive joint properties due to the possible deformation of the adherends.

However, careful attention to the experimental conditions permits the determination of the adhesive resistance to rupture, R , and other related properties. If E is the Young modulus of the adherend, e its thickness, h the wedge height and l_0 the fracture length:

$$R = \frac{3Eh^2e^3}{16l_0^4} \quad (1)$$

† Presented at the Tenth Annual Meeting of The Adhesion Society, Inc., Williamsburg, Virginia, U.S.A., February 22–27, 1987.

provided that there is no plastic deformation in the substrate and no energy dissipated or yielding in the adhesive layer.

Thus the measure of the fracture length gives the resistance to fracture through Eq. (1) and its relation to surface parameters or environmental conditions. Experimental verification was already given for the case of two long strips of glass joined together with silicone oil. In these conditions R was equal to twice the oil surface tension as would be expected.¹

1 EXPERIMENTAL CONDITIONS

Two rectangular plates made from flat ($\pm 5 \mu\text{m}$ over 5 cm) metal strips are assembled with a liquid adhesive deposited as a central line using a syringe. The plates are filed at one end in order to form a mouth where the wedge can easily be introduced (Figure 1) and

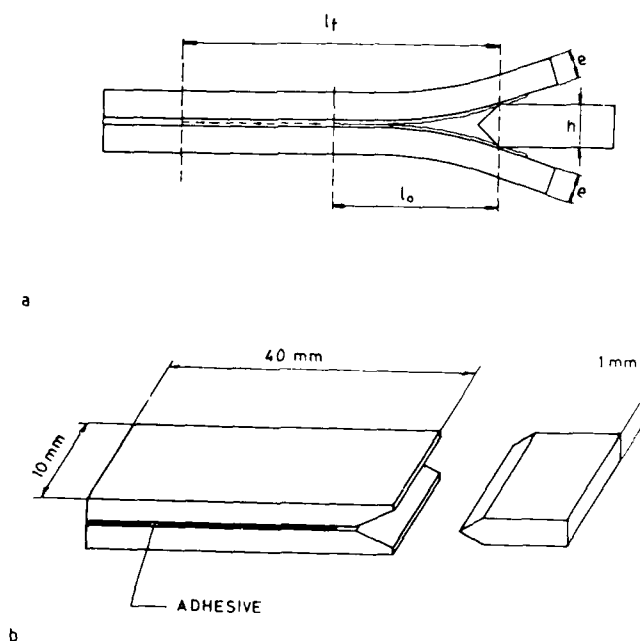


FIGURE 1 Schematic drawing of the wedge-test geometry.

then positioned and maintained with two clips. Polymerisation is carried out following the procedure recommended by the manufacturer. The resulting adhesive layer is very thin, of the order of $20\text{ }\mu\text{m}$ and it appears that thickness variations of the order of plus or minus $10\text{ }\mu\text{m}$ have little effect.

The wedge is introduced by means of a micrometric device (Figure 2) so that its edge protrudes some 2 mm from the mouth. This creates a crack, the length of which is measured by the distance separating the line where the wedge touches the beam and the crack tip. In order to locate the crack tip a micrometer is opened to the height of the assembly $+0.01\text{ mm}$; the crack tip is the point where the micrometer touches the assembly (Figure 3).

In general the metal used is hardened stainless steel AISI 304 of spring quality which avoids plastic deformation of the adherends. The adhesives used are formulations based on Shell, Ciba-Geigy and EMS-Chemie resins. The simplest formulation gives higher experimental scatter whereas filled adhesives give more reproducible results and also an initial cohesive failure. They will be designed by reference to the caption of Figure 6. The commercial adhesive AV 118 is used for purposes of comparison.



FIGURE 2 Micrometric device used to introduce the wedge.

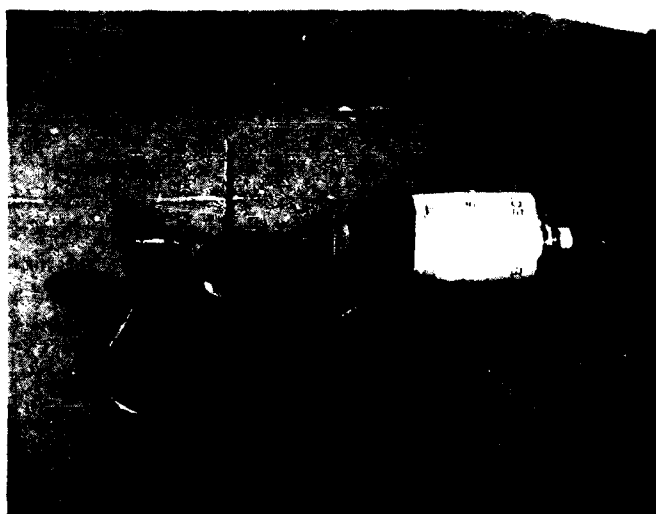


FIGURE 3 Determination of the position of the tip with a micrometer.

2 EQUILIBRIUM CONDITIONS

The kinetics of the fracture propagation has not been studied yet, thus the time necessary to attain equilibrium is not known precisely. Since driving potential for fracture propagation is the difference between the elastic strain energy release rate, G , and the energy of fracture, W_s ,[†] crack growth becomes very slow when G approaches W_s . Nevertheless our latest results, obtained over one year, confirm our previous estimations^{3,4} that in many cases the crack length is stable after one day in a dessicator. In Figure 4 the energies of fracture deduced from the crack length of five different epoxy adhesives are given. Only one rubber-modified epoxy adhesive shows slight crack progression which may be attributed to yielding. A joint made of the same adhesive, but filled, did not show any progression of fracture; neither did various epoxy-nylon adhesives. The wedge test is in fact, a double cantilever beam submitted to a constant displacement and thus the conclusions of S. S. Wang⁵ *et al.* should be valid.

[†] At equilibrium R and W_s are identical.

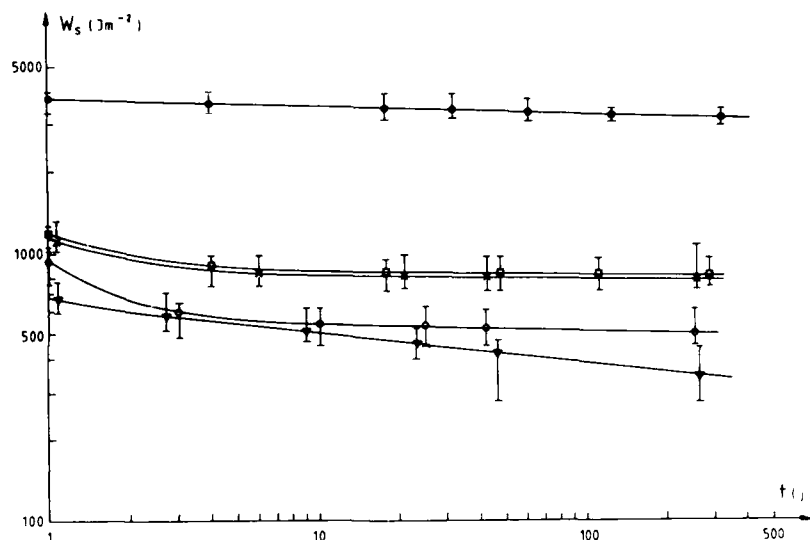


FIGURE 4 Variation of the energy of fracture with time for 5 adhesives. Only the unfilled, rubber-modified epoxy shows some variation probably due to yielding. ● epoxy nylon, □ epoxy-rubber modified, × filled epoxy-rubber modified, ○ epoxy nylon, ▼ epoxy-rubber modified (unfilled).

These authors used finite elements analysis and found, in the case of purely elastic behaviour, that the stress at the crack tip is similar to that in a monolithic system and may be described by the stress intensity factor K_I and the strain energy release rate G_I which are related to each other by $G_I = K_I^2/E_I$. Furthermore, they found that G_I is independent of the adhesive thickness as our experimental results⁴ suggest.

3 INFLUENCE OF THE EXPERIMENTAL GEOMETRY

3.1 Influence of the wedge-height

In our configuration the substrate beam should have a limited length, l , and the crack length should be maintained below $l/2$. Since R varies as l_0^4 the accuracy is very low for small cracks in strong adhesives; therefore, l_0 values of some 10 mm are preferred.

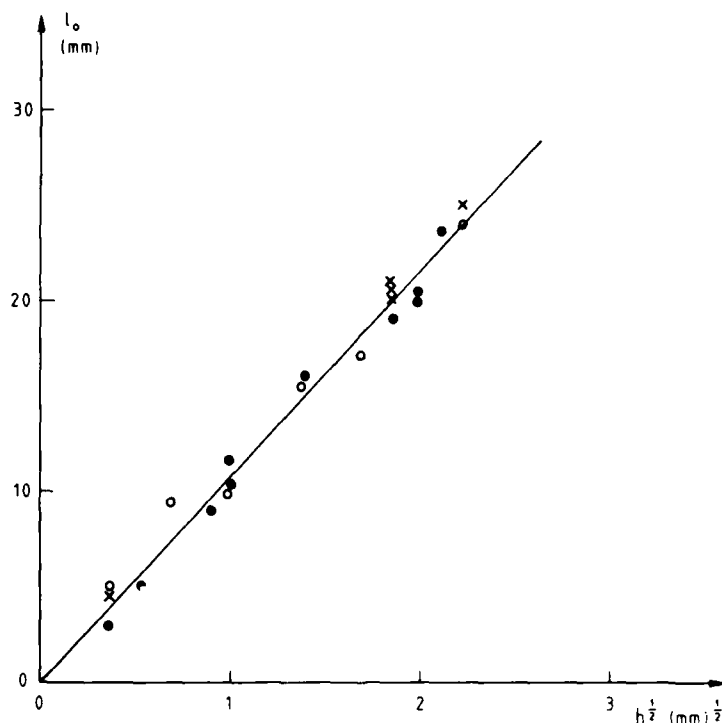


FIGURE 5 Variation of the fracture length with the square root of the wedge height.

The choice of the wedge height permits the variation of the crack length. Equation (1) applies for the joint [stainless steel-adhesive C (20μ) - stainless steel] cleaved by wedges of height varying from 0.15 to 5 mm as we have shown. From the experimental parameters, Eq. (1) becomes

$$W_S^{0.25} = \frac{1.47}{l_0} h$$

and the slope of Figure 5 gives $W_S = 340 \text{ Jm}^{-2}$ where h is 1 mm.

3.2 Application of the wedge-test to various substrates: influence of Young's modulus

Much of our work has been carried out on stainless steel of spring quality which is sometimes coated with another material.

In some cases it would be useful to study directly the adhesion to another metal. From Eq. (1) it can be seen that the simplest way to do this is to adapt the thickness of the substrate plates taking into account their elasticity. For example, titanium (BSTA 6) is easily deformed and has a modulus of 103 MPa. In order to cleave an assembly between two titanium beams 2 mm thick plates are used. In these conditions a 1 mm thick wedge provokes a cohesive fracture of 20 ± 2 mm in the joint using adhesive C18 which was polymerised at 140°C. Following Eq. (1):

$$W_s = \frac{1.54 \times 10^{-4}}{t_0^3 \text{ (m)}} \text{ Jm}^{-2}$$

The above values correspond to an energy of fracture of $1200 \pm 300 \text{ Jm}^{-2}$. In contrast, adhesive fracture on stainless steel or gold gives 500 and 100 Jm^{-2} respectively.

Kennedy *et al.*⁶ studied the cleavage of Redux 312/5 adhesive between titanium beams ($e = 2.10 \times 10^{-3}$) cleaved by a 3.17 mm wedge and found 53 mm of fracture length, corresponding to a resistance to fracture of 1515 Jm^{-2} . This was very close to that which we observed with our formulation C.

4 INFLUENCE OF HUMIDITY

4.1 The debonding of adhesive joints

The debonding of adhesive joints in outdoor environments is highly undesirable and its origin is still not completely understood.

The cleaved adhesive joint placed in humid conditions clearly illustrate this phenomenon. When a cleaved assembly, which has its fracture in equilibrium with the laboratory atmosphere, is placed in a humid environment the fracture length increases. The kinetics of the variation depends upon the type of the adhesive for a given wedge-test configuration. As shown in Figure 6 some adhesives will debond very fast at 40°C and 90% RH (for example the plasticised resin D) while others (such as adhesive A) show a very slow evolution. The debonding process in humid conditions, in common with all environmental delamination, is always interfacial. When the initial fracture is cohesive it progresses to the interface and proceeds along it (Figure 7) whilst it is maintained in a humid atmosphere.

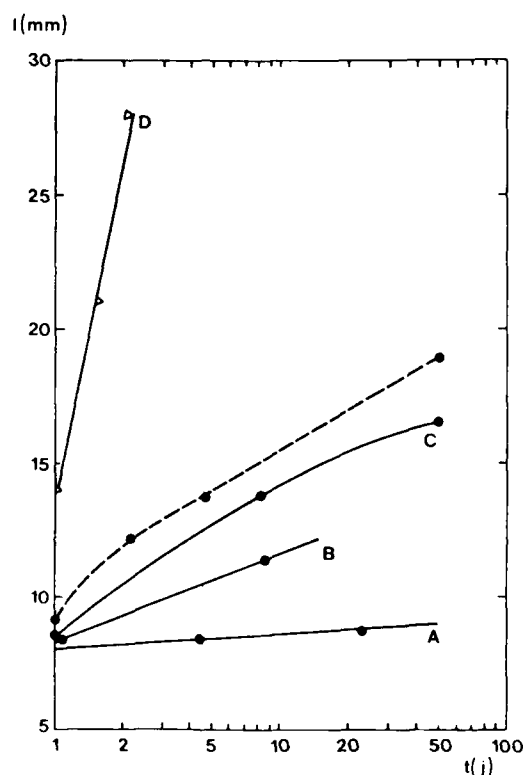


FIGURE 6 Evolution of the crack length with exposure time in humid conditions for different epoxy adhesives. A—filled nitrile epoxy, B—epoxy-nylon, C—epoxy-nitrile, D—plastified epoxy, - - - - - commercial adhesive AV 118.

4.2 Influence of a silane treatment of the surface of stainless steel on the resistance to humidity of an adhesive bonded joint

A study has been made with the plasticised adhesive D which, as mentioned above, is very sensitive to humidity and delamination. Two series of joints cleaved by the same process differ only in that one is silane treated and the other not. Upon cleavage the initial fracture is cohesive in both cases and runs over 14 mm, corresponding to a resistance to fracture $R = 75 \pm 25 \text{ Jm}^{-2}$. After 24 hours in hot humid conditions (40°C; 90% RH) the crack length reaches 28 mm for the silane treated substrate while it exceeds 30 mm for the untreated samples (see Table I). After 4 days of exposure all the

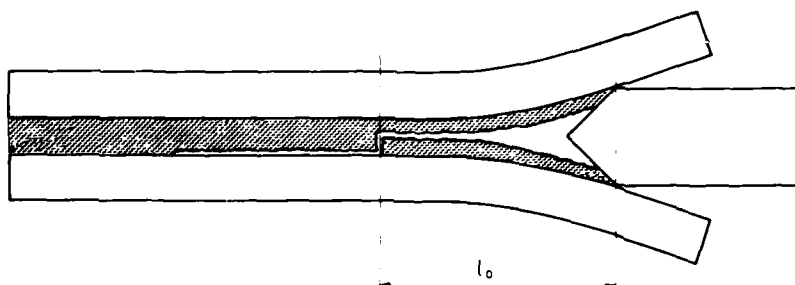


FIGURE 7 Crack always proceeds along interface in humid conditions. An initially cohesive fracture progresses to the interface and proceeds along it when maintained in the humid atmosphere.

TABLE I

Values of the crack length of joints in mm using adhesive *D*, between two stainless steel beams untreated or silane treated. l_0 is the initial fracture length $l(t)$ its value after time t of exposure to 40°C 90% RH

Stainless steel Silane treated	l_0	(24h)	$l(4j)$
	16	29	33
	16.8	25	31
	16.8	28	32
	16.2	28	32
	14.8	26	32
	16.2	26	33
Without treatment	17.8	34	debond
	13.8	35	debond
	16.3	26	debond
	17.8	36	debond
	14.8	35	debond
	17.5	36	debond

untreated samples are debonded while the silane-treated ones still have a resistance to fracture of some 5 Jm^{-2} ($\pm 0.5 \text{ Jm}^{-2}$) showing the benefit of the silanisation.

5 THE DISTRIBUTION OF THE FRACTURE LENGTH FOR VARIOUS SAMPLES FOLLOWS WEIBULL STATISTICS

The mechanical properties of adhesive joints show a more pronounced scatter in the case of simple formulations and unfilled

resins, as compared to commercial filled adhesives. Similar scatter is found for ceramics. For these materials it has been shown that the reliability of a given property, for example resistance to rupture, follows a Weibull statistics, that is $\ln \ln P_i^{-1} = m \ln \sigma - m \ln \sigma_0$ where P_i is the probability that σ is given value σ_i .⁷ The observation that Weibull statistics can also be applied to cured bulk epoxy resins has recently been shown.⁸ This led us to consider its possible applicability to the resistance to fracture in the wedge-test.

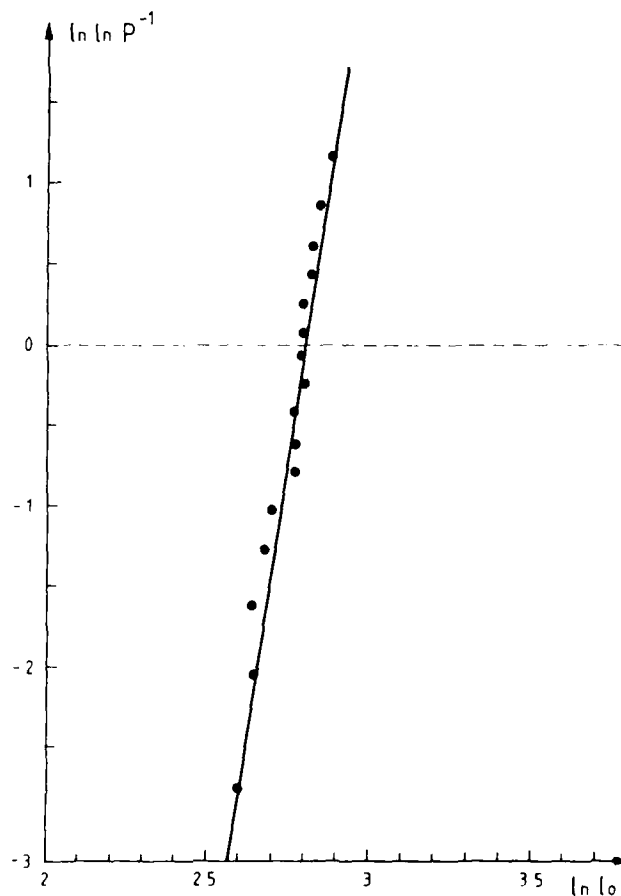


FIGURE 8 Weibull plot of the initial fracture length.

TABLE II
Values of the initial crack length for wedge-tests using adhesive D between stainless steel, in order of increasing value. P_i is the probability that l will be higher than l_i

No	l_0 (mm)	$P = 1 - \frac{i}{17}$	$\ln \ln P^{-1}$	$\ln l_0$
1	13.5	0.94	-2.78	2.60
2	14	0.88	-2.05	2.64
3	14	0.82	-1.61	2.64
4	14.5	0.76	-1.29	2.67
5	15	0.70	-1.03	2.70
6	16	0.64	-0.80	2.77
7	16	0.58	-0.61	2.77
8	16	0.52	-0.42	2.77
9	16.5	0.46	-0.25	2.80
10	16.5	0.40	-0.08	2.80
11	16.5	0.34	+0.07	2.80
12	16.5	0.28	-0.24	2.80
13	17	0.22	+0.41	2.83
14	17	0.16	+0.60	2.83
15	17.5	0.10	+0.83	2.86
16	18	0.04	+1.17	2.89

We have considered many adhesives and found that, in each case, the logarithm of the initial value of the length of fracture was a linear function of $\ln \ln P$. An example is given in Figure 8 for adhesive D , which has the highest scatter among the adhesives considered in this work. The law of probability P is obtained from the rank i of the N values of l_0 , put in order of increasing length as shown in reference 7b.† From the values given in Table II, one finds the Weibull modulus for adhesives D : $m = 13.7$. Values of P give the probability that the fracture length reaches a given value and allows the quality control of the adhesive. In the case of adhesive D the probability that the fracture length exceeds 18 mm is 4% and that it exceeds 19 mm is 0.0009. In other words, there can only be 1/1000 joints which have a resistance to fracture below 30 Jm^{-2} (corresponding to $l_0 = 19 \text{ mm}$).

Although Weibull statistics apply well to the initial fracture this is not so as far as the progression in humid atmosphere is concerned, which prohibits any prediction of the behaviour in such conditions.

† $P = 1 - \frac{i}{N+1}$.

What is actually observed is that those adhesive joints which are initially weaker (that is having the greater length of fracture) are also those that are more sensitive to humidity. For these joints, the progression of the fracture in a humid environment is much faster than it is for stronger joints.

CONCLUSION

The tests currently available to measure the properties of adhesive joints do not provide the data required for mechanical engineering. Quantitative use of the wedge-test can give the resistance to fracture of an adhesive joint and its variation with the parameters defining the adhesion problem. More work is needed to check the influence of thickness, internal stress and general applicability of the results. The main drawback in the method is that the locus of failure is only known at the end of the test by destruction of the assembly. Nevertheless, we have shown that sound results (comparable to other more time consuming and expensive methods) may be obtained which allow a much better characterisation of the joints than was available up to the present time. In addition, knowledge of the fracture behaviour permits the prediction of the lifetime in service at least for indoor applications.

Acknowledgements

Thanks are due to MM.F. Chabloz and C. Ganguillet for their careful experimental work.

References

1. S. J. Burns and B. R. Laus, *Int. J. Fract. Mech.* **4**, 339-345 (1968).
2. Cary, S. A. CH-2400 Le Locle.
3. J. Cognard, *J. Adhesion* **20**, 1-13 (1986).
4. J. Cognard, *Int. J. Adh. Adh.* **6**, 215-220 (1986).
5. S. S. Wang, J. F. Mandell and F. J. McGarry, *Int. J. Fract.* **14**, 36-58 (1978).
6. A. C. Kennedy, R. Kohler and P. Poole, *Int. J. Adh. Adh.* **3**, 133-139 (1963).
7. (a) R. W. Davidge, *Mechanical Behaviour of Ceramics* (Cambridge Univ. Press, 1979), Chap. 9.
(b) *Idem* p. 136.
8. H. R. Beer and T. Kaiser, manuscript in preparation.

Reactive Hot Melts on the Basis of Polyester and Polyamide†

F. ANNIGHÖFER

EMS-Chemie AG, 7013 Domat/Ems, Switzerland

(Received October 24, 1986)

Hot melts show many advantages over other adhesives, for instance, their lack of solvent and their very short setting time just by cooling. The weak point of hot melts in comparison to thermosetting resins is their limited thermal resistance. There is no doubt that the high performance hot melts on the basis of polyester and polyamide show a better heat performance than the widely-used rubbery hot melts. Nevertheless, it is true that the thermal resistance is limited by the melting point of the hot melt. To improve the heat performance, without losing the favourable hot melt properties, crosslinkable hot melts have been created. For the example, copolyamide/blocked isocyanate blends, it can be shown that crosslinkable hot melts are achievable in a wide range of reactivities. After curing, which takes place during the bonding process, these hot melts withstand temperatures of over 220°C even if the melting point of the initial hot melt was 100°C.

KEY WORDS Crosslinked hot melt adhesives; blocked isocyanates; high performance; polyamides; polyesters; thermal resistance.

INTRODUCTION

Hot melt adhesives consist of thermoplastic polymers. Melting point and melt viscosity of hot melt adhesives are relatively low compared to those of thermoplastic materials in general. The bonding with hot melts is performed by wetting the substrate surfaces with the hot polymer melt while joining them. Final bond strength is achieved

† Presented at the Tenth Annual Meeting of The Adhesion Society, Inc., Williamsburg, Virginia, U.S.A., February 22-27, 1987.

after cooling the hot melt. The main advantage of hot melts over other adhesives is their lack of solvent and their very short setting time.

The weak point of hot melts in comparison to thermosetting adhesives is their thermal resistance. There is no doubt that polyester and polyamide hot melts show a better heat performance than the widely used ethylene vinylacetate copolymers (EVA) or styrene diene block copolymers (SBS, SIS).^{1,2} Nevertheless, it is true that the thermal resistance is limited by the melting point of the hot melt. The melting point on the other hand defines the processing temperature which itself is limited by the thermal stability of the substrates.

To overcome this problem we have created crosslinkable hot melts which hold the advantages of hot melts but show a better heat performance.

High performance hot melts

The so-called high performance hot melts are semicrystalline polymers on the basis of polyester or polyamide.³ Melting points in the usual range of 80–200°C are achieved by copolymerizing different monomers. Figure 1 shows the chemical structure of a polyester hot melt. The usual monomers are terephthalic acid, isophthalic acid and several aliphatic diacids and glycols. The polymer contains hydroxyl and/or carboxyl endgroups. A typical copolyamide hot melt, as shown in Figure 2, is polymerized from caprolactam, laurilactam and several aliphatic diacids and diamines.⁴ The endgroups in this case are carboxyl and/or amine.

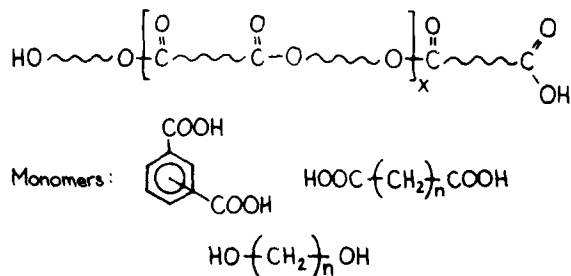


FIGURE 1 Chemical structure of a copolymer hot melt.

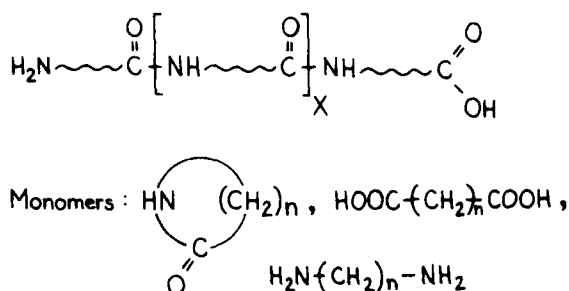


FIGURE 2 Chemical structure of a copolyamide hot melt.

Possibilities for crosslinking

Chemically these polyester or polyamide hot melts can be cross-linked *via* their functional endgroups. Possible crosslinking agents are multi-functional epoxies, isocyanates, oxazolines and so on. The crosslink density of the cured hot melt depends on the chain length of the polymer; it is relatively low compared to thermosetting resins.

Higher crosslink densities are achievable by using functionalized copolymers. In this way polymers with higher concentrations of hydroxyl, carboxyl or amine groups can be produced. Other functional groups, such as double bonds, can be introduced in the same manner.

The chemical possibilities in finding crosslinkable combinations with polyesters or polyamides are virtually unlimited. Unfortunately, the mixtures of the said reactive compounds with the hot melt are not storage stable; the reaction already starts during the blending process.

To combine the properties of long shelf life and fast crosslinking, the reactivity has to be inhibited. Possibilities are a chemical masking of functional groups or a physical microseparation of the components. Another consideration is crosslinking with humidity. It is not possible to expand on all these possibilities in this paper; however, a chemically-blocked system will be concentrated on. It will be shown that the boundaries with physically-inhibited systems or humidity-reactive systems are smooth.

Blocked isocyanates

A well known example of the chemical masking of reactive compounds is the blocking of isocyanates.⁵ The reaction of isocyanates with proton donors, H-B, like phenols, lactams, malonic esters and so on is an equilibrium reaction as illustrated in Figure 3. The

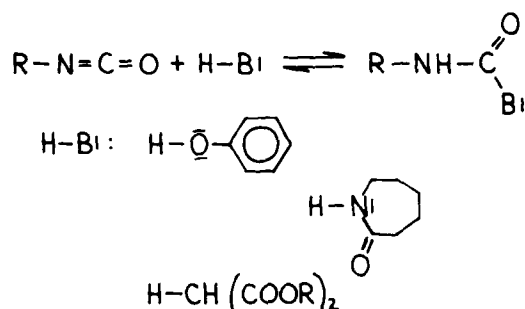


FIGURE 3 Chemistry of blocked isocyanates.

equilibrium shifts to the left side of the equation at elevated temperatures. In other words, blocked isocyanates form free isocyanates when heated. The cleaving temperature depends on the chemistry of the isocyanate and the blocking agent. In the presence of a crosslinkable polymer the crosslinking reaction starts as soon as free isocyanate has been formed.

The reaction kinetics of isocyanates or blocked isocyanates with hydroxyl, carboxyl or amine groups can be investigated by differential scanning calorimetry (DSC). Unfortunately, these experiments can be only conducted on low molecular weight model compounds as, for instance, hexane diol, adipic acid or hexamethylene diamine. In the case of polymeric hot melts with molecular weights in the range of 10,000 to 15,000 g/Mole the concentration of reacting groups is too small to be detected by DSC. Nevertheless, the DSC measurements on low molecular model compounds give useful information about the kinetics of polymeric systems as well.

RESULTS AND DISCUSSION

Table I shows the reaction temperatures of variously blocked MDIs, which have been stoichiometrically mixed with different reaction partners. The given reaction temperatures are the onset and the maximum of the reaction exotherm measured by DSC at a heating rate of 20°C/min.

The first experiments (1–3) indicate decreasing affinity of the isocyanate in the grading: alcohol > acid > amine. The poor reactivity of the hexane diamine seems not to be dependent on the chain lengths.⁴ Small amounts (0.1%) of triethylamine as a catalyst, on the other hand, decrease the reaction exotherm by 30°C.⁵

Because none of these mixtures with unblocked MDI is storage stable, the following measurements will refer to blocked species. From the literature, it is known that lactam-blocked isocyanates are less reactive than phenol-blocked isocyanates; and the latter are less reactive than free isocyanates.⁵ The experimentation data on that topic^{6–9} are, at first glance, disappointing. Nearly no difference is

TABLE I
Reaction temperatures of differently blocked MDIs measured by
DSC (heating rate: 20°C/min)

	Blocking agent	Reaction partner	Reaction temperature/°C	
			onset	maximum
1	unblocked	hexane diol	70	90
2	unblocked	adipinic acid	130	155
3	unblocked	hexane diamine	170	185
4	unblocked	dodecane diamine	170	185
5	unblocked	hexane diamine/cat.	145	155
6	caprolactam	hexane diol	175	190
7	caprolactam	adipinic acid	185	220
8	caprolactam	hexane diamine	170	185
9	phenol	hexane diol	180	190
10	caprolactam ^a	hexane diol	150	190
11	caprolactam ^a	adipinic acid	180	210
12	caprolactam ^a	hexane diamine	155	180
13	caprolactam ^a	hexane diamine/cat.	145	160

^a amorphous

visible between the reaction temperatures in respect to blocking agents and reaction partners. The explanation for this behavior can be given by experiments 10–13, which have been conducted using a different, caprolactam-capped MDI.

The first measurements have been carried out with a pure, crystalline material with a melting point of 197°C (caprolactam-capped, Grilbond® IL-6 (EMS-CHEMIE AG)), respectively 186°C (phenol-capped, Grilbond® IPH). The last measurements have been made with a nearly amorphous, caprolactam-blocked MDI. In the case of the amorphous, capped MDI the reactivities depend upon the reaction partner. Therefore, it seems that both the cleaving temperature of the blocked isocyanate and its melting point have to be exceeded in order to initiate the reaction. What is present is a combination of a chemical and a physical inhibition.

Bonding with hot melts

Before transferring the kinetic results from the DSC-measurements to polymers, something must be mentioned about the basic properties of the hot melts themselves. Otherwise, there would be a risk of creating a crosslinkable polymer which is no longer a hot melt.

Provided that the chemical structure is adapted to the required chemical resistance, the most important properties of the hot melt are the melting point and the temperature dependence of the melt viscosity. These properties define the processing temperature and the apparatus to be used for processing, the optimum bonding temperature and the wetting of the substrates and, last but not least, the thermal resistance of the finally-bonded structure.

Figure 4 shows the viscosity-temperature relationship of a copolyester hot melt with a melting point of 130°C. The hot melt in this example has an optimum temperature range for bonding of 140–180°C. At temperatures lower than 140°C the viscosity is too high to be able to wet the substrate or *vice versa*: this temperature marks the thermal resistance of the finally-bonded structure. The upper temperature limit for bonding is determined by the type of substrates. With textile materials there is a substantial risk of seepage if the temperature increases too much, that is, if the viscosity decreases too much. Also, the thermal stability of the substrates has to be taken into account.

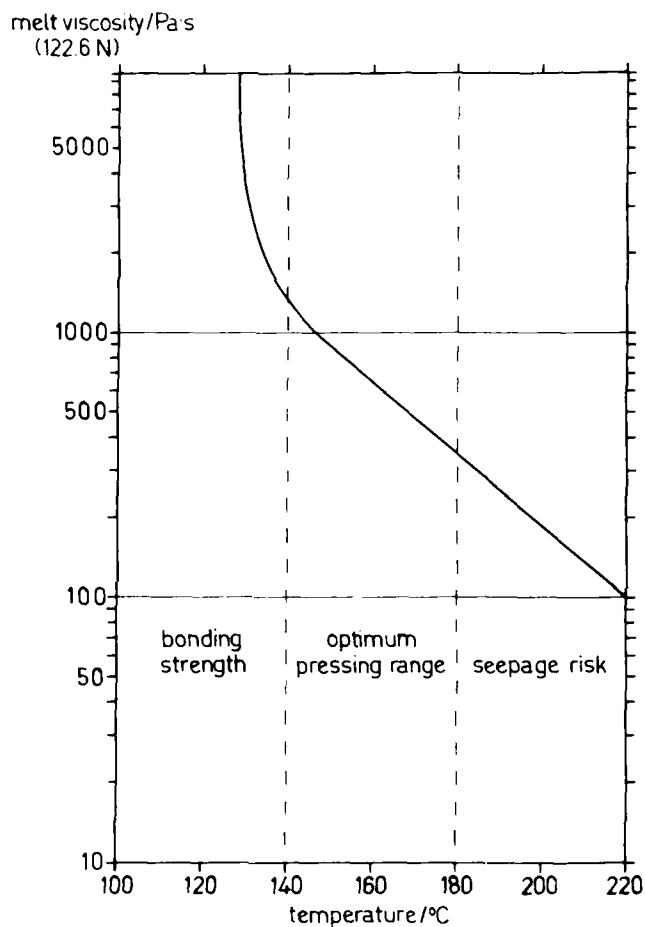


FIGURE 4 Viscosity-temperature relationship of the copolyester hot melt Griltex® 6 (EMS-CHEMIE AG) with a melting point of 130°C.

Crosslinking hot melts

In the case of crosslinkable hot melts the viscosity depends not only on the temperature but also on the time at a given temperature. An illustration for this additional time dependence is given in Figure 5. shown are melt viscosities of a copolyamide hot melt blended with 5 and 10% by weight of a caprolactam-blocked isocyanate. Unfortunately, this type of measurement gives only poorly reproducible

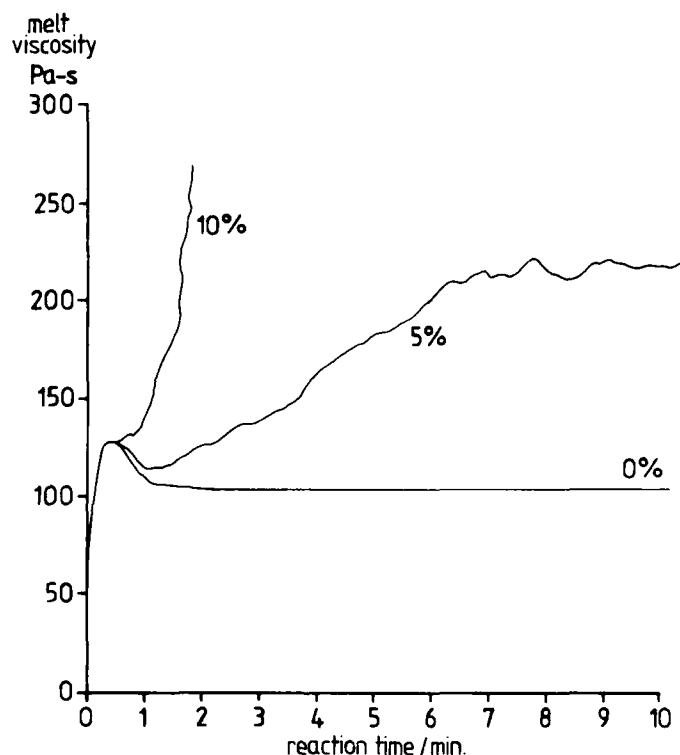


FIGURE 5 Viscosity increase of reactive copolyamide hot melts measured with a cone-plate viscosimeter at 200°C.

results in the case of highly reactive systems. But it is extremely useful to give an idea of the complexity of the viscosity-time-temperature dependence of reactive hot melts.

First, the latent reactive system has to be storage-stable for as long as possible. Then it has to be heated above its melting point, retaining a low viscosity until the substrates which are to be bonded are wetted. Afterwards, in the last step, the crosslinking reaction has to occur as quickly as possible.

The crosslinking kinetics of hot melts which are blended with blocked isocyanates depend upon several factors. The following discussion is based on discontinuous measurements of the relative viscosity. The reactive mixtures have been heat-treated for a fixed

time and, afterwards, the viscosity has been measured in solution (0.5% in m-cresol).

The first parameter to be investigated is the ratio of the reactive component in the hot melt. Figure 6 shows viscosity-time relationships of a copolyamide hot melt (Griltex[®] 4) which contains various percentages of a caprolactam-capped MDI (Grilbond[®] IL-6). For a one-to-one stoichiometry the isocyanate amounts to 5.9%. The continuous acceleration of the viscosity increase from 5% to 15% crosslinking agent indicates that there must be a side reaction in addition to the endgroup reaction. Possible, but still unproven, is a coupling of the isocyanate with the amide groups in the polymer chain, or a reaction of isocyanate with urea groups which are formed through the amino endgroup reaction.

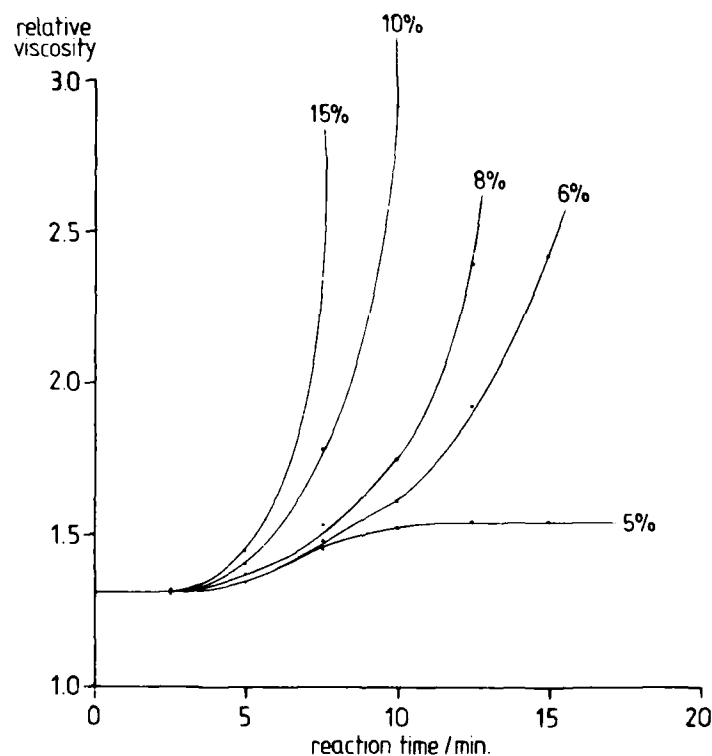


FIGURE 6 Viscosity-time dependence of copolyamides with different amounts of caprolactam-capped MDI, measured at 200°C.

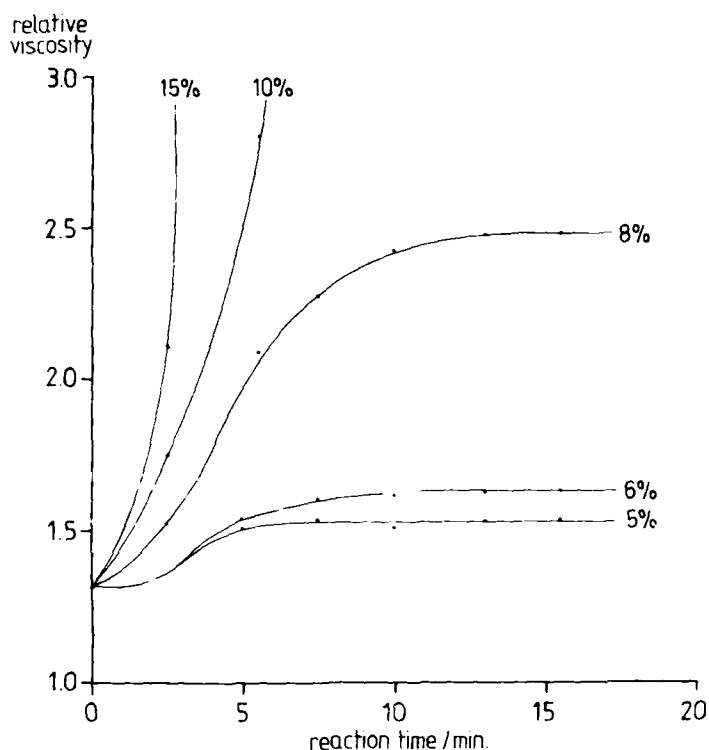


FIGURE 7 Viscosity-time dependence of copolyamides with different amounts of caprolactam-capped MDI, measured at 250°C.

The influence of the temperature on the curing time is illustrated in Figure 7. The measurements are conducted on the same uncatalysed blends of copolyamide with caprolactam-capped MDI as above. What is different is the reaction temperature of 250°C instead of 200°C. This rise in temperature quickens the reaction by at least a factor of two, but the 6 and 8% samples do not crosslink as before.

The effect of the type of blocking agent is shown in Figure 8. The phenol-blocked MDI (Grilbond® IPH) reacts much quicker than the caprolactam-blocked MDI. An uncapped MDI cannot be blended with the copolyamide without increasing the viscosity during the blending process.

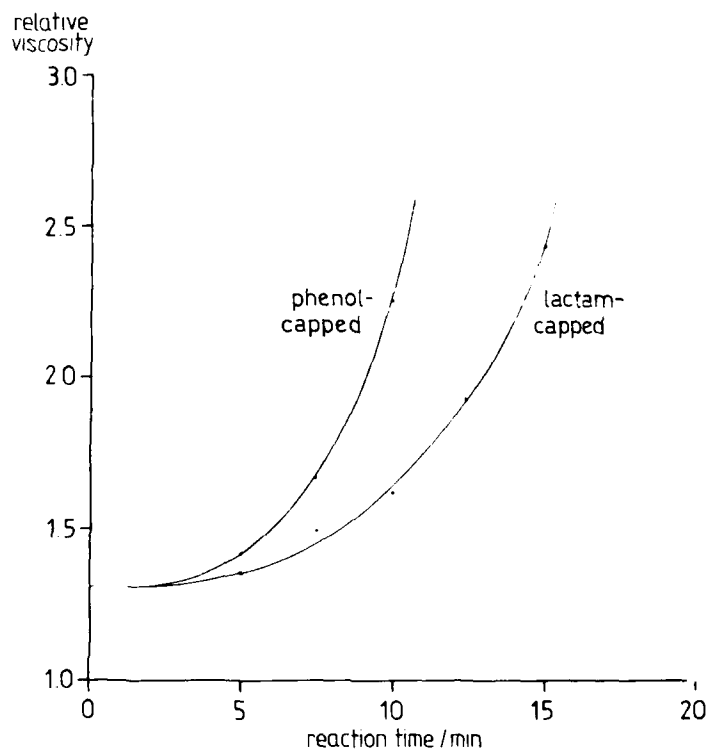


FIGURE 8 Comparison of the reactivities of caprolactam- and phenol-blocked MDI both 6% blended into copolyamide.

An accelerating effect on the increase of the viscosity is to be expected when the number of functional groups per molecule is increased. The corresponding experiments cover a three-functional caprolactam-blocked isocyanate, and a triamino copolyamide. The multi-functional isocyanate is a more highly condensed MDI-type isocyanate with an average functionality of 2.9, which has been capped with caprolactam. The multi-functional copolyamide has been synthesized using a small amount of triamine comonomer. The viscosity data of the mixtures containing multi-functional components are given in Figures 9 and 10. Besides the different functionalities Figure 10 contains data of hot melts with different

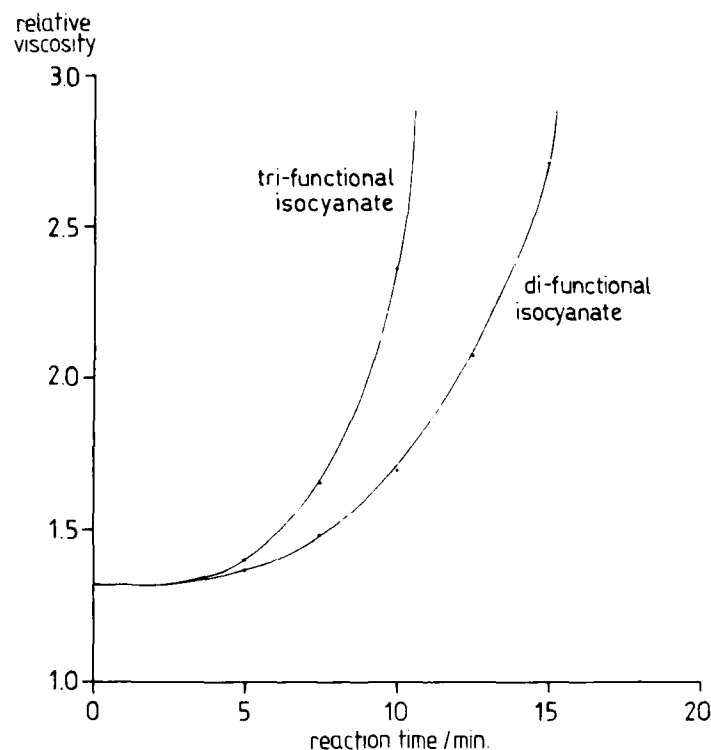


FIGURE 9 Comparison of the viscosity increase of di- and tri-functional caprolactam-blocked MDI, both 7% blended into copolyamide.

endgroups and different initial viscosities. Curve A is the copolyamide with mainly carboxyl endgroups (Griltex® 4) discussed above. Curve C shows an analogous copolyamide with amino endgroups which happens to react in about half of the time. D represents a trifunctional copolyamide of about the same molecular weight as A and C. The B-data are measured on a higher molecular weight hot melt.

Upon summarizing the kinetic data, it can be said that copolyamide hot melts can be crosslinked with capped isocyanates and the velocity of the reaction can be varied *via* the chemistry of the hot melt and the blocked isocyanate over a wide range, without losing the storage stability of the system.

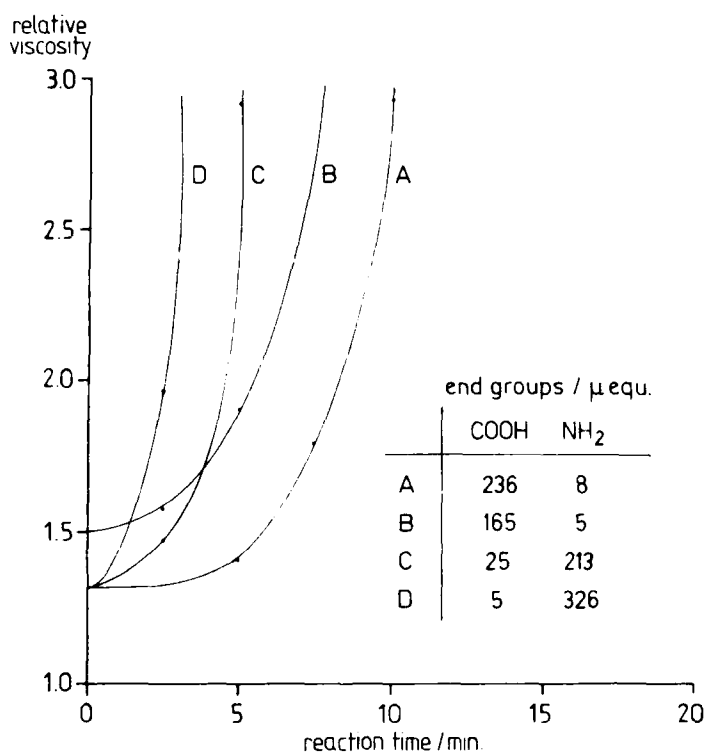


FIGURE 10 Reactivities of copolyamides with different endgroups in mixtures with 10% caprolactam-blocked MDI.

Thermal resistance

So far the discussion has concentrated on the velocity of cross-linking and consequent viscosity increase. What is left to be demonstrated is that a hot melt which has been modified in the described manner shows an improved thermal resistance. The experiments which have been conducted to reveal the heat performance are shown in Figure 11.

The first test related to the resistance of the hot melt material itself. For this test a hot melt foil (0.5 mm) was heated at a rate of 1°C/min under a stress of 1N/mm² until it failed. The result of this series of experiments can be summarized very easily. In all cases

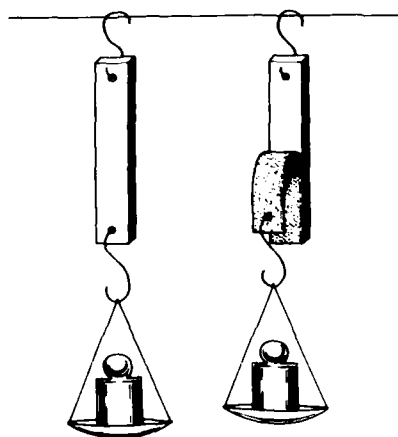


FIGURE 11 Left: test of the heat resistance of hot melt foils, right: heat peel test of hot melt bonded laminates.

where the insolubility in *m*-cresol indicates a crosslinked system, the hot melts withstand more than 220°C, even when the melting point of the basis polymer was 100°C. The not-completely-crosslinked systems fail in a range of 5–20°C above their melting point.

For characterizing the thermal resistance of bonded structures peel tests under a load of 1N/5 cm have been carried out. For this test, polyester carpet which was scatter-coated on its reverse side with 100 g/m² of hot melt powder (200–500 μm) was heat-pressed to phenolic-resin-cured backings. Laminates of this type are in use for door trims and rear shelves in car interiors.⁶

The experimentation data confirm the necessity of completely crosslinking the hot melt to get an essential rise in the heat stability. In the cases where the adhesive is crosslinked the bond remains intact until the carpet starts to degrade at about 220°C.

But the interdependencies between pressing temperature and time, hot melt reactivity and wetting behavior increase the complexity. The data in Table II may illustrate the influencing factors. The first three columns represent measurements on a low-viscosity, fast-reacting hot melt. Under the bonding conditions 100°C/30s a good wetting is achieved, resulting in a high peel strength. As visible from the thermal resistance, crosslinking has not occurred. A rise in the bonding temperature up to 140°C results in crosslinking.

TABLE II
Application properties of different crosslinking hot melts

Melting point/°C	80		120			
Initial melt viscosity (122.6 N, 160°C), Pa · s	25		1000			
pressing temperature/°C	100	140	180	130	150	200
pressing time/s	30	30	30	30	30	30
thermal resistance/°C	85	>190	>190	130	>190	>190
peel strength/N/5 cm	>25*	15	3	13	>25*	>25*

* substrate failure

The thermal stability increases to more than 190°C. In parallel, the peel strength decreases because the hot melt has soaked into the carpet. This effect is amplified at a bonding temperature of 180°C.

On the right side of Table II, bonding data of a high-viscosity, medium-reactive hot melt are shown. In this case, there is no decrease in the peel strength with increasing bonding temperature. On the other hand, the minimum bonding temperature is shifted to about 150°C because of the poorer wetting effect and the slower crosslinking reaction.

This short excursion into the application properties shows that crosslinked hot melts offer many possibilities. But it also shows that the type of hot melt and the bonding parameters have to be carefully selected with regard to each specific bonding problem.

CONCLUSION

Crosslinkable hot melts are a new class of adhesives. They are created to improve the heat performance of hot melts without losing the advantages of hot melts, for instance, their lack of solvent and their very short setting time. As shown, crosslinkable hot melts tremendously exceed their uncrosslinked counterparts in respect to thermal resistance. Only time will tell whether the requirement of more closely observing the application conditions will be accepted for achieving the described advantage.

References

1. F. Eichhorn and Th. Reiner, *Elektro-Anzeiger* **34**/7, 33 (1981).
2. A. J. Kettleborough, *Polymers, Paint & Colour Journal* **11**, 62 (1978).

3. F. Annighöfer, *Proceedings of the 2nd Adhesives, Sealants and Encapsulants (ASE) Conference*, London (1986).
4. S. Schaaf, *Textilveredelung* **9**/1, 14 (1974).
5. R. G. Arnold, J. A. Nelson and J. J. Verbanc, *Chem. Rev.* **57**, 47 (1957).
6. R. Nüssli, *European Adhesives and Sealants* **12**, 18 (1985).

The Repair of Concrete Structures by Injection With Epoxide Resin†

A. C. ROULIN-MOLONEY* and A. R. BERCHTEN**

** Laboratoire de Polymeres, Swiss Federal Inst. of Technology, Lausanne, Switzerland.*

*** Suisselectra Consulting Engineers SA, 4010 Basel, Switzerland.*

(Received October 24, 1986)

The factors to be considered in selecting a material suitable for the repair of concrete structures are discussed. The repair work of the Zeuzier Arch Dam in Switzerland is described including the special problems encountered in this particular application and the supporting experimental programme.

KEY WORDS Application properties; cracked concrete structure; epoxy resin; field repair; mechanical properties; application properties.

INTRODUCTION

Concrete structures may be damaged as a result of inadequate design or poor fabrication such as insufficient provision of expansion joints or cracking due to shrinkage on setting. Existing structures may be damaged by overloading; for example, most bridges built in the early part of this century are now required to bear loads vastly superior to the original design.¹ Other causes of damage are seismic activity, the settlement of foundations and chemical reactions.² For many years the problem of cracked concrete was ignored since no effective method of repair was available.³ However, cracks provide sources of stress concentrations and hence reduction in the strength

† Presented at the Tenth Annual Meeting of The Adhesion Society, Inc., Williamsburg, Virginia, U.S.A., February 22-27, 1987.

of the structure, they often lead to corrosion in pre-stressed concrete and may give rise to leakage of water and other fluids.

The case which stimulated this work was the Zeuzier Arch Dam in the canton of Valais, Switzerland. This 156m. high Dam which is situated at an altitude of 1778 m. functioned perfectly normally for 21 years. The central pendulum in the Dam regularly recorded deformations in a 30×70 mm. envelope due to thermal changes throughout the year and to the variation in lateral water loads. However, in the autumn of 1978 the pendulums indicated an abnormal movement of the Dam in the upstream direction even though the Dam was almost completely full. The Dam was immediately drained but extensive investigations could only commence in the spring of 1979 due to the climatic conditions. After comprehensive examination of the structure of the Dam it was concluded that the Dam had settled 11 cm., that there was a shortening of the arch chord at the level of the Dam crest of 6 cm. and that an upstream displacement had occurred measuring 11 cm. at the Dam crest. These movements inevitably caused cracking in the Dam structure:

- an opening of the vertical construction joints on the upstream face
- cracks on the downstream face extending locally into the rock abutment
- cracks visible in the inspection galleries essentially towards the abutments.

A schematic diagram of the Dam and the crack network is shown in Figure 1. Extensive investigations as to the causes of the settlement of the Dam were conducted and their results have been published.⁴ It was demonstrated that the movements of the Dam were due to a regional settlement caused by the drainage of an exploratory adit for a new motorway tunnel through the Alps. This adit was under construction a distance of 1.5 km. from the Dam and 400 m. lower in altitude than the base of the Dam. It was concluded that a repair of the Dam would be possible if a suitable agent was found. This repair operation was also stimulated by the fact that the Societe de l'Electricite de la Lienne would lose about 6M Sfr. per year by only operating as a "run of river" station rather than accumulating water in summer and generating when demand is high in winter.

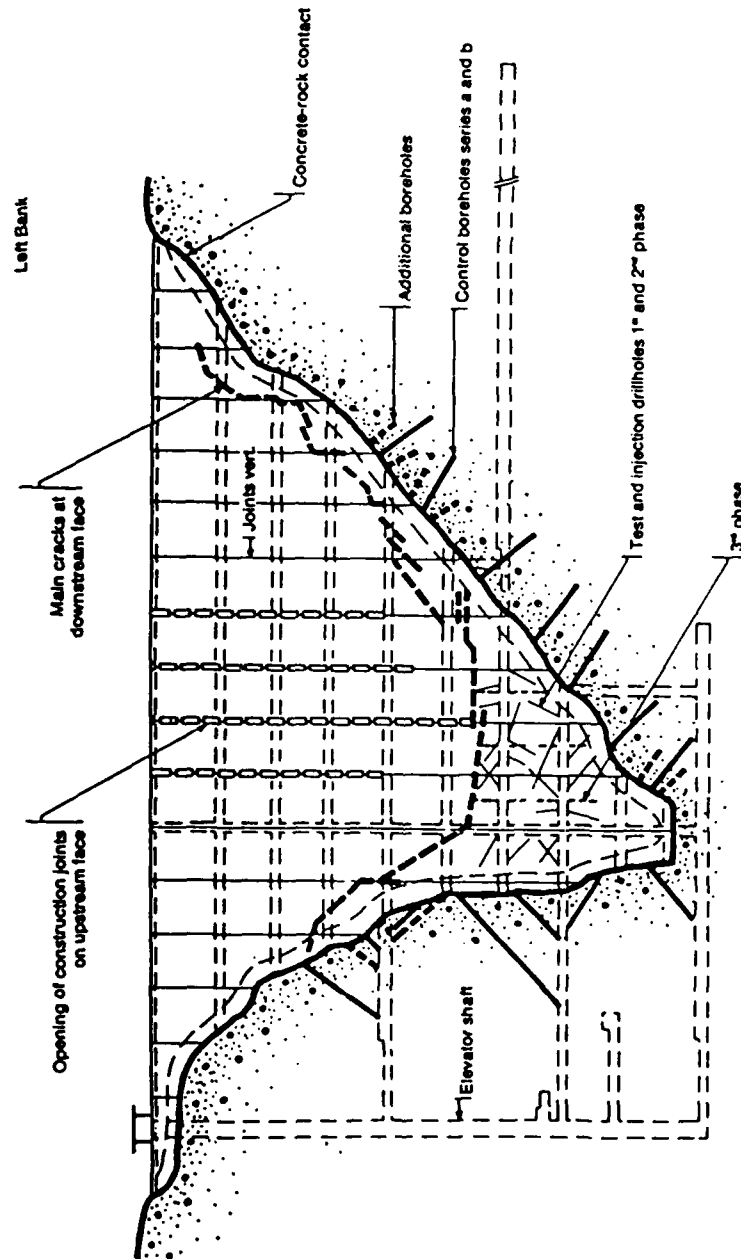


FIGURE 1 Schematic diagram of the Zeuzier Arch Dam showing the main crack network and the test boreholes (after Berchien Ref. 5).

A number of parameters had to be considered in order to select a suitable material for the repair.

- the viscosity must be sufficiently low to penetrate a network of fine cracks, in this case down to 0.2 mm. in thickness and of dimensions up to 5m. by 30m.
- the adhesion to concrete must be good even in wet conditions
- the material must have a high Young's modulus, tensile and compressive strength
- the pot life must be sufficiently long to allow injection before gelation
- the curing reaction must be possible at the working temperature of between 3 to 7°C inside the Dam which results from the altitude of 1778 m.

These requirements restricted the choice to an epoxide resin but since the properties may be considerably varied by the choice of resin and hardener chemistry, the presence of additives such as fillers and diluents, further specification was necessary. The Federation Internationale de la Précontrainte had made certain recommendations for epoxides used in construction.⁵ The compressive modulus should be at least 8 GPa, the compressive strength at least 75 MPa after 7 days and the pot life a minimum of 20 minutes. On the basis of these recommendations Suselectra Consulting Engineers asked for a resin with the following characteristics for the repair of the Zeuzier Dam:

- viscosity at 23°C: 500 mPa s
- minimum cure temperature: 5°C
- modulus of elasticity: 8 GPa
- compressive strength (min.): 60 MPa
- tensile strength (min.): 10 MPa
- bond strength to wet concrete: 3 MPa

The modulus of cured epoxide resins is always in the range of 2.5 to 3.5 GPa depending on their chemical structure. Thus, in order to increase this value it is necessary to incorporate high modulus mineral fillers in the form of particles. As a general rule the higher

the volume fraction of filler the higher the modulus, the higher the viscosity of the uncured mixture and the lower the adhesive strength. Thus the quantity incorporated involves a compromise between these parameters. For this type of application typical fillers are silica flour, glass beads and barium sulphate.

MATERIALS

The principal materials used in these tests were Rodur 510 and 520, the resins selected for the repair work of the Zeuzier Dam (produced by Sika SA, Zurich). The two products have differing viscosities and can be mixed to give an intermediate viscosity appropriate to the working temperatures and the dimensions of the cracks.

REPAIR WORK ON SITE

The repair was carried out in several stages; firstly, by injection of the cracks visible on the Dam faces and in the inspection galleries. Secondly, by drilling holes 46 mm. in diameter from the inspection galleries and the Dam faces between each vertical joint perpendicular to the axis of the gallery. In total, 228,000 kg. of resin was injected into the Dam during the repair.

The epoxide resin was supplied in cans ready for mixing. The hardener component was poured directly into the can containing the resin component and the two mixed with a pneumatic tool. This procedure avoids the necessity for accurate weighing on site. The injections were carried out up to maximum pressures of 20 bars. The amount of resin injected decreased with each stage indicating the effectiveness of the treatment. Samples of the same mixes were also poured into $4 \times 4 \times 16$ cm. moulds and allowed to harden. These prisms were then labelled with the date of casting, the resin system and the location within the Dam. In addition, core samples were removed from the structure (diameter 100 mm.) in order to verify the filling of the cracks and to measure the properties of the injected concrete and the adhesion to concrete.

EXPERIMENTAL WORK AND RESULTS

(A) Quality control of the resin injected into the Dam

During the period 1980 to 1983 the prisms cast on site were tested. The density, compressive modulus, compressive and flexural strength were measured. Similar specimens were cast in the Laboratory for comparison. The results are given in Table I which represents data from nearly 300 specimens. It can be noted that over the three-year period there was a distinct improvement in the mechanical properties probably due to the increased experience of the employees. The values are shown in the histograms in Figure 2. In 1982 a series of low values of modulus were noted. This results from incomplete cure either due to inadequate mixing or due to leaving too much time in between the mixing and the casting. The resin component which includes the particulate filler has a density of 2.23 gdm^{-3} and the hardener of 1.02 gdm^{-3} and thus with time the two tend to separate out. One of the principal parameters which must be controlled on site is the homogeneity of the mixture since, if this is assured, the resin has reproducible properties. In

TABLE I
Properties of resin samples cast on site and in the laboratory

Place/ Material	Density g dm^{-3}	Flexural modulus GPa	Flexural strength MPa	Compressive strength MPa
Site 1980 (510)	—	3.80 ± 0.61	—	54.7 ± 3.4
Site 1980 (510/520)	—	5.33 ± 0.2	—	—
Site 1982 (510)	2.02 ± 0.01	4.93 ± 0.05	35.1 ± 2.2	88.5 ± 1.6
Site 1982 (510/520)	1.88 ± 0.05	3.62 ± 0.4	29.5 ± 1.5	66.8 ± 2.9
Site 1983 (510)	1.97 ± 0.02	5.08 ± 0.5	36.0 ± 0.6	90.4 ± 0.7
Lab. 1981 (510)	1.93 ± 0.02	4.88 ± 1.6	41.9 ± 3.5	97.7 ± 3.6
Lab. 1982 (510)	2.00 ± 0.01	4.69 ± 0.11	50.5 ± 3.0	88.8 ± 2.5
Overall mean	1.97 ± 0.01	4.89 ± 0.06	35.8 ± 0.6	87.8 ± 0.9

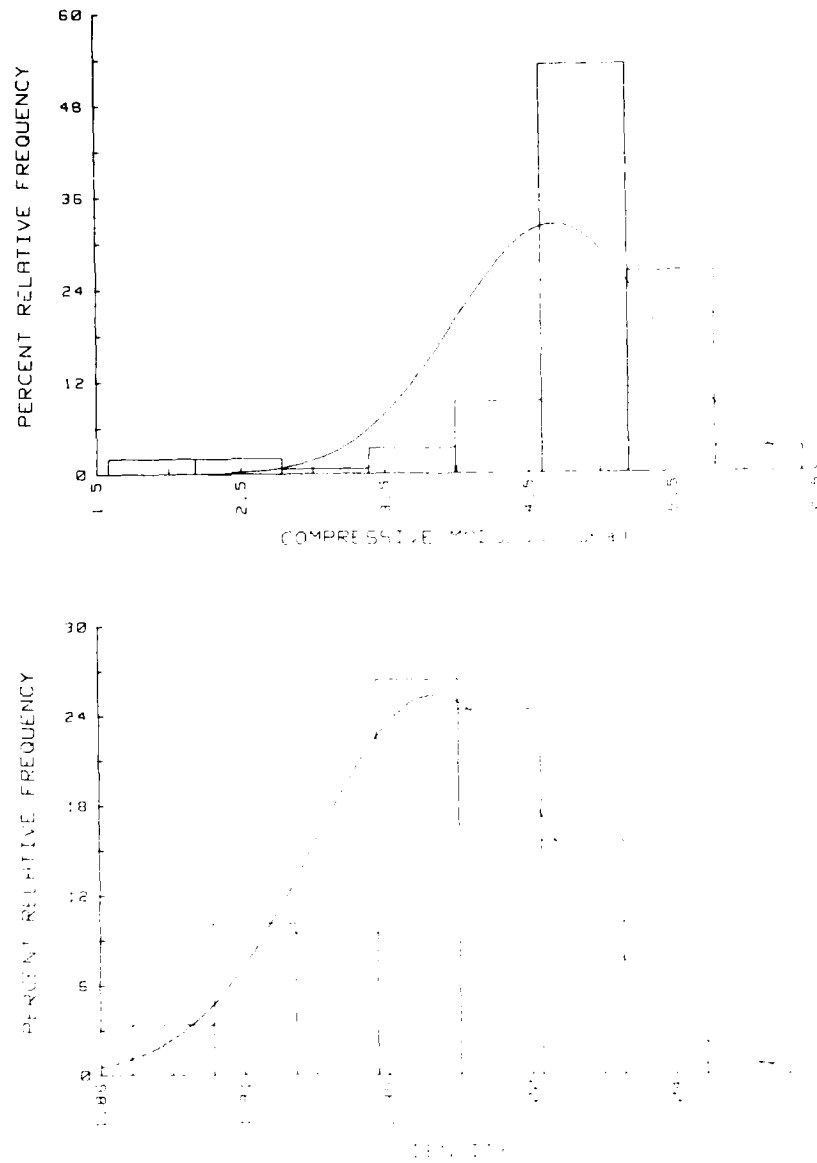


FIGURE 2 Histograms of density, modulus, flexural and compressive strength for resin samples cast on site during the repair.

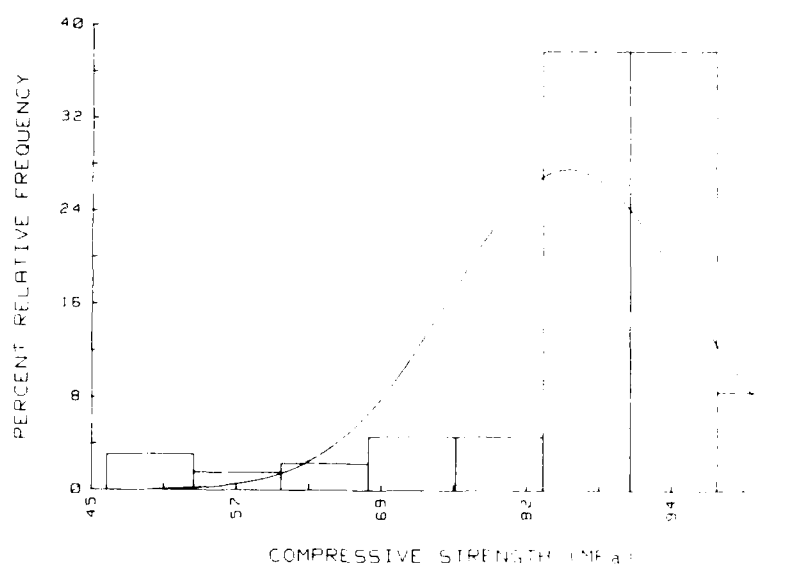
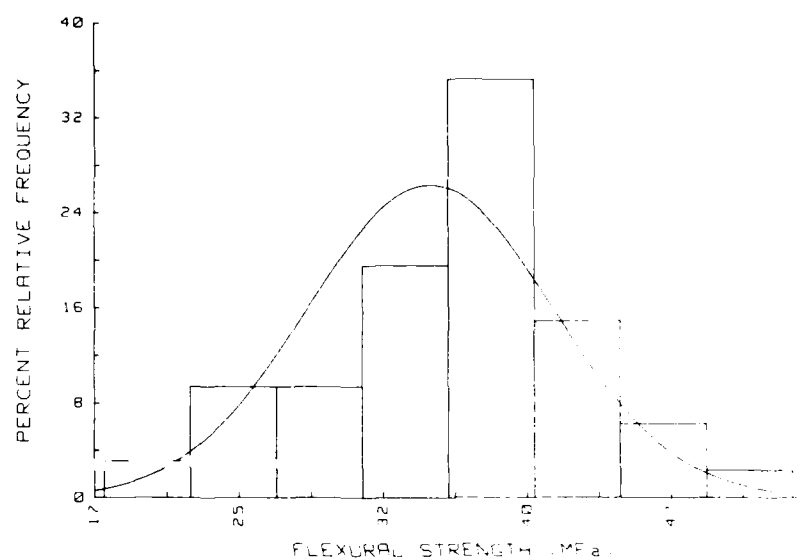


FIGURE 2 (continued)

Figure 3, the mechanical properties of the Rodur have been compared with the density; there is some correlation between density fluctuations and the modulus and compressive strength.

(B) Verification of the properties of Rodur

The properties measured were the density, viscosity, the pot life, filler content, flexural strength and the bond strength to wet concrete. The viscosity was measured using a Rheomat 30 turboviscometer. Following the practice of the resin manufacturer, the pot life was taken as the time for a mixture of 1 kg to rise in temperature from 20 to 40°C. The filler content was measured by burn off tests at 400°C. The bond strength to wet concrete was obtained by using 7×7×16 cm blocks of concrete which were submerged in tap water for 7 days. After alignment in aluminium jigs the resin was poured into the glue line (1.5 mm) and the samples immediately re-immersed in water. After 7 days cure under water the samples were ruptured in four-point bending. The results of these tests are given in Table II.

(C) Cure of resin at low temperatures

It was necessary to establish whether the cure of the resin was still possible at temperatures as low as 0°C, especially in thin layers. The cure reaction being exothermic accelerates the reaction and cure time is strongly dependent on the volume of the mixture. For these tests the resin, hardener and steel moulds were pre-cooled to 0°C. Mixing, casting and curing were carried out at this temperature. The flexural modulus and strength were measured after 1000 h cure at 1°C. These 1 mm thick samples gave values of 3.85 GPa and 40.8 MPa respectively. This indicated that curing was possible at low temperature and in layers of thickness comparable to the cracks in the Dam. The evolution of flexural modulus with cure time at 5°C for 4 mm. thick samples is given in Figure 4. Under these conditions the gelation time is approx. 24h. and the mechanical properties reach plateau values after 600 h. The final values are in good agreement with those measured for the large prisms (*cf* Table II).

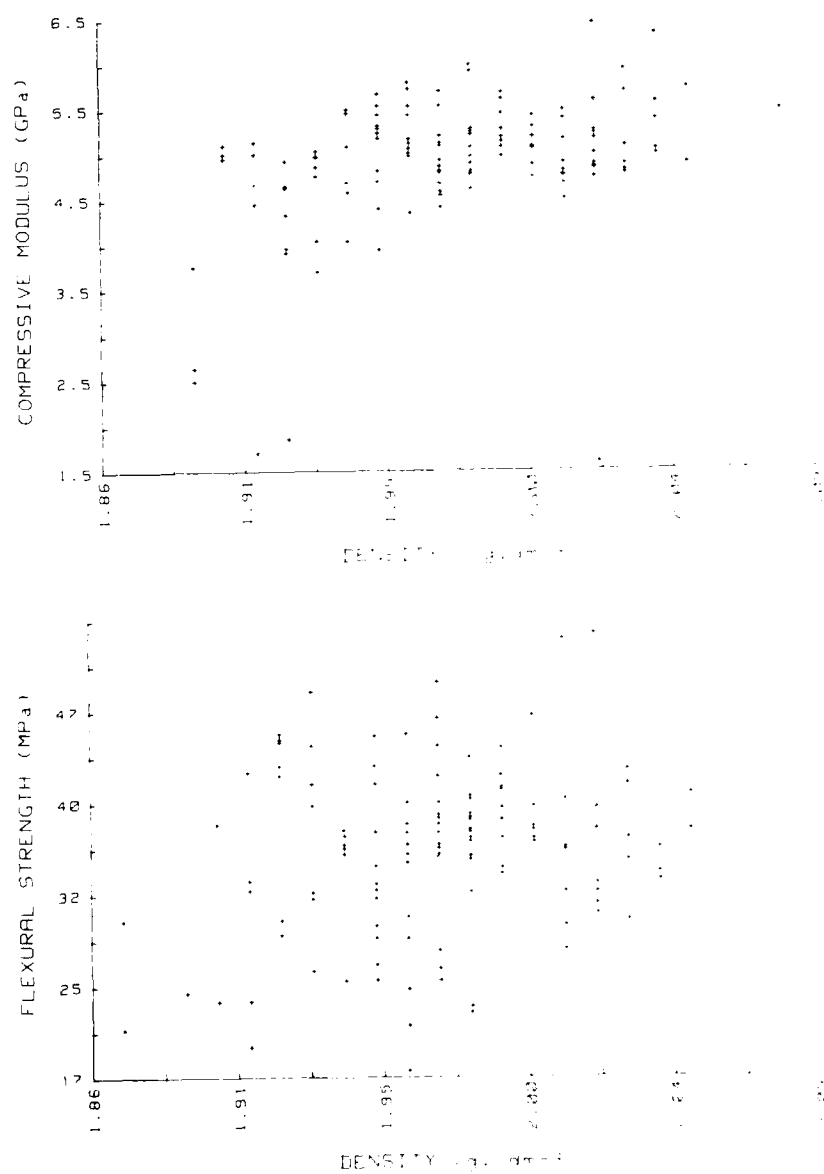


FIGURE 3 Properties of resin samples cast on site during the repair.

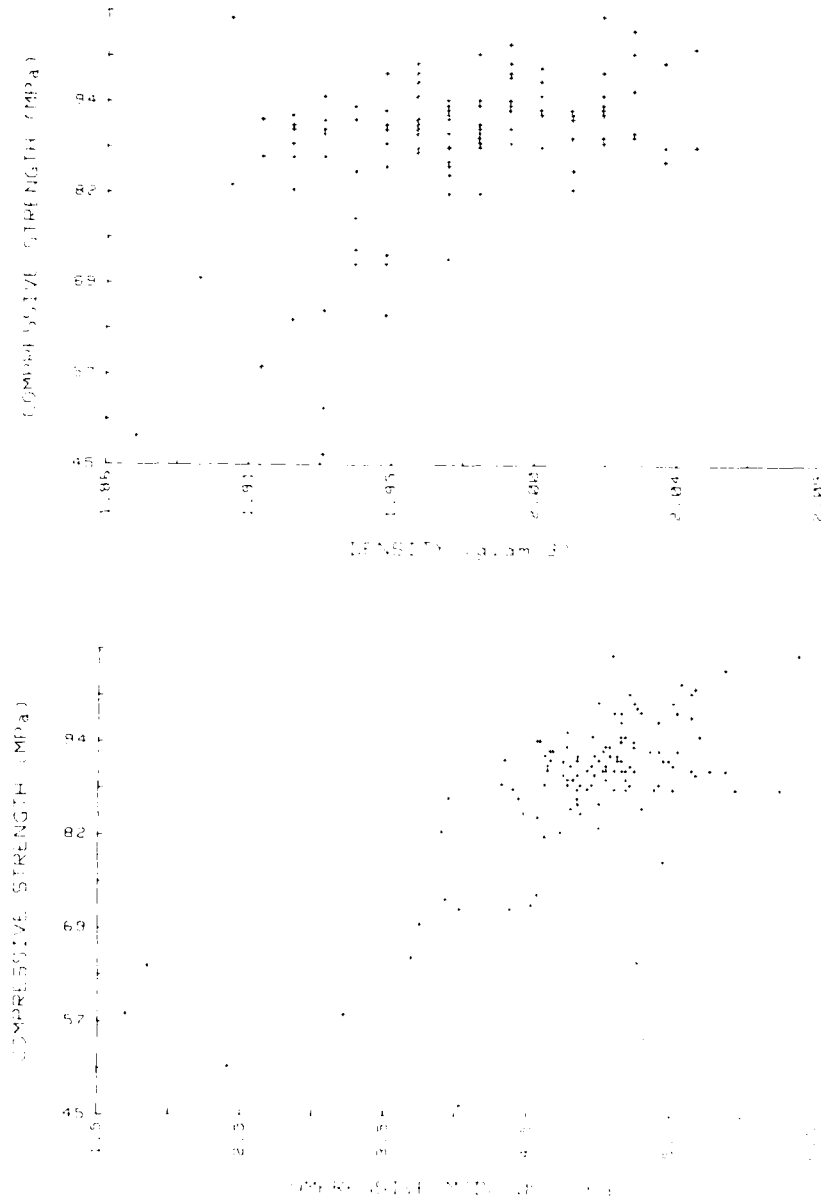


FIGURE 3 (continued)

TABLE II
Properties of Rodur 510

Density	(g dm ⁻³)	2.02
Viscosity of uncured mixture	(mPas)	2500
Pot life/20°C/1 kg	(min)	57
Filler weight ratio		1:1.6
Compressive strength		
10 d. at 20°C	(MPa)	88.8
Flexural strength		
10 d. at 20°C	(MPa)	50.5
42 d. at 1°C	(MPa)	40.8
Flexural modulus		
10 d. at 20°C	(GPa)	4.69
42 d. at 1°C	(GPa)	3.85
Bond strength to wet concrete	(MPa)	3.00

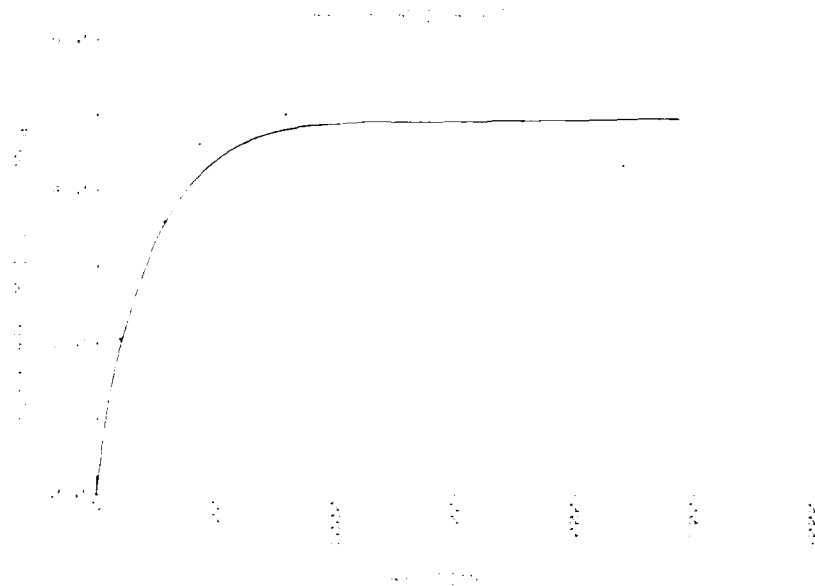


FIGURE 4 Flexural modulus as a function of cure time at 5°C

DISCUSSION

The experience gained on site and the tests carried out in the Laboratory have indicated that an epoxide resin such as the Rodur system can be used to repair concrete structures such as the Zeuzier Dam. Removal of core samples showed that even cracks down to 0.2 mm. in width were penetrated. Thus, a viscosity of up to 2500 mPas is suitable even for a network of very fine cracks. The Federation de la Précontrainte recommended that epoxide resins in construction should have a modulus of 8 GPa. However, this is extremely difficult to achieve taking into account the viscosity requirements and the low cure temperature in this particular application. Their recommendation for compressive strength and tensile strength (75 MPa and 10 MPa respectively) may be obtained easily since most epoxide resins have properties superior to these values.

A factor of considerable importance in the repair of such a large scale structure is when injections should take place. It has been suggested that cracks should be injected when they are completely open, that is in the early morning or in winter.⁶ This may be valid for isolated cracks but not for extensive repair work in a structure such as a Dam. If injections are performed in such conditions tensile stresses develop when the structure re-heats and this could result in new cracking on the opposite face on the Dam. In addition, injection pressures must be carefully controlled especially in the final stages of the repair. Excess pressures could also induce new cracks in the structure. In the Zeuzier Dam supplementary gauges were installed with valves to cut off the resin flow in order to avoid this problem.

The repair of the Zeuzier Dam required consideration of the climatic conditions in the Alps and, in particular, this area. Access to the Dam for the purposes of the repair was possible just from June to September or October each year. The repair of the Zeuzier Dam was completed in 1984.⁷ The instrumentation in and around the Dam has been considerably increased by installing dilatometers, piezometers, strain gauges and remote reading seismometers and thermometers in order to measure rapidly and very accurately the behaviour of the Dam. The seismometers are so sensitive that it is claimed they can detect movements caused by the wind on the ridge

of the Rohrbachstein some 1500 m. above the left bank of the Dam. The Swiss Government has approved a refilling programme over a period of 6 years. If the behaviour of the Dam during the refilling procedure continues to be completely normal the maximum storage will be reached again in 1988, ten years after the original incident.

References

1. F. Hugenschmidt, "Strengthening of existing concrete structures with bonded reinforcements", Ciba Geigy, Basle, Sept. (1981).
2. Ann. Inst. Tech. Bat. Trav. Pub. No. 366 Nov. 1978 Chap. VI "Principales applications des résines synthétiques dans les domaines du bâtiment".
3. R. W. Gaul and E. P. Smith in *Epoxies with Concrete* Amer. Concrete Inst. SP-21 (1968), p. 29.
4. Wasser, Energie, Luft, Special issue for the Int. Congress on Large Dams, Rio de Janeiro, 74 (3), 1982.
5. Federation Int. de la Précontrainte, "Proposal for a standard for acceptance tests and verification of epoxy bonding agents for segmental construction, March (1978).
6. P. Wolf, Ann Inst. Tech. Bat. Trav. Pub. No. 349, April (1977), "Les injections de résines utilisées pour réstituer leur monolithisme aux structures fissurées ou cavernueuses".
7. A. R. Berchten, Int. Congress on Large Dams, Lausanne. 1985, "Repair of the Zeuzier Arch Dam in Switzerland".

Thermoset Matrices for Structural Adhesives: Imidazole-Catalysed Curing of Epoxy Resins†

JÜRGEN VOGT

Ciba-Geigy SA, Research Centre Plastics and Additives, CH 1701 Fribourg, Switzerland

(Received October 24, 1986)

The thermoset epoxy systems of diglycidyl ether of bisphenol-A (DGEBA) and different imidazoles (unsubstituted imidazole, N-methyl-im., 2-methyl-im., 4(5)-methyl-im., 2-ethyl,4-methyl-im., 2-ethyl-im., 2-phenyl-im.) as catalytical curing agents were characterized. From microcalorimetric experiments it was deduced that each molecule of imidazole induces more than 20 epoxy groups to undergo polyaddition. Therefore, optimum glass transition temperature-ranges can be obtained with 0.025 to 0.05 mol of catalyst/equivalent of epoxy. The different alkyl- and aryl-substituted imidazoles show rather similar catalytic effects, with the kinetics differing by a factor of 3 at most. Mechanical properties (flexural modulus and strength, ultimate strain and fracture toughness) at ambient temperature do not correlate with the crosslinking density of the polymer network.

KEY WORDS Imidazoles; catalysed curing; epoxy resins; mechanical properties; structural adhesives; thermoset matrices.

INTRODUCTION

Structural bonding with organic adhesives is now accepted in many industries as a viable joining method. Adhesives based on epoxide resins are versatile materials mainly because of the following

† Presented at the Tenth Annual Meeting of The Adhesion Society, Inc., Williamsburg, Virginia, U.S.A., February 22-27, 1987.

advantages:

- good adhesion to many substrates
- cure without evolution of volatiles
- adaptable, by formulation, to various application forms, cure conditions and performance properties
- good resistance to chemical and environmental exposure.

With the great number of possible combinations of formulation components and their relative amounts on one hand, and the legion of possible applications, substrates and designs on the other hand, a countless number of tests would be necessary to find the optimal adhesive system for a specific application. To avoid unlimited testing, some sort of basis set of material data for each principal adhesion formulation might be sufficient to choose an appropriate system and to supply property data for computer-aided construction and design programs.

In this work, the basic physico-chemistry of a rather simple thermoset epoxy resin system is correlated with its materials science data. Some more practical-application-oriented adhesive systems are dealt with in an accompanying paper.¹

EXPERIMENTAL

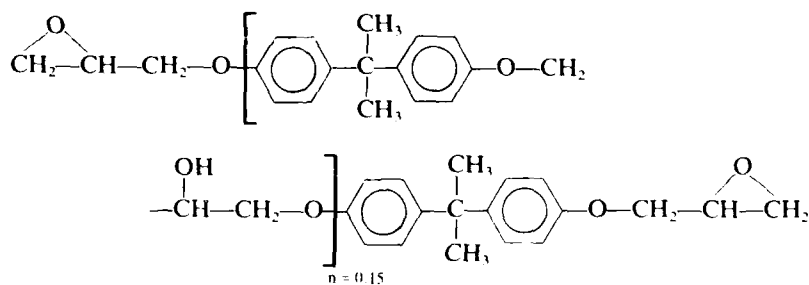
Materials and methods

DGEBA (Araldite GY 250, Ciba-Geigy), Im (Fluka), N-Me-Im (Araldite DY 070, Ciba-Geigy), 2-Me-Im, 4(5)-Me-Im, 2-Et,4-Me-Im, 2-Et-Im (Aldrich) and 2-Phe-Im (Merck) were used as supplied. Resin/catalyst mixtures were prepared at 30 to 50°C, vacuum degassed and cured in aluminum moulds using a forced air circulation oven. Microcalorimetric measurements were performed on a DuPont TA 9000 Thermoanalyser System, dynamic scans at 10 K/min. For dynamic mechanical analysis, a Lonza Torsional Pendulum was used at a heating rate of 1 K/min. Mechanical tests were performed at room temperature on a Schenck servohydraulic testing equipment. Test specimens were cut from 1 and 4 mm sheets. Fracture toughness was determined on the compact tension specimen⁸ of dimension $26 \times 26 \times 4$ mm.

RESULTS

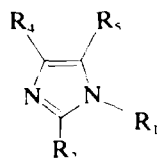
Imidazole-catalysed cure of epoxy resin

In order to illustrate the dependence of polymer physical and mechanical properties on formulation and cure cycle parameters, we studied the thermoset system of a basic commercial epoxy resin, diglycidyl ether of bisphenol-A (DGEBA, Araldite GY 250, Ciba-Geigy),



(1)

and a series of catalytic hardeners, in our case several substituted imidazoles (Table I).



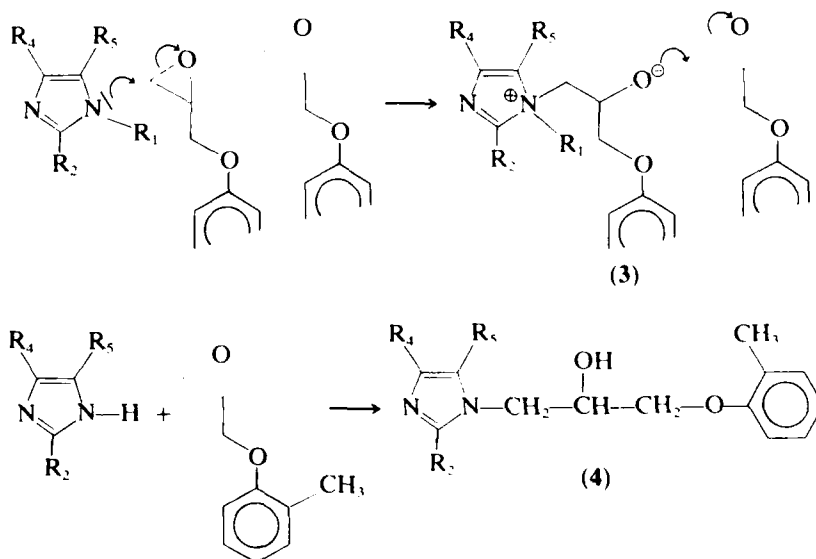
(2)

TABLE I
Substituted imidazoles used as catalytic curing agents

Designation	R ₁	R ₂	R ₄	(R ₅)
Im	H	H	H	H
N-Me-Im	CH ₃	H	H	H
2-Me-Im	H	CH ₃	H	H
4(5)-Me-Im	H	H	CH ₃	H
2-Et,4-Me-Im	H	C ₂ H ₅	CH ₃	H
2-Et-Im	H	C ₂ H ₅	H	H
2-Phe-Im	H	C ₆ H ₅	H	H

Although the imidazoles are well known epoxy curing agents, systematic work has been published predominantly on the reaction with non-crosslinking, monofunctional epoxies such as phenyl glycidyl ether²⁻⁴ or *p*-cresol glycidyl ether⁵ with emphasis on the elucidation of the reaction mechanism. Some data were published on the imidazole cure of technically relevant epoxies,⁶ mainly discussing the kinetics, but giving only few data on their mechanical behaviour.

Polyaddition of glycidyl ether compounds is induced by imidazole through nucleophilic addition to the epoxide ring, thereby forming the *t*-amine-alcoholate intermediate 3 as chain propagating species.³ For *N*-unsubstituted imidazoles, the primary reaction is the addition of the imidazole to an epoxy ring to form the *N*-substituted imidazole 4, which then acts as the catalytically active species.^{1,3} This primary addition of *N*-unsubstituted imidazoles can be detected in the dynamic DSC-experiment as an exothermic peak at lower temperatures than the onset of the principal polyaddition reaction (Figure 1, upper trace). This extra peak disappears (Figure 1, lower trace), if a 1:1 molar adduct of the unsubstituted imidazole and a monofunctional epoxy compound such as *o*-cresol glycidyl ether is used as catalyst 4. The secondary hydroxyl groups in, *e.g.*, 1 and 4 act as co-catalysts.⁵



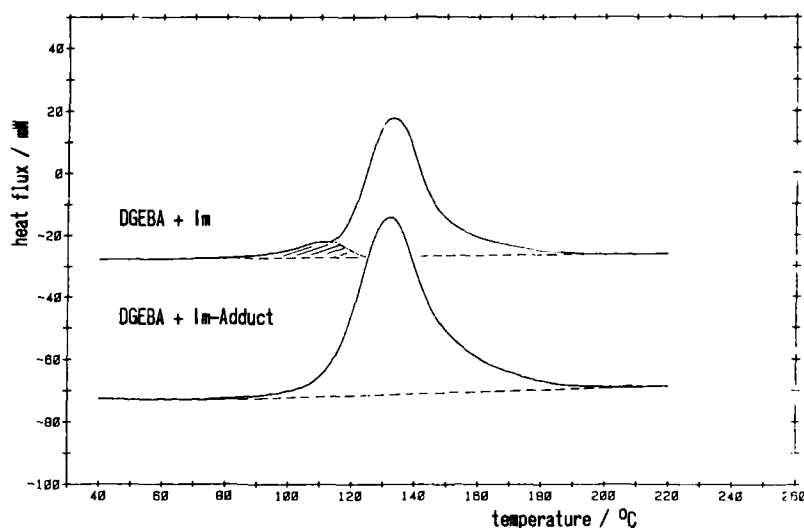


FIGURE 1 Differential scanning calorimetric characterization of the DGEBA polyaddition induced by Im (upper trace) and the Im/o-cresol glycidyl ether adduct (lower trace).

Dynamic cure (10 K/min), in the DSC instrument, of DGEBA with different amounts of catalyst, reveal that under these conditions up to about 20 epoxy groups can be induced to undergo polyaddition by one molecule of imidazole. This ratio corresponds to a catalyst concentration of 0.05 mol/equiv. of epoxy. As can be deduced from the dependence of heats of reaction on catalyst concentration (Figure 2), more than 0.05 mol catalyst/equiv. of epoxy give fully cured systems yielding 99 ± 5 kJ/equiv. of epoxy (*cf.* dotted curve in Figure 2). This value is rather close to 92 kJ/equiv. of epoxy reported for the t-amine catalyzed epoxy polyaddition.⁷

Below the optimum catalyst concentration, the heat of reaction per mol of catalyst remains rather constant near 2000 kJ/mol, indicating that although more than 20 reactive epoxy groups are present per molecule of imidazole, the excess remains unreacted. This is accompanied by a decrease in the glass transition temperature-range T_g (Figure 3). The T_g also decreases at catalyst concentrations higher than 0.05 mol/equiv. of epoxy (Figure 3), due

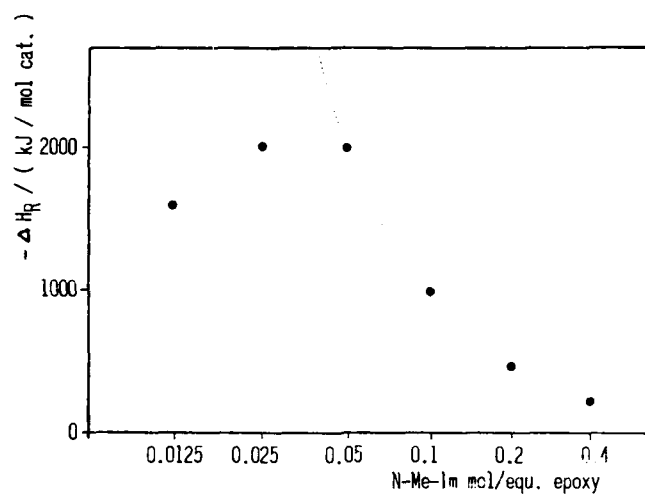


FIGURE 2 DGEBA polyaddition catalysed by N-Me-Im. Heats of reaction per mol catalyst in function of catalyst concentration.

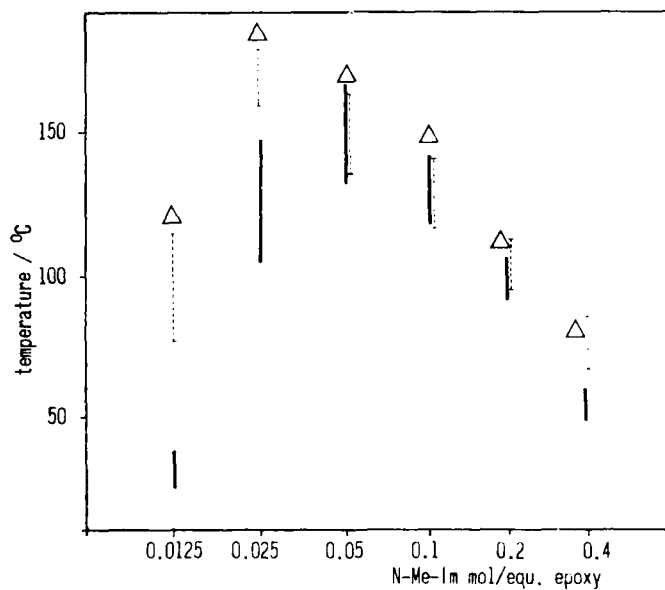


FIGURE 3 DGEBA polyaddition catalysed by N-Me-Im. Glass transition temperatures after dynamic cure (10 K/min, —), after cure cycle 6h 80°C + 4h 180°C determined by DSC (---) and DMA (max. of loss factor, Δ).

to the fact that each molecule of imidazole acts as a chain end group, thereby lowering the crosslinking density.

With a different curing cycle (slow gelation at 80°C, 6 h, and post-cure at 180°C, 4 h), slightly higher T_g values can be obtained. The conversion per mol of catalyst can be increased, resulting in high T_g ranges with 0.025 mol cat./equiv. of epoxy (Figure 3).

For comparison, the dynamic mechanical characterizations of DGEBA resin cured with different concentrations of N-Me-Im are given in Figure 4. These results are in agreement with the microcalorimetric data discussed above. As expected, the increasing crosslinking density leading to a higher T_g is also reflected in an increased shear modulus above T_g . Furthermore, the maximum of the loss factor with temperature essentially coincides with the corresponding upper limit of the calorimetrically determined T_g -range (*cf.* Figure 3). For all catalyst concentrations a broad β -relaxation is observed near -60°C.

This type of catalyst-concentration effect on the cure of DGEBA is typical of all imidazoles studied. The T_g ranges obtained after dynamic cure with 0.05 mol cat./equiv. of epoxy are depicted in Figure 5. The rather similar T_g ranges indicate that the different alkyl or aryl substituents do not have an important influence on the

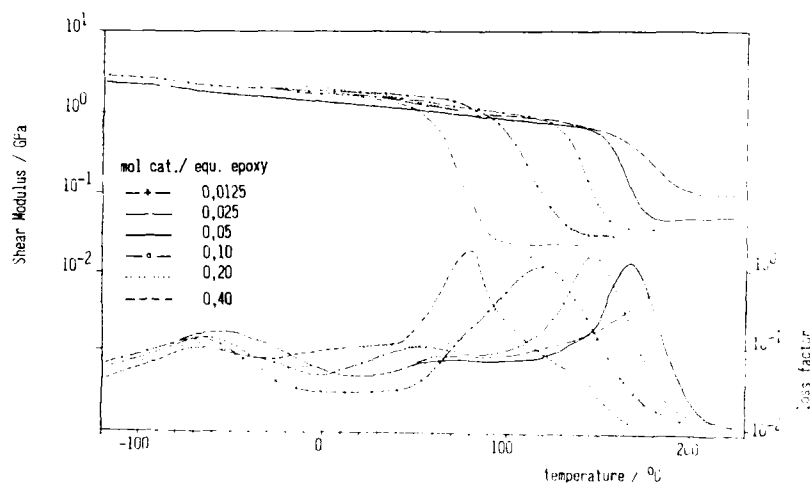


FIGURE 4 DGEBA polyaddition catalysed by N-Me-Im. Effect of catalyst concentration on complex shear modulus.

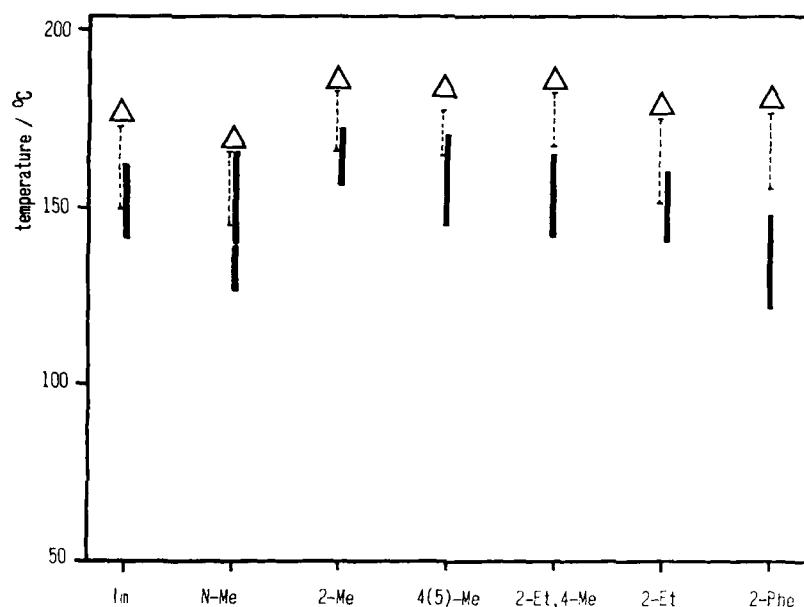


FIGURE 5 DGEBA polyaddition catalysed by different imidazoles. Glass transition temperatures obtained with 0.05 mol cat./equ. epoxy (designation as in Fig. 3).

network structure. Some minor substituent effects were observed on the polyaddition kinetics, resulting in gel times differing at most by a factor of 3 (Figure 6). From the Arrhenius plot of the temperature dependence of gel times (Figure 6), overall activation energies for gelation can be determined (Table II). The close similarity of the activation energies observed using various imidazole derivatives is taken to indicate a common reaction mechanism.

The similarity of cure induced by the different imidazoles also becomes evident from the corresponding dynamic mechanical analysis data. In Figure 7, the temperature dependence of shear modulus and loss factor of the DGEBA/imidazole systems are shown. These data reveal that up to 150°C the complex shear modulus is essentially independent of the type of imidazole. Only above this temperature do small differences in T_g differentiate the systems under study.

Most often the glass transition temperature is chosen as the main criterion for the development of thermosets, although their usual

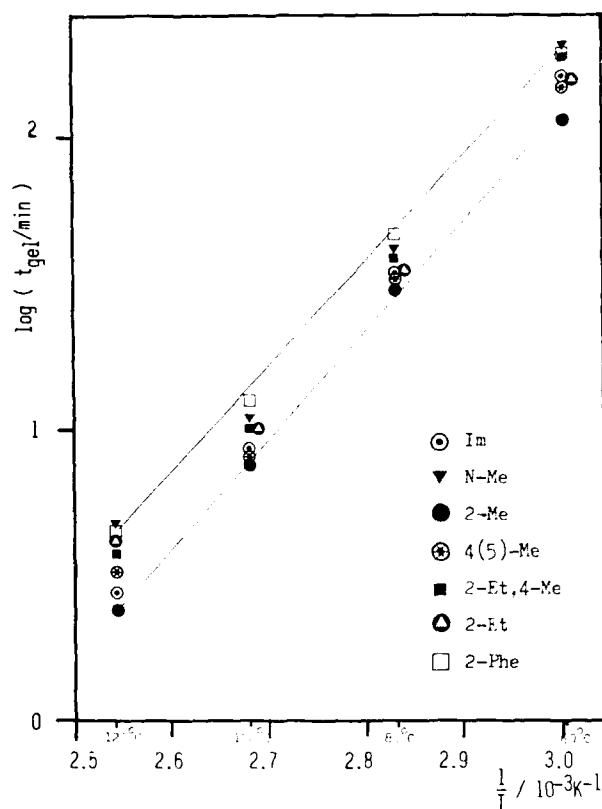


FIGURE 6 Arrhenius-plot of gel times (DGEBA + 0.05 mol. cat./equ. epoxy).

TABLE II
Activation energies for imi-
dazole-catalyzed epoxy poly-
addition from gel times (cf.
Figure 6)

Catalyst	E_a /kJ/mol
Im	70
N-Me-Im	71
2-Me-Im	74
4(5)-Me-Im	75
2-Et, 4-Me-Im	71
2-Et-Im	66
2-Phe-Im	68

application in adhesives or engineering plastics occurs at temperatures much below T_g . As is demonstrated with the series of different concentrations of N-Me-Im and DGEBA, quite a range of different T_g s and, therefore, different polymer network properties are "adjustable". Though, important material properties such as the flexural modulus E and the flexural strength σ show a non-monotonic dependence on T_g , as becomes evident from the data in Figure 8. E and σ have a common behaviour in dependence on catalyst concentration with an apparent local minimum at 0.025 mol cat./equiv. of epoxy, where the T_g has its maximum. Below that concentration, E and σ rise, although the polymer network is poorly crosslinked due to more unreacted epoxy groups. Both E and σ reach their local maximum at 0.2 mol cat./equiv. of epoxy, where T_g has an intermediate value. Surprisingly enough, the specific mass ρ (Figure 8) of the cured resin follows the catalyst concentration dependence of E and σ , indicating that at temperatures much below T_g , the packing density of polymer segments determines E and σ . The packing density in this temperature range depends only rather indirectly on the crosslinking density.

At the highest crosslinking density (slow cure, 0.025 mol cat./equiv. of epoxy, maximum T_g), the free volume reaches its

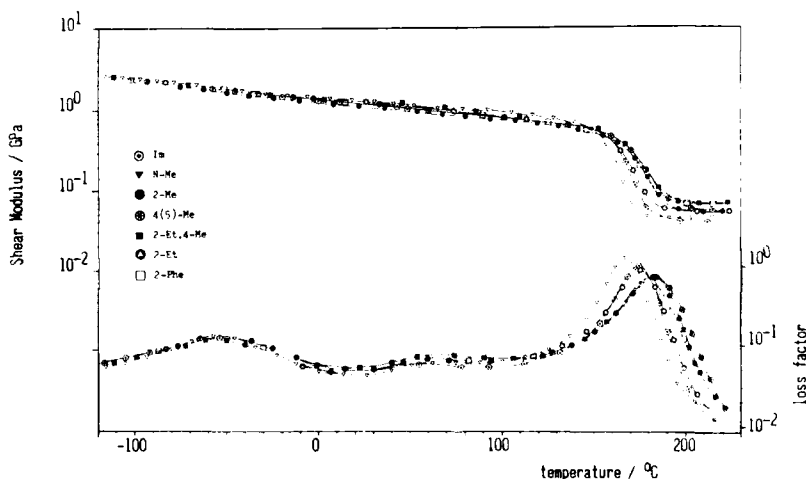


FIGURE 7 DGEBA polyaddition catalysed by different imidazoles. DGEBA + 0.05 mol cat./equ. epoxy, cure 6h 80°C + 4h 180°C, dynamic mechanical analysis.

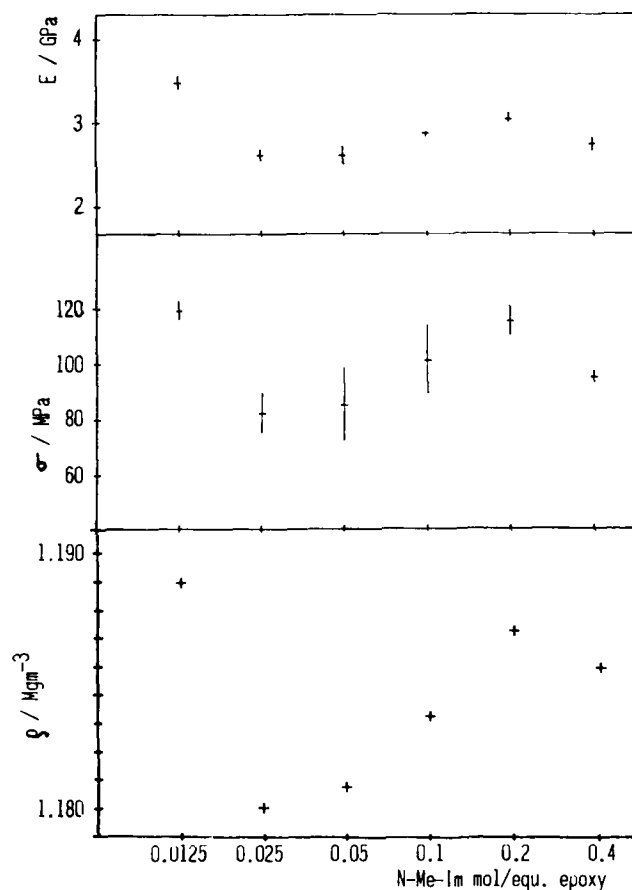


FIGURE 8 DGEBA/N-Me-Im, cure 6h 80°C + 4h 180°C. Effect of catalyst concentration on flexural modulus E , flexural strength σ and specific mass ρ .

maximum due to the high built-in disorder of the polymer network. With decreasing cross-linking density, obtained at higher or lower catalyst concentrations, the polymer segments can relax, due to their higher mobility, into a more closely packed structure. Above 0.2 mol cat./equiv. of epoxy, the specific mass of the cured resin drops again, most probably due to the large portion of the low density catalyst $\rho(\text{N-Me-Im}, 23^\circ\text{C}) = 1.04 \text{ Mg/m}^3$, against $\rho(\text{DGEBA}, 23^\circ\text{C}) = 1.17 \text{ Mg/m}^3$.

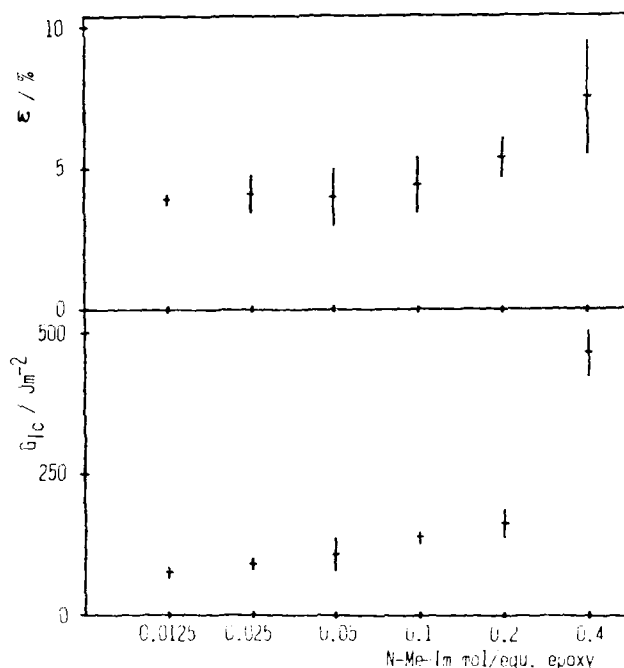


FIGURE 9 DGEBA/N-Me-Im, cure 6h 80°C + 4h 180°C. Effect of catalyst concentration on ultimate strain ϵ and fracture toughness G_{IC} .

The effect of catalyst concentration upon ultimate strain and fracture toughness takes again a different course (Figure 9). Both properties are fairly constant or only slowly rising over the range 0.025 to 0.1 mol cat./equiv. of epoxy, with a sharp increase above 0.2 mol cat./equiv. of epoxy. This behaviour can be rationalized considering the increasing number of imidazole-terminated polymer segments fixed to the network only with one end. They increase the plasticity through orientation and chain sliding during deformation while simultaneously lowering the T_g , as discussed above.

CONCLUSIONS

In conclusion, the seemingly simple system of DGEBA and different amounts of imidazole catalysts reveal rather complicated

dependencies between the polymer physical data and the macroscopic mechanical properties. Since practical applications need well-chosen optimizations of several material properties, the knowledge of such dependencies and their intercorrelations help considerably to reduce effort and time for the development of adhesives or engineering plastics specifically adapted to a certain performance profile.

Acknowledgement

Specimen preparation and careful measurements by Mrs. C. Irrgang, Mrs. E. Pürro and Dr. K. Jud are gratefully acknowledged.

References

1. U. T. Kreibich and A. F. Marcantonio, paper presented at the Tenth Annual Meeting of The Adhesion Society, Williamsburg, Virginia 1987, *J. Adhesion* **22**, 153-165 (1987).
2. A. Farkas and P. F. Strohm, *J. Appl. Polym. Sci.* **12**, 159 (1968).
3. F. Ricciardi, M. M. Jouille, W. A. Romanchick and A. A. Griscavage, *J. Polym. Sci. Polym. Lett. Ed.* **20**, 127 (1982).
4. F. Ricciardi, W. A. Romanchick and M. M. Jouille, *J. Polym. Sci. Polym. Chem. Ed.* **21**, 1475 (1983).
5. J. Berger and F. Lohse, *J. Appl. Polym. Sci.* **30**, 531 (1985).
6. W. A. Harding and S. H. Christie, *Amer. Chem. Soc., Div. of Organic Coatings and Plastics Chemistry Preprints* **24**(2), 309 (1964); T. J. Dearlove, *J. Appl. Polym. Sci.* **14**, 1615 (1970); C. A. Glandt and J. K. Gillham, *Amer. Chem. Soc., Div. of Polym. Chem. Preprints*, **16**(1), 694 (1975).
7. H. Lee and K. Neville, *Handbook of Epoxy Resins* (McGraw-Hill, New York, 1967), Chap. 6.
8. A. J. Kinloch and R. J. Young, *Fracture Behaviour of Polymers* (Elsevier, London, 1983), Chap. 3.

New Developments in Structural Adhesives for the Automotive Industry†

U. T. KREIBICH

CIBA-GEIGY AG, Subdivision Plastics, CH-4002, Basel, Switzerland

A. F. MARCANTONIO

CIBA-GEIGY Formulated Systems Group (Automotive Center), Madison Heights, MI 48071, U.S.A.

(Received October 24, 1986)

Recently developed epoxy paste adhesives, reactive hot melts, adhesive film tape and polyurethane adhesives are presented for structural bonding in the automotive industry. Paste adhesives usually require a precure stage to obtain handling strength of the joints and to guarantee wash-out resistance of the adhesive in the paint baths. This step can be omitted with reactive hot melts and adhesive film tape, which are solid before and after their application. In addition they allow an improved working hygiene. Some mechanical properties of the adhesives are shown such as lap shear strength and peel strength as well as lap shear strength as a function of the bondline thickness. Results of the excellent durability of epoxy one-component pastes, reactive hot melts and adhesive film tape are given from cyclic environmental and salt spray tests.

KEY WORDS Epoxy adhesives; polyurethane adhesives; reactive hot melts; adhesive film tape; mechanical properties; environmental resistance.

1 INTRODUCTION

During recent years adhesive joints have received increasing interest in the automotive industry with emphasis

– to reduce and even eliminate spotwelding of steel,

† Presented at the Tenth Annual Meeting of The Adhesion Society, Inc., Williamsburg, Virginia, U.S.A., February 22–27, 1987.

- to improve corrosion resistance,
- to bond substrates, especially polymers, which cannot be joined by conventional fastening techniques,
- to allow engineers new ways in the construction of vehicles and to reduce the number of parts of a car,
- to improve the efficiency of production lines.

Similar to adhesives for the aircraft industry, structural adhesives used by the automotive industry have to fulfill demanding performance profiles with respect to the mechanical and environmental properties of the joint, the application and curing properties of the system as well as to its storage conditions (see Figure 1). Critical for good adhesion are defined chemical and physical properties of the substrate surface and its interactions with the adhesive.¹⁻³ In contrast to the well-defined surfaces of the aircraft industry, *e.g.* pretreated aluminium,^{4,5} car manufacturers extensively use oily steel and are reluctant to invest in surface pretreatment because of the incurred cost premium.

Major developments are ongoing to fulfill the requirements for engineering adhesives. Out of these only a few highlights can be given now on epoxy paste adhesives, reactive hot melts, adhesive film tape and two-part polyurethane adhesives.

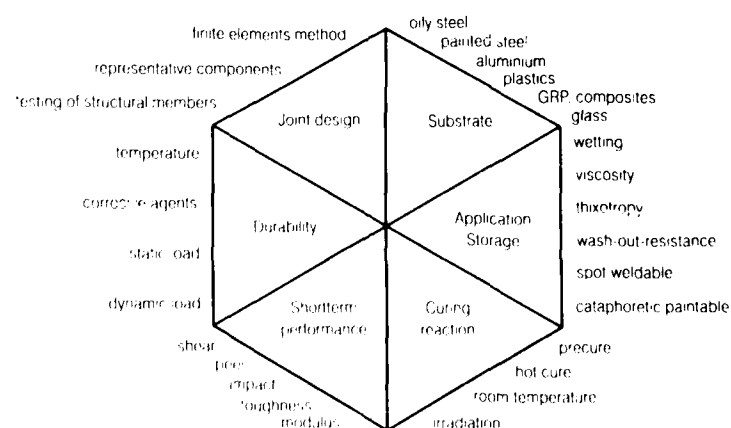


FIGURE 1 Major factors determining performance of an adhesive for the automotive industry.

Some typical and important aspects of their application and curing characteristics, their mechanical strength and their environmental durability will be dealt with.

2 APPLICATION AND CURING PROPERTIES

When epoxy or polyurethane adhesives crosslink in a polyaddition reaction, a polymer is formed with a glass transition, T_g , varying with the structure.⁶ The T_g shifts to higher temperatures as the degree of reaction and the crosslinking density increases.⁷ Figure 2 shows the typical scanning calorimetric profile of the reaction of the epoxy resin bisphenol-A diglycidylether with the hardener diaminodiphenylmethane, at different stages of cure. Towards increasing temperatures T_g is followed by an exothermic peak, until complete cure has been accomplished. The area of the peak is calculated to give the reaction enthalpy and the degree of cure. The higher the degree of cure, the better normally becomes the mechanical and environmental performance.⁸

Figure 3 shows the typical curing reaction of bisphenol-A

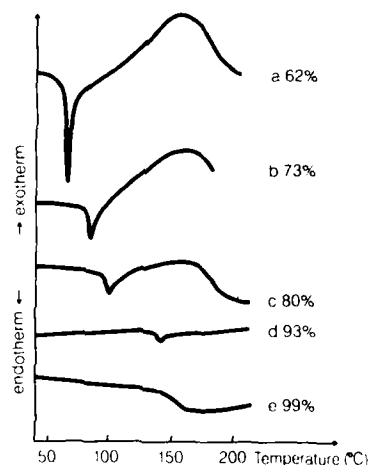


FIGURE 2 Glass transition, T_g , and exothermic reaction of an epoxide system as a function of the degree of reaction (DSC-diagram, heating rate = $10^\circ/\text{min}$). Epoxide system: Bisphenol-A diglycidylether + diaminodiphenylmethane.

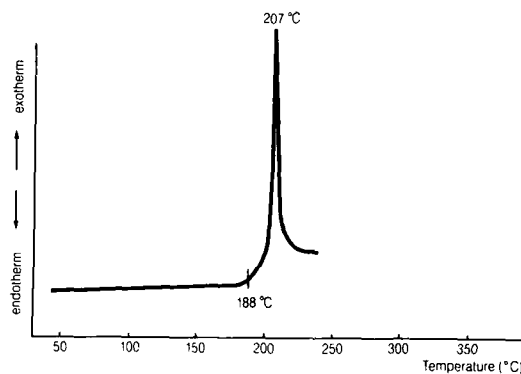


FIGURE 3 Curing reaction of bisphenol-A diglycidyl ether with dicyandiamide (DSC-diagram, heating rate = 20°C/min).

diglycidyl ether with dicyandiamide in air atmosphere. When the exotherm is measured as a function of time, in the isothermal mode, the extent of cure can also be calculated. Small amounts of accelerators or catalysts can be seen to shift the exotherm to lower temperatures, as seen in Figure 4.

Another important property, the rheological behaviour of a

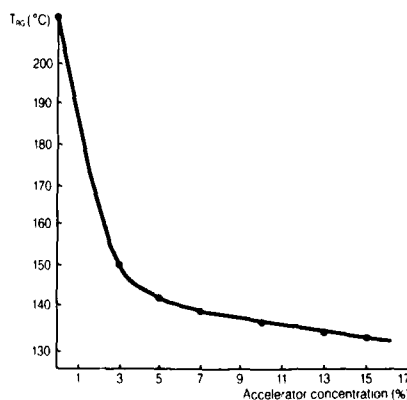


FIGURE 4 Temperature T_{RG} of the exothermic reaction maximum of an epoxy system as a function of the amount of accelerator (experimental product).

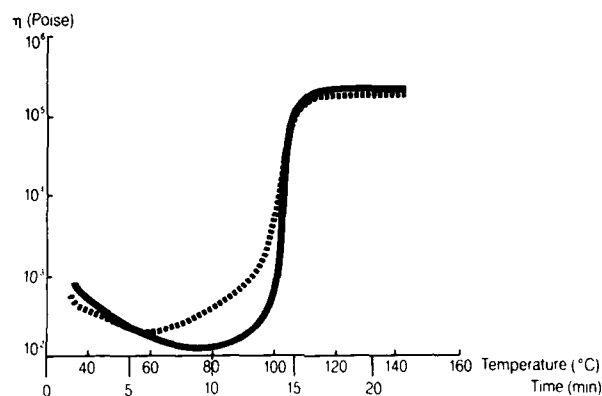


FIGURE 5 Dynamic flow viscosity of epoxy-2-part adhesives as a function of temperature and time. — XW 455-A2 and --- LSU 202-41, both cured with XW 441-B2.

typical thermoset adhesive, is shown in Figure 5. The dynamic flow viscosity of the epoxy resin is automatically plotted with time and temperature (Rheometrics RDA-700 Dynamic Analyzer). The viscosity of the adhesive can be obtained at any temperature or time at a specific heating rate before gelation occurs.⁹ A graph of the viscosity at constant temperature with time measures the stability of the adhesive (see Figure 6).

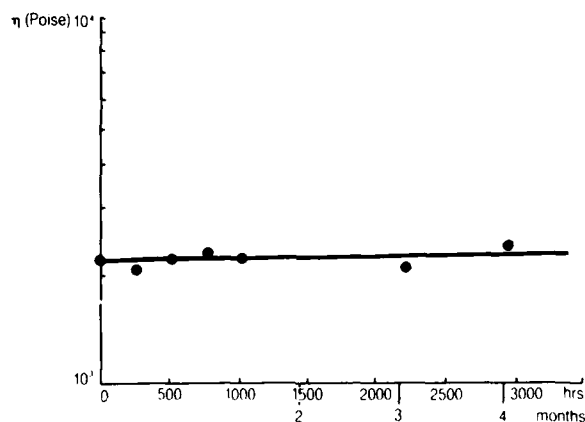


FIGURE 6 Stability of an epoxy-1-part adhesive, RW 213-37, at 75°C as a function of its storage time at RT from measurements of the dynamic flow viscosity.

The basic relationship between the chemical structure of the components of a system, the curing reaction and the material properties have to be used in order to fulfill the demanding performance profiles of adhesives for the automotive industry. Usually, the best performance can be achieved with heat curing systems. In the car industry the heat of the paint baking process is used to effect this cure. However, for the handling of parts on a production line an initial or green strength is needed for an adhesive joint prior to passing through the ovens for paint baking. In addition, the solidification prevents paste adhesives from contaminating cataphoretic paint baths. Depending on the chemical structure of the reaction partners, adhesives can be formulated with a tailor-made precure time to achieve handling strength (see Figure 7). This green strength is already obtained for new one-component epoxy paste adhesives after a few seconds of induction precure or some minutes of oven precure. These minimum reaction times at certain bondline temperatures can be increased, if required for application.

With two-part epoxy adhesives handling strength at room temperature is obtained after a reaction time of 10–20 min, which decreases with higher temperatures. The low heat conductivity of parts made from fibre-reinforced polyester, *e.g.* sheet molding compound (SMC), bulk molding compound (BMC) etc., increases

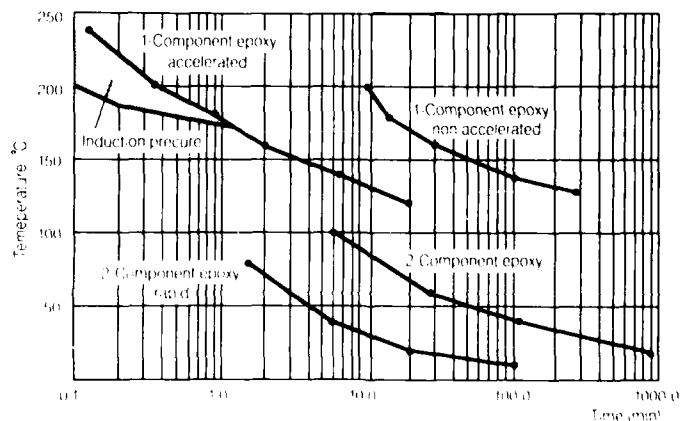


FIGURE 7 Time until handling strength at different temperatures for various 1- and 2-part epoxy adhesives.

the time required for the curing cycle. Therefore, more reactive adhesives are needed. So two-part epoxy adhesives have been formulated with cycle times for manufacturing of even 1.5 min at 80°C at a pot life of about 4 min.

Another important factor for adhesive application is its physical form, which is again dependent upon the chemical formulation. Although car manufacturers are more and more using application robots on production lines, working hygiene gains increasing interest. New adhesives have been developed which are applied in the solid state as adhesive film tape and interest is now being expressed in adhesives which are solidified during application as reactive hot melts. Such adhesives are wash-out resistant and save the precuring step.

3 MECHANICAL PROPERTIES

With the application of adhesive to bond primary structures, impact resistance is of some concern to the automotive makers. Epoxy adhesives are thermally durable, but can be quite brittle unless modified for impact resistance.¹⁰⁻¹³ Both the chemistry of modifying adhesive epoxy systems for impact resistance, while allowing little or no sacrifice to processing, mechanical properties, and environmental resistance, and methods development for toughness evaluation, are currently the subjects of intensive research efforts. A great deal of attention has been focused on the toughness (impact resistance) of thermoset matrix resins used in composite technology.^{14,15} Similar methods can be applied to the toughness of adhesives.

Typical examples of the lap shear strength, the T-peel, and the roller peel of one-component pastes, of reactive hot melts, and of adhesive film tape are presented in Figure 8 to illustrate the possibilities of formulation and flexibilization. The T-peel of one-component paste adhesives, a critical property in engineering, can be significantly improved by formulation as seen from the comparison of pastes 1 and 2. New reactive hot melts are under development. They can be formulated to have properties varying from those of high strength adhesives to sealant type products. With film adhesives the possibilities of formulation to change properties is

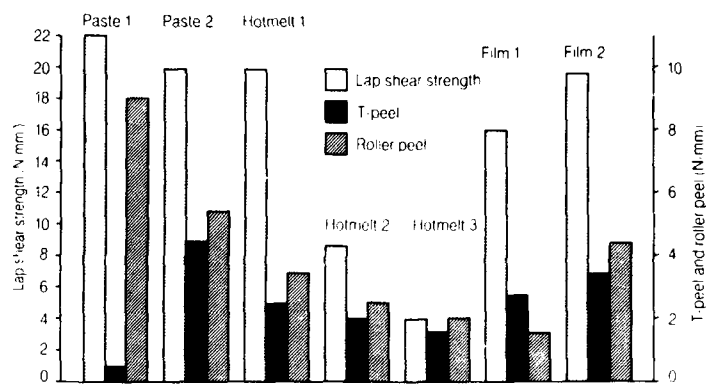


FIGURE 8 Lap shear strength, T-peel and roller peel of epoxy-based 1-part paste adhesives, reactive hot melts and adhesive film tape. Cure: 30 min at 180°C. Substrate: Steel, oiled.

more restricted. So the key to a high performance adhesive, fulfilling the demanding specifications of the automotive industry, is the creative choice and careful balance of the ten or more compounds making up an adhesive, many of which can react or interact with each other. Of course, the adhesive strength depends on its relaxation behaviour with temperature. A significant change is observed during the glass transition.

The strength of an adhesive joint strongly depends on the stresses imposed during the tests. Especially the most common test methods such as the lap shear test and the peel test show rather inhomogeneous stress distributions depending on the geometry of the test specimen and the stress environment.¹⁶ Adhesive strength is also influenced significantly by the bondline thickness. Joints of aluminium and SMC with epoxy adhesives show a decay of the lap shear strength with increasing bondline thickness (see Figure 9). The effect is the more pronounced, the higher the resistance of the adhesive and of the substrate is to deformation.

In Figure 9 the reactive hot melt shows cohesive failure in the bondline of the aluminium joints, whereas material failure is observed in the SMC, *i.e.* pull-out of glass fibres, with two-part epoxy and polyurethane adhesives at all bondline thicknesses considered. The fact, that SMC fails at different levels of load (see Figure 9) can be explained by the increased resistance of the lap

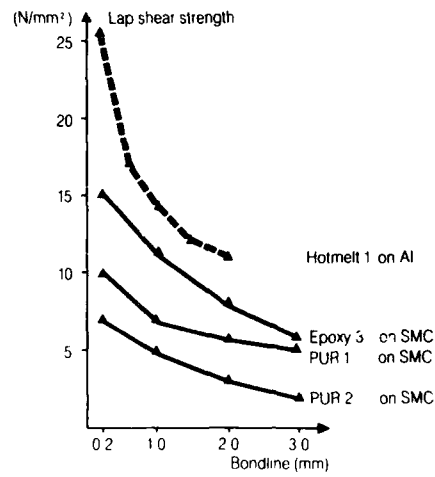


FIGURE 9 Lap shear strength of a reactive hot melt and of epoxy and polyurethane 2-part adhesives as a function of the bondline thickness. Substrates: SMC with E-modulus 10000 N/mm², Aluminium, Test: Lap shear strength after ISO 4587.

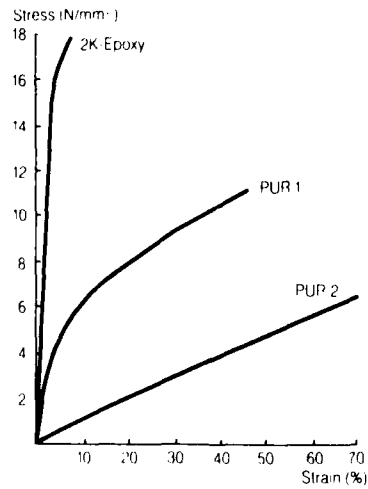


FIGURE 10 Stress-strain-diagrams of epoxide and polyurethane 2-part adhesives. Test: Tensile test after ISO R 527.

shear specimens towards bending moments and plastic deformations under stress depending on the elastic modulus of the adhesives used. Stress-strain diagrams in Figure 10 show the higher elastic modulus of the epoxy adhesive compared with the polyurethane adhesives with higher energy absorption and higher elongation.

This comparison of data illustrates the importance of stress analysis which affects the components as shear stresses, normal stresses and their superpositions. The choice of the test method and the test geometry is crucial, in order to obtain relevant results from calculations for design with adhesives. Suitable data are provided, *e.g.*, by measurements of tubular, blunt-joined test specimens in the tensile-torsion test.¹⁷

4 ENVIRONMENTAL DURABILITY

Adhesives for the automotive industry have to match with the lifetime of a car without inajor changes in strength and aspects of failure. The durability of adhesive joints in corrosive environments heavily depends on the chemical interlocking of the adhesive and

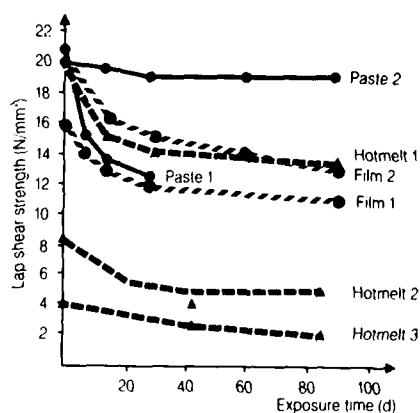


FIGURE 11 Cyclic environmental resistance of epoxy-based 1-part adhesives, reactive hot melts and adhesive film tape as a function of the exposure time (cycles: -20°C to $+70^{\circ}\text{C}$ /100% rel. humidity). Cure: 30 min at 180°C . Substrate: Steel, oiled, Test: Lap shear strength after ISO 4587.

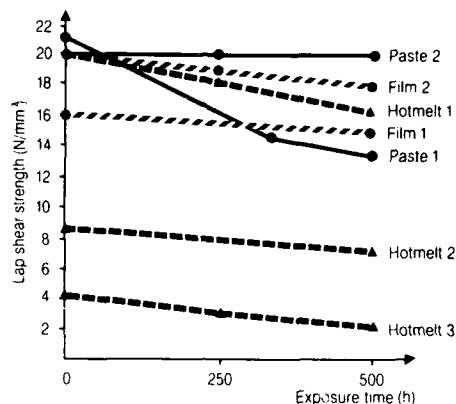


FIGURE 12 Saltspray resistance of epoxy-based 1-part adhesives, reactive hot melts and adhesive film tape in function of the exposure time. Cure: 30 min at 180°C. Substrate: Steel, oiled. Test: Lap shear strength after ISO 4587.

the substrate surface. Cyclic environmental and salt spray test are well established methods to predict the durability of adhesive joints from accelerated aging. They combine the effect of plastification and the chemical effect of degradation of the adhesive joint by water or salt solutions, which reduce the adhesive strength. The evidence of these tests is, however, limited, especially if they are performed at elevated temperatures. Then the polymer can be in the rubbery state. This facilitates the penetration of humidity and solutions into the polymer network over that in the glassy state, which is the typical physical state of many structural adhesives in the joint.

Figure 11 shows the excellent corrosion resistance of adhesive joints of oily steel with the epoxide paste adhesive 2, the reactive hot melt 1 and the adhesive film types for 90 days exposure. But, also, the semistructural and the sealant type reactive hot melts 2 and 3 show improved durability, always at cohesive fracture of the adhesive. This is especially remarkable, since the flexible, rubbery phase dominates in highly flexible adhesives.

Salt spray tests after DIN 50021 with lap shear samples (see Figure 12) also show an outstanding durability of the new paste generation 2, the reactive hot melts and the adhesive film tape.

5 CONCLUSION

New generation paste adhesives are under development. They show handling strengths after short induction cure, improved toughness and environmental resistance. Excellent mechanical properties and durability can also be achieved with new solid adhesives. They are applied as reactive hot melts with different degrees in flexibility or as adhesive film tape. Comparisons of strength data obtained with different test methods show the big influence of geometry of the specimens, the stresses applied and the bondline thickness. In addition, the modulus and the behavior in plastic deformation of both substrate and adhesive are determining factors. This needs proper consideration and the design of adhesive joints for optimum strength now becomes a crucial factor for the usage of adhesives in the automotive industry.

Acknowledgement

The authors would like to thank H. Lehmann, Dr. K. Mechera, Dr. H. Simon, K. Urech, Dr. J. Weber and J. Hack for their valuable contributions.

Designations of Experimental Products (all are from Ciba-Geigy)

EP-Paste 1	= XD 911
EP-Paste 2	= Le 10193.6
EP-Hotmelt 1	= JW 873.6
EP-Hotmelt 2	= JW 974.2
EP-Hotmelt 3	= JW 973.1
EP-Film 1	= KU 868
EP-Film 2	= KU 920
Epoxy 3	= Le 10192 + Le 10168 (1:1)
PUR 1	= HS 1212 + HS 1308 (1:1)
PUR 2	= HS 1026 + HS 1116 (1:1)

References

1. D. H. Kaelble, *Physical Chemistry of Adhesion* (Wiley Interscience, New York, 1971).
2. W. A. Zisman, in *Handbook of Adhesives*, I. Skeist, Ed. (Van Nostrand Reinhold, New York, 1977).
3. L.-H. Lee, *Adhesive Chemistry, Developments and Trends* (Plenum Press, New York and London, 1984).

4. W. Brockmann, O. D. Hennemann, H. Kollek, and C. Matz, *Adhesion* **7/8**, 31 (1986).
5. W. D. Saunders, *Adhesives Age*, August, 1986, p. 39.
6. U. T. Kreibich and H. Batzer, *Angew. Makromol. Chem.* **83**, 57 (1979).
7. H. Batzer, F. Lohse, and R. Schmid, *Angew. Makromol. Chem.* **29/30**, 349 (1973).
8. T. Daniels, *Thermal Analysis* (John Wiley and Sons, New York, 1973).
9. C. W. Macosko, *Adhesives Age* **20**, 35 (1977).
10. E. Forster, in H. Batzer, *Polymere Werkstoffe, Band III, Technologie 2* (Georg Thieme Verlag, Stuttgart, New York, 1984).
11. U. T. Kreibich, E. Lohse, R. Schmid, and G. Wegner, Einfluss Struktureller Merkmale, in H. Batzer, *Polymere Werkstoffe, Band I, Chemie und Physik* (Georg Thieme Verlag, Stuttgart, New York, 1985).
12. A. J. Kinloch, in K. Dusek, *Epoxy Resins and Composites I* (Springer-Verlag Berlin, Heidelberg, New York, Tokyo, 1985).
13. A. F. Yee and R. A. Pearson, *J. Mater. Sci.* **21**, 2462 (1968) and 2472 (1986).
14. "Standard Tests for Toughened Resin Composites", NASA Reference Publication 1092 (1983).
15. J. Harper-Tervet, *27th National SAMPE Symposium* **27**, 292 (1982).
16. R. D. Adams and W. C. Wake, *Structural Adhesive Joints in Engineering* (Elsevier Applied Science Publ., London, New York, 1984).
17. J. Engasser and A. Puck, *Kunststoffe* **70**, 423 (1980).

44

SESSION OF AUSTRALIA

The Interaction Parameter and the Strength of Adhesive Joints†

R. W. CHERRY and P. B. EVELY‡

Department of Materials Engineering, Monash University, Victoria, Australia 3168.

(Received October 3, 1986)

A "blister test" technique has been used to determine the fracture surface energy of a range of adhesive joints formed using a polyurethane adhesive and a range of solid substrates. For each adhesive pair examined the work of adhesion was calculated from the contact angles formed by liquids for which the polar and dispersion force components of the surface tension are known. For each adhesive pair, the solubility parameter of adhesive and substrate were determined by swelling measurements in a range of liquids. Although cohesive failure of the joints was observed for some of the pairs for which the solubility parameters were matched, this was not true for all such pairs and an explanation of this behaviour has been sought in a new calculation of the volume interaction component of the molecular interaction parameters.

KEY WORDS Adhesive fracture surface energy; adhesive joint strength; blister test; interaction parameter; solubility parameter; work of adhesion.

INTRODUCTION

Since the Adhesive Fracture Surface Energy of an adhesive joint is controlled by the molecular interactions across the interface, it must be a function of the Work of Adhesion.¹ The problems of measuring the interfacial energy for the interface between two solid materials are considerable and many approaches to the problem are

† Presented at the Tenth Annual Meeting of The Adhesion Society, Inc., Williamsburg, Virginia, U.S.A., February 22-27, 1987.

‡ Currently at The Shell Company of Australia Ltd., 155 William Street, Melbourne, Australia.

based upon the Girifalco and Good² expression for the work of adhesion

$$\omega_a = 2\phi(\gamma_a\gamma_s)^{1/2} \quad (1)$$

where γ_a and γ_s are the surface energies of the adhesive and substrate respectively and ϕ is the so-called "interaction parameter". The interaction parameter is³ the product of the molecular attraction parameter ϕ_l and the volume interaction parameter ϕ_v . The former may be written as the ratio of the geometric mean of the attractive constants for the individual phases to the attractive constant for the two-phase system. The latter can be calculated assuming a specific form for the intermolecular potential energy function and a specific form for the combining relationships between the attractive and repulsive constants. Good⁴ has suggested that the molecular attraction parameter is approximately unity whenever the intermolecular forces in the two phases are of the same type and has shown that when the intermolecular forces in the two phases are dissimilar then it can fall to values as low as 0.5. Gardon⁵ has similarly shown that the volume interaction parameter when calculated on the assumption that the intermolecular distance across the interface is the arithmetic mean of the intermolecular distances in the bulk materials of the two phases, does not differ significantly from unity and that a ratio of 5 to 1 in the molecular volumes will only reduce the volume interaction parameter to 0.93.

Although the relationship between adhesive fracture surface energy and the work of adhesion was demonstrated by Andrews and Kinloch⁶ they had to use the method of Owens and Wendt⁷ to calculate the work of adhesion. In so doing they used a value for the interaction parameter which remained constant with a value of approximately unity for all the adhesive substrate pairs used. The relationship between the fracture surface energy and the work of adhesion apparently broke down when cohesive failure took place due to covalent bonding across the interface and it also broke down when the surface energy of the substrate was less than that of the adhesive.

Equation (1) suggests that if the interaction parameter is constant, then for a given substrate there will be an increase in the adhesive joint strength with surface tension of the adhesive. However the wetting criterion for the formation of an adhesive joint

put forward by Zisman⁸ leads to the conclusion that such a relationship between work of adhesion and fracture surface energy can only apply when the surface tension of the adhesive is less than the critical surface tension of the substrate. This is because under those conditions when the adhesive surface tension is greater than that of the substrate, the joint strength must be weakened by the flaws at the interface introduced by poor wetting. The combination of the two effects therefore suggests a peak in the relationship between Adhesive Fracture Energy and the Adhesive Surface Tension. Such a peak can be inferred from the results of Iyengar and Erikson.⁹

The peak in the relationship between the adhesive fracture surface energy and the surface tension of the adhesive has been advanced by some workers as evidence that the adhesive fracture surface energy is controlled by the interfacial energy for the system. An examination of the factors controlling the interfacial free energy has led these workers to postulate that the maximum adhesive fracture surface energy should be attained when the solubility parameters of adhesive and substrate are matched. This hypothesis, sometimes known as the mutual solubility approach to adhesive bonding was originally based upon the work of Hansen¹⁰ and has been justified by the results of Harrison.¹¹

The relationship between the surface tension and the solubility parameter may be expressed in the form¹²

$$\gamma = K\delta^2V^{1/3} \quad (2)$$

where δ is the solubility parameter, V is the molar volume and K a constant. The peak in the curve relating joint strength to solubility parameter⁶ would therefore not be predicted by the combination of Eqs (1) and (2). If it is assumed that variations in the molar volume between different adhesives are unlikely, when reduced to the one-third power, to make a material difference to the proportionality between the surface tension and the square of the solubility parameter then the work of adhesion would increase monotonically with the surface tension of the adhesive. However, variations in the molar volume may also affect the volume interaction component of the interaction parameter, therefore one objective of the present work is to examine the dependence of joint strength on adhesive surface tension at the same time as examining values of the

interaction parameter, in order to see whether the changes in the different components of the interaction parameter are capable of explaining the variation of joint strength.

EXPERIMENTAL AND RESULTS

A suitable experimental system for the examination of the interaction parameter and its influence on the failure of an adhesive joint was designed as follows. A number of joints were constructed with the same adhesive and a range of substrates (each substrate had a different surface energy or solubility parameter). To avoid the complicating effects of compositional changes and hence possible changes in the surface energy of the adhesive, a solvent-free, castable polyurethane elastomer was used. The use of the castable polyurethane elastomer and sheets of commercially produced polymers produced a joint ideally suited to the blister test method for measuring the fracture surface energy.

Measurement of fracture surface energy

The blister test was developed by Williams¹³ to measure the fracture surface energy between an elastic adhesive and a rigid substrate. During the blister test a pressurised fluid (which may be gas or liquid) is applied through a hole in the substrate, to the underside of a Teflon® disc. Since the disc is located at the interface between the adhesive and the substrate, the pressurized fluid forms a blister. The pressure is then increased until failure occurs (Figure 1). The fracture surface energy is calculated from a knowledge of the pressure at which the crack propagates, the geometry of the specimen and the modulus of the adhesive. The blister test has been used in many diverse applications such as the adhesion between rocket liners and propellants¹⁴ and the adhesion of molluscs and dental adhesives.¹⁵

The relationship between the fracture surface energy and the experimental variables can be written in a general form (Equation 3),

$$R = P_{cr}/[E \times Q(h/a)] \quad (3)$$

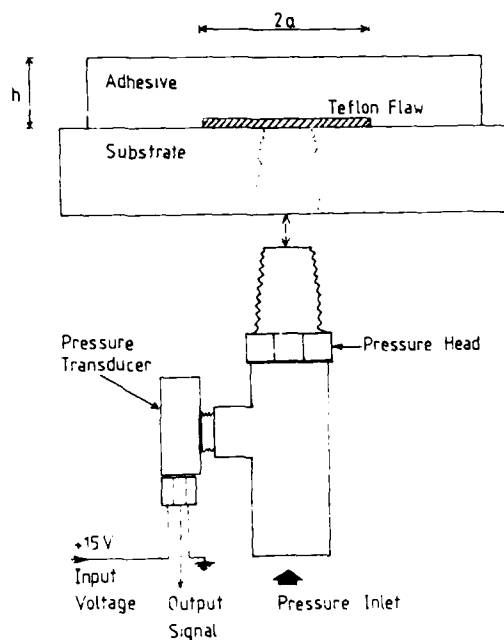


FIGURE 1 Blister test specimen.

here " $Q(h/a)$ " is a geometry factor which accounts for the variation of the fracture surface energy with the geometry of the joint. Andrews and Stevenson¹⁶ have derived an analytical expression for the geometry factors. P_{cr} is the pressure at which the flaw propagates, a is the radius of the flaw, h is the height of the adhesive and E is the modulus of the adhesive.

Two different blister test rigs were built, a low-pressure source test rig and a high-pressure source test rig. Each relies on a different method of producing and also controlling the pressure applied to the interface of the specimen. The specimen in the low-pressure rig is part of a closed volume system which allows the pressure to be increased by reducing the volume of the system using a piston and cylinder arrangement. The second type of rig which is capable of higher pressures uses a regulated air supply. With both test rigs the specimen was attached to the pressure head, by screwing a 1/8 B.S.P. tapered male fitting into the bottom of the substrate.

Characterisation of the adhesive and substrate

Both the surface energy as measured according to the method of Owens and Wendt⁷ and the solubility parameters of the adhesive and substrate were determined.

The solubility parameters of the adhesive and the substrates used in the experimental programme were determined by measuring the swelling of each polymer in a range of organic solvents. The swelling was measured using the percentage mass increase of the polymer as a function of immersion time in the solvent.¹⁷ The swelling measurements were taken at different time intervals to obtain the equilibrium swelling, as some solvents were found to approach equilibrium faster than others. The equilibrium swelling values were then plotted against the solubility parameter of the solvents, and the solubility parameter of the polymer was taken to be that of the solvent which produced the largest equilibrium swelling. The results are shown in Table I.

The contact angles of methylene iodide and water were measured

TABLE I

Substrate	Contact angle measurements				Solubility parameter
	θ_1	θ_2	γ_s^d mJ/m ²	γ_s^p mJ/m ²	
H.M.W.P.E.	56	103	31.4	0.1	8.6
Polypropylene	62	98	26.4	1.0	8.6
Polystyrene	38	83	38.3	2.8	9.2
P.M.M.A.	33	70	38.3	7.7	9.5
Rigid P.V.C.	40	86	37.9	1.9	9.7
Acetal resin	36	79	38.6	4.0	9.3
Epoxy resin	41	78	35.6	5.0	9.3-9.5
COO4 urethane	32	84	41.5	2.0	10.2
Polycarbonate	37	83	38.7	2.6	10.6
P.E.T.	26	76	42.8	4.1	10.9
Nylon 6-6	34	70	37.5	8.2	14.5
Nylon 6	39	61	33.1	14.2	15.0
Polyurethane	68	94	22 ¹	2.4	9.3
Adhesive					

θ_1 refers to the contact angle of methylene iodide.

θ_2 refers to the contact angle of water.

γ_s^d refers to the dispersion component of the surface energy.

γ_s^p refers to the polar component of the surface energy.

on the adhesive and the substrates used in the blister tests. According to Owens and Wendt⁷ this allows the calculation of the components of the surface energy of the adhesive and the substrate. The contact angles were measured using a contact angle analyzer (manufactured by IMass of the USA). The results are also shown in Table I.

The fracture surface energy measured in the blister test versus the solubility parameter of the substrate is presented in Figure 2. The maximum fracture surface energy is associated with a change of the failure mode from interfacial failure to cohesive failure. The maximum occurs for some substrates when the difference between the solubility parameters of the adhesive and the substrate is small. This indicates that the toughness of the interface for these joints

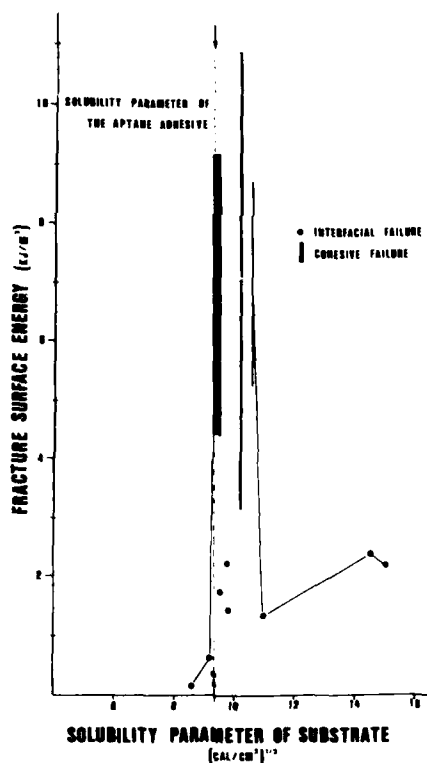


FIGURE 2 Blister test results.

goes through a maximum as the differences between the solubility parameter decreases. However, a close examination of the blister test results shows that significant differences exist between the results of the blister test experiments and the results obtained by Iyengar and Erickson. The experimental results of Iyengar and Erickson suggest a matching of the solubility parameters maximises the fracture surface energy. However, it can be seen that this is not always the case as some joints with the same solubility parameter for the adhesive and the substrate failed interfacially. It has been suggested earlier that variations in the interaction parameter may be responsible for such effects and consequently this is now examined more closely.

DISCUSSION

The value of the work of adhesion was calculated by the method of Owens and Wendt⁷ and this is shown in Table II. For a system in which the adhesive is a constant for all joints, the dissipative energy losses should be nearly the same for all joints and hence the work of adhesion should vary linearly with the fracture surface energy. The ratio of the work of adhesion to the fracture surface energy is shown in Table II and it can be seen that this is far from constant and, in fact falls into three groups. There is a group of substrates including HMWPE, PP, PS and PMMA for which the calculated work of

TABLE II

Substrate	R J/m^2	w_A mJ/m^2	R/w_A $\times 10^3$	γ_c mJ/m^2
H.M.W.P.E.	142	50.6	2.8	26.0
Polypropylene	128	51.3	2.5	25.6
Polystyrene	629	63.3	9.9	31.6
Acetal resin	336	64.6	3.5	32.3
P.M.M.A.	1,770	66.7	5.0	33.4
Rigid P.V.C.	2,267	62.1	28	31.1
Epoxy resin	9,165	63.0	145	31.5
COO4 urethane	10,908	64.9	168	32.5
Polycarbonate	8,732	63.4	137	31.7
P.E.T.	1,375	65.4	21	33.9
Nylon 6-6	2,284	66.5	34	33.2
Nylon 6	2,417	65.7	36	32.9

adhesion appears to be high, and a group of substrates for which (because the failure is cohesive) the calculated work of adhesion is apparently low. The reason for this is not clear.

The epoxy resin, the polycarbonate and the polyurethane substrates all yielded a cohesive failure with a large cohesive work of fracture. The wetting approach to bonding would suggest that cohesive fracture would always occur when the surface tension of the adhesive is less than the critical surface tension of the substrate. The appropriate critical surface tension is, however, that which would be found if it were determined using a range of liquids which have the same polarity (ratio of the polar to the dispersion components of the surface energy) as the substrate. This may be calculated for the adhesive used as follows. On the basis of the Owens and Wendt formulation then since

$$\gamma_a(1 + \cos \theta) = 2(\gamma_s^d \gamma_a^d)^{1/2} + 2(\gamma_s^p \gamma_a^p)^{1/2} \quad (4)$$

and $\cos \theta = 1$ when $\gamma_A = \gamma_c$

$$\gamma_c = (\gamma_s^d \gamma_a^d)^{1/2} + (\gamma_s^p \gamma_a^p)^{1/2} \quad (5)$$

or for the adhesive used

$$\gamma_c = 4.70(\gamma_s^d)^{1/2} + 1.55(\gamma_s^p)^{1/2} \quad (6)$$

The calculated value of the critical surface tension for each substrate which is appropriate to a liquid of the polarity of the adhesive is shown in Table II. This reveals that the adhesive has a lower surface tension than the critical surface tension of any of the substrates and hence that the failure should have been cohesive in all cases.

The mutual solubility approach to adhesive bonding has some success in predicting the joint strength in that there is a maximum in the strength and the failure becomes cohesive when the cohesive energy densities of substrate and adhesive are matched. The approach is less successful in predicting the strength in the case of polystyrene, acetal, Perspex and rigid PVC for which the failure was adhesive.

If, following Gardon,⁵ the volume interaction parameter is put approximately equal to unity then the interaction parameter is a function only of the molecular attraction parameter and can be calculated from equation (1) expressed in terms of the fractional

polarities.

$$\phi_A = (p_u p_s)^{1/2} + (d_u d_s)^{1/2} \quad (7)$$

The values of the molecular attraction parameter were calculated for each of the blister test pairs using equation (7) and it can be seen from Table III that it does not deviate significantly from unity.

The small deviation of the molecular attraction parameter values in Table III from unity would suggest that the interaction parameter is not a significant variable. However, the small variation is difficult to reconcile with the fact that for water/organic liquid systems the measured values of the interaction parameter range from 0.55 to 1.13.² The lower values are typical of non-polar liquids such as the hydrocarbon liquids in contact with water. Furthermore, Good⁴ has shown that the molecular attraction parameter reduces to one only when dispersion forces predominate on both sides and across the interface. This is in direct conflict with the treatment proposed by Owens and Wendt. Calculations based on Owens and Wendt treatment for substrates with large polar components such as Perspex, the epoxy resin, and nylon 6-6 all yield interaction parameter values of 0.99 according to equation (7) and similar results are obtained with reported surface energy components for such unlikely combinations as P.V.C./Polyethylene, P.V.C./Nylon 6-6, Epoxy/P.M.M.A. and Epoxy/Polyethylene.

Since the molecular attraction parameters calculated and shown in Table III do not reveal the reason for the observed relationship

TABLE III

Substrate	d	p	ϕ_i	ϕ_u
H.M.W.P.E.	0.9975	0.0025	0.9646	0.7938
Polypropylene	0.9510	0.0037	0.9510	0.8731
Polystyrene	0.9310	0.0690	0.9987	0.9740
P.M.M.A.	0.8320	0.1680	0.9944	0.9629
Rigid P.V.C.	0.9520	0.0480	0.9954	0.8726
Acetal resin	0.8766	0.1234	0.9991	1.0442
Epoxy resin	0.8766	0.1234	0.9991	1.0442
COO4 urethane	0.9534	0.0466	0.9951	0.9999
Polycarbonate	0.9369	0.0631	0.9980	0.9940
P.E.T.	0.9125	0.0875	0.9998	0.9985
Nylon 6-6	0.8196	0.1804	0.9925	1.0690
Nylon 6	0.6994	0.3006	0.9654	0.9930

between the fracture surface energy and the properties of the adhesive and substrate, an examination of the volume interaction parameter was attempted.

If a Lennard-Jones potential energy function is used to describe the intermolecular attraction between the two phases then the volume interaction parameter can be calculated by assuming the appropriate combining relationships between the function constants for the interfacial interactions and those for the intermolecular interactions in the individual phases. Girifalco and Good² used a geometric mean relationship for both attractive and repulsive constants. Kong, however,¹⁸ has developed a more rigorous method for the calculation of the repulsive constant which yields

$$B_{12} = (B_{11}/2^{13})[1 + (B_{22}/B_{11})^{1/3}]^{13}$$

where B_{11} , B_{22} and B_{12} are the Lennard-Jones repulsive constants for the interactions between molecules within one phase and across the interface. If this combining relationship is used then the volume interaction parameter can be calculated from an expression of the form

$$\phi_v = \left(\frac{V_{22}}{V_{11}}\right)^{5/6} \left(\frac{\delta_{22}}{\delta_{11}}\right)^{1/3} \left[\frac{2}{1 + ((\delta_{22}/\delta_{11})^2 (V_{22}/V_{11})^5)^{1/3}} \right]^{13/3} \quad (8)$$

The results of such calculations are shown in Table III.

From Table III it can be seen that all the systems which failed cohesively had a high value for the volume interaction parameter. Although the P.E.T. and nylon joints appear to be exceptions to this, it is suggested that the molecular interaction parameter may be smaller in this case than is indicated by the Owens and Wendt calculation.

CONCLUSIONS

Interfacial failure is possible even with systems in which the adhesive is capable of wetting the substrate. Although the fracture surface energy of the joint (which measures the work of adhesion) demonstrates a general increase as the surface energy of the substrate increases, this relationship is perturbed within the region where cohesive failure occurs. The cohesive failure occurs when the

solubility parameters of adhesive and substrate approach one another but only if the volume interaction parameters of the system are high.

References

1. B. W. Cherry and M. I. Hakeem, *Adhesion* 10, K. W. Allen, Ed. (Elsevier Applied Science Publishers, London, 1986), Chapter 4, pp. 42-56.
2. L. A. Girifalco and R. J. Good, *J. Phys. Chem.* 61, 904-9 (1957).
3. R. J. Good, L. A. Girifalco and G. Kraus, *J. Phys. Chem.* 62, 1418 (1958).
4. R. J. Good in *Adhesion and Adhesives*, R. L. Patrick, Ed. (Edward Arnold, London, 1967), Chapter 2, pp. 9-68.
5. J. L. Gardon in *ibid.*, Chapter 8, pp. 269-324.
6. E. H. Andrews and A. J. Kinloch, *Proc. Roy. Soc. A* 332, 385-99 (1973).
7. D. K. Owens and R. C. Wendt, *J. Appl. Poly. Sci.* 13, 1741-7, (1969).
8. W. A. Zisman in *Advances in Chemistry Series No. 43*, R. F. Gould, Ed. (Amer. Chem. Soc., Washington, D.C., Chapter 1, pp. 1-51).
9. Y. Iyengar and D. E. Erickson, *J. Appl. Poly. Sci.* 11, 2311-24 (1967).
10. C. M. Hansen, *Ind. Eng. Chem. Prod. Res. Dev.* 8, 2 (1969).
11. K. W. Harrison, in *Adhesion* 3, K. W. Allen, Ed. (Applied Science Publishers, London, 1979), Chapter 9, pp. 143-70.
12. A. F. M. Barton, *J. Adhes.* 14, 33-62 (1982).
13. M. L. Williams, *J. Appl. Poly. Sci.* 13, 19-38 (1969).
14. J. D. Burton, W. B. Jones and M. L. Williams, *Trans. Soc. Rheol.* 15, 39-50 (1971).
15. G. P. Anderson, S. J. Bennet and K. L. DeVries, *Analysis and Testing of Adhesive Bonds* (Academic Press, New York, 1977), pp. 58-68.
16. E. H. Andrews and A. Stevenson, *J. Matls. Sci.* 13, 1680-8 (1978).
17. S. Takahashi, *J. Appl. Poly. Sci.* 28, 2847-66, (1983).
18. C. L. Kong, *J. Chem. Phys.* 59, 2464-7, (1973).

A Thermodynamic Model of the Adhesive Bond†

W. S. GUTOWSKI

CSIRO Division of Building Research,‡ Melbourne, Australia

(Received August 30, 1986)

An adhesive bond is considered as a thermodynamic system in which the properties of components are expressed in relevant thermodynamic terms. Two hypotheses are analysed, (i) that the maximum strength of the bond is achieved when the interfacial energy is a minimum, and (ii) that only those systems which exhibit a true zero-interfacial energy can be considered stable in terms of their durability.

Conditions are found expressed by the 'critical energy ratio', α^{CRIT} , under which the thermodynamic work of adhesion becomes negative and, accordingly, the strength of the adhesive bond is zero.

Thermodynamic Equilibrium Diagrams are constructed which allow analysis of bond performance in order to determine conditions for maximum strength, zero strength, and the 'no-bond' area, indicating zero-strength or spontaneous delamination tendency.

KEY WORDS Work of adhesion; Interfacial energy; Critical energy ratio; Thermodynamic equilibrium diagrams; Delamination; Adhesive bonds.

INTRODUCTION

In order to predict the performance of an adhesive bond under service conditions it is necessary to know (1) the conditions in terms of properties of bond components which promote the maximum strength, (2) the conditions under which a zero-strength or spontaneous delamination of the bond can be expected, (3) the strength

† Presented at the Tenth Annual Meeting of The Adhesion Society, Inc., Williamsburg, Virginia, U.S.A., February 22-27, 1987

‡ Postal address: PO Box 56, Highett, Victoria 3190, Australia

deficiency of the bond (compared to the maximum achievable) outside the optimum point, and (4) the durability (stability under adverse environments) of the bond during its service.

Answers to the above are possible if an adhesive bond is considered as a thermodynamic system whose properties are described in terms of relevant thermodynamic parameters such as surface energies of components, and wettability characteristics.

BASIC TERMS AND ASSUMPTIONS

Conditions for the maximum strength

It has been claimed by numerous researchers that either the thermodynamic work of adhesion,^{1,2,3,4} critical surface tension for wetting,^{4,5,6} solubility parameter^{7,8} or interfacial energy^{4,5,9} are responsible for the strength of adhesive bonds. It can be shown, however, that all of these are interrelated with thermodynamic properties of bond components, as expressed by surface energies.

A knowledge of surface energies of substrate and adhesive, as well as a wettability characteristic, provides sufficient data for estimation of interfacial energies. Based on experimental evidence and analytical prediction we postulate, therefore, that (I) the minimum interfacial energy between bond components corresponds to maximum strength and durability of the adhesive bond, and (II) only those 'substrate/adhesive' systems that exhibit true zero interfacial energy under their conditions of service can be treated as stable in terms of their durability.

Conditions for zero-strength of adhesive bond

Adhesive bonding is governed by intermolecular forces exerted across the surface of contact between two phases. The force of attraction between two semi-infinite idealized bodies (*e.g.* substrate and cured adhesive) is described by a derivative of the energy of interaction which in a simplified example can be represented by the Lennard-Jones¹⁰ potential (see Appendix for terms used in equations), *i.e.*

$$F = \frac{d}{dr} \left[\frac{A}{r^6} + \frac{C}{r^{12}} \right]. \quad (1)$$

This function is illustrated in Figure 1.

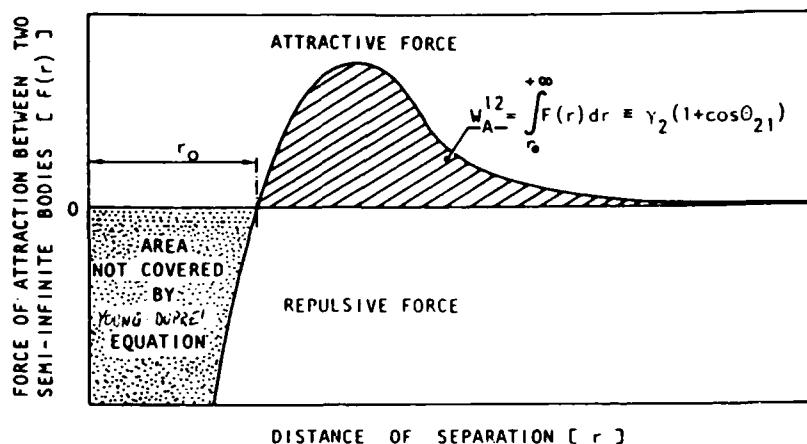


FIGURE 1 The area of relevance of the Young-Dupré equation for thermodynamic work of adhesion in respect to a character of the gross intermolecular force acting across a substrate-adhesive interface as determined from Lennard-Jones potential.

Conditions under which $W_A = 0$ are relevant where there is no net force across the interface phase 1/phase 2.

When $W_A < 0$ the existence of net repulsive forces cannot be excluded, *i.e.* conditions at the interface are such that the system may exhibit zero strength or may delaminate spontaneously.

Accordingly, we postulate that thermodynamic conditions at the interface under which $W_A = 0$ correspond to zero-strength of the adhesive bond.

Basic equations

We assume that the following equations for adhesion are valid:

(a) Dupré equation:

$$W_A = \gamma_1 + \gamma_2 - \gamma_{12} \quad (2)$$

(b) Young-Dupré equation:

$$W_A = \gamma_2(1 + \cos \theta_{21}) \quad (3)$$

where θ_{21} is an equilibrium in contact angle made by phase 2, whilst liquid, in contact with phase 1.

It is assumed for the simplicity that the equilibrium spreading pressure $\pi_e = 0$.

Wettability characteristic of the solid

The relationship between $\cos \theta_{21}$ and γ_2 is known as the wettability characteristic and was first described by Fox and Zisman,¹¹ *i.e.*

$$\cos \theta_{21} = 1 - b_0[\gamma_2 - \gamma_{C(1)}]. \quad (4)$$

There is some controversy as to the profile of the wettability characteristic.^{11,12,13,14} We assume, however, that it can be well approximated in a linear fashion, as Figure 2 illustrates.

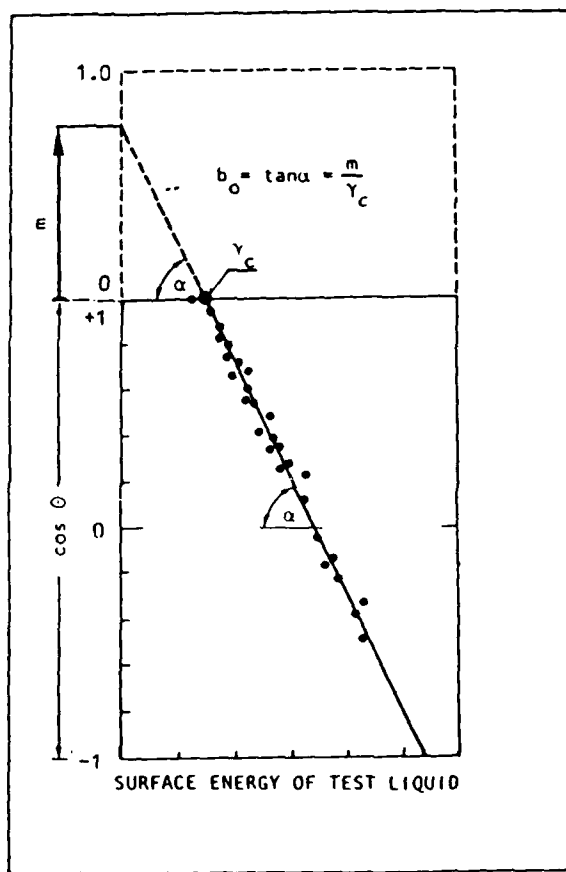


FIGURE 2 Graphical illustration of the wettability characteristic approximated in a rectilinear fashion, with the explanation of the sense of parameter 'm' as an intercept of axis parallel to $\cos \theta$.

Introducing the energy ratio 'a' of the substrate-adhesive system:

$$a = \gamma_1 / \gamma_2, \quad (5)$$

and a specific bonding efficiency factor Φ_0 , i.e.:

$$\Phi_{0(1)} = [\gamma_{C(1)} / \gamma_1]^{1/2} \quad (6)$$

we have:

$$\cos \theta_{21} = 1 - m_1 \left[\frac{1}{a \Phi_{0(1)}^2} - 1 \right]. \quad (7)$$

THERMODYNAMIC CONDITIONS FOR MAXIMUM STRENGTH OF ADHESIVE BOND

It has been postulated above that the maximum strength and durability of an adhesive bond are achieved under conditions where the interfacial energy is minimum under service conditions. The expression for the interfacial free energy of the system is obtained by rearrangement of Eqs. (2) and (3):

$$\gamma_{12} = \gamma_1 - \gamma_2 \cos \theta_{21}. \quad (8)$$

Further substitution of Eq. (7) in Eq. (8) and introduction of a physical limitation for complete wetting at $(\cos \theta_{21})^{\text{MAX}} = 1.0$, lead to either

$$\gamma_{12} = \gamma_1 - \gamma_2(1 + m_1) + m_1 \frac{\gamma_2^2}{\gamma_{C(1)}} \quad \text{for } \gamma_2 \geq \gamma_{C(1)} \quad (9)$$

or

$$\gamma_{12} = \gamma_1 - \gamma_2 \quad \text{for } \gamma_2 \leq \gamma_{C(1)}. \quad (10)$$

Conditions for the minimum interfacial energy are found from the first derivative of Eq. (9) with respect to γ_2 and they occur at the energy ratio:

$$a_{\text{MIN}} = \frac{2m_1}{(1 + m_1)\Phi_{0(1)}^2}. \quad (11)$$

The minimum interfacial energy is found by substituting Eq. (11) into Eq. (9)

$$\gamma_{12}^{\text{MIN}} = \gamma_1 - \frac{(1 + m_1)^2 \cdot \gamma_1 \Phi_{0(1)}^2}{4m_1}. \quad (12)$$

THERMODYNAMIC CONDITIONS FOR MAXIMUM BOND STABILITY (DURABILITY)

Conditions for the maximum bond stability are achieved when the 'substrate-adhesive' system exhibits a true zero-interfacial energy under service conditions. This is satisfied [see Eq. (9)] when the slope of the wettability characteristic yields the value of the parameter m

$$m_1^D = \frac{2}{\Phi_{0(1)}^2} [1 - (1 - \Phi_{0(1)}^2)^{1/2}] - 1. \quad (13)$$

THERMODYNAMIC CONDITIONS FOR ZERO-STRENGTH

As postulated earlier, conditions for zero-strength of an adhesive bond correspond to $W_A = 0$. It follows from Eqs. (3) and (7) that this occurs for any energy ratio:

$$a \leq a_1^{\text{CRIT}} = \frac{m_1}{(2 + m_1)\Phi_{0(1)}^2}. \quad (14)$$

The following can be determined from Eq. (14):

- a) The surface energies of phase 1 and 2 at which adhesive bonding becomes impossible because the bond strength equals zero;
- b) Those property values at which a change of thermodynamic properties of bond components at the interface (*e.g.* γ_1 , γ_2 , p_1 , d_1 , p_2 , d_2) produces the energy ratio $a \leq a^{\text{CRIT}}$. This phenomenon relates to the tendency to spontaneous interfacial delamination of the bond and failure of the structure. This may be brought about by environmental attack, *e.g.* absorption of water or fuel by adhesive, aging of the adhesive, oxidation or corrosion of the substrate's surface, etc.

Another condition for zero-strength of an adhesive bond is determined from the thermodynamic equation of state for adhesion proposed by the author,¹⁵ *i.e.*:

$$\begin{aligned} W_A &= \gamma_1 + \gamma_2 - \gamma_{12} = \gamma_2(1 + \cos \theta_{21}) \\ &= \gamma_1(1 + \cos \theta_{12}) = \text{CONSTANT} \end{aligned} \quad (15)$$

The right-hand side of Eq. (15) defines another equilibrium contact angle, θ_{12} . It is explicitly exhibited by a liquid deposited on a cured adhesive, or appears in an implicit form when thermodynamic wetting takes place in the case of two solids in immediate contact. When a cured adhesive is regarded as a solid of surface energy γ_2 then, from Eq. (15):

$$\gamma_{12} = \gamma_2 - \gamma_1 \cos \theta_{12}. \quad (16)$$

The wettability characteristic of the cured adhesive is determined from reference to Figure 2:

$$\cos \theta_{12} = (1 + m_2) - \frac{m_2}{\Phi_{0(2)}^2} \frac{\gamma_1}{\gamma_2}, \quad (17)$$

where

$$\Phi_{0(2)} = [\gamma_{C(2)}/\gamma_2]^{1/2}. \quad (18)$$

Conditions for $W_A = 0$, pertaining to the wettability characteristic of cured adhesive, are found by rearranging Eqs. (17), (18) and the right part of Eq. (15). It follows that $W_A = 0$ for

$$a \geq a_2^{\text{CRIT}} = \frac{(2 + m_2)\Phi_{0(2)}^2}{m_2}. \quad (19)$$

It can be noted that a_2^{CRIT} , as expressed by Eq. (19), unexpectedly corresponds to the area of complete thermodynamic wetting of substrate by cured adhesive (*i.e.* $\theta_{21} = 0^\circ$) of constant surface energy γ_2 .

THERMODYNAMIC EQUILIBRIUM DIAGRAMS (TED) FOR DETERMINING BOND PERFORMANCE

From the above relations Thermodynamic Equilibrium Diagrams (TED) can be developed from which the performance of adhesive bonds can be determined in terms of (a) maximum strength, (b) zero-strength, (c) zero-contact angle, and (d) no-bond area.

Data necessary for the construction of TED are (i) surface energies of phase 1 and phase 2, *i.e.* γ_1 and γ_2 , and (ii) wettability characteristic of phase 1 or phase 2 to gain parameters: ' m ' and γ_C .

TED may be in the coordinates:

a) γ_2 vs. $\gamma_{C(1)}$; for a procedure based on the wettability characteristic of substrate, or;

b) γ_1 vs. $\gamma_{C(2)}$: for a procedure based on the wettability characteristic of cured adhesive.

For convenience, a procedure based on the wettability characteristic of a cured adhesive is presented (see Figure 3).

Conditions for maximum strength in TED

Conditions for maximum strength are described by Eq. (11). The optimum surface energy of the substrate, γ_1^{OPT} , can be determined if

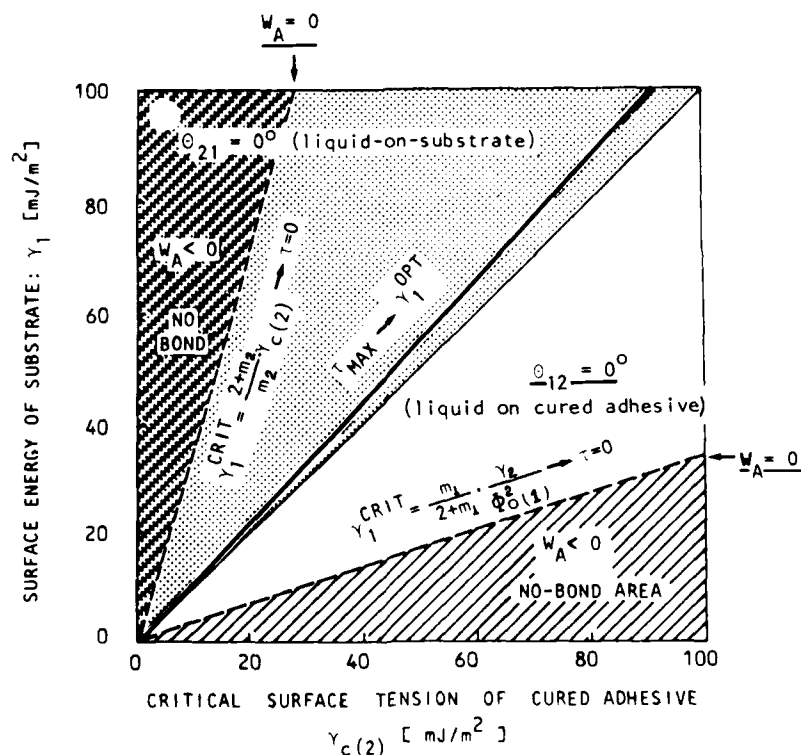


FIGURE 3 Thermodynamic Equilibrium Diagram (TED) based on the wettability characteristic of cured adhesive. (a) representation of conditions for the maximum strength [Eq. (20)] and zero-strength in TED [Eq. (22) and (23) for $m = 0.8$] with indicated areas of no-bond [as corresponding to $W_A \leq 0$]; and (b) the influence of value of parameter 'm' on location of γ_1^{CRIT} and γ_1^{OPT} .

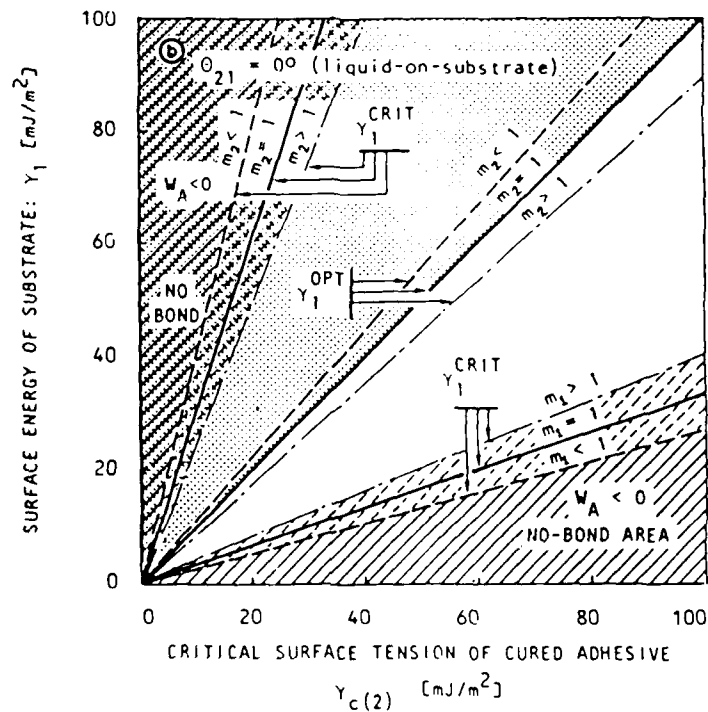


FIGURE 3 (contd.)

the energy ratio $a = \gamma_1/\gamma_2$ and Eq. (18) are introduced to modified Eq. (11), e.g.:

$$\gamma_1^{\text{OPT}} = \frac{1 + m_2}{2m_2} \cdot \gamma_{C(2)} \quad (20)$$

Equation (20) is illustrated in Figure 3.

In the engineering terms, Eq. (20) indicates the optimum surface energy of the substrate, to be obtained through its surface treatment (e.g. etching, adsorption of adhesion promoters, etc) in order to achieve the maximum strength with a given adhesive (as characterized by $\gamma_2:m_2:\gamma_{C(2)}$).

Conditions for zero-contact angle θ_{12} in TED

Conditions relevant to complete wetting of the cured adhesive are physically achieved when

$$\gamma_1 \leq \gamma_{C(2)} \quad (21)$$

which is represented in TED (Figure 3a) by a straight line with a constant slope of 1, *independent* of the parameter 'm'. Thus, the area below and including $\gamma_1 = \gamma_{C(2)}$ represents conditions which correspond to the thermodynamic wetting of the surface of the cured adhesive. The dotted area above $\gamma_1 = \gamma_{C(2)}$ relates to the complete wetting of substrates by a given adhesive of constant surface energy γ_2 , *e.g.* $\theta_{21} = 0^\circ$ in this zone.

Conditions for zero-strength and no-bond areas in TED

Conditions for zero strength of an adhesive bond are achieved when $W_A = 0$, as expressed by the right-hand side of equation of state (15). The first boundary value of surface energy of the substrate, γ_1^{CRIT} , at which $W_A = 0$ is determined from Eq. (19) *i.e.*:

$$\gamma_1^{\text{CRIT}} \geq \frac{2 + m_2}{m_2} \cdot \gamma_{C(2)}. \quad (22)$$

Physically, the line expressed by Eq. (22), as illustrated in Figure 3a by an upper broken line, constitutes a boundary for areas indicating conditions for existence and non-existence of adhesive bonds.

The hatched area between axis γ_1 and γ_1^{CRIT} relates to the conditions under which $W_A \leq 0$, as corresponding to no-bond in the system (*e.g.*: 'substrate-adhesive', etc.). The Young-Dupre equation, restricting W_A to positive values only, becomes irrelevant here as attractive forces across the interface do not exist (see Figure 2). The second boundary value where the surface energy of the substrate yields $W_A = 0$ with a given adhesive is found from Eq. (14), namely

$$\gamma_1^{\text{CRIT}} \leq \frac{m_1}{2 + m_1} \cdot \frac{\gamma_2}{\Phi_{0(1)}^2}. \quad (23)$$

Equation (23) is graphically represented by a lower broken line in Figure 3a located within the area of incomplete wetting of the

substrate by a given adhesive (*i.e.*, $\theta_{21} > 0^0$) [note that it corresponds to the complete thermodynamic wetting of the cured adhesive as indicated by θ_{12}]. Thus, any point located on or below the line equivalent to Eq. (23) falls into the zone where $W_A \leq 0$, *i.e.*, where zero-strength of an adhesive bond can be expected or spontaneous delamination occurs.

The above observations indicate that there are two different sets of conditions for $W_A \leq 0$ and therefore zero-strength of an adhesive bond. These are (I) as given by Eq. (22), relevant to complete wetting of the substrate by the adhesive and (II) as given by Eq. (23), which occurs within the area of no wetting.

The influence of wettability characteristic parameters on the value of demarcation points in TED.

Interesting observations may be made from the analysis of the influence of parameters related to the wettability characteristics of substrates and adhesives (*e.g.*: m , γ_c and Φ_0) on the values of γ_1^{OPT} and γ_1^{CRIT} described in the previous sections. For the maximum strength of the bond, the slope of the wettability characteristic of a cured adhesive has the following implications (see Figure 3b).

a) when $m < 1.0$, the maximum strength of the bond corresponds to thermodynamic conditions relevant to a zero contact angle θ_{21} at the 'substrate/adhesive' interface as exhibited by adhesive-on-substrate. [Note: this corresponds to a finite value of the imaginary contact angle: θ_{12}].

b) when $m = 1.0$, τ_{MAX} is achieved for thermodynamic conditions corresponding to a zero contact angle θ_{21} at the line $\gamma_1 = \gamma_{c(2)}$.

c) when $m > 1.0$ τ_{MAX} is achieved for condition corresponding to a finite angle θ_{21} , [Note: this relates to a zero—imaginary contact angle θ_{12}].

The above explains the long known but not explained dilemma: why in some cases the zero-contact angle of adhesive-on-substrate (*i.e.* θ_{21}) coincides with condition for the maximum strength whilst in others it does not.

Further analysis of Eqs. (20) and (22) indicates that decreasing the slope of the wettability characteristic (as relevant to decreasing

' m ') extends the area of positive adhesive bonding (*i.e.* when $\tau > 0$). This is illustrated by broken lines for γ_1^{CRIT} in Figure 3b which are relevant to the lower and higher limits for $\tau = 0$ respectively. In technical terms this means that the adhesive becomes more 'forgiving' (when ' m ' decreases) in respect to the successful bonding and, which applies to a larger difference between γ_2 and γ_1 .

An increase in the value of the parameter ' m ' has an adverse effect, indicated by the lines denoting γ_1^{CRIT} in Figure 3, and the area of positive bonding is narrowed.

Contact angle at the conditions for the maximum strength

It follows from the above argument that a finite contact angle *i.e.* $\theta_{21} > 0^\circ$, relates to the conditions for the maximum strength when the wettability characteristic of the substrate is such that $m_1 < 1.0$. Value of this contact angle, *i.e.* θ_{21}^{OPT} , is determined if Eq. (11) for the energy ratio a_{MIN} at γ_{12}^{MIN} (as corresponding to τ_{MAX}) is

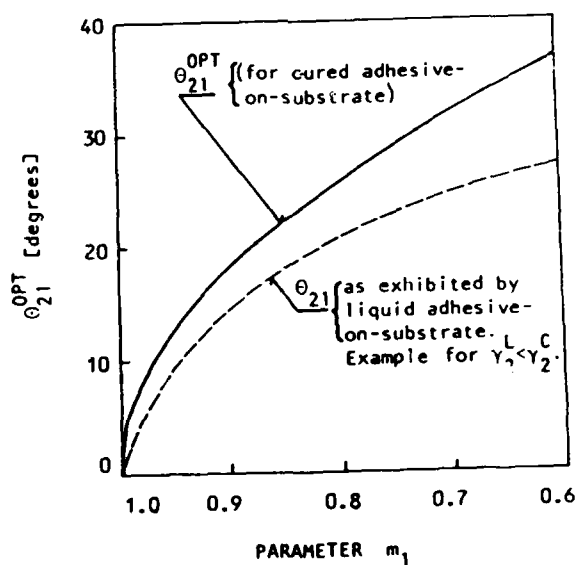


FIGURE 4 Contact angle θ_{21}^{OPT} corresponding to conditions for the maximum strength in relation to the slope of the wettability characteristic (as represented by ' m ').

substituted into Eq. (7), e.g.:

$$\theta_{21}^{\text{OPT}} = \cos^{-1} \frac{1 + m_1}{2}. \quad (26)$$

Equation (26), graphically presented in Figure 4, shows that only in the case where the slope of the wettability characteristic of the substrate yields $m = 1.0$, can the zero-contact angle, i.e. $\theta_{21} = 0$ indicate conditions for the maximum strength (when $\gamma_2 = \gamma_2^{\text{OPT}}$).

For any $m < 1.0$ (more shallow wettability characteristic), the value of θ_{21}^{OPT} is SIGNIFICANTLY higher than zero. When, for instance, $m = 0.99$, $\theta_{21}^{\text{OPT}} = 5.73^\circ$ whilst for $m = 0.8$ value of θ_{21}^{OPT} is as high as 25.84° .

The surface energy of the cured adhesive in most cases is higher than in its liquid state. Therefore, the value of θ_{21} [see Eq. (7)] as exhibited by a liquid adhesive on a substrate is lower than that corresponding to θ_{21}^{OPT} as calculated by Eq. (26) for a cured adhesive. This difference is clearly illustrated in Figure 4. The above indicates that in order to utilize θ_{21} (liquid adhesive on a substrate) as a technological indicator for optimum treatment of substrate, it is necessary to know the adhesive's surface energy in both the liquid and cured state.

References

1. N. A. De Brune, *Nature* **180**, 262 (1957).
2. L. E. Raraty and D. Tabor, *Proc. of Roy. Soc. A* **245**, 184 (1958).
3. M. J. Barbaris, *Nature* **215**, 383 (1967).
4. K. L. Mittal, in *Polymer Science and Technology*, Vol. **9A** (Plenum Press, New York, 1975), p. 129.
5. M. Levine, G. Ilkka and P. Weiss, *Polym. Lett.* **2**, 915 (1964).
6. Y. Kitazaki and T. Hata, *J. Adhesion* **4**, 123 (1972).
7. E. P. Plueddemann, *J. Paint Technol.* **40**, (316) 1 (1968).
8. Y. Iyengar and D. E. Erickson, *J. Appl. Polym. Sci.* **11**, 2311 (1967).
9. G. A. Dykerhoff and P. J. Sell, *Angew. Macromol. Chem.* **21**, 169 (1972).
10. R. J. Good, in *Treatise on Adhesion and Adhesives* Vol. 1, R. L. Patrick, Ed.), (Marcel Dekker Inc., New York, 1967), Chapt. 2.
11. H. W. Fox and W. A. Zisman, *J. Coll. Sci.* **5**, 514 (1950).
12. R. J. Good, *J. Coll. Int. Sci.* **59**, 398 (1977).
13. D. H. Kaelble and K. C. Uy, *J. Adhesion* **2**, 51 (1970).
14. J. H. Brooks, J. Mingins and N. F. Owens, *J. Coll. Int. Sci.* **61**, 215 (1977).
15. W. Gutowski, "Thermodynamic Model of Adhesive Bond and its use for Prediction of Bond Performance". *J. Adhesion* (submitted for publication).

Appendix

NOMENCLATURE

γ_1, γ_2	total surface energy of phase 1 or 2
γ_c	critical surface tension for wetting
γ_{12}	interfacial energy
W_A	thermodynamic work of adhesion
θ	equilibrium contact angle
θ^{OPT}	θ , corresponding to the minimum interfacial energy
m	parameter dependent upon the slope of the wettability characteristic
m^D	' m ' for system durable under service conditions
Φ_0	specific bonding efficiency factor
$\gamma_{12}/\gamma_2,$ γ_{12}/γ_1	relative interfacial energy
$W_A/\gamma_2,$ W_A/γ_1	relative work of adhesion
$a = \gamma_1/\gamma_2$	energy ratio of the system
a^{CRIT}	critical energy ratio for $W_A = 0$, corresponding to zero-strength
a_{MIN}	optimum energy ratio for γ_{12}^{MIN} and $[\gamma_{12}/\gamma_1]_{\text{MIN}}$, corresponding to the maximum strength
γ_1^{CRIT}	γ_1 corresponding to the zero-bond strength (when phase 1 bonded with given phase 2)
γ_1^{OPT}	γ_1 corresponding to the maximum bond strength (when phase 1 bonded with given phase 2)
F	force of attraction
A	attractive constant
C	repulsive constant
r	distance of separation
τ	bond strength

Silane Coupling Agents as Adhesion Promoters for Aerospace Structural Film Adhesives†

W. THIEDMAN,‡ F. C. TOLAN, P. J. PEARCE and C. E. M. MORRIS

Materials Research Laboratories, Defence Science and Technology Organisation, Ascot Vale, Victoria 3032, Australia

(Received August 30, 1986)

The performance of eight organofunctional silane coupling agents as adhesion promoters for the bonding of aluminium with two 121°C and two 177°C curing structural film adhesives was investigated and compared to the chromic acid (FPL) etch pre-treatment process and two non-chemical pretreatments. Aspects considered were shear strength of joints at ambient and elevated temperatures and durability, as judged by the wedge test.

The epoxy silane, γ -glycidoxypyltrimethoxy silane, was found to be a very efficient adhesion promoter with all film adhesives evaluated. The cationic styryl silane, a neutral diamine monohydrochloride, showed promise with two adhesive systems. Four other neutral silanes were less effective.

Performance of amine functional silanes was mixed. Although the shear strength of joints with the primary amine silane at its natural pH of ~ 10.3 was relatively good, durability was poor. However, good durability was obtained if the primer was first adjusted to pH 8 with hydrochloric acid, but not if acetic or phosphoric acids were used. Diamine silane was not an effective adhesion promoter at either its natural pH or when acidified with hydrochloric acid.

KEY WORDS Silane coupling agents; Aerospace film adhesives; Aluminium; Durability; Lap shear tests; Wedge tests.

† Presented at the Tenth Annual Meeting of The Adhesion Society, Inc., Williamsburg, Virginia, U.S.A., February 22–27, 1987.

‡ Present address: Chemistry Department, Deakin University, Geelong, Australia.

INTRODUCTION

It is well established that the surface treatment prior to bonding is of paramount importance in developing the optimum strength and durability of a structural adhesive assembly. Currently, the surface preparation applied to aluminium alloys in the aerospace industry involves alkali cleaning and vapour degreasing followed by the most important stage—an oxidising treatment, frequently a Chromic Acid Etch¹ or Phosphoric Acid Anodization (PAA)². Although adhesive joints prepared using a chromic etch yield high lap shear strength at room and elevated temperatures, some systems have been shown to lack long term durability, particularly in a moist environment. The PAA treatment is considered superior in terms of durability,³ but the process is lengthy and more complex than the chromic etch. Clearly, neither treatment is convenient in locations remote from ideal workshop conditions or when carrying out *in-situ* bonded aircraft repairs.

Organofunctional silanes, used originally for enhancing the bonding properties of glass fibres in reinforced plastics,⁴ are now finding utility as primers or adhesion promoters for improving the hydrothermal stability of metal to metal adhesive bonds.⁴ Silanes have the distinct advantage that their mode of application is simple (usually *via* immersing the parts to be bonded in 1% solutions), and the operation may be performed at room temperature.

Theories proposed to explain the mechanism by which silane coupling agents function are numerous but support for the presence of chemical bonding is well founded.⁵⁻⁷ The structure is commonly $X_3Si(CH_2)_nY$, where X is a hydrolysable alkoxy group and Y an organofunctional group. Thus, the theory of chemical bonding suggests that Si—O bonds are formed by elimination of water between Si—OH groups of the hydrolysed silane and surface OH groups of the substrate, leaving the organic end of the molecule to interact with the matrix resin.

The commercial range of coupling agents includes a variety of silanes containing organofunctional groups tailored to be compatible with a wide range of polymers. Several have been suggested as suitable for epoxy systems.⁴

Previous studies undertaken to investigate the effectiveness of silane adhesion promoters for the bonding of metals with structural

adhesives have been mostly concerned with the dry and wet strengths of aluminium, iron or titanium lap-shear or butt joints bonded with simple two-part epoxy systems and utilizing either γ -aminopropyltriethoxy silane or γ -glycidoxypyltrimethoxy silane.⁸⁻¹¹ Work on two unspecified film adhesives is included in ref. 8.

This paper reports on an investigation of the efficiency of eight organofunctional silanes as adhesion promoters in the bonding of aircraft-grade aluminium with a range of epoxy based structural film adhesives. Joint strength is measured in terms of lap shear strength at both room and elevated temperature and durability is monitored using the Boeing wedge test. Results are compared with both degrease/sandblast and FPL etch surface pretreatments.

EXPERIMENTAL

Materials

Details of the eight silanes and four structural film adhesives used in this work are given in Tables I and II, respectively. All materials were used as received. Aluminium used in the testing procedures was Alclad 2024-T3 of thickness 1.6 mm for lap-shear joints and 3.2 mm for wedge test specimens.

Surface treatments

Silane The adherends were solvent wiped with acetone, vapour degreased with 1,1,1-trichloroethane, grit blasted with $<230\mu$ zircon sand, immersed for 20 mins in 1% silane solutions, drained and allowed to dry for 1 hour at 110°C.

Neutral silanes (Z6040, Z6030, Z6076, Z6075 and A172) were hydrolysed with aqueous 0.1% acetic acid (pH 4) and diluted with methanol to give a 95% methanolic solution. A1100 (primary amine) was used initially at its natural pH of 10.3 in 95% methanol. In further durability studies aqueous solutions were either used at pH 10.3 or adjusted to pH 8 with 1 M hydrochloric, phosphoric or acetic acids. Z6020 (diamine) was used at its natural pH of 10.3 in

TABLE I
Silane coupling agents

Trade name	Type	Name	Organofunctional group
Z6040 ^a	Epoxy	γ -Glycidoxypropyltrimethoxy silane	$\begin{array}{c} \text{O} \\ \diagup \quad \diagdown \\ \text{CH}_2\text{CHCH}_2\text{O}(\text{CH}_2)_3 \end{array}$
Z6030 ^a	Methacrylate	γ -Methacryloxypropyltrimethoxy silane	$\begin{array}{c} \text{CH}_3 \\ \\ \text{CH}_2=\text{C}-\text{COO}(\text{CH}_2)_3 \end{array}$
Z6076 ^a	Chloropropyl	γ -Chloropropyltrimethoxy silane	$\text{Cl}(\text{CH}_2)_3$
A1100 ^b	Primary amine	γ -Aminopropyltriethoxy silane	$\text{NH}_2(\text{CH}_2)_3$
Z6020 ^a	Diamine	N-(β -aminoethyl)- γ -aminopropyltrimethoxy silane	$\text{NH}_2(\text{CH}_2)_2\text{NH}(\text{CH}_2)_3$
Z6075 ^a	Vinyl	Vinyltrimethoxy silane	$\text{CH}_2=\text{CH}$
A172 ^b	Vinyl	Vinyltriethoxy silane	$\text{CH}_2=\text{CH}$
Z6032 ^a	Cationic styryl	N- β -(N-vinylbenzylamino)-ethyl- γ -aminopropyltrimethoxy silane monohydrochloride	$\begin{array}{c} \text{CH}_2\text{NHCH}_2\text{NH}(\text{CH}_2)_3 \\ \\ \text{styryl} \quad \text{HCl} \end{array}$

^a Dow Chemical Co.^b Union Carbide.

95% methanol initially but in some later experiments aqueous solutions were adjusted to pH 8.0 with 1 M hydrochloric acid. Z6032 (cationic styryl) was used at its natural pH of ~ 7.0 as an aqueous solution.

Acid etching Adherends were solvent wiped and degreased as described previously and immersed in a chromic acid bath (FPL

TABLE II
Film adhesives

Name	Manufacturer	Type	Cure conditions
FM-73	American Cyanamid	Rubber modified epoxy	60 mins at 121°C
FM-300		Nitrile rubber modified epoxy	60 mins at 177°C
AF-130	3M	Unmodified epoxy	60 mins at 177°C
AF-163		Polyether rubber modified epoxy	60 mins at 121°C

etch composition—3750 g H_2O + 680 ml conc. H_2SO_4 + 500 g $\text{K}_2\text{Cr}_2\text{O}_7 \cdot 2\text{H}_2\text{O}$) for 10 mins at $65^\circ\text{C} \pm 2^\circ\text{C}$. On removal from the bath the panels were washed with cold running tap water for approximately 10 mins, then dried at 65°C for 1 hour.

Adhesive joint testing

Joints were made in a heated platten press using the recommended cure cycle for the film adhesive (see Table II). For lap shear strength, joint geometry and test methods were conducted according to ASTM D1002-72. Strengths at ambient and elevated temperatures were assessed using an Instron 1185 Materials Testing Machine. Wedge tests were performed according to ASTM D3762-79. Specimens were exposed to a controlled environment of 96% RH at 50°C for periods of up to 350 hours. Crack growth was monitored at suitable intervals using a stereo microscope and plotted as a function of time^{1/2}.

Adhesive joint test results were generally based on the average of six replicates showing coefficients of variation of around 3%.

RESULTS

Shear strength

Using 121°C curing adhesive FM-73 (American Cyanamid), lap shear strength as a function of test temperature for aluminium joints primed with seven silanes was compared with the FPL etch and degrease or degrease/sandblast surface treatments. It can be seen from Table III and Figure 1 that the FPL treatment gave superior strength at all test temperatures and that most of the silane-primed joints were only marginally lower in strength at ambient. In contrast, joint performance at elevated temperatures showed significant differences with only the primary amine and epoxy types approaching the FPL values. Results obtained from the degrease and degrease/sandblast treatments were generally inferior to those obtained from primed joints.

Examination of the bonded surfaces after testing showed that all pretreatments resulted in >90% cohesive failure when tested at

TABLE III
Effect of pretreatment on lap shear strength of FM-73

Surface treatment	Lap shear strength (MPa)			
	Ambient	80°C	90°C	100°C
Chromic acid etch	38.7	26.3	24.7	22.1
Epoxy silane	36.8	23.8	21.8	17.2
Methacrylate silane	36.7	20.9	18.5	11.2
Chloropropyl silane	36.5	19.8	18.3	12.6
Amine silane	35.6	22.5	22.4	18.3
Diamine silane	35.4	23.1	20.6	13.8
Vinyltriacetoxysilane	34.4	20.5	18.1	12.5
Vinyltrimethoxysilane	31.1	19.6	16.3	12.5
Degrease	31.2	19.6	14.6	10.2
Degrease/sandblast	27.9	17.6	15.0	11.4

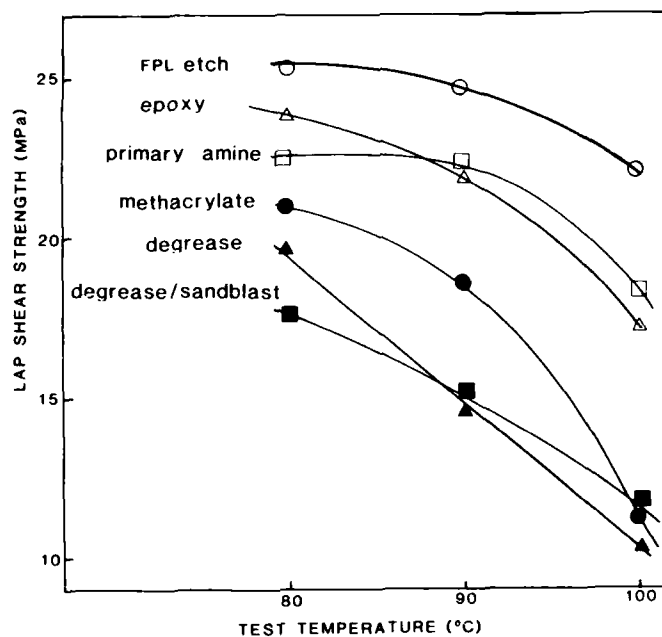


FIGURE 1 Effect of pretreatment on lap shear strength at elevated test temperatures—selected systems, FM-73 adhesive.

TABLE IV
Effect of pretreatment on lap shear strength of
AF-130

Surface treatment	Lap shear strength (MPa)	
	Ambient	177°C
FPL Chromic etch	18.9	19.6
Epoxy silane	15.6	15.0

ambient but only the FPL etch maintained this performance at elevated temperatures. The degrease/sandblast and all silane treatments, with the exception of the diamine type, resulted in approximately 80%–90%, 60%–75% and 50%–60% cohesive failure at test temperatures 80°C, 90°C and 100°C respectively. The diamine silane and degrease-only treatments produced essentially adhesive (*i.e.*, interfacial) failures at the higher temperatures, particularly at 100°C.

Using the 177°C curing adhesive AF-130 (3 M Company), lap shear strength was determined at ambient and 177°C on joints primed with epoxy silane and compared with the performance of FPL-etched joints. The shear strengths obtained after the silane pretreatment were about 20% lower than FPL etched joints at both test temperatures (Table IV). All failures were cohesive.

Durability

Bond durability has been assessed in terms of crack propagation resistance during exposure to a hostile environment (50°C and 96% RH) using the wedge test. Although this relatively simple test simulates forces and effects at the metal-adhesive interface in a purely qualitative manner, results obtained have been shown to be more reliable than methods using lap shear or peel tests when predicting the environmental durability of adherend surface preparations.¹²

The qualitative nature of the wedge test is, to a large extent, the result of variation in initial crack length, and hence initial joint stress, due to the inherent fracture toughness of the adhesive under test. Thus, a comparison of crack propagation rates between

different adhesive systems must be treated with caution. For any particular adhesive system, regardless of adherend surface pretreatment, the initial crack length remains fairly constant if cohesive failure occurs. The range of initial crack lengths observed in this work was AF-163 26.2–29.7 mm, FM-73 30.4–32.6 mm, FM-300 37.8–40.8 mm, AF-130 53.3–54.2 mm.

The crack propagation resistance of bonded joints made using four silane primers (primary amine, diamine, epoxy and methacrylate), the FPL etch and sandblast/degrease pretreatments is shown in Figure 2 for the 121°C curing adhesive FM-73. Results indicate a large variation in crack propagation rates between different adhesives.

To assess the potential of silane primers with a range of structural film adhesives, the durability of two 121°C and two 177°C curing systems was assessed from wedge specimens prepared using the

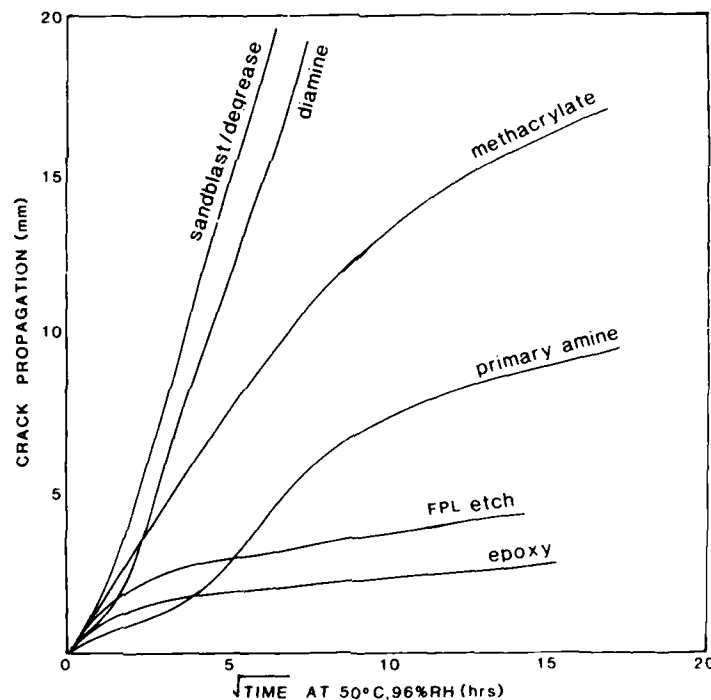


FIGURE 2 Effect of pretreatment on crack propagation, FM-73 adhesive.

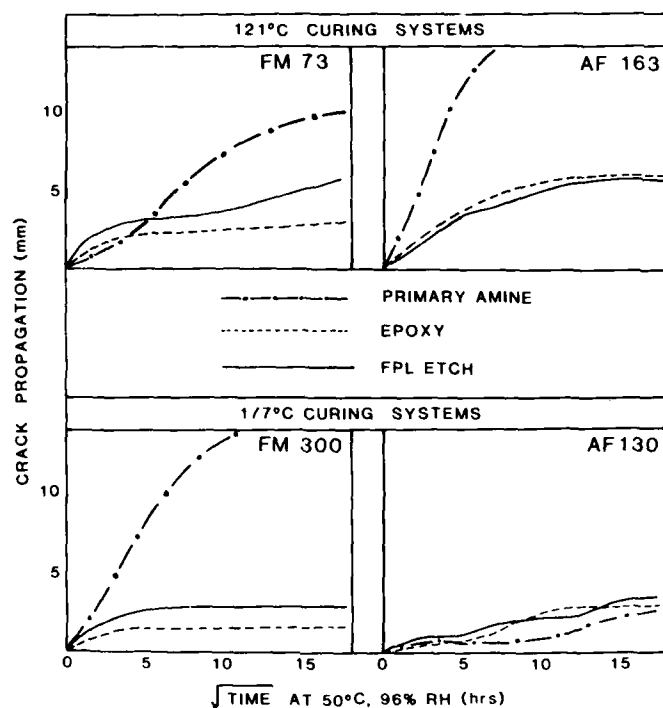


FIGURE 3 Effect of adhesive type on crack propagation—epoxy silane, primary amine silane and FPL etch pretreatments, four adhesives.

primary amine and epoxy silane. A comparison with FPL etched specimens is shown in Figure 3. With each of the four adhesives, the epoxy silane and FPL etch treatments produced good to excellent crack resistance in contrast to the primary amine treatment which was variable.

Further studies with primary amine silane

Drying time FM-300 bonded wedge specimens pretreated with primary amine silane and dried at 110°C for 16 hours under vacuum were compared with joints prepared using the normal drying schedule of 1 hour at 110°C. Only a small improvement in crack propagation resistance occurred after the extended drying period.

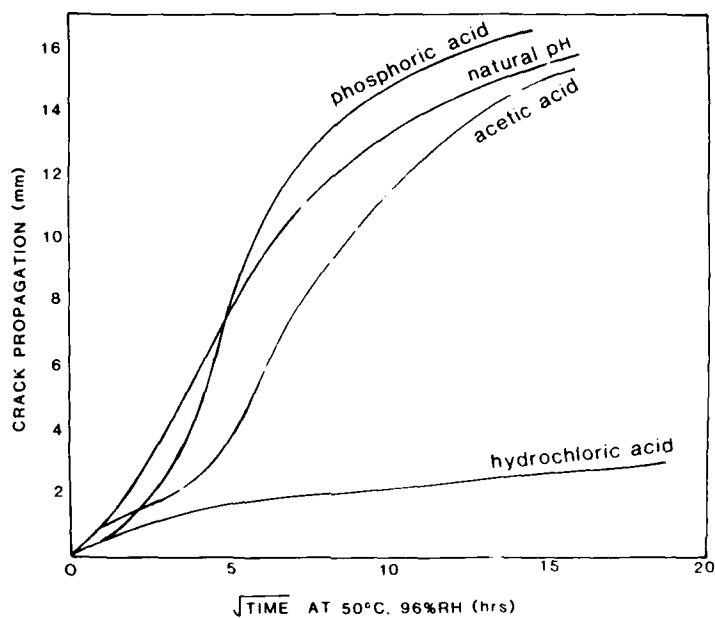


FIGURE 4 Effect of primer pH on crack propagation—primary amine silane adjusted to pH 8 with various acids, FM-300 adhesive.

pH effect Crack propagation rates of FM-300 bonded wedge specimens, pretreated with primary amine silane solutions adjusted to pH 8.0 with 1 M solutions of hydrochloric, phosphoric or acetic acids, were compared with joints prepared using the silane at its natural pH of ~ 10.3 . As seen in Figure 4, the acetic and phosphoric acid modified solutions did not significantly improve the poor performance obtained with joints prepared at the natural pH but, in contrast, specimens obtained from the hydrochloric acid modified solution showed excellent crack resistance.

Hydrochloric acid modification of amino silanes

To assess the general effectiveness of the hydrochloric acid modification on amino silanes, FM-300 and FM-73 bonded wedge specimens were prepared after the following silane surface pretreatments: primary amine adjusted to pH 8, diamine adjusted to pH 8

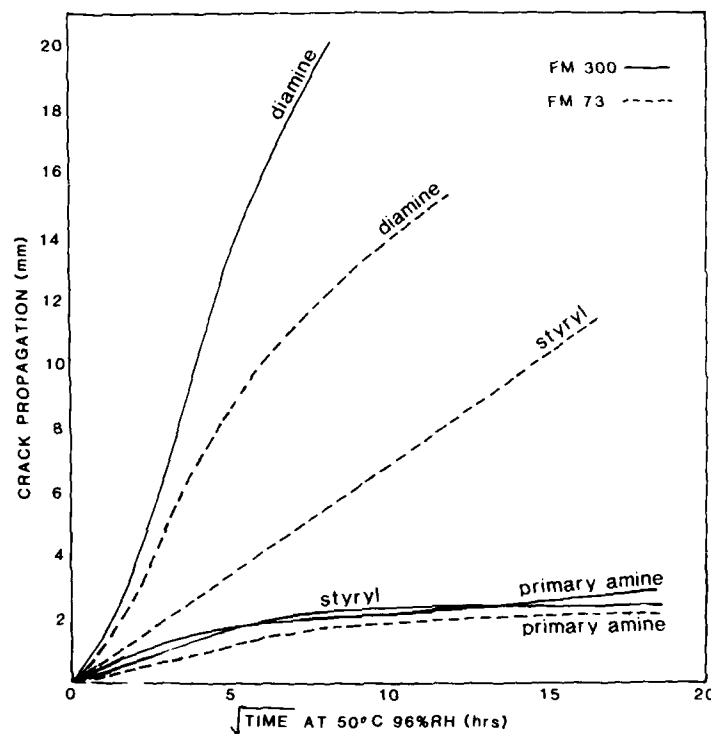


FIGURE 5 Effect of primer pH on crack propagation—primary amine and diamine silanes adjusted to pH 8 with HCl, cationic styryl silane at its natural pH, FM-73 and FM-300 adhesives.

and the cationic styryl (which is supplied as the monohydrochloride). Results, illustrated in Figure 5, indicate that joints primed with the primary amine silane and bonded with FM-73 gave excellent performance. The cationic styryl silane also performed well with FM-300 but was less successful with FM-73. In contrast, diamine silane treated joints showed poor crack resistance, particularly with FM-300.

DISCUSSION

Lap shear measurements on aluminium with the 121°C curing adhesive FM-73 highlighted the differences between a range of

silane primers by showing that at the highest test temperatures only the amine and epoxy functionalities approached the values obtained using the FPL treatment (Table III). Since the strength differences between the silane and FPL treatments were much greater at elevated temperatures, and only the former treatments showed signs of adhesive failure, the possibility that the T_g of the polysiloxane network was a dominating influence was considered. Indeed, the literature has reported a T_g of around 108°C for the amine silane after prolonged drying.¹³ However, joints primed with the epoxy silane and bonded with the 177°C curing adhesive AF-130 when tested at 177°C gave relatively good shear strength, compared with the FPL treatment, and failed cohesively (Table IV).

Durability studies showed a similar trend: in crack propagation experiments with a representative range of pretreatments on wedge test specimens bonded with FM-73, only the epoxy silane primed joints matched the durability exhibited by the FPL etch. Examination of the crack resistance of joints made from AF-163, AF-130 and FM-300 confirmed that treatment with epoxy silane matched the durability of the FPL treatment in all cases.

Since silanes containing an amino functionality should be chemically reactive in epoxy systems, it was felt that their relatively poor performance in terms of durability should be investigated further. Previous work, based on the dry and wet strengths of aluminium lap shear joints primed with primary amine silane and bonded with a simple, two-part epoxy system, showed that durability was a function of silane solution drying conditions¹⁰ and pH⁷. Our study, using the primary amine silane with the 177°C curing adhesive FM-300, has shown that extended drying gives only a small improvement to the poor durability found using normal drying conditions. Experiments using the same system but with the amine silane adjusted to pH 8.0 produced a vast improvement in durability when hydrochloric acid was employed but no such improvement if either phosphoric or acetic acid was used to modify the pH. The reason for this is unclear and is being examined further.

Further experiments designed to investigate the general applicability of the HCl pH adjustment gave mixed results. The modified primary amine silane treatment produced good durability with both FM-73 and FM-300 but no improvement was noted with the diamine silane with either adhesive. The cationic styryl silane,

which contains diamine functionality and is supplied as the monohydrochloride, gave encouraging results without further modification (Fig. 5).

CONCLUSIONS

- 1) The epoxy silane (γ -glycidoxypyriltrimethoxy silane) is versatile as an adhesion promoter for aluminium and confers acceptable lap shear strength and durability on a range of epoxy-based structural film adhesives.
- 2) The remaining neutral silanes evaluated (methacrylate, chloropropyl, vinyl triacetoxo and vinyl trimethoxy functionalities) are less effective.
- 3) The primary amine silane (γ -aminopropyltriethoxy silane) is a good adhesion promoter after treatment with hydrochloric acid. (Manufacture of this product as the hydrochloride, if feasible, might be beneficial).
- 4) The cationic styryl silane {N- β -(N-vinylbenzylamino)-ethyl- γ -aminopropyltrimethoxy silane monohydrochloride} shows considerable promise in the systems examined.
- 5) The diamino silane is not an effective adhesion promoter for epoxy film adhesives.

Acknowledgement

The authors gratefully acknowledge the technical assistance provided by Mr A. W. Camilleri.

References

1. H. W. Eichner and W. E. Scholwaller, Forests Products Lab., Madison, WI, Report No. 1813, 1950.
2. G. S. Kabayaski, and D. J. Donnelly, Boeing Corp., Seattle, WA, Report No. D6-41517, Feb 1974.
3. W. M. Scardino, and J. A. Marceau, *J. Appl. Polym. Sci.: Appl. Poly. Symp.* **32**, 51 (1977).
4. E. F. Pleuddemann, *Silane Coupling Agents* (Plenum Press, New York, 1982).
5. M. Gettings and A. J. Kinloch, *J. Mater. Sci.* **12**, 2511 (1977).
6. S. R. Culler, H. Ishida, and J. L. Koenig, *J. Colloid Interface Sci.* **106** (2), 334 (1985).

7. F. J. Boerio, and J. W. Williams, *Proc. Ann. Conf. Reinf. Plast./Compos., Soc. Plast. Ind.* **36**, Section 2-F (1981).
8. M. E. Schrader, and J. A. Cardamone, *J. Adhesion* **9**, 305 (1978).
9. R. A. Gledhill, and A. J. Kinloch, "Weathering of Plastics and Rubbers", *Conf. Proc., Plastics and Rubber Inst.*, London, 1976, page D12.1.
10. A. Kaul, N. H. Sung, I. J. Chin, and C. S. P. Sung, *Polym. Prep.* **26** (2), 113 (1985).
11. F. J. Boerio, R. G. Dillingham, and A. R. Snow, *Org. Coat. Plast. Chem. Prepr.* **50**, 444 (1984).
12. A. W. Bethune, *SAMPE J* **11** (3), 4 (1975).
13. A. Kaul, N. H. Sung, I. Chin, and C. S. P. Sung, *Polym. Eng. Sci.* **24**, 493 (1984).

SESSION OF ISRAEL

Correlation Between the Total Morphology of an Epoxy System and Some of its Properties†

DOV KATZ and ELI ALON

Department of Materials Engineering, Technion-Israel Institute of Technology, Haifa, Israel

(Received October 3, 1986)

Due to the ever growing use of epoxy resins for structural applications, more information is required about their structure-properties relationship. Much work was done on this subject by us and by others, but many questions still remain unanswered. Some problems which require more detailed studies are the influence of factors like compositional changes in the resin (ratio of prepolymer-curing agent), postcuring and cooling of the polymerized resin from temperatures above T_g to room temperature, on physical properties of the product.

KEY WORDS Amine cure; epoxy resin; mechanical properties; morphology; structure/property correlation; thermal effects.

In order to learn more on these subjects we continued to investigate a model system used by us in some previous studies, namely Epon Resin 826 crosslinked with various amounts of metaphenylene diamine. The experimental work included preparation of suitable specimens, measurement of their glass transition temperatures, analysis of $\log G_{(10)}$ vs. T curves and of DSC thermograms, bending tests at different temperatures and rates of strain and use of scanning electron microscopy in order to study the failure surface structure of the samples fractured by bending. The influence of

† Presented at the Tenth Annual Meeting of The Adhesion Society, Inc., Williamsburg, Virginia, U.S.A., February 22-27, 1987.

accelerated aging (annealing) and of the testing procedure on properties of the polymers was investigated. An attempt was made to correlate the total morphology (chemical and physical structure) of the investigated polymers with some of their properties and the assumption of occurrence of microheterogeneities in the form of supermolecular structures seems to contribute to understanding of this relationship.

INTRODUCTION

The evergrowing use of epoxy resins in structural applications for adhesives and matrices in composites requires more information about the structure-properties relationship. Much work was done in this field, but many questions still remain unanswered. Some of the problems which require further and more detailed study are the influence of compositional changes in the resin (ratio of prepolymer-curing agent) and of the process of post-curing and cooling of the polymerized resin from temperatures above T_g to room temperature, on physical properties of the product. In order to learn more about these subjects which have been recently studied quite extensively,¹⁻⁷ we continued to investigate a model resin system used by us in some previous studies⁸⁻¹⁰ and tried to correlate the total morphology (chemical and physical structure of the polymers) with some of their properties.

EXPERIMENTAL

Materials

The materials used were EPON RESIN 826, mainly diglycidyl ether of bisphenol A (DGEBA), a product of Shell Chemicals Ltd. and metaphenylene diamine (MPDA) cat. 98% pure, made by Fluka A.G. For sample preparation casting molds were made from RTV 630, a product of General Electric. Determination of the thermal expansion and of the torsion moduli of the specimens was performed in silicone oil M 200/200 (produced by BDH) used as heating medium.

Sample preparation

Proper weight ratios of Epon 826 and MPDA were heated to 50–60°C, mixed thoroughly, degassed by pressure lowering to about 10 mm Hg for 10 minutes and cast into preheated RTV molds. The molds contained specimens for torsion modulus *vs.* temperature measurements (2 × 3 × 50 mm) and for determination of linear expansion of the resins (4 × 4 × 50 mm). The samples were cured and postcured in the molds in predetermined conditions of temperature and time and then, after removal from the molds, they were cooled overnight to room temperature by switching off the heating. (The specimens were removed from molds at temperatures above their T_g in order to avoid introduction of stresses because of the larger linear thermal expansion coefficient of the rubbery mold than of the glassy epoxy resin.) All the resin samples were cast in the same conditions, heated for 1 hr at 120°C and postcured for 3 hrs at 172°C. Several resin compositions were investigated but, since the behavior of all of them follows a similar general path, most of the results presented and discussed in this paper refer to these with molar ratios of Epon 826 to MPDA-1:0.69, 1:1, 1:1.44.

Testing apparatus and procedure

The tests included: (A) measurement of linear thermal expansion of the polymers as a function of temperature by use of slightly modified standard equipment;¹¹ (B) differential scanning calorimetry (DSC) by use of a Mettler TA 3000 apparatus; (C) measure-

TABLE I
Composition of investigated specimens

Composition	MPDA phr	Epon 826:MPDA Molar Ratio ^a
A	7.14	1:0.49
B	10.00	1:0.69
C	14.49	1:1
D	20.83	1:1.44
E	25.00	1:1.72

^a Since Epon 826 does not consist of pure DGEBA and its MW is 360–376, the weight ratio Epon 826:MPDA = 6.9:1 was assumed to be stoichiometric.

ment of the 10-sec torsion modulus *vs.* temperature by use of a modified Gehman apparatus;¹² (D) density determination of the polymers at room temperature from sample weight in air and in distilled water containing a small amount of a detergent; (E) three-point bending test of specimens $4 \times 4 \times 25$ mm executed at room temperature, 100 and 150°C in an Instron testing machine at rates of strain: 50 mm/min, 5 mm/min, 0.005 mm/min; (F) scanning electron microscopy, by use of a JEOL apparatus Model JSM 840, of Au/Pd (90/10) vacuum-coated failure surfaces of samples fractured in bending experiments. All numerical data cited as experimental results represent an average of 3–5 experiments.

EXPERIMENTAL RESULTS

(A) Linear thermal expansion

From measurements of linear thermal expansion of the samples heated at a rate of 1°C/min over a large range of temperatures the glass transition temperatures, T_g of the polymers were determined. In order to check the influence of the testing procedure (heating the sample over a wide temperature range for a relatively long time) a second test was performed on the same samples shortly after they cooled down to room temperature from the first experiment. A difference was found in T_g values in the two consecutive determinations and a higher value was obtained in the second run.

(B) Differential scanning calorimetry

DSC measurements were used in order to follow enthalpy changes in the investigated polymers and for determination of their glass transition temperatures. The scans were performed at a rate of heating of 10°C/min. Data obtained for T_g from the first thermogram and from the second scan performed on the same sample after it cooled down to room temperature, are listed in Table II. As in the measurements of linear thermal expansion, the T_g values obtained from the second scan were higher in all cases than the values of T_g derived from the first DSC scan.

TABLE II
Glass transition temperatures of different
Epon 826-MPDA resin compositions

Composition (molar)	T_g^a °C		T_g^b °C	
	I ^c	II ^d	I	II
A	64	84	45	46
B	121	122	104	112
C	169	171	154	163
D	129	127	133	137
E	91	109	121	121

^a From linear thermal expansion; ^b From DSC thermograms; ^c First determination; ^d Second determination.

(C) Torsion Modulus-Temperature Relationship

A typical curve obtained in experiments with the investigated resins is shown in Figure 1 and four characteristic values were marked on the curves: T_g , T_i —inflection temperature at $G_{10} = 10^9$ dynes/cm², T_R —the temperature and G_{10R} the torsion modulus of the beginning of the rubbery plateau region. From values obtained for G_{10R} , the molecular weight of an average network chain was calculated by use

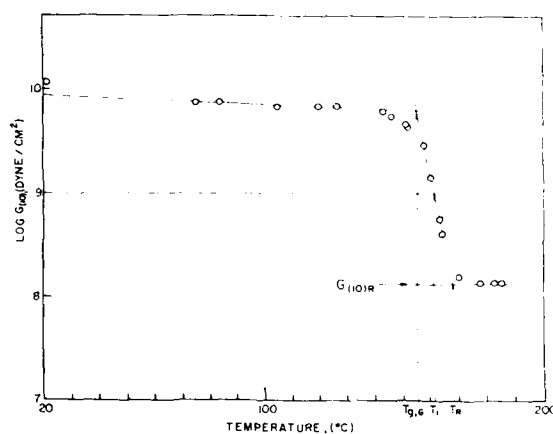


FIGURE 1 10 sec-Torsion modulus vs. temperature curve of an Epon 826-MPDA resin.

TABLE III
Data from strain modulus vs. temperature measurements
of Epon 826-MPDA resins

	Composition, (molar)				
	A	B	C	D	E
T_g , °C I ^a	49	98	165	127	104
II ^b	50	106	166	130	109
T_i , °C I	63	114	171	138	141
II	63	121	173	114	118
T_R , °C I	84	135	178	156	128
II	86	138	182	156	132
G_{10R} I	0.26	0.73	1.38	0.67	0.41
dyne/cm ² × 10 ⁸ II	0.13 ^c	0.78	1.46	0.81	0.42
M_c I	865	412	317	431	579
II	2933 ^c	398	306	394	570

^a I—First determination, ^b II—Second determination on the same specimen. ^c The anomalous results are probably due to the extreme softness of the specimen.

of the equation $M_c = 293 d / \log G - 7$.¹³ Once again, the influence of the experimental procedure was checked—by performing a second test on the same samples shortly after they cooled down to room temperature. The data for T_g , T_i , G_{10R} and T_R are listed in Table III.

(D) Density determination

Data obtained from density measurements of the polymer are presented in Table IV:

TABLE IV
Density of different Epon 826 MPDE resin compositions at
25°C

Composition (molar)	A	B	C	D	E
d , gr/cm ³	1.2164	1.2167	1.2155	1.2194	1.2211

The density of postcured samples decreases with the increasing amount of MPDA from MPDA-deficient molar ratios of the resin, reaches a minimum value for the stoichiometric composition and increases again with further increase in the amount of MPDA.

Mechanical testing

The modulus of elasticity was calculated from results obtained in bending tests of the investigated specimens and the data are listed in Table V.

TABLE V
Modulus of elasticity (in bending) of different Epon
826-MPDA resins compositions, in GPa

Composition (molar)	Rate of strain (mm/min)	Test Temperature °C			
		RT	RT ^a	100	150
A	0.05	3.39			
	5	4.01			
	50	7.61			
B	0.05	3.12	3.03	1.15	0.06
	5	3.45	3.50	2.56	0.04
	50	5.85	4.53	3.96	0.04
C	0.05	2.72	2.90	1.83	0.80
	5	2.78	2.96	2.04	1.03
	50	3.71	5.43	3.60	1.45
D	0.05	2.72	3.06	2.69	0.05
	5	2.85	3.25	2.88	0.04
	50	4.71	5.43	4.45	0.10
E	0.05	3.38			
	5	3.64			
	50	6.43			

^a After annealing at 130°C for 336 hrs.

AGING EXPERIMENTS

Postcured specimens with three resin compositions were annealed at 130°C for different lengths of time and some of their properties were measured. If the measurement involved heating of the

specimen above 130°C, the experiment was repeated shortly after the specimen cooled down to room temperature. The experiments with annealed samples included measurements of their thermal expansion, DSC scans and three-point bending tests performed at room temperature.

DISCUSSION

The highest T_g in the investigated system was obtained for the resin with a stoichiometric Epon 826-MPDA ratio. This result agrees with data obtained in previous works on other epoxy-amine systems.^{2,4,5,7} Since our determinations of T_g were made by several methods, the numerical values are slightly different, but the general picture remains the same. Similarly, values of T_i , T_R and G_{10R} , derived from torsion modulus *vs.* temperature measurements were the highest for the polymer with the stoichiometric ratio of the epoxy and amino compounds. In all cases, a second test performed on the same specimen, after it cooled down from the first experiment, showed an increase in the values of T_g , T_i , T_R and G_{10R} . Such behavior of the investigated polymers can be explained by assuming that additional polymerization (crosslinking) took place in the samples during the heating procedure connected with the previous testing, resulting in nonreversible changes in the chemical network structure. The changes occur in all polymers and it seems that the crosslinking process in all heating conditions applied in this study was not complete. The effect of additional heating was most pronounced in the Epon-rich resins. This is probably due to the fact that the bifunctional prepolymer, when attached by only one end to the MPDA molecules, acquires relatively high mobility at higher temperature, which allows the active epoxy group to come close enough to residual nonreacted amine functions and continue the polymerization. It is also possible that some of the excess epoxy groups react with hydroxyl groups created during earlier opening of the epoxy rings in reaction with MPDA.

The low values of M_c for the stoichiometric resin calculated from G_{10R} (lower than M_c of the prepolymer) is probably due to the presence of entanglements trapped during crosslinking.

Density measurements as well as determination of modulus

values from bending experiments produced results which seem at first rather strange. The density, as well as the modulus, of the polymer with a stoichiometric ratio of components, both measured at room temperature, are the lowest when compared with data obtained for resins from the same series with a deficiency or with an excess of the crosslinking agent. Similar results were obtained by others who referred to them as "odd, unexpected, unusual, peculiarities" *etc.*^{4-7,14-16} Most authors explain this behavior of glassy polymers by assuming that they are in nonequilibrium state below T_g and by consideration of changes occurring in the free volume of the resins. Upon regular cooling or quenching from above T_g to room temperature, the polymers preserve conformations and inter- and intramolecular structure characteristic for their glass transition temperatures. The frozen-in structures, built and kept together to a large extent by secondary forces, are not equilibrium ones at room temperature. The free energy excess and lower entropy in the nonequilibrium state are driving forces in the polymer's tendency to reach equilibrium structures at room temperature, but this process is opposed by secondary forces acting below T_g . These forces are quite considerable in the investigated resin system due to its highly polar character; this approach and the nature of the structures was discussed earlier by one of the authors.^{8-10,17} Polymers with compositions closer to the stoichiometric ratio of reactants have higher glass transition temperatures than those with an epoxy or MPDA excess and, consequently, their equilibrium structures at room temperature are further from those frozen in at T_g . Additional parameters that should be considered are the less-dense crosslinking in "non-stoichiometric" polymers and the plasticizing effect of the reagent in excess, which even if not free in the final product, reacted with only a part of its available functional groups. When a stoichiometric polymer with the highest T_g in the series is cooled from above that temperature, large fluctuational holes are frozen-in at T_g . This leads to a low packing density at room temperature. In non-stoichiometric polymers, the free volume derived from fluctuational holes frozen-in at their T_g is small and products with a larger room temperature density are obtained.¹⁵ In search for additional arguments related to the reason why the modulus of the stoichiometric polymer is the lowest in room temperature, when compared with moduli of non-stoichiometric resins from the same series, some

more facts have to be considered. One of them is the occurrence of residual thermal stresses in the resins, due to their contraction during the process of cooling. These stresses are much smaller in non-stoichiometric polymers (lower T_g , plastification, *etc.*); a method for calculation of those stresses, based upon a thermorheologically complex viscoelastic model with aspects of non-linearity was suggested by Weitsman.¹⁸ Another point for consideration is the nodular structure of the polymer distinguished when SEM and TEM micrographs of the fractured specimens are studied. The resin with a stoichiometric composition in the series contains the smallest and probably also the most dense microheterogeneities chemically linked to the less dense interstitial polymer.¹⁹⁻²¹ These considerations, together with the ones based on the free volume approach, may also contribute to explanation of the fact that, when the glassy polymers are heated, the difference between the modulus values of the nonstoichiometric polymers and the stoichiometric one decreases, see Table V and Ref. 7.

In earlier works reported by others and by us,^{8-10,17,23-32} the presence of micron size heterogeneities, named by Lipatov "macroheterogeneities",²⁷ was observed. These heterogeneities, which are much larger (by up to three orders of magnitude) than the nodular microheterogeneities occurring because of local differences in cross-link density of the polymer, are built up by agglomeration of smaller structures held together mainly by intra- and intermolecular secondary forces and are formed during and after polymerization. The size and the shape of these structures are influenced by many factors and the subject was reviewed earlier.¹⁷ Since it was assumed by some scientists that the fracture behavior of polymers may be associated with the nature of the large supermolecular structures,^{28,30,31} we continued to investigate the subject by studying failure surfaces mainly of the two non-stoichiometric samples B and D (with a deficiency and excess of the crosslinking agent). The samples were fractured by bending at different rates of strain (0.05, 5, 50 mm/min) at room temperature and at 100°C. A few micrographs of failure surfaces of the fractured samples are shown in Figures 2 and 3 and in all cases regions with globular, deformed globular and/or elongated (fibrillar) structures can be seen. The structures are easy to detect in places where deeper crevices appear in the failure surfaces or where secondary cracks,



FIGURE 2 Micrographs of failure surfaces of Epon 826-MPDA samples with molar ratio 1:0.69 fractured by bending: a, b, c—at room temperature; d, e, f—at 100°C. Rates of strain: a, d—0.05; b, e—5 and c, f—50 mm/min.

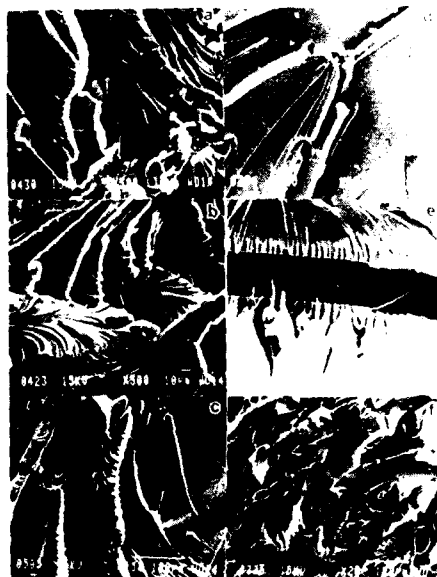


FIGURE 3 Micrographs of failure surfaces of Epon 826-MPDA samples with molar ratio 1:1.44 fractured by bending: a, b, c—at room temperature; d, e, f—at 100°C. Rates of strain: a, d—0.05; b, e—5 and c, f—50 mm/min.

perpendicular to the failure surfaces, occurred. As expected in both compositions, B and D, with the increase in rate of bending strain, an increase in the modulus can be noted. Again as expected, in both compositions with the decrease in rate of strain in samples fractured at 100°C, the failure surface became smoother and less structural details can be detected in SEM micrographs. Comparison of results obtained by investigation of both compositions is rather interesting. T_g of the Epon-rich composition (B) is considerably lower than T_g of the resin with an excess of MPDA and its modulus of elasticity in bending in room temperature is higher at all rates of strain than in samples of the resin D. In bending experiments, executed at different rates of strain at 100°C, the modulus of composition B drops quite considerably, while the drop of modulus values of resin D samples is moderate, similar to the behavior of the resin C with a component ratio of 1:1; this can be explained by the fact that the bending experiments were carried out at a temperature close to T_g of the resin B. SEM micrographs show very clearly, especially in the case of composition B fractured at 100°C, Figure 2d, e, f, the ample presence of globular structures of different sizes built up from smaller globules in the failure surface of specimens bent at a rate of 50 mm/min, a decrease in the amount of globules and occurrence of many fibrillar structures formed by interconnected globules in samples fractured at a rate of 5 mm/min, and almost smooth fibrils present in specimens which failed at a rate of strain of 0.05 mm/min. Also, micrographs of fracture surfaces of samples D with an excess of crosslinking agent, which failed in bending at a rate of 5 mm/min in 100°C, show the presence of fibrils derived from larger globular structures, Figure 3e. In general, the SEM micrographs resemble those obtained and reported earlier, in investigation of the Epon 826-MPDA and Epon 826-DETA resins with the molar ratio of reactants 1:1.^{8-10,17} Those, and previous observations, prove that there is a correlation between the rate of strain and the characteristics of supermolecular structures found in the failure surfaces of specimens fractured at a certain temperature. There is a distinct difference in structure of the fractured surfaces of the two resin compositions, the one with an excess and the other with a deficiency in the amount of crosslinking agent.

In spite of the fact that the whole study is in its initial stages only and it is very difficult to come up with conclusive statements, a few

qualitative remarks supporting previous assumptions¹⁷ can be made. By stressing the polymer specimens, a higher order of organization which depends on the rate of strain, is introduced into the material due to alignment of the existing globular structures, their deformation in the direction of straining and eventually creation of fibrils. Those new structures, which may or may not interact, persist mainly thanks to inter- and intramolecular physical forces acting inside the material. These forces are quite strong in the investigated epoxy system because of its highly polar character. Although the new supermolecular structures are of non-permanent character, (due to internal energy differences between the oriented and nonoriented state), their disintegration into non-oriented, randomly-dispersed globules is opposed by strong inter- and intramolecular secondary bonds and the relaxation times of the new structures may be very long, especially at temperatures far below the T_g of the resin. The stress-oriented structures may change considerably such characteristics of the original material as σ_b , ϵ_b , E , toughness, density, etc., but since the system contains nonequilibrium structures, those characteristics will tend to change with time and with temperature increase in order to reach the values they had before the stress application. This is one of the aspects of physical ageing of the polymer. Further investigation on the correlation between the total morphology of the epoxy system and its properties is taking place.

Accelerated aging in sub- T_g temperatures

Detailed description of experimental results, their analysis and discussion of problems regarding accelerated aging of the Epon 826-MPDA system in sub- T_g temperatures for different lengths of time will be presented separately. In this paper only a part of the results, mainly those related to irreversible changes occurring during the annealing process, are mentioned. A typical picture of the influence of accelerated aging on the investigated polymers, annealed at $T_a = 130^\circ\text{C}$ is shown in Figures 4 and 5. The effect, noticed also by others,^{14,15,32} which is quite pronounced in resins with a deficiency or an excess of MPDA, is much weaker in the stoichiometric polymer, mainly due to the large difference between T_a and the T_g of the stoichiometric polymer. In all cases, in the first measurement of Δl as a function of temperature after annealing, a

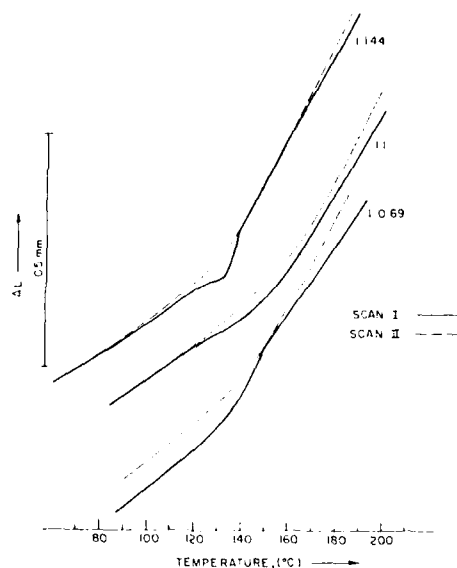


FIGURE 4 Linear thermal expansion *vs.* temperature of Epon 826-MPDA resins annealed for 336 hrs at 130°C.

volume relaxation can be noticed below the T_g of the polymer. However, the second measurement, performed on the same sample, showed that, although the thermoreversible annealing effect disappeared, due to heating of the sample above its T_g in the first experiment, a permanent small increase in the value of T_g occurred.

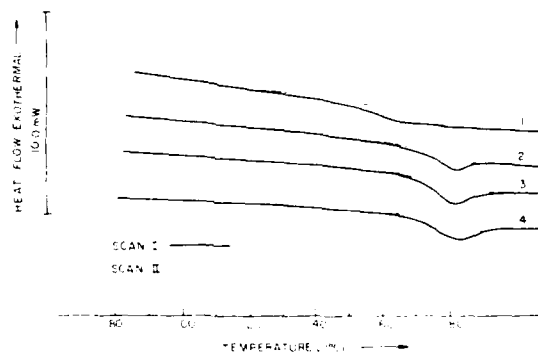


FIGURE 5 DSC thermograms of the stoichiometric Epon 826-MPDA resin: 1—as postcured; 2, 3, 4—annealed at 130°C for 99, 336 and 668 hrs, respectively.

Figure 4. Similar results can be seen in Figure 5, in which enthalpy changes occurring during the accelerated aging of the stoichiometric resin are recorded in the form of DSC scans. Again, heating above T_g in the first measurement erases the thermoreversible physical aging effect, but a small change of permanent character takes place as a result of the experiment and of the length of the annealing period. That permanent change is far less pronounced under the same annealing conditions in the stoichiometric resin, than in those with an excess of one of the components.

Acknowledgements

Support of this work by Technion V.P.R. Fund—Lawrence Deutch Research Fund and by The Fund for the Promotion of Research at the Technion is gratefully acknowledged.

References

1. T. D. Chang, S. H. Carr and J. O. Brittain, *Polym. Eng. Sci.* **22**, 1213 (1982).
2. N. D. Daniele, *J. Polym. Sci., Chem. Ed.* **19**, 2443 (1981).
3. J. B. Enns and J. K. Gillham, *J. Appl. Polym. Sci.* **28**, 2831 (1983).
4. V. B. Gupta *et al.*, 29th National SAMPE Symp., 901 (1984).
5. J. D. Lemay, B. J. Swetlin and F. N. Kelley, *ACS Symp.* **243**, 165 (1984).
6. S. Yamini, R. J. Young, *J. Mater. Sci.* **15**, 1814 (1980).
7. V. B. Gupta, L. T. Drzal, C. Y.-C. Lee and M. J. Rich, *J. Macromol. Sci.-Phys.* **B23** (4-6), 435 (1984-85).
8. D. Katz and A. Buchman, *J. Polym. Sci. Chem. Ed.* **16**, 597 (1978).
9. D. Katz and A. Buchman, *J. Appl. Polym. Sci., Appl. Polym. Symp.* **35**, 49 (1979).
10. A. Buchman and D. Katz, *Polym. Eng. Sci.* **19**, 923 (1979).
11. *ASTM Stand. Ann. Book* **44**, D696-70 (ASTM, Philadelphia, 1979).
12. *ASTM Stand. Ann. Book* **37**, D1053-73 (ASTM, Philadelphia, 1984).
13. L. E. Nielsen, *Mechanical Properties of Polymers and Composites*, 2nd ed., Vol. I (Marcel Dekker, New York, 1974), Chap. 4, p. 177.
14. E. S. W. Kong, *ACS Symp. Series* **243**, 125 (1984).
15. E. F. Oleinik, *Pure and Appl. Chem.* **53**, 1567 (1981).
16. K. Shelby and L. E. Miller, *J. Mater. Sci.* **10**, 12 (1975).
17. D. Katz, in *Polymer NDE*, K. H. G. Ashbee, Ed. (Technomic Publ. Co. Inc., Lancaster-Basel, 1986), pp. 19-30.
18. Y. Weitsman, *J. Appl. Mech.* **46**, 563 (1979).
19. J. Mijovic and J. A. Koutsky, *Polymer* **20**, 1095 (1979).
20. D. Katz and L. T. Drzal, unpublished results (1984).
21. J. Mijovic, J. G. Williams and T. Donnellan, *J. Appl. Polym. Sci.* **30**, 2351 (1985).
22. V. A. Kargin, *J. Polym. Sci.* **30**, 247 (1958).
23. E. H. Erath and R. A. Spurr, *J. Polym. Sci.* **35**, 391 (1959).

24. R. E. Cuthrell, *J. Appl. Polym. Sci.* **12**, 391 (1968).
25. D. Katz and I. G. Zewi, *J. Polym. Sci., Part C, Polym. Symp.* **46**, 139 (1974).
26. D. Katz and O. G. Zewi, *J. Polym. Sci., Chem. Ed.* **13**, 654 (1975).
27. Yu. S. Lipatov, *Pure and Appl. Chem.* **43**, 273 (1975).
28. R. J. Morgan and J. E. O'Neal, *Chemistry and Properties of Crosslinked Polymers* (Academic Press Inc., New York 1977), p. 289.
29. D. Katz and I. G. Zewi, *J. Polym. Sci.* **16**, 597 (1978).
30. P. J. Aspbury and W. C. Wake, *Br. Polym. J.* **11**, 17 (1979).
31. R. A. Gledhill and A. J. Kinloch, *Polym. Eng. Sci.* **19**, 82 (1979).
32. L. C. E. Struik, *Annals of N.Y. Acad. of Sci.* **279**, 78 (1976).

Room Temperature Curing Epoxy Adhesives for Elevated Temperature Service†

H. DODIUK, S. KENIG and I. LIRAN

M.O.D. P.O. Box 2250, Haifa 31021, Israel

(Received July 10, 1986)

Room Temperature curing compositions of epoxy resins with high temperature service capability (95–120°C) were formulated and evaluated. The compositions were based on selected high functionality aromatic epoxy polymers and multicomponent polyamine curing agent systems. Toughening was achieved by addition of a rubbery phase either by prereaction of the epoxy resin with carboxyl terminated (CTBN) or by amine terminated (ATBN) poly butadiene acrylonitrile. The latter elastomeric component served as a part of the polyamine curing agent.

Best results were achieved with an adhesive formulation comprising tetra glycidyl-4-4'-diaminodiphenylmethane (TGDDM) and triglycidyl ether of p-aminophenol with triethylenetetramine and addition of ATBN with a felt carrier.

Lap shear strengths of aluminum/aluminum specimens primed by silane coupling agent in the order of 22 MPa at 25°C and 11 MPa at 120°C with T-Peel strengths of 1.6 N/mm at 25°C and 0.52 N/mm at 120°C, were obtained.

The thermal behaviour and transitions, the chemical and mechanical properties, the microstructure and morphology of the selected adhesive formulation were studied, using DSC, Gehman, FTIR, mechanical testing and SEM analysis, respectively.

Experimental results showed that the selected compositions could develop good high temperature (120°C) properties while cured at room temperature. Furthermore, their high temperature performance compares favorably or even exceeds that of commercially available room-temperature-curing adhesive compounds, and are competitive with elevated temperature cured film adhesives.

KEY WORDS epoxy; mechanical properties; morphology; room temperature curing; rubber toughening; DSC.

† Presented at the Tenth Annual Meeting of The Adhesion Society, Inc., Williamsburg, Virginia, U.S.A., February 22–27, 1987.

INTRODUCTION

High temperature service is a common requirement for adhesives and fiber-reinforced composites, especially for aerospace applications. Epoxy resins with their high strength properties, toughness, corrosion resistance, excellent electrical properties and processing characteristics, have emerged as the most important adhesive and matrix materials for high-performance fiber reinforced structures. However, in order for epoxy to develop its optimal properties at elevated temperatures, heat has to be applied during curing. In most cases the maximum curing temperature has to exceed the expected service temperatures.

Perhaps the most outstanding characteristic of epoxy resins is their versatility,^{1,2} depending upon their physical and chemical nature, the type and amount of the curing agents, fillers and other additives used as well as the curing conditions employed. By proper selection it is possible to obtain cured materials with a wide range of highly-reproducible, tailor-made properties.

Recently the possibility of employing room temperature curing resins with high temperature service characteristics has aroused considerable interest, especially for structural adhesives and fiber-reinforced composites. Room-temperature-curing resin systems could lower manufacturing cost of the composites and adhesives and simplify their processing, especially under field repair conditions.

The formulation of room-temperature-curing epoxy with high temperature service capability has been attempted by a number of approaches using specific types of polyfunctional epoxies and various curing agents comprising modified highly functional amines and aromatic dianhydrides.^{3,4}

The primary objective of the present study has been aimed at developing a two-part paste adhesive for field repair that can be cured at ambient temperature with final properties equivalent to high-temperature-cured epoxy film adhesives.

Elevated-temperature-curing adhesive formulations and synthesis of new polymers for field repair of damaged structures was not within the scope of this study, although there were some successful efforts in these directions during the last years.⁵⁻¹³

In the course of the present investigation an extensive screening of commercially available epoxy resins and curing agents has been

carried out and, consequently, a few multi-component room temperature curing epoxy compositions were developed. The selected formulations exhibited remarkably high service temperature capabilities. Results obtained were evaluated and compared to various commercially available structural adhesives.

EXPERIMENTAL

Materials and processes

The compounds used in this work are listed in Table I. In all cases the adhesive comprised a multi-component formulation. Two principal cases were studied.

In the first case, one part of the composition was the product of a carboxyl-terminated liquid rubber prereacted with a blend of two epoxy resins. In this way linear epoxy rubber chains were obtained. The second part of the adhesive was an amine curing agent (Procedure A).

In the second case, one part was a blend of two epoxy resins and the second part included the amine curing agent which was partially composed of an amine terminated reactive liquid rubber (Procedure B). Details are given in the next section and the list of the adhesive formulations are given in Tables II and III.

Adhesives compositions were first characterized by determining their shear and peel properties. Testing specimens were prepared from aluminum (A1-2024-T351) that has been chromic acid anodized without sealing in accordance with MIL-A-8625, Type I, Class I. Before the application of adhesive, the substrates were vapor degreased in a TF-35 solution (manufactured by DuPont) for 5-10 minutes. Silane Primer (2% A-187 in 80/20 V/V ethanol-water) was applied by dipping and allowed to dry for $\frac{1}{2}$ hour at R.T. and 1 hour at 100°C. The adhesive was applied by brushing. When a felt carrier was used, it was impregnated with the adhesive, evacuated for 5 minutes at 5 mm/Hg (absolute pressure) and excess resin was squeezed out. The felt used was FIBERMAT IC-650 (3M, U.S.A.).

The test specimens were permitted to cure at ambient temperature for 6 days, prior to testing. The 95°C and 120°C test data are reported after 10 min soak at testing temperature. In order to

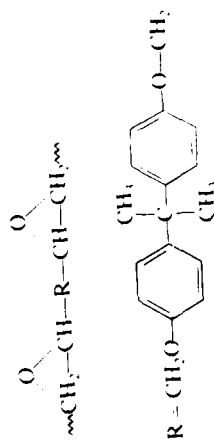
TABLE I
Chemical formula

Materials	Chemical formula	Trademark
Epoxy Resin EE* = 183 gr/eq		EPN138 CIBA GEIGY
Epoxy Resin EE = 128 gr/eq	<p style="text-align: center;">$R = \text{CH}_2-\text{CH}(\text{O})-\text{CH}_2$</p>	MY720 CIBA GEIGY
Epoxy Resin EE = 107 gr/eq	<p style="text-align: center;">$R = \text{CH}_2-\text{CH}(\text{O})-\text{CH}_2$</p>	ERL510 CIBA GEIGY

RT CURING EPOXY ADHESIVES

343

EPON828
Miller
Stephenson
Chem. Co



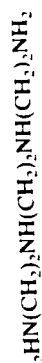
Epoxy Resin
EE = 190 ± 20 gr/eq

ER0163
CIBA GEIGY

Tetra functional,
unknown chemical formula.

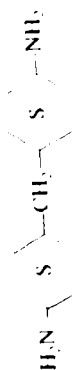
Epoxy Resin
EE = 200 ± 260 gr/eq

TETA
Miller
Stephenson
Chem. Co.



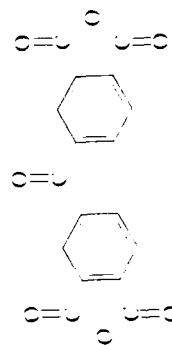
Curing Agent
AE^b = 40 ± 3 gr/eq

PACM20
DuPont



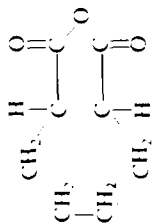
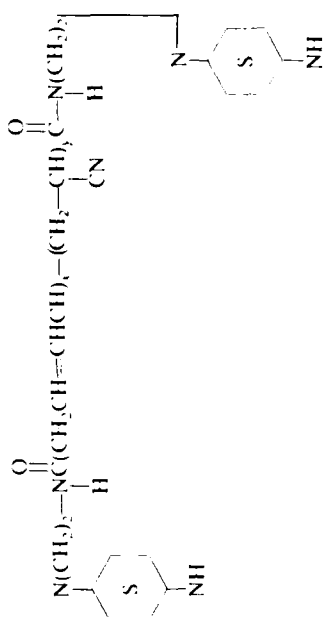
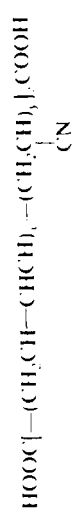
Curing Agent
AE = 111 gr/eq

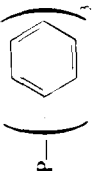
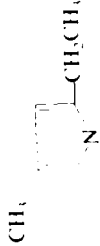
BTDA
Gulf
Advanced
Materials



Curing Agent

TABLE I (continued)

Materials	Chemical formula	Trademark
Curing Agent		HHPA Miller Stephenson Chem. Co.
Rubber ATBN		Hycar ATBN 1300 x 16
AE - 1160 gr/cq		BF GOODRICH Chem. Co.
Rubber CTBN		Hycar CTBN 1300 x 8
COOH No. = 2000 ± 150	$\alpha = 5, \gamma = 1, \delta = 10$	BF GOODRICH Chem. Co.

Catalyst		T.P.P. (Tri Phenyl Phosphine) Aldrich
Curing Agent		EMI (2-Ethyl- 4-Methyl- Imidazole) Aldrich
Primer	Unknown	EA9203 HYSOL Division
Coupling Agent	$\text{HNCH}_2\text{CH}_2\text{CH}_2\text{Si}(\text{OCH}_2)_3$	A-187 UNION CARBIDE
γ -Glycidoxypropyl-trimehtoxy-silane		

^a EE - Epoxy Equivalent.
^b AE - Amine Equivalent.

TABLE II
Lap shear strengths of room temperature curing high functionality epoxy resin systems

Epoxy resin formulation	Lap shear strength, ^b MPa.	
	25°C	120°C
1. Epoxy Resin 0163/EPON828/TETA 60/40/18	7.2 ± 1 ^a	inconvenient
2. EPN 1138/EPON828/TETA 60/40/13	8.8 ± 2.5 ^a	10.9 ± 0.5 ^a
3. MY 720/EPON828/TETA 60/40/16.4	9.6 ± 4.9 ^a	9.6 ± 0.3 ^a
4. ERL510/EPON 828/TETA 72/40/12	9.3 ± 1.5 ^a	2.2 ± 0.2 ^a
5. ERL510/HHPA/BTDA 49/29/20	2.6 ± 0.6 ^a	9.6 ± 1.4 ^a
6. MY720/ERL510/PACM20 50/40/45	5.4 ± 0.4 ^a	15.6 ± 1.4 ^a
7. MY720/ERL510/HHPA/BTDA 50/40/53/36	9.9 ± 0.8 ^a	14.6 ± 1.4 ^a
8. MY720/ERL510/TETA 50/40/20	14.7 ± 1.6 ^a	10.2 ± 4.8 ^a

^a Adhesive failure.

^b Average of 5 test specimens ± standard deviation.

evaluate the influence of soaking at testing temperature on the shear strength, tests were conducted after 2 minutes, 5 minutes and 10 minutes at 120°C. It should be noted that the test specimen reached the 120°C after 2 minutes soaking at that temperature. Results (shown in Table III, footnote e) indicated that the shear strength did not change markedly during the soaking period. Similar behaviour was found for the other formulations, within the experimental error.

Sample preparation

Epoxy and CTBN prepolymers were prereacted to ensure the formation of an epoxy rubber intermediate. The mechanisms of this

TABLE III
Lap shear and T-Peel strengths of high functional room temperature curing epoxy compositions formulated in the present study, and selected commercial adhesives

Adhesive composition	Adhesive type	Manufac-turer	Lap shear strength (MPa) ^(b)				T-Peel Strength (N/mm) ^(b)		
			25°C	85-95°C	120°C	25°C	95°C	120°C	
9. MY720/ERL510/TETA/CTBN ^(d) 50/40/20/14.9	R. T. Cure Epoxy	M.O.D.	22 ± 3.5 ^a	—	8.5 ± 1.4 ^a	0.29 ^a	—	0.5 ^a	
10. MY720/ERL510/TETA/CTBN/ EMI ^(d) 50/40/20/14.9/4	R. T. Cure Epoxy	M.O.D.	28.3 ± 5.9 ^a	—	11.7 ± 0.9 ^a	—	—	—	
11. MY720/ERL510/TETA/ATBN 50/40/18.6/36	R. T. Cure Epoxy	M.O.D.	23.0 ± 2.3 ^a	16.2 ± 3.2 ^a	9.3 ± 0.9 ^a	1.1 ± 0.1 ^a	0.2 ± 0.03 ^a	0.2 ± 0.02 ^a	
12. MY720/ERL510/TETA/ATBN/EMI 50/40/18.6/36/4	R. T. Cure Epoxy	M.O.D.	27.3 ± 3.5 ^a	15.8 ± 1.5 ^a	15.0 ± 1.7 ^a	0.30 ± 0.03 ^a	0.19 ± 0.03 ^a	0.12 ± 0.02 ^a	
13. MY720/ERL510/TETA/ATBN + felt 50/40/18.6/36	R. T. Cure Epoxy	M.O.D.	21.5 ± 1.2 ^a	—	10.6 ± 1.2 ^{a,c}	1.6 ± 0.09 ^a	—	0.52 ± 0.05 ^a	
14. EA9321	R. T. Cure Epoxy	HYSOL	29.4 ± 0.98 ^a	7.6 ± 0.49 ^a	2.94 ± 0.69 ^a	0.5 ± 0.1 ^a	0.3 ± 0.03 ^a	0.12 ± 0.03 ^a	
15. EA9309	R. T. Cure Epoxy	HYSOL	24.5 ± 0.9 ^a	3.0 ± 0.7 ^a	2.5 ± 0.3 ^a	5.3 ± 0.6 ^a	0.3 ± 0.1 ^a	0.07 ± 0.02 ^a	
16. EA9330	R. T. Cure Epoxy	HYSOL	22.1 ± 1.2 ^a	3.9 ± 0.3 ^a	2.5 ± 0.2 ^a	3.6 ± 0.5 ^a	0.12 ± 0.04 ^a	0.05 ± 0.01 ^a	
17. FM300K	177°C/35 psi Cure Epoxy	American Cyanamid	27.9 ± 1.9 ^a	—	19.6 ± 2 ^a	1.4 ± 1.5 ^a	—	—	
18. Versilok 204/Ac4	RT Cure Acrylic	Hughson	24.2 ± 2.7 ^a	—	—	—	—	—	

^a Adhesive failure.

^b Average of 5 test specimens ± standard deviation.

^c Cohesive failure

^d Without primer 187

^e After 2 minutes soaking at 120°C—8.1 ± 1.1 MPa.

After 5 minutes soaking at 120°C—9.0 ± 0.9 MPa.

After 10 minutes soaking at 120°C—9.4 ± 0.6 MPa.

reaction has been discussed by Siebert and Riew.¹⁵ The epoxy-rubber prepolymer was prepared at 150°C, with mechanical stirring under nitrogen flow, using triphenyl phosphite (0.15 percent) as catalyst. The reaction advancement was monitored by titration of the carboxyl groups with 0.1 N KOH/ETOH. Reaction continued to 1 percent of the initial EPHR. Following preparation, the intermediate prepolymer was stored at 0°C and used in appropriate amount as described in Procedure A (see below).

Since ATBN reacts directly with the epoxy end groups (it was used as one of the curing agents¹⁶), it was added directly to the epoxy as described in Procedure B (see below).

Two typical formulations (Tables II and III), were prepared as described by the following procedures:

Procedure A: MY720/ERL510/TETA/CTBN (50/40/20/3.3).

10 grams of prereacted mixture of MY720/ERL510/CTBN (95/76/72 W/W) was added to 41.2 grams of MY720 and 33.0 grams of ERL510 and was mixed to a homogeneous mixture which contained 3.7% CTBN (epoxy resin basis). Then, 18 grams of the TETA curing agent was mixed with the combination of the epoxy resins. This formulation has a low enough viscosity to be easily mixed and applied.

Procedure B: MY720/ERL510/TETA/ATBN (50/40/19.3/13.5).

To a resin mixture of 50 grams MY720 and 40 grams of ERL510, a curing agent mixture of 19.3 grams of TETA and 13.5 grams of ATBN was added. This formulation (which contains 15% ATBN on the epoxy resin basis) was mixed to a homogeneous mixture.

In some cases, preheating of some components was needed to lower their viscosity and promote mixing.

Testing techniques

Tensile lap shear specimens (L.S.S) were prepared according to ASTM D1002-72. T-Peel specimens were prepared according to ASTM D1867. Five specimens were fabricated for each test by compression, using a special mold. Bondline thickness for all specimens was 0.10 ± 0.03 mm. Mechanical properties were determined using a 10-ton Instron machine—crosshead speed 2 mm/

min (L.S.S.) and 200 mm/min (T-peel) at 25°C, 95°C and 120°C. The mode of failure (adhesive or cohesive) was evaluated by visual inspection.

The selected compositions were characterized in bulk using tensile samples that were cut from cast specimens and loaded at an extension rate of 5 mm/min. In this way, Young's modulus and maximum stress and strain to failure were obtained.

Densities of the cast cured epoxy specimens were measured at ambient temperature, according to ASTM D3800-79.

Specific heats and extent of cure were determined using a 910 DSC unit of DuPont 1090 Thermal Analyzer at a heating rate of 10°C/min. The T_g was determined from the plot of 10-sec flexural modulus *versus* temperature, using a modified Gehman apparatus according to ASTM D1043-58 (rate of heating 1°C/min).

Infrared spectra of the aluminum adherend surfaces after fracture were obtained in a FTIR Nicolet 5DX. The External Specular Reflectance mode was used. In addition, it was equipped with a horizontal stage in a near-to-normal incidence, with gold mirror for reference.

SEM/EDAX analysis of fracture surfaces was obtained using a Jeol SEM, Model JSM-840, equipped with an energy dispersive analyzer link model 290. Prior to observation, the specimens were sputter-coated with a thin layer (~20 nm) of platinum to obtain a conductive surface and reduce charging.

RESULTS AND DISCUSSION

Methodology

The special combination of room-temperature curing with elevated-temperature service performance places a few restrictions on the potential use of certain constituents and calls for special considerations.

The primary demand for high temperature preformance and thermal stability dictates that the selected epoxy resins should be capable of creating a high cross-linking density. This, in turn, limits one to the use of polyfunctional epoxy resins and curing agents.

Preferably, all of the components should consist of aromatic rings for enhanced thermal stability.

The use of polyfunctional epoxy resins with high aromaticity results in brittle solids with low toughness. To remedy this consequence, reactive elastomers and a thermoplastic carrier have to be incorporated in the formulation, preferably without sacrifice of the high temperature performance.

The other most important requirement of room temperature curing capability demands the use of reactive room temperature curing agents and low viscosity resins and other components.

In this study another restriction was imposed, namely, all resins, curing agents and additives should be commercially available. On the basis of these considerations all of the materials used in the present study were selected.

Optimization of adhesive compositions

As previously described, the basic approach in the present study was the use of high functionality and high aromaticity epoxy resins and hardeners to yield a high level of cross-linking and consequently improved stability.

The selected epoxy resins, as described in Table I, were:

- MY720—This resin is a tetra functional epoxy with high aromaticity.
- ERL510—A very low viscosity trifunctional epoxy. It was added to MY720 to reduce its viscosity and to allow easy mixing.
- EPON828—A general purpose difunctional epoxy.
- EPN1138 and ER0163—Are high functionality epoxies. However, they are less convenient since they are solids at RT.

In this investigation, two curing agent types were used. One initiated reaction at a moderate temperature, the other provided high temperature stability.

High functionality aromatic amine curing agents have been selected as they have high reactivity and introduce good thermal stability.⁵ PACM-20 has been selected because it has fast cure times with epoxy resins and gives products with good thermal stability.^{10,11} Being a low viscosity liquid, it could be readily mixed with the resin.

BTDA and HHPA are tetrafunctional anhydrides which result in products with good thermal stability.³ A list of the evaluated formulations is presented in Tables II and III.

Table II summarizes the initial lap shear results at both ambient and elevated temperature (120°C). Results indicated that high functionality epoxy resins such as EPN1138/EPON828, MY720/EPON828 and MY720/ERL510 can be incorporated with a curing agent such as TETA to produce room-temperature-curing compositions having a respectable high temperature shear strength. More specifically, formulations 2, 5, 6, 7 of Table II were not completely cured at room temperature during 7 days, as shown by the bond strength enhancement at 120°C. Lap shear strengths values of formulations 1 and 4 (Table II) decreased markedly at 120°C. However, those of formulations 3 and 8 are particularly interesting with regard to both the initial and 120°C values obtained, with some advantage of formulation 8 at 25°C. Consequently, at that stage, the high functionality epoxy resin with the TETA curing agent was selected for further investigation. However, as expected, it was brittle and its T-Peel strength was very low (~ 0.12 N/mm), as shown in Figure 1.

In the next step, the fracture toughness as manifested by the peel strength had to be improved in order to engineer an adhesive which not only would possess high shear strength but also substantial resistance to peel stresses.

Extensive work has been carried out and reported on the mechanical properties of rubber-modified epoxy resins, usually heat cure formulations. It has been shown that a substantial increase in fracture toughness can be achieved by using carboxyl terminated acrylonitrile-co-butadiene rubbers (CTBN).¹⁴⁻²⁷ Furthermore, it has been shown that similar results can be obtained with amine-terminated rubbers (ATBN).^{16,27}

Figure 1 demonstrates the effect of ATBN and CTBN content on the shear and peel strengths in the various epoxy formulations. As shown, T-Peel strength at 25°C increases with increasing rubber content until some optimal limit is obtained ($\sim 40\%$ ATBN and $\sim 12\%$ CTBN). Moreover, at higher temperatures (95°C, 120°C) the general behaviour is different for ATBN and CTBN. Generally, lap shear strength decreases while T-Peel increases for CTBN-containing formulations, while for ATBN both shear and peel strengths decrease. It is evident from Figure 1 that the ATBN

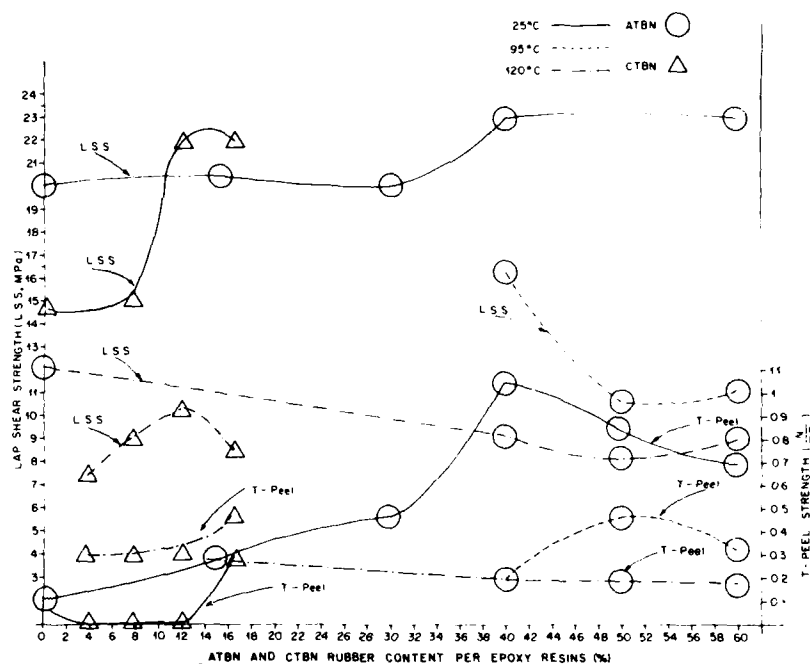


FIGURE 1 Lap shear and T-Peel strengths as a function of ATBN and CTBN rubber concentration in epoxy (%).

formulations exhibit somewhat higher elongation than the CTBN ones. These property differences may be attributed to a greater degree of chemical bonding between the ATBN and epoxy compared to CTBN and the epoxy. At 40% ATBN, the material exhibits the best combination of shear and T-Peel strengths. Moreover, epoxy resin systems, toughened by ATBN that serves also as a curing agent, demonstrate good adhesive strength at elevated temperatures.

Thorough experimental work¹² has confirmed that the presence of imidazole species in the curing agent could substantially enhance the high temperature performance of epoxy resin compositions while ATBN could contribute to toughness. Data are shown in Table III that substantiate the effect of imidazole addition to these epoxy resin systems. Results indicate that the inclusion of the 2-ethyl-4-methyl imidazole has enhanced the 120°C lap shear

performance but has degraded the T-Peel performance. Though the role of imidazole as an effective curing agent for epoxy has long been recognized,¹² the beneficial effects of such a compound as shown in this investigation are not fully understood. Hence, formulation 11 (without imidazole) was selected for further investigation, as an adhesive.

To improve the durability of aluminum-epoxy and avoid interfacial failure, a silane coupling agent was used. As can be seen in Figure 2, the coupling agent has caused a dramatic change in the failure mode which becomes cohesive. To study the environmental durability of the selected epoxy formulation, a number of specimens were exposed to a combination of heat and humidity (50°C/95% RH) for 15 days and their shear and T-Peel strengths were measured. As depicted in Figure 2, significant improvement in bond strength has been achieved. In both cases, (with and without the

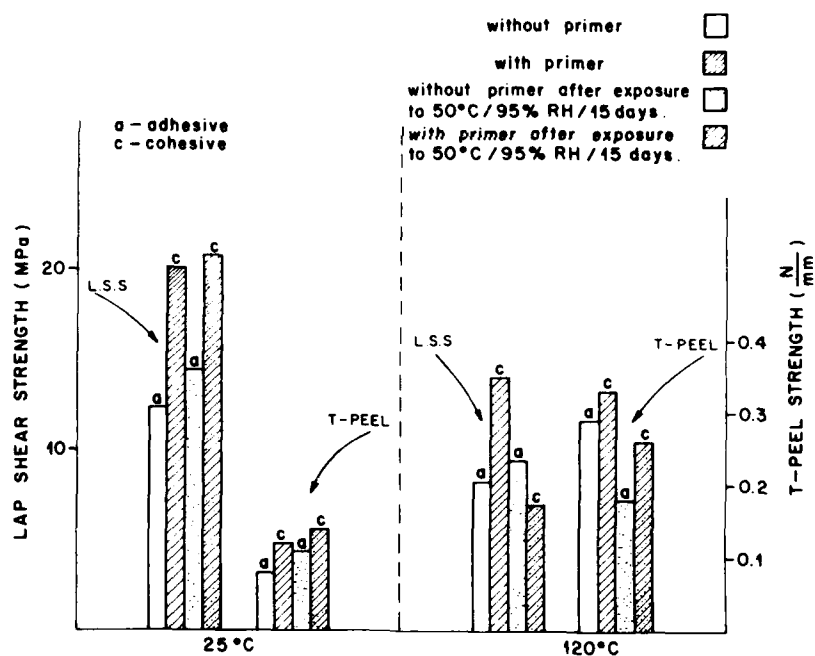


FIGURE 2 The effect of primer on the lap shear and T-Peel strengths of the MY720/ERL510/TETA/CTBN (50/40/20/10.8) formulation in ambient and 50°C/95% RH/15 days conditions.

silane primer) bond strength slightly increased after exposure to humidity and heat at 25°C, while at 120°C a pronounced reduction was observed. These results indicate that at elevated temperature the adhesive joint is more sensitive to environmental conditions as the effect of water/humidity is accelerated.

In the last phase of the investigation, the effect of a carrier on the toughness and bond line thickness was studied. Generally, shear and T-Peel strengths showed an improvement of 10 to 50% (Table III). It seemed that the addition of the thermoplastic carrier had increased the toughness and the resistance to crack propagation. Figure 3 shows the failure surfaces of the T-Peel specimen. The mode of failure is cohesive and both surfaces are covered completely with the adhesive and felt.

The results obtained in this study are impressive when compared to typical commercially available room-temperature-curing adhesive systems. Table III compares the lap shear and T-Peel strength properties, at various temperatures, of a number of such commercial structural adhesives with the present room-temperature-curing resin systems. The commercial adhesives included epoxy and acrylic types. For information purposes, lap shear and T-Peel strengths of a commercial structural autoclave curing adhesive are also shown. The five compositions (9-13) exhibited superior properties, especially at 120°C. Formulation 13 demonstrated the best combination of properties compared to the various room-temperature-cured commercial adhesives, but somewhat inferior to FM-300K.



FIGURE 3 Failure surfaces of formulation 13 including carrier.

The improved performance of these high functionality epoxy resin compositions at elevated temperature, *e.g.*, 120°C, should be regarded as most noteworthy and certainly promising for further development and optimization.

Adhesive characterization

Following the adhesive compositional optimization, formulation 13 was further characterized and evaluated as to its thermal properties and transitions, chemical structure, mechanical behavior and microstructure.

(1) *Thermal behavior and transitions* DSC (Differential Scanning Calorimetry) was used to determine the degree of cure, curing temperature, and exotherm of the partially cured polymers. Figure 4 depicts the first and second run thermograms of the cured epoxy resin. The first run, (a), shows that the resin system has a peak cure exotherm at 90–100°C, indicating that curing is not complete after 6

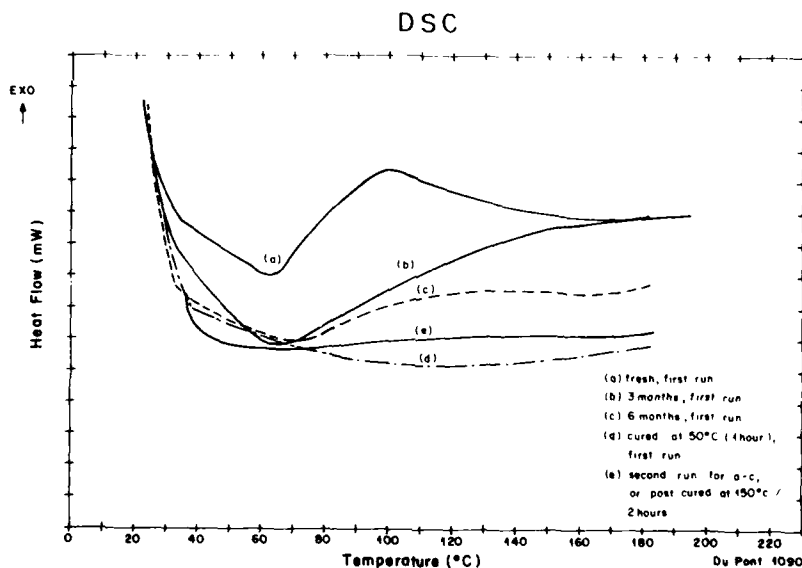


FIGURE 4 DSC scans of MY720/ERL510/TETA/ATBN (50/40/18.6/36) formulation, cured at various conditions.

days at ambient temperature. It can be seen that after 3 and 6 months at ambient temperature, the curing process continues, and the exotherm decreases (Figure 4, b,c). When cured at 50°C for 1 hour (Figure 4, d) or post cured at 150°C/2 hr, (e), no exotherm was observed, which indicates in turn that curing has been completed. The second runs (e) confirm that the epoxy matrix is in a fully-cured state following the first heat treatment of the first run.

Based on the above DSC results, it is evident that even if curing is incomplete after 6 days at RT, it could be completed either by 50°C/1-hour curing or after longer periods of time at RT. Furthermore, as can be concluded from the ambient temperature and moderate temperature (50°C) cure, the selected formulation is highly reactive. Hence, the thermal history that the adhesive is exposed to during thermal characterization changes its degree of cure and consequently the glass transition temperature.

Determination of the glass transition temperature was carried out by means of a modified Gehman apparatus. As can be seen in Figure 5, typical curves of $\log G(10)$ vs. T indicated that the T_g is

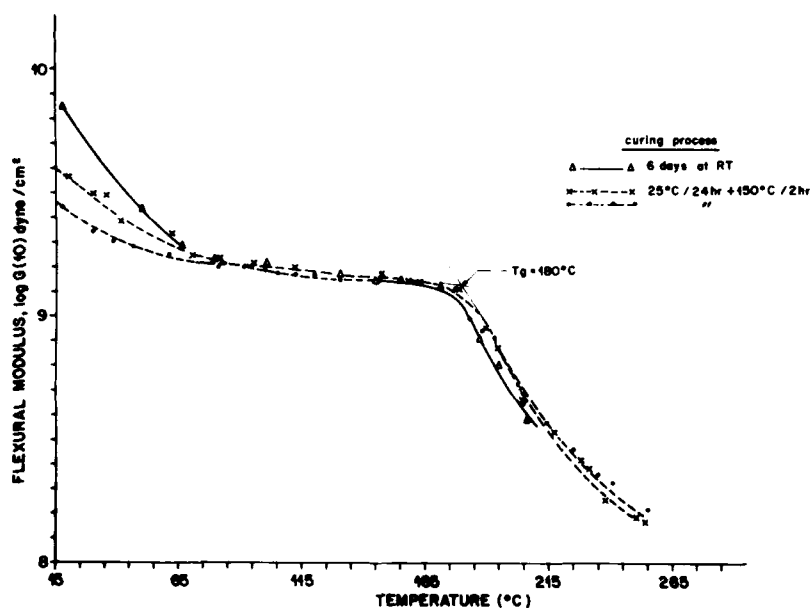


FIGURE 5 Log $G(10)$ vs. Temperature for MY720/ERL510/TETA/ATBN (50/40/18.6/36) formulation, cured at various conditions.

close to 180°C for both samples; *i.e.*, cured 6 days at ambient temperature, and postcured for 2 hours at 150°C. The flexural modulus at low temperatures (15–35°C) was surprisingly higher by 25% for the RT-cured epoxy formulation compared to the elevated temperature (150°C/2 hr) cured resin. Similar results were observed when tensile properties of bulk specimens were determined, as will be discussed in the following section. It should be emphasized that the selected adhesive formulation exhibited a relatively high T_g compared to other epoxy adhesives, especially to those cured at low and medium curing temperatures (25–60°C).

(2) *Chemical structure.* FTIR (Fourier Transform Infra-Red) was used to monitor the rate at which reactive molecular species such as epoxide group disappear during cure.²¹ Figure 6 shows, for example, the fracture surface FTIR spectrum of the selected epoxy formulation. The spectrum does not have a noticeable epoxide band (at 906 cm^{-1}) which indicates that curing is almost complete. In addition to hydroxyl and ether bands in the region of 3400 cm^{-1} and

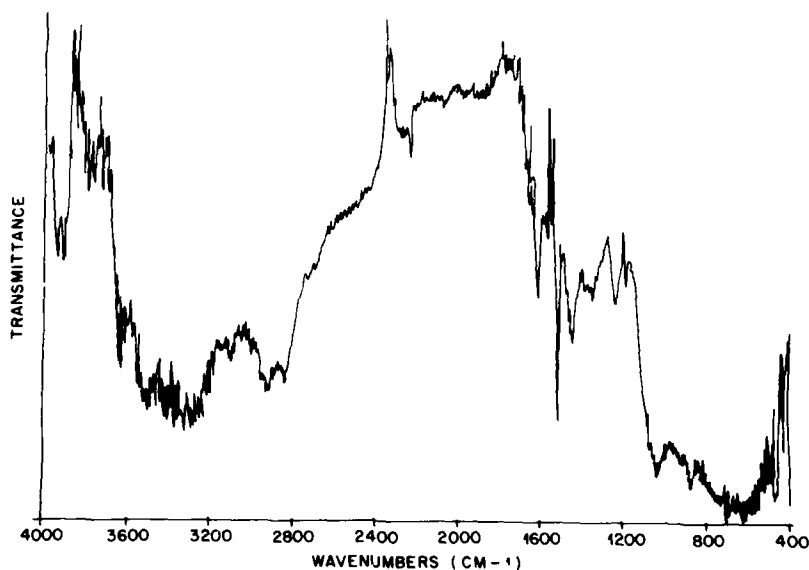


FIGURE 6 FTIR spectrum of Al/Al fracture surface of specimens bonded with MY720/ERL510/TETA/ATBN (50/40/18.6/36) formulation.

at 1040 cm^{-1} respectively, phenyl bands at 830, 1187, 1238, 1363, 1448 and 1517 cm^{-1} are present and remain constant regardless of epoxide reactions. The absorption at $2235\text{--}2242\text{ cm}^{-1}$ is due to the presence of ATBN's cyano-functional group.

(3) *Mechanical behaviour* The high functionality resin systems look promising as adhesives that cure at ambient temperatures. The degree of curing of this formulation at RT was verified by lap shear and bulk testing. As can be seen in Table IV, lap shear and T-Peel strengths were not improved after post-cure at 150°C for 2 hours.

Mechanical properties of the bulk adhesive showed significant differences under various cure conditions, as shown in Table IV, Figure 5 and Figure 7. In general, it could be observed that the epoxy formulation showed highest mechanical properties and lower density following cure at 25°C for 6 days. The mechanical properties obtained after post-cure at 150°C or two months at ambient temperature were similar to RT cure but had higher density.

TABLE IV
Effect of cure conditions on mechanical properties of epoxy formulation
(MY720/ERL510/TETA/ATBN, 50/40/18.6/36)

Mechanical property	Curing process		
	25°C/24 hr + 150°C/2 hr	25°C 6 days	25°C 2 months
$\rho(\text{g/ml})$ Density	1.1507 ± 0.0007	1.1441 ± 0.0020	—
σ_B (MPa) Stress at break	17.5 ± 1.9	30.5 ± 3.9	18.1 ± 3.5
Σ_B (%) Strain at break	1.21 ± 0.1	1.80 ± 0.2	0.83 ± 0.2
E (MPa) Young's Modulus	1631 ± 48	1792 ± 98	1551 ± 1.25
Lap Shear Strength (MPa)	$14.7 \pm 0.8^{(c)}$	$20.1 \pm 2.8^{(c)}$	—
T-Peel Strength $\left(\frac{\text{N}}{\text{mm}}\right)$	$0.21 \pm 0.02^{(c)}$	$0.22 \pm 0.04^{(c)}$	—

^(c) Cohesive failure.

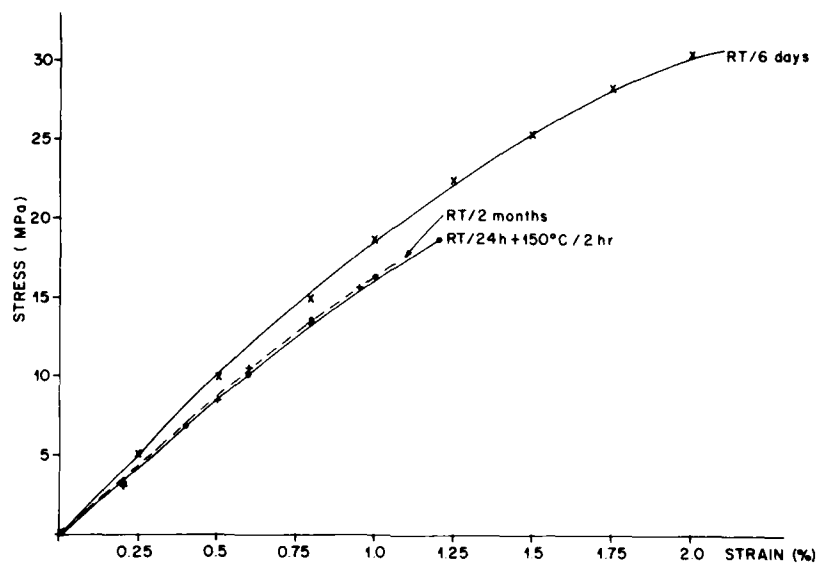


FIGURE 7 Stress-strain plot of MY720/ERL510/TETA/ATBN composition following various curing procedures.

Curing conditions are expected to influence the mechanical properties such as Young's modulus, stress and strain at break and density. However, the direction of the changes were unexpected.²⁸ It seems that the additional post-curing or ambient-temperature-curing for longer periods (two months) does not improve and even reduces the bulk and the adhesive mechanical properties.

The effect of curing conditions on the mechanical properties and densities of epoxy resins were studied by Gillman *et al.*^{17b} The results of this latter investigation do not agree with the present ones. While Gillham^{17b} reported high Young's modulus accompanied by high density at low temperature curing, the present investigation indicated that ambient temperature cure resulted in lower densities and higher moduli compared to elevated temperature cure.

(4) *Microstructure and Morphology.* SEM (Scanning Electron Microscope) micrographs of fracture surfaces from specimens cured at ambient temperature for 6 days are given in Figure 8. The

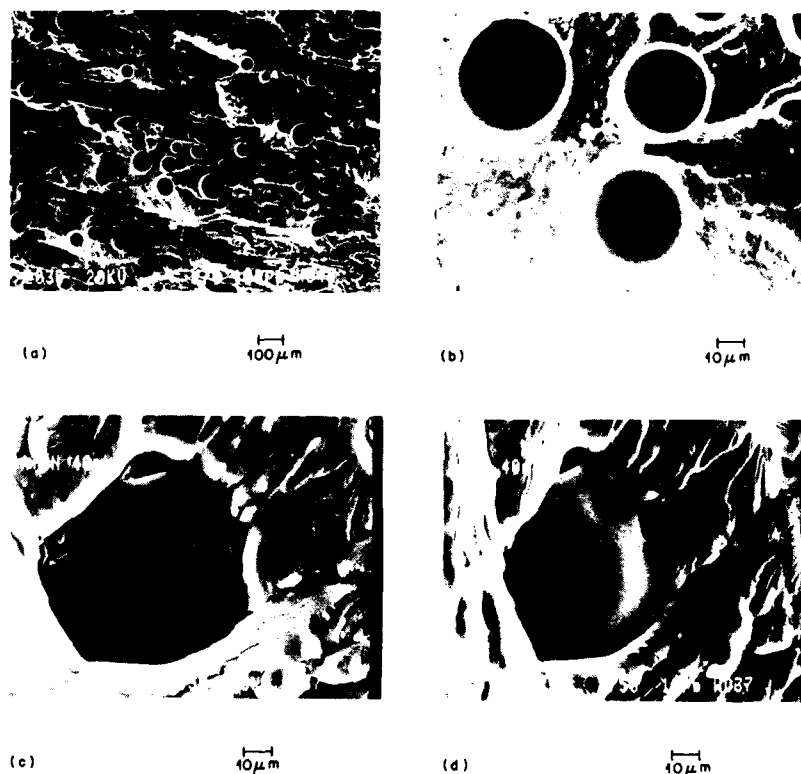


FIGURE 8 Scanning electron photomicrographs taken from fracture surfaces of 40% ATBN modified epoxy resin at various magnifications (a— $\times 70$, b— $\times 400$, c— $\times 750$ $\theta = 0^\circ$, d— $\times 750$ $\theta = 43^\circ$).

outstanding observation is that the particle diameters are very large—up to $100\ \mu\text{m}$. The properties of the ATBN/epoxy formulations are strongly dependent on the relative amounts of the two components. This is manifested in the marked increase of the number of large particles as the rubber content increases and uneven distribution of small particles (Figure 8, a,b). ATBN particles show highly irregular contours which often appear as agglomerated islands of smaller particles. As can be seen from Figure 8, c and d, the relatively giant rubber spheres create a discontinuous phase. There is a bimodal distribution of rubber particles; $80\text{--}100\ \mu\text{m}$ and $15\text{--}30\ \mu\text{m}$. Both spheres are much bigger

in size than the CTBN and ATBN rubber spheres reported earlier^{14-18, 22-23}, except those reported by H. N. Nae^{17c}, A. J. Kinloch *et al.*¹⁹ and Z. Nir *et al.*²⁰

In general the morphology develops during the cure cycle and depends on the rubber-epoxy compatibility, the temperature and time of cure, and elastomer concentration. A possible mechanism for morphology development was suggested by Nae.^{17c} At the beginning of polymerization the system behaves like a compatible solution. As the network grows, the rubbery segments are segregated from the main chain, and agglomerates are formed.

Such agglomerates were also observed in other trifunctional systems.^{17c} In these systems containing CTBN, rubber particles as large as 80–120 μm were observed, similar to the present system containing tri- and tetra-functional epoxy resin.

Results point out that ATBN in large quantities is a better toughening agent than CTBN rubber.¹⁶ In addition, most of the studies reported show well-bonded particles as a consequence of the chemical reactivity of the rubber. Poor interfacial bonding was observed in the ATBN/epoxy formulation, as evident in the fracture surface shown in Figure 8, d. Similar description was given by Kinloch.¹⁹ In the latter case (contrary to the present study) it has been specifically designed by using an unreactive system.

CONCLUSIONS

Room-temperature-curing epoxy formulations for elevated temperature use have been developed. Results have shown that the fundamental lap-shear and peel strengths at ambient and high temperature of the proposed composition are superior to commercially-available, room-temperature-cure adhesive systems. Moreover, they are only marginally inferior to high-temperature-cured film adhesives.

The thermal, mechanical and chemical characterizations that accompanied the composition development have shown that, although curing has not come to completion after six days at room temperature, the resulting properties are satisfactory and termination of cross-linking is achieved after 3–6 months cure at ambient temperature or 1 hour at 50°C.

in size than the CTBN and ATBN rubber spheres reported earlier^{14-18, 22-23}, except those reported by H. N. Nae^{17c}, A. J. Kinloch *et al.*¹⁹ and Z. Nir *et al.*²⁰

In general the morphology develops during the cure cycle and depends on the rubber-epoxy compatibility, the temperature and time of cure, and elastomer concentration. A possible mechanism for morphology development was suggested by Nae.^{17c} At the beginning of polymerization the system behaves like a compatible solution. As the network grows, the rubbery segments are segregated from the main chain, and agglomerates are formed.

Such agglomerates were also observed in other trifunctional systems.^{17c} In these systems containing CTBN, rubber particles as large as 80–120 μm were observed, similar to the present system containing tri- and tetra-functional epoxy resin.

Results point out that ATBN in large quantities is a better toughening agent than CTBN rubber.¹⁶ In addition, most of the studies reported show well-bonded particles as a consequence of the chemical reactivity of the rubber. Poor interfacial bonding was observed in the ATBN/epoxy formulation, as evident in the fracture surface shown in Figure 8, d. Similar description was given by Kinloch.¹⁹ In the latter case (contrary to the present study) it has been specifically designed by using an unreactive system.

CONCLUSIONS

Room-temperature-curing epoxy formulations for elevated temperature use have been developed. Results have shown that the fundamental lap-shear and peel strengths at ambient and high temperature of the proposed composition are superior to commercially-available, room-temperature-cure adhesive systems. Moreover, they are only marginally inferior to high-temperature-cured film adhesives.

The thermal, mechanical and chemical characterizations that accompanied the composition development have shown that, although curing has not come to completion after six days at room temperature, the resulting properties are satisfactory and termination of cross-linking is achieved after 3–6 months cure at ambient temperature or 1 hour at 50°C.

12. W. Brenner and J. Arnon, "Room Temperature Curing Epoxy Resin Compositions High Temperature Service Capability for Fiber Reinforced Structures, Adhesives and Sealants," NTIS Report AD-A115025, May 1981.
13. L. H. Peebles, "Adhesive Joint Formation under Field Conditions," NTIS Report AD-D011478, 1984.
14. (a) R. Drake, A. Siebert, *SAMPE Quarterly* **6**(4), 1 (1975). (b) B. F. Goodrich Chemical Company, Product Literature, "Toughen Epoxy with Hycar RLP," Bulletin RLP-2.
15. C. K. Riew, E. M. Rowe and A. R. Siebert, in *Toughness and Brittleness of Plastics*, R. D. Deanin and A. H. Grignala, Eds. *Adv. Chem. Series*, **154** (Am. Chem. Soc., Washington, D.C., 1976), pp. 326-343.
16. R. S. Drake, "Formulating Epoxy Structural Adhesives with Amine Reactive Polybutadiene/Acrylonitrile Liquid Polymers," Proceedings of The Int. Adhesion Conf., 12-14 September, 1984, Univ. of Nottingham, U.K., p. 11.
17. (a) H. N. Nae and J. K. Gillham, *ACS Div. Org. Coat. Plast. Chem. Prep.* **48**, 566 (1983). (b) J. B. Enns and J. K. Gillham, *J. Appl. Polym. Sci.* **28**, 2831 (1983). (c) H. N. Nae, *ibid.*, **31**, 15 (1986).
18. J. H. Cranmer, "Dynamic Mechanical Analysis of Elastomer Modified Epoxies," *SAMPE Quarterly*, **16**(2), 1 (1985).
19. A. J. Kinloch, "Multiphase Thermosetting Adhesives," 8th Annual Meeting, The Adhesion Society, February 24-27, 1985.
20. Z. Nir, W. J. Gilwee, D. A. Kourtises and J. A. Parker, *Polymer Composites* **6**, 65 (1985); **6**, 72 (1985).
21. R. E. Smith, F. N. Larsen and C. L. Long, *J. Appl. Polym. Sci.* **29**, 3713-3726 (1984).
22. A. V. Pocius, "Elastomer Modification of Structural Adhesives," Presented at a meeting of the Rubber Division, American Chemical Society, Denver, Colorado, Oct. 23-25, 1984; *B. Rubb. Chem. and Tech.* **58**, 622-636 (1985).
23. S. C. Kunz, J. A. Sayre and R. A. Assink, *Polymer* **23**, 1897 (1982).
24. N. C. Paul, D. H. Richards and D. Thompson, *Polymer* **18**, 945 (1973).
25. J. N. Sultan and F. J. McGarry, *Polym. Eng. Sci.* **13**, 29 (1973).
26. P. Bartlet, J. G. Pascault and H. Sautereau, *J. Appl. Polym. Sci.* **30**, 2955-2966 (1985).
27. G. Levita, A. Marchetti and E. Butta, *Polymer* **26**, 1110-1116 (1985).
28. S. K. Joneza, *Research & Development* **27**, 4 (1985).

SESSION OF CANADA

Polymer Mixing and the Thermodynamics of Cell Adhesion at Fluid Interfaces†

DONALD J. L. McIVER‡^(1,2) and SAMUEL SCHÜRCH⁽³⁾

Departments of Pharmacology and Toxicology⁽¹⁾ and Biophysics,⁽²⁾ University of Western Ontario, London, Ontario, N6A 5C1 and Faculty of Medicine,⁽³⁾ University of Calgary, Calgary, Alberta, T2N 4N1, Canada

(Received December 22, 1986)

The mechanism of adhesion of cells to other cells or to non-cellular surfaces is a central problem in cell biology and biotechnology. The present studies were carried out to investigate the relationships between cell surface thermodynamics, the kinetics of cell adhesive behaviour and the molecular and morphological structure of the cell surface, when cell adhesion is elicited by defined physiological stimuli. The surface thermodynamic studies are applications of classical capillarity in which we measure the wetting of cell surfaces (the surface affinity or work of adhesion) by aqueous phase separated polymer solutions of dextran and poly (ethylene glycol), before and after exposure of the cells to the adhesive stimuli. For the phase system used here {4%/4% w/w dextran mol. wt. 2×10^6 /poly (ethylene glycol) mol. wt. 2×10^4 in HEPES buffered physiological saline}, the measured interfacial free energy was $4.02 \times 10^{-6} \text{ J m}^{-2}$. Isolated leukocytes were exposed to adhesion-promoting chemoattractant stimuli (for example, the tripeptide N-formyl methionyl leucyl phenylalanine or serum complement activated yeast particles). We observed increases in the work of cell adhesion to the dextran phase which were proportional to the stimulus dose; at the maximally effective doses, the cell-liquid-liquid contact angles changed by about 50° , corresponding to $2 \times 10^{-6} \text{ J m}^{-2}$ changes in the work of adhesion. In parallel with the thermodynamic measurements we measured the kinetics of cell activation to provide the time scale of cell behaviour which is missing from the equilibrium surface energy measurements. Infrared photometry (optical density and perpendicular light scattering) provided information on the kinetics of cell adhesion and morphological responses to stimuli; simultaneous measurements of oxygen free radical-dependent chemiluminescence and spectrophotometric measurements of

† Presented at the Tenth Annual Meeting of The Adhesion Society, Inc., Williamsburg, Virginia, U.S.A., February 22-27, 1987.

‡ To whom correspondence regarding this paper should be addressed.

enzyme activity defined the kinetics of biochemical activation. The thermodynamic studies were carried out during the plateau of the time-response curves; under these conditions both the kinetic and thermodynamic measurements have similar stimulus dose-response curves, suggesting that both types of process are manifestations of the same cell surface events. The exact relation of the surface affinity changes to the molecular mechanism(s) of cell adhesion is not yet clear, however. Synthetic structural studies (model membrane reconstitution) indicate that the cell surface/polymer phase affinity is a function of the concentration, molecular weight and conformational state of the cell surface glycopolymers (the "glycocalyx"). Analytic studies have shown correlations between surface affinity changes and the molecular weight/concentration profiles of isolated cell membrane glycoproteins. Modelistic considerations suggest that the cell surface glycoproteins which determine the phase wetting behaviour have concentrations in the micromolar range. If these aqueous phase reactive glycocalyx proteins are the molecules which mediate cell adhesion elicited by small specifically recognised ligands, then it may be necessary to modify the current model of cell adhesion which proposes that adhesion results from a balance between "specific bonding and non-specific repulsion." For example, in stimulus induced leukocyte adhesion a "specific induction, non-specific execution" model may be more useful.

KEY WORDS Bioadhesion; cell adhesion; fluid interfaces; polymer mixing; properties of cell surfaces; thermodynamics.

1 INTRODUCTION: MEASURING AND MODELLING CELL ADHESION

*"Until our assays of adhesion are improved considerably we will remain ignorant of the relative contributions of strength and permanence in adhesion interactions."*¹

The mechanism of adhesion of cells to other cells or to non-cellular surfaces is a central problem in cell biology and biotechnology. Any detailed understanding of these processes must account for

- 1) the physical strength (thermodynamics) of cell adhesion and its relation to the nature and range of the forces between the adhering molecules;
- 2) the permanence (kinetics) of cell adhesion, and
- 3) the way that chemical selectivity (structure) operates in different cellular adhesive events.

The term "cell adhesion" encompasses a wide variety of adhering cells and surfaces, ranging from such processes as the aggregation of

cells in flowing blood to the adherence of cells to plastic tissue culture dishes or implanted biomaterials. The molecular details of these events remain only partially characterised, but it seems unlikely from the outset that any single method of measurement or model of adhesion would suffice to describe the diversity of these adhesive processes.

In this communication, we will focus on the ways in which surface thermodynamic studies highlight the similarities rather than the differences in cell adhesion. Historically, this has been the role of thermodynamics: to provide a framework for describing the magnitude and direction of diverse natural processes, without requiring or using molecular information. Eventually, of course, a full understanding of adhesion requires that the thermodynamic measurements be related to the structure of the adhering surfaces.²

Measuring cell adhesion

The variety of methods that has been employed to measure cell adhesion seems only to emphasise this diversity. The experimental approaches that have been used to quantify cell adhesion include *adherent particle counting*,³ *force-displacement measurements*,⁴ *particle size distribution*,⁵ *hydrodynamic shearing of cells in suspension*^{6,7} or *attached to surfaces*,^{8,9} *light scattering*^{10,11} and *surface thermodynamics*.¹² Each of these approaches has features to commend it, but all have their limitations. So far none has permitted the detailed, simultaneous correlation of adhesive energies and kinetics with the biochemical structure of the cell surface that is necessary to formulate and test critical theories of the mechanism(s) of cell adhesion.

The traditional biological approach to quantifying cell adhesion is the direct counting of the "adhering" cells, using morphological, chemical or radiochemical detection methods.¹³ The biological advantage of this approach is that it necessarily provides a functional assessment of adhesion. The major difficulty is that what is observed (the quantity of adherent cells) depends on the distraction procedure, *i.e.*, on the method used to separate "bound" and "free" cells in these kinds of measurements. The cell responses are quantized (*i.e.*, cells are either "stuck" or "not stuck"), so it is difficult to make estimates of graded adhesion energies. The forces

required to remove adherent cells do not necessarily provide information about adhesive energies; the large hysteresis between the energies of cell attachment and detachment probably arises because detachment includes contributions from time-dependent (irreversible) work as well as from the reversible work of adhesion.³²

The traditional physical approach to the energies of surface interaction is to measure the force required to produce a measured surface displacement. Provided reversibility can be guaranteed (no easy task when dealing with phenomena that are usually time- and path-dependent), this will probably always be the most informative method of studying adhesion. In aqueous media—the predominant biological milieu—this approach has been applied with increasing refinement over the past decade: micromechanical¹⁴ or osmotic force¹⁵ measurements, coupled with multiple beam optical interference¹⁴ or X-ray diffraction¹⁵ measurements of surface separation have revealed a wealth of information about the range and magnitude of surface forces. However, the technical requirements of these measurements—molecular smoothness or structural repetition which yields an X-ray diffraction pattern—have so far limited their application to non-cellular systems. When micro-mechanical force-displacement measurements are carried out on living cells the fine details of the range of the surface forces are lost, and an integral of work and distance is recorded.⁴

The distribution of particle sizes in either microscopic optical measurements¹⁶ or electronic sizing channelizers⁵ has been a useful way of following the growth of cell clumps due to aggregation. These procedures provide evidence of cell-cell adhesion, but once again estimates of adhesion forces are not readily obtainable.

Light scattering measurements have also been widely employed to study cell adhesion. When a suspension of particles is illuminated with a beam of collimated light, some of the light may be absorbed, some transmitted and some scattered. Measuring the luminous intensities of each of these processes is a powerful tool for obtaining information on the morphological properties of the components of the suspension—the size, shape, state of aggregation, etc. Born¹⁰ introduced transmittance photometry to the study of blood platelet aggregation, and showed that microscopic aggregation was time correlated with increased light transmittance. Since then, measure-

ments of light transmittance and scattering by cell suspensions have been widely used to study cell responses to stimuli.¹⁷ The light scattering approach has two major virtues. First, it has good kinetic sensitivity (providing a millisecond time scale for cell behaviour). Second, it has good statistical reliability, being based on measurements of large numbers of cells (typically 10^5 – 10^7). In addition, other spectral data may be obtained at the same time as scattering is used to investigate morphology. Information on interaction forces is not readily obtainable, however, and the results of scattering experiments have usually been interpreted empirically, mostly in terms of light or electron microscopy.

Surface thermodynamics has been used as a tool for investigating cell adhesion for more than 50 years.¹⁸ While this is also a potentially powerful approach, it has suffered from the limitation of identifying the cell surface thermodynamic potential functions which are *relevant* to studying cell adhesion. The problem is essentially one of the macrocosm and the microcosm: given the microheterogeneity of cell surfaces, it is not clear what a macroscopically averaged "surface energy" measurement on a multicomponent cell surface really means. Nevertheless, measurements of cell surface thermodynamics have shown a number of correlations with cell behaviours such as phagocytosis and adhesion to synthetic polymeric surfaces.¹⁹ A related approach which has been widely investigated as a tool in cell surface analysis is the partition of cells between liquid phases.²⁰ Surface thermodynamics contributes to the partition behaviour of cells, via the difference in interfacial energy of the cells in each phase but there are other factors at work as well: external forces in addition to interfacial work (such as hydrodynamic flow and gravity) also influence cell partition.²¹

Modelling cell adhesion

Based on these kinds of measurements, the current model of cell adhesion is that of a "competition between non-specific repulsion and specific bonding."²² According to this model, cell adhesion occurs when a sufficient number of cross-bridging molecules bind to the surfaces of adjacent cells and oppose the distracting forces which tend to keep the cells apart. Lectins,²³ antibodies²⁴ and "Cell

Adhesion Molecules" (or CAM's²⁵) are examples of molecules which cross-bridge specific binding sites; non-specific cell cross-linking (the so-called rouleau formation) may also be mediated by binding of molecules such as dextran or fibrinogen.²⁶

The mechanics and thermodynamics of the "non-specific repulsion, specific bonding" model (which we shall subsequently call "model 1" for short) have been developed in detail, both for the cases where the bridging molecules are continuously²⁷ or discretely²⁸ distributed on the cell surface; direct micromechanical force measurements of cell cross-bridging under equilibrium conditions have confirmed the predictions of this model. Model 1 explicitly assumes that the same molecular mechanisms are responsible for recognising and executing cell adhesion. For both the specific and non-specific macromolecular cross-bridging (agglutination) reactions described above, this is a reasonable assumption.

For many types of cell adhesion, however, we suggest that model 1 is not adequate; the agglutination described by model 1 is a sufficient but not necessary condition for cell adhesion. There are many cellular adhesive events where the specificity of adhesion arises from a low molecular weight adhesion-inducing ligand which is of itself too small to provide the specific cross-bridging required by model 1. An important example of such a process is the leukocyte aggregation induced by the chemoattractant tripeptide N-formyl methionyl leucyl phenylalanine;¹⁶ the stimulation of cell adhesion to foreign surfaces by activated complement²⁹ may well be a similar phenomenon. A considerable amount is known about the recognition of these specific adhesion-inducing ligands, but much less is known about the sticky molecules—the glue—which actually mediate the cell adhesion. Given the fact that activated leukocytes, for example, may stick quite indiscriminately to a variety of surfaces, we suggest that small-ligand-induced adhesion may be better described by the reverse of model 1 or a "specific induction, non-specific execution" model, which we call model 2 for short. The idea behind model 2 is not new (for example, see Refs. 30, 31). What is new is the availability of methods for testing it.

These methods, which are predominantly applications of classical thermodynamics to cells in liquid polymer solution phases, are based on measuring the static (equilibrium) affinity of cell surfaces

for fluid interfaces under conditions where the cell adhesiveness is varied by environmental manipulation, and where parallel studies of the kinetics, morphology and biochemistry of the adhering cells allow these events to be correlated. From a knowledge of the composition of the liquids used for the affinity measurements, it is possible to make some testable inferences about changes in the cell surface under defined conditions of adhesion, and to relate these inferences to the energies between the adhering molecules.

2 SURFACE THERMODYNAMIC APPROACHES TO CELL ADHESION

In principle, an approach which could yield information about the time- and path-independent (*i.e.*, equilibrium) adhesive forces between cell surfaces is one based on surface thermodynamics. This idea is not new either: attempts to describe cell adhesion in terms of the formalisms of classical thermodynamics had already been made by the second decade of this century.¹⁸ These early approaches regarded cell adhesion as arising from a "a pure surface tension . . . and the fluidity of the protoplasm";¹⁸ in more modern terminology this balance of opposing forces would be described as the resultant of surface affinity (the surface free energy reduction on contact, or work of adhesion) and cell deformability.³² However, after this seminal early work (and for no apparently decisive reasons), enthusiasm waned for using equilibrium thermodynamics as a tool in analysing cell adhesion. At least two influences were likely responsible. On the one hand, the growing appreciation of the biochemical complexity of cells may have pointed to the improbability of usefully describing microscopically heterogeneous cell surfaces in terms of macroscopically averaged potential functions. For example, the fact that cell receptors for drugs and hormones only covered a small fraction of the cell surface was already widely appreciated by 1933.³³ In addition, the growing recognition of irreversibility in biology³⁴ may have made equilibrium approaches to what is manifestly a non-equilibrium phenomenon, seem unrealistic. The strengths and limitations of the equilibrium approach to cell surface interactions have recently been

discussed.²² In Section 7 we will briefly discuss the relations between microscopic receptor distribution and equilibrium macroscopic surface thermodynamics in relation to the question of cell adhesion induced by low molecular weight, structurally specific ligands which do not *per se* have the capacity to stick cells together.

In the early 1960's thermodynamic approaches to cell adhesion were taken up again, this time from the viewpoint that whole cells could be regarded as miscible or immiscible liquids.³⁵ Despite its limitations, we believe that elements of this theory remain useful for modelling some important aspects of cell adhesion, in particular, those aspects which primarily involve the isotropic polymer solution-like behaviour of the cell surface glycoproteins (the glycocalyx) rather than the thixotropic or viscoelastic behaviour of membrane or cytoplasmic deformation. Subsequently, the thermodynamic analysis of cell adhesion phenomena received a considerable impetus from advances in the study of contact angles and their application to a variety of cell-substrate and cell-particle interactions.¹²

The latter studies take as their starting point the equation developed by Thomas Young in 1805³⁶ to describe the equilibrium relationship at the three-phase line between two fluids and an ideal, non-deformable solid substrate (Figure 1):

$$\gamma_{23} = \gamma_{13} + \gamma_{12} \cos \theta \quad (1)$$

where γ_{12} , γ_{13} and γ_{23} are the interfacial free energies between the three phases (denoted 1, 2 and 3) and θ is the contact angle at the three-phase line. Deviations of real contact angles from Young's equation are usually attributed to metastable wetting states arising from chemical heterogeneity or surface roughness.³⁷ The scale of microscopic irregularities which result in macroscopic contact angle changes is a current area of active research concern; as far as heterogeneity is concerned, modelistic considerations indicate that dimensions $< 0.1 \mu\text{m}$ will not give rise to macroscopic contact angle hysteresis;³⁸ since most cell surface chemical heterogeneities are expected to be much smaller than this, macroscopic contact angles on living cells should reflect an equilibrium average of the effects of the chemical determinants of the surface. The exact influence of the second cause of contact angle hysteresis—microscopic surface roughness—still remains unsettled.

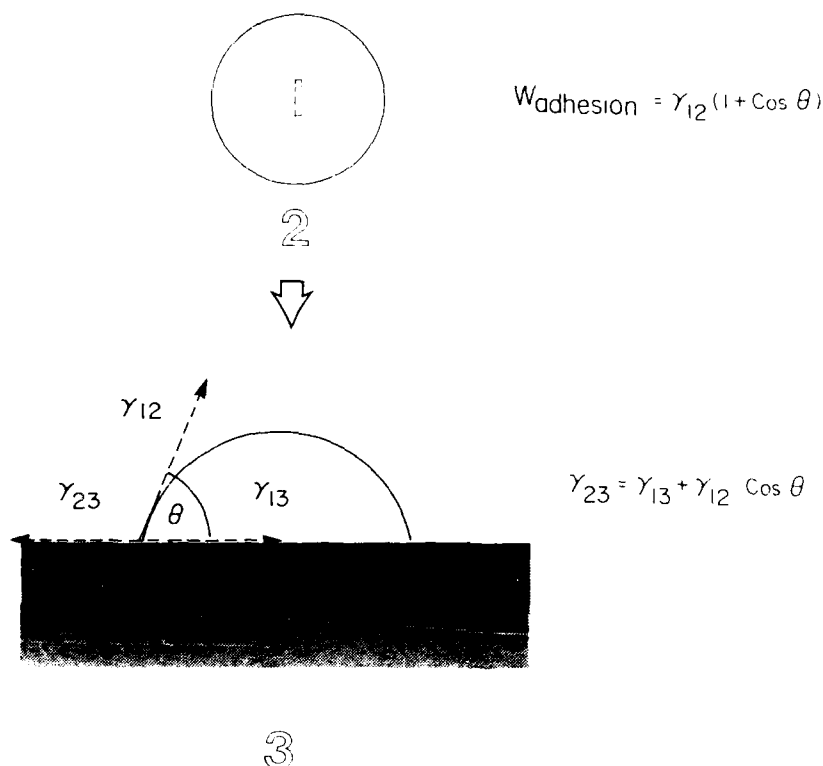


FIGURE 1 Relationships between the interfacial free energies, γ , and the contact angle θ , at a three-phase boundary.

The last decade has seen a great increase in the application of surface thermodynamics to the investigation of a variety of cell surface phenomena (for a recent review, see Ref. 19), as well as the appreciation of some of the problems associated with it.

Like the methods described above, our own approach to cell adhesion has been based on the measurement of contact angles at cell surfaces, and the estimation of the work of cell adhesion under various biological conditions. Our approach differs from those described above in that it uses aqueous solutions, rather than the vapour phase, as the reference state for calculating cell surface thermodynamic potentials.

3 CELL SURFACE CONTACT ANGLES IN LIQUID-LIQUID SYSTEMS

In our early studies of cell surface contact angles in liquid/liquid systems (*e.g.*, Ref. 39) we used droplets of polar hydrocarbon oils immersed in saline solutions to measure angles at the oil/saline/cell interface. Figure 2A illustrates the application of this approach to

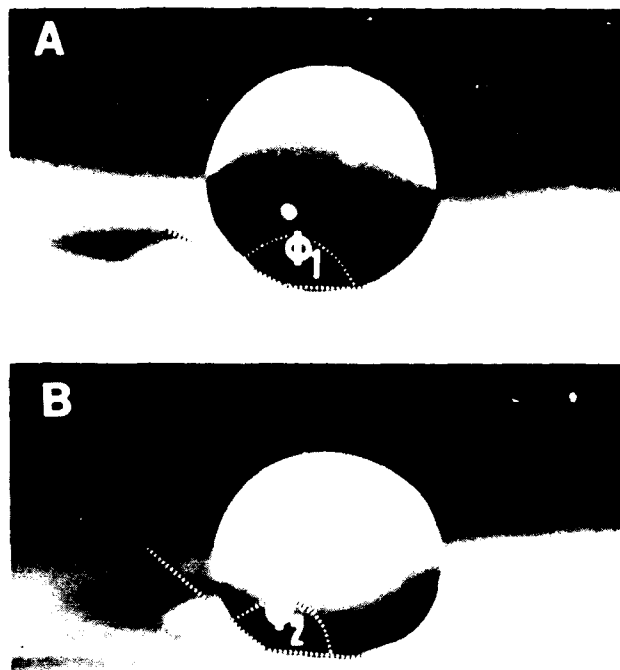
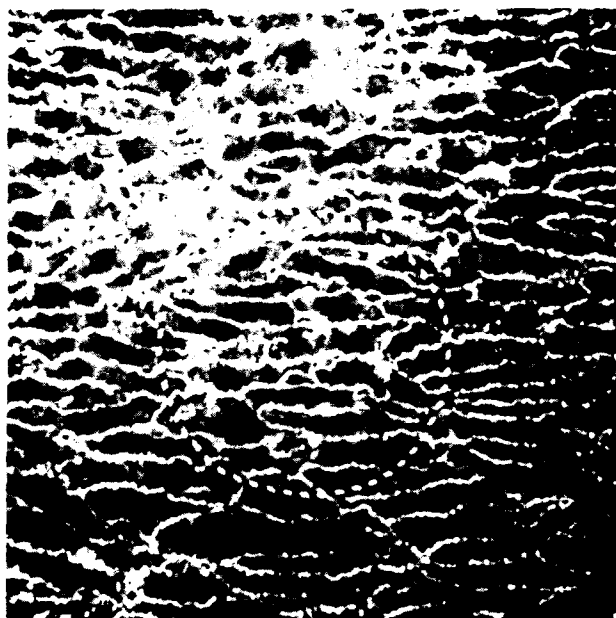


FIGURE 2 Adhesion of endothelial cells at oil-water interfaces. A A droplet of isopropyl salicylate ($\gamma_{12} = 13.3 \text{ mJ m}^{-2}$) resting on the endothelial surface of the aorta from a healthy rabbit. The contact angle is 150° . B A droplet of isopropyl salicylate resting on the surface of an endothelial lesion from an animal with advanced diet-induced atherosclerosis. The contact angle is 137° . Both droplets are approximately 1 mm in diameter. C Scanning electron micrograph of specimen A, stained with silver to highlight the endothelial cell boundaries, and showing the intact endothelial cell monolayer. The endothelial cells range in length from 30 to $50 \mu\text{m}$; the dotted line shows the approximate boundary of the three phase line which would be formed by droplet A at a contact angle of 90° . Adapted and reproduced from Ref. 39.



60 μm

FIGURE 2 (continued)

the endothelial cell surface of isolated arteries. The measured contact angles and liquid-liquid interfacial free energies, and a semi-empirical equation of state (see equation [2]⁴⁰) indicated that the cell-saline interfacial free energy was very low, $\sim 10^{-2} \text{ mJ m}^{-2}$ or less. This value is one order of magnitude lower than direct measurements of bilayer interfacial free energies,⁴¹ and two orders of magnitude lower than interfacial free energies calculated from measurements of contact angles on lipid monolayers at oil-water interfaces,⁴² indicating that the contact angles at the cell/saline interface were a result of non-lipid surface active materials in the cell membrane (*i.e.* membrane proteins), an idea originally proposed by Davson and Danielli.⁴³ Interestingly, these cell/oil/water adhesion studies also showed that pathological processes (in this

case, advanced diet-induced atherosclerosis, which resulted in focal changes in the endothelial surface) resulted in changes in the interfacial free energies of the cells which could be distinguished from healthy control animals or from non-affected cells in the diseased animals (Figure 2B). Morphological studies (Figure 2C) showed that the cell layer remained intact through the experimental procedure. On the basis of these liquid/liquid adhesion measurements, we suggested that this kind of study might be a useful approach to assessing one of the factors thought to be involved in the initiation of atherosclerosis: an altered adhesion potential of the blood vessel wall for blood elements such as platelets or leukocytes.³⁹

However, the use of oil-water interfaces in these studies created a problem of sensitivity: because of the high values of the cell/oil/water contact angles (a consequence of the high oil/water interfacial free energy, and the low cell/water interfacial free energy) it proved impossible to obtain contact angles of less than 150° on normal cells; the difficulty of accurately measuring such high angles introduced a substantial uncertainty into the cell/saline free energy estimates. In addition, since cells do not usually live in a hydrocarbon environment, the biological effects of this procedure may not be innocuous.

Accordingly, most of our subsequent studies of cell surface thermodynamics have been carried out using a procedure which minimises these problems: aqueous phase separated polymer systems. These systems have been extensively studied by Albertsson and co-workers,²⁰ and have both of the characteristics required for studies of the surface thermodynamics of living cells: ultralow interfacial free energies ($\sim 10^{-3} \text{ mJ m}^{-2}$) and excellent biocompatibility. These polymer systems resemble blood plasma in their physiochemical properties (indeed, dextran solutions have been in clinical use as plasma expanders for many years), and they may be buffered, sterilised, rendered isotonic and provided with many of the factors required for normal cell function. They have been used extensively for dynamic studies of cell separation by phase partition.⁴⁴

Measurements of static contact angles of polymer phase drops with living cells were carried out independently in our laboratory⁴⁵ and that of Fisher.⁴⁶ Since then we have studied the effects of

environmental factors on the thermodynamic properties of the cell surface revealed by this method, seeking to correlate biochemical and biophysical information about the cell surface, its relation to the mechanisms of cell adhesion, and its alteration by pathological processes.

The method is illustrated in Figures 3A and 3B. A droplet of the denser polymer phase (4% dextran, ave. mol. wt. 2×10^6) is formed in the lighter phase (4% polyethylene glycol, ave. mol. wt. 2×10^4 , PEG) and the interfacial free energy is determined from the deformation of the drop profile by gravity. Tables of drop profile parameters⁴⁶ may be used for this calculation. The drop is allowed to fall onto the surface of interest, and it spreads until a final advancing contact angle is achieved. If suitable digitising and computing facilities are available, a more precise analytic procedure is provided by the computer programme of Rotenburg, Boruvka and Neumann,⁶⁸ which uses a least squares algorithm to fit a LaPlacian curve to the drop profile, and which calculates the interfacial free energy, the drop volume and surface area, and the contact angle formed by the drop. Depending on the polymer concentration, for drops of the size illustrated in Figure 3B (0.1–1 mm), spreading takes 1–4 minutes.

Figure 3B shows the drop from Figure 3A, after it has reached its stationary state on the cell surfaces. In this case, the cells were a purified (~99%) population of lung alveolar macrophages cultured on a cellulose acetate filter for 24 hours before the contact angle measurements were made. At this magnification (60 \times) the individual cells (12–15 μ m in diameter) can just be resolved. Each drop samples about 7×10^3 cells. The contact angle (calculated either by direct measurement with a protractor eyepiece, or by the computer curve fitting procedure),⁶⁸ is 95°, corresponding to an affinity (work of adhesion) of the cell surface for the dextran phase in the PEG phase of 4×10^{-3} mJ m⁻². Subsequent studies, described below, have shown that the polymer phase contact angle is quite sensitive to changes in the cell surface induced by a variety of different means, and that the chemical basis of these changes probably lies in alterations in the amount, molecular weight or conformation of cell surface glycoproteins. The method has also been used to investigate the effects of mechanical removal of endothelial cells from the arterial wall.⁵⁰

A**B**

0.1mm

A horizontal scale bar with vertical end caps, indicating a length of 0.1mm.

4 EQUIVALENT SOLUTION PROPERTIES OF THE CELL SURFACE

Abandoning the vapour phase as the reference state for cell surface thermodynamics may arguably have some benefits in terms of sensitivity and biocompatibility (*e.g.*, Ref. 69), but it definitely carries a price: in the absence of an independent relation between the contact angle and the interfacial free energies Young's equation cannot be solved for solid substrates. Hence, contact angle measurements on solid surfaces yield only the difference in interfacial free energies of the solid surface between the two fluid phases. An empirical functional relation (an equation of state) between the free energies in three-phase systems has been proposed⁴⁰ having the form,

$$F(\gamma_{13}, \gamma_{23}, \gamma_{12}) = 0 \quad (12)$$

but so far this relation applies only to the type of two-component systems for which it was derived, where γ_{12} (using the terminology of Figure 1) is of the magnitude of the energy of the hydrocarbon-vapour interface, *i.e.*, in the mJ m^{-2} range.⁴² For systems of $\mu\text{J m}^{-2}$ interfacial free energies (such as the aqueous polymer phases of interest here), the empirical equation of state does not hold.⁴⁹

In order to stay with thermodynamics, therefore, we are restricted to expressing contact angle data in terms of the difference in free energy of the substrate with respect to the two fluid phases. Quantitatively, this difference is expressed as the work of adhesion, W_{adh} , where

$$W_{\text{adh}} = \gamma_{12}(1 + \cos \theta) \quad (13)$$

Equivalently, and for a constant γ_{12} , the difference in interfacial

FIGURE 3 Adhesion of isolated cells in phase-separated aqueous polymer systems. A A pendant drop of the denser (dextran-rich) phase hanging in the less dense (polyethylene glycol-rich) phase of a 4%/4% dextran (ave. mol. wt. 2×10^6)/polyethylene glycol (ave. mol. wt. 2×10^4) phase system. The aqueous phase is Hank's balanced salt solution, pH 7.4. The interfacial free energy of this system is $4.02 \times 10^{-3} \text{ mJ m}^{-2}$. The maximum drop diameter is approximately $100 \mu\text{m}$. Differential interference (Nomarski) contrast. B The droplet shown in A resting on a layer of pig alveolar macrophages sedimented onto a cellulose acetate filter. The final advancing contact angle is 95° . Individual cells can just be distinguished at this magnification ($60\times$). Polarization contrast. Reproduced from Ref. 45.

free energy between two situations can be expressed as the change in the cosine of the contact angle, $\Delta \cos \theta$ (e.g., see Figure 10). In general, we express the liquid-liquid adhesion measurements in terms of the work of adhesion of the cells to a drop of the dextran phase immersed in the polyethylene glycol phase.

Here, however, we want to explore briefly an extra-thermodynamic approach to interpreting the polymer phase contact angle measurements. The strategy is based on an analogy with Zisman's operational parameter, the so-called "critical surface tension for spreading" or " γ_c ").⁵¹ For low energy solid/liquid/vapour surfaces and negligible equilibrium spreading pressure, Zisman defined γ_c as the limiting value of a cosine plot of the contact angle *versus* the liquid surface tension. As Zisman was careful to point out, γ_c is not a thermodynamic property of the surface, and it therefore cannot be used in a thermodynamic analysis. However, along with molecular considerations, a critical spreading type of approach does offer some useful insights into the interaction of polymer phases with cell surfaces.

The approach is illustrated in Figure 4. In 4A, droplets from the dextran-rich phase of three different two-phase systems are shown on sedimented layers of isolated human erythrocytes. As the polymer concentration is reduced, the contact angle is progressively lowered. In the Zisman approach, a " γ_c "-like parameter would be defined as the limiting liquid surface tension when θ approaches zero. We have also used a " γ_c " type of parameter to express the properties of the cell surface;⁴⁵ it is not clear, however, what a " γ_c " determined under these conditions really means. More informative perhaps is the limiting value of the polymer *concentration* when θ approaches zero. Assuming that the interfacial free energy between the cell and the test droplet in this case is very low (certainly a minimum, and possibly zero: Ref. 52), at this point the polymer phase in the test drop is equivalent in composition to a polymer phase comprised of the molecules making up the cell surface. We call this limiting composition of the test droplet phase, determined as the contact angle approaches zero, an "equivalent solution" to the cell surface. For equivalent molecular weights and conformations (*i.e.*, polymer-solvent interactions), the time- and space-averaged polymer compositions of the two systems (the cell surface and the test drop) should be identical.

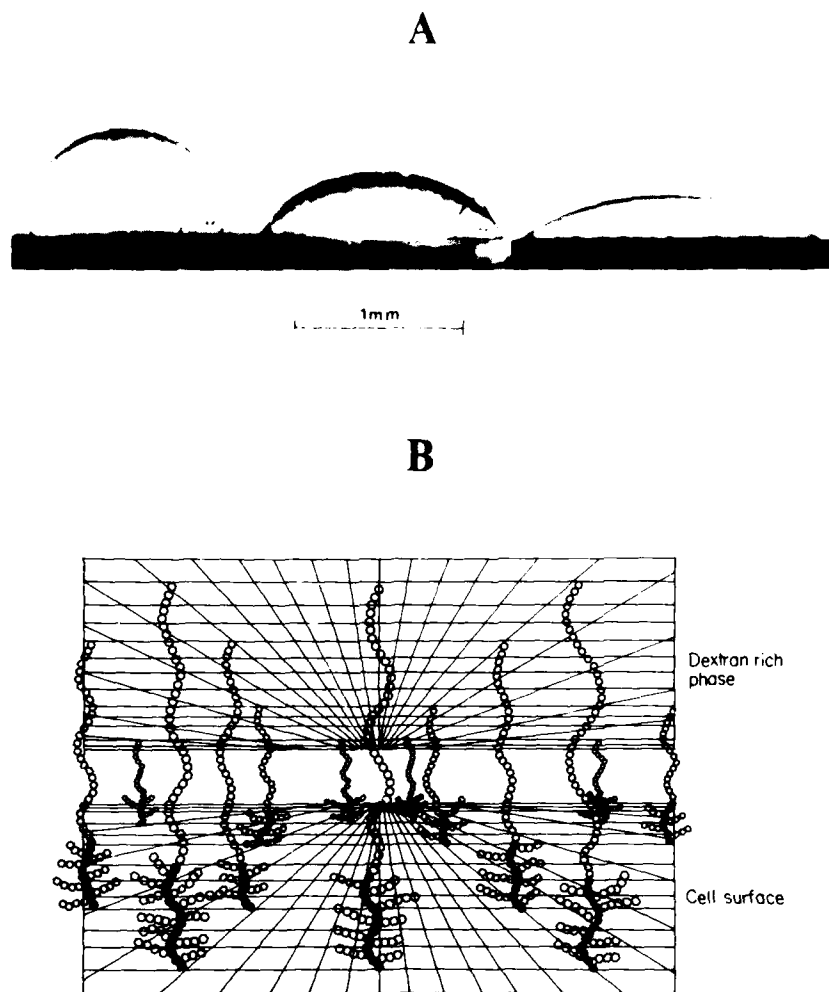


FIGURE 4 "Critical spreading" of polymer phases on isolated cells. A Variation of contact angle with polymer concentration of dextran/polyethylene glycol droplets on layers of human erythrocytes for dextran (ave. mol. wt. 5×10^5) polyethylene glycol (ave. mol. wt. 2×10^4) phase systems. The concentrations (w/w) of the polymers and the contact angles are: 5%, 106° (left); 3.7%, 61° (middle) and 3.3%, 38° (right). The droplet diameters are approximately 1 mm. Polarization contrast. Reproduced from Ref. 45. B Schematic quasi-lattice model of polymer-polymer interactions at an idealised cell surface as the contact angle and the cell/dextran phase interfacial free energy approach zero. Reproduced from Ref. 48.

This hypothesis is illustrated schematically in Figure 4B, a quasi-lattice model of polymer-polymer interactions between the polymer segments at the cell surface and in the aqueous phase.⁴⁸ In this model, lowered contact angles (lowered interfacial free energies or increased work of adhesion of the cell surface to the dextran phase) correspond to increased mixing between the two phases, while raised contact angles (increased interfacial free energies or increased adhesion to the PEG phase) correspond to phase de-mixing. From a consideration run on to next page (15) of the phase diagrams of these phase systems (*e.g.*, Refs. 20, 45) these changes could be mediated by changes in the molecular weight or the concentration of cell surface polymers. In addition, polymer solution theory (*e.g.*, Ref. 53) predicts that alterations in polymer-solvent interactions (conformation) at the cell surface will be expected to influence such mixing behaviour.

We have not yet obtained any direct evidence that the latter factor (cell surface polymer conformation) exerts an influence on cell surface/polymer phase interactions, but several experiments are consistent with the hypothesis that changes in the molecular weight and amount of cell surface polymer influences cell-medium contact angles.

5 CELL SURFACE COMPOSITION AND SURFACE THERMODYNAMICS

Our approaches to the experimental investigation of the relationships between cell surface composition and surface thermodynamics have taken two routes: synthesis and analysis. First, we carried out some simple recombination experiments in which the surface thermodynamic behaviour of model (synthetic) surfaces made of defined chemical components was compared with the behaviour of intact cells. The other route was correlating contact angle measurements with biochemical analysis of the membrane composition of cells cultured under conditions which produce well-defined permanent changes in membrane composition.

The experimental basis of the synthetic approach is the ability to measure contact angles on defined molecular monolayers at defor-

mable interfaces. The experimental procedure is chosen to facilitate both contact angle measurements and analysis of interface shape, while at the same time circumventing the problems of surface film leakage which attend traditional film balances of the Langmuir-Wilhelmy type.⁵⁴ This is achieved in a "mini surface balance," illustrated schematically in Figure 5A. A five-phase system is used: a hydrophilic substrate (*e.g.*, 1% agar gel) provides a leakproof base for a lipid monolayer spread at an oil/water interface. By adding or removing oil the area of the monolayer can be controlled just as in a Langmuir trough. The choice of a dense hydrophobic and oleophobic liquid fluorocarbon ("FC40," perfluoromethyldecalin, 3M Company) allows the creation of a fluid oil/water interface which is deformed by gravity, but not by the hydrocarbon test drop, whose density (1.02 g/ml) is chosen to be slightly greater than that of the aqueous phase (1.01 g/ml), but much less than that of the fluorocarbon (1.85 g/ml). We call this system a pseudo-solid, since with respect to hydrocarbon/water contact angles the fluorocarbon oil behaves as a solid. That is to say, because of the density differences the usual "Neumann triangle" relationship associated with deformation at fluid three-phase lines⁵⁴ does not occur. As a "solid" this system is rather unusual: since the surface monolayer is both smooth and homogeneous, it is free from contact angle hysteresis, and the contact angles measured on this surface are unambiguously equilibrium angles. With respect to profile analysis, however, the fluorocarbon behaves as a true fluid. Figures 5B illustrates this experimental arrangement when a phospholipid monolayer is spread at the oil-water interface: the contact angle of 105° corresponds to a measured monolayer-water interfacial free energy of 3.6 mJ m⁻² on this partially compressed monolayer.

When isolated membrane proteins are added, the wetting behaviour of intact cells can be reproduced. Figure 6 shows the effects of progressive addition of membrane components on the wetting behaviour of synthetic and native erythrocyte surfaces. In 6A, the left-hand photograph shows a hydrocarbon test droplet resting on top of a fluorocarbon drop (diameter 1 cm); the hydrocarbon has spread to a contact angle of about 5°, since in so doing the high energy (50 mJ m⁻²) fluorocarbon/water interface is replaced by the lower energy hydrocarbon/water interface (in this case, 22.5 mJ m⁻²). In the adjacent photograph a phospholipid

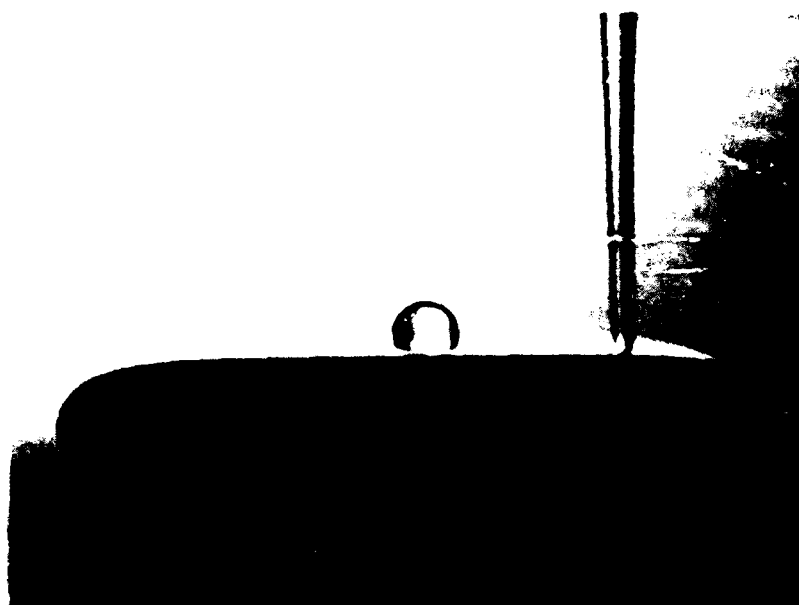
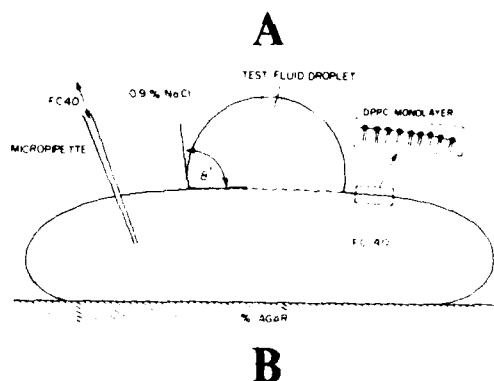


FIGURE 5 Simultaneous equilibrium contact angle measurement and shape analysis at fluid interfaces. A Schematic diagram of the mini-surface balance with a dense "pseudo-solid" (fluorocarbon) subphase. B Hydrocarbon droplet contact angle (the test drop is a 1:1 mixture of dibutyl/dioctyl phthalate, density 1.02 g/ml, interfacial free energy 22.5 mJ m^{-2}) and interface profile of a dipalmitoyl phosphatidylcholine monolayer at a fluorocarbon oil-water interface. The contact angle is 105° and the monolayer-water interfacial free energy is 3.6 mJ m^{-2} . Reproduced from Ref. 42.

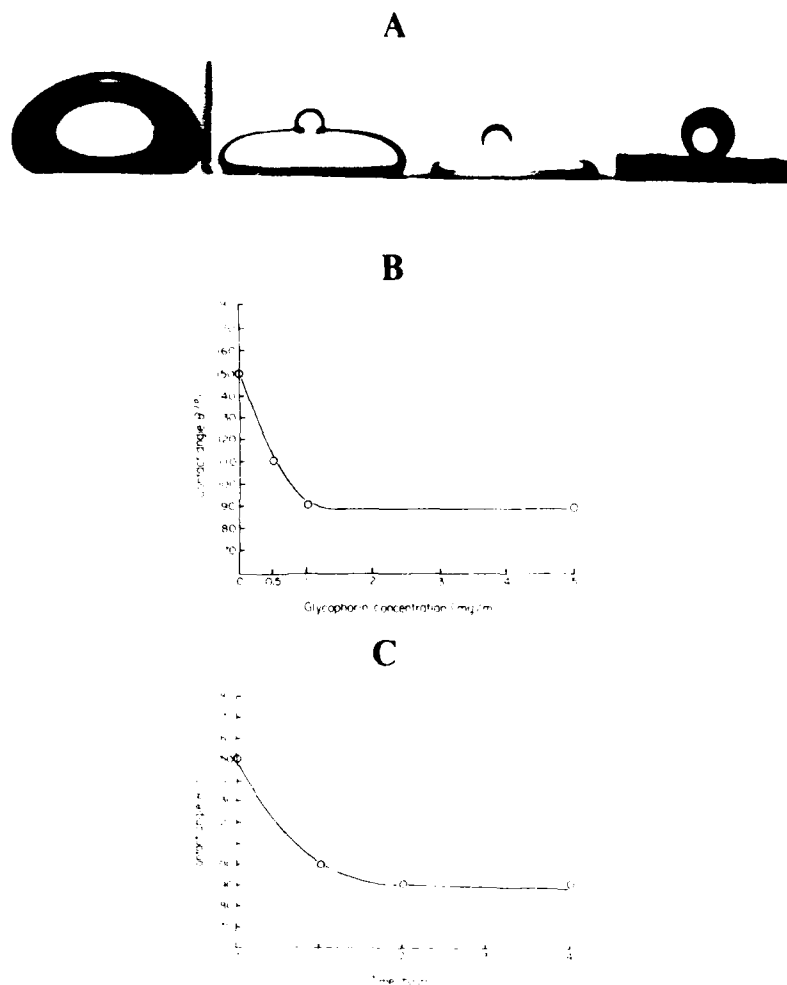
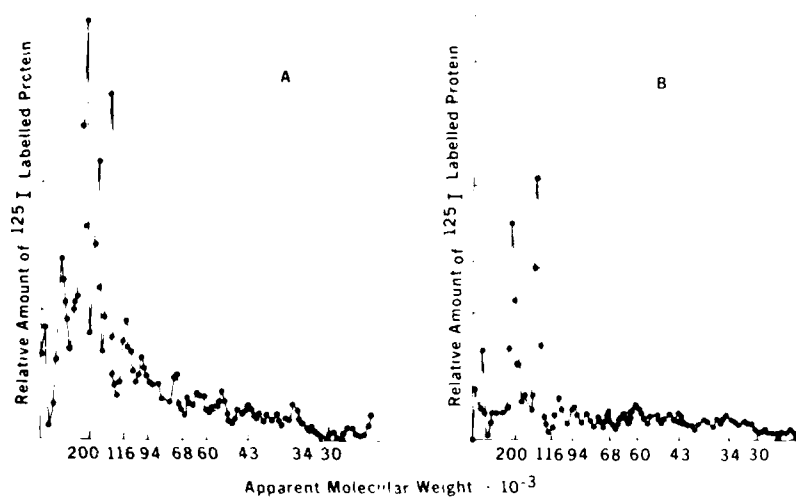


FIGURE 6 Interfacial free energies of native and model (reconstituted) cell surfaces. A Surface wetting by oil droplets (1:1 dibutyl phthalate/dioctyl phthalate). a: fluorocarbon/water interface, $\theta = 5^\circ$; b: phospholipid/water interface, $\theta = 90^\circ$; c: phospholipid/glycophorin/water interface, $\theta = 175^\circ$; d: intact erythrocytes, $\theta = 175^\circ$. B Effect of bulk phase glycophorin concentration on dextran/polyethylene glycol contact angles at the oil/phospholipid/water interface. 4%/4% phase system. C Kinetics of glycophorin effects on dextran/polyethylene glycol contact angle at the oil/phospholipid/water interface. 4%/4% phase system. Reproduced from Ref. 49.

monolayer (dipalmitoyl phosphatidylcholine) has been spread at the fluorocarbon/water interface: the equilibrium balance between interfacial free energy and the gravitational force arising from the density difference between the FC40 and aqueous phases now occurs with substantial deformation and flattening of the FC40 drop, and an increase in the contact angle to 90° , at a monolayer-water interfacial free energy of 5 mJ m^{-2} . Next, addition of the major erythrocyte membrane glycoprotein glycophorin to the bulk phase results in the same wetting behaviour as observed in intact erythrocytes (right-hand photograph): contact angles of 175° are observed in both cases. When polymer phase systems are used instead of oil droplets, the glycophorin addition is associated with similar wetting behaviour to that observed in intact cells, except that the wetting changes are in the opposite direction: glycophorin causes the dextran contact angles to decline. This decline shows saturation with respect to bulk phase protein concentration (6B) and constancy with respect to time (6C). Of course, the correlations between the wetting behaviour of these model membranes and real cells are only semi-quantitative, since the monolayer glycophorin concentration is not known in these experiments. However, the experiments do suggest that the contact angles are indeed a function of the cell surface protein concentration. This conclusion was corroborated by experiments in which the amount of radiolabelled protein adsorbed at the interface was directly correlated with the reduction in dextran contact angle.^{55,56}

In complementary experiments, the protein composition of cell membranes was varied *in vivo* by manipulating the growth conditions of cells in culture, and the measured contact angles compared with the measured glycoprotein composition of the isolated membranes.⁵⁷ V79 fibroblasts were exposed to varying oxygen concentrations, a procedure known to induce long-lasting

FIGURE 7 Environmental effects on membrane composition and surface thermodynamics of cultured V 79 fibroblasts. A Radiodensitometric profile of membrane glycoproteins from normal aerobic (A) and hypoxic (B) fibroblasts. ^{125}I -concanavalin A was used to label the membrane glycoproteins separated by polyacrylamide gel electrophoresis. B Comparison of contact angles formed by dextran droplets from a 4%/4% phase system on layers of V79 fibroblasts grown under aerobic (a) and hypoxic (b) culture conditions. Reproduced from Ref. 57.

A**B**

a



b



changes in membrane protein composition and in substrate adhesion. The isolated cell membrane proteins were separated by gel electrophoresis, and labelled with a radioactive ligand, the mannose binding lectin concanavalin A. The densitometric profiles of the autoradiograms of the isolated proteins are shown in Figure 7A: hypoxia induces a reduction in both amount and molecular weight of the membrane proteins. As expected on the basis of the discussion in section 3 above, these changes are associated with increased dextran contact angles (B). Since both concentration and molecular weight changed, these experiments cannot clearly assign the contact angle changes to either factor and more quantitative work in this area is needed. About the relationship of surface wetting to the third factor—macromolecule conformation—we can as yet say nothing, except to propose that polymer phase wetting studies like these reported here may turn out to be a useful probe of the configuration of macromolecules at surfaces.

6 STIMULUS-RESPONSE COUPLING AND CELL SURFACE WETTING

In the experiments just described, altering the cell culture conditions was associated with morphological evidence of reduced cell-substrate adhesion,⁵⁷ and the increased dextran contact angles observed on the less-adherent cells support the hypothesis that adhesion and cell surface/polymer phase thermodynamics are somehow related. However, the hypoxia experiments represent rather drastic changes in cell behaviour and are not a very sensitive test of the hypothesis. We have, therefore, examined several cellular responses which are related to more physiological adhesive events *in vitro*, and we have examined in some detail the time- and dose-relationships between cell surface thermodynamic changes and the stimuli which elicit the cellular responses.

One cell adhesion process which has been studied in considerable depth by a number of workers is the response of blood neutrophils to the chemotactic peptide N-formyl methionyl leucyl phenylalanine (fMLP). This low molecular weight ligand elicits several behavioural responses from the neutrophil, including both increased cell-substrate and cell-cell adherence (aggregation), and a variety of

biochemical responses including the production of oxygen-free-radicals.⁵⁸ Figure 8A shows the dose-response relationships for three photometric indices of these responses: perpendicular light scattering, light transmission and oxygen-radical-dependent chemiluminescence.^{59,72} The light scattering changes predominantly reflect polarisation of the cells, the light transmission changes are

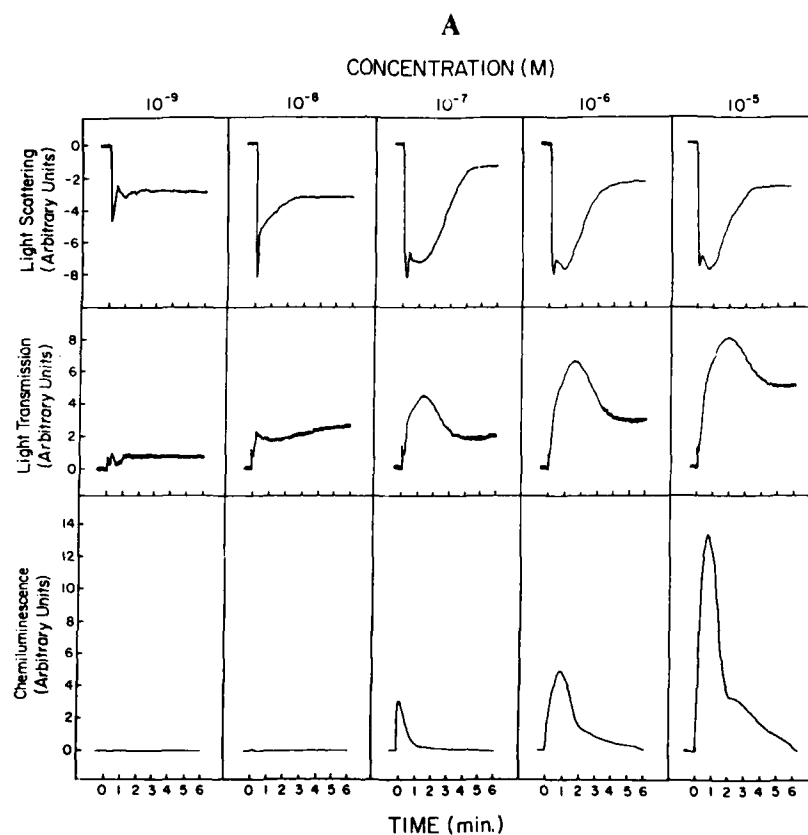


FIGURE 8 Effects of the soluble chemoattractant tripeptide N-formyl methionyl leucyl phenylalanine (fMLP) on human blood neutrophil behaviour and surface thermodynamics in polymer phases.⁵⁹ A Dose-response curves for photometric measurements of the responses of human neutrophil suspensions to fMLP. B Dose-response relations of neutrophil contact angle changes associated with exposure to fMLP. Left: 10^{-6} M ($\theta = 60^\circ$); centre 10^{-7} M ($\theta = 73^\circ$); right: control ($\theta = 95^\circ$).

B

0.1 mm

FIGURE 8 (continued)

associated with cell adhesion (aggregation), and the chemiluminescence reflects the biochemical activation of the cells. All of these responses show a dose-dependence on the fMLP concentration. So do the changes in the cell/dextran phase contact angles illustrated in Figure 8(B), which show a 50% increase in the work of adhesion to the dextran phase between the control and maximally fMLP-stimulated cells, *i.e.*, a ΔW_{adh} of $2.0 \mu\text{J m}^{-2}$.

Macrophages are another type of cell which show dose-response relations for stimulus-induced adhesion in polymer phases. When macrophages are exposed to particulate stimuli (Figure 9) they show dose relations between measurements of biochemical activation (the production of oxygen radicals and the secretion of lysosomal enzymes) and changes in the adhesion of the cells to the polymer phases.⁶⁰ Figure 10A is a comparison of the potency of a number of stimuli in eliciting changes in macrophage surface thermodynamics: serum-treated yeast particles (opsonized zymosan) are the most potent stimulators of changes in adhesion to the polymer phases, followed by the protein kinase C activator phorbol myristate acetate

(PMA) and the arachidonic acid metabolite leukotriene D (LTD₄).⁶¹ As with the effects of fMLP on neutrophils, the contact angle dose-response curve for leukotriene D₄ (Figure 10B) indicates a sensitive and specific relationship between the surface thermodynamic measurements and cell stimulation by the ligand.⁶¹

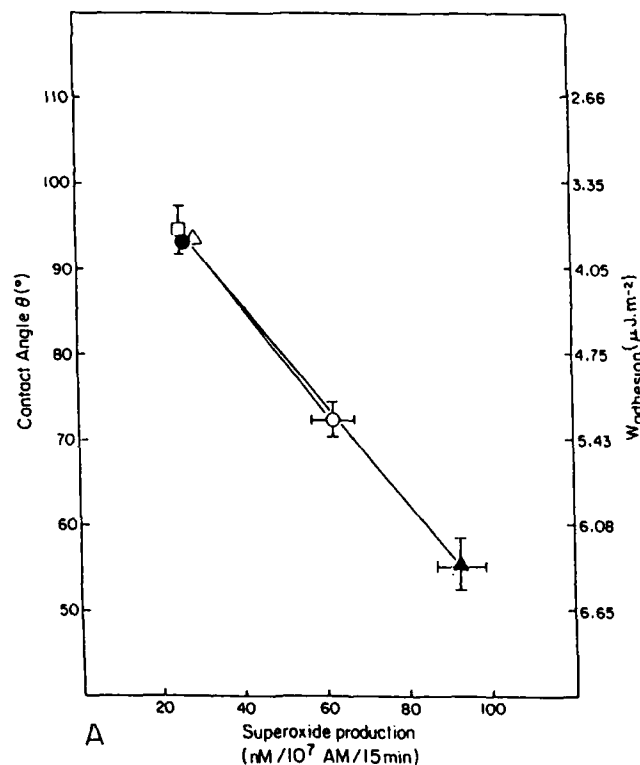


FIGURE 9 Effects of the particulate stimuli opsonized zymosan and non-opsonized silica on porcine alveolar macrophage surface thermodynamics and enzyme activity.⁶⁰ A Relation between contact angles, work of adhesion and superoxide anion production by macrophages exposed to zymosan (circles) or silica (triangles). Opsonized particles are indicated by filled symbols, non-opsonized particles by open symbols. Control cells are indicated by the square. 4%/4% phase system. B Relation between contact angles, work of adhesion and lysosomal enzyme release by alveolar macrophages exposed to zymosan or silica particles. Symbols as denoted in A. Dotted line indicates release of N-acetyl beta glucosaminidase, solid line release of arylsulfatase. 4%/4% phase system. Each point is the mean \pm S.E. mean of 6 separate enzyme determinations or 30–40 separate contact angle measurements.

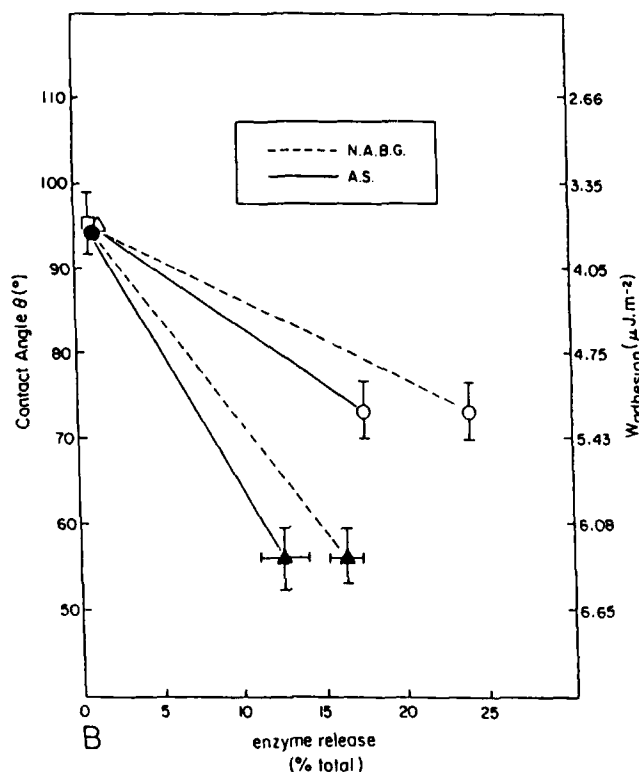
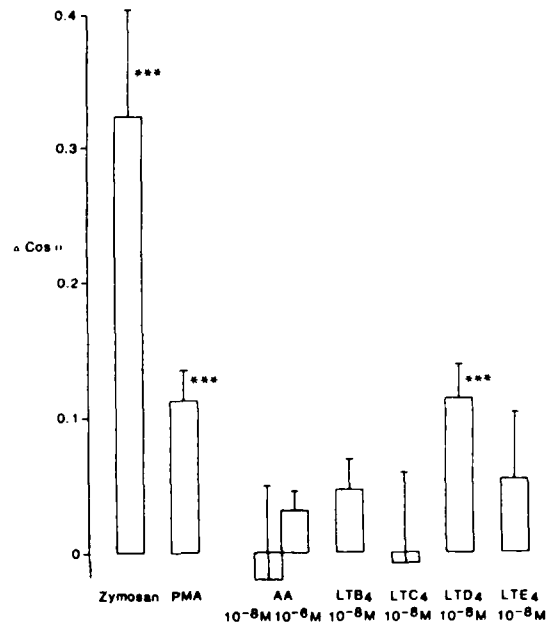
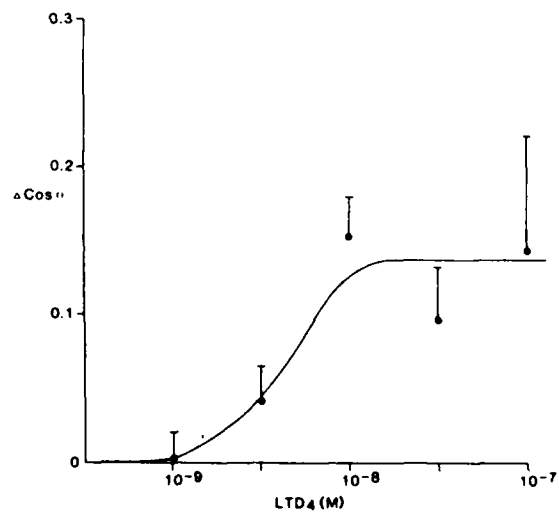


FIGURE 9 (continued)

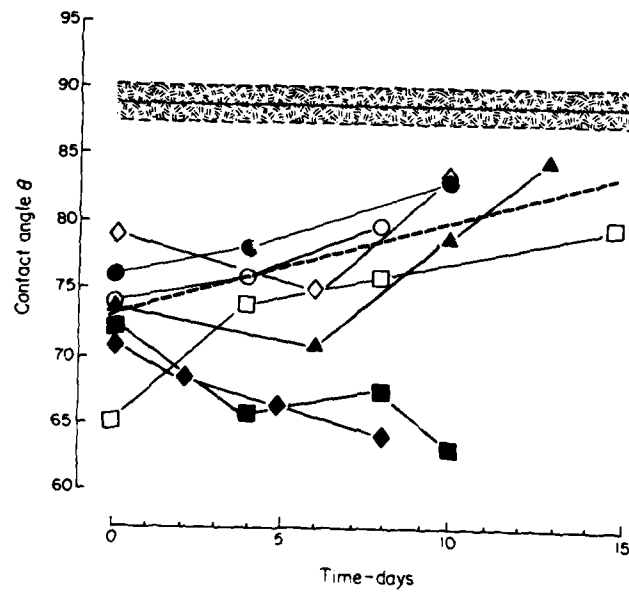
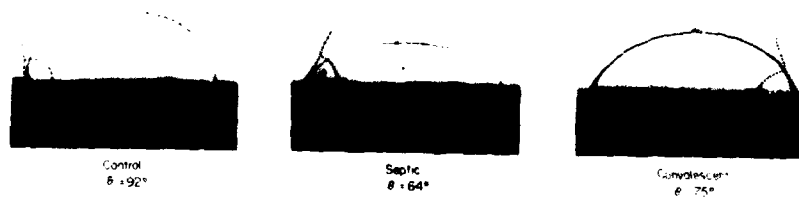
FIGURE 10 Effects of particulate and soluble stimuli on surface thermodynamics of alveolar macrophages in the 4%/4% phase system.^{61,62} A Comparison of the surface thermodynamic effects of the particulate stimulus opsonised zymosan with the effects of various soluble ligands. Differences in surface free energy are expressed as the change in the cosine of the contact angle between control and treated cells. Asterisks indicate differences in $\cos \theta$ which are significant at the $p < 0.001$ level. PMA, phorbol myristate acetate; AA, arachidonic acid; LTB_4 - C_4 - D_4 and - E_4 , leukotrienes B to E.⁶¹ B Dose-response curve for the effects of LTD_4 on alveolar macrophage surface free energy in the dose range 10^{-9} M to 10^{-7} M. Each point is the mean \pm S.E. mean of 20-30 separate contact angle measurements in 6 different experiments.⁶²



A



B

A**B**

Finally, Figure 11 shows the results of a study of human neutrophil surface thermodynamics in a clinical disorder which is associated with massive intravascular neutrophil adhesion, the Adult Respiratory Distress Syndrome, or "A.R.D.S."^{70,71} In Figure 11(A) the contact angles on isolated neutrophils from 7 patients with A.R.D.S. are compared with normal age- and sex-matched controls. In this small sample, two trends are apparent: first, there is a significant lowering of the neutrophil contact angles in all patients when compared with the control group and, second, there is a correlation with clinical course. The two patients who died showed continuously lowered contact angles, while the convalescing patients showed a gradual return towards control values. The contact angle changes shown in Figure 11(B) are reminiscent of the *in vitro* response of isolated neutrophils to fMLP, suggesting that the changes may be due to *in vivo* activation of the cells by chemoattractants.

These studies collectively point to a general association between stimulus-specific cell activation and increased cell adherence to the dextran phase of the polymer phase systems; these associations do not however, prove that there is necessarily any causal relationship between the changes in the cell surface which produce the contact changes, and the molecular events which actually mediate cell-cell, cell-particle or cell-substrate interactions. That is to say, it may not be the adhesive events *per se* which produce the contact angle changes, but some other, rather ubiquitous process associated with cell surface activation. In the absence of information about the molecules actually responsible for mediating any particular adhesive events, this conjecture cannot be directly tested. The only proof of a causal relationship between cell adhesion and the surface thermo-

FIGURE 11 Neutrophil surface thermodynamic changes in a clinical disorder of neutrophil adhesion, the Adult Respiratory Distress Syndrome (A.R.D.S.).⁷¹ A Contact angles and clinical courses of 7 patients with A.R.D.S. and 4 normal controls (hatched area). The standard errors of the mean (not shown) are around 3%. The two downward sloping curves (black diamonds and squares) were for non-survivors; the remainder of the patients survived. Each point is the mean of 30-40 separate contact angle measurements. B Contact angles on neutrophils isolated from a patient with A.R.D.S. associated with systemic sepsis (the patient represented by the open squares in A.), compared with those from a healthy age- and sex-matched control subject.

dynamic measurements would be the demonstration that the isolated molecules which actually do mediate the ligand-induced adhesive interaction(s) described above could reproduce the wetting changes in recombination experiments such as those described in section 5. In the meantime, we propose a working hypothesis which we believe is consistent with the data so far, and which suggests a somewhat different way of looking at the thermodynamics of ligand-specific cell adhesion from the sequence of events described by model 1.

7 POLYMER MIXING AND CELL ADHESION

The hypothesis is that the binding of structurally specific, adhesion promoting stimuli (such as fMLP) to cell surface receptors induces changes in cell surface molecules which are responsible for adhesion of the cells both to polymer phases and to other cells or substrates.

The experimental results discussed above indicate that specific ligand-induced cell adhesion to foreign particulate surfaces (phagocytosis) or to other cells (aggregation), and such biochemical evidence of cell activation as enzyme activity or secretion can all be correlated in a ligand dose-dependent fashion with changes in the surface affinity of the cells for polymer phase solutions. In general, when cells become stickier to substrates or to each other they also become stickier to the dextran phase of the dextran/PEG phase system. Some evidence also suggests the opposite behaviour: inhibition of adhesion is associated with an increased affinity for the PEG phase.^{57,70} These general trends are similar to the surface tension studies reported by Neumann and co-workers¹⁹ for a variety of cell-particle and cell-substrate adhesive processes, where lower surface tension (more hydrophobic) cells are generally less adhesive than higher surface tension (more hydrophilic) cells.

None of these correlations proves that any averaged thermodynamic properties of the cell surface are causally related to any of the adhesive events occurring in these experiments. The correlations could be merely with some effect of cell activation on cell surface chemistry which happens to occur under the same conditions as adhesion; such coincidences, while they might be interesting in their own right, would not be expected to contribute much insight into the mechanisms of adhesion.

On the other hand, it is possible that the correlations actually are causally related to the adhesion occurring in these experiments, and that the changes in cell/polymer phase affinity do reflect the intermolecular forces which drive cell adhesion under these conditions. If this is the case, then it is necessary to modify the "specific bonding, non-specific repulsion" model for cell adhesion elicited by small ligands.

We suggest that adhesion elicited by structurally specific low molecular weight, non-cross linking ligands may be better described by a "specific induction, non-specific execution" model, *i.e.*, model 2. In circumstances where large bridging molecules such as lectins or multivalent antibodies provide both recognition and adhesion functions, model 1 serves well. But where the recognition and adhesion are separate molecular processes, and particularly in those kinds of rapid, reversible adhesion events such as the ones studied here (typically the kind of adhesion encountered in the blood and in host defence mechanisms), model 2 suggests that it may be useful to analyse cell adhesion as a problem in polymer phase mixing.

The simplest form of such a model is based on a proposal like that of Steinberg,³⁵ that cell adhesion occurs when the free energy of the adherent state is lower than that of the non-adherent state. An equilibrium approach to cell adhesion requires that the adhesion is measured on a time scale that is slower than biochemical transients such as those shown in Figure 8. In other words, that the cell surface is considered constant with respect to irreversible metabolic processes which may move the cell from one metastable state to another.²² The approach describes simply what the adhesion molecules prefer to do and where they prefer to go after they have been synthesised, and before they have been degraded. Such an approach has definite limitations: it will not, for example, account for processes such as cell "grip" which depend on the expenditure of contractile energy.⁶³ However, to the extent that the model will not include irreversible sources of cell adhesive behaviour, it may in fact allow an experimental separation of those processes which depend on pure adhesion ("stick") and those which depend on "grip." That is to say, the failures of the model may be as useful as its successes.

Consider two cell types, a and b: equilibrium adhesion between the two cells can only take place if the free energy of adhesion.

(W_{a-b}) is negative

$$\text{i.e., } W_{a-b} < 0 \quad (4)$$

the condition

$$W_{a-b} = 0 \quad (5)$$

corresponds to a non-adherent dispersion of the cells; the condition

$$W_{a-b} > 0 \quad (6)$$

(i.e., a positive free energy of adhesion) corresponds to de-mixing or repulsion of the cells.

For the three types of adhesion $a-a$ (homotypic aggregates of a), $b-b$ (homotypic aggregates of b) and $a-b$ (heterotypic aggregates of a and b), and the three conditions $W < 0$ and $W > 0$, ten different combinations can be distinguished.³⁴ In the blood, for example, Eq. (4) could correspond to the margination of leukocytes, Eq. (5) to the free mixing of non-adhering cells in the plasma and Eq. (6) to the repulsion of the normal endothelium for blood components.

Let us now take one of the simplest possible models of a cell—a non-deformable particle coated with a completely deformable (liquid-like) polymer solution. The free energies of adhesion in Eq. [4–6] may be replaced with a polymer interaction parameter, such as the Flory–Huggins χ .⁵³ Equivalent treatments (e.g., Refs 64, 65) attribute positive (repulsion) or negative (attraction) interaction energies to an effective polymer “excluded volume.” In terms of surface thermodynamics in polymer phases, adhesion ($W < 0$) corresponds to phase mixing (minimum interfacial free energy or a contact angle of 0° as in Figure 4B), while repulsion (maximum interfacial free energy or a contact angle of 180°) corresponds to phase separation. To the extent that cells are actually deformed on contact, deformation energies will also enter into the balance of forces between polymer affinity and the work of cell deformation.^{17,31}

If this cell surface phase mixing and demixing behaviour does in fact mediate the kind of cell adhesion events described by model 2, the contact angle changes are clearly stating that the adhesion molecules must be quite widely distributed on the cell surface. The equivalent solution of an activated neutrophil is a 3.2% phase of

dextran 2×10^6 . Assuming, for example, that the adhesion molecules have an average molecular weight of 200 k daltons (*e.g.*, see Figure 7A), then the surface concentration of the adhesion molecules could well be in the 0.3% or micromolar range. This is many orders of magnitude higher than the concentrations at which most ligands activate their specific receptors in cell membranes;⁶⁴ it may be noteworthy however that the fibrinogen binding site in blood platelets (the so-called glycoprotein IIB-III complex) actually constitutes 18% of the platelet membrane protein.⁶⁷

Model 1 describes the situation where the specificity of both recognition and adhesion lies in the agglutinating molecules. By contrast, model 2 describes cell adhesion as a problem in polymer phase mixing, and attributes adhesion (either positive or negative) to stimulus-induced changes in the concentration, molecular weight or conformation of glycocalyx polymers, and consequent changes in their free energies of mixing with polymers on the surfaces of other cells or substrates.

Supported by Grants from the Medical Research Council of Canada (D.M., S.S., E.T. and N.P.) and the Heart and Stroke Foundation of Ontario (D.M.).

References

1. J. M. Lackie, and P. C. Wilkinson, in *White Cell Mechanisms: Basic Science and Clinical Aspects*, Kroc Foundation Series volume 16, (H. J. Meiselman, M. A. Lichtman and P. L. LaCelle, Eds.) (New York, Liss, 1983).
2. R. J. Good, *J. Colloid Interface Science* **59**, 398 (1977).
3. R. L. Hoover, *et al.*, *J. Cell Sci.* **45**, 73 (1980).
4. E. A. Evans, *Biophys. J.* **30**, 365 (1980).
5. J. T. O'Flaherty, H. J. Showell, E. L. Becker, and P. A. Ward, *Am. J. Pathol.* **95**, 433 (1979).
6. A. S. G. Curtiss, *J. Embryol. Exp. Morph.* **22**, 305 (1969).
7. H. L. Goldsmith, and J. C. Marlow, *Proc. Roy. Soc. B.* **182**, 351 (1973).
8. R. M. Hochmuth, N. Mohandas and P. L. Blackshear, *Biophys. J.* **13**, 747 (1973).
9. J. V. Forrester and J. M. Lackie, *J. Cell. Sci.* **70**, 93 (1984).
10. G. V. R. Born, *Nature* **194**, 927 (1962).
11. P. Latimer, G. V. R. Born and F. Michal, *Arch. Biochem. and Biophys.* **180**, 151 (1977).
12. C. J. van Oss, C. F. Gillman and A. W. Neumann, in *Phagocytic engulfment and cell adhesiveness as surface phenomena* (Marcell Dekker, New York, 1975).
13. M. A. Hubbe, *Prog. Surface Sci.* **11**, 65 (1981).
14. J. N. Israelachvili, *Intermolecular and Surface Forces* (Academic Press, New York, 1985).
15. D. M. Le Neveu, R. B. Rand and V. A. Parsegian, *Nature* **259**, 601 (1976).

16. S. T. Hoffstein, R. S. Friedman and G. Weissmann, *J. Cell. Biol.* **95**, 234 (1982).
17. P. Latimer, *Ann. Rev. Biophys. Bioeng.* **11**, 129 (1982).
18. W. O. Fenn, *J. Gen. Physiol.* **4**, 373 (1922).
19. A. W. Neumann, *et al.*, *Ann. N.Y. Acad. Sci.* **416**, 276 (1983).
20. P. A. Albertsson, *Partition of cell particles and macromolecules*, 2nd Ed. (Wiley Interscience, New York, 1971).
21. K. A. Sharp, E. A. Evans and D. E. Brooks, "Cell partitioning in aqueous polymer two phase systems and cell surface free energies related through contact angles," *ACS Colloid Symposium, Toronto*, **A216**, (1983).
22. G. I. Bell, M. Dembo, and P. Bongrand, *Biophys. J.* **45**, 1051 (1984).
23. W. A. Frazier, L. Glaser and Gottlieb, *Cellular Recognition* (Alan R. Liss, Inc., New York, 1982).
24. W. R. Springer and W. R. Barondes, *Proc. Natl. Acad. Sci. USA.* **79**, 6561 (1982).
25. G. M. Edelman, *Science* **219**, 450 (1983).
26. G. Thorsen and H. Hint, *Acta Chir. Scand. Suppl.* **154**, 1 (1950).
27. E. A. Evans, *Biophys. J.* **48**, 175 (1985).
28. E. A. Evans, *ibid.* **48**, 185 (1985).
29. P. R. Craddock, *et al.*, *J. Clin. Invest.* **59**, 879 (1977).
30. G. B. Mackaness, *J. Inf. Dis.* **123**, 439 (1971).
31. A. S. G. Curtiss, *Symp. Soc. Exp. Biol.* **32**, 51 (1978).
32. E. A. Evans and V. A. Parsegian, *Ann. N.Y. Acad. Sci.* **416**, 13 (1983).
33. A. J. Clark, *The Mode of Action of Drugs on Cells* (Arnold, London, 1933).
34. L. von Bertalanffy, *Science* **111**, 23 (1950).
35. M. S. Steinberg, in *Cellular membranes in development*, M. Locke, Ed. (Academic Press, NY, 1963), p. 321.
36. T. Young, *Miscellaneous Works, Vol. 1* G. Peacock, Ed. (Murray, London, 1985), p. 418.
37. R. J. Good, *J. Amer. Chem. Soc.* **74**, 5041 (1952).
38. A. W. Neumann, in *Advances in Colloid and Interface Science, Vol. 4*, M. Kerfer, Ed. (Academic Press, New York, 1974) p. 105.
39. J. Boyce, S. Schürch and D. J. L. McIver, *Atherosclerosis* **37**, 361 (1980).
40. A. W. Neumann, R. J. Good, C. J. Hope and M. Sejpal, *J. Colloid Interface Sci.* **49**, 291 (1974).
41. H. T. Tien, *J. Phys. Chem.* **71**, 3395 (1976).
42. S. Schürch and D. J. L. McIver, *J. Colloid. Interface Sci.* **83**, 301 (1981).
43. J. T. Danielli and H. Dawson, *J. Cell. Comp. Physiol.* **5**, 494 (1935).
44. D. E. Brooks, G. V. F. Seaman and H. Walter, *Nature (London) New Biol.* **234**, 61 (1971).
45. S. Schürch, D. F. Gerson and D. J. L. McIver, *Biochem. Biophys. Acta* **640**, 557 (1981).
46. F. D. Raymond and D. Fisher, *Biochim. Biophys. Acta* **596**, 445 (1980a).
47. S. Hartland and R. W. Hartley, *Axisymmetric Fluid-liquid Interfaces* (Elsevier, New York, 1976) p. 552.
48. D. J. L. McIver and S. Schürch, "Free energies at the biosurface-water interface estimated from contact angles in two-phase aqueous polymer systems," in *The Biophysics of Water*, Felix Franks, Ed. (John Wiley, NY, 1982), p. 151.
49. D. J. L. McIver and S. Schürch, *Biochim. Biophys. Acta* **691**, 52 (1983).
50. J. F. Boyce P. C. Wong, S. Schürch and M. R. Roach, *Circ. Res.* **53**, 372 (1983).
51. A. W. Zisman, in *Contact Angles, Wettability and Adhesion, Advances in Chemistry, Vol. 43* (Applied Publications; American Chemical Society, Washington, D.C. 1964), Chapter 1.

52. L. A. Girifalco and R. J. Good, *J. Phys. Chem.* **61**, 904 (1957).
53. P. J. Flory, *Principles of Polymer Chemistry* (Cornell University Press, Ithaca, N.Y., 1953).
54. A. W. Adamson, *Physical Chemistry of Surfaces*, 3rd Ed. (John Wiley and Sons, New York, 1976).
55. S. Schürch, K. Ellis and D. J. L. McIver, "Protein adsorption at a lipid-water interface investigated by using phase separated aqueous polymers" *American Chemical Society, 57th Colloid and Surface Symposium*, **A222** (1983).
56. S. Schürch, J. A. Wallace, M. H. Wilkinson and D. J. L. McIver, in *Surfactants in Solution*, K. L. Mittal, Ed. (Plenum, 1987), in press.
57. S. A. Johnstone, *et al.*, *Biochem. Biophys. Acta* **815**, 159 (1985).
58. H. B. Kaplan, H. S. Edelson, R. Friedman and G. Weissman, *Biochim. Biophys. Acta* **721**, 55 (1982).
59. D. J. L. McIver and S. Schürch, Unpublished results.
60. D. J. L. McIver, S. Schürch and N. A. M. Paterson, *Langmuir*, submitted, 1987.
61. N. A. M. Paterson, D. J. L. McIver and S. Schürch, *Immunology* **56**, 153 (1985).
62. N. A. M. Paterson, D. J. L. McIver and S. Schürch, *Prostaglandins, Leukotrienes and Medicine* **25**, 147 (1986).
63. D. A. Rees, C. W. Lloyd and D. Thom, *Nature (London)* **267**, 124 (1977).
64. N. G. Maroudas, *ibid.* **254**, 695 (1975).
65. A. Silberberg, *Ann. N.Y. Acad. Sci.* **416**, 83 (1983).
66. R. Snyderman and E. J. Goetzl, *Science* **213**, 830 (1981).
67. L. K. Jennings and D. R. Phillips, *J. Biol. Chem.* **257**, 10458 (1982).
68. Y. Rotenberg, L. Boruvka and A. W. Neumann, *J. Colloid Interface Sci.* **93**, 169 (1983).
69. M. Hato, T. Sakai and B. A. Pethica, *Langmuir* **1**, 541 (1985).
70. W. J. Sibbald, *et al.*, *Ann. N.Y. Acad. Sci.* **384**, 496 (1982).
71. D. J. L. McIver, W. J. Sibbald and S. Schürch, Unpublished results.
72. H. Valencia and D. J. L. McIver, *C.F.B.S.* **29**, 169 (1986).

Surface Characteristics of Hydroxyapatite and Adhesive Bonding. I. Surface Characterization†

D. C. SMITH,‡ D. G. MURRAY,* J. D. ZUCCOLIN and N. D. RUSE

*University of Toronto and *Medipro Sciences, Toronto, Canada*

(Received November 15, 1986)

Adhesion to hydroxyapatite (HA), the mineral phase of calcified tissues, is important in cellular attachment and bonding of synthetic adhesive materials. The surface preparation of HA was found to affect the adhesion greatly. A pure synthetic HA was studied to examine the effect of commonly-used preparative techniques on surface morphology and activity. Surface grinding and polishing and organic acid etching gave rough surfaces that were hydrophobic. Etching with HCl or HNO₃ and firing at 800°C gave hydrophilic surfaces. ISS, SIMS and ESCA studies showed various degrees of organic and inorganic contamination. Plasma cleaning removed hydrophobic contaminants but inorganic contamination from the plasma vessel increased as time of exposure was increased. It was evident that current preparative procedures give highly variable surfaces that would be expected to influence adhesion of both monomer-polymer adhesive systems and cells.

KEY WORDS Adhesion; dentistry; morphology; preparative techniques; surface characterization; synthetic hydroxyapatite.

INTRODUCTION

Hydroxyapatite (HA), $\text{Ca}_{10}(\text{PO}_4)_6(\text{OH})_2$, is the principal inorganic (mineral) phase of calcified tissues. The outer enamel layer of teeth

† Presented at the Tenth Annual Meeting of The Adhesion Society, Inc., Williamsburg, Virginia, U.S.A., February 22-27, 1987.

‡ To whom correspondence regarding this paper should be addressed at University of Toronto, Faculty of Dentistry, 124 Edward Street, Toronto, Ontario M5G 1G6 Canada.

is almost 98% HA and the inner dentin and bone both contain about 60% HA. These tissues consist of a mass of small crystallites bonded together by a protein aqueous gel.¹ Adhesion between proteins and the HA is obviously important to structural integrity; protein binding is also important in relation to cellular attachment of the soft tissues and to the attachment of bacteria as in the instance of bacterial plaque accumulation on teeth. In addition to the adhesion of *in vivo* substances to HA, there is considerable interest in bonding extra-corporeal materials to the mineral phase of teeth and bones for reconstructive surgery and dentistry.

In dentistry, extensive use is made of acid etching of enamel to bond polymerizable coating and filling materials;² recently, so-called "dentin-bonding agents" have been developed that are of interest also as systems that have potential for adhesion to bone in surgical reconstruction.³ These latter materials are monomer systems, based on polycarboxylic acid or polyphosphate or phosphonate derivatives,³⁻⁵ which are polymerized after application through free radical initiation by a peroxide-amine system or by visible light-activated diketones.⁶ Their use may be preceded by an acid etch treatment procedure. In principle, bonding occurs through chemisorption and complex formation of functional groups to the Ca in the HA.³ A second dental adhesive system is based on aqueous polyacrylic acid cements.^{5,7,8} These zinc polyacrylate and glass ionomer cements show substantial bonding *in vivo* via the polyacrylate anion interaction with the Ca^{++} of the enamel and dentin. The latter mechanism has been established by a variety of investigations.⁸⁻¹² Little work has been done on the mechanism of attachment of the polymerizable monomer systems, however, although numerous studies of bond strength have been carried out.^{3,13-15}

The mineral phase of bone and teeth is a defect HA containing numerous other ions, notably F.¹ However, synthetic hydroxyapatite produced by sintering the precipitated material under controlled conditions¹⁶ has well-defined reproducible properties^{16,17} and has been shown to be similar to enamel in properties such as fluoride uptake,¹⁸ bacterial plaque attachment¹⁹ and bone adherence.²⁰ The majority of the existent commercial and experimental dentin adhesive systems have been formulated on the basis of specific reactivity towards HA^{3,4} and should, therefore, display bonding to both the synthetic and natural substrates.

The purpose of the present work was to study factors affecting the potential bonding of representative adhesive systems to synthetic HA to establish a more basic approach to improved materials. In these experiments the attachment of various reactive monomers and primers to a synthetic HA has been investigated.

Preliminary work showed that the adsorption and stability of attachment of primers to HA was greatly affected by the surface preparation. Thus, a necessary approach to the problem was first to characterize the HA surface better and this is the subject of the present report.

MATERIALS AND METHODS

(A) Hydroxyapatite

A commercial pure sintered hydroxyapatite[†] was used in the present work. The preparation and properties of the basic material have been described elsewhere.^{16,17} Sintered sheets of the material were cut into plates 10 × 10 × 2 mm. The experimental surface was ground with a 400 and then a 600 grit silicon carbide slurry under water cooling. The plates were finally cleaned ultrasonically using acetone/methanol and, finally, distilled water. This was the as-received state. A 1 mm diam. hole was drilled in one corner of each plate and two similar holes 1 mm deep in the non-test face to facilitate handling the plate without contamination. The prepared plates were suspended in test solutions by a 316L stainless steel wire loop and handled only at the edges with PTFE coated forceps.

When required, the experimental surface was reground (Lunn Major Grinder, Struers, Denmark) manually to 600 grit SiC paper with water cooling and a virgin paper surface for each movement. Polishing was carried out using a Minimet Polisher (Buehler Inc.) and three successive series of diamond polishing pastes: 6, 1 and 0.25 micrometres (Grades M.6, H.1 and H.1/4, Micro Metallurgical Ltd.). After grinding and polishing, the plates were cleaned ultrasonically in 0.5% aqueous Pluronic 31R4, distilled water, methanol and distilled water.

Certain plates were suspended in a Harrick Plasma Cleaner

[†] Durapatite[®]—Sterling-Winthrop Research Institute.

(Harrick Scientific Corp., Ossining, N.Y.) and cleaned in air at a pressure of 0.3 to 0.5 Torr for a period of 5–15 minutes using a power setting of 7–10. The plasma cleaner itself was purged with creation of a plasma several times before use.

(b) Reagents

Solvents, inorganic acids and other compounds were purified grades, in most cases meeting "reagent grade" ACS standards. Polyacrylic acid (PAA) of average molecular weight 20,000 was prepared by us using the method of Smith.²¹ The material was dialyzed and the test solutions filtered through a polycarbonate membrane with 5 μ m pores (Nuclepore Corp.). Distilled water was obtained from our own still; for all of the contact angle experiments "Omnisolv" distilled water (BDH Chemicals, Toronto) was used. Deuterium oxide was a gift from D. W. Priddle, Department of Chemistry, University of Toronto. Sources of other materials were: disodium ethylenediaminetetraacetate (EDTA)—Fisher Scientific #S-311; lactic acid—J. T. Baker #0194 (88% aqueous solution containing lactic acid and its anhydride); Pluronic 31R4—BASF Wyandotte (block copolymer of ethylene oxide and propylene oxide).

(c) Procedures

1. *Etching*—Etching of HA surfaces was carried out by suspending the prepared plates in aqueous solutions of one of the appropriate reagents as follows: (a) 0.5% solutions of hydrochloric, nitric, and lactic acids and 1% EDTA for 10 min (b) 0.5% EDTA for 2 min and (c) 0.5% PAA for 20 min. The plates were then washed with copious amounts of water or methanol and air dried in a glass chamber.

2. *Firing*—Certain test plates were fired in air in an electric furnace up to 800° over a 2 hr period followed by cooling over 1 hr to 300°C before storage in a glass chamber.

3. *Surface energy from measurements of contact angles*—The advancing contact angle of water on test surfaces was determined

using a sessile drop method. An $0.8\ \mu\text{L}$ drop of water was pipetted on to the surface and the contact angle measured immediately using a lens with protractor eyepiece. Four determinations at different locations were made and the mean calculated. For very hydrophilic surfaces, accurate determination was not attempted for angles below 10° . The surface tension of water was determined by measuring the force exerted by the liquid when in contact with a platinum plate attached to a microbalance. The plate was cleaned in a methanol flame just before use. The energy of the surface was calculated by the method of Neumann *et al.*²² from the surface tension and mean advancing contact angle using a computer programme furnished by Professor A. W. Neumann, Department of Mechanical Engineering, University of Toronto.

4. *Surface analysis*—SIMS and ISS spectra of the prepared HA surfaces were obtained using a 3M-Kratos Model 535 BX combined ISS/SIMS spectrometer with the assistance of Dr. G. R. Sparrow (Advanced R and D Inc.) A surface area of about $6\ \text{mm}^2$ was examined for SIMS and about $2\ \text{mm}^2$ for ISS. The positive ions beams used were He or Ar with a beam energy of 2 keV or, more rarely, 4 keV.

ESCA spectra were obtained using a McPherson ESCA 36 instrument and Mg K-alpha X-radiation. (Surface Science Western, University of Western Ontario). Additional ESCA spectra were obtained using a Surface Science Labs SSX-100 spectrometer with the assistance of Dr. N. S. McIntyre (Surface Science Western, University of Western Ontario) and Dr. B. Ratner (National ESCA Center for Biological Materials, University of Washington).

SEM and EDX observations were carried out using an ISI-60 scanning electron microscope fitted with a Princeton Gamma Tech energy dispersive analysis system.

RESULTS

(a) Morphological findings

Typical ground surfaces of a HA plate as-received and after resurfacing with 600 SiC grit are shown in Figures 1 and 2 respectively. These features were little altered by firing.



FIGURE 1 Ground surface of as-received HA plate (SEM, $\times 1500$).

Etching by the acids resulted in significant dissolution of the surface layer. HCl treatment led to separation of segments of a surface film which remained insoluble. Almost all the film separated in 10 min under the chosen conditions. Repetition of this procedure on a treated plate resulted in no further separation of a film or particles. HNO_3 etching did not cause separation of intact film segments but small white particles did separate from the surface during the first few minutes of etching. SEM observations showed that these mineral acids gave pitted surfaces (Figures 3, 4, 5). The small craters (about $0.5 \mu\text{m}$) may be due to the removal of individual

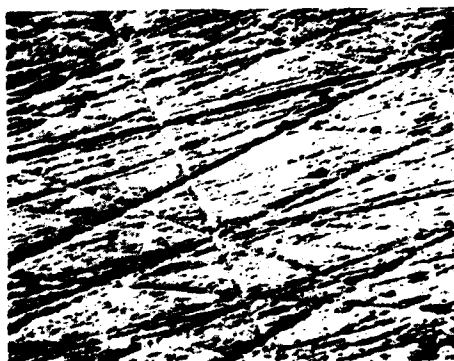


FIGURE 2 Surface of HA plate ground with 600 SiC grit and ultrasonically cleaned with methanol and water (SEM, $\times 1000$).

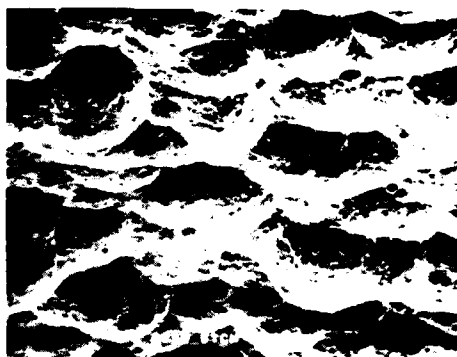


FIGURE 3 HA plate etched with 0.5% HCl for 10 min, washed in water (SEM, $\times 1500$).

HA crystallites whereas the large craters of 7–20 μm diam. may be due to loss of aggregates. Washing with methanol to remove HCl after etching (Figure 4) did not result in any insoluble surface precipitation as contrasted to water rinsing (Figure 3).

Etching with the organic acids resulted in quite different microstructures. Lactic acid gave a generalized rough, porous appearance with some cavitation (Figure 6) whereas PAA showed localized pitting (Figure 7). The EDTA-treated surface resulted in a roughened appearance with some cavitation, though less so than the lactic acid (Figure 8).



FIGURE 4 HA plate etched with 0.5 HCl for 10 min, washed with methanol (SEM $\times 1500$).

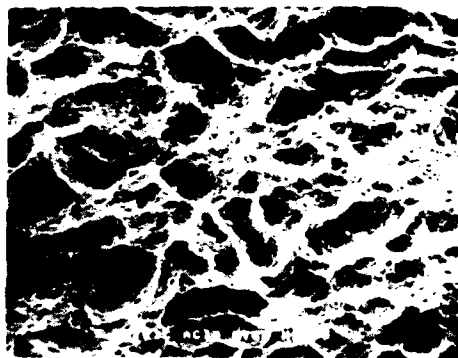


FIGURE 5 HA plate etched with 0.5% HNO₃ for 10 min, washed with methanol (SEM $\times 1500$).

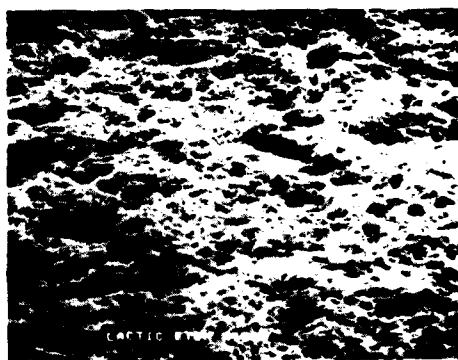


FIGURE 6 HA plate etched with 0.5% lactic acid for 10 min, (SEM, $\times 1500$).

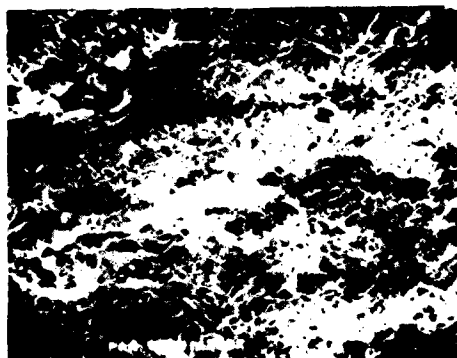


FIGURE 7 HA plate etched with 0.5% polyacrylic acid for 10 min (SEM $\times 1500$).



FIGURE 8 HA plate etched with 0.5% EDTA for 2 min (SEM $\times 1500$).

(b) Surface energy changes

Table I shows that an as-received HA plate had a hydrophobic surface with the low surface energy of 34 ergs/cm^2 indicating organic contamination during preparation. Samples of these plates were then subjected to a variety of surface preparation methods, as listed in Table I, including grinding, polishing, ultrasonic cleaning, immersion in boiling water and heating to 190°C in air or in vacuum. The resulting surface energies (Table I) were quite variable. Some surfaces had even lower energies than the untreated plates but most had higher energies, *i.e.*, were more hydrophilic. Removal of the (presumed) organic contamination was variable and dependent on the original plate as shown by entries 5 and 6 where energies of 57 and 72 ergs/cm^2 respectively were obtained using the same procedure on different plates. Polishing procedures produced low energies (entries 10–12) though exposure to boiling water improved the situation. In contrast, plasma cleaning (entry 13) gave a completely hydrophilic surface with a contact angle of less than 10° and a surface energy greater than 72 ergs/cm^2 .

Removal of organic contaminants by firing the plates at 800°C for 3–5 hours gave surface energies equal to or greater than 72 ergs/cm^2 for 4 plates tested (Table II). Surface energies of plates etched by the various agents are also given in Table II. Only HCl and HNO_3 produced markedly hydrophilic surfaces (Table II; entries 2–4). Washing the HCl-etched plates with water gave variable results

TABLE I
Surface energies of hydroxyapatite plates after various cleaning procedures

Entry #	Surface treatment	Surface energy (ergs/cm ²)	Advancing contact angle
1	None	34	84 ± 1°
2	Immersed in boiling water for 2 hours	44	68 ± 0°
3	Heated at 190° for 2 hours at atmospheric pressure	38	87 ± 2°
4	Heated at 190° for 2 hours in a vacuum of ~1 mm	26	97 ± 3°
5	a. Ground with 600 grit SiC paper; b. cleaned in ultrasonic bath.	57	47 ± 3°
6	As above, different plate	72	15 ± 2°
7	a. Ground with 600 grit SiC paper, b. cleaned in ultrasonic bath, c. immersed in boiling water for 2 hours	63	36 ± 5°
8	a. Ground with 600 grit SiC paper b. cleaned in ultrasonic bath, c. heated at 190° for 2 hours at atmospheric pressure	51	57 ± 2°
9	a. Ground with 600 grit SiC paper, b. cleaned in ultrasonic bath, c. heated at 190° for 2 hours in a vacuum of ~1 mm	34	84 ± 4°
10	a. Polished with 6μ, 1μ, and finally ½μ diamond paste, b. cleaned ultrasonically.	33	86 ± 2°
11	a. Polished with 6μ, 1μ, and finally ½μ diamond paste, b. cleaned ultrasonically, c. immersed in boiling water for 2 hours	61	40 ± 0°
12	a. Polished with 6μ, 1μ, and finally ½μ diamond paste, b. cleaned ultrasonically, c. heated at 190° for 2 hours at atmospheric pressure.	43	71 ± 2°
13	Plasma cleaned.	>72	<10°

perhaps because of localized slow drying and absorption of atmospheric contaminants. Washing with methanol was much more consistent and the hydrophilicity did not change on exposure to boiling water (entry 3). The organic agents gave much lower and comparable energies (Table II; entries 5–8) suggesting residual organic materials.

TABLE II
Surface energy of hydroxyapatite plates cleaned by firing at 800°C or by etching with acids

Entry #	Surface treatment	Surface energy ergs/cm ²
1	Fired at 800°C	≥ 72
2	HCl etch (0.5% for 10 min; methanol wash)	≥ 72
3	a. HCl etch, as above, b. immersion in boiling water for 2 hours	72
4	Nitric acid etch (0.5% for 10 min; methanol wash)	~ 72
5	Lactic acid etch (0.5% for 10 min; water wash)	46 ± 4
6	EDTA etch (0.5% for 2 min)	37 ± 1
7	EDTA etch (1% for 10 min)	45 ± 2
8	PAA etch (0.5% for 10 min; water wash)	47 ± 4

(c) Surface spectroscopy

Selected plates subjected to the various "cleaning" procedures were examined using ISS, SIMS and ESCA as noted previously. Figure 9 shows the ISS spectrum of an as-received plate. Curve A is the sum of many scans taken during the first 16 secs. of sputtering and represents the outer atomic layers whereas curve B resulted from

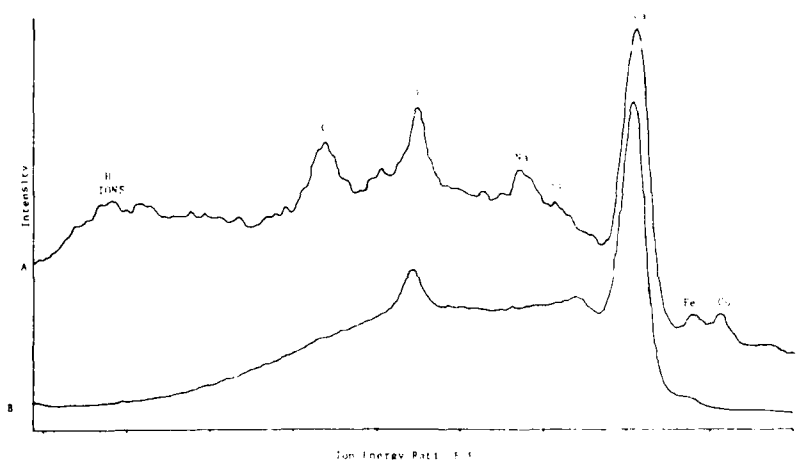


FIGURE 9 ISS spectra of as-received HA plate (A) and after 128 secs of sputtering (B).

128 secs of sputtering when about 1 nm would have been removed. Figure 10 shows a set of sequential ISS spectra giving a depth profile of the plate. The successive curves show the spectra after the indicated interval of sputtering.

SIMS spectra of the as-received plates are given in Figures 11–13. In the positive spectrum shown in Figure 11, curve A corresponds to the ions collected during the first 40 seconds of sputtering, and Curve B corresponds to the ions collected during a later 40-second period from the 80th second of sputtering to the 120th second of sputtering. Barium does not show up in the spectra in Figure 11, which were obtained with a helium ion beam, but it does appear in the spectrum in Figure 12, which was determined using a beam of argon ions. Figure 13 shows the negative $^3\text{He}^+$ SIMS spectrum. Since negative SIMS is sensitive to electronegative elements such as carbon, nitrogen, oxygen, and the halides, the prominence of m/e 16 (oxygen) from the hydroxyapatite and m/e 12 and 13 (C and CH from the organic surface layer) is expected.

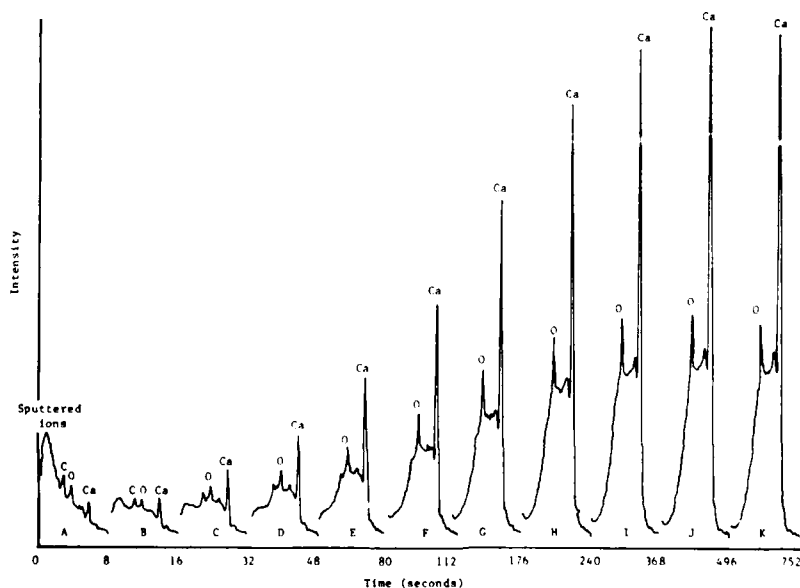


FIGURE 10 Sequential ISS spectra of as-received HA plate showing changes in major surface peaks with time of sputtering.

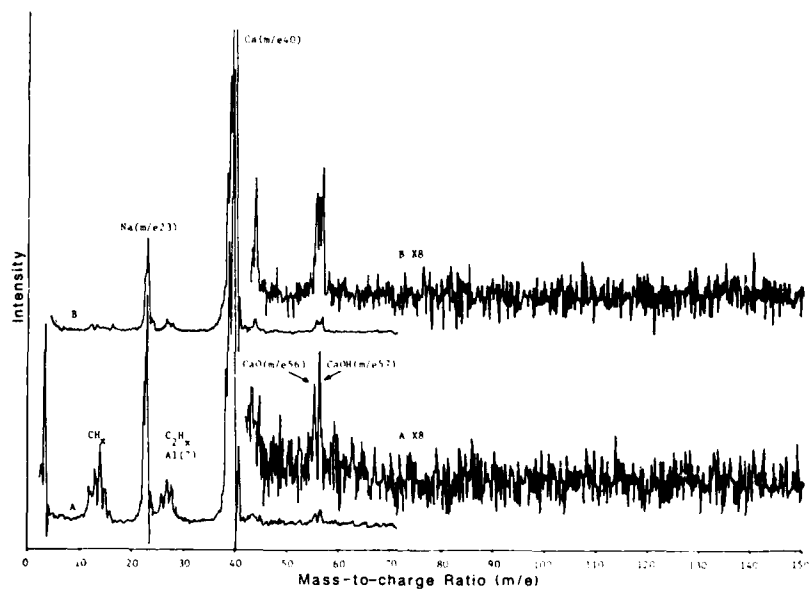


FIGURE 11 Positive SIMS spectra (He^+ : 2 KeV) of as-received HA plate, showing initial state (A) and after 120 secs of sputtering (B).

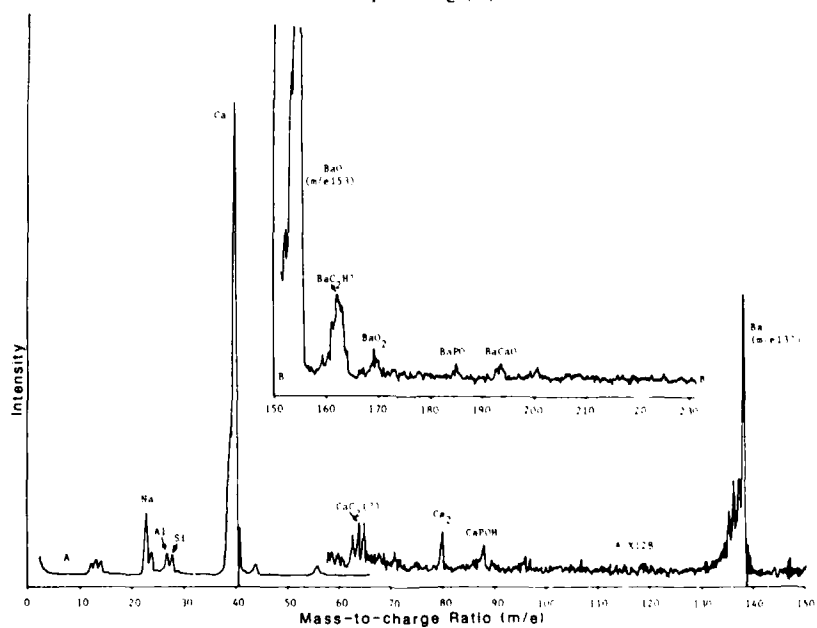


FIGURE 12 Positive SIMS spectra (40 Ar^+ : 2 KeV) showing presence of Ba (compare Figure 11).

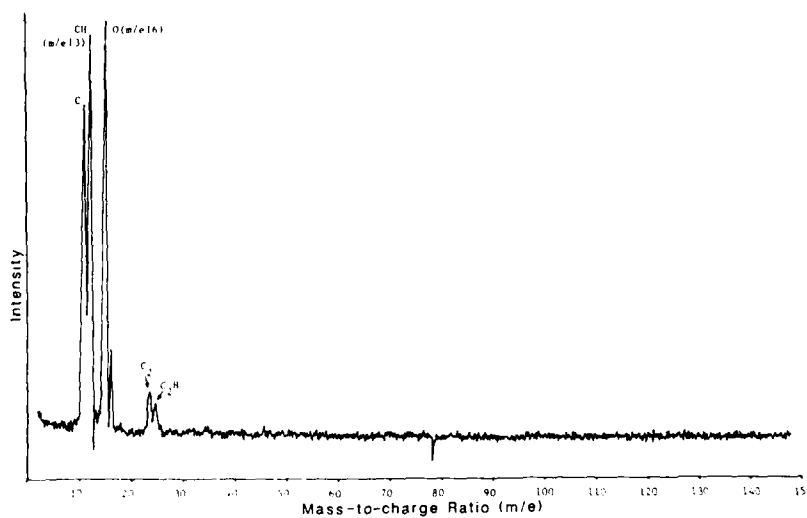


FIGURE 13 Negative SIMS (He: 2 KeV) of as-received HA plate after sputtering for 80 secs.

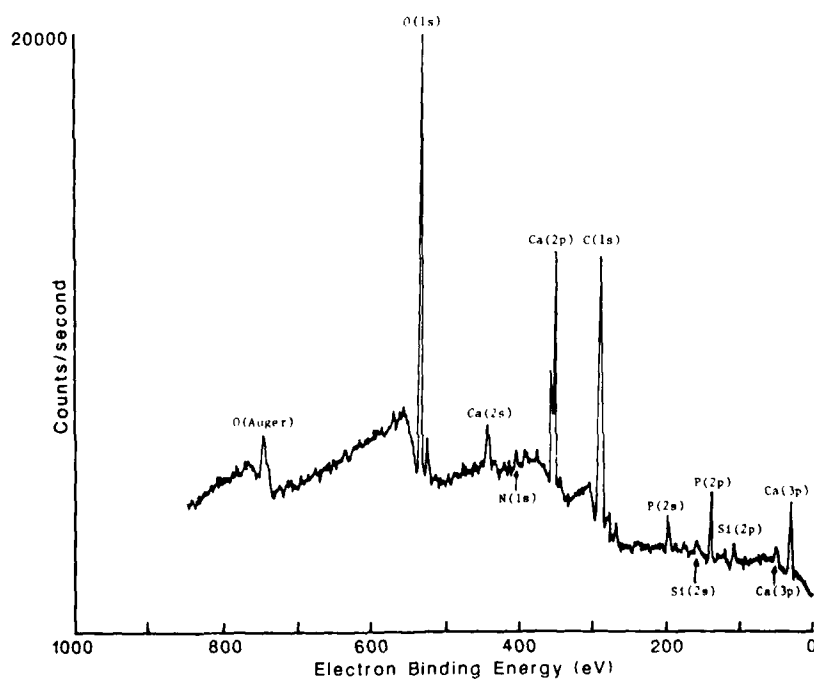


FIGURE 14 ESCA spectrum of as-received HA plate.

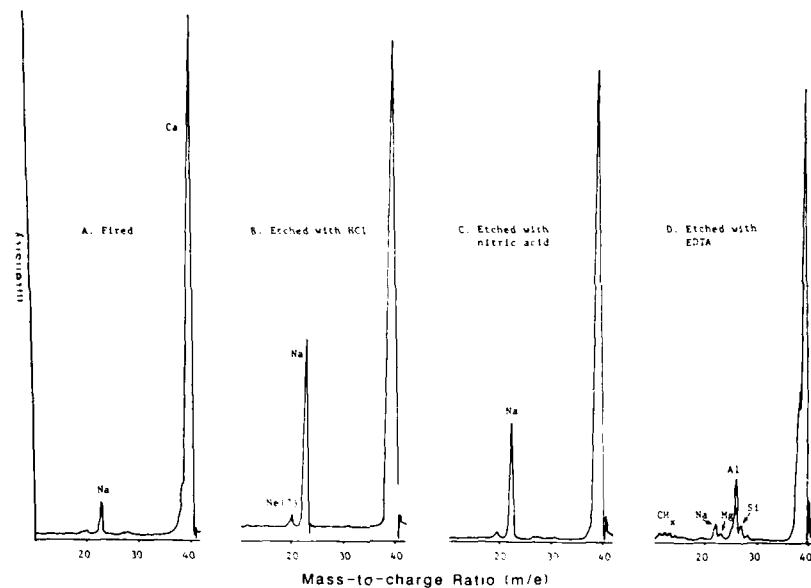


FIGURE 15 Sectional positive SIMS (He^+ : 2 KeV) spectra for HA surfaces exposed to various firing and etching procedures.

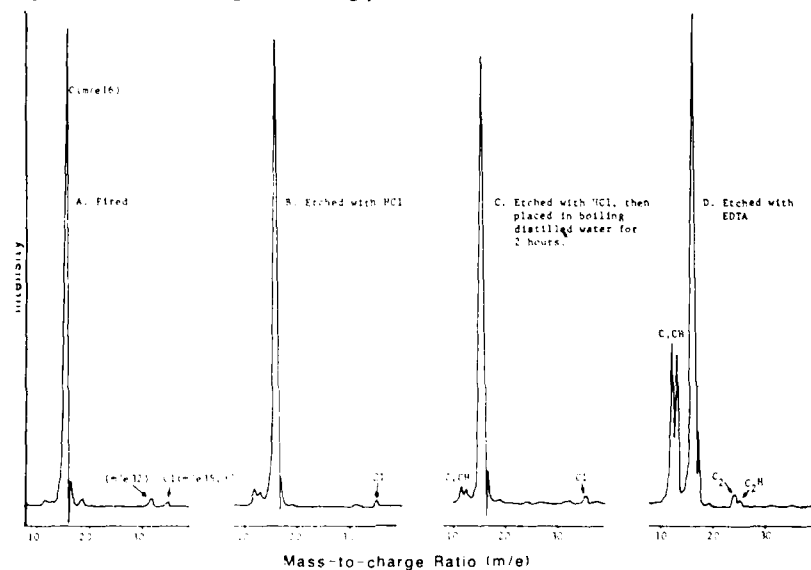


FIGURE 16 Negative SIMS (He^+ : 2 KeV) sectional spectra of HA surfaces exposed to various firing and etching procedures.

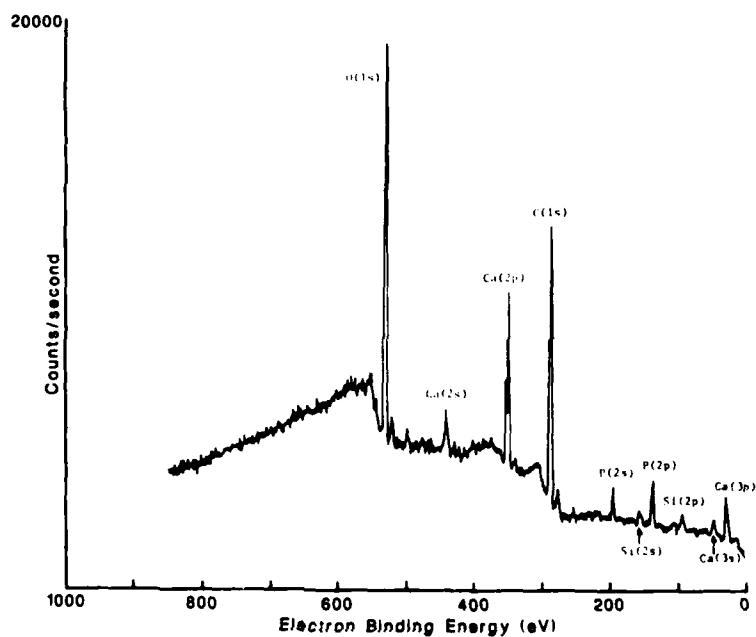


FIGURE 17 ESCA spectrum of HA plate etched with lactic acid.

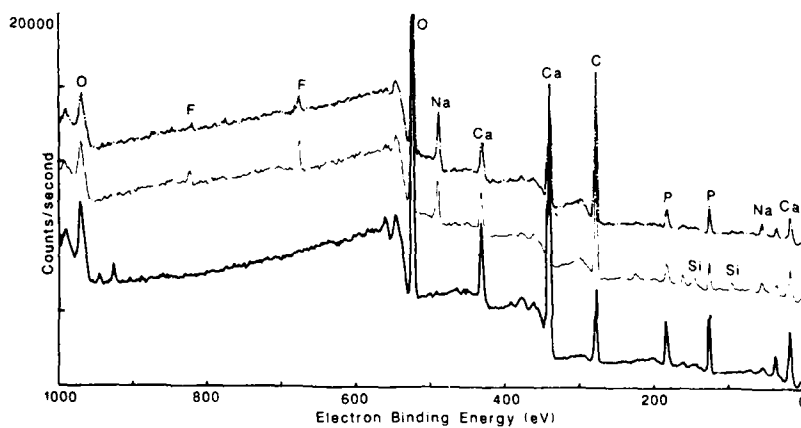


FIGURE 18 ESCA spectra of HA plates subjected to argon plasma for 1 min (bottom), 5 min (top), 15 min (middle).

Figure 14 shows an ESCA spectrum of the as-received surface.

Figure 15 shows positive $^3\text{He}^+$ SIMS spectra of fired, HCl-etched, nitric acid-etched, and EDTA-etched plates.

Figure 16 shows negative SIMS spectra for the fired, HCl-etched, HCl-etched followed by immersion in boiling water, and EDTA-etched plates.

The ESCA spectrum of a lactic acid-etched late is shown in Figure 17.

Figure 18 shows the ESCA spectrum of a plasma-cleaned plate that was subjected to various cleaning periods in an argon atmosphere as opposed to air.

DISCUSSION

Bonding to hydroxyapatite both *in vivo* and *in vitro* on enamel, dentin and bone as well as synthetic HA normally involves machined, ground, polished or etched surfaces^{2-6,11,13-15,18-20} which vary in their adherence and biocompatibility. The extent of the influence of residual cutting debris (on teeth, the 'smear' layer²³) and contaminants, both inherent and acquired, on the adhesion is uncertain as are the techniques for removal to effect durable bonding.^{3,23} The surfaces examined in the present work are thus reasonable models of those currently used in adhesion investigations.

As might be expected, the morphological and spectral data show the presence of a variety of inorganic and organic contaminants. Figures 1 and 2 illustrate that the roughened debris-laden surface of the as-received surface was converted to a well-defined abraded surface after grinding and ultrasonic cleaning. This surface was less hydrophobic than the original (Table I, entry 1) both as supplied and after exposure to boiling in water or heating at 190°C (Table I, entries 2-4). One ultrasonically cleaned-ground specimen was hydrophilic with a contact angle of 15° but washing, drying and polishing procedures applied to this surface generally resulted in greater hydrophobicity (entries 7-12) through, probably, adsorbed adventitious organic contaminants. Boiling water treatment showed some tendency to improve wetting but only plasma cleaning of the

hydrophobic surfaces resulted in easily wettable surfaces with contact angles of 10° or less and a surface energy greater than 72 ergs/cm^2 (Table I, entry 13), thus supporting the hypothesis that stripping off surface organic films with little change in morphology resulted in a hydrophilic surface.

These data illustrate the difficulty of avoiding surface contamination when customarily-used grinding or polishing procedures are employed. Arends *et al.*²⁴ have recently published work on the surface tensions of tooth enamel and related materials including this synthetic HA (Durapatite). The specimens "were polished on chemically pure cotton in a slurry of Al_2O_3 powder with distilled water" before measurement. They found the contact angle of distilled water on the polished Durapatite surface to be $42 \pm 16^\circ$ (standard deviation for six measurements). In a separate study,²⁵ the same investigators found that the contact angle of distilled water on polished enamel, after removal of 100–200 microns by grinding, was $47 \pm 9^\circ$ (standard deviation for 29 patients). They concluded that "Durapatite is not a reliable substitute for human enamel as far as contact angle measurements are concerned". Our results suggest that their HA surface was contaminated. It also seems probable that their measurements and calculations on enamel and the other minerals studied are erroneous because of surface contamination. To test this hypothesis, an experiment was carried out on polished enamel surfaces to determine the contact angle before and after plasma cleaning. One human incisor and one bovine incisor tooth, both of which had been stored in water following extraction, were first ground on the buccal side with 600 grit SiC paper (Carbimet, Buehler, Inc.) with water cooling until roughly 0.4 mm had been removed at the centre of the flat surface created. The flat surface was then polished with a slurry of 1 micron aluminum oxide powder (Linde C Polishing Powder) in distilled water on a cotton cloth (Metcloth, Buehler, Inc.) and was finally washed with a stream of distilled water and dried in air. The contact angle with distilled water of the ground and polished human enamel surface was $44 \pm 2^\circ$ (mean and mean deviation of two drops), and that of the bovine enamel surface was $33 \pm 1^\circ$ (mean and mean deviation of 4 drops). The teeth were then plasma cleaned, and the contact angles of the ground and polished surfaces were re-determined. In both cases the contact angle was less than 10° .

Removal of organic surface contaminants by firing seemed to be a simple alternative to plasma cleaning. Firing at 800°C for 3.5 hours gave surface energies equal to or greater than 72 ergs/cm² (Table II). However, firing has the disadvantage of not removing inorganic contaminants and the possibility of changing surface composition through diffusion or contamination from other materials in the furnace. Acid etching resulted in removal of the original surface though with morphological changes. The etchants reveal the microstructure (Figures 3, 4, 5) as shown previously by Jarcho *et al.*¹⁶ but only hydrochloric and nitric acids produced markedly hydrophilic surfaces (Table II). Flooding the etched surface with methanol after HCl etching rather than distilled water produced hydrophilic surfaces more consistently, perhaps because of more rapid drying in vacuo. The hydrophobicity showed little change after treatment with boiling water for 2 hours (Table II, entry 3). Treatment with the organic agents resulted in more hydrophobic surfaces (though the concentrations used were not optimized) even though significant roughening occurred (Figures 6–8). These results suggested residual adsorbed contaminants.

Some light was thrown on these observations by the surface spectra. The ISS spectra from the as-received plates (Figure 9) demonstrate a high level of surface organic contamination in the outermost layers (curve A) whereas after about 1 nm of the surface had been removed by sputtering the C peak almost disappeared as was also the case for Na, Si, Fe and Cu. It should be emphasized that the different elements have different sensitivities and the relative peak heights do not correspond to relative concentrations. Under the operating conditions the sensitivity of C is about 1/15 that of Ca so that on a normalized basis the C peak would be about 15 times higher. The sequential ISS depth profile (Fig. 10), after various sputtering intervals up to a total of 752 seconds, demonstrates the gradual disappearance of surface impurities and changes in the Ca/O ratio up to about 300 secs *i.e.* after about 2.5 nm had been removed.

In the positive SIMS spectra for the as-received surface (Fig. 11), the presence of the organic material on the surface is shown by the C, CH, CH₂, CH₃ cluster at mass-to-charge (*m/e*) ratios of 12, 13, 14 and 15. The cluster of peaks around *m/e* 27 may be due to aluminum and silicon (*m/e* 28) as well as C₂H_x. Positive SIMS is

especially sensitive to alkali metals and the strong sodium peak (m/e 23) does not necessarily indicate that it is present on the surface in high concentration. In curve B the organic and sodium peaks are less prominent relative to Ca (m/e 40) after the longer sputtering interval. The argon spectrum (Figure 12) reveals the presence of Ba and more prominent peaks for Al and Si. The increased attenuation in curve B shows that most of the ion clusters contain Ba. The negative SIMS spectrum in Fig. 13 shows prominent organic C peaks; minor F (m/e 19) and chlorine (m/e 35 and 37) peaks were detected (see Figure 16).

An ESCA spectrum of the as-received surface (Figure 14), which inherently relates to information from a greater depth, showed a prominent C peak indicating an organic coating though it was relatively thin, perhaps a few monolayers. Manual deconvolution of the expanded C1s peak suggested some of the organic layer contained carboxylic groups. The most prominent major impurity was silicon; it constituted about 2% of the outer 3–4 nm to which the instrument was sensitive.

It is of interest to compare the major inorganic surface contaminants of the as-received HA plates as shown in the foregoing spectra with the impurities found in the bulk of the material. The principal surface impurities were Na, Ba, Al, Si, Fe, F and Cl. Semi-quantitative spectrographic analysis of the same batch of material supplied by the manufacturer indicated that strontium was the main impurity; boron, silicon, aluminum, manganese, iron, magnesium, and chromium were also detected but at levels less than 0.01%. The preparative procedures for the plates have clearly resulted in a differential variation in surface elemental distribution as well as adventitious contamination. This was illustrated by further ISS and SIMS spectra that were obtained for a plate that had been ground to 600 grit and then subjected to several ultrasonic cleaning cycles. The spectra showed that an organic coating was present but much thinner, or perhaps patchy, in accordance with the lower hydrophobicity (Table I, entry 5) as compared with the as-received material. Na, Ba, F, Cl and Fe levels were also reduced but Cu and As (or Sr) had been increased.

These effects are apparent in the sectional positive SIMS spectra (Figure 15) for the HA surfaces subjected to the various firing and etching procedures. After firing, minimal C contamination was

present but Na is prominent in this and in the hydrophilic mineral acid-etched surfaces. The EDTA-etched surface showed a cluster of peaks around m/e 13 due to organic contamination in addition to a relatively high Al and low Si and Na peaks corresponding to the moderately hydrophobic surface (Table II). The negative SIMS spectra (Fig. 16) confirm only a minimal level of organic contamination on the fired and HCl etched surfaces as compared with the as-received material (Figure 13). It is interesting to note the effect of immersion in boiling distilled water. Residual adsorbed material from the EDTA is again prominent.

An ESCA spectrum for a lactic acid-etched HA plate that was also moderately hydrophobic (Table II) is shown in Figure 17. Comparison with the spectrum of the as-received plate (Figure 14) indicates a similar level of organic contaminants. Since EDTA and polyacrylic acid are both known to adsorb to HA, it may be assumed that this is a layer of adsorbed lactic acid. However, this was ruled out on the basis of the shape of the expanded C1s peak which did not indicate any carboxylic C content.

Variation in exposure time and the carrier gas in the plasma cleaning process also produced significant variations in surface ion concentration.

ISS spectra of the reground plates subjected to an air plasma for 15 minutes showed very little carbon but prominent peaks for F, Si, Fe, Cu and Ba. The presence of these elements was confirmed by positive SIMS using both 3He^+ and 40Ar^+ . These spectra showed also the presence of B and Sr. This was similar to the earlier findings but the Si and F were particularly prominent and appeared to increase with longer times. Corresponding plates were subjected to an argon plasma for 1, 5, 15 and 30 minutes. The data suggested that C removal was reduced compared to the air plasma but that Na, F and Si became increasingly prominent with time. This is evident in the comparative spectra for 1, 5 and 15 minutes shown in Figure 18. Thus, additional inorganic contamination, presumably from the walls of the plasma vessel, was being acquired with time. This spectral data confirms the findings of Baier *et al.*^{26,27} that a maximum time of exposure of 3–5 min is desirable for air or argon plasma cleaning. Further investigation is needed to establish optimum plasma cleaning conditions for HA.

The present data show that the surface of HA resulting from

commonly-used adhesion preparative procedures is highly variable and dependent on the precise technique. These morphological and chemical variations would be expected to influence adhesion both of monomer-polymer systems and cells. While this variability may be overcome by the use of reactive adhesive systems for clinical application, a defined preparative approach is desirable. Thus, further studies are indicated of the present procedures and others such as UV-ozone²⁸ to establish reproducible surfaces for *in vitro* investigation and a foundation for clinical techniques.

References

1. A. R. Ten Cate, *Oral Histology* 2nd Ed. (CV Mosby, St. Louis, 1985).
2. S. J. Gwinnett and D. C. Smith, in *Biocompatibility of Dental Materials*, D. C. Smith and D. F. Williams, Eds. (CRC Press, Boca Raton, 1982), Chap. 2, Vol. II, pp. 15-49.
3. E. Asmussen and E. C. Munksgaard, in *Posterior Composite Resin Dental Restorative Materials*, G. Vanherle and D. C. Smith, Eds. (3M Co., St. Paul, 1985), Section IV, pp. 217-230.
4. N. Nakabayashi, *Crit. Rev. Biocompat.* **1**, 25 (1985).
5. D. C. Smith, *Oper. Dent.* **7**, 14 (1982).
6. I. E. Ruyter, in *Posterior Composite Dental Restorative Materials* (CRC Press, Boca Raton, 1985), Sec. II, pp 109-135.
7. D. C. Smith, *Brit. Dent. J.* **125**, 381 (1968).
8. A. D. Wilson, *Chem. Soc. Rev.* **7**, 265 (1978).
9. W. J. Peters, R. W. Jackson and D. C. Smith, *J. Biomed. Mater. Res.* **8**, 53 (1974).
10. D. R. Beech, *Arch. Oral Biol.* **17**, 907 (1972).
11. S. Crisp, H. J. Prosser and A. D. Wilson, *J. Mater. Sci.* **11**, 36 (1976).
12. T. Nasu, *J. Biomed. Mater. Res.* **20**, 347 (1986).
13. R. L. Bowen, *Int. Dent. J.* **35**, 155 (1985).
14. N. Nakabayashi, *Int. Dent. J.* **35**, 145 (1985).
15. K. F. Leinfelder, *et al.*, *J. Ala. Dent. Ass.* **70**, 15 (1986).
16. M. Jarcho, *et al.*, *J. Mater. Sci.* **11**, 2027 (1976).
17. M. B. Thomas, *et al.*, *J. Mater. Sci.* **15**, 891 (1980).
18. M. Jarcho, *et al.*, *J. Dent. Res.* **57**, 917 (1978).
19. M. Jarcho, J. R. O'Connor and D. A. Paris, *J. Dent. Res.* **65**, 151 (1977).
20. M. Jarcho, *et al.*, *J. Bioeng.* **1**, 79 (1977).
21. D. C. Smith, U.S. Pat. 3,605,605 (1972).
22. A. W. Neumann, *et al.*, *J. Coll. Interfac. Sci.* **49**, 291 (1974).
23. W. R. Cotton, *Oper. Dent.* **9**, Suppl. 3 (1984).
24. H. P. de Jong, *et al.*, *Surface and Colloid Phenomena in the Oral Cavity: Methodological Aspects*, (R. M. Frank, Ed. IRL Press, London, 1982), p. 106.
25. H. P. de Jong, *et al.*, *J. Dent. Res.* **61**, 11 (1982).
26. R. E. Baier and V. A. DePalma, Calspan Corporation Report no. 176, 1982.
27. R. E. Baier, *et al.*, *J. Biomed. Mater. Res.* **18**, 337, (1984).
28. J. R. Vig, in *Surface Contamination: Genesis, Detection and Control*, Vol. 1, K. L. Mittel, Ed. (Plenum Press, New York, 1979), pp. 235-254.

Component Interaction and Properties of Pigmented Epoxy Systems[†]

SYLVIA PONCE, R. BAZINET and H. P. SCHREIBER

Department of Chemical Engineering, Ecole Polytechnique of Montréal, P.O. Box 6079, Stn. "A", Montréal, Québec, Canada H3C 3A7

(Received October 16, 1986)

Acid-base interaction parameters have been measured for components of epoxy resins, including various pigmenting solids, using the method of inverse gas chromatography. The influence of acid-base interactions was then evaluated in terms of cure rates and the performance of the epoxy formulations as adhesives in metal joints. It has been found that non-polar particulates do not affect cure rates significantly; strongly acidic and basic pigments such as an iron oxide and a rutile, both retard the reaction, while a mildly basic CaCO_3 filler tended to accelerate the curing process. The initial bond strength of joints using the epoxy as sealant also varied with the choice of particulate, as did bond strength retention following exposure to selected temperature-humidity cycles. The effects exerted by the particulates are postulated as being due to selective sorption mechanisms. It is believed that the strongly basic rutile immobilizes the mildly acidic epoxy molecule, while the strongly acid iron oxide tends to immobilize basic catalyst and accelerator molecules. Both tend to slow reaction rates, but only the immobilization of epoxy by a basic particulate surface also produces benefits in bond strength and bond durability.

KEY WORDS Acid-base interaction; adhesive properties; component interaction; epoxy systems; fillers; peel strength.

INTRODUCTION

In recent years considerable attention has been given in our laboratory to the measurement of interactions among the com-

[†] Presented at the Tenth Annual Meeting of The Adhesion Society, Inc., Williamsburg, Virginia, U.S.A., February 22-27, 1987.

ponents in multi-phase polymers, and to the effects of interactions on polymer properties. As to measuring interactions among the components, the inverse gas chromatography (IGC) method^{1,2} has been adapted for the purpose. By standardizing on vapors known to be Lewis acids and bases,³ it is possible to define an interaction potential parameter, Ω , which ranks polymeric and other non-volatile stationary phases in the IGC experiment as to their donor-acceptor tendencies.³ This technique has been used with thermoplastic polymers, their blends and composites, in order to clarify the importance of interaction balances on mechanical and rheological properties, among others.^{4,5}

A logical extension to the cited work involves thermosetting, crosslinked polymers. In the present instance epoxy systems have been chosen as representative of this polymer category. Specifically, we report on the influence of pigments on crosslinking phenomena and on the adhesion of joints with the epoxy as sealant. The use of pigments and other particulates in epoxy formulations is, of course, well known.⁶ Such materials as mica, CaCO_3 , talc, inorganic and organic colorants are present frequently to modify a host of characteristics, ranging from moisture sensitivity and thermal expansion coefficients to the amount of heat liberated during hardening reactions.^{6,7,8} In this work, particulates have been chosen from the pigment group as well as from the range of solids usually added to reduce cost or to control specific properties of the composite. Attempts are made to rationalize modifications in crosslinking and adhesion characteristics brought on by the additives in terms of the specific interactions represented by Ω values. We intend thereby further to evolve an understanding of behavior patterns in multi-component polymer systems.

EXPERIMENTAL SECTION

i) Materials

The epoxy resin used in this work was Epon R-2004, a commercial product supplied by Shell Canada Ltd. Its fusion point was found to be 70°C. Two crosslinking agents were used. One was Epon P-100, an imidazole compound produced by Shell, with a fusion tempera-

ture of 64°C. The second, also from Shell, was Epon P-108, a dicyandiamide containing imidazole as accelerator, with a fusion point at 203°C.

The following were the particulates involved in the study:

- TiO_2 -rutile; a commercial surface treated pigment with an average particle size of $0.2\ \mu\text{m}$ and a BET surface area of $8.9\ \text{m}^2/\text{g}$.
- Fe_2O_3 -ferric oxide; a commercial specimen with average particle size of $0.8\ \mu\text{m}$.
- Mica-phlogopite mineralization; a platelet solid screened to provide fraction in the $-40 + 70$ size range.
- CaCO_3 ; a commercial, surface-treated sample, B.E.T. surface area $5.5\ \text{m}^2/\text{g}$, and average particle size of $1.2\ \mu\text{m}$.

ii) Procedures

Compounding All Epons were dried under vacuum for 24 h prior to use, and all particulates were heated to 150°C under vacuum prior to compounding. To prepare test compounds, materials were tumble-blended for 30 min on a roll mill, then re-ground in a Wiley mill and tumble-blended again (1 h) to ensure uniform distribution. The composition of specimens was as follows:

I. Epon R-2004 . . .	100 parts
Epon P-100 . . .	5 parts
Particulate . . .	10 parts

II. As above, but Epon P-108 replacing P-100.

Interaction characteristics Columns for IGC experiments were prepared by mixing one part of each of the solids individually with ten parts inert glass beads (0.5 mm radius). In all cases the solids content was between 3–5 g; a column containing glass beads was used to provide a correction to the retention data generated in columns containing the active agents in our compounds. The details of IGC experiments were described previously;^{4,5} *n*-octane, *t*-butanol and butylamine were neutral, acid and base vapor probes respectively. At least triplicate elution trace determinations were used to evaluate retention times and specific retention volumes (V_g°), following the conventions described in Reference 4. Interac-

tion parameters Ω were calculated for acidic solids (Vg butanol < Vg° butylamine) from

$$\Omega = 1 - (Vg^\circ)_{\text{amine}} / (Vg^\circ)_{\text{alcohol}} < 0 \quad (1)$$

and for basic solids (Vg butanol > Vg° butylamine) from

$$\Omega = (Vg^\circ)_{\text{alcohol}} / (Vg^\circ)_{\text{amine}} - 1 > 0 \quad (2)$$

The parameters were obtained from 30–120°C, with a repeatability better than 5%. Though it would be desirable to extend the Ω data over the entire temperature range of crosslinking reactions, the sharp decrease in Vg° at higher temperatures made this impractical.

Reaction processes A Perkin–Elmer DSC-2 differential scanning calorimeter was employed to measure reaction exotherms in the range 50°–280°C at linear heating rates of 5, 10 and 20°C/min. Isothermal determinations of reaction heats were also conducted at selected points within that temperature range. The degree of conversion (α) from initial to final products was evaluated following Barton,⁹ using ratios of reaction exotherms at any time t and at equilibrium,

$$(\alpha) = \Delta H_t / \Delta H_\infty \quad (3)$$

Whenever possible, isothermal experiments were also used to determine the induction times, t_1 , for the onset of exothermic reactions. This was done to show the degree to which component interactions may accelerate or attenuate crosslinking reactions in the chosen epoxy formulations.

Adhesion performance Adhesive joints were prepared for peel strength testing, according to ASTM D903-49.¹⁰ Samples were prepared by applying a 300 mg sample of epoxy formulation to a 20 cm × 2 cm test panel sheet (Bonderite-1000 Cold-Rolled steel) and covering this with aluminium foil cut to 40 cm × 2.5 cm dimension. All metallic parts of the joint were previously cleansed in trichloroethylene vapor under reflux, then washed in distilled water and dried at 150°C under N_2 . The assembled parts were then exposed to 70°C at 10,000 lb/in² (743 kg/cm²) for 1 min to form a cohering “sandwich”. These structures were then cured at a temperature in the range 120–170°C for 10 mins.

Peel testing was done on six samples of each formulation, using

an Instron table model tester. This pulled the flexible aluminium foil from the assembly at a 180° angle and a separation speed of 10 cm/min.

Adhesive properties were measured on samples as prepared (initial properties) and after specimens had been subjected to accelerated aging routines (residual properties). In one cycle of this routine, the specimen is conditioned for 24 h at ambient conditions, then is placed in a chamber at 60°C and 80% R.H. for 24 h, then in a dry compartment (24 h) at -55°C, before being returned to ambient conditions for a final 24 h. Up to 20 cycles were applied to certain samples, and peel test evaluations were performed after selected numbers of cycles.

RESULTS AND DISCUSSION

i) Interaction Characteristics

Values of Vg° and Ω for the particulates and the epoxy components are given in Table I. Also indicated in the Table are the ratios of Vg° values at the extreme temperatures—*i.e.* $(Vg^\circ)_{120^\circ}/(Vg^\circ)_{30^\circ}$ so as to show the extent of temperature variations in the retention characteristics.

As might be expected from their chemical structures,¹¹ the epoxy and the two crosslinking agents are respectively acid and base. Of the two crosslinkers, Epon P-100 is the stronger base, its Ω value attaining values >1.0 at temperatures above 60°–70°C. Among the particulates, the rutile represents a strong base, the surface of Fe_2O_3 is a relatively strong acid and $CaCO_3$ is a weak base. The mica has Ω values sufficiently close to zero to be considered, in essence, as a solid surface in which dispersive forces dominate over polar forces. The evident temperature dependence of Ω is due, presumably, to the differences in bonding energies between solid-vapor pairs exhibiting acid-base coupling and those in which van der Waals forces dominate, or where polar force repulsion can be envisaged. The ratios of Vg° at 120° and 30° provide a rough guideline in this regard. Assuming octane to be a non-polarizable molecule, it is evident that regardless of which solid is being contacted, dispersion-force bonds generate a ratio of about 0.3. In

TABLE I
IGC parameters for epoxy and particulate components

Material		(Vg°): nC ₈	n but. amine	t. butanol	Ω
Epon R2004: @ °C	30	27.6	35.2	28.7	-0.23
	60	20.3	30.3	23.0	-0.32
	90	14.3	24.0	17.3	-0.39
	120	9.9	18.5	11.6	-0.59
Epon P-100: @ °C	30	20.4	19.5	29.4	0.51
	60	15.1	14.8	24.4	0.65
	90	10.3	9.3	20.9	1.25
	120	6.7	6.1	18.3	2.00
Epon P-108 @ °C	30	33.7	31.5	41.0	0.30
	60	25.6	25.8	32.7	0.27
	90	19.1	19.1	26.9	0.41
	120	11.7	11.5	20.8	0.81
Mica @ °C	30	40.5	26.8	27.7	0.03
	60	31.3	19.5	21.6	0.11
	90	19.4	10.8	11.3	0.05
	120	12.0	7.9	10.0	0.27
TiO ₂ : @ °C	30	167	132	299	1.26
	60	113	106	274	1.58
	90	75.2	80.1	230	1.87
	120	53.9	57.2	288	2.29
Fe ₂ O ₃ : @ °C	30	116	128	89.8	-0.43
	60	81.9	106	73.6	-0.44
	90	55.3	93.2	60.4	-0.54
	120	37.4	70.7	40.0	-0.77
CaCO ₃ : @ °C	30	27.0	22.8	30.9	0.35
	60	20.1	17.4	23.1	0.33
	90	16.6	13.5	18.1	0.34
	120	9.7	8.8	13.4	0.51

the pairs where strong acid-base coupling appears to occur—namely TiO₂-butanol and P-100-butanol, the Vg° ratio is near or above 0.6, while for moderate bonding the ratio value may be expected to lie in the range 0.4–0.5. If these guidelines truly reflect the interaction phenomena at interfaces, then with a substrate such as mica, the presence of polar hydroxyl and amino groups in the vapor probe contributes little to the bond strength. Similarly in cases such as P100-butyl amine, CaCO₃-butyl amine, and possibly R2004-butanol, the vapor molecules appear to be so oriented at the solid surface as to interact with it through (predominantly) dispersion forces.

ii) Reaction Processes

Two parameters have been chosen to illustrate the crosslinking processes taking place in the defined epoxy formulations. As already indicated, these are the degree of conversion, α , of epoxy to crosslinked resin, obtained from reaction isotherms,⁹ and the induction time, t_1 , for the onset of reaction. Additional parameters, including total exothermic heats of reaction will be reported in a subsequent publication. A number of the reaction isotherms for reference compositions, without particulate additives, are shown in Figure 1. These differentiate strongly between the crosslink effectiveness of the two agents; P-108, containing imidazole accelerator, triggers significant reaction at temperatures above about 100°C, while no significant signs of reaction could be detected by present methods below 120°C when P-100 was involved. At the upper end of the temperature scale, above ~180°C reaction rates were too rapid to be analyzed meaningfully with P-108 reagent, but could be followed to ~220°C with P-100. The presence of the accelerator, clearly exerts a strong influence on the reaction processes.

Referring to Table I, and assuming that trends in the temperature variations of Ω are maintained beyond 120°C, stronger acid-base coupling would be expected in the Epoxy-P-100 system than in the

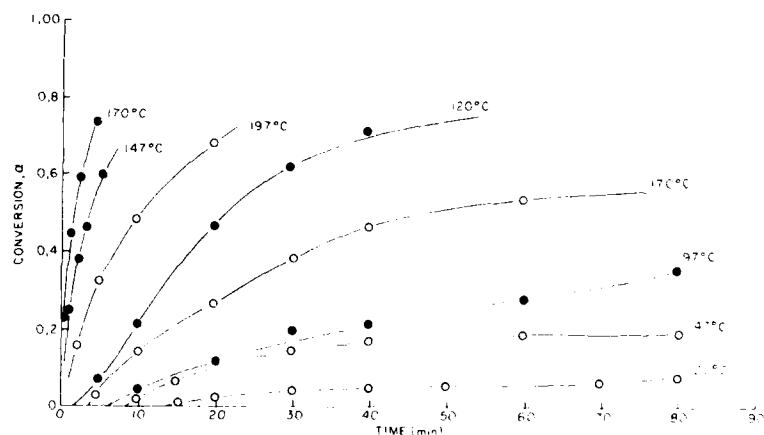


FIGURE 1 Rates of epoxy conversion as function of temperature and catalyst choice.

○ P-100 catalyst ● P-108 catalyst

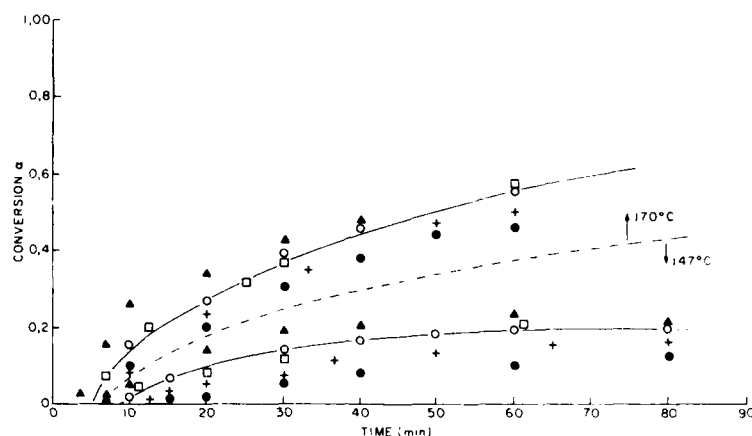


FIGURE 2 Influence of particulates on isothermal epoxy cure processes: System epoxy/P-100.

○ No filler ▲ CaCO₃ + TiO₂
 □ Mica ● Fe₂O₃

corresponding P-108 system. Apparently this is not an important factor in the determination of reaction rates in the unpigmented compounds.

The effect of particulates on reaction processes, however, does appear to depend on specific interactions among the components. An illustration is given in Figure 2, showing the response of the system epoxy-P-100 to the presence of the particulates. Isotherms at 147°C and 170°C have been chosen for the illustration which typifies the trends at other reaction temperatures, and also serves as an example of similar trends noted in the epoxy-P-108 system. As shown in Figure 2, mica has virtually no modifying effect on the crosslinking process. The CaCO₃ acts as a mild accelerator, the influence being particularly noted in the initial stages of reaction. In contrast, both TiO₂ and Fe₂O₃ reduce the rate of conversion and seem to produce final products with lower degrees of conversion and thus, lower crosslink densities.

An analogous effect is noted in t_1 . The temperature dependence of this parameter is shown for epoxy-P-100 in Figure 3, and for epoxy-P-108 in Figure 4. The choice of abscissa was dictated by the empirical observation that such a representation produced very satisfactory linear functions. The effects in these cases are internally

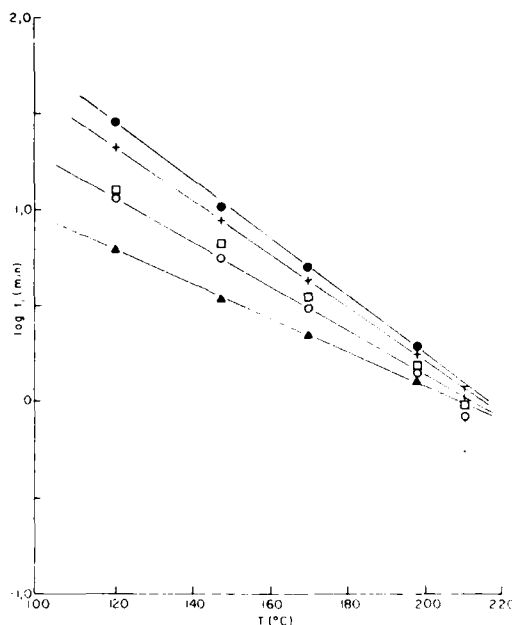


FIGURE 3 Induction time vs. temperature for epoxy cure reaction: System epoxy-P-100.

○ No filler ▲ CaCO₃ + TiO₂
 □ Mica ● Fe₂O₃

consistent. A decrease in the induction time is produced by the CaCO₃, while TiO₂ and Fe₂O₃ attenuate the onset of reaction appreciably. Again, in neither case does mica influence the induction time for reaction.

Qualitatively, these observations may be rationalized in terms of apparent acid-base interactions, and selective sorption phenomena which arise as a result. In this scheme mica reflects its weakly interacting surface, and does not sorb effectively any of the chemical reactants. The present rutile and iron oxide samples, with Ω ratings in the strong basic and acidic group, may be assumed to sorb their counterparts selectively, as demonstrated by analogous work reported by Fowkes and coworkers.¹² Accordingly, rutile will tend to immobilize the epoxy molecule, while the basic imidazole and dicyandiamide molecules will tend to be immobilized by the acidic iron oxide pigment. The (partial) immobilization either of

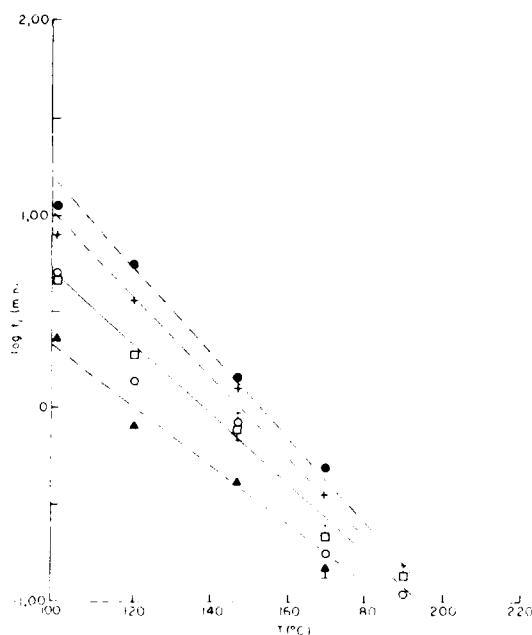


FIGURE 4 As in Figure 3: System Epoxy-P-108.

epoxy or crosslinking chemical reduces the reaction rate and increases the induction time for reaction. Of the two, the sorption of crosslinking agent appears to be the more effective route to slowing the thermosetting reaction, since relatively larger effects are noted due to the presence of Fe_2O_3 than to that of the present rutile specimen. The most interesting, and complex case, is that of CaCO_3 . This mildly basic surface accelerates reaction parameters; for consistency, therefore, there cannot be effective immobilization of the epoxy molecule in this instance. The question of effective immobilization then would depend on the difference in the Ω values for interacting species. At present, no guidelines can be offered from theoretical considerations as to what represents a minimum $\Delta\Omega$ for strong interaction. Empirically, using 120°C as a representative reaction temperature, it follows from Table I that $\Delta\Omega \geq 1.5$ produces partial immobilization leading to an attenuation of reactions. The $\Delta\Omega$ for epoxy- CaCO_3 , near 1.0, may be sufficient to reduce the free mobility of the epoxy without, however, inhibiting

its chemical reactivity. Thereby the crosslinking process is accelerated. Some further discussion of this interpretation follows below. Clearly, however, additional experiments will be needed to test the validity of the concept.

iii) Adhesion Performance

Initial bond strengths of control and filled epoxy formulations, determined by peel testing as outlined above, are reported in Table II. The data—at 120° and at 170°C—represent the full temperature range for cure, and are typical of all results obtained. Two features are immediately evident: Firstly, the choice of catalyst significantly affects the initial bond properties; secondly, the presence of particulates may alter these bond properties in either direction. Increases in peel strength, 40–60% in magnitude, may be realized by using the dicyandiamide/imidazole catalyst (P-108) in place of the imidazole compound (P-100) alone. The differences, observed both in control and filled compounds, suggest that different network morphologies, and perhaps different surface energetics, are produced by these catalysts. Evidence supporting the generation of distinctive network morphologies by these catalyst classes has been reported by Cagle.¹³

The ability of particulates to affect bond performance is not dependent on the catalyst involved but appears to vary significantly with the interaction potential of the filler. Mica, which did not affect crosslinking processes, again fails to exert significant influence. The initial bond properties, when mica is present, are within the

TABLE II
Initial adhesive bond strength for variously filled epoxy systems

Catalyst Cure condition: (°C/min)	Adhesive Bond Strength (kg cm ⁻¹)			
	P-100		P-108	
	120°/10	170°/10	120°/10	170°/10
Additive:				
None-control	0.58	1.12	0.95	1.62
TiO ₂	0.86	2.07	1.63	2.86
Fe ₂ O ₃	0.53	0.97	0.84	1.40
CaCO ₃	0.64	1.22	1.09	1.91
Mica	0.59	1.07	0.91	1.55

experimental error of control structures. Rutile and CaCO_3 increase peel strength, the former predominantly by 60–80%, the latter by some 10–20%. As suggested by the relevant acid-base parameter (Ω) values, the rutile should interact with or sorb the epoxy strongly, while weaker interaction would be expected between epoxy and CaCO_3 . The iron oxide, which would be expected to interact with the basic catalysts, decreases initial bond characteristics, typically by some 10–15%.

The contribution of fillers to bond properties is even more evident in samples which had been aged by the temperature-humidity cycles described earlier in this article. Figures 5 and 6 document the point, the former showing percent changes in bond properties for epoxy-P-100 systems, the latter for corresponding epoxy-P-108 formulations. The most obvious contrast is between the ability of TiO_2 to stabilize and of Fe_2O_3 to destabilize bond properties. CaCO_3 retains a mild stabilizing tendency, while mica again appears not to be involved in the interfacial characteristics of these structures. Qualitatively, these findings are consistent with the

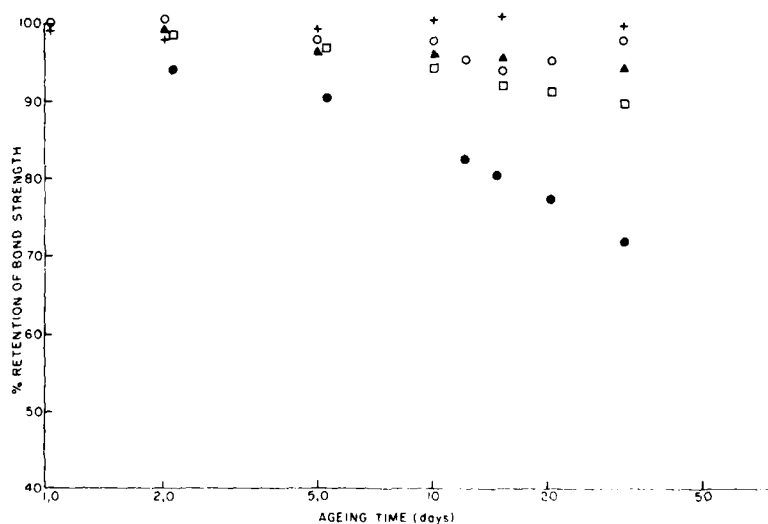


FIGURE 5 Retention of bond strength in joints using pigmented epoxy/P-100 system as adhesives. Cure conditions $170^\circ\text{C}/10$ min.

○ No additive ▲ CaCO_3 + TiO_2
 □ Mica ● Fe_2O_3

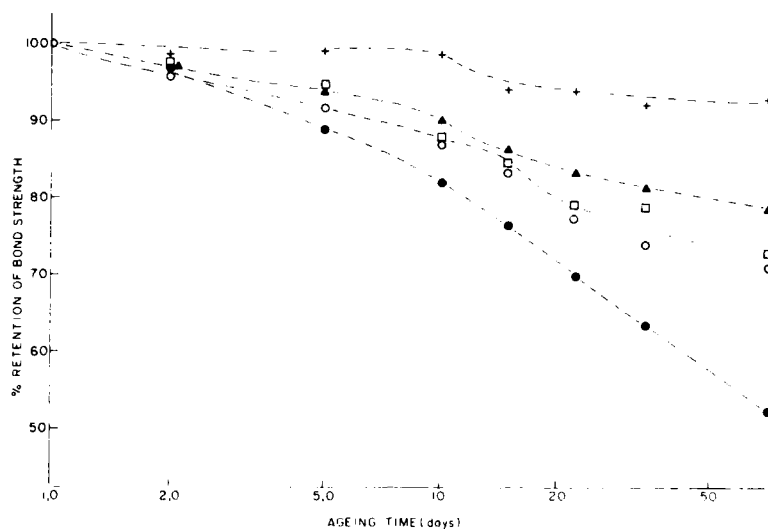


FIGURE 6 As in Figure 5: System epoxy/P-108 as adhesive.

suggestion that fillers sorbing the epoxy molecule become integral parts of the crosslink structure in the cured resin, while the inherent incompatibility between the epoxy and acidic particulates, such as the present iron oxide,[†] produce a crosslink structure with imperfections or microvoids in the region of the particulates. This would account for the differences in initial bond strengths; furthermore, since imperfections in the particulate/matrix interphase would act as routes for the intrusion of water, for the concentration of mechanical strains, etc., more rapid deterioration of bond and mechanical properties would be expected.

The final point to be considered here is the origin in acid-base interaction tendencies of the time-dependent changes in bond properties. Following the notions introduced above, the percent changes in bond strength were plotted against the Ω values of particulates. Figure 7 illustrates the result, using the data after 60 days of aging cycles. Entirely analogous results are obtained at other aging times, showing that the increasing stability in bond

[†] Since most commercial particulates have been surface treated, we stress that present remarks pertain to the specific specimens examined and do not necessarily apply to other versions of the particulates.

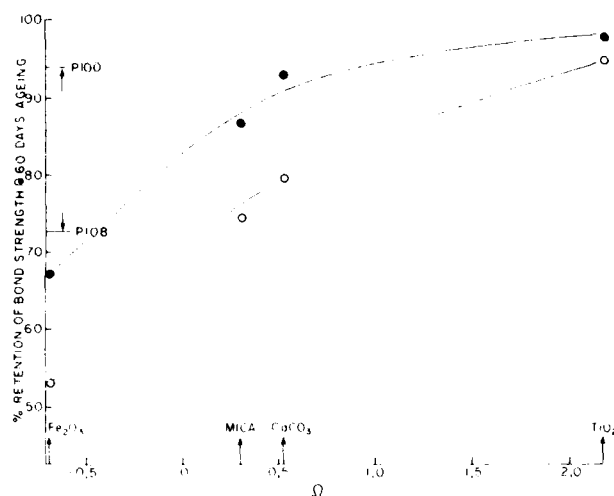


FIGURE 7 Apparent relationship between bond strength retention and acid-base interaction among components in epoxy formulations.

○ P-108 catalyst ● P-100 catalyst

strength and increasing basicity of the particulate are directly linked. Thus, for the acidic epoxy used here, the acid-base interaction concept seems to provide a useful guideline both to the initial bond properties and to their time-dependent variations in aggressive environments. Further work is planned to clarify the many implications of these findings.

Acknowledgment

This work was supported by operating grants from the Natural Sciences and Engineering Research Council, Canada.

References

1. J. M. Braun and J. E. Guillet in *Progress in Gas Chromatography*, J. H. Purnell, Ed. (Wiley and Sons, New York, 1976).
2. D. G. Gray, *Progress in Polym. Sci.* **5**, 1, (1977).
3. H. P. Schreiber, Y. M. Boluk and Yongming Li in *Proc. International Congress on Composite Interfaces*, H. Ishida, Ed. (Plenum Press, New York), in press.
4. Y. M. Boluk and H. P. Schreiber, *Polym. Eng. Sci.*, in press.
5. H. P. Schreiber, M. R. Wertheimer and M. Lambla, *J. Appl. Polym. Sci.* **27**, 2269 (1982).

6. W. G. Potter, *Use of Epoxy Resins* (Chemical Publishing Co., New York, 1976, Ch. 4, 5).
7. H. Lee and K. Neville, *Epoxy Resins* (McGraw-Hill Publishing Co, New York, 1957), pp. 150-155.
8. C. A. May and Y. Tanaka in *Epoxy Resins* (Marcel Dekker Inc., New York, 1973), Ch. 10.
9. J. M. Barton, *J. Macromol. Sci. (Chem.)* **A-8**, 25 (1974).
10. A.S.T.M. ANSI/ASTM D903-49 (Reapproved 1978). Annual Book of ASTM Standards, Part 22 (ASTM, Philadelphia, 1980), p. 231.
11. R. S. Bauer, H. E. De La Mare, J. M. Klarquist and S. F. Newman in *Epoxy Resins and Epoxides* (Shell Development Co., Houston, TX., 1973).
12. F. M. Fowkes and M. A. Mostafa, *Ind. Eng. Chem. Prod. Res. Dev.* **17**, 3 (1978).
13. C. V. Cagle, *Handbook of Adhesive Bonding* (McGraw-Hill Publishing Co., New York, 1973), Section I-14.

Adhesion of Hydrophilic Particles to Polymer Substrates Immersed in Aqueous Media†

DARRYL R. ABSOLOM and A. WILHELM NEUMANN

Department of Mechanical Engineering and Institute of Biomedical Engineering, University of Toronto, Toronto, Ontario, Canada M5S 1A4
and

Research Institute, The Hospital for Sick Children, Toronto, Ontario, Canada M5G 1X8

(Received October 16, 1986)

Various factors affecting the extent of adhesion of hydrophilic particles to polymer surfaces have been evaluated. Specifically the kinetics of adhesion, and the influence of substrate surface tension, ionic strength, pH, and surface tension of the suspending liquid medium have been investigated. In addition the role of divalent cations has been assessed. The substrates examined exhibit a wide range of wettability and the hydrophilic particles used were both fresh and glutaraldehyde-fixed human erythrocytes.

For experiments in which the particles are suspended in solutions with an ionic strength of 0.15 or greater the kinetic studies reveal that the extent of adhesion increases rapidly initially and reaches a plateau value after approximately 30 mins. There is no evidence for a lag-time in the onset of particle adhesion, suggesting that electrostatic double layer forces are negligible under these experimental conditions. For a bulk particle concentration 1×10^6 cells/ml the plateau value of adhesion corresponds to a surface coverage of no more than 10% for the most densely covered substrate. For a given set of experimental conditions the level of saturation adhesion is determined by the wettability of the substrate material. The extent of particle adhesion to any given substrate material is influenced considerably by the respective surface tension of the adhering particles (γ_{PV}), the substrate material (γ_{SV}) and the suspending liquid media (γ_{LV}). For conditions where $\gamma_{LV} > \gamma_{PV}$ the extent of

† Presented at the Tenth Annual Meeting of The Adhesion Society, Inc., Williamsburg, Virginia, U.S.A., February 22–27, 1987.

Address correspondence to: D. R. Absolom, Research Institute, The Hospital for Sick Children, Toronto, Ontario, Canada M5G 1X8.

particle adhesion decreases with increasing substrate surface tension, γ_{SV} . For conditions where $\gamma_{LV} < \gamma_{PV}$ the opposite pattern of behaviour is found.

The extent of particle adhesion to various polymer surfaces is also a function of solution pH and ionic strength. At a constant pH of 6 virtually no erythrocyte adhesion occurs at ionic strengths less than 0.05. Adhesion increases with increasing ionic strength and reaches a limiting plateau value at an ionic strength of approximately 0.1. The actual level of the plateau value is quite different for each polymer. Particle adhesion is also pH dependent. For conditions of constant ionic strength and variable pH the extent of erythrocyte adhesion at and below pH 6 is constant for each polymer substrate and extends over a substantial domain of high ionic strength and low pH. As the pH is increased erythrocyte adhesion decreases and reaches a second plateau at pH 8 and above.

The pH and ionic strength studies suggest that at low ionic strength double layer repulsion plays a critical role in preventing particle adhesion. With increasing ionic strength the double layer becomes more compressed allowing a closer approach of the particles to the substrate and hence an increased van der Waals attraction giving rise to increased erythrocyte adhesion.

KEY WORDS Adhesion kinetics; cell-surface interactions; particle adhesion; polymer surfaces; erythrocyte adhesion; effect of pH, ionic strength and surface tension on adhesion.

1 INTRODUCTION

There is widespread interest in particle adhesion to various substrates for theoretical^{1,2} as well as practical reasons.^{3,8} Understanding of the process of particle adhesion has direct implications for a large number of fields including artificial organs; electrophotography; separation of liquid-solid mixtures in filtering, screening and flocculation; sintering, pelleting and briquetting; fluidizing and pneumatic conveyance of powders; reactor fouling and various cleaning processes. In the present article we wish to review our work on hydrophilic particle adhesion to polymer substrates immersed in aqueous solutions. The presence of the liquid medium alters considerably the interaction energies involved and needs to be considered as will be discussed later in this article.

2 EXPERIMENTAL ASPECTS

(a) Hydrophilic Particles

The hydrophilic particles examined in this work are glutaraldehyde-fixed human erythrocytes (red blood cells). Our reasons for

selecting these objects as our model particles include the following:

(1) Erythrocytes are readily available in large quantities and exhibit remarkably homogeneous batch properties including size, shape and chemical composition;

(2) Glutaraldehyde-fixation results in the preparation of particles which are stable over long periods of time and in virtually all environmental conditions;

(3) Fixation prevents the loss of proteins and glycoproteins from the cell surface which might otherwise preadsorb onto carefully prepared substrates rendering interpretation of the experimental data more difficult;

(4) Fixation increases cell rigidity, thereby stabilizing the area of contact between the cell and the substrate material.

(5) Fixation produces only a small change in the net surface charge of the cell surface⁹ or in the local distribution of the charge-bearing glycoproteins in the membrane lipid bilayer.¹⁰

(6) The hydrophilicity of fixed erythrocytes has been determined by a number of independent methods.¹¹ The surface tension of fixed human erythrocytes is approximately 65 ergs/cm².

Thus these cells represent a well-characterized, readily-available source of hydrophilic particles ideally suited for studies of the type described here.

(b) Polymer Substrates

The adhesion experiments were performed using the substrate materials listed in Table I. Preparation of the substrates was performed as described previously.¹² Smooth films of these polymers (with the exception of polystyrene and sulphonated polystyrene which are commercially available as thin films) were made in a hydraulic heat press (Wabash, Ind.) by pressing strips of the polymers between chromic-acid-cleaned glass slides. All surfaces with the exception of sulphonated polystyrene have no ionizable groups or semi-permanent charges. They are also inert in the sense of not containing chemical reactive groups such as hydroxyl, amine or isocyanate. These polymers thus represent a class of materials

TABLE I
Solid substrates used in the erythrocyte adhesion experiments

Material	Source	Preparation	Contact angle θ_{H_2O} with water	Surface tension γ_{SV} (ergs/cm ²)
Fluorinated ethylene-propylene copolymer (FEP)	Commercial Plastics, Toronto, Canada	Heat Press	110 \pm 3	16.4
Dimethyl-dichlorosilane (SIL)	Eastman-Kodak, Rochester, N. Y.	Vapour deposition	108 \pm 2	17.6
Polystyrene (PS)	Central Research Lab., Dow Chemical Co.	Film	95 \pm 2	25.6
Low density polyethylene (LDPE)	Commercial Plastics, Toronto, Canada	Heat press	84 \pm 4	32.5
Acetal resin (Ac)	Commercial Plastics, Toronto, Canada	Heat press	64 \pm 1	44.6
Sulfonated polystyrene (SPS)	Central Research Lab., Dow Chemical Co.	Film	24 \pm 3	66.7

whose principal property, insofar as it affects particle adhesion, is their surface tension, γ_{sv} . The surface tension of the polymers (*cf.* Table I) was calculated from contact angle data using the equation of state approach.¹³

(c) Suspending Liquids

For the purpose of the experiments to be described here the fixed-erythrocytes were suspended at a concentration of 1×10^6 cells/ml in aqueous solutions of various ionic strengths, pH and liquid surface tensions. The specific experimental conditions are described at the appropriate position in the text.

(d) Static Adhesion Test

Particle-substrate adhesion has been investigated in a number of different experimental systems including the inclined plane,¹⁴⁻¹⁶ centrifuge methods,¹⁷⁻¹⁹ aerodynamic or hydrodynamic methods,²⁰ gravimetric methods^{1,6,7,12} the rotating disc method²¹⁻²⁴ and powdered methods.^{25,26} The present results were obtained using a static adhesion test which involves the deposition of particles onto a flat horizontal surface from a stagnant suspension. This system has the advantage that it avoids the complexities such as turbulence, shear forces, *etc.*, which might arise as the result of fluid flow. The method has been described in detail previously^{6,7,12} and hence will be discussed only briefly here. One millilitre of the particle suspension, at a concentration of 1×10^6 cells/ml, was placed on the surfaces and was retained in wells formed in Teflon[®] molds separated from the polymers by Silastic[®] gaskets. The height of the cell suspension is approximately 1 cm. The system is then incubated for the desired time and at the selected temperature. Thereafter the surfaces are placed, without exposure to air, in a large volume of the suspending fluid and rinsed under standardized conditions in order to remove any non-adherent particles. For this purpose we employ a rinsing device described previously.²⁷ Thereafter the substrates are air-dried. Then the number of particles adhering to the various surfaces is determined, after brief immersion in deionized distilled water to dissolve any salt crystals, using an automated image analysis system (Omnicon 3000, Bausch and Lomb, Roches-

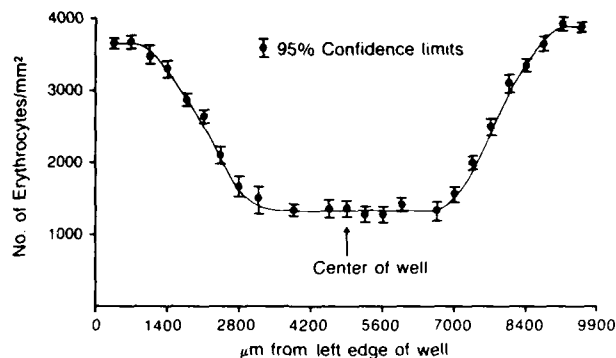


FIGURE 1 The influence of "wall-effects" in determining the extent of particle (glutaraldehyde-fixed erythrocytes) adhesion to a FEP surface. The erythrocytes, at a concentration of 1×10^6 cells/ml in Hanks Balanced Salt Solution (pH 7.2, ionic strength of 0.15) were retained in a Teflon[®] mold. Contact time was 30 minutes.

ter, NY). For this purpose a Wild-Leitz Metalloplan microscope connected to a Bosch camera containing a Chalnicon tube was used. A 32X, long-working-distance objective lens was employed. Computer controlled automation of the microscope stage permitted rapid evaluation of 126 separate fields of view of known area for each well. In view of "wall-effects" in these adhesion tests, illustrated in Figure 1, only the central portions of each well are assessed. The data from each of these individual fields measurements were then averaged and expressed as the number of particles (erythrocytes) adherent per unit surface area of substrate material. For each experiment at least six wells per type of polymer surface were examined. Each experiment was repeated at least three times.

3. THEORETICAL ASPECTS

It is generally accepted that the main forces responsible for the adhesion of small particles, suspended in a liquid, to a solid surface are long-range interactions which result from a combination of van der Waals forces and electrostatic forces. Both of these primary forces may under certain circumstances be either attractive or repulsive. The actual strength of the subsequent adhesive bond may

also depend on factors such as substrate roughness and deformability, particle size and shape, the nature of the particle, surface contamination. At the present time it is widely accepted that particle adhesion is best described in terms of the DLVO theory.^{28,29}

(a) DLVO Predictions of Particle Adhesion

In recent years a theoretical description of particle sedimentation and adhesion to flat horizontal substrates out of stagnant suspensions, such as described in the present work, has become available.^{30,31} In the essence this approach takes into account the rate of sedimentation of the particles in the suspending medium and the rate of escape over the potential barrier as given by the DLVO theory. The authors give an expression for the number of particles adhering to a solid surface as a function of time. Denoting t^* as the time needed for the furthest cell to reach the surface by diffusion, then for times $t < t^*$ the number of particles adhering to the surface is given by:

$$n = C_0 V \left(t + \frac{e^{-Pt} - 1}{P} \right) \quad (1)$$

where n is the number of particles adhering per unit area; C_0 is the initial bulk concentration of the particles in suspension; V is the sedimentation velocity and P is the probability per unit time that a particle will adhere to the solid surface. For time t larger than $3/P$, Eq. (1) can be approximated by:

$$n = C_0 V \left(t - \frac{1}{P} \right) \quad (2)$$

The rate at which particles adhere to the solid surface is then proportional to the sedimentation velocity V . For time t greater than t^* , the authors³¹ obtained an expression which predicts that all available particles will adhere to the solid surface.

Overall, the theoretical predictions are as sketched in Figure 2. For a different solid surface, P may vary and hence the extrapolated intersection with the time axis may be different. However, as may be seen from Eq. (2), at times $t < t^*$ but $t > 3/P$, the rate of particle adhesion would be independent of the solid surface. Thus this

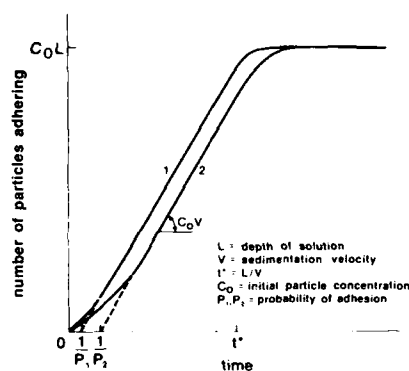


FIGURE 2 Theoretical plot of particle adhesion as a function of time—from Ruckenstein, *et al.*^{30,31} Schematic curves shown for two different probabilities of adhesion. L = depth of solution; V = sedimentation velocity; $t^* = L/V$; C_0 = initial particle concentration; P_1, P_2 = probability of adhesion.

DLVO model predicts that the process of particle adhesion would be kinetically controlled and should lead to complete coverage of the substrate material.

4. EXPERIMENTAL VERIFICATION

In an attempt to test this theoretical model we have examined the kinetics of particle adhesion to a number of different substrates.^{7,32,33} Shown in Figures 3 and 4 are the results of experiments with both fresh and glutaraldehyde-fixed erythrocytes, suspended in Hanks Balanced Salt Solution, pH 7.2 and an ionic strength of 0.15. For details of the experimental conditions see legends to the figure. It should be noted that the general features of the curves for the two types of hydrophilic particles are identical.

Comparing the curves of Figures 3 and 4 with the theoretical predictions^{30,31} as given in Figure 2 and described by Eqs (1) and (2), we note that these relations do not describe our results adequately. According to this theory, for times greater than $3/P$, but less than t^* , the rate of particle adhesion to various solid surfaces would have to be identical. In other words, after lag times possibly different for the various substrates the curves would all

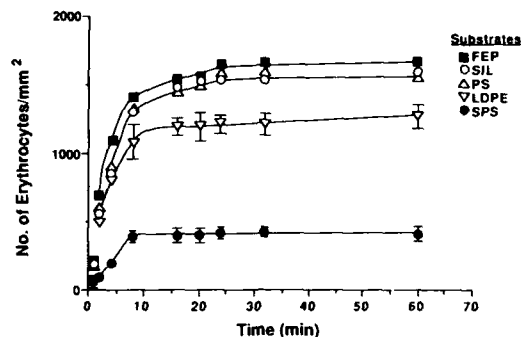


FIGURE 3 Kinetics of glutaraldehyde-fixed human erythrocyte adhesion to various surfaces. Cell concentration is 1×10^6 cells/ml in Hanks Balanced Salt Solution (pH 7.2; ionic strength = 0.15). Substrates as indicated. The associated error limits are 95% confidence limits. (For graphical reasons errors are shown only for selected cases; errors are similar in all cases.)

have to be parallel to each other. This is clearly not the case. There is no evidence in the experimental curves for the existence of lag times, and the slopes of the curves are a function of the surface tension of the substrate, as discussed previously.^{6,7,12,32,34} Furthermore, the derived theoretical expressions imply that the rate of adhesion will remain constant until it reaches t^* . For a depth of the

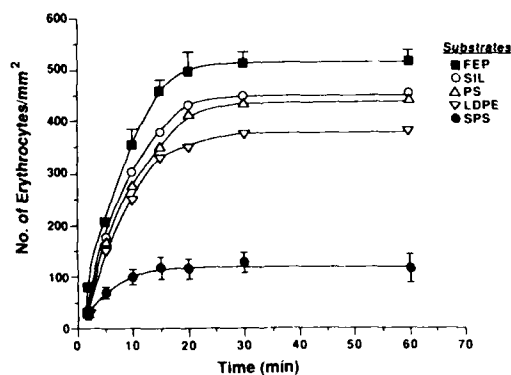


FIGURE 4 Kinetics of fresh human erythrocyte adhesion to various surfaces in Hanks Balanced Salt Solution (pH 7.2; ionic strength = 0.15). Cell concentration is 1×10^6 cells/ml. Substrates as indicated. The associated error limits are 95% confidence limits. (For graphical reasons error are shown only for selected cases; errors are similar in all cases.)

solution in the well of approximately 1 cm as in these experiments, t^* is of the order of 10 hrs, in contrast to the 20–30 minutes after which no more particles adhered to the surface. The extent of adhesion is most pronounced on the hydrophobic FEP surface. At the saturation level of adhesion on the FEP surface a maximum surface coverage of only approximately 10–15% is observed. Thus the traditional DLVO type of description of particle adhesion fails on two accounts to describe the experimental observations of the present work: (1) Within the limits of these experiments no lag time in the adhesion process is noted; and (2) Complete surface coverage of the substrate is not observed. Thus we conclude that the process of particle adhesion out of a solution with an ionic strength of 0.15 or greater is not transport controlled but is determined by properties of the solid substrate, *cf.* Figures 3 and 4.

Both the rate of adhesion and the saturation level of particle adhesion to each of the surfaces is substrate dependent. Plots of the number of particles adhering per unit surface area for the various substrates as a function of substrate surface tension for the various contact times result in a generally linear decrease in the extent of particle adhesion with increasing substrate surface tension.

5. THERMODYNAMIC MODEL FOR PARTICLE ADHESION

These observations are consistent with a theoretical description of particle adhesion based on surface thermodynamic considerations. Such an approach indicates that a properly identified thermodynamic potential, the grand canonical potential, which we simply call the free energy,⁷ will be minimized at equilibrium. This implies that the process under consideration, *e.g.* particle adhesion, will be favoured if the process itself causes the thermodynamic function to decrease. The process will not be favoured if it would cause the free energy function to increase.

In order to make quantitative predictions about the likelihood of a particular process, it is necessary to "model" the process: Consider a particle (P) initially suspended in a liquid (L) attaching to a solid (S) which is also immersed in the same liquid as illustrated schematically in Figure 5. In the absence of specific interactions the

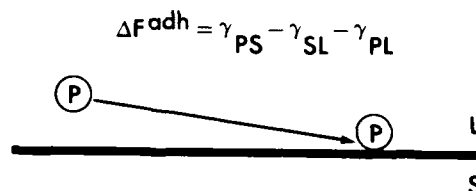


FIGURE 5 Schematic representation of the process of particle adhesion. *P*, particle; *L*, suspending liquid; *S*, substrate materials.

change in free energy (ΔF^{adh}) due to the process of adhesion is

$$\Delta F^{\text{adh}} = \gamma_{PS} - \gamma_{PL} - \gamma_{SL} \quad (3)$$

where γ_{PS} , γ_{PL} and γ_{SL} are the particle–solid, particle–liquid and solid–liquid interfacial tensions, respectively. The validity and restrictions of this model have been described in detail elsewhere.^{11,35,36} It should be emphasized that this model considers only van der Waals interactions. The relationship between interfacial tensions and van der Waals forces has been described in detail elsewhere.^{37,38}

It is clear from Eq. (3) that the free energy of adhesion of a particle to a surface depends not only on the surface tension of the adhering particles and the polymer surface but is also dependent on the surface tension of the suspending liquid. As an illustration shown in Figure 6 is the theoretical free energy of adhesion (ΔF^{adh}) for fixed-erythrocytes to substrates of various surface tensions, for two conditions of the liquid surface tension. The input data required for the development of such a plot are the respective surface tensions of the adhering particles (γ_{PV}), the polymer substrates (γ_{SV}) and the suspending liquid medium (γ_{LV}). This information is given in the legend to this figure. Consideration of such theoretical calculations as illustrated in Figure 6 lead to a distinction between two situations: For

$$\gamma_{LV} > \gamma_{PV} \quad (4)$$

ΔF^{adh} becomes more positive with increasing γ_{SV} predicting a decrease of particle adhesion with increasing substrate surface tension, γ_{SV} , over a comparatively wide range of γ_{SV} values. On the

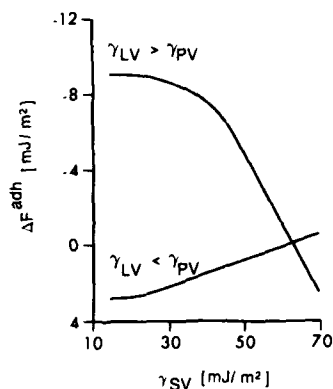


FIGURE 6 The free energy of adhesion (ΔF^{adh}) for fixed human erythrocytes as a function of substrate surface tension, γ_{SV} . (A) $\gamma_{LV} > \gamma_{PV}$: $\gamma_{LV} = 72.8 \text{ ergs/cm}^2$ and $\gamma_{PV} = 64.6 \text{ ergs/cm}^2$. (B) $\gamma_{LV} < \gamma_{PV}$: $\gamma_{LV} = 59.8 \text{ ergs/cm}^2$ and $\gamma_{PV} = 64.6 \text{ ergs/cm}^2$.

other hand, when

$$\gamma_{LV} < \gamma_{PV} \quad (5)$$

the opposite pattern of behaviour is predicted.^{6,34} For the limiting case of the equality

$$\gamma_{LV} = \gamma_{PV} \quad (6)$$

ΔF^{adh} becomes equal to zero independently of the value of γ_{SV} implying that under these conditions the extent of particle adhesion does not depend on substrate surface properties and in principle should be zero if no other effects, such as electrostatic interactions, come into play.

6. EXPERIMENTAL VERIFICATION

As an illustration of the influence of the substrate surface tension on the extent of erythrocyte adhesion shown in Figure 7 are photomicrographs of the substrate after rinsing to remove non-adherent cells. In Figures 7a and 7b the suspending liquid surface tension was 72.8 ergs/cm^2 and the two substrates, fluorinated ethylene-propylene copolymer (FEP) and sulphonated polystyrene (SPS), have surface tensions of 16.4 and 66.7 ergs/cm^2 , respectively. In

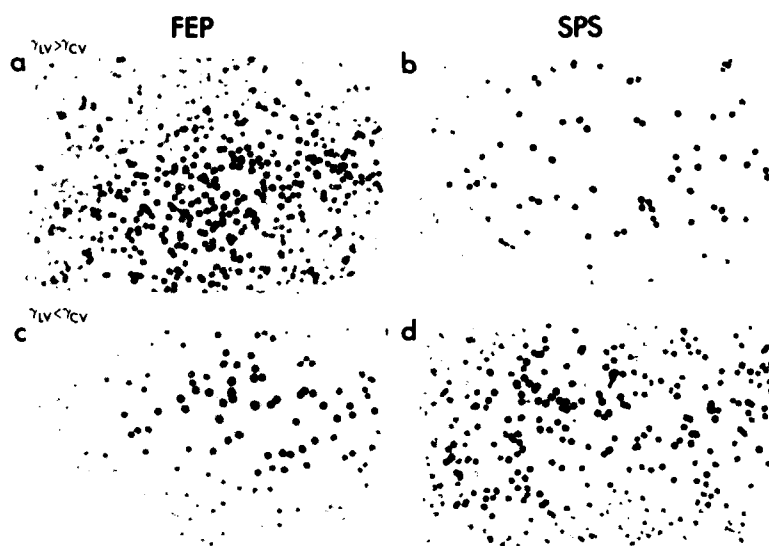


FIGURE 7 Photomicrographs of erythrocyte adhesion under varying experimental conditions. (a) Fluorinated ethylene-propylene (FEP, $\gamma_{SV} = 16.4$ ergs/cm²); $\gamma_{LV} = 72.8$ ergs/cm². (b) Sulphonated polystyrene (SPS, $\gamma_{SV} = 66.7$ ergs/cm²); $\gamma_{LV} = 72.8$ ergs/cm². (c) Fluorinated ethylene-propylene (FEP, $\gamma_{SV} = 16.4$ ergs/cm²), $\gamma_{LV} = 59.8$ ergs/cm². (d) Sulphonated polystyrene (SPS, $\gamma_{SV} = 66.7$ ergs/cm²); $\gamma_{LV} = 59.8$ ergs/cm².

Figure 7c and 7d we show photomicrographs of the extent of adhering erythrocytes to the same two surfaces when the liquid surface tension had been substantially lowered to a value of $\gamma_{LV} = 59.8$ ergs/cm². A comparison of Figure 7a and 7b with Figures 7c and 7d reveals quite clearly that as the liquid surface tension is varied so the pattern of adhesion is changed. As the surface tension of the suspending liquid medium is lowered from 72.8 to 59.8 ergs/cm², the number of adhering particles per unit surface area decreases in the case of FEP but increases for SPS under otherwise identical conditions. The effect of varying γ_{LV} on the extent of particle adhesion is perhaps even more clearly illustrated by considering one and the same substrate and two different γ_{LV} values, e.g. by comparing Figure 7a with Figure 7c or Figure 7b with Figure 7d.

The quantitative results of experiments in which the particles, at a constant bulk concentration, are suspended in various aqueous mixtures having different surface tensions are summarized in Figure 8. For the purpose of these experiments the fixed erythrocytes were suspended, at a bulk concentration of 1×10^6 erythrocytes/ml. in buffered Hanks Balanced Salt Solutions containing varying amounts of dimethyl sulfoxide (DMSO), a surface-tension-lowering additive. The pH and temperature of these solutions was held constant at pH 7.2 and 25°C respectively. The surface tension, measured by means of the Wilhelmy Plate Method,³⁹ of these solutions are given in Table II. For complete experimental details see legend to Figure 8. The theoretical predictions inherent in Figure 6 and their implications are substantiated experimentally as shown in Figure 8. At the lowest DMSO concentration, corresponding to the highest surface tension, γ_{LV} , of the suspending medium, particle adhesion *decreases* with increasing substrate surface tension γ_{SV} . As the DMSO concentration is increased and the surface tension γ_{LV} correspondingly lowered, the change in the extent of particle adhesion with increasing γ_{SV} become less pronounced. At a certain intermediate γ_{LV} , particle adhesion becomes independent of γ_{SV}

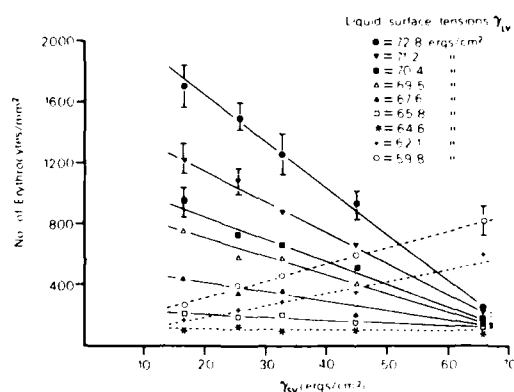


FIGURE 8 Erythrocyte adhesion as a function of substrate surface tension γ_{SV} for various liquid surface tensions. The cells at a concentration of 1×10^6 cells/ml were suspended in Hanks Balanced Salt Solution containing varying amounts of a surface tension lowering additive, dimethylsulfoxide (DMS). The pH of the solution was 7.2. Indicated error limits are 95% confidence limits. (For graphical reasons error limits are given only for selected cases; the errors are similar in all cases.)

TABLE II
Suspending media for the erythrocyte adhesion experiments

Medium	Concentration	Surface tension γ_{LV} (ergs/cm ²)
HBSS ^a	—	72.8
HBSS-DMSO 1 ^b	1% (vol/vol) DMSO	71.2
HBSS-DMSO 3	3% (v/v)	70.4
HBSS-DMSO 5	5% (v/v)	69.5
HBSS-DMSO 10	10% (v/v)	67.6
HBSS-DMSO 12	12% (v/v)	65.8
HBSS-DMSO 12.5	12.5 (v/v)	64.6
HBSS-DMSO 15	15% (v/v)	62.1
HBSS-DMSO 18	18% (v/v)	59.8
H ₂ O-DMSO 12.5	12.5% (v/v)	64.4

^a Hanks Balanced Salt Solution, comprising in mg/L: anhydr. CaCl₂: 140.0; KCl: 400.0; KH₂PO₄: 60.0; MgCl₂ · 6H₂O: 100.0; MgSO₄ · 7H₂O: 100.0; NaCl: 8000.0; NaHCO₃: 350.0; NaHPO₄ · 2H₂O: 60.0; glucose: 1000.0; ionic strength, μ = 0.15; pH 7.26.

^b Dimethyl sulfoxide.

and finally, at yet lower values of the surface tension γ_{LV} , particle adhesion *increases* with increasing γ_{SV} . Aside from the practical interest of these data there are two further points to be made. First the thermodynamic model underlying Eq. (3) describes the qualitative features of erythrocyte adhesion remarkably well. The agreement between theoretical predictions and experimental observations suggests for the present experimental conditions (ph 7.2, ionic strength \approx 0.15) that the extent of particle adhesion to polymer surfaces is primarily governed by van der Waals forces. Secondly, the thermodynamic model predicts that in the case of $\gamma_{LV} = \gamma_{PV}$ (Eq. (6)), ΔF^{adh} should be independent of γ_{SV} , implying that the extent of adhesion should be independent of γ_{SV} , a situation that is indeed contained in the data of Figure 8. To investigate this concept further, the slopes of the straight lines in Figure 8 were plotted *versus* γ_{LV} in Figure 9, by means of a second order polynomial curve fit. It is inferred that the slope becomes equal to zero at a value of γ_{LV} which is characteristic for the adhering particles. This value, according to the predictions of the thermodynamic mode, is equal to the surface tension, γ_{PV} , of the particles themselves. Figure 9 reveals that for the fixed human erythrocytes the adhesion

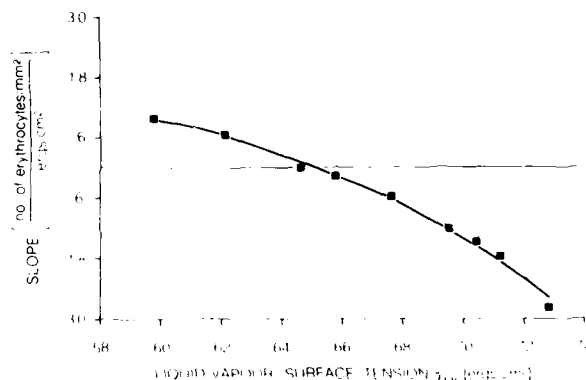


FIGURE 9 Slopes of the straight lines of Figure 8 versus liquid surface tension. The slope is equal to zero for $\gamma_{LV} = \gamma_{PV}$.

slope becomes equal to zero when $\gamma_{LV} = 64.6$ ergs/cm², implying that the surface tension of these particles is equal to 64.6 ergs/cm² at 25°C. This is in good agreement with the surface tension values obtained for these particles by means of other independent techniques.^{11,32,40} This issue is discussed in more detail later in this article.

Thus the thermodynamic model for particle adhesion proposed in Eq. (3) and illustrated in Figure 6 can be used to describe qualitatively erythrocyte adhesion to a range of polymer surfaces under conditions of varying γ_{LV} . The model, however, does not describe entirely all the features of the pattern of particle adhesion. When $\gamma_{LV} = \gamma_{PV}$ there is an absence of van der Waals interactions and hence the extent of erythrocyte adhesion is expected to be *independent* of the surface properties of the substrate materials, and

$$\Delta F^{\text{adh}} = 0 \quad (7)$$

Under these conditions ($\gamma_{LV} = \gamma_{PV}$), however, a small level of adhesion to all the polymer surfaces was observed. In this case, particle adhesion cannot be ascribed to van der Waals attraction; in a polar liquid such as water, electrostatic interactions may be implicated. To investigate this possibility further, the adhesion of erythrocytes was measured at the liquid surface tension close to the cell surface tension of 64.6 ergs/cm². This was done at 12.5% (v/v) DMSO concentrations at an ionic strength $\mu \approx 0.15$ (in HBSS), *i.e.*

just as in Fig. 8, and similarly at $\mu = 0.075$ (half-strength HBSS) and at $\mu = 0$. The results are given in Figure 10. At $\mu = 0.15$, and in the absence of van der Waals interactions, an average of 104 adhering particles per square millimeter is observed, while at $\mu = 0.075$ considerably fewer (≈ 68) particles per unit surface are found. At $\mu = 0$ only 6 particles per square millimeter were observed. Thus, lowering the ionic strength of the suspending medium significantly decreases the residual level of particle adhesion under these experimental conditions, *i.e.*, when the van der Waals forces are zero. This reduction in the number of adhering cells may be due to electrokinetic phenomena such as a decrease in ionic strength being accompanied by an increase in ζ -potential as discussed below.

Plurivalent cations, *e.g.* Ca^{2+} ions, are often implicated in particle adhesion studies. Since these ions were present in the buffer system (HBSS) used in these studies, a divalent chelating agent, Na_2EDTA , was admixed into the buffer in order to bind and effectively remove these cations. As shown in Fig. 10, this indeed resulted in a significant decrease in the extent of particle adhesion to the polymer surfaces. These results together with the data presented in Figure 8 suggest that, in the absence of any specific interactions, two major types of forces play a role in determining the overall extent of particle adhesion to polymer surfaces: van der Waals attractive

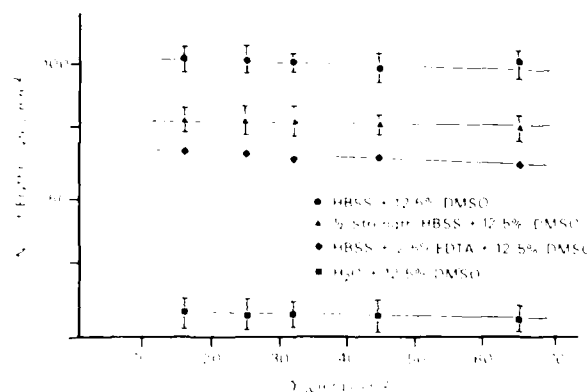


FIGURE 10 Erythrocyte adhesion as a function of substrate surface tension γ_{st} in high and low ionic strength media and in the presence of a chelating agent. Indicated error limits are 95% confidence limits.

forces (between the adhering particles and the polymer substrate) and plurivalent cationic bridging.

The data presented thus far would suggest that the most important of these forces are, by a large margin, the van der Waals interactions; the level of particle adhesion out of HBSS onto a Teflon® surface is ≈ 1700 cells/mm². When the van der Waals attraction is reduced to zero, and under otherwise identical conditions, the level of particle adhesion is reduced to approximately 100 cells/mm² ($\approx 6\%$). Under these conditions both plurivalent cationic bridging and ionic strength effects contribute to the residual level of particle adhesion. These conclusions are based on experiments in which the particles are suspended in buffered solutions having an ionic strength of 0.15 and pH 7.2.

7. ROLE OF SOLUTION pH AND IONIC STRENGTH

The effect of ionic strength has been briefly referred to above. In order to define its role in particle adhesion more precisely a systematic study was undertaken. The data contained in Figure 8 and in 10 are surprising since there is an apparent absence of electrical double layer effects on particle adhesion. In order to address this question a study on the role of solution pH and ionic strength in determining the extent of particle adhesion to polymer surfaces was undertaken. Experimental details have been reported elsewhere.³⁴

(a) Solution pH

Results of experiments to determine the effect of pH on particle adhesion are shown in Fig. 11. These experiments were performed at a constant ionic strength of 0.15, *i.e.* the particles were suspended in 150 mM NaCl solutions buffered to the described pH with 3×10^{-4} M sodium bicarbonate. The pH range examined extended from pH 5.0 to pH 9.0 at 0.5 pH intervals. This range was selected since it has been established^{41,42} that the particles' surface charge density did not vary over this pH range as assessed by electrophoretic mobility measurements in 0.15 M NaCl at the various pH values. Thus, changes in the extent of particle adhesion cannot be

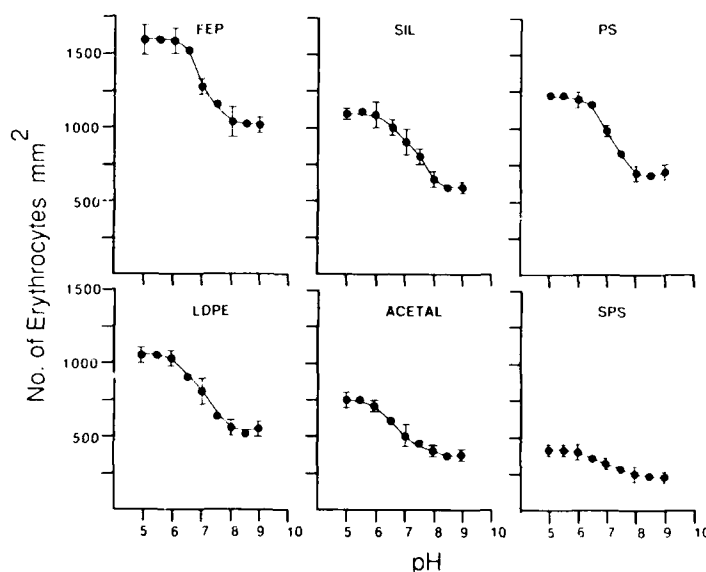


FIGURE 11 The effect of pH on erythrocyte adhesion to polymers of different surface tension. The cells, at a concentration of 1×10^6 cells/ml, were suspended in various buffered pH solutions at a constant NaCl concentration of 150 mM. Errors indicated are 95% confidence limits.

ascribed to changes in particle zeta-potential and must be due to other factors.

There are several points to be made about the data contained in Fig. 11. First we note that a decrease in pH below 6.0 does not result in any further change in the level of particle adhesion for any of the polymer substrates examined (Plateau No. 1). As the pH of the suspending solution is increased above pH 6.0 there is a marked decrease in the level of particle adhesion until a pH value of approximately 8.0 is reached. Thereafter, the level of particle adhesion does not change anymore, *i.e.* a second plateau is reached for each substrate (Plateau No. 2). The values of these plateau levels of particle adhesion are determined by substrate surface properties in agreement with earlier observations with respect to Figures 3, 4 and 8. This is illustrated in Figure 12 in which the two plateau levels of particle adhesion are plotted as a function of substrate surface tension. We note that the two plateau levels of

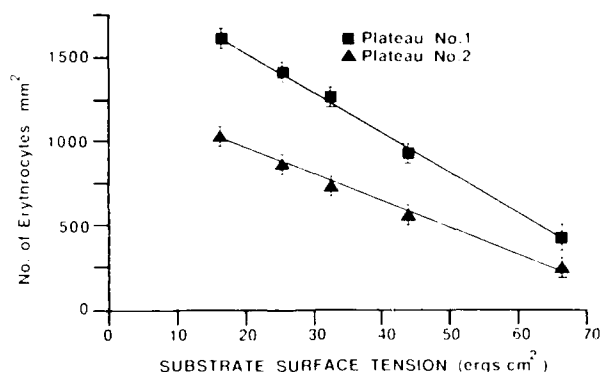


FIGURE 12 Plateau values of erythrocyte adhesion plotted as a function of substrate surface tension. Errors indicated are 95% confidence limits.

adhesion each give rise to a straight-line plot of the extent of particle adhesion with increasing substrate surface tension. Particularly noteworthy, however, is the observation that the slopes of these two lines are different. These differences are significant and suggest that the particle-polymer interaction is altered as a result of the pH changes. As discussed above these changes cannot be ascribed to differences in the effective zeta-potentials and an alternative explanation must be sought.

Interpreting the two straight lines naively from the point of view of the thermodynamic model described earlier and the associated stipulation that only van der Waals forces are operative, one would conclude for the present case of constant liquid surface tension that the Plateau No. 2 curve belongs to particles having a surface tension which is different from that of the particles described by Plateau No. 1. To be specific, the thermodynamic model would suggest that the particles of Plateau No. 2 have a higher surface tension (*i.e.* are more hydrophilic) than those of Plateau No. 1. The implication of these conclusions is that changes in pH conditions have, in some as yet undetermined manner, altered the surface tension of the particles whilst the net surface charge of the particles remains unchanged.

(b) Ionic Strength

The results of experiments performed in order to assess the effect of solution ionic strength on hydrophilic particle adhesion are summarized in Figure 13. For the purpose of these experiments the pH of the solution was maintained at a constant value of 6.1. This pH value was selected since it falls within the pH range giving rise to one of the two plateaux in Fig. 12. Thus, the points corresponding to an ionic strength of 0.15 (*i.e.* 150 mM NaCl concentration) in Figure 13 are identical to those of pH 6.1 in Figure 12. We note from Figure 13 that the level of particle adhesion is near zero for the lowest ionic strengths and increases with increasing ionic strength. Finally, at ionic strengths near 0.1 (*i.e.* sodium chloride concentrations of 100 mM) the extent of erythrocyte adhesion reaches a limiting plateau value. In general, this plateau level of particle adhesion decreases with increasing substrate surface tension. A plot of this level of particle adhesion as a function of

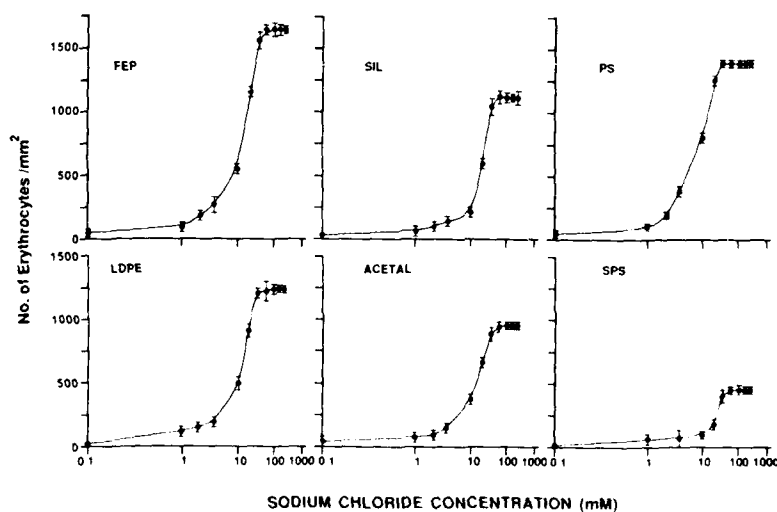


FIGURE 13 The effect of ionic strength on erythrocyte adhesion to polymers of different surface tension. The cells at a concentration of 1×10^6 cells/ml were suspended in various ionic strength solutions at a constant pH of 6.1. Errors indicated are 95% confidence limits.

substrate surface tension has already been given in Figure 12 (Plateau No. 1).

These findings suggest that at low ionic strength double layer repulsion prevents particle adhesion more or less completely. With increasing ionic strength the double layer thickness decreases so that the particles can approach the solid substrates more closely so that the van der Waals forces will become appreciable, causing particle adhesion. For ionic strengths of 0.1 (corresponding to a NaCl concentration of 100 mM) and above, the van der Waals forces apparently overpower all electrostatic effects.

8. IRREVERSIBLE PARTICLE ADHESION

Adhesion of fixed erythrocytes to polymer surfaces out of solution of high ionic strength (0.15) is irreversible in the sense that subsequent immersion of the substrate in deionized-distilled water does not result in particle detachment. This observation is valid for all pH conditions examined. This is illustrated in Table III in which it is shown that there is no significant difference in the level of particle adhesion to any of the polymer surfaces, for each of the pH conditions examined, when the surfaces are rinsed either in water or in high-ionic-strength (150 mM NaCl) media. The implication of this observation is that under experimental conditions of a suspending solution ionic strength of 0.15 and a solution pH in the range of 5–9, particle adhesion is irreversible, a pattern of behaviour which is characteristic of a process that has occurred at the primary energy minimum.²⁹ It has yet to be established whether solutions of low ionic strength also give rise to irreversible adhesion or whether under such experimental conditions particle adhesion is reversible reflecting a process occurring at the secondary energy minimum.

9. DISCUSSION

Earlier in this article we discussed the apparent failure of a typical DLVO approach to describe the experimental results of erythrocyte adhesion to a wide range of substrate surface properties. It appears that a pH of approximately 7.0 and an ionic strength of 0.1 or

TABLE III
Effect of ionic strength on erythrocyte detachment. For the initial cell-polymer exposure the erythrocytes were suspended in the various pH solutions as indicated with an ionic strength of 0.15. Errors are 95% confidence limits assuming a Student *t*-distribution

Polymer surface	150 mM NaCl rinse					Deionized distilled water rinse				
	5.0	6.0	pH 7.0	8.0	9.0	5.0	6.0	7.0	8.0	9.0
FEP	1610 ± 100	1602 ± 90	1524 ± 60	1021 ± 120	1000 ± 76	1645 ± 80	1590 ± 110	1545 ± 78	1008 ± 75	1000 ± 69
SIL	1098 ± 56	1103 ± 68	897 ± 104	644 ± 80	597 ± 42	1051 ± 70	1146 ± 85	909 ± 60	665 ± 75	578 ± 56
PS	1418 ± 26	1382 ± 55	1180 ± 30	882 ± 40	870 ± 68	1447 ± 56	1359 ± 42	1162 ± 38	877 ± 52	853 ± 36
LDPE	1243 ± 58	1217 ± 54	998 ± 86	756 ± 45	747 ± 58	1236 ± 61	1238 ± 76	1049 ± 58	743 ± 38	719 ± 31
Acetal	926 ± 68	898 ± 47	709 ± 64	580 ± 42	559 ± 30	949 ± 25	861 ± 89	748 ± 60	570 ± 45	518 ± 24
SPS	393 ± 38	386 ± 48	316 ± 15	237 ± 40	226 ± 31	406 ± 42	365 ± 31	297 ± 24	260 ± 52	216 ± 45

higher, erythrocyte adhesion is primarily governed by van der Waals interactions between the particles and the various substrate materials. The experimental data can be predicted in large part by means of a thermodynamic model which implicitly considers that van der Waals forces only are operative. Under the stated experimental conditions particle adhesion is irreversible, a pattern of behaviour which is consistent with a process occurring at the primary energy minimum.

Critical to the success of the thermodynamic model for particle adhesion is the ability to determine the surface tension of the adhering particles. Over the past decade several strategies have been developed to determine the surface tension of small particles. These strategies include contact angle measurements,⁴³ the adhesion strategy,^{6,12,33} droplet sedimentation^{44,45} and sedimentation volume⁴⁶⁻⁴⁹ studies, and the freezing front method.^{37,38,50-55} These techniques have recently been reviewed in detail elsewhere.^{11,40} A comparison of the results obtained with these independent techniques for glutaraldehyde-fixed human erythrocytes is given in Table IV. As illustrated it is clear that the results obtained with the different techniques are in good agreement. As yet we have not been able to perform contact angle measurements on fixed-erythrocytes. We believe this is because of the rigid nature of these cells.

As noted earlier, the extent of particle adhesion decreases with increasing substrate surface tension. There is, however, one minor, although significant, exception to this general trend. Adhesion to a siliconized glass surface is considerably less than that noted on a

TABLE IV
Surface tension of glutaraldehyde-fixed human erythrocytes obtained *via* different techniques.
Corrected to 22°C assuming $\frac{d\gamma}{dT} = 0.1$ ergs/cm²°C

Method	Particle surface tension (ergs/cm ²)
Adhesion	64.6
Freezing Front	64.2
Droplet Sedimentation	64.3
Sedimentation Volume	64.5

hydrophobic FEP surface even though these surfaces both have the same surface tension of approximately 17 ergs/cm². Generally, the level of erythrocyte adhesion on a siliconized surface is similar to that observed on a polystyrene surface which has a surface tension of approximately 26 ergs/cm². This observation is illustrated in Figures 3 and 4, respectively. Thus, siliconized glass behaves as one would expect of a more hydrophilic surface. There are two possible, not mutually excluding, explanations for this pattern of behaviour: 1. The hydrocarbon (silane) layer may not be complete and would thus allow contact between the hydrophilic glass surface and the erythrocytes. This possibility, however, is not likely since contact angle measurements performed on various sections of the siliconized surface suggest a homogenous surface. 2. The second possibility, which may be operative even if the silane coating is perfect, is a phenomenon known as "screening".^{2,56,57} This is due to the fact that the depth of the van der Waals interaction between two phases is of the same order as the separation distance between the two phases. Thus, since the silane layer is probably only a few Angstroms thick, and since the van der Waals interaction are appreciable over hundreds of Angstroms, the approaching cells will interact not only with the silane layer, but also with the underlying glass substrate. This type of apparent anomaly in the behaviour of siliconized surfaces has been observed not only with respect to particle adhesion³² but also with macromolecule (protein) adsorption.⁵⁸

Acknowledgements

Supported by research grants from the Natural Science and Engineering Research Council (A-8278, UO-408), the Medical Research Council (MT 5462, MT 8024, MA 9114) of Canada and the Ontario Heart and Stroke Foundation (AN 402). One of us (D.R.A.) acknowledges receipt of an Ontario Heart and Stroke Foundation Senior Research Fellowship.

References

1. M. Corn in *Aerosol Science*, C. N. Davis, Ed. (Academic Press, London, 1966), pp. 359.
2. H. Krupp, *Adv. Colloid Interface Sci.* **1**, 111 (1967).
3. M. T. Broughey, R. M. Duckworth, A. Lips, and A. L. Smith *Chem. Soc. Faraday Trans. I*, **74**, 2200 (1978).

4. G. Thomson, N. Kallay and E. Matijevic, *Chem. Eng. Sci.* **38**, 1901 (1983).
5. P. Gherardi and E. Matijevic, *J. Colloid Interface Sci.* **109**, 57 (1986).
6. D. R. Absolom, *et al.*, *J. Colloid Interface Sci.* **104**, 51 (1985).
7. A. W. Neumann, *et al.*, *J. Biomed. Mater. Res.* **14**, 499 (1980).
8. L. Weiss, *Int. Rev. Cytol.* **9**, 187 (1960).
9. P. S. Vassar, *et al.*, *J. Cell Biol.* **53**, 809 (1972).
10. P. J. Pinto da Silva, *J. Cell Biol.* **53**, 77 (1972).
11. A. W. Neumann, *et al.*, *Annals N.Y. Acad. Sci.* **416**, 276 (1983).
12. A. W. Neumann, D. R. Absolom, C. J. van Oss and W. Zingg, *Cell Biophys.* **1**, 79 (1979).
13. A. W. Neumann, R. J. Good, C. J. Hope and M. Sejpal, *J. Colloid Interface Sci.* **49**, 291 (1974).
14. D. K. W. Smith and J. A. Kitchener, *Chem. Eng. Sci.* **33**, 1631 (1978).
15. S. N. Omenyi, J. Chappuis and A. W. Neumann, *J. Adhesion* **13**, 131 (1981).
16. E. Cremer, Th. Kraus and F. Conrad, *Angew. Chem.* **64**, 10 (1952).
17. J. W. Beams, J. B. Breazeale and W. L. Bart, *Phys. Rev.* **100**, 1657 (1955).
18. M. C. Kordecki and C. Orr, *Arch. Environ. Health* **1**, 13 (1960).
19. G. Böhme, *et al.*, *Z. Angew. Phys.* **19**, 265 (1965).
20. A. J. Goldman, R. G. Cox and H. Brenner, *Chem. Eng. Sci.* **22**, 653 (1967).
21. P. H. Tewari and A. B. Campbell in *Recent Developments in Separation Science*, Vol. 4, N. N. Li, Ed., (CRC Press, New York, 1978), p. 83.
22. G. E. Clint, J. H. Clint, J. M. Corkhill and T. Walker, *J. Colloid Interface Sci.* **44**, 121 (1973).
23. M. Hull and J. A. Kitchener, *Trans. Faraday Soc.* **65**, 3093 (1969).
24. J. K. Marshall and J. A. Kitchener, *J. Colloid Interface Sci.* **22**, 342 (1966).
25. E. J. Clayfield and E. C. Lumb, *Discussions Faraday Soc.* **42**, 285 (1966).
26. E. J. Clayfield and A. L. Smith, *Env. Sci. Technol.* **4**, 413 (1970).
27. O. S. Hum, A. W. Neumann and W. Zingg, *Thromb. Res.* **7**, 461 (1975).
28. B. V. Deryagin and L. D. Landau, *Acta Phys.—Chim. (URSS)* **14**, 63 (1941).
29. E. J. W. Verwey and J. T. G. Overbeek, *Theory of the Stability of Lyophobic Colloids* (Elsevier, Amsterdam, 1948).
30. E. Ruckenstein, A. Marmur and S. R. Rakower, *Throm. Haemostas. (Stuttgart)* **36**, 334 (1976).
31. R. Srinivasan and E. Ruckenstein, *J. Colloid Interface Sci.* **79**, 390 (1981).
32. D. R. Absolom, *et al.* (In preparation).
33. D. R. Absolom, *et al.*, *Colloids and Surfaces* **17**, 143 (1986).
34. D. R. Absolom, *et al.*, *Colloids and Surfaces* (Accepted for publication).
35. D. R. Absolom, W. Zingg and A. W. Neumann in *Comprehensive Biotechnology*, Vol. III, C. C. Cooney and A. E. Humphrey, Eds. (Pergamon Press, N.Y., 1985), pp. 433.
36. R. P. Smith, D. R. Absolom, J. K. Spelt and A. W. Neumann, *J. Colloid Interface Sci.* **110**, 521 (1986).
37. A. W. Neumann, S. N. Omenyi and C. J. van Oss, *Colloid and Polymer Sci.* **257**, 413 (1979).
38. A. W. Neumann, S. N. Omenyi and C. J. van Oss, *J. Phys. Chem.* **86**, 1267 (1982).
39. A. W. Neumann, *Adv. Colloid Interface Sci.* **4**, 105 (1974).
40. D. R. Absolom, R. P. Smith and A. W. Neumann, "Techniques for Determining the Wettability of Small Particles" (In Preparation).
41. D. H. Heard and G. V. F. Seaman, *J. Gen. Physiol.* **43**, 635 (1960).
42. D. H. Heard and G. V. F. Seaman, *Biochim. Biophys. Acta* **53**, 366 (1961).

43. D. R. Absolom, W. Zingg and A. W. Neumann, *J. Colloid Interface Sci.* (In Press).
44. S. N. Omenyi, *et al.*, *J. Colloid Interface Sci.* **81**, 402 (1981).
45. S. N. Omenyi, *et al.*, *J. Dispersion Sci. Technol.* **3**, 307 (1982).
46. E. I. Vargha-Butler, *et al.*, *Chem. Eng. Comm.* **33**, 255 (1985).
47. E. I. Vargha-Butler, *et al.*, *Colloids and Surfaces* **15**, 233 (1985).
48. E. I. Vargha-Butler, T. K., Zubovits, H. A. Hamza and A. W. Neumann, *J. Dispersion Sci. Technol.* **6**, 357 (1985).
49. D. R. Absolom, *et al.*, *J. Colloid Interface Sci.* (Accepted).
50. S. N. Omenyi, R. P. Smith and A. W. Neumann, *J. Colloid Interface Sci.* **75**, 117 (1980).
51. S. N. Omenyi, A. W. Neumann and C. J. van Oss, *J. Appl. Phys.* **52**, 789 (1981).
52. R. P. Smith, S. N. Omenyi and A. W. Neumann in *Physicochemical Aspects of Polymer Surfaces*, Vol. I, K. L. Mittal, Ed. (Plenum Press, NY, 1983), p. 155.
53. J. K. Spelt, *et al.*, *Cell Biophys.* **4**, 113, (1982).
54. D. R. Absolom, *et al.*, *Cell. Biophys.* **7**, 267 (1985).
55. A. W. Neumann, E. I. Vargha-Butler, H. A. Hamza and D. R. Absolom, *Colloids and Surfaces* **17**, 131 (1986).
56. D. Langbein, *J. Adhesion* **1**, 37 (1969).
57. J. Visser, *Adv. Colloid Interface Sci.* **55**, 664 (1976).
58. D. R. Absolom, W. Zingg and A. W. Neumann, *J. Biomed. Mater. Res.* (In Press).

SESSION OF FRANCE

Recent Developments in the Spectroscopic Characterization of Modified Surfaces for Adhesive Bonding or Painting†

M. ROMAND, F. GAILLARD, M. CHARBONNIER and A. ROCHE

*Département de Chimie Appliquée et Génie Chimique, (CNRS, UA 417),
Université Claude Bernard, Lyon I, 43 Bd. du 11 Novembre 1918, 69622
Villeurbanne cedex, France*

(Received December 10, 1986)

Low-Energy Electron-Induced X-ray Spectroscopy (LEEIXS) and X-Ray Fluorescence Spectroscopy (XRFS) have been used to study the near-surface chemistry of metallic substrates submitted to various pre-bonding or pre-painting chemical or electrochemical treatments. Applications given in this paper concern firstly stainless-steel and Ti-6Al-4V adherends and secondly steel and galvanized steel sheets. Experiments provide the information necessary to understand how treatments such as anodization, chemical conversion, rinsing . . . affect the chemistry and properties of surfaces. So, specific examples are shown, outlining how the chemistry of the adherend surface may be correlated with its bondability, the strength of bonded joints being determined using a three-point flexure test. In addition, it is discussed why the information available through the spectroscopic techniques used are quite complementary to the ones provided by more sophisticated surface analysis instrumentations.

KEY WORDS Adhesion; Low-Energy Electron-Induced X-ray Spectroscopy (LEEIXS); near-surface chemistry; prebonding treatments; steels; Ti-6Al-4V adherends.

† Presented at the Tenth Annual Meeting of The Adhesion Society, Inc., Williamsburg, Virginia, U.S.A., February 22-27, 1987.

1 INTRODUCTION

During the past two decades many new spectroscopic techniques have been developed and refined further to provide information on the chemical composition of solid surfaces and interfaces. This effort is fully justified by the increasing recognition of the decisive role played by the surface of a material in determining its properties on a macroscopic scale. So, surface-sensitive techniques such as X-ray photo-electron spectroscopy (XPS), Auger electron spectroscopy (AES), secondary ion mass spectroscopy (SIMS) and ion scattering spectroscopy (ISS) have been largely employed and their usefulness has been amply demonstrated in many areas.

In the particular field of adhesion these methods have been essentially applied to the study of either the surface properties of the metallic adherend materials or the interfacial interactions between organic polymer (adhesive or paint) systems and various metals or alloys (see, for instance, References 1-8). In these studies, it is shown that numerous parameters may play a major role in the formation of a metal-polymer bond, in the initial strength of the bond and in its durability in various aggressive environments. One of these parameters, the chemistry of the metallic substrate, is particularly important. Indeed, the overall performances of adhesive or paint/metallic substrate systems have been shown to be clearly dependent, among other factors, on the nature and manufacturing process of the substrate and on the nature of the pretreatments and treatments used to modify its surface before it is bonded or painted. In these studies, it has been also shown that these techniques, which offer different sensitivities, information depths, lateral resolutions, etc . . . provide complementary data and that a more or less complete understanding of a problem involves at least, the use of a multi-method approach. In these conditions, and account being taken of their specificities and their potential uses, these techniques undoubtedly will be, in the future, more and more employed in the study of the effects of surface chemistry on the bond characteristics of adhesives or paint coatings on various substrates. However, it is also clear that a definite need exists for techniques able to provide surface information not only from the outermost atomic layers but equally from thicker zones (e.g. of several tens of nanometers or more), the chemical properties of

which may change considerably when substrates are submitted to pre-bonding or pre-painting treatments. In this context, the main objective of the present paper is to describe results of surface characterization experiments using non destructive (*i.e.* without sputtering) and largely unexploited X-ray emission techniques (XRFS, LEEIXS) and to demonstrate their large interest for obtaining the information necessary to develop a better adhesion on metallic substrates and a better durability of the relevant systems.

2 EXPERIMENTAL

X-ray fluorescence spectrometry (XRFS) is an emission technique based on excitation of the atoms constitutive of the sample to be analysed. In general, excitation is produced by a primary X-ray beam emitted by a Coolidge tube. The wavelength (wavelength dispersive spectrometry/WDS) or energy (energy dispersive spectrometry/EDS) of the emitted photons (secondary X-rays) is measured to determine what elements are present in the specimen (qualitative analysis) and the intensity of the corresponding characteristic X-rays is a direct or non-direct measure of the amount of each element in the specimen (quantitative analysis). Despite largely spread ideas to the contrary, XRFS must be considered as a surface technique⁹⁻¹¹ when the X-rays being measured only originate from ultra-thin or even thin films, *i.e.* when the surface layer of interest contains elements not present in the substrate. In these conditions, the intensity of a relevant X-ray signal is generally a direct function of the surface concentration of the element being investigated. Obviously such a statement is essentially valuable for elements which can be detected with a sufficient sensitivity (*i.e.*, in routine, for elements of $Z \geq 11$).

Low-energy electron-induced X-ray spectrometry (LEEIXS) is a new soft and ultra-soft X-ray emission spectroscopy.¹⁰⁻¹⁴ The device used is a wavelength-dispersive (WDS) X-ray spectrometer, equipped with a gas discharge tube (or cold cathode tube) operating in the primary vacuum of the spectrometer. This source is used to bombard the sample surface with a quasi-monoenergetic electron beam, the energy of which is selectable over the range 0.5 to 5 keV. The probed depth, depending among other parameters upon the

incident electron beam energy and upon the sample nature, typically ranges from 5 to 100 nm, the probed area being about 1 cm². This technique allows both atomic (qualitative and quantitative) and molecular (qualitative) analysis. It is suited very well to the analysis of light elements (B, C, O, N, F . . .) and so, to the measure of oxide layer thicknesses by using either an external standard or an auto-standardization method.

The three-point flexure test¹⁵⁻¹⁸ used in this work is a useful mechanical method developed in order to determine the practical adhesion¹⁹ (*i.e.* the forces or the work required for the disbondment either at the interface or in the interfacial region) of adhesive or paint/metallic substrate systems. This test has already shown its potential not only in evaluating the effects of various adherend treatments but in optimizing, for a given treatment, the experimental conditions to be chosen in order to produce better adhesion. Flat adherend sheets, about 1 mm in thickness, are prepared by die-cutting to provide identically-sized strips (50 × 10 mm) and then are submitted, prior to bonding, to different surface treatments. The single adherend/adhesive specimen geometry and the specimen preparation fixture have been previously described.¹⁵⁻¹⁷ A three-point flexure tester (FLEX 3 from IRSAP, France) is used and fitted to an APPLE IIe microcomputer in order to monitor the cross-head displacement, to record the load/displacement curve and to calculate the parameters of interest {slope of the load-displacement (P vs. d) curve in the linear zone, ultimate load (P_{\max}) and displacement (d_{\max}) before sample failure}.

3 RESULTS AND DISCUSSION

3.1 Prebonding treatments of metallic adherends

Many chemical etchings and oxidising treatments are commonly used on metals and alloys in order to produce a strong and durable surface layer which enables good long-term properties of the adhesive-substrate interfacial zone even in aggressive environments. Anodization is one of these treatments. It has been largely used for aluminum, titanium and their respective alloys (see, for instance, References 20-22 and cited literature). Recent investigations con-

cerning stainless steels²³⁻²⁵ show that the formation of "thick" films by such a process can also produce steel/adhesive bonds which are stronger than those obtained using other, more widespread, pre-bond treatments²⁶⁻²⁹ such as acid etchings or mechanical roughenings.

The first examples described here are relative to stainless steel adherends. The specimens used are industrial quality AISI 304 L sheets, acetone degreased, acid pickled and then galvanostatically anodized in a hot sulfuric acid-potassium dichromate bath. The effect of anodization of steel surfaces can be followed using LEEIXS. Spectra (a) and (b) in Figure 1 are typical of such substrates which are subjected (a) to chemical pickling (in 15% HNO_3 , 5% HF at 22°C for 5 min) and to rinsing in deionized water and (b) to anodization ($j = 1 \text{ mA cm}^{-2}$) in a hot (70°C) concentrated ($400 \text{ g l}^{-1} \text{ K}_2\text{Cr}_2\text{O}_7 - 475 \text{ g l}^{-1} \text{ H}_2\text{SO}_4$) electrolyte for 15 min. These spectra are obtained using an electron beam of 3 keV at a current density of 0.3 mA cm^{-2} and using a TIAP dispersing crystal ($2d = 2.571 \text{ nm}$). Under the energy conditions used in these experiments,

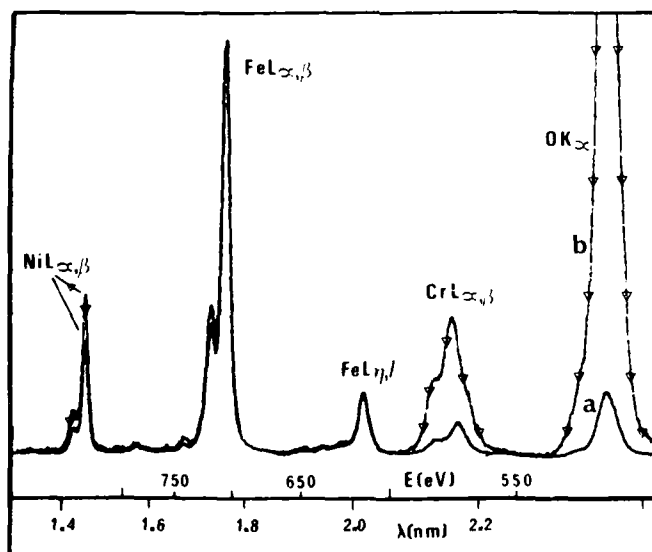


FIGURE 1 LEEIXS spectra of a stainless steel surface (a) before and (b) after anodization in a hot H_2SO_4 - $\text{K}_2\text{Cr}_2\text{O}_7$ bath.

the maximal depth of analysis is about 50 nm in the metallic matrix (case a) and 90 nm in the $\text{Cr}_2\text{O}_3/\text{Fe}_2\text{O}_3$ oxide matrix (case b). More particularly, the comparison of these spectra shows evidence of the formation of a "thick" oxide film on the sample surface (a large increasing of the OK_α emission band intensity can be observed). It is also to be noticed that the intensity of the OK_α signal from spectrum (a) is associated with a residual oxide, the thickness of which is about 6 nm. In addition, it can be seen that the surface treatment used modifies the superficial concentrations of the alloying elements (significant changes in the relative intensities of Ni, Fe and Cr $\text{L}_{\alpha,\beta}$ emission bands can be reported). Figure 2 graphs the results of a quantitative analysis. It shows, as a function of

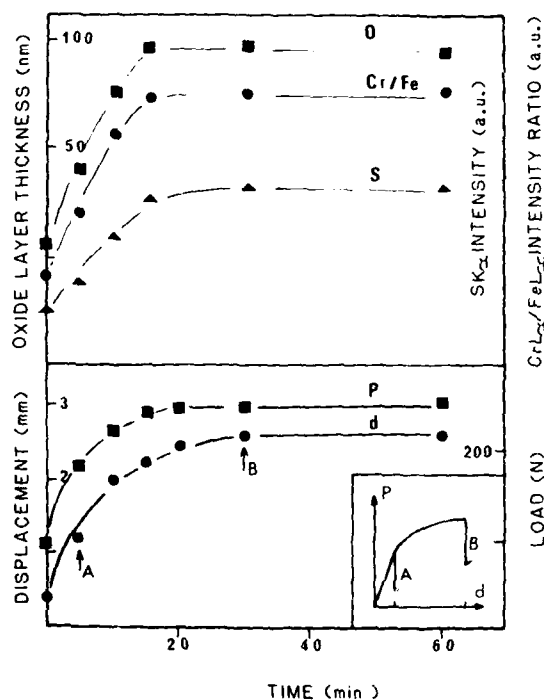


FIGURE 2 Anodization of stainless steels in a hot $\text{H}_2\text{SO}_4\text{-K}_2\text{Cr}_2\text{O}_7$ bath. Effects of anodization duration firstly on oxide film thickness, sulfur impurity incorporation (SK_α variations), Cr/Fe superficial concentration changes ($\text{CrL}_\alpha/\text{FeL}_\alpha$ variations) and secondly on ultimate load (P_{\max}) and ultimate displacement (d_{\max}) of bonded specimens.

GF

treatment duration, firstly the variation in thickness of the oxide films formed during the electrochemical process ($K_2Cr_2O_7$ concentration: 400 g l^{-1} ; bath temperature: 70°C ; current density: 1 mA cm^{-2}) and secondly the corresponding SK_α intensity and the CrL_α/FeL_α intensity ratio variations. It is noteworthy that the oxide thickness determination requires the measurement of the OK_α signal intensity and a standardization using either a self-calibration method or a specimen, the oxide thickness of which is known (e.g. measured by another technique).³⁰ Also to be noted is that those results concerning OK_α intensity measurements are obtained using an electron beam energy (4.5 keV) such that the thickness of the probed material is always greater than those of the oxide films. This condition is absolutely necessary for obtaining a direct relation between OK_α intensity and oxide layer thickness all along the investigated thickness range.

It is quite clear from the data presented in Figure 2 that: (i) the larger oxide thicknesses (90 nm or so) are obtained for treatment durations equal to or greater than 15–20 minutes, (ii) sulfur impurities are incorporated (probably in the anionic form SO_4^{2-}) into the anodic oxides and that to an amount roughly proportional to the film thickness, (iii) the sample surfaces become markedly more and more chromium-enriched (as Cr^{3+}) when the oxide film thickness increases. This enrichment seems to be consistent with a relative insolubility of this element compared to that of iron and nickel in the sulfo-chromic medium. It should be noted here that FeL_α and CrL_α intensity measurements are performed using a 3 keV primary electron beam and that, in these conditions, the maximal analysed thickness (i.e. 90 nm in the case of the fully oxidized matrix and less when a part of the metallic substrate is analysed) is roughly the one of the thickest oxide layer. This fact explains why the Cr/Fe ratio remains constant for treatment durations greater than 15–20 minutes.

Figure 2 also represents (in the inset) typical load-displacement curves (P vs d) obtained, using the three-point flexure test, from two anodized stainless steel/epoxy systems (treatment duration of the adherend being respectively 5 and 60 minutes). The adhesive used is a two-component epoxy resin (Araldite AY 103 with hardener HY 991). The bonded specimens are submitted to curing for 2 hours at 80°C , stored for 24 hours in a dessicator and then

exposed to a humid environment for 72 hours at 70°C, 95% R.H. before testing. This procedure is used here because non-aged specimens exhibit such good interfacial properties that they undergo failure within the adhesive. Lastly, Figure 2 shows the variations, *versus* anodization duration, of both ultimate load (P_{\max}) and displacement (d_{\max}). It should be noted that P_{\max} and d_{\max} show quite similar evolutions. It is now of particular interest to point out, by comparing all the results presented in Figure 2, that there exists a remarkable correlation between the increasing of the oxide layer thickness and of the Cr/Fe ratio and the increasing of d_{\max} or P_{\max} . In other words, the strength of the joint varies with the two former parameters.

In the same manner, Figure 3 shows, as a function of anodization current density, respectively the variation in thickness of the oxide films formed during the electrochemical process ($K_2Cr_2O_7$ concentration: 400 g l⁻¹; bath temperature: 70°C; treatment duration: 15 min), the variation of SK_{α} intensity and $CrL_{\alpha}/FeL_{\alpha}$ intensity ratio and the variation of P_{\max} and d_{\max} for the corresponding anodized stainless steel/epoxy systems. From these curves several conclusions are evident. Firstly, the thickest layers (90 nm or so) are associated with current densities about 1 mA cm⁻². Secondly, sulfur impurity incorporation and chromium enrichment (compared to that of iron) are, as in the previous experiments, directly dependent upon the oxide film thickness. Both these observations are consistent with the formation of an ever thicker oxide layer when current density increases in the range 0–1 mA cm⁻². Similarly, it can be noted that there is a drastic improvement in the mechanical properties of the bonded specimens (as shown by d_{\max} increasing). In addition, for current densities above 1 mA cm⁻², the oxide film dissolution becomes the predominant phenomenon. The slight decrease of d_{\max} is associated with thinner oxide layers when current density increases. However, the relevant mechanical properties remain strong. This fact can be explained by the presence at the adherend outermost surface layers of a very chromium-enriched zone as that has been observed by Auger electron spectroscopy.³¹ Obviously, in this particular case, LEEIXS is not the more appropriate investigation method, on account of its relatively large analysis depth compared to the very low thickness of the modified zone remaining at the sample surface. Lastly, it should be noted, in

contrast with the previous case (Figure 2), that P_{\max} and d_{\max} exhibit here quite different evolutions. The inset of Figure 3 emphasizes, in the present case, that d_{\max} is the more significant parameter.¹⁸ Indeed, the failure occurs in a P vs d curve zone for which, roughly, P_{\max} does not vary while d_{\max} goes on increasing.

These studies concerning anodizations *versus* process duration or current density highlight the major role played in the overall performances of the stainless steel/epoxy bonded joints by oxide thickness and surface chromium enrichment. However, this last parameter, as shown in Figure 3, seems to be the predominant factor. Some complementary studies (performed either by varying

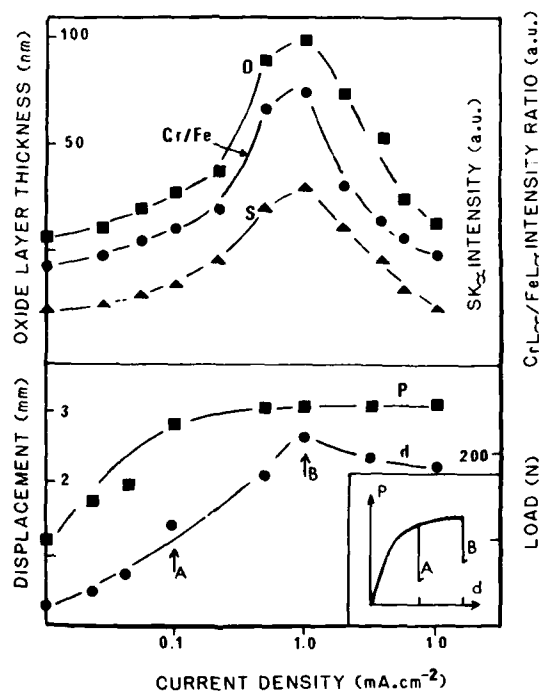


FIGURE 3 Anodization of a stainless steels in a hot $\text{H}_2\text{SO}_4\text{-K}_2\text{Cr}_2\text{O}_7$ bath. Effects of anodization current density firstly on oxide film thickness, sulfur impurity incorporation (SK_α variations), Cr/Fe superficial concentration changes ($\text{CrL}_{\alpha_2}/\text{FeL}_{\alpha_2}$ variations) and secondly on ultimate load (P_{\max}) and ultimate displacement (d_{\max}) of bonded specimens.

other parameters such as electrolyte concentration and bath temperature or by using other oxidizing acid media such as nitric acid solutions) confirm this fact.^{24,25}

The second example described here is relative to Ti-6Al-4V alloy adherends treated with a conventional phosphate-fluoride process (*i.e.* an aqueous solution containing 5% trisodium phosphate, 0.9% sodium fluoride and 2.6% hydrofluoric acid; treatment duration: 2 min at room temperature). This industrial surface preparation process, often described as a conversion treatment, is known to produce relatively thick "oxide" layers. However, con-

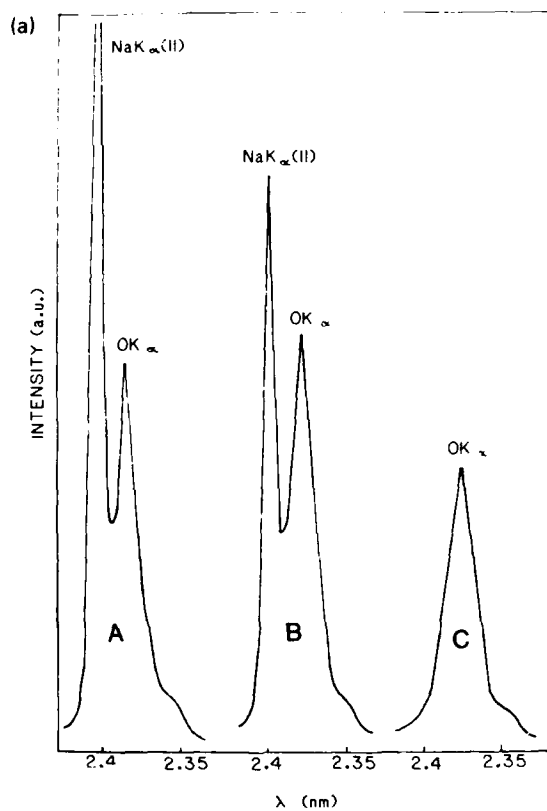


FIGURE 4 NaK_α(II), OK_α and FK_α LEEIXS spectra from the surface of a Ti-6Al-4V substrate submitted to a phosphate-fluoride process and rinsed for 10 (A), 30 (B) and 60 (C) seconds.

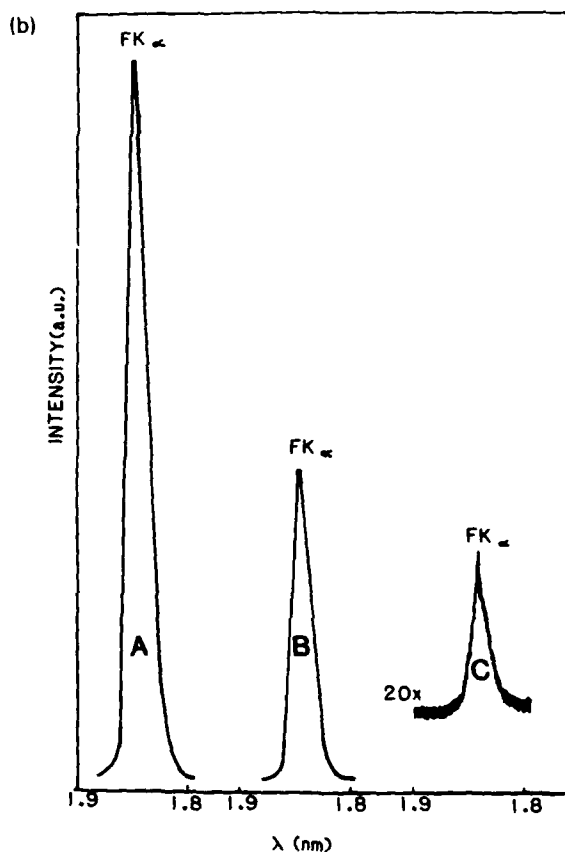


FIGURE 4 (continued)

troversial data have been reported concerning their thickness and composition as well as their crystallographic structure.³²⁻³⁸ So, Hamilton *et al.*³²⁻³⁴ show, using XPS, that the conversion coating is basically a titanium oxide TiO_2 which contains "impurities" such as F, P, Na, Al and C while Roche *et al.* infer, from AES, SIMS, ISS and LEEIXS studies, that the main surface compounds are titanium and sodium fluorides (TiF_4 and NaF).^{13,39,40} As a matter of fact, the composition of the conversion coating is strongly influenced by the action of the rising procedure subsequent to the conversion stage. Figures 4a and b contain NaK_{α} (II), OK_{α} and FK_{α} LEEIXS spectra

from Ti-6 Al-4 V panels treated as described above and rinsed in running tap water for 10 (A), 30 (B) and 60 (C) seconds, respectively. In addition, Figure 5 summarizes the effects of this treatment by following, as a function of rinsing time, the variations in intensity of CK_{α} , OK_{α} , FK_{α} , NaK_{α} and PK_{α} . It should be noted here that intensities of these signals cannot be directly compared, practical emission yields being very dependent upon the wavelength of the corresponding radiations. However, interesting observations can be made firstly about the largely decreasing amounts of fluorine and sodium with rinsing time and secondly about the presence (as impurities) of phosphates {quite similar PK_{α} and OK_{α} intensity variations can be seen during the first 100–150 s, the sharp increase during the very first seconds being associated with the removal of

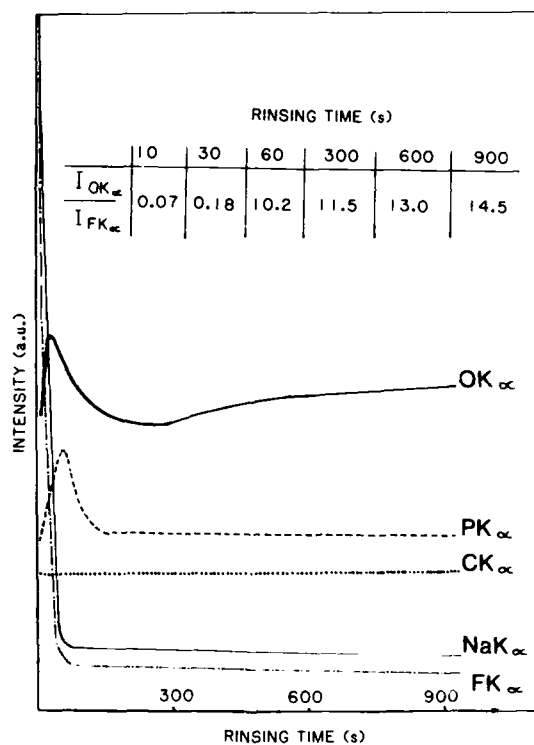


FIGURE 5 Effects of rinsing time of a Ti-6Al-4V substrate submitted to a phosphate-fluoride process on CK_{α} , OK_{α} , FK_{α} , NaK_{α} and PK_{α} intensity variations.

the outermost layers which are constituted of highly solubles compounds (TiF_4 and NaF). In addition, Figure 6 represents the X-ray emission bands $\text{TiL}_{\alpha,\beta}$ characteristic of the conversion coating after 10 s (A) and 600 s (B) rinsing time, a degreased titanium alloy substrate (C) covered only by its residual oxide layer, the thickness of which is about 5 nm and a TiF_4 standard (D). Let us point out here that an X-ray emission band is associated with electronic transitions between valence levels and a core level of a given atom. The chemical bonding influencing the electronic distribution in the valence levels, the structure of the X-ray emission band may also suffer this influence. The spectral modifications (named chemical effects) can, therefore, be used with the intent of characterizing the

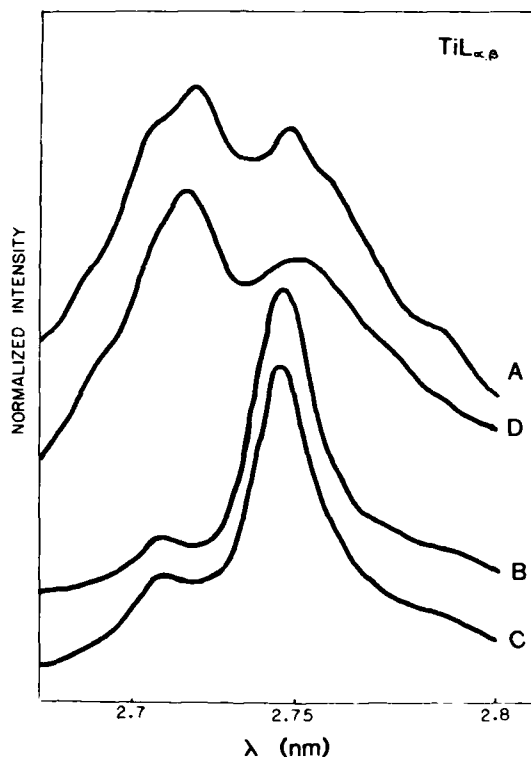


FIGURE 6 $\text{TiL}_{\alpha,\beta}$ LEEIXS emission bands from a Ti-6Al-4V substrate submitted to a phosphate-fluoride process after 10 (A) and 600 (B) seconds rinsing time, from a degreased Ti-6Al-4V substrate (C) and from a TiF_4 standard (D).

chemical state of some elements incorporated in a solid surface layer.¹⁴ In the case studied here, comparison of the $\text{TiL}_{\alpha,\beta}$ spectra from Figure 6 and from other standards such as TiF_3 , TiO and TiO_2 ^{13,40} confirms that titanium fluorides are largely present in the conversion film (spectrum A is typically characteristic of the TiF_4 species) and that these titanium fluorides also undergo dissolution during the rinsing states. In addition, both the comparison of (B) and (C) emission bands (Figure 6) and the marked increase of the $\text{OK}_{\alpha}/\text{FK}_{\alpha}$ intensity ratio (see Figure 5 inset and note that emission yield for FK_{α} is greater than for OK_{α}) clearly indicate that rinsing for a sufficiently long time leaves the surface mainly covered by a titanium oxide which is about 10 nm in thickness and which still contains "impurities" such as P and F. Lastly, it should be noted that (i) the thickness of the remaining oxide is directly determined by comparing OK_{α} intensities of the sample under investigation and of a standard obtained by anodization of a Ti-6Al-4V substrate,⁴⁰ (ii) another recommended rinsing procedure (15 min soak in deionized water at 90°C) leaves a slightly thicker oxide layer (15–20 nm) and (iii) these last thickness values are quite small in comparison with those relative to conversion coatings claimed by different authors (for example, from 150 to 300 nm^{33,41}) but are in good agreement with those reported by Wegman *et al.*³⁵

3.2 Pre-painting treatments of metallic substrates

Many chemical or electrochemical treatments of metallic substrates have also been commonly used both to promote adhesion of thin polymeric coatings such as paint or varnish films and to protect them against corrosion. Indeed, as noted by Dwight and Wightman "corrosion is closely related to adhesion; the appearance of corrosion is indicative of loss of adhesion between the paint and the underlying substrate."⁴² Generally, the substrate can be any metal but it is usually aluminum, zinc, steel, tin-plated, galvanized or electro-galvanized steels, and among the treatments extensively employed we may especially note phosphatizing and chromating.

The example described here is relative to steel and galvanized steel sheets for automotive applications. It concerns the deposit of phosphate conversion layers, such substrate/coating systems being usually post-passivated by chromating. This rinse in a Cr^{3+} or

$\text{Cr}^{3+}/\text{Cr}^{6+}$ solution is known to provide an additional corrosion resistance probably owing to the incorporation of chromium ions mainly between the phosphate crystals but equally at the surface of these crystals.⁸ In Figure 7 the effect of an alkaline solution at $\text{pH} = 12$ on unchromated and chromated specimens is demonstrated. The interest of such studies has recently increased considerably because (i) during wet corrosion, hydroxyl ions may be formed beneath the paint films, (ii) during cataphoretic paint deposition, the pH at the electrode surface may locally increase up to 12. In such conditions an attack of the phosphate crystals occurs and changes in the surface composition may be responsible for adhesion loss. These experimental results obtained by XRFs give, as a function of immersion duration in the alkaline solution, the intensity variations of the PK_α radiations emitted by the phosphate crystals remaining after each leaching step. In each case, the decrease of the analysed signal represents the dephosphating of the surface layer and consequently should the solubility of the phosphate crystals at high pH . In addition it can be seen that: (i) the dissolution rate varies largely with the type of substrate, (ii) chromating does not necessarily improve the behaviour of the galvanized substrates in the alkaline solutions, (iii) chromating alone ($t = 0$) is responsible for a partial dissolution of the phosphate layer. The two former observations are not quite wholly explained

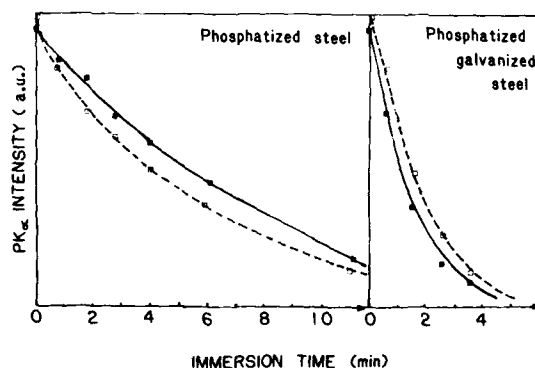


FIGURE 7 Behaviour of chromated (—) and unchromated (---) phosphated steel and galvanized steel in a alkaline solution at $\text{pH} = 12$. Effects of immersion duration on PK_α intensity (measured by XRFs).

at present but are probably associated with different phosphate compositions and morphologies since the corresponding crystals are grown on different substrates. In these preliminary experiments, XRF is used to probe the entire thickness of the phosphate layers. In contrast, LEEIXS is able to provide information only from the surface of these layers. Figure 8 shows a partial LEEIXS spectrum from the surface of a galvanized steel sheet after a Zn-Ni phosphatizing. The main elements which are considered are oxygen, phosphorus, nickel and zinc. Figure 9 illustrates the applicability of LEEIXS to a Zn-Ni-Mn phosphatized steel surface analysis. It shows the comparison between the OK_{α} , PK_{α} , MnL_{α} , FeL_{α} , NiL_{α} and ZnL_{α} intensities before and after a sample immersion in an alkaline solution of $pH = 12$ during about 10 minutes. These results firstly confirm the dephosphating of the surface layers and secondly point out the corresponding increase of the $(Fe + Mn + Ni)/Zn$ ratio. Furthermore, the slight decrease of the OK_{α} intensity would be in agreement with the transformation of phosphates into ferric zincates as that has been proposed by Van Ooij *et al.*⁸ Although these studies are still under investigation (and then will largely be pursued in the future), it is evident that use of such spectroscopic methods will strongly help to understand the specimen behaviour in

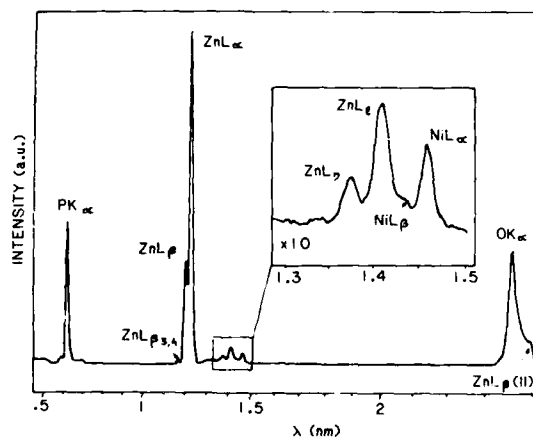


FIGURE 8 LEEIXS spectrum of a galvanized steel surface after a Zn-Ni phosphatizing.

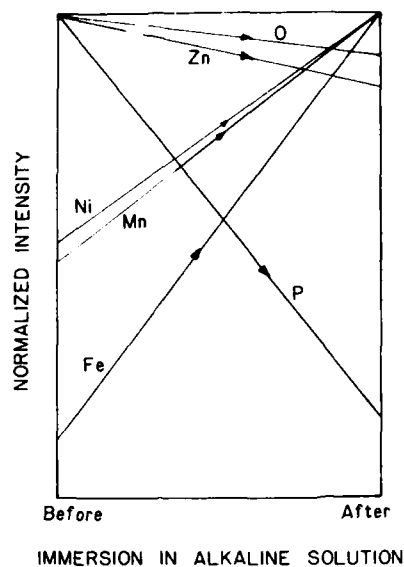


FIGURE 9 Behaviour of a Zn-Ni-Mn phosphatized steel in a alkaline solution at pH = 12. Normalized OK_{α} , PK_{α} , MnL_{α} , FeL_{α} , NiL_{α} and ZnL_{α} intensities before and after a 10 minute immersion.

service or test and then to formulate more corrosion-resistant and adherent new products.

4 CONCLUSIONS

In this paper, we have carried out a number of LEEIXS and XRFS studies emphasizing the potential of the relevant techniques to the characterization of metallic surfaces which have been chemically or electrochemically modified. A major conclusion from the applications described here is that significant progress in adhesion and paint sciences can be achieved by using suitable X-ray emission techniques and their specific advantages. More particularly, this statement is based on the fact that the techniques used are capable of giving both qualitative and quantitative chemical information about the composition of surface layers over a relatively larger

range of thickness than real surface techniques like XPS, AES, SIMS or ISS. In other words, the methods of investigation used are able to provide extra information necessary to understand how chemical or electrochemical treatments affect the surface properties of adherends and various substrates and, therefore, are able to bring solutions as to the best processes and experimental conditions to be used in the preparation of surfaces.

References

1. W. L. Baun, in *Adhesion Measurement of Thin Films, Thick Films and Bulk Coatings* (ASTM-STP-640, Philadelphia, 1978), pp. 41-53.
2. J. S. Solomon and W. L. Baun, in *Surface Contamination—Its Genesis, Detection and Control*, Vol. 2 (Plenum Press, New York, 1979), pp. 609-634.
3. G. D. Davis and J. D. Venables, in *Durability of Structural Adhesives* (Appl. Science Publ., London, 1982), pp. 43-84.
4. J. M. Walls and A. B. Christie, in *Surface Analysis and Pretreatment of Plastics and Metal* (Appl. Science Publ., London, 1982), pp. 13-44.
5. W. L. Baun, *ibid.*, pp. 45-72.
6. W. L. Baun, in *Adhesive Joints—Formation, Characterization and Testing* (Plenum Press, New York, 1984), pp. 3-17.
7. W. J. van Ooij, in *Physicochemical Aspects of Polymer Surfaces*, Vol. 2 (Plenum Press, New York, 1981), pp. 1035-1100.
8. W. J. van Ooij, T. H. Visser and M. E. F. Biemond, *Surf. Interface Anal.* **6**, 197 (1984).
9. J. V. Gilfrich, in *Characterization of Solid Surfaces* (Plenum Press, New York, 1974), pp. 275-306.
10. M. Charbonnier, M. Romand, A. Roche and F. Gaillard, *Int. J. Adhesion and Adhesives*, In press.
11. M. Romand, M. Charbonnier and E. Sahakian, *XVIII Fatipex Congress*, Venice, Italy, September 1986, Vol. 2/A, pp. 77-107.
12. R. Bador, M. Romand, M. Charbonnier and A. Roche, *Adv. X-Ray Anal.* **24**, 351 (1981).
13. A. Roche, *et al.*, *Appl. Surf. Sci.* **9**, 227 (1981).
14. M. Romand, R. Bador, M. Charbonnier and F. Gaillard, *X-Ray Spectrometry*, In press.
15. A. A. Roche, J. S. Solomon and M. J. Romand, in *Microscopic Aspects of Adhesion and Lubrication* (Elsevier, Amsterdam, 1982), Tribology Series 7, pp. 333-342.
16. A. A. Roche, A. K. Behme and J. S. Solomon, *Int. J. Adhesion and Adhesives* **2**, 249 (1982).
17. A. A. Roche, M. J. Romand and F. Sidoroff, *Adhesive Joints—Formation, Characteristics and Testing* (Plenum Press, New York, 1984), pp. 19-30.
18. A. Roche, F. Gaillard, M. Romand and M. von Fahnestock, *J. Adhesion Science and Technology*, Submitted.
19. K. L. Mittal, in *Adhesion Measurements of Thin Films, Thick Films and Bulk Coating* (ASTM-STP-640, Philadelphia, 1978), pp. 5-17.
20. D. M. Brewis, in *Durability of Structural Adhesives* (Appl. Science Publ., London, 1982), pp. 215-254.

21. A. Mahoon, *ibid*, pp. 255-279.
22. A. C. Moloney, in *Surface Analysis and Pretreatment of Plastics and Metals* (Appl. Science Publ., London, 1982), pp. 175-197.
23. R. P. Haak and T. Smith, *Int. J. Adhesion and Adhesives* **3**, 15 (1983).
24. F. Gaillard, M. Romand, H. Hocquaux and J. S. Solomon, *Surf. Interface Anal.*, In press.
25. F. Gaillard and M. Romand, *Matériaux et Techniques*, In press.
26. M. Gettings and J. Kinloch, *Surf. Interface Anal.* **1**, 165 (1979).
27. T. L. Sterrett, *Int. J. Adhesion and Adhesives* **1**, 208 (1981).
28. W. L. Baun, Air Force Materials Laboratory, Technical Report TR-79-4138 (1979), Wright-Patterson AFB, Ohio.
29. W. Brockmann, in *Durability of Structural Adhesives* (Appl. Science Publ., London, 1982), pp. 281-316.
30. A. Roche *et al.*, *J. Microsc. Spectrosc. Electron.* **4**, 351 (1979).
31. F. Gaillard *et al.*, Results to be published.
32. W. C. Hamilton, *Appl. Polym. Symp.* **19**, 105 (1972).
33. W. C. Hamilton and G. A. Lyster, Picatinny Arsenal, Technical Report 4185 (1971).
34. W. C. Hamilton, G. A. Lyster and G. Frohnsdorff, *ibid*, 4362 (1972).
35. R. Wegman, M. C. Ross, S. A. Slota and E. S. Duda, *ibid*, 4186 (1971).
36. F. Dalard, C. Montella and J. Gandon, *Surf. Technol.* **8**, 203 (1979).
37. T. Smith and D. H. Kaelble, Air Force Materials Laboratory, Technical Report TR-74-73 (1974), Wright-Patterson AFB, Ohio.
38. M. Natan, J. D. Venables and K. R. Breen, 27th National SAMPE Meeting, San Diego, CA (1982).
39. A. A. Roche, Air Force Materials Laboratory, Technical Report TR-80-4004 (1980), Wright-Patterson AFB, Ohio.
40. A. Roche, Thesis, Lyon (1983).
41. C. L. Hendricks and S. G. Hill, *Sampe Q.* **12**, 32 (1981).
42. D. W. Dwight and J. P. Wightman, *Surface Contamination—Its Genesis, Detection and Control*, Vol. 2 (Plenum Press, New York, 1979), pp. 569-586.

Elementary Mechanisms in the Interaction of Organic Molecules with Mineral Surfaces†

C. BOIZIAU,^{1‡} S. LEROY,¹ C. REYNAUD,¹ G. LECAYON,²
C. LE GRESSUS² and P. VIEL²

¹IRF—DPhG—SPAS

²IRD—DPC—SES

C.E.N. Saclay—91191 Gif-sur-Yvette Cédex, France.

(Received November 3, 1986)

Model systems are used to reproduce the actual situations encountered during the interaction of organic molecules with mineral solids under controlled experimental conditions.

The role of local electrical fields produced by surface heterogeneities and the influence of the electronic properties of the functional groups of the organic molecule and of the surface are demonstrated and discussed.

This study enables modelling of the basic mechanisms in the organic molecule-mineral solid bond and of the polymerization process of the organic film.

The results given here may be used to produce theoretical models of predictive nature in the field of adhesion and structural bonding.

KEY WORDS Adhesion; metal oxides; acrylonitrile; electrochemistry; chemisorption; acid-base reactions.

INTRODUCTION

Although the problems of structural bonding and the adhesion of organic films to mineral surfaces are generally well-mastered in the

† Presented at the Tenth Annual Meeting of The Adhesion Society, Inc., Williamsburg, Virginia, U.S.A., February 22–27, 1987.

‡ To whom correspondence regarding this paper should be addressed.

field of industrial applications, they still raise a number of questions from the design point of view.

Precise answers to these questions would clearly ensure better control of the use of adhesives and improve the laws of behaviour of assembled materials.

Unfortunately, such an approach cannot be made using samples taken from industrial materials, owing to their complexity and also to the lack of reproducibility of such samples which would, anyway, be difficult to describe suitably at an atomic or molecular scale.

It is, therefore, necessary to deal with the problem posed under simplified conditions enabling the production of models which can be experimentally controlled. We can then make a serious approach to the following questions:

- the mechanisms of interaction between organic molecule and mineral substrate in terms of surface physico-chemistry,
- the mechanisms of polymerization and possible changes in the resulting polymer in terms of molecular chemistry,
- the behaviour of the mineral organic compound in terms of solid state physics.

The purpose of this article is to describe the results achieved with the system Acrylonitrile-oxidizable metal. The first part will be devoted to a methodological explanation and a brief description of the experimental equipment used. The second part will describe the mechanisms governing the organic molecule/mineral solid bond. In the third part, we shall discuss the influence on this bond of the condition of the mineral surface (electronic properties and chemical composition). A set of results concerning the laws of behaviour of assembled materials will be evoked in the conclusion.

I METHODOLOGY—INSTRUMENTATION

I-1 The surfaces of true mineral solids

In practice, except for a few noble metals, the surfaces of mineral materials are nearer to those of insulating substances than those of metals. This is obviously the case for solid insulating substances but also applies to most metals whose surface is always either naturally

or as a result of treatment covered by a layer with non-metallic properties (oxide, nitride, carbide, organic coating, etc.). It should also be noted that following the machining processes to which they have been subjected, the surface of these metallic materials is morphologically different from their volume: the external layer of the material is in a microcrystalline or even amorphous state, and its properties are very different from the solid in volume.¹

It naturally follows, from the point of view of electronic properties, that there are considerable variations depending on the depth with respect to the surface of the sample, the density of the electronic states being either that of an insulator (perfect or not) or that of a metal.

Thus, it is not possible, in the case of a true mineral, to consider its surface properties as similar to those which it possesses in volume. Moreover, the main properties of this surface are very different from those of a perfect insulating substance: not only do stoichiometry faults produce localized levels which invade the forbidden band but electrostatic charges (positive and negative) localized on these defects, together with the presence of dangling bonds presenting emergent orbitals and, finally, impurities either included or resulting from chemical adsorption cause considerable roughness of the isopotential curves. Very intense local fields (range approximately 1 to 2 nm, $|E| > 10^8 \text{ V} \cdot \text{m}^{-1}$) are caused by this roughness.²

In fact, the surface of a true mineral can be described as a mosaic of sites which either give or accept electrons to a varying extent, with positive or negative electrical fields associated with the existence of these sites.

I-2 Role of functional groups on organic molecules

We know that the polymerization of a monomer may be the result of addition reactions which can be described in terms of acid-base reactions as intended by Lewis.

In the case of a monomer with one extremity A of an acid nature (electrophil) and the other extremity B of a basic nature (nucleophil), the polymerization reaction can be written: $AB + AB \rightarrow ABAB$. This type of reaction (ion polymerization) is, in particular, extremely active when the monomer is a polar and

polarizable molecule. The presence of outside agents (electrical field, chemical aggression, plasma aggression) accelerates the polymerization process. We can now see why during an interaction between polymerizable molecules and a true mineral surface (creation of an adhesive bond) we obtain an adhesive/substrate interface, characterized by very strong bonds immediately adjacent to a layer where the adhesive is extremely fragile: the active extremities of the molecules close to the mineral solid interact strongly with the antagonistic active sites of the surface rather than participating in the polymerization mechanism.

I-3 Experimental simulation of these phenomena

An attempt at modelling this seemingly complex situation involves the inclusion of all the parameters while, at the same time, creating conditions favourable to an unambiguous demonstration of their role.

In order to overcome the random nature of distribution of the active sites on the mineral substrate surface, we must on the one hand create a surface which is well-defined chemically (pure metal), and on the other hand give it an even acid or basic character; electrochemistry is well suited to this aim, the working electrode either emitting or receiving electrons, depending on its polarization (cathode or anode). Electrochemistry is also useful for creating intense even and isotropic fields, produced on the surface of the electrode by the formation of the double layer once the system is polarized above the null charge potential. As for the monomer molecule, it must have the necessary characteristics (acid and basic extremities and polarizability) while remaining sufficiently simple to be calculable, so as to enable the production of a model whose validity can be checked out by experimental results. As a first approach, the acrylonitrile (AN) seems well studied to this aim. A complete study of this molecule was therefore carried out, combining experience and theoretical chemistry.³

I-4 Study techniques

In parallel with electrochemistry performed in a strictly controlled organic environment⁴ and used to follow the interaction kinetics

activated by the double layer electrical field, we had to simulate the case of surface sites without an intense electrical field. For this we used the normal methods of the physico-chemistry of surfaces, the acrylonitrile molecule being in an ultra-vacuum environment in the gaseous phase: its interaction with the surface of the sample then results exclusively from the intrinsic properties of the two bodies.

In this latter case, we required spectroscopic techniques which were both sensitive and non-destructive: the association of UV photo-electron spectroscopy (UPS) and metastable de-excitation spectroscopy (MDS)⁵ resulted in a good description of the chemisorption mechanism. In fact, the escape depth of the photo-electrons is approximately 2 nm. It is therefore possible to "see" the substrate through one or more chemisorbed molecular layers whereas the MDS, being sensitive to emergent orbitals only, gives electronic and structural data on the solid-vacuum interface.

Finally, UPS and MDS were associated with infrared absorption spectroscopy (IRAS) and Auger electron spectroscopy (AES) for the study of samples obtained after electrochemical treatment.

II RESULTS OBTAINED—INTERPRETATION

The acrylonitrile molecule was, therefore, subjected to three types of interaction with a polycrystalline metal surface:

- ~ non-polarized metal surface;
- ~ negatively-polarized metal surface (basic character imposed), the molecular being situated in the cathode double-layer field;
- ~ positively-polarized metal surface (acid character imposed), the molecule being situated in the anode double-layer field.

In all three cases, the metal was a transition metal offering a high density of occupied states below the Fermi level.

II-1 Chemisorption of acrylonitrile on nickel

Before each measurement, the nickel surface is cleaned by ion bombardment. The acrylonitrile is introduced into the experimental chamber in gaseous form; exposure to acrylonitrile is measured in

Langmuirs ($1L = 10^{-6}$ Torr · s) and carried out at pressures between 10^{-8} and 10^{-7} Torr, the basic pressure of the installation being 10^{-10} Torr. The sample is maintained at ambient temperature.

The interpretation of the experimental data⁶ shows that like molecules of the type C_2H_2 , C_2H_4 and C_6H_6 ⁷ and CH_3CN ,⁸ the acrylonitrile molecule is absorbed flat on the surface of the metal (Figure 2b) without modifying the metallic nature of this surface from the point of view of electronic properties. The covalent bonds between the molecule and the surface result from electronic exchanges: on the one hand between the π and anti-bonding orbitals of the vinyl extremity and the d-levels of the nickel; and on the other hand between the π orbitals of the CN group and the bottom of the valence band of the metal.⁹

This situation is obviously unfavourable for any subsequent polymerization process. Moreover, the energy of the molecule + surface bond is low enough to enable the adsorbate to be desorbed by heating at moderate temperature ($T \sim 600K$).¹⁰

II-2 Interaction of acrylonitrile with a negatively-polarized surface

The surface of polycrystalline nickel is used as a cathode in an electrolytic cell containing organic solution (solvent: acetonitrile; salt: perchlorate of tetraethylammonium; the acrylonitrile acting as a co-solvent). The potentiodynamic characteristics ($I(V)$ curves) in Figure 1 show the changes of Faradaic current with respect to electrode potential: in the presence of acrylonitrile an inhibition peak appears, showing an irreversible modification of the surface of the electrode. This irreversible modification has its origin in two important phenomena: on the one hand the oxide layer which initially covers the surface of the electrode is reduced (visible result on the $I(V)$ curve without acrylonitrile); on the other hand, in the presence of acrylonitrile a polymer film is deposited on the electrode; identified by IRAS in polarized light, this film is composed of polyacrylonitrile chains (PAN) perpendicular to the plane of the electrode, the pendant nitrile groups being themselves oriented in this direction (Figure 2c); the direction of this orientation (nitrogen atom pointing towards the outside of the film) is controlled by MDS: the AN—Ni bond is therefore made by means of the carbon in the β -position to the CN and polymerization results

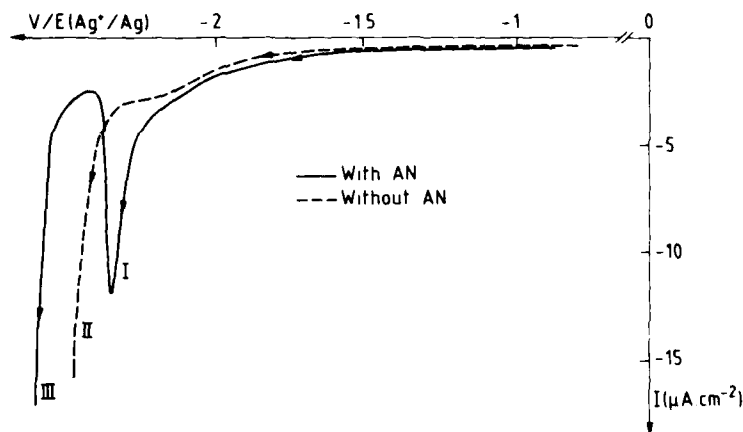


FIGURE 1 Interaction of AN with a negatively-polarized metal. In the presence of AN, the Faradaic current shows an inhibition peak located between the reduction region of the oxide (I) and that of the intense Faradaic current (III).

from an addition reaction involving the vinyl doublet of the molecule.¹¹

II-3 Modelling of the interaction between acrylonitrile and a cathode

Negative polarization of the electrode corresponds to the formation of a double-cathode layer. An intense electrical field ($|E| \sim 10^7 \text{ V} \cdot \text{cm}^{-1}$) oriented towards the surface of the electrode in a direction perpendicular to its plane results from the antagonism of positive ion/cathode charges (double electrochemical layer).

Given the dipolar moment of the CN group, the acrylonitrile molecule is oriented in such a way that its CH_2 extremity interacts with the metal surface (Figure 3b). Moreover, polarization of the vinyl bond under the inductive effect of the dipolar moment of the CN group is reinforced by the electrical field, such that the CH_2 extremity of the molecule begins to lack electrons, which reinforces its acid character in the sense intended by Lewis. The acid-base reaction between molecule and electrode can then occur, leading to the establishment of a chemisorption bond (Figure 3c). The transfer from the electronic pair from ex-vinyl bond to the CH extremity of

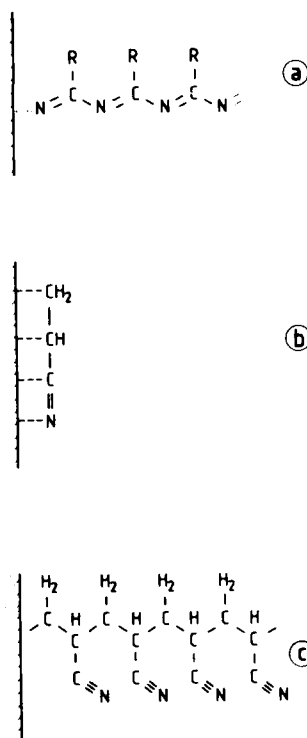


FIGURE 2 Different forms of AN/Metal interaction. a—Metal polarized positively (anode). b—Metal non-polarized (classical chemisorption). c—Metal polarized negatively (cathode).

the molecule results in a shift of the basic character, initially located on the surface of the electrode, such that the acid-base reaction can be propagated from monomer to monomer and leads to the formation of polymer (PAN). Figure 3d illustrates this mechanism. As the film thickens, the surface of the electrode moves towards the solution: functioning of the cell (from the electro-chemical point of view) is ensured with respect to Faradaic current by hole conduction from CN group to CN group, owing to the existence of π electrons; the monomer supply of the reactional area (double-layer) results from diffusion of the acrylonitrile from the solution.

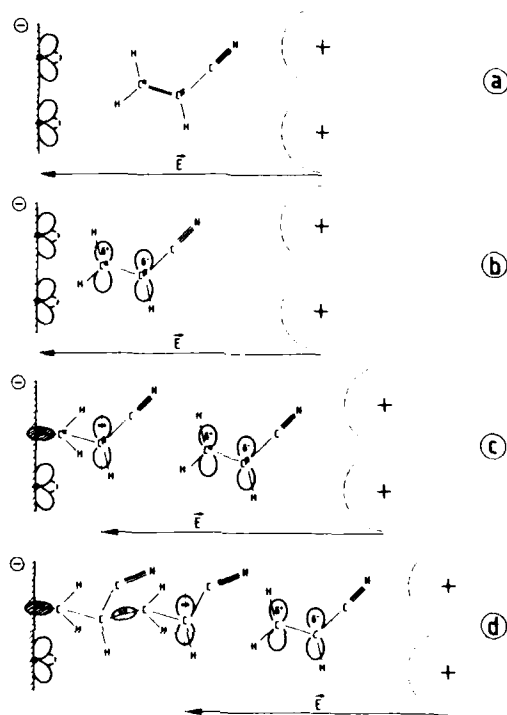


FIGURE 3 AN/Cathode interaction. a—AN molecule without interaction. b—AN molecule oriented and polarized by the field of the double layer. c—AN molecule bonded to the surface: the basic character is transferred to the carbon in α of CN. d—Polymerization results from propagation of the acid-base reaction.

II-4 Interaction of acrylonitrile with a positively-polarized surface

Returning to the diagram in Figure 3b, the electrode now occupies the space previously occupied by positive ions, the double-layer in this case being formed by the accumulation of negative ions in front of the anode; as for the electrical field of this new configuration, it is the same direction and the same orientation as on Figure 3b. We can see immediately that if an interaction is to occur between molecule and surface, it will necessarily involve the nitrogen atom from the CN group. As in the previous case, the reaction will be acid-base type, as described by Lewis: in fact the electronic lone

pair of the nitrogen atom is the cause of a basic character as defined by Lewis, while positive polarization gives the electrode an acid character.

However, unlike the previous case (propagation of the basic character of the cathode to the CH extremity of the vinyl bond), the nitrogen-metal bond can occur without the carbon atom in the CN group lacking electrons, *i.e.* taking on a marked acid character. Under these conditions, the polymerization process can only occur by opening of a π bond in the CN group under the effect of an attack of this bond by an oxidizing radical.¹² We can therefore predict, on the one hand, a much slower reaction speed than that which occurs on the cathode, and on the other hand a resulting polymer built around a skeleton composed of —C=N— conjugate bonds. Experimental results confirm these assumptions: it requires several minutes on the anode to create a 100 nm thick film (whereas on the cathode, one second is enough to achieve this thickness); moreover, electron spectroscopies (UPS and MDS) indicate the presence of a broad valence band, characteristic of an organic semi-conductor, attributable to conjugate —C=N— bonds. Finally, infrared absorption spectroscopy can be used to identify the nature of the *R* radicals in a pendant position on the skeleton: these are —CH=CH_2 (from the acrylonitrile) —CH_3 (from the acetonitrile) and —O—CH_3 and —O—CH=CH_2 , resulting from attack of the π bond by an oxidizing radical.

II-5 Summary of results

In this way, using electrochemistry and physico-chemistry of surfaces techniques, it has proved possible to reproduce experimentally the various situations encountered on actual material.

These results are summarized in Figure 2: in the absence of a local electrical field (sites with low potential roughness), the molecule is chemisorbed on the flat, is unsuitable for any subsequent polymerization process and the molecule-surface bond is weak (Figure 2b). However, in the presence of intense electrical fields (sites with high potential roughness) only one extremity of the molecule is involved in the bond with the substrate, the other extremity being available for polymerization processes.

Molecule-surface adhesion is governed by an acid-base reaction,

as described by Lewis which, as we shall show here later, produces a strong bond. Depending on the direction of the local electrical field, acrylonitrile is adsorbed either by the carbon from its CH₂ extremity (Figure 2c) or by the nitrogen from its CN group (Figure 2a). Finally, reproduction of the initial conditions at each stage of the polymerization (in particular direction and orientation of electrical field) produces parallel polymer chains, whose abundance depends on the number of available sites on the surface of the electrode and the steric bulk of the molecules. This creates favourable conditions for filling of the volume occupied by the film with useful material for adhesion.

III INFLUENCE OF THE ELECTRONIC PROPERTIES OF THE SURFACE

The results given in the previous chapter show that adhesion of the organic molecule to the metal results from an acid-base reaction as described by Lewis, *i.e.* on the sharing of an electronic pair supplied by one of the two elements. For a given organic molecule, we can therefore see that the electronic properties existing on the surface of the mineral material will play an important role in the quality of the bond achieved and, as a result, in the qualities of the polymer film.

For the purpose of the study which follows, there are two types of consideration to be taken into account:

- this research should stay close to actual problems (which therefore means priority examination of cases in which the mineral is constituted from a common and therefore oxidizable metal);
- the possibility of unambiguous interpretation of the results obtained with respect to the nature and structure of the film.

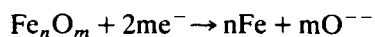
We therefore chose to favour cathode studies (electrochemistry on reduction) which, as we have seen above, lead to the generation of PAN films which can be easily characterized. In this context, various types of situations may be encountered:

- transition metal (with tight-binding electrons) with non-stoichiometric oxide (this is the case of iron)
- transition metal with stoichiometric oxide (such as nickel);

- alloy of transition metals with passivating surface segregation (stainless steel A316L)
- metal with free electrons coated with a fairly thick layer of oxide (with a wide forbidden band) which is fairly disturbed (aluminium can be used for this study).

III-1 Interaction of acrylonitrile with a negatively-polarized iron surface

In the initial state, the surface of the electrode is covered with various oxides,¹³ reduced once cathode polarization is established, in accordance with the reactions:



The oxygen thus released is discharged from the double-layer by the electrical field; this mechanism helps to create a uniform layer of pure iron on the surface of the electrode, whose electronic properties are shown in Reference 14.

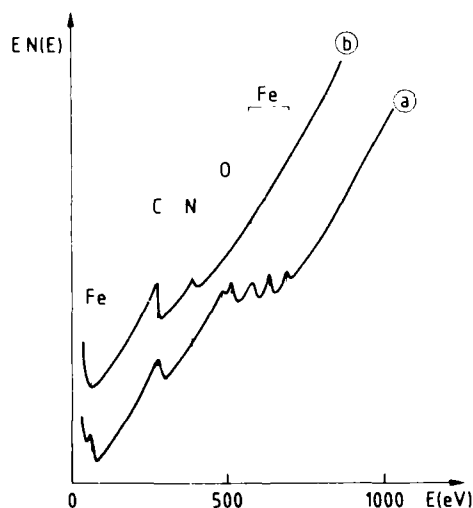


FIGURE 4 AN/iron interaction (cathode area). a—Initial chemical composition of the surface (AES). b—Chemical composition of the surface after electrolysis (AES). c—Curve $I(V)$ in the presence of AN (0.5 M). d—Curve $I(t)$ in the presence of AN (0.5 M) for $V = -2.8V$.

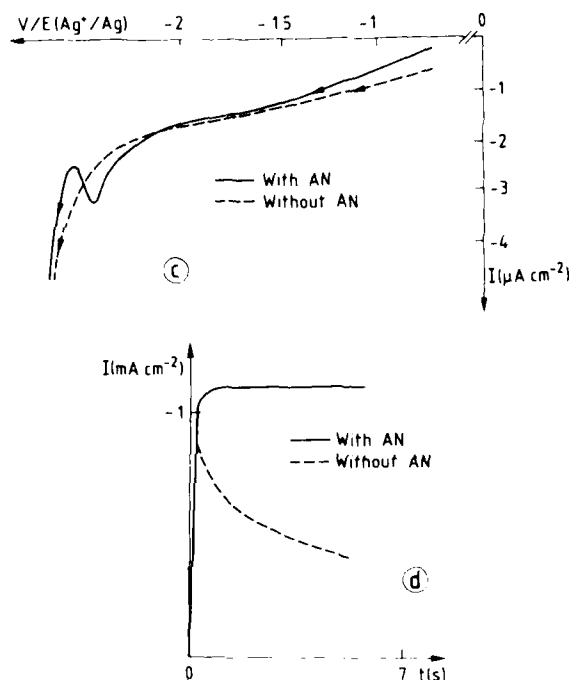


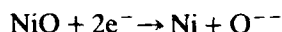
FIGURE 4 (continued)

The electrode is composed of Armco iron, mechanically polished (final particle size $1\mu\text{m}$), then coated by cathode bombardment with a film of iron of the same quality, approximately $1\mu\text{m}$ thick. Following exposure to the air of the laboratory, the surface showed traces of atmospheric contamination detected by AES (Figure 4a). The potentiodynamic characteristic (curve $I(V)$ in Figure 4c) obtained during an electrolysis shows three separate areas: after a period of reduction of the oxide (I), there appears a Faradaic activity inhibition peak, indicating modification of the surface of the electrode (II) and, finally, at (III) a region of intense Faradaic activity which favours rapid growth of the thickness of the film. It is, however, interesting to note that the Faradaic intensity is independent of the thickness of the film, as shown by the potentiostatic characteristic in Figure 4d: the thickening film does not offer any particular resistance to passage of current. However, as shown in Figure 4b obtained by AES on the electrode after electrolysis, the

film of polyacrylonitrile covers the entire surface as the characteristic Auger lines of the iron have disappeared.

III-2 Interaction of acrylonitrile with negatively-polarized nickel surface

The nickel electrode is prepared in a similar way to that of the mechanically polished iron, followed by deposit of $1\text{ }\mu\text{m}$ of Marz nickel by cathode bombardment. Here again, cathode polarization helps to reduce surface oxide:



However, unlike iron, nickel has a stable stoichiometric oxide (formation enthalpy $\Delta G = -101.2\text{ kcal} \cdot \text{M}^{-1}$). The reduction kinetics of the oxide layer are, in this case, influenced by its thickness and the presence of stoichiometric faults which alter its stability: we then obtain results fairly close to those obtained with iron, which is

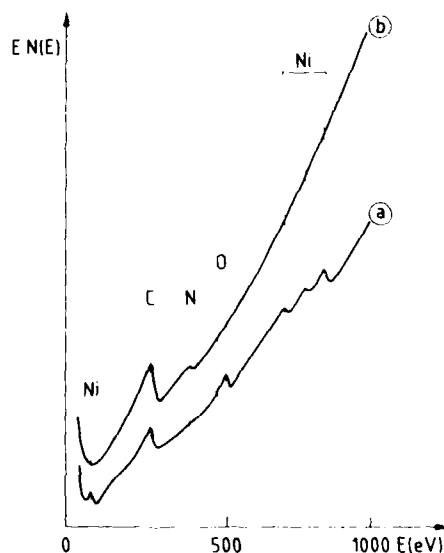


FIGURE 5 AN/nickel interaction (cathode area). a—Initial chemical composition of the surface (AES). b—Chemical composition of the surface after electrolysis (AES). c—Curve $I(V)$ in the presence of AN (0.5 M). d—Curve $I(t)$ in the presence of AN (0.5 M) for $V = -2.8\text{ V}$.

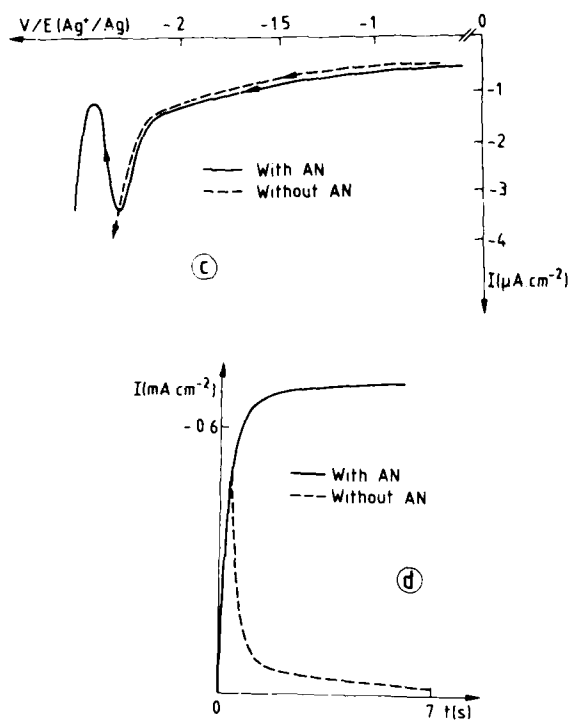


FIGURE 5 (continued)

explained to the extent to which electronic properties of these two metals are fairly similar.¹⁴ In spite of surface contamination due to exposure to the air (Figure 5a), the potentiodynamic (Figure 5c) and potentiostatic (Figure 5d) characteristics are similar to those in Figure 4; similarly, the film of PAN obtained after electrolysis is total (Figure 5b). Following ion abrasion of the film (disappearance of the Auger line from the nitrogen and reappearance of Auger lines of the nickel), we note that the oxide initially present on the surface of the nickel has been completely eliminated: chemisorption of AN has occurred on the sites released by reduction of NiO.

However, if we compare the results achieved by MDS (surface electronic structure) from the three samples (Figure 6):

— one exposed to electrolysis without acrylonitrile (Figure 6a);

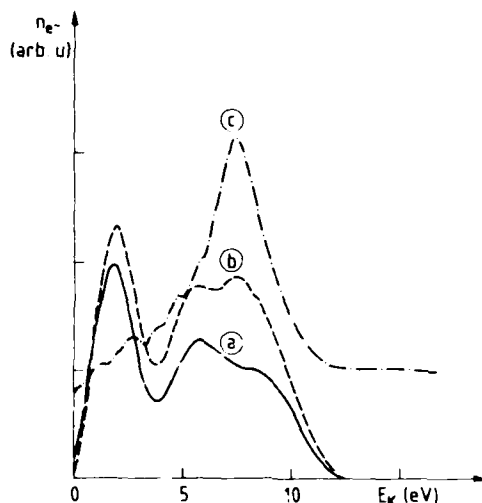


FIGURE 6 Modification by electrolysis of the surface of nickel with respect to thickness of the oxide (MDS spectrums). a—Crude nickel surface. b—Nickel surface (highly oxidized) after electrolysis. c—Nickel surface (slightly oxidized) after electrolysis.

- another exposed to electrolysis with acrylonitrile but initially very oxidized (Figure 6b);
- the third, exposed to the same electrolysis as the second, but initially only lightly oxidized (Figure 6c),

we note that sample no. 2 has hardly been modified by the presence of acrylonitrile in the electrolytic cell, whereas sample no. 3 shows an intense electronic emission band characteristic of the acrylonitrile CN group. In the case of nickel, therefore, there is a direct correlation between the possibility of reducing surface oxide and the possibility of obtaining an even, total and structurally well-defined film of PAN.

III-3 Interaction of acrylonitrile with negatively-polarized stainless steel

The stability of stainless steel A316L with respect to corrosion and oxidation is due to the surface segregation of one of its components

(chrome) whose stoichiometric oxide (Cr_2O_3) is particularly stable (formation enthalpy $\Delta G \approx -168.8 \text{ kcal} \cdot \text{M}^{-1}$). Let us therefore consider two samples:

- STAINLESS STEEL 1, mechanically polished,
- STAINLESS STEEL 2, mechanically polished, then subjected to ion abrasion (Ar^+ , $E_p = 3 \text{ keV}$, $I_p = 1 \mu\text{A}$), designed to destroy its surface layer of natural oxide.

Both samples are subjected to the same type of measurements as the previous samples. The spectra shown in Figures 7a and b are Auger spectra obtained from STAINLESS STEEL 1 before and after electrolysis: oxygen is still present after electrolysis (reduction

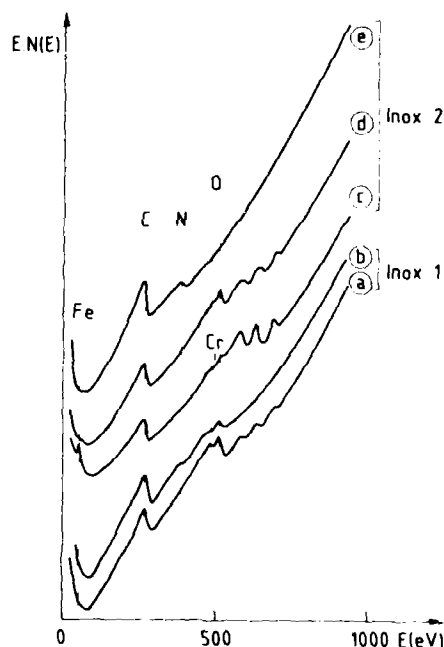


FIGURE 7 AN/Stainless steel interaction (cathode area). a—Initial chemical composition of the surface (as polished). b—Chemical composition of the surface of the sample after electrolysis. c—Initial chemical composition of the surface after ion abrasion. d—Chemical composition of the surface of the same sample after exposure to air (2 minutes). e—Chemical composition of the surface of the same sample after electrolysis. f—Curve $I(V)$ in the presence of AN (0.5 M) of the 1st sample. g—Curve $I(V)$ in the presence of AN (0.5 M) of the 2nd sample.

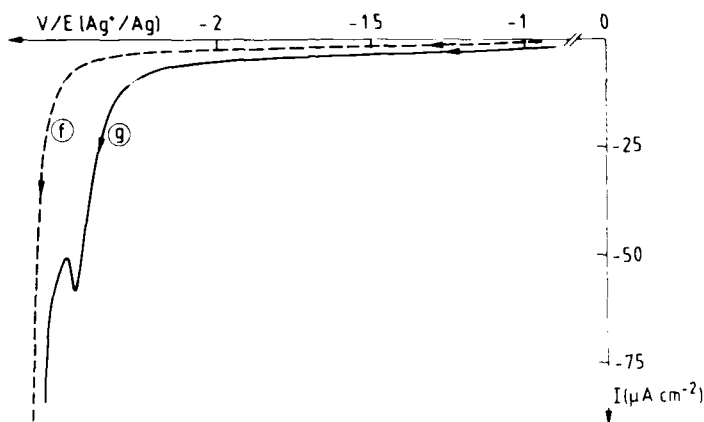


FIGURE 7 (continued)

has been very incomplete); however, the Auger line of the nitrogen indicates the presence of PAN, whereas the disappearance of Auger lines from the iron indicates that it is the areas of high iron concentration on the surface of the sample, which have above all been coated with PAN.

Let us now examine the potentiodynamic characteristic (Figure 7f). The Faradaic activity inhibition peak observed in the case of iron does not appear here, which confirms the results obtained by AES: the surface of the electrode is not completely modified by the deposit of a film of PAN during electrolysis.

However, the results obtained with STAINLESS STEEL 2 are quite positive, in that they show great similarity to those obtained with iron. Following ion abrasion, the surface of the sample contains only iron, chromium and carbon (Figure 7c). Brief exposure to air (corresponding to transfer of the sample from the ion abrasion apparatus to the electrolytic cell) causes the formation of a fine layer of oxide (Figure 7d) which can easily be reduced. An even and total film of PAN can then be obtained (Figure 7e), as is confirmed by the potentiodynamic characteristic (Figure 7g): the Faradaic activity inhibition peak appears, indicating complete modification of the surface of electrode.

Thus, as in the case of nickel, the presence of stoichiometric oxide with a strong formation enthalpy (therefore difficult to reduce) constitutes a block to the adhesion process.

III-4 Interaction of acrylonitrile with the surface of a negatively-polarized aluminium electrode

The situation is worsened in the case of aluminium, which has an oxide whose formation enthalpy is very high ($\Delta G = -258.2 \text{ kcal} \cdot \text{M}^{-1}$). An initial mechanically-polished sample AL1 shows a highly oxidized surface, contaminated by carbon (Figure 8a) which, following electrolysis, appears only thinly covered with PAN: the Auger lines of the aluminum and the oxygen are still clearly visible (Figure 8b). The potentiodynamic characteristic (Figure 8f) shows no inhibition peak. Moreover, the Faradaic

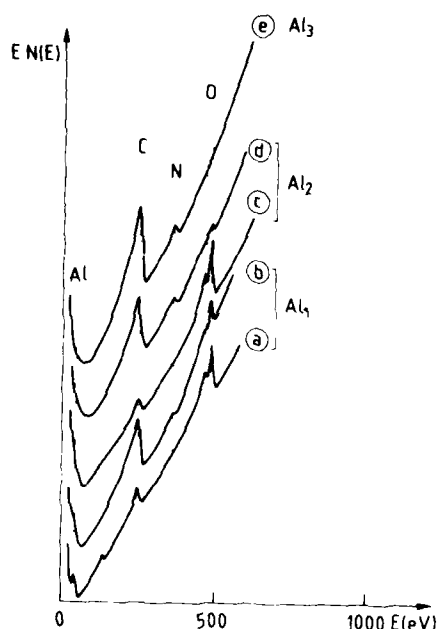


FIGURE 8 (AN/Aluminium interaction (cathode area). a—Initial chemical composition of the surface (as polished). b—Chemical composition of the surface of the same sample after electrolysis. c—Initial chemical composition of the surface after ion abrasion and exposure to air (2 minutes). d—Chemical composition of the surface of the same sample after electrolysis (0.5 M). e—Chemical composition of the surface of an identical sample after electrolysis (2.5 M). f—Curve I(V) in the presence of AN (0.5 M) of the 1st sample. g—Curve I(V) in the presence of AN (0.5 M) of the 2nd sample. h—Curve I(V) in the presence of AN (2.5 M) of the 3rd sample.

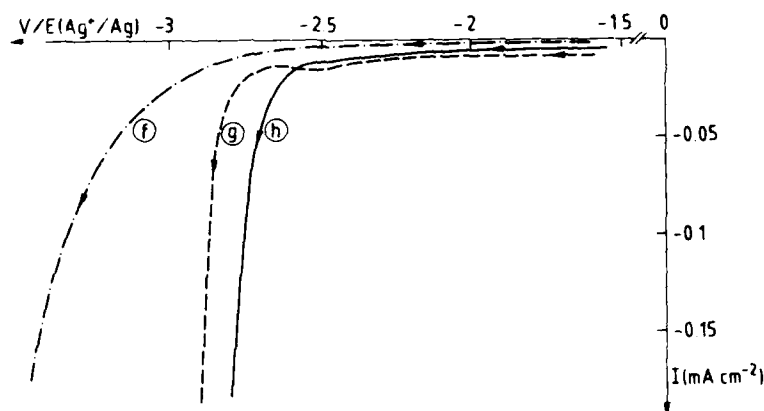


FIGURE 8 (continued)

activity of this electrode is very weak, indicating that its electrical resistance is high.

A second mechanically polished sample AL2 was subjected to ion abrasion until it was perfectly clean (*in situ* test by AES). The short exposure to air necessary for the transfer of the sample from the ion abrasion apparatus to the electrolytic cell caused the formation of a native oxide contaminated by carbon (Figure 8c). However, after electrolysis, the surface of this sample is almost completely covered with PAN (low intensity of aluminium and oxygen Auger lines (Figure 8d). Moreover, the potential-dynamic characteristic (Figure 8g) shows, on the one hand, very high Faradaic activity of the electrode (low resistance); in addition, there is a plateau in the area of the inhibition peak, if any.

We repeated this second experiment but under different conditions (concentration of AN in the solution 5 times higher than in all other experiments). This time, the surface of electrode AL3 was completely covered with PAN (Figure 8e) and a clear inhibition peak appeared on the potential-dynamic characteristic (Figure 8h).

These results extend and complete those obtained with other metals. The thick and even oxide layer present on AL1 cannot be reduced: there is no film. Much thinner, the oxide layer on AL2 (native oxide) can be attacked locally by the reduction process, thus creating conditions favourable to the formation of PAN islands. In the case of AL3, the increase in the concentration of AN assists the

polymerization reaction: the apparently complete coverage of the surface of the electrode results not from abounding of the PAN chains (as in the case of iron and nickel) but from the formation of adjacent organic aggregates grafted locally onto the substrate.

III-5 Interpretation of results

It is worthwhile interpreting all the results obtained.

As shown in Ref. 14, when uncoated, all the metals used show a high density of occupied electronic states at around their Fermi level which is obviously favourable to an acid-base type reaction, in which the metal plays the part of electron donor. However, their oxides, which are characterized by localization of electrons on the $2p$ levels of the oxygen, show only a very low density of occupied electronic states at the Fermi level (this is the case of iron and certain crystalline faces of nickel); this electronic localization may also lead to the establishment of a forbidden band ΔV , whose size increases with the formation enthalpy of the oxide (as an example $\Delta V \text{ O/Ni/111} \approx 3 \text{ eV}$; $\Delta V \text{ Al}_2\text{O}_3 \approx 9.5 \text{ eV}$). The wider the forbidden band and the less reducible the oxide, the less likely is the acid-base reaction.

It is now possible to suggest an energy diagram for the metal, oxide and electrolytic solution system (Figure 9).

Figure 9a shows, as an ordinate, the bonding energies of the active electronic levels with the non-polarized system. The electrons in the oxide layer are too bonded to be involved in an acid-base reaction with the LUMO (lowest unoccupied molecular orbital) of the acrylonitrile or with the unoccupied orbital of the ion $\text{N}(\text{C}_2\text{H}_5)_4^+$ of the supporting electrolyte: the system is stable. It is no longer stable when the electrode is polarized (Figure 9b):

- reduction of the oxide causes electronic re-occupation of the surface below the Fermi level;
- polarization of the vinyl bond of the AN in the double layer causes degeneracy of the LUMO and HOMO (highest occupied molecular orbital) and their shift;
- the unoccupied orbital of $\text{N}(\text{C}_2\text{H}_5)_4^+$ is lowered with respect to the vacuum level of the electrode.

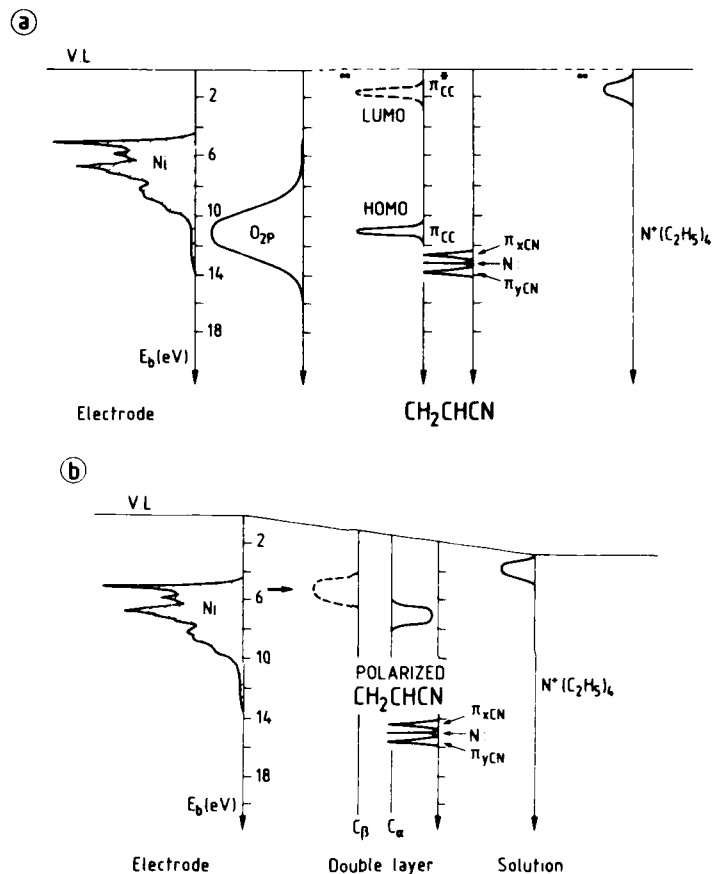


FIGURE 9 Energy diagram of the An-Ni system in the cathode area. a—System without interaction. The bonding energies are given with respect to the vacuum level. b—Polarized system. Establishment of the chemical bond (acid-base reaction) is shown by the small thin arrow; the Faradaic transfer from the electrode to the $N^+(C_2H_5)_4$ ion is produced by tunnelling throughout the double layer.

Under these conditions, the acid-base reaction between metal and AN can occur, the resulting hybridization leading to a chemisorption bond. At the same time, the orbital resulting from the degeneracy of HOMO (and which is an electronic pair carrier) becomes, in turn, suitable for involvement in an acid-base reaction if a new AN molecule is available in its immediate vicinity (see Figure 3c and d).

This model has been established for a particularly simple case but its generalization can be very interesting for the technical applications: a preliminary study (experience, theory or bibliography) of the partners (mineral material and organic molecule) allows one to predict their ability for adhesion. It can also suggest and eventually help to determine what surface treatments can improve this ability, and how to modify the joining methods in order to benefit from the main properties of the organic molecule.

CONCLUSION

The results described in this article have been obtained by means of laboratory work designed to reproduce experimentally, and in a controlled and reproducible fashion, the various actual situations encountered during the production of organic coatings on mineral substrates and during the making of adhesive joints. They have enabled us to demonstrate the elementary mechanisms which govern organic molecule-mineral substrate bonds and the conditions necessary for optimization of the adhesion and reticulation processes.

Apart from the influence of the electronic properties of the monomer molecule, we have demonstrated the influence of the electronic states of the mineral surface and of the local electrical fields on the chemical reactions involved, and also on the properties of the resulting product.

The correlation between the elementary properties and the structure of the organic mineral system at atomic scale has been established and generalization methods proposed.¹⁵⁻²⁰

Finally, results, as yet incomplete, show that the same approach can be adopted for a systematic study of the behaviour laws of such a system when subjected to a variety of stresses, and will be soon published.

References

1. J. C. Pivin, J. Perreau, C. Reynaud, J. Takadoum. *J. of non-cryst. solids* 86 (1986) 161.
2. G. Lecayon, C. Boiziau. *Proceedings of Adhecom*, 15-18th April 1986—Bordeaux (France), p. 259.

3. J. Perreau, C. Reynaud, G. Lecayon, Y. Ellinger, *J. Phys. B* **19**, 1497 (1986).
4. C. Boiziau, G. Lecayon, *Scanning Electron. Microsc.* **I**, 109 (1986).
5. C. Boiziau, *Scanning Electron. Microsc.* **III**, 949 (1982).
6. C. Reynaud-Matrat, Thesis, Université Paris-Sud-Orsay (France), July 1, 1986.
7. J. E. Demuth, D. E. Eastman, *Phys. Rev. B* **13**, 1523 (1976).
8. K. Kishi, S. Ikeda, *Surf. Sci.* **107**, 405 (1981).
9. J. Perreau, *et al.*, *Surf. Sci.* **162**, 776 (1985).
10. C. Reynaud, C. Juret, C. Boiziau, *Surf. Sci.* **126**, 733 (1983).
11. G. Lecayon, *et al.*, *Chem. Phys. Letts.* **91**, 506 (1982).
12. G. Tourillon, P. C. Lacaze, J. E. Dubois, *J. Electroanal. Chem.* **100**, 247 (1979).
13. J. C. Pivin, C. Roques-Carmes, G. Slodzian, *Int. J. of Mass Spectrom. and Ion Phys.* **31**, 293 (1979).
14. Landolt-Bornstein, *Numerical data and functional relationships in science and technology.* **III. 13**, C (Springer-Verlag, Berlin, 1984).
15. C. Boiziau, *et al.*, *Scanning Electron. Microsc.* **IV**, 1187 (1984).
16. C. Boiziau, *et al.*, *ibid.* **IV**, 1385 (1985).
17. S. Leroy, *et al.*, *J. Molecular Structure* **128**, 269 (1985).
18. C. Reynaud, *et al.*, **11**, 159 (1985).
19. S. Leroy, *et al.*, *Materials Letts.* **3**, 239 (1985).
20. G. Lecayon, *et al.*, *Scanning Electron. Microsc.* (1986) (in press).

The Role of the Interface in Carbon Fibre-Epoxy Composites†

J. SCHULTZ, L. LAVIELLE and C. MARTIN

Centre de Recherches sur la Physico-Chimie des Surfaces Solides, C.N.R.S., 24, avenue du Président Kennedy, 68200 Mulhouse, France

and

Laboratoire de Recherches sur la Physico-Chimie des Interfaces de l'Ecole Nationale Supérieure de Chimie de Mulhouse 3, rue Alfred Werner, 68093 Mulhouse Cedex, France

(Received February 24, 1987)

The final performance of a composite material depends strongly on the quality of the fibre-matrix interface. The interactions developed at the interface were studied using the acid-base or acceptor-donor concept.

The surface characteristics of the carbon fibres and the epoxy matrix were studied using a tensiometric method and the inverse gas chromatography technique. Acid-base surface characters could be determined allowing the interactions at the interface to be described by a specific interaction parameter.

It was shown that the shear strength of the interface, as measured by a fragmentation test, is strongly correlated to this specific interaction parameter, demonstrating the importance of acid-base interactions in the fibre-matrix adhesion.

KEY WORDS Acceptor-donor interactions; acid-base interactions; carbon-fibre/epoxy composite; fibre-matrix interface; inverse gas chromatography; wetting.

INTRODUCTION

It is generally accepted nowadays that the final performance of a composite material depends, to a large extent, on the adhesion of

† Presented at the Tenth Annual Meeting of The Adhesion Society, Inc., Williamsburg, Virginia, U.S.A., February 22-27, 1987.

the polymer matrix to the reinforcing fibre and, therefore, on the quality of the interface which is formed between the two solids.

When interactions of physical origin are being exchanged at the interface, the reversible energy of adhesion can be determined from the surface energies of both the fibre and the matrix.

For many years, the surface energy γ_s of a solid has been described by a sum of two terms, the dispersive component γ_s^D and the polar component γ_s^P . However, more recently, it appears that the non-dispersive interactions may be better described in terms of the electron acceptor or -donor (acid-base) characters of the solids. Both polar and acceptor-donor aspects will be considered in this study.

The purpose of the present study is to examine the role of these specific interfacial interactions in the adhesion between carbon fibres and an epoxy matrix.

MATERIALS

Three high-strength PAN based carbon fibres corresponding to different stages of manufacturing have been used in this study:

- the untreated fibre ①,
- the untreated fibre having received a proprietary surface treatment designated oxidized fibre ②,
- the oxidized fibre having received a supplementary sizing treatment denoted coated fibre ③.

The fibres were handled as little as possible to prevent surface contamination or damage.

SURFACE PROPERTIES OF CARBON FIBRES

1 Wetting technique

The surface energy γ_s of solids, in particular their dispersive component γ_s^D and polar component γ_s^P , are usually determined through wetting experiments. The method consists of measuring contact angles of a series of liquids of known surface energy

components on the solid surface. In the case of high surface energy solids however, virtually all liquids spread spontaneously on the surface. Moreover the spreading pressure can generally not be neglected. Therefore, for such solids, a two-phase liquid method has been developed.^{1,2} Experimentally, as shown on Figure 1, the single fibre is attached to the arm of an electro-balance and immersed first in the non-polar liquid phase (hydrocarbon), and then in both the hydrocarbon and the non-miscible polar liquid (formamide)³. From the resulting weight increase, the contact angle of formamide on the fibre in the presence of hydrocarbon is determined. The same analysis as that used for flat surfaces², may be applied and allows us to determine the surface energy components of the carbon fibres. The results are presented on Table I.

It is observed that the untreated and oxidized fibres have a rather high dispersive term of the order of $50 \text{ mJ} \cdot \text{m}^{-2}$ whereas that of the coated fibre is only about $34 \text{ mJ} \cdot \text{m}^{-2}$. On the contrary, the surface polarity of the untreated fibre is low, whereas that of the two other fibres is relatively high. These values are in rather good agreement with published data of surface energy of carbon fibres measured by a tensiometric method,^{4,5} but are much lower than those obtained on graphite.^{6,7}

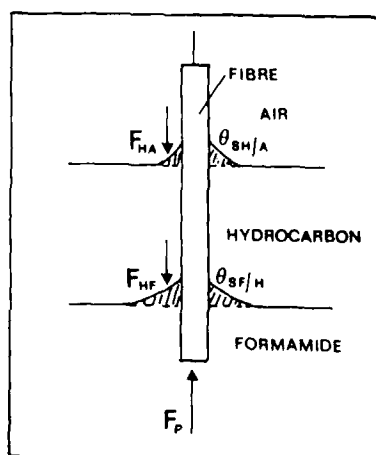


FIGURE 1 Representation of the two-liquid-phase technique applied to a carbon fibre.

TABLE I
Surface energy components of carbon fibres
(Wettability technique) (in $\text{mJ} \cdot \text{m}^{-2}$)

Carbon fibre	γ_s^D	γ_s^P	γ_s
Untreated (1)	50 ± 8	7 ± 3	57
Oxidized (2)	48 ± 10	15 ± 4	63
Coated (3)	34 ± 6	13 ± 3	47

It must be noted that the tensiometric method gives good precision concerning the evaluation of γ_s^P , but is less reliable for γ_s^D . Moreover, given the small diameters of the fibres and the range of forces measured, the method requires a great deal of patience and painstaking effort.

2 Inverse gas chromatography at infinite dilution^a

In the inverse gas chromatography (IGC) technique, the surface characteristics of the solid are determined by injection of probes of known properties into the column containing the solid. The retention times of these probes measured at "infinite" dilution or near zero surface coverage, allow us to determine the interactions between the probes and the solid in the absence of interactions between the probe molecules themselves.

Measurements were carried out with an Intersmat IGC DLF chromatograph equipped with a flame ionization detector of high sensitivity. The retention data were obtained with a stainless steel column of 0.6 m length and 4.4 mm internal diameter packed with 3 to 5 g of carbon fibres. The amount of each probe injected corresponds to the limit of sensitivity of the detector (10^{-4} to 10^{-3} ppm) in order to ensure practically zero surface coverage. Optimum working conditions allowed us to record quite symmetrical peaks obeying, in all cases, the laws of linearity and ideality required for interpretation.

The net retention volume V_N was calculated from:

$$V_N = jD(t_R - t_0) \quad (1)$$

where t_R is the retention time of the given probe, t_0 , the zero retention reference time measured with a non adsorbing probe such

as methane, D , the flow rate, and j , a correction factor taking into account the compressibility of the gas.

Simple thermodynamic considerations applied to the inverse gas chromatography technique at infinite dilution lead to the following general relationship:

$$\Delta G_D^0 = -\Delta G_A^0 = RT \ln \left(\frac{V_N P_0}{S \cdot g \pi_0} \right) \quad (2)$$

where ΔG^0 is the free enthalpy of desorption (or adsorption) of 1 mole of solute from a reference adsorption state defined by the bidimensional spreading pressure π_0 of the adsorbed film to a reference gas phase state defined by the partial pressure P_0 of the solute, S is the specific surface area of the fibres and g is the weight of fibres in the column.

Two reference states are generally considered⁸:

—the reference states of Kemball and Rideal

where $P_0 = 1.013 \times 10^5$ Pa and $\pi_0 = 6.08 \times 10^{-5}$ Nm⁻¹,

—the reference states of De Boer

where $P_0 = 1.013 \times 10^5$ Pa and $\pi_0 = 3.38 \times 10^{-4}$ Nm⁻¹.

ΔG^0 can therefore be written:

$$\Delta G^0 = RT \ln V_N + K \quad (3)$$

K being a constant depending on the chosen reference states.

To a first approximation, ΔG^0 is related to the energy of adhesion W_A between the probe and the solid, per unit surface area, by

$$\Delta G^0 = \mathcal{N} a W_A \quad (4)$$

\mathcal{N} being Avogadro's number and a the surface area of the probe molecule.

a) *Dispersive interactions* According to Fowkes⁹, the energy of adhesion W_A , in the case of dispersive interactions, for instance with n -alkanes probes, is given by:

$$W_A = 2(\gamma_S^D \gamma_L^D)^{1/2} \quad (5)$$

Therefore, combining Eqs. (3), (4) and (5) leads to:

$$RT \ln V_N = 2\mathcal{N}(\gamma_S^D)^{1/2} a (\gamma_L^D)^{1/2} + C' \quad (6)$$

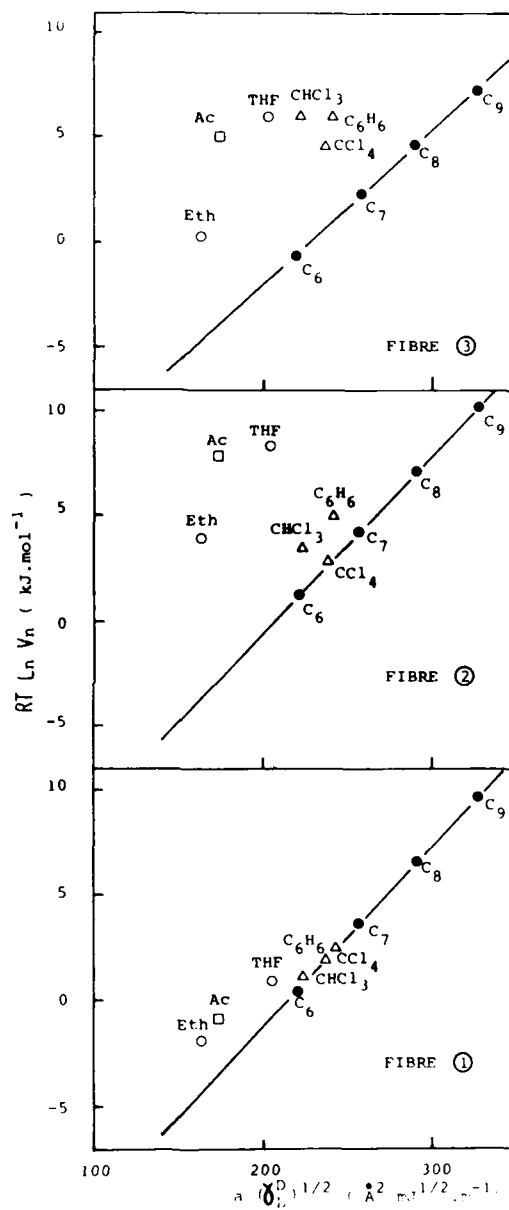


FIGURE 2 $RT \ln V_N$ vs $a(\gamma_L^D)^{1/2}$ diagram for the 3 carbon fibres.

This analysis is confirmed, on the examples shown in Figure 2, where it is observed that for a series of n -alkanes, $RT \ln V_N$ is a linear function of the quantity $a(\gamma_L^D)^{1/2}$. The slope of the straight line leads to the values of γ_S^D of the three carbon fibres listed on Table II.

Gray¹⁰ uses a similar method for the determination of γ_S^D by considering the increment of ΔG^0 per methylene group in the n -alkanes series of general formula C_nH_{2n+2} . The increment $\Delta G_{(CH_2)}^0$ defined by $\Delta G_{(C_{n+1}H_{2n+4})}^0 - \Delta G_{(C_nH_{2n+2})}^0$ leads to:

$$\gamma_S^D = \frac{\left[RT \ln \frac{V_N C_{n+1} H_{2n+4}}{V_n C_n H_{2n+2}} \right]^2}{4N^2 a_{CH_2}^2 \gamma_{CH_2}} \quad (7)$$

where a_{CH_2} is the surface area of a CH_2 group, *i.e.* 6 \AA^2 and γ_{CH_2} the surface energy of a CH_2 group, *i.e.*, of a surface constituted of close packed CH_2 groups analogous to polyethylene and given by:

$$\gamma_{CH_2} = 35.6 + 0.058(20 - T), \text{ in mJ} \cdot \text{m}^{-2}$$

The values of γ_S^D obtained by using Gray's method are also presented on Table II.

It must be noted that the chromatographic method leads to values of γ_S^D much more precise than the ones obtained by wetting, although they agree satisfactorily. The untreated and oxidized fibres have rather high values of γ_S^D whereas the coated fibre exhibits a somewhat lower value close to the one of a polymer.

b) *Specific interactions* Non-dispersive interactions have usually been referred to in terms of polar interactions. More recently, the works of Drago^{11,12} Gutmann¹³ and Fowkes^{14,15} stress the fact that the non-dispersive or specific interactions are essentially Lewis

TABLE II
Dispersive component of the surface energy of carbon fibres (IGC method)

Carbon fibres	γ_S^D (mJ . m ⁻²)	
	Our method	Gray's method
Untreated (1)	50 ± 4	48 ± 4
Oxidized (2)	49 ± 2	50 ± 4
Coated (3)	36 ± 3	33 ± 3

acid-base interactions or electron acceptor-donor interactions. According to this new concept, strong interactions develop only between an acid and a base. Materials of the same character, both acids or both bases, even with high surface polarities will exchange nearly zero specific interaction.

According to Gutmann¹³ for instance, liquids can be characterized by donor or acceptor numbers:

– the donor number DN defining the basicity or electron-donor ability is the molar enthalpy value for the reaction of the electron-donor D with a reference acceptor SbCl_5 .

– the acceptor number AN characterizing the acidity or electron acceptor ability is defined on a different basis. It is the NMR chemical shift of ^{31}P contained in $(\text{C}_2\text{H}_5)_3\text{PO}$ when reacting with the acceptor A.

In this study, several specific probes have been chosen, exhibiting either a strong donor (base) character or a strong acceptor (acid) character, or both characters (amphoteric).

Table III shows the main characteristics of some of the probes used in this work. The surface area a of the probe molecules has been determined by injecting the probes on neutral reference solids

TABLE III
Characteristics of some probes

	a (\AA^2)	γ_L^D ($\text{mJ} \cdot \text{m}^{-2}$)	DN	AN	Specific character
C_6H_{14}	51.5	18.4	—	—	Neutral
C_7H_{16}	57.0	20.3			
C_8H_{18}	62.8	21.3			
C_9H_{20}	68.9	22.7			
THF	45	22.5	20.0	8.0	Base
Ether	47	15	19.2	3.9	
CHCl_3	44	25.9	0	23.1	Acid
CCl_4	46	26.8	0	8.6	
C_6H_6	46	26.7	0.1	8.2	
Acetone	42.5	16.5	17.0	12.5	Amphoteric
Ethyl-Acetate	48	19.6	17.1	9.3	

(PTFE, poly-ethylene, graphitized carbon black, . . .). The dispersive component γ_L^D has been measured by the contact angle method on reference solids. The values of DN and AN are taken from tables published by Gutmann¹³.

In order to be able to determine quantitatively these specific interactions, we consider, to a first approximation, that the specific interactions are simply added to the dispersive interactions defined previously.

Therefore, the experimental point corresponding to a specific probe having an acid or base character will always lie well above the reference straight line of $RT \ln V_N$ vs $a(\gamma_L^D)^{1/2}$ corresponding to the *n*-alkanes as schematically illustrated in Figure 3.

At a given value of $a(\gamma_L^D)^{1/2}$, the difference of ordinates between the point corresponding to the specific probe and the reference line leads to the value of the free enthalpy of desorption ΔG_{sp}^0 corresponding to specific acid-base interactions.

$$RT \ln \frac{V_N}{V_N^{ref}} = \Delta G_{sp}^0 \quad (8)$$

Such experiments have been carried out on the three carbon fibres at various temperatures. An illustration of the $RT \ln V_N$ vs $a(\gamma_L^D)^{1/2}$ diagrams obtained at 40°C are presented in Figure 2.

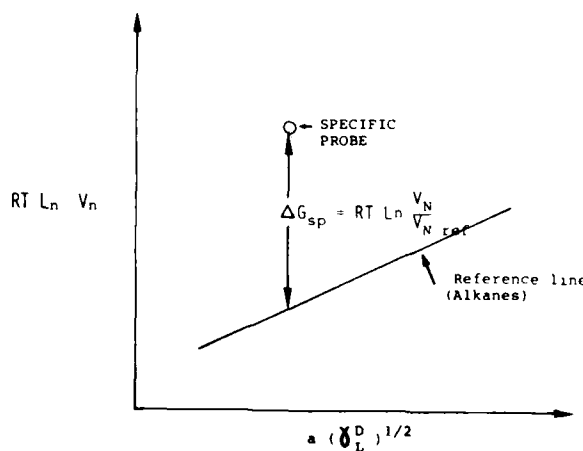


FIGURE 3 Schematic representation of a general $RT \ln V_N$ vs $a(\gamma_L^D)^{1/2}$ diagram.

It can easily be concluded, on a qualitative basis, that:

–the untreated fibre (1) has an average acid or acceptor character and practically no base or donor character,

–the oxidized fibre (2) has a strong acid character and a rather low base character,

–the coated fibre (3) could be called “amphoteric” since it exhibits a strong acid character together with a high base character.

In order to get at least a semi-quantitative estimate of the acid-base surface properties of the carbon fibres, the enthalpy of desorption ΔH_{sp}^0 corresponding to the specific interactions has been determined by the intercept at the origin of the variation of ΔG^0 with temperature T according to

$$\Delta G_{sp} = \Delta H_{sp} - T \Delta S_{sp} \quad (9)$$

An example is presented in Figure 4. Following Papirer's approach¹⁶, we assume that:

$$\Delta H_{sp} = K_A \cdot DN + K_B \cdot AN \quad (10)$$

where DN and AN are Gutmann's numbers for the probes and K_A and K_B are numbers describing the acid and base characters of the fibres.

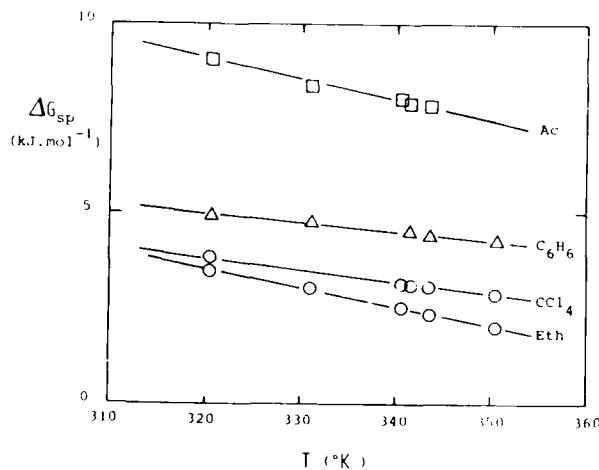


FIGURE 4 The variation of the free energy of desorption, ΔG_{sp} , with temperature.

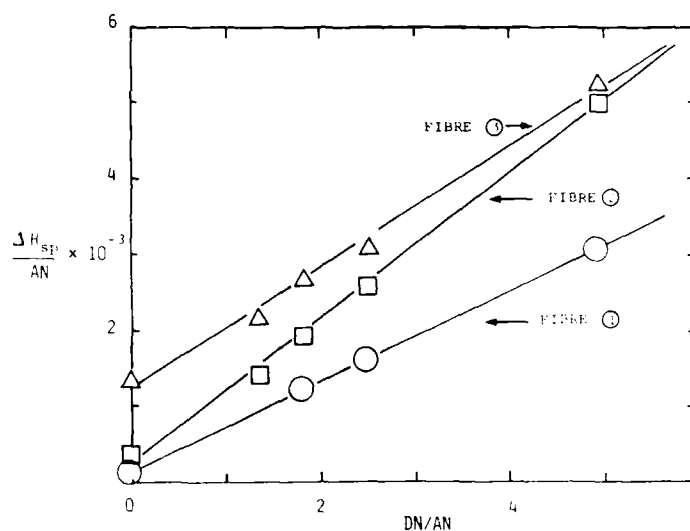


FIGURE 5 $\frac{\Delta H_{sp}}{AN}$ vs $\frac{DN}{AN}$ diagram.

Equation (10) can be written:

$$\frac{\Delta H_{sp}}{AN} = K_A \frac{DN}{AN} + K_B \quad (11)$$

It is shown in Figure 5 that a plot of $\Delta H_{sp}/AN$ vs DN/AN is actually linear. Therefore K_A and K_B can be determined from the slope and intercept at the origin of this straight line.

Table IV gives the values of K_A and K_B found for the three carbon fibres. We are aware that, given the approximations used in the chromatographic analysis, K_A and K_B can only be considered as semi-quantitative values of the surface acidity and basicity of the

TABLE IV
Acceptor-donor (acid-base) character
of the carbon fibres (arbitrary units)

Carbon fibres	K_A	K_B
Untreated (1)	6.5	1.5
Oxidized (2)	10.0	3.2
Coated (3)	8.6	13.0

TABLE V
Surface properties of the epoxy matrix

γ_s^D (Wettability)	γ_s^P	γ_s^D	K_A (IGC)	K_B
40	4	40	7.6	6.2

TABLE VI
Specific interaction parameter A between carbon fibres and epoxy resin (in arbitrary units)

Carbon fibres	A
Untreated (1)	52
Oxidized (2)	86
Coated (3)	152
Coated (4)	127

fibres, allowing comparison to be made. This semi-quantitative approach leads to the same conclusions as the ones drawn from the qualitative examination.

The same type of study has been effected on an epoxy matrix (DGEBA-DDS) after grinding at low temperature in an inert atmosphere. Its surface properties are shown in Table V.

Knowing the K_A and K_B values for the fibres and matrix and by analogy with relation (10), it is now possible to define a "specific interaction parameter" A describing the acid-base interaction between the fibre (f) and the matrix (m) by:

$$A = K_A^f K_B^m + K_A^m K_B^f \quad (12)$$

The calculated values of A for the three fibres, together with the one for a commercial fibre of different characteristics (Coated Fibre ④), are shown in Table VI. It is seen that the specific interaction increases when going from the untreated to the coated fibre. As expected the amphoteric coated fibre 3 leads to the highest acid-base interaction with the amphoteric epoxy matrix.

FIBRE-MATRIX ADHESION

The fibre-matrix adhesion has been evaluated by using the fragmentation method^{17,18}.

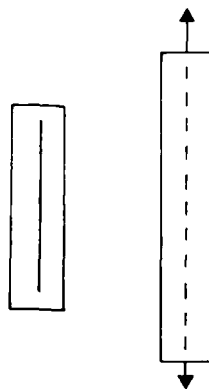


FIGURE 6 Schematic representation of the fragmentation technique.

As shown schematically in Figure 6, the elementary carbon fibre is embedded in the epoxy matrix and the parallelepipedic test piece is submitted to an uniaxial tensile stress in the direction of the fibre. The fibre-matrix adhesion, *i.e.*, the capacity of the interface to transfer the stress from the matrix to the fibre, is evaluated from the shear resistance τ of the interface. By applying a tensile force, the single fibre is broken into small fragments until the shear strength of the interface is reached. τ can, therefore, be calculated from the average length of the fragments and the tensile strength of the fibre at this average length. Weibull statistics have been used to determine both parameters.

The values of τ given in Table VII have been calculated assuming that the shear strength is maximum at the extremities of the fibre fragments.^{19,20} The adhesion of the coated fibre 3 is roughly 30% higher than the adhesion of the untreated fibre 1.

TABLE VII
Fibre/matrix adhesion

	τ (MPa)	A (a.u.)	$I^D + I^P$ (mJ . m ⁻²)
Untreated fibre 1	101	52	101
Oxidized fibre 2	113	86	105
Coated fibre 3	135	152	87
Coated fibre 4	128	127	—

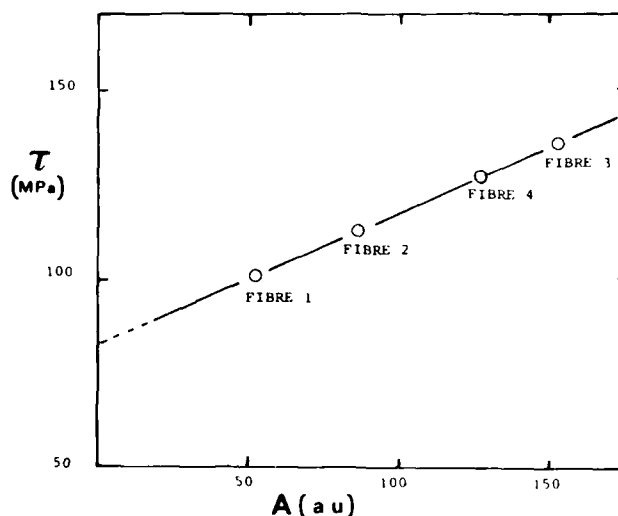


FIGURE 7 Interfacial shear resistance τ vs specific interaction parameter A .

As shown on Table VII, the increase of adhesion obtained by the oxidation treatment and by the coating cannot be explained by assuming that the interactions at the interface are the result of dispersive and polar forces. There is no correlation between τ and the sum ($I^D + I^P$).

However, as shown on Figure 7, there is a very strong correlation between τ and the specific interaction parameter A . This could mean that the interfacial adhesion principally results from acid-base or acceptor-donor interactions between the fibre and the matrix, assuming that the dispersive interactions are of the same order of magnitude. The meaning of the value of τ obtained by the intercept at the origin of the straight line, of the order of 80 MPa, is not clear yet; this value could be considered, to a first approximation, as being the contribution of the dispersive interactions to the shear resistance of the interface.

CONCLUSIONS

Tensiometric and chromatographic methods for the study of the surface of carbon fibres have been developed. The inverse gas

chromatography technique appears to be a very powerful tool for the characterization of solids in terms of the dispersive component of the surface energy and of the acid-base or acceptor-donor character.

The concept of acid-base interactions constitutes an interesting, if not universal, approach to a better understanding of the interfacial properties of composite materials and could constitute a basis for a better choice for the surface treatments of the fibres.

However, we do now claim that acid-base specific interaction is the only explanation for the increased adhesion of the coated fibre, since other mechanisms could intervene such as interdiffusion or co-cross-linking.^{21,22}

Acknowledgements

This work was supported by the Société Nationale Elf Aquitaine and FIMAC, subsidiary of Elf Aquitaine and Pechiney. The authors wish to thank Drs. J. Bednarick and M. Biensan for their help throughout this study.

References

1. J. B. Donnet, J. Schultz and K. Tsutsumi, *Proc. 4th Intern. Conf. on Chem. Thermodynamics*, Montpellier (France) **7**, 126 (1975).
2. J. Schultz, K. Tsutsumi and J. B. Donnet, *J. Colloid Interf. Sci.* **59** (2), 272 (1977) and **59** (2), 277 (1977).
3. J. Schultz, C. Cazeneuve and M. Shanahan, *J. Adhesion* **12** (3), 221 (1981).
4. L. T. Drzal, J. A. Mescher and D. L. Hall, *Carbon* **17**, 375 (1979).
5. S. K. Li, R. P. Smith and A. W. Neumann, *J. Adhesion* **17** (2), 105 (1984).
6. C. Cazeneuve, J. B. Donnet, J. Schultz and M. Shanahan, *Proc. 14th Biennial Carbon Conf.*, 216 (1979).
7. J. B. Donnet, J. Schultz and M. Shanahan, *Proc. Intern. Symp. on Carbon*, Toyohashi, 57 (1982).
8. J. R. Conder and C. L. Young, *Physicochemical Measurements by Gas Chromatography*, (J. Wiley, New York, 1979).
9. F. M. Fowkes, *Ind. Eng. Chem.* **56** (12), 40 (1964).
10. G. M. Dorris and D. G. Gray, *J. Coll. Interf. Sci.* **77**, 353 (1980).
11. R. S. Drago, G. C. Vogel and T. E. Needham, *J. Am. Chem. Soc.* **93**, 6014 (1971).
12. R. S. Drago, L. B. Parr and C. S. Chamberlain, *ibid.* **99**, 3203 (1977).
13. V. Gutmann, *The Donor-Acceptor Approach to Molecular Interactions*, Plenum Press, New York (1983).
14. F. M. Fowkes, *Rubber Chem. Tech.*, **57**, 328 (1978).
15. F. M. Fowkes and S. Maruchi, *Org. Coatings Plast. Chem.*, **37**, 605 (1977).
16. C. Saint-Flour and E. Papirer, *Ind. Eng. Chem., Prod. Res. Dev.* **21**, 666 (1982).
17. A. T. Di Benedetto and L. Nicolais, *Plast.* **10** (5), 83 (1979).

18. W. D. Bascom and R. M. Jensen, *J. Adhesion* **19**, 219 (1986).
19. H. Simon, F. Bomo and J. Schultz, *Proc. Europ. Plast. Conf.* (Paris), **4** (9), 1 (1982).
20. H. Simon: PhD Thesis, Université de Haute-Alsace (France), 1984.
21. L. T. Drzal, M. J. Rich and P. F. Lloyd, *J. Adhesion* **16**, 1 (1982).
22. L. T. Drzal, M. J. Rich, M. F. Koenig and P. F. Lloyd, *ibid.* **16**, 133 (1983).

Adherence of Elastomers: Fracture Mechanics Aspects†

D. MAUGIS

Equipe de Recherche de Mécanique des Surfaces (CNRS) L.C.P.C., 58, Bd. Lefebvre, 75732 Paris Cédex 15, France

(Received February 24, 1987)

The adhesion forces which link two solids together are of the same nature as those which insure cohesion of solids (Van der Waals, ionic, covalent or metallic), and their thermodynamic transcription is the Dupré energy of adhesion $w = \gamma_1 + \gamma_2 - \gamma_{12}$, where γ_2 is the surface energy and γ_{12} are interfacial energy. Its maximum value is about 2 J/m² for strong binding. However, the force to separate two solids in contact (pull out force or adherence force) depends on a number of parameters including the shape of the solids in contact, their rheological properties, the withdrawal velocity, and the stiffness of the measuring apparatus (soft or hard machines). Adherence is thus characterized by a coupling between mechanics and surface effects and can be studied by fracture mechanics, a field where such a coupling appeared for the first time (Griffith, 1920).

KEY WORDS Adherence; adhesion; cracking; elastic solids; viscoelastic solids; fracture mechanics.

ADHERENCE OF ELASTIC SOLIDS

For two solids in contact over an area A , the edge of the contact can be seen as a crack tip, advancing when the area decreases and receding when the area increases. The energies involved are simply elastic energy U_E , potential energy U_P and total surface energy $U_S = -wA$. Thermodynamics tells us that the crack is in equilibrium when the thermodynamic potential (Gibbs free energy at fixed load

† Presented at the Tenth Annual Meeting of The Adhesion Society, Inc., Williamsburg, Virginia, U.S.A., February 22-27, 1987.

P , Helmholtz free energy at fixed grips) is extremum, i.e. $G = w$ (Griffith criterion) where G is the strain energy release rate. The equilibrium is stable, unstable or neutral according to the sign of the second derivative of the thermodynamic potential, i.e. $(\partial G/\partial A)_P$ at fixed load, or $(\partial G/\partial A)_\delta$ at fixed grips, and thus depends on the shape of the solids and on the stiffness of the loading system. For peeling or double cantilever beam (DCB) with applied momentum, equilibrium is neutral, for a flat punch on a plane or DCB with dead load equilibrium is unstable, DCB with a wedge inserted in it is stable, for a sphere or a cone on a plane it is stable over a range of loads or displacements and becomes unstable at a critical load or displacement. The adherence force is the load corresponding to neutral or unstable equilibrium (at which the crack propagates until complete separation). For a sphere on a plane, for which

$$G = \left(\frac{a^3 K}{R} - P \right)^2 / 6\pi a^3 K$$

where a is the radius of contact, and K , an elastic constant, the adherence force is $P = -(3/2)\pi w R$ at fixed load and $-(5/6)\pi w R$ at fixed grips (JKR theory, Ref. 1). The adherence force is not always proportional to w , but can vary as $w^{1/2}$ for flat punch or DCB, or as w^2 for cones.

In the Griffith description, the crack tip has an elliptical shape which leads to singularities at the crack tip, the intensity of which is described by the stress intensity factor K_I . In fact, as pointed out by Barenblatt,² such infinite stresses are physically unrealistic. Instead of appearing abruptly at the crack tip, the adhesion or cohesion forces increases progressively, reaching the theoretical strength σ_{th} at the crack tip. They deform the crack as would do any stress system applied to the crack lips, and the crack has a short acute tip (the Barenblatt tip) with no singular stress (stress intensity factors due to external load and to cohesion forces cancel one another). It is this theoretical stress σ_{th} which moves with the crack and breaks the bonds one by one as a tip fastener does. It is also these adhesion or cohesion forces that provoke crack healing when external loading is insufficient ($G < w$). In fact the adherence force between two solids, in contact over an area A , is essentially due to the adhesion forces acting in the Barenblatt tip. For example, in $\pi/2$ peeling

adherence is independent of the contact area and a hung load P is sustained only by the forces in the Barenblatt tip. For a sphere on a plane, the pull-out force is almost totally dependent on the value of w at the edge of the contact. This shows that the characterization of an adhesive joint by the mean stress at rupture is nonsense; fracture mechanics concepts must be used.

Since w is the integral of adhesion forces in the Barenblatt tip, the Griffith theory ($G = w$) gives a correct result as long as the Barenblatt tip is small compared to the crack length or to the contact radius. For adherence of soft tiny spheres, the JKR theory ($G = w$) leads to mean stress well above σ_{th} , and it not valid. The profile of the deformed sphere becomes smooth and the adherence is $P = -2\pi w R$ (DMT theory, Ref. 3). A simplified version of the Barenblatt model is the Dugdale model where the adhesion or cohesion force is assumed to have a constant value σ_0 over a length d at the crack tip. In this case, G , or more precisely the integral J , becomes simply $\sigma_0 \delta_i$, where δ_i is the crack opening displacement at the limit of the cohesion zone. (A good example is liquid bridges where σ_0 is the Laplace pressure γ/r (r is the radius of the meniscus), and $\delta_i = 2r \cos \theta$ the crack opening displacement, hence $J = G = 2\gamma \cos \theta$. Evaluating G from the variation of potential energy at constant volume of the liquid bridge gives the force of adherence.⁴

ADHERENCE OF VISCOELASTIC SOLIDS

Elements of volume near the trajectory of a moving crack undergo a cycle of stress when the crack tip comes on and then comes off, whose characteristic time is of the order of d/v (where d is the length of the cohesion zone and v the crack velocity) and whose magnitude is proportional to σ_{th} and hence to w . In a dissipative material energy is lost during such a cycle, and the crack instead of continuously accelerating until the Rayleigh velocity, takes a limit velocity v , which is a function of the generalized force $G - w$ that moves the crack. In a viscoelastic solid the drag force on the crack will be proportional to w and a function of the loss modulus E'' , a frequency dependent quantity, so that in the absence of inertial effects, one can write (Andrews and Kinloch,⁵ Maugis and

Barquins⁶)

$$G - w = w\phi(a_T v)$$

or

$$G = w\phi(v) \quad (1a)$$

(the factor a_T holds for temperature-velocity equivalence) which generalizes, for any geometry, the equation given by Gent and Schultz⁷ for peeling. Inertial effects can be accounted for by writing

$$G = w\phi(a_T v) - \frac{dU_K}{dA} \quad (2)$$

where U_K is the kinetic energy of the system. Eq. (1) holds only for viscous drag which cancels with the crack velocity. A static friction term has certainly to be added for materials such as metals, where a finite stress must be applied to dislocations before they move and dissipate energy. Eq. (1) was quite well verified in all its consequences for adherence of glass on elastomers when only Van der Waals forces act, with crack propagation for $G > w$, and crack healing for $G < w$.^{6,8} For polyurethane the variation of $\phi(v)$ as $v^{0.6}$ at low velocity was correlated with the variation of E'' as $\omega^{0.6}$ at low frequency.

At high frequencies the loss modulus generally decreases, and the loss function $\phi(v)$ decreases above a critical velocity v_c corresponding to a critical value G_c . As a negative resistance branch cannot be observed, the crack velocity jumps, sometimes over several decades, on a second positive branch, giving catastrophic failure. In the presence of an active medium reducing w , *i.e.* the forces in the Barenblatt tip, the $G(v)$ curve is shifted as long as the active medium can follow the crack velocity. If it can follow it until the velocity v_c , a loading that would have given subcritical crack growth, gives a catastrophic failure. This is the essence of Rehbinder embrittlement effects.⁹ If, for specimen with stable geometry factor, *i.e.* $(\partial G/\partial A) > 0$, as peeling or double torsion, one tries to impose a mean velocity V in the negative resistance branch $d\phi/dv < 0$, stick-slip motion is observed. The classical picture of a relaxation oscillation cycle between G_c , the second positive branch, G_{\min} , and the first positive branch, is valid only in absence of inertial effects. For peeling of an adhesive tape, Eq. (2), when variation of peel

angle is neglected, leads to a Lienard differential equation which gives limit cycles in the phase place $G(v)$, quite distinct from the $\varphi(v)$ curve, with Hopf bifurcation at G_c and G_{\min} .^{10,11} Three first order differential equations appear with peel angle variation, that can explain chaotic motion in some ranges of the parameters.

OTHER LOSSES

Besides the viscoelastic losses $w\varphi(a_T)$ due to the stresses moving with the crack, other losses can act and drag the crack. For instance, the presence of a liquid can reduce the surface energy and shift the $G(v)$ curve, but also gives rise to viscous drag larger than viscoelastic ones above a critical velocity, until cavitation occurs, as observed by Carré and Schultz¹² for peeling, and Michalske and Frechette¹³ for rupture of glasses in water.

When weak binding (*e.g.* Van der Waals) occurs between a solid and a polymer, the threshold value G_0 for vanishing crack speed is the thermodynamic work of adhesion w . However, for strong interfacial bonds, values up to 100 J/m^2 for G_0 are easily reached, which are of the same order of magnitude as the value G_0^* obtained for bulk polymers (*e.g.*, by tearing). In this case, it is probable that molecular chains strongly held at the interface are drawn from the polymer as in crazing, and one can tentatively add to $w\varphi(a_T v)$ a friction term $\nu f L$ where ν is the density of strong chemical bonds at the interface, L the length of polymer chains and f their friction coefficient, as proposed by de Gennes¹⁴ for refracture of polymers after healing. Such an equation could account for the results of Ahagon and Gent¹⁵ and Chang and Gent¹⁶ on the proportionality of G_0 to the concentration of interfacial bonds and on the influence of crosslinking. The maximum value of ν is of the same order of magnitude as the number of chains broken by a crack in a bulk polymer and varies as $M^{-1/2}$. As L varies with the molecular weight M , the maximum value of G_0 is the G_0^* of the bulk polymer and varies as $M^{1/2}$ as observed by Gent and Tobias.¹⁷ The problem of adherence in the presence of strong bonds is thus quite similar to that of fracture of bulk polymers where chains or fibrils are extracted and broken if too long. In the latter case G becomes independent of the molecular weight as discussed recently by

Prentice.¹⁸ As the stress in the craze zone is nearly constant, this zone is a perfect example of a Dugdale zone at a crack tip¹⁹.

References

1. K. L. Johnson, K. Kendall and A. D. Roberts, *Proc. Roy. Soc.* **A324**, 301–313 (1971).
2. G. I. Barenblatt, *Adv. Appl. Mech.* **7**, 55–129 (1962).
3. B. V. Derjaguin, V. M. Muller and Yu. Toporov, *J. Colloid Interface Sci.* **53**, 314–326 (1975).
4. D. Maugis, *J. Adhesion Sci. Technol.* (in Press).
5. E. H. Andrews and A. J. Kinloch, *Proc. Roy. Soc.* **A332**, 385–399 (1973).
6. D. Maugis and M. Barquins, *J. Phys. D: Appl. Phys.* **11**, 1989–2023 (1978).
7. A. N. Gent and J. Schultz, *J. Adhesion* **3**, 281–294 (1972).
8. D. Maugis and M. Barquins, in *Adhesion and Adsorption of Polymers*, part A, H. L. Lee, Ed. (Plenum Press, New York, 1980), pp. 203–277.
9. D. Maugis, *J. Mater. Sci.* **20**, 3041–3073 (1985).
10. M. Barquins, B. Khandani and D. Maugis, *C.R. Acad. Sci. Paris, série II*, **303**, 1517–1519 (1986).
11. D. Maugis, *C.R. Acad. Sci. Paris* (in press).
12. A. Carre and J. Schultz, *J. Adhesion* **18**, 207 (1985).
13. T. A. Michalske and V. D. Frechette, *J. Amer. Ceram. Soc.* **63**, 603–609 (1980).
14. P. G. de Gennes, *C.R. Acad. Sci. Paris*, **B291**, 219–221 (1980).
15. A. Ahagon and A. N. Gent, *J. Polymer. Sci. Polym. Phys. Ed.* **13**, 1285–1300 (1975).
16. R. J. Chang and A. N. Gent, *ibid.* **19**, 1619–1633 (1981).
17. A. N. Gent and R. H. Tobias, *J. Polym. Sci. Polym. Phys. Ed.* **20**, 2051–2058 (1982).
18. P. Prentice, *J. Mater. Sci.* **20**, 1445–1454 (1985).
19. H. R. Brown and I. M. Ward, *Polymer* **14** 469–475 (1973).

SESSION OF THE
UNITED STATES. I

Synthesis and Characteristics of Novel Poly(Imide Siloxane) Segmented Copolymers†

R. H. BOTT, J. D. SUMMERS, C. A. ARNOLD, L. T. TAYLOR, T. C. WARD and J. E. McGRATH‡

Department of Chemistry, Polymer Materials and Interfaces Laboratory and Center for Adhesion Science, Virginia Polytechnic Institute and State University, Blacksburg, VA 24061, U.S.A.

(Received January 31, 1987)

New poly(imide siloxane) copolymers for possible use as tough environmentally stable structural matrix resins and structure adhesives have been prepared. Thus, 3,3'-4,4'-benzophenone tetracarboxylic dianhydride was reacted with various Mn aminopropyl-terminated polydimethylsiloxane oligomers and a meta-substituted diamine "chain-extender" such as 3,3'-diaminodiphenyl sulfone or 3,3'-diaminobenzophenone to produce the siloxane-modified poly(amic acid). Thin films were cast from the reaction mixtures and subsequent thermal dehydration produced the poly(imide siloxane) block or segmented copolymers. Upper "cure" temperatures of 300°C were used to insure complete imidization. By varying the amount and molecular weight of the siloxane oligomer, a variety of novel copolymers of controlled composition have been synthesized. Tough, transparent, flexible soluble films were produced by this method. The thermal and bulk properties of films having low to moderate siloxane content closely resemble those of the unmodified polyimide controls. However, toughness and surface behavior can be enhanced.

KEY WORDS Segmented Copolymers; Poly(imide siloxanes); Moisture Durability; Atomic Oxygen Resistance; Surface Segregation; Synthesis.

INTRODUCTION

Polyimides synthesized from aromatic monomers are of great interest for high performance applications due to their excellent

† Presented at the Tenth Annual Meeting of The Adhesion Society, Inc., Williamsburg, Virginia, U.S.A., February 22-27, 1987.

‡ To whom correspondence regarding this paper should be addressed.

thermal and mechanical properties. However, these polymers are often insoluble in their fully imidized form unless carefully designed. Many approaches to enhancing the solubility and processability of polyimide systems have been investigated which also attempt to maintain their high performance properties. Successful attempts to accomplish this goal have involved the incorporation of flexible bridging units into either the diamine or dianhydride monomers, which imparts mobility to the otherwise rigid polyimide backbone.¹⁻³ Incorporation of bulky side groups⁴ and utilization of diamines containing meta linkages^{5,6} also enhance processability.

Incorporation of flexible siloxane segments into the polyimide backbone can yield soluble, processable copolyimides while still maintaining fairly good thermal-mechanical properties.⁷ In addition to enhanced solubility, incorporation of polysiloxane blocks imparts a number of other desirable characteristics, such as improved weatherability to aggressive environments, improved impact resistance, decreased sensitivity to water absorption and surface modification.^{7,8}

This improved processability and environmental resistance to moisture and atomic oxygen suggests these materials as candidates for specialized adhesive applications. Although the low surface energy of poly(dimethyl siloxane) suggests that it should behave as a release agent, preliminary results in our laboratories suggest that the decrease in bond strength due to incorporation of low levels of siloxane (<20% w/w) is small. Thus, these materials may find utility in applications where environmental resistance is paramount. It is also expected that the hydrophobic nature of the polysiloxane segments should add an improved degree of resistance to moisture over the unmodified polyimides. This paper will describe the synthesis, characterization and initial adhesive properties of several novel poly(imide-siloxane) copolymers having the representative structure shown in Figure 1.

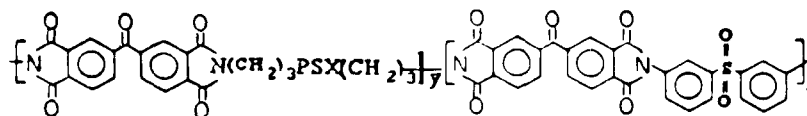


FIGURE 1 Representative structure for poly(imide siloxane) segmented copolymers.

EXPERIMENTAL

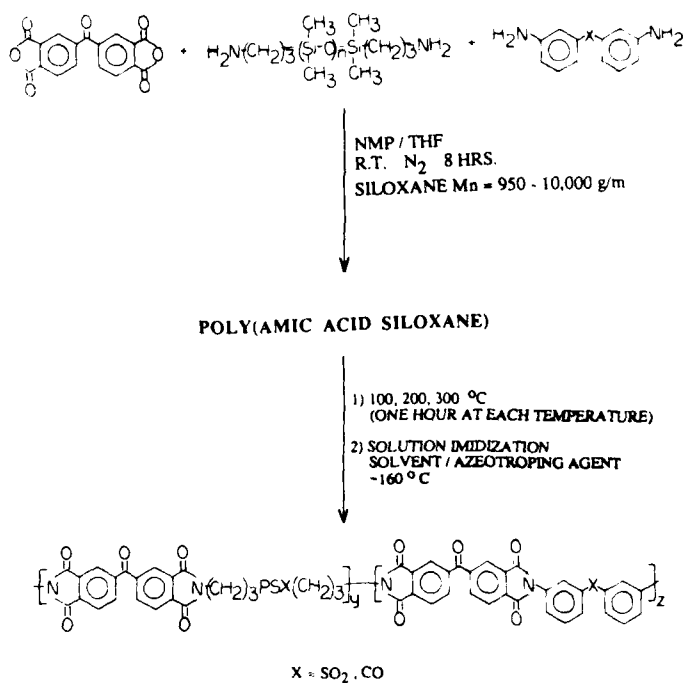
Synthesis of Poly(imide-siloxane) Copolymers of Controlled Composition

The 3,3'-4,4'-benzophenone tetracarboxylic dianhydride (BTDA) was obtained in high purity from the Chriskev Company and subjected to a thermal treatment prior to use. 3,3'-diaminodiphenylsulfone (DDS) was obtained from FIC Corporation and recrystallized from a deoxygenated methanol/water solution (90% yield, m.p. 172–173°C). The α , ω -aminopropyl polydimethylsiloxane oligomers were synthesized by methods previously disclosed⁹ and their corresponding molecular weights were determined by potentiometric titration of the amine end groups. N-methylpyrrolidinone (NMP, Fisher), tetrahydrofuran (THF, Fisher), and N-cyclohexylpyrrolidinone (CHP, GAF) were distilled from calcium hydride under reduced pressure and stored in round bottom flasks sealed with rubber septa.

Synthesis of the poly(amic acid siloxane) intermediates was conducted in a 3-neck, 250 mL round bottom flask fitted with a mechanical stirrer, nitrogen inlet, drying tube, and addition funnel. The actual cosolvent ratio used to synthesize the amic acids varied with the amount of siloxane oligomer to be incorporated. A representative synthetic procedure will be outlined to synthesize a copolymer containing 10 weight percent of a siloxane oligomer whose molecular weight is 950 g/m.

The entire apparatus was assembled and flamed to remove residual moisture from the system. BTDA (11.3546 g, 0.0352 moles) was added to the flask and rinsed in with 40 mL of NMP and 30 mL of THF. Next, 2.0000 g of the siloxane oligomer (0.0009 moles) and 20 mL of THF were placed in the addition funnel and added dropwise to the stirring dianhydride solution. After stirring for an additional 15 min, 6.7016 g (0.0334 moles) of 3,3'-DDS was added as a chain extender along with 20 mL of NMP and 10 mL of THF. The reaction was allowed to proceed for 8 hours. The resulting clear viscous solution was stored at $\sim 10^{\circ}\text{C}$ until needed.

"Curing" of the poly(amic acid siloxane) intermediate to the imide form was accomplished by casting the amid acid solution onto glass plates at thicknesses ranging from 5 to 50 mils. The plates were



ALL FILMS ARE TRANSPARENT AND CREASABLE

FIGURE 2 Synthetic scheme for poly(imide siloxane) segmented copolymers.

then placed in a vacuum oven to remove the reaction solvents. After this treatment, the films on the plates were imidized in a forced air convection oven at temperatures of 100°C, 200°C and 300°C, each for one hour. The synthetic scheme is summarized in Figure 2.

Characterization of poly(imide-siloxane) copolymers

Viscosity measurements Intrinsic viscosity measurements yielded relative molecular weights and were performed in NMP at 25°C using a Cannon-Ubbelohde viscometer.

Thermal analysis Differential scanning calorimetry (DSC) was used to determine the glass transition temperatures (*T_g*) of the

copolymers with a Perkin-Elmer Model DSC-4. Scans were run at 10°C/min with a sensitivity of 10 mcal/sec in a nitrogen atmosphere. Reported values were obtained from a second scan after heating and rapid cooling. Some copolymer transitions were obtained by dynamic mechanical thermal analysis (DMTA) at a frequency of 1 Hz using a Polymer Laboratories instrument.

Thermal gravimetric analysis and thermal mechanical analysis TGA was performed on a Perkin-Elmer TGS-2 instrument on samples in film form. Scans were run at 10°C/min in an air atmosphere. TMA was performed on a Perkin-Elmer TMS-2 with a 10°C per minute heating rate with a 50 gram quartz penetration probe.

Stress strain analysis An Instron Model 1122 was used to determine the mechanical behavior of dogbone-shaped specimens of the copolymers. Specimen gauge lengths were 10 mm. Specimen widths were 2.76 mm. The extension rate was 5 mm per minute.

Contact angle measurements Water contact angles were measured on samples prepared by spin-coating the amic acid intermediate in its reaction solution onto a ferrotype plate and then imidizing by thermal treatment. In some cases, recast fully imidized films were also examined.

X-ray photoelectron spectroscopy Samples for XPS were prepared by spin-coating the amic acid intermediate in its reaction solution onto ferrotype plates which had been washed in hexane three times prior to coating. The samples were covered with a watchglass to prevent contamination during thermal imidization by the standard method in a forced air convection oven. After imidization, the samples were thrice washed in hexane and placed in clean glass containers with lids. Analysis was performed on a Kratos instrument at exit angles of 15° and 90°.

Oxygen plasma stability Samples of the siloxane-polyimide copolymers were analyzed in an oxygen plasma environment to determine qualitative physical degradation and weight loss. A Plasmod unit from the Tegal Corporation of Richmond, CA, was used. Film samples were maintained in an oxygen-charged environment for

45 minutes, under a vacuum of 1.5 torr. The applied radio frequency was 50 KHz. Oxygen flow rate to the analysis chamber was approximately 30 cc per minute.

Initial adhesion results Single lap shear specimens were prepared by sandwiching a scrim cloth (112 E glass) coated with the poly(imide siloxane) resin between two primed titanium adherends. The poly(amic acid siloxane) solution in NMP/THF, which was molecular weight controlled by the addition of phthalic anhydride, was coated onto the scrim cloth and cured in a forced air convection oven using the following schedule:

60° - $\frac{1}{2}$ hr
100° - $\frac{1}{2}$ hr
160° - $\frac{1}{2}$ hr
160 in vac - $\frac{1}{2}$ hr.

This procedure was repeated until an overall thickness for the cloth and resin of 9-13 mils was achieved.

The titanium adherends were sandblasted, treated with Pasa Jell 107, ultrasonically cleaned, and immediately primed with a coating of amic acid solution to preserve the surface treatment. This primer coat was imidized using the same thermal schedule as the scrim cloth.

Single lap shear specimens ($\frac{1}{2}$ -inch overlap) were prepared by pressing the coated scrim cloth between two primed adherends using the following bonding cycle:

R.T. to 325°C, apply 200 PSI at 280°C
Hold for 15-60 min, @ 325°C
Cool under pressure.

RESULTS AND DISCUSSION

Thermal analysis and thermal stability

Values of the upper glass transition temperatures of the siloxane modified polyimides were found to be a function of both the level of incorporated siloxane as well as the siloxane molecular weight (Table I). Generally, the upper transition temperature will increase

TABLE I
Upper glass transition temperatures of poly(imide siloxane) copolymers

PSX wt%	PSX Mn	DSC	Tg(°C) DMTA
Control	—	272	—
10	950	256	260
10	2100	267	267
10	5000	264	—
10	10,000	264	266
20	950	246	248
20	2100	259	—
20	5000	262	—
40	950	†	225

† No transition detected in DSC scan.

with greater siloxane oligomer molecular weight and with decreasing siloxane incorporation. In many cases, the copolymers' upper transition temperature is depressed only slightly relative to that of the control, indirectly indicating that good microphase separation was achieved. The lower temperature siloxane transition is difficult to detect by DSC for low levels of siloxane incorporation, <20 weight percent. At greater levels of incorporation, however, the transition is detected by both DSC and DMTA within the range -117 to -123°C, representing 20 to 50 weight percent siloxane, respectively.

Copolymer thermal stability also varied with both siloxane oligomer molecular weight (Figure 3) and level of siloxane incorporation (Figure 4), increasing with the former variable and decreasing with the latter. From this observation, one may conclude that thermal degradation begins at the aliphatic *n*-propyl segments linking the siloxane oligomers to the polyimide matrix. As the siloxane oligomer molecular weight is increased, the concentration of *n*-propyl linkages in the copolymer backbone decreases, thus increasing the overall thermal stability. Copolymers containing higher amounts of siloxane show decreased resistance to probe penetration by TMA (Figure 5). The TGA traces indicate, however, that the copolymers possess fairly high stability values at elevated temperatures. Even at high siloxane levels of 60 weight

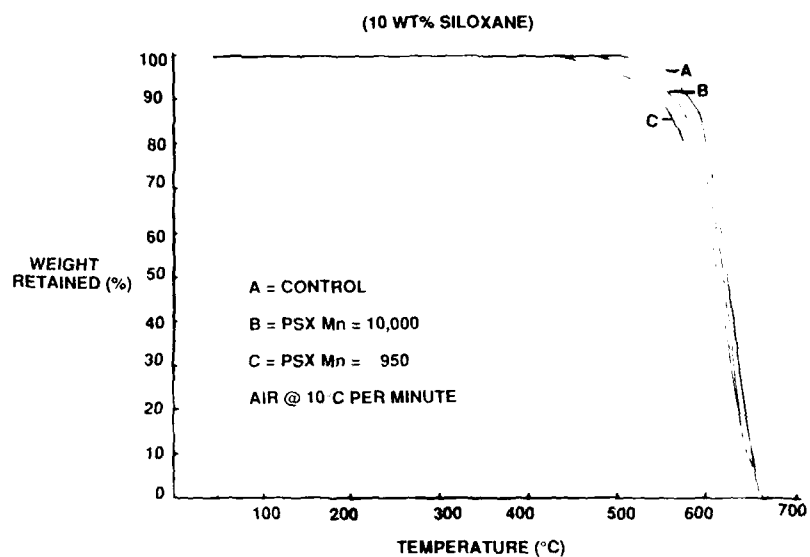


FIGURE 3 Thermogravimetric analysis of poly(imide siloxane) copolymers (10 weight % siloxane).

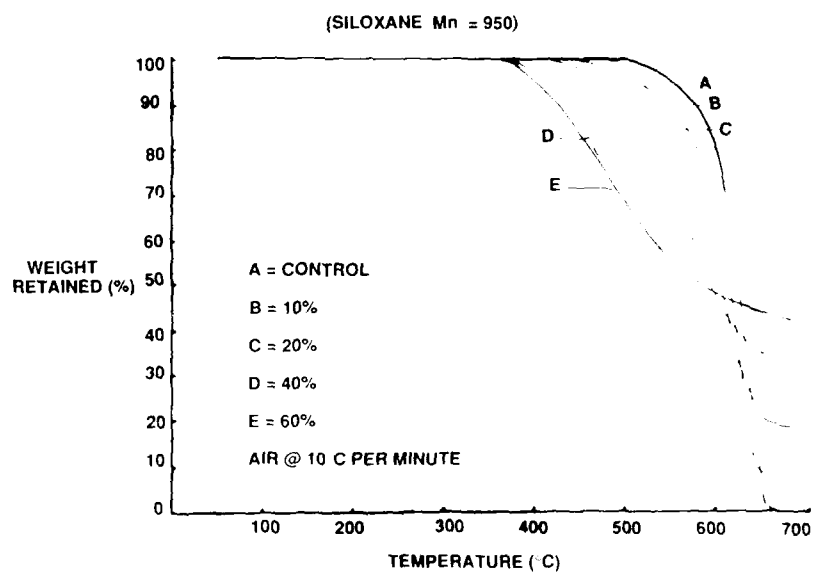


FIGURE 4 Thermogravimetric analysis poly(imide siloxane) copolymers (siloxane Mn = 950).

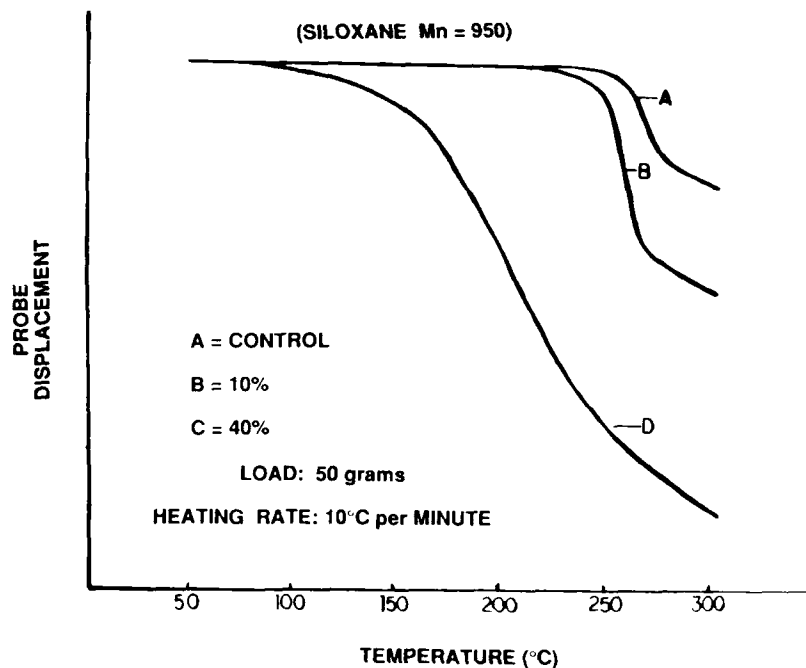


FIGURE 5 TMA penetration curves for poly(imide siloxane) copolymers.

percent, the copolymers maintained good thermal stability, although as the siloxane content is increased, degradation occurs at lower temperatures. The char yield at high temperatures, proportional to the siloxane content, suggests that a silicate-type structure is the principal degradation product in an air atmosphere.

Mechanical property analysis

An initial investigation of the mechanical behavior of these copolymers indicated that this property is highly dependent upon the level of siloxane incorporation (Figure 6). While copolymers containing low to moderate amounts of siloxane maintained good rigidity and ductile mechanical properties, a significant decrease in modulus and an increase in elongation occurred for high amounts of siloxane, no doubt due to inversion of the imide matrix to a continuous siloxane phase in the latter case.

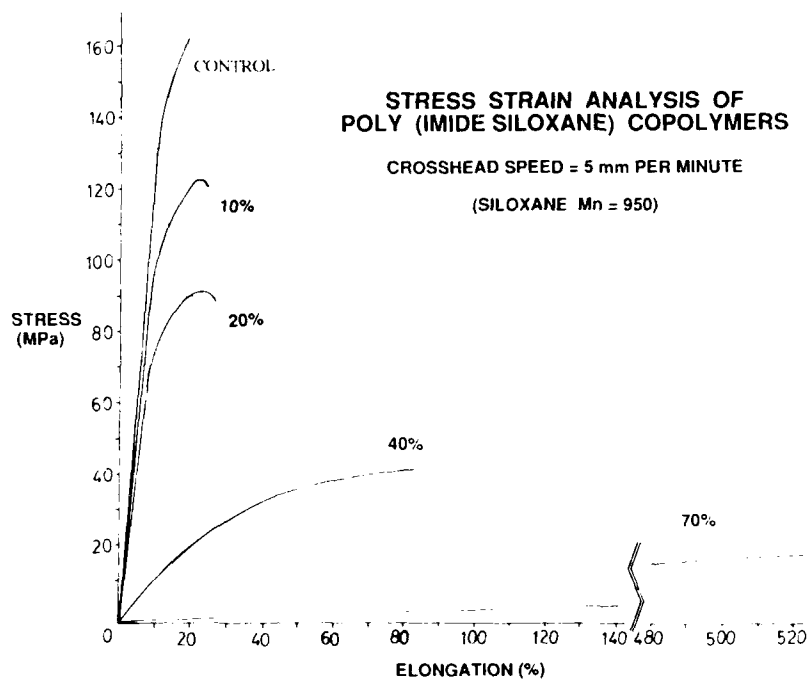


FIGURE 6 Stress strain analysis of poly(imide siloxane) copolymers.

Surface properties

Since the surface composition of these macromolecular materials is directly related to such properties as coefficient of friction and atomic oxygen stability, X-ray photoelectron spectroscopy (XPS or ESCA) was employed in order to characterize the surface composition of the siloxane-modified polyimide copolymers. By varying the angle of the sample relative to the analyzer, different depths of the polymer were sampled, such that a 15° grazing take-off angle characterizes molecules from the uppermost surface (~ 10 to 20 \AA) more so than molecules from the bulk. The 90° take-off angle, on the other hand, yields compositional information more characteristic of the subsurface regions (~ 50 to 70 \AA).

The results of the XPS experiments are listed in Table II. The results conclusively demonstrate that the siloxane component dominates the surface of the copolymer. Furthermore, the extent of

TABLE II
XPS analysis of poly(imide siloxane) copolymers

PSX wt%	PSX Mn	Take-off angle	wt% PSX at surface
5	950	15°	85
5	950	90°	34
10	950	15°	77
10	950	90°	35
10	10,000	15°	87
10	10,000	90°	39
20	950	15°	87
20	950	90°	53
40	950	15°	86
40	950	90°	63

Grazing angles (15°) sample depths of ~10–20 Å; normal angles sample depths of ~50–70 Å.

TABLE III
Water contact angle measurements of poly(imide siloxane) copolymers

PSX wt%	PSX Mn	Water contact Angle (degrees)
Control	----	68
5	950	92
10	950	98
10	2100	100
10	5000	98
10	10,000	100
20	950	101
20	2100	102
20	5000	102
40	950	106
40 (recast)	950	105
60	2100	106

domination is independent of the weight percent of the siloxane incorporated into the copolymer. Thus, one is able to achieve a surface characteristic of the siloxane component while tailoring the physical properties which are characteristic of the bulk.

These results are supported by the data obtained by contact angle measurements. Unlike XPS, however, contact angle measurements provide no direct quantitative information.

Water contact angle measurements are listed in Table III. A significant increase in contact angle is observed between the unmodified control and copolymer samples containing only 5 to 10 weight percent siloxane. In fact, the copolymer contact angles approach those of pure polydimethylsiloxane. The water absorption is also significantly reduced upon siloxane incorporation. Both of these properties are attributed to the hydrophobicity of siloxanes.

Oxygen plasma stability

The copolymers examined were based upon BTDA-PSX-DDS as well as their oxydianiline (ODA) analogue, and had siloxane

TABLE IV
Oxygen plasma stability of poly(imide siloxane) copolymers (PSX Mn of 1000; based upon either 3,3'-DDS or 3,3' ODA; averages of multiple runs)

Sample	Weight loss (Mg per cm ²)
Kapton	0.86
DDS-Control	0.86
DDS-10% PSX	0.75
DDS-20% PSX	0.67
DDS-30% PSX	0.24
DDS-50% PSX	0
ODA-Control	1.13
ODA-30% PSX	0.30
ODA-50% PSX	0.14
DDS-30% PSX on kapton†	0.35
DDS-50% PSX on kapton†	0.10

† Spray-coating of poly(imide siloxane) copolymer ~0.03 mm thickness on kapton.

contents of 30 and 50 weight percent and siloxane segment molecular weights of 1000. Results obtained thus far are listed in Table IV. In every run, the DDS-based 50 weight percent siloxane samples lost no weight after exposure to the oxygen environment and their ODA analogues performed similarly well. Interestingly, the ODA-based systems seemed to perform somewhat less successfully than the DDS-based copolymers. Additionally, the 30 weight percent siloxane copolymers lost more weight during exposure than the 50 weight percent siloxane analogues, in both the DDS and ODA systems. Consistently, Kapton[®] lost more weight than either the DDS- or ODA-based siloxane-modified polyimides, and coating Kapton with the DDS-based copolymers enhanced the stability of the Kapton film under the aggressive environment for both the 30 and 50 weight percent siloxane levels. Under these latter conditions, the performance of the Kapton-coated film resembled the performance of the siloxane-modified polyimides which constituted the coated layer.

Initial adhesion results

Preliminary adhesive data on controlled molecular weight copolymers are shown as lap shear strengths in Table V. The incorporation of low to moderate amounts of siloxane ($M_n = 950$ g/m) does not significantly alter the adhesive characteristics of these materials. Only at high levels of siloxane do the lap shear strengths fall below 2000 psi, indicating the potential utility of these materials as atomic oxygen resistant structural adhesives.

The data presented in this table represent tests on a comparable series of polymers synthesized using the same techniques and

TABLE V
Compositions, molecular weight considerations and preliminary adhesive results

PSX wt%	PSX Mn	$[\eta]$ 25°C, NMP	Lap shear strength (psi)
Control	—	—	2500
5	950	—	2400
10	950	0.40	2300
20	950	0.36	2100
40	950	0.34	1800

bonded using the same cure schedules. This is significant since these materials are only produced in 1–10 gram quantities at present, and there has been continuing improvement in both synthesis and bonding techniques. The goal of this adhesion research is to evaluate the potential utility of this class of new materials for specialized applications without becoming overwhelmed with optimization of processing variables. The cure and bonding cycles chosen have been used in similar systems and were therefore thought to be appropriate for this initial evaluation.⁶ The failures of these bonds were cohesive in the polymer/scrim cloth layer.

More recently, attention has been focused on the measurement and comparison of bond durability in a hot/wet environment for these poly(imide-siloxane) copolymers. This testing involves the use of lap shear specimens which are placed under load (some percentage of the ultimate strength measured at R.T.) then placed into an 80°C, 100% R.H. environment. The time to failure is then measured. Initial results in this area have been promising although only a limited number of samples have been tested to date. In this study a comparison was made between the polyimide sulfone control and a poly(imide-siloxane) containing 10% by weight of a ~900 (g/m) poly(dimethyl siloxane) segment. The control polymer (no siloxane) had a room temperature lap shear strength of 2500 psi, and the polymer containing 10% siloxane was approximately equal at 2560 psi. This difference does not appear significant in light of the data scatter evident in this test. However, in terms of durability a significant difference is apparent. When these specimens were tested in a hot/wet environment, the control polymer was loaded to 1100 psi for a 0.5 in.² overlap sample corresponding to ~40% of the ultimate load at room temperature. The 10% siloxane containing sample was loaded to 1700 psi or 66.7% of the ultimate R.T. strength. Interestingly, both samples failed after the same amount of time in the 80°C/100% R.H. environment: 60 hrs. This result, although not conclusive due to the limited number of samples tested, does suggest an enhancement of durability with respect to moisture in the case of the siloxane containing material. Also of interest is that again in this durability test, both samples failed cohesively so that material rather than interfacial properties appears to control the ultimate bond strength. Currently, new synthetic methods which involve the imidization of the copolymer

prior to bonding are being explored in order to evaluate the role of the amic acid in bonding as well as the effect of volatiles. In the present cases, thermogravimetric analysis suggests that up to 5% (w/w) volatiles due to water of imidization and residual solvent may be lost during the bonding cycle. This relatively high percent volatiles is expected to be reduced significantly due to prior imidization of the copolymer and solubility in more volatile solvents which could be more thoroughly removed prior to bonding. More extensive durability testing on a series of siloxane containing copolymers is also underway.

CONCLUSIONS

High molecular weight, randomly coupled, segmented siloxane modified polyimides were synthesized. These materials show good mechanical and thermal properties. Preliminary adhesive results suggest that incorporation of low levels of siloxane does not detract significantly from the room temperature lap shear strength compared to the unmodified controls. Also, preliminary durability studies at 80°C in a 100% relative humidity environment suggest that the incorporation of hydrophobic siloxane segments may significantly enhance the durability of those materials under these conditions.

Acknowledgements

The authors would like to acknowledge the Environmental Effects Research Branch of NASA Langley Research Center for funding of this project. We are also indebted to the late Mr. George Sykes for his enthusiasm and continued support throughout the course of this work.

References

1. H. D. Burks and T. L. St. Clair, *Polyimides: Synthesis, Characterization, and Applications*, 1, K. L. Mittal, Ed. (Plenum, NY, 1984), pp. 117-135.
2. P. R. Young and N. T. Wakelyn, *Proceedings from the 2nd International Conference on Polyimides* (Ellenville NY, 1985), pp. 414-425.
3. J. P. Critchley and M. A. White, *J. Polym. Sci., Polym. Chem. Ed.* **10**, 1809 (1972).

4. F. W. Harris, *et al.*, *Polymides: Synthesis, Characterization, and Applications*, **1**, K. L. Mittal, Ed. (Plenum, NY, 1984), pp. 3-14.
5. A. K. St. Clair, T. L. St. Clair and E. N. Smith, *Polymer Preprints* **17**, 359 (1976).
6. T. L. St. Clair and D. A. Yamaki, *Polymides: Synthesis, Characterization, and Applications*, **1**, K. L. Mittal, Ed. (Plenum, NY, 1984), pp. 99-116.
7. B. C. Johnson, I. Yilgor and J. E. McGrath, *Polymer Preprints* **25**(2), 54 (1984); B. C. Johnson, Ph.D. Thesis, VPI and SU, 1984; B. C. Johnson, J. D. Summers, J. E. McGrath, *J. Poly. Sci.* (in press, 1987); J. E. McGrath, P. M. Sormani, C. S. Elsbernd, S. Kilic, *Makromol. Chemie* (accepted, 1986); P. M. Sormani, R. J. Minton, J. E. McGrath, *Ring Opening Polymerization: Kinetics, Mechanisms and Synthesis*, J. E. McGrath, Ed., ACS Symposium Series, No. 286 (1985), Chapter 11, pp. 147-161.
8. J. E. McGrath, *et al.*, *Final Report for NASA Langley Research Center Grant No. NAG-1-343*, Suppl. 10 (October 1986).
9. P. M. Sormani, R. J. Minton and J. E. McGrath, *Ring Opening Polymerization: Kinetics, Mechanisms, and Synthesis*, J. E. McGrath, Ed., ACS Symposium Series, No. 286 (1985), Chapter 11, pp. 147-161.

Adhesion Tensile Testing of Environmentally Exposed Ti-6Al-4V Adherends†

H. M. CLEARFIELD, D. K. SHAFFER, J. S. AHEARN, and
J. D. VENABLES

*Martin Marietta Laboratories, 1450 S. Rolling Road, Baltimore, MD 21227,
U.S.A.*

(Received September 4, 1986)

The structural and bonding properties of Ti-6Al-4V adherends, prepared by chromic acid anodization (CAA), were studied as a function of exposure in high-temperature environments such as vacuum, air, boiling and pressurized water, and steam. Subsequent to the environmental exposure, bonds were produced and the adhesive tensile strengths measured. Long-term exposure to high temperature, dry environments did not cause structural changes to the adherend oxide but did result in poor bond strength. The failure mode in these cases was within the oxide, which was apparently weakened by the exposure. The water- and steam-exposed oxides underwent a transition from amorphous to crystalline TiO_2 (with an accompanying change in oxide morphology); however, bond strength was maintained for moderate exposures at $T \leq 250^\circ\text{C}$. For exposure at $T = 300^\circ\text{C}$, the bond strength was degraded severely. The latter result can be explained by a lack of porosity in the transformed oxide. SEM and XPS measurements were made on debonded surfaces to determine the loci of failure.

KEY WORDS Titanium adhesive bonding; oxide morphology; environmental exposures; adherend surface analysis; Ti-6Al-4V; oxide stability.

I INTRODUCTION

Adhesively bonded materials that are stable at high temperatures are becoming increasingly important for the performance of

† Presented at the Tenth Annual Meeting of The Adhesion Society, Inc., Williamsburg, Virginia, U.S.A., February 22–27, 1987.

advanced military and aerospace systems. The proposed operating temperature range, from 100–400°C, presents special problems for all components of the bonded system, *i.e.*, adherend, primer and adhesive must all be stable in severe environments. Several classes of metal adherends are used (or have been proposed) for such systems, including titanium alloys, nickel-based superalloys, and high-temperature steels. One, Ti-6Al-4V, is a particularly good baseline material for the adherend because its mechanical properties are retained at high temperatures.

In previous studies of both Ti¹ and Al^{2,3} adhesive bonding systems, it was shown that initial bond strength was enhanced by physical interlocking between the adherend oxide and the adhesive; porous oxides maximized this interlocking and hence provided the best overall bond strength. Additionally, in Al adherends, humidity-induced changes in the oxide led to bond degradation. The primary cause of failure in that case was the transformation of the original oxide to a hydroxide that is loosely bound to the Al substrate.³ Certain organic inhibitors were later used to slow down such a transformation, thereby increasing bond durability.⁴

The oxide of Ti, typically formed by anodization in a chromic acid solution (CAA), is much more stable than that of Al and hence the bonds exhibit markedly better durability. However, the unbonded Ti oxide was found to undergo a transition from amorphous TiO₂ to crystalline TiO₂ (anatase) when immersed in water at 85°C for as little as 20 hours.⁵ The transformation was accompanied by a change in morphology—from a porous, honeycomb structure to a more needle-like structure. Although some porosity was retained after this transformation, it was later shown that exposure to humid environments for longer times or at higher temperatures results eventually in a rather smooth, nodular-like oxide that lacks porosity.⁶

The observation that a CAA oxide that was transformed at lower temperatures retained porosity suggests that such an oxide might couple mechanically to an adhesive. It would be desirable to use such a transformed oxide in a bondline, if the oxide-base metal interfacial strength were maintained, because the crystalline Ti oxide phases are more stable thermodynamically than the amorphous phase.⁷ Although anatase is not the most stable form of TiO₂,⁷ none of the other crystalline TiO₂ phases has been observed

in earlier Ti adherend studies (the anatase to rutile transformation occurs at $\sim 650^\circ\text{C}$ at atmospheric pressure—the earlier studies were conducted at lower temperatures).^{5,6} Thus, by bonding to a crystalline adherend oxide, *i.e.*, anatase, large-scale morphology changes that normally occur during accelerated testing could presumably be avoided, thereby increasing bond durability.

In this study, we have investigated the strength of bonds formed on Ti-6Al-4V adherends after they were subjected to high-temperature environments such as vacuum, air, boiling water, pressurized water and steam. The CAA oxide was chosen as the baseline adherend because it provides excellent bond durability for Ti adhesive bonds.¹ Coupons were anodized, exposed, bonded to an Al stud (see below), and tested with an instrument that applies a tensile force normal to the adherend surface. The test was designed to determine the adhesion of the (transformed) oxide to the underlying substrate. Adherends were characterized before and after tensile testing by high-resolution scanning electron microscopy (SEM) and X-ray photoelectron spectroscopy (XPS). These measurements allowed the identification of the loci of failure in the adhesion tensile tests. The failure mechanisms were then correlated with the respective oxide morphologies.

II EXPERIMENTAL

A Sample preparation

Coupons of Ti-6Al-4V were anodized in a solution containing 5% chromic acid (CAA). Details of the procedure are given elsewhere.^{6,8} Transmission electron micrographs show that the resultant oxide is ~ 120 nm thick and amorphous.⁶

Coupons subjected to heat alone were placed in a vacuum furnace for periods of 72 and 160 hr at 400°C , and at a pressure of 3×10^{-4} Pa. Although there was no residual gas analyzer on the furnace, we estimate the partial pressure of oxygen to be less than 5×10^{-5} Pa.⁹ Any residual water vapor was pumped away during warmup. Additionally, some coupons were exposed to air in an ordinary laboratory furnace at 330°C . Exposure times varied from 160–1200 hr. The relative humidity in the furnace was not determined.

The boiling water exposures were conducted by immersion of the coupons in water maintained at 95–100°C. For higher temperature water exposures, a high-pressure autoclave was used. In this case, a sufficient volume of water was used at each temperature to maintain an equilibrium between liquid and vapor at the saturation vapor pressure. Some coupons were immersed in the liquid; others were exposed only to the vapor. Exposures ranged from 3–120 hr at temperatures of 150, 200, 250 and 300°C.

B Adhesion testing

A pneumatic adhesion tensile testing instrument (SEMicro, Rockville, MD) was used for the adhesion tests. A schematic drawing of the testing geometry is shown in Figure 1. A 1.25-cm-diameter Al stud (that had been etched previously in FPL solution) was bonded to the pre-exposed adherend with an epoxy resin (3M 1838). The bonding area was defined with a Teflon ring. The adhesive was cured under a pressure of 0.4 MPa for 72 hr at room temperature; the thickness of the bondline was not determined. Prior to testing, the Teflon ring was replaced by a stainless steel ring and the bonded system was mounted in a jig that prevents the adherend from flexing. The stud was screwed into a pneumatic piston which applies the tensile force (increasing at ~4 MPa/min) normal to the adherend surface. The force required to remove the stud thus provides a relative indication of the bond strength of the oxide.

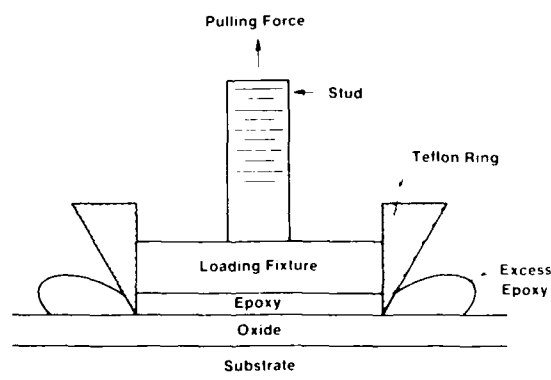


FIGURE 1 Schematic diagram of adhesion tensile testing geometry.

C Analysis

A JEOL JEM 100-CX STEM, used in the SEM mode, provided the resolution needed to examine the morphology of the CAA oxide and the bond-failure surfaces. Samples were cut to 1 cm \times 2 mm and coated with \sim 5 nm of Pt to eliminate charge buildup on the oxide. The stereo micrographs shown in this study were obtained at \pm 7 deg tilt.

XPS was used to determine the surface composition of the oxides and the debonded surfaces. The spectrometer, an SSL SSX-100, was equipped with a differentially-pumped ion sputter gun. For compositional analysis, the analyzed area was 600 μ m in diameter, which was large enough to represent the average over the entire coupon surface. For depth profiles, a 300- μ m-diameter area at the center of a 3 mm \times 3 mm crater was used.

III RESULTS AND DISCUSSION

A Morphology of exposed adherends

A stereo micrograph of a typical, as-anodized CAA oxide is shown in Figure 2. It is characterized by a multilevel, porous structure with cell dimensions on the order of 40 nm. At lower magnifications (Figure 2a), it is evident that the porous structure covers the entire surface. The multilevel morphology is due to differential etching of the two-phase alloy.

Samples that were exposed to vacuum at 400°C for as long as 160 hr showed no change in morphology when examined by SEM. *i.e.*, the porous, honeycomb morphology was retained. However, in a micrograph of a sample exposed to air at 330°C for 1200 hr, Figure 3, the honeycomb structure is still evident but the cell walls have thickened slightly. Additionally, some peeling of the oxide seems to have occurred at the grain boundaries.

CAA oxides immersed in boiling water developed crystallites, consistent with earlier results.^{1,5} After as little as 3 hr immersion, the honeycomb cell walls begin to thicken. By 24 hr, crystallites can be observed and the cells have nearly closed up. By 72 hr, the adherend surface is covered with crystallites and the honeycomb structure has disappeared, as seen in Figure 4. Some fusion of the

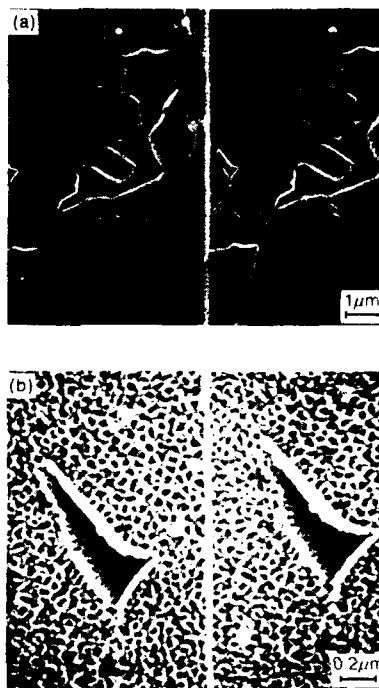


FIGURE 2 Scanning electron micrographs at a) low and b) high magnification, showing the oxide surface resulting from the anodization of Ti-6Al-4V adherends in a solution containing 5% chromic acid.



FIGURE 3 CAA oxide after heating in air at 330°C for 1200 hours. Some thickening of the cell walls has occurred.

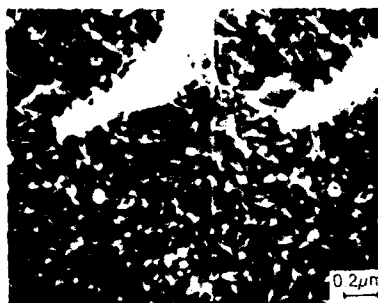


FIGURE 4 CAA oxide after immersion in water at 100°C for 72 hours.

crystallites has also occurred. A dissolution/precipitation mechanism for this change in morphology has been proposed in Reference 6.

As already mentioned, some CAA oxides exposed to water in the autoclave were immersed in the liquid, while others that hung above the liquid were exposed only to the vapor. The evolution of the oxide is different for the two exposures, as can be seen in the sequence of Figures 5a-c. Those immersed in the liquid at 300°C were completely covered by needle-like crystallites after as little as 3 hr (Figure 5a). By 24 hr (Figure 5b), the crystallites began to fuse and the surface appears somewhat flatter. Finally, at 120 hr (Figure 5c), the crystallites became nodular in shape, leaving an oxide that was relatively smooth (compared to the as-anodized oxide). For vapor-exposed oxides, no needle-like crystallites were observed. Rather, the honeycomb structure evolved into a more nodular-like oxide (Figure 5a). Selected area diffraction (SAD) patterns generated in the TEM show these nodules to be anatase TiO_2 . With continued exposure, the nodules began to fuse (Figure 5b) until, by 120 hr, the oxide surface was again relatively smooth, *i.e.*, lacking porosity (Figure 5c). The diameter of the vapor-exposed nodules was approximately one-half that of the corresponding liquid-exposed nodules.

B Adhesion tensile tests

1 *As-anodized adherends* The tensile test used in this study measured the relative adhesive strength of the oxide-base metal

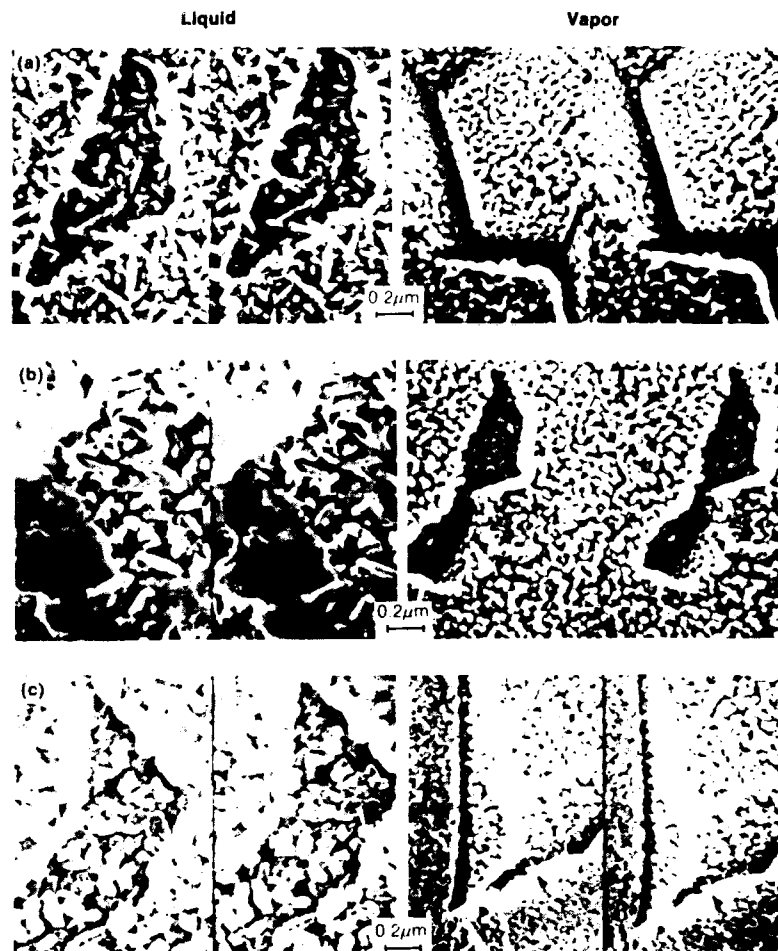


FIGURE 5 CAA oxide after exposure to water in liquid and vapor phases in an autoclave at 300°C: a) 3, b) 24 and c) 120 hours.

interface. The results are presented in Table I. The greatest bond strength was obtained with the as-anodized CAA oxide. Visual examination of the debonded surfaces showed both to have the same appearance—rough and of the same color as the adhesive—suggesting that the failure mode was cohesive. To confirm this, we examined the surfaces by SEM and XPS. Scanning electron

TABLE I
Adhesion tensile test results

Exposure	Ti-6Al-4V (CAA 5%) Pull strength (MPa)
As-anodized	9.2 ± 0.5(cohesive)*
Vacuum ($T = 400^{\circ}\text{C}$)	0-0.7(oxide)
Air 330°C, 160 hr	3.5(mixed)
Air 330°C, 1200 hr	0-0.7(oxide)
Boiling/pressurized water, steam ($T \leq 250^{\circ}\text{C}$)	6.2-8.3(mixed)
Pressurized water, steam ($T = 300^{\circ}\text{C}$)	0-0.7(adhesive)

* Failure mode is indicated in parentheses.

micrographs showed an adhesive-like morphology on both sides with large (20- μm -diameter; Figure 6) filler particles consisting primarily of Al and Si. The XPS spectra obtained from the metal and the adhesive sides of the failure are nearly identical to each other, as shown in Figure 7, and to spectra obtained from the cured adhesive alone. The C and O concentrations are indicative of the adhesive component, and the Al and Si from the filler particles are evident. We conclude that 9.2 MPa (Table I) represents the cohesive strength of the adhesive in this testing geometry. This value is significantly less than that quoted by the manufacturer, and can be attributed to some flexing of the adherend. Thicker adherends used in the same geometry yield cohesive strengths that approach the manufacturers' value.¹⁰

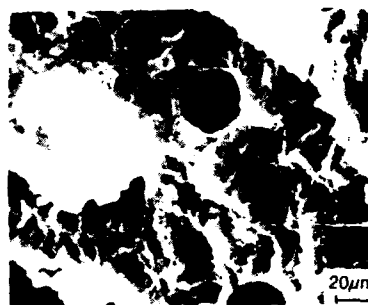


FIGURE 6 Typical scanning electron micrograph of both debonded surfaces of an as-anodized Ti-6Al-4V adherend. The morphology is indicative of adhesive on both sides of the failure.

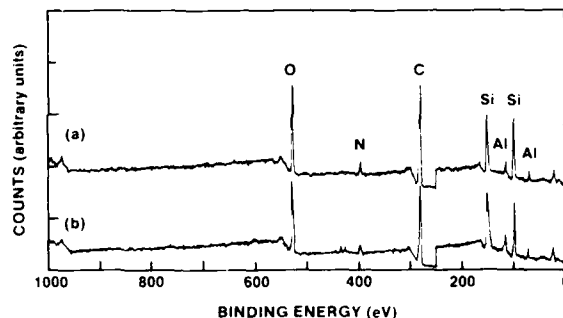


FIGURE 7 X-ray photoelectron spectra of a) metal and b) stud sides of an as-anodized Ti-6Al-4V adherend after tensile testing. The spectra are typical of adhesive.

2 Vacuum- and air-exposed adherends Most of the high-temperature vacuum- and air-exposed specimens failed prior to testing as the Teflon ring was being removed. Those that were tested failed at pressures less than 0.7 MPa. The debonded surfaces appeared metallic on both the stud and the metal sides, indicating failure entirely within the oxide layer or at the oxide-metal interface. The precise location was determined by SEM and XPS depth profiles. As seen in Figure 8 (the stud side), the original CAA oxide cell walls are evident and have lifted away from the base metal. The micrograph from the metal side shows a complementary



FIGURE 8 Debonded surface from the stud side of a Ti-6Al-4V adherend exposed to air for 1200 hr at 330°C, after tensile testing. A replica of a honeycomb structure is evident, indicating that the oxide has been lifted from the adherend.

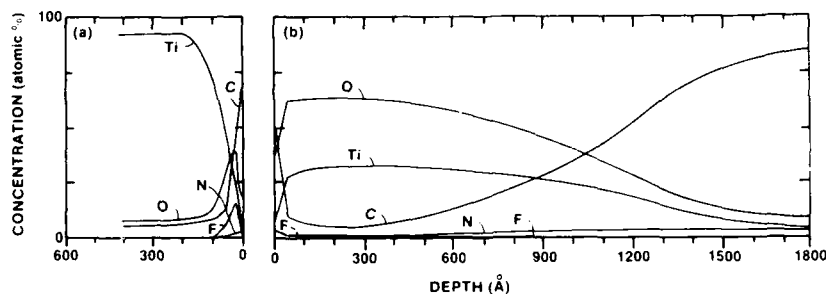


FIGURE 9 XPS depth profiles of the debonded surface from the a) metal and b) stud side of a Ti-6Al-4V adherend exposed to air for 1200 hr at 330°C, after tensile testing.

image. XPS survey spectra of both surfaces were identical; however, depth profiles show different oxide layer thicknesses. On the metal side, Figure 9a, the oxide-metal interface is abrupt and appears at a depth less than 10 nm as judged by the rapid increase in the Ti signal with depth (the greatest oxide layer thickness on the metal side of any of these samples was ~ 30 nm). In Figure 9b, the stud side, the oxide-adhesive interface is not well defined due to penetration of the adhesive into the honeycomb structure. One feature common to both depth profiles is the accumulation of F at both debonded surfaces. Previously, we found an accumulation of F near the oxide-metal interface in as-anodized and air-exposed oxides.⁶ Cross-sectional TEM revealed that the oxide consisted of a 20- to 30-nm-thick barrier layer under the honeycomb structure (~ 100 nm thick). Thus, the depth profile in Figure 9b can be described in terms of three distinct regions: at depths less than 30 nm, the profile is dominated by the steady level of the Ti and O signals, and C is at its background level. This corresponds to the barrier layer. Between 30 and 140 nm, the steady rise in C concentration indicates that the adhesive penetrated the oxide. At depths greater than 140 nm, the C signal is dominant, indicative of the adhesive layer. We conclude from the micrographs and the depth profiles that the debonding occurred within the barrier layer at or very near the oxide-metal interface.

The failure at low stress levels of vacuum- and air-exposed oxides was surprising in view of the retention of the honeycomb structure

after exposure, especially since earlier studies indicated that porous oxides were important for bond durability. In an effort to understand this, we subsequently cycled some of the pre-exposed adherends from room temperature to 400°C several times under vacuum. The vacuum- and air-exposed adherends developed large cracks eventually whereas water-exposed adherends did not. The cracks may have developed due to stress between the untransformed oxide and the base metal (at the barrier layer) during cycling. This is reasonable in that there is a 5% difference between the thermal expansion coefficients of Ti and TiO₂.¹¹ Earlier cross-sectional TEM measurements of the water-exposed oxides showed that the barrier layer had disappeared with the transformation to the anatase phase.⁶ Therefore, the water-exposed oxides may not have experienced the same stresses as the vacuum-exposed oxides during thermal cycling and did not develop cracks.

An alternate explanation for the loss of bond strength is a change in the microstructure of the Ti-6Al-4V during heating. Typically, Ti-6Al-4V is rolled into sheets at $T \approx 900^\circ\text{C}$ and subsequently cooled rapidly. This results in a non-equilibrium microstructure that contains a significant volume fraction of metastable beta phase (*i.e.*, V-stabilized). Annealing at $T \geq 300^\circ\text{C}$ can cause the metastable beta to transform to the alpha phase, thereby disrupting the oxide-metal interface. Optical micrographs obtained from as-anodized and air-exposed adherends support this hypothesis.¹²

3 Boiling, pressurized water- and steam-exposed adherends CAA oxides exposed to both liquid and vapor environments at temperatures below 250°C retained almost all of their bond strength, as seen in Table I. Although these debonded surfaces were not examined by XPS, the appearance of adhesive material on all of them suggests that the failure mode was predominantly cohesive in each case (although small areas of adhesive failure could be delineated). It should be noted that the tensile strength values listed for water-exposed adherends in Table I represent the averages of many samples. Some of these exhibited tensile strengths comparable to those obtained for the as-anodized adherends.

Adherends exposed to humid environments at 300°C for 24 hr or more failed at low stress levels. In these cases, the two debonded surfaces appeared different, suggesting an adhesive failure mode.

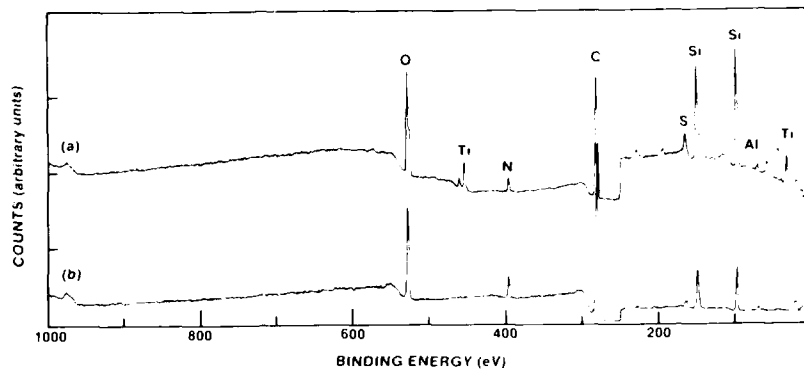


FIGURE 10 X-ray photoelectron spectra of a) metal and b) stud side of a Ti-6Al-4V adherend exposed to steam in a high-pressure autoclave for 120 hours at 300°C, after tensile testing.

This was confirmed by XPS measurements. In Figure 10a, the spectrum obtained from the metal side contains a significant concentration of Ti although the C and Si concentrations are much greater than those observed for the as-anodized surface. Two explanations for the enhanced C and Si are plausible: the increased concentrations may be due either to a very thin adhesive layer (2–4 nm thick) left after the tensile test or to contamination during transfer to the XPS vacuum system. The spectrum of the stud side, Figure 10b, shows no Ti but is typical of the adhesive alone. Scanning electron micrographs show adhesive on the stud side and the nodular oxide on the metal side of the failure.

Selected area diffraction patterns obtained from water- and vapor-exposed adherends show that the oxide is crystalline TiO_2 . The tensile test results indicate, at least for temperatures below 250°C, that the integrity of the oxide-metal interface is retained despite the amorphous-to-crystalline (structural) transformation—the transformed oxide itself can be bonded with nearly the same strength as the as-anodized oxide. This result is in contrast with those obtained for Al adherends that were exposed while bonded, in which chemical changes result in weak bonding to the base metal.³ It is apparent from the SEM micrographs that porosity exists in water-exposed surfaces even after the transformation and,

therefore, the adhesive can penetrate and interlock mechanically with the oxide.

The lack of porosity can explain the reduced bond strength in adherends exposed to humid environments for the longest times and/or at the highest temperatures. In these instances, the adhesive cannot penetrate the oxide and, therefore, no mechanical coupling can occur. The adhesive merely pulls away from the oxide under very little tensile force.

IV SUMMARY

Tensile testing of Ti-6Al-4V adherends that were exposed to a variety of high-temperature environments prior to testing indicate that the mode of failure depended on the nature of the environmental exposure. The as-anodized adherends all failed cohesively (within the adhesive itself). Although the original CAA morphology was retained after high-temperature exposures in vacuum and air, adherends subjected to these environments at temperatures greater than (or equal to) 330°C degraded severely and failed within the oxide. Oxides subjected to moderate, humid environments retained almost all of their initial bond strength although long-term or high-temperature exposures resulted in adhesive failures.

The tensile tests were not designed to simulate phenomena that would occur in a bondline. Such simulations are usually done using, for instance, wedge-crack propagation tests. Structural transformations of the magnitude we have observed would likely result in drastic bond failures if they occurred in a bondline. Rather, the tensile test results suggest that a pre-transformed, crystalline oxide might be used as a suitable alternative to an amorphous oxide in a bondline because the crystalline oxide is more stable thermodynamically. It has been shown that annealing alone can transform amorphous TiO₂ films to crystalline ones¹³ so it may also be possible to transform the oxide in a non-humid environment. We are presently exploring these possibilities.

Acknowledgements

We acknowledge useful discussions with D. McNamara, G. Davis and A. Desai. G. Cote acquired much of the XPS data. P. Martin assisted with the tensile tests. The

financial support of DARPA/ONR under contract number N00014-85-C-0804 is gratefully acknowledged.

References

1. B. M. Ditchek, *et al.*, *Proc. 25th Natl. SAMPE Symp. Exhib.*, San Diego, CA, U.S.A., 1980 (SAMPE, Azusa, CA, 1980).
2. Reviews of some earlier Ti and Al adhesive bonding studies can be found in J. D. Venables, *J. Mater. Sci.* **19**, 2431 (1984) and A. J. Kinloch, *J. Mater. Sci.* **17**, 617 (1982).
3. J. D. Venables, *et al.*, *Proc. 12th Natl. SAMPE Tech. Conf.*, Seattle WA, U.S.A., 1980 (SAMPE, Azusa, CA, 1980).
4. D. A. Hardwick, J. S. Ahearn, A. Desai and J. D. Venables, *J. Mater. Sci.* **21**, 179 (1986).
5. M. Natan and J. D. Venables, *J. Adhesion*, **15**, 125 (1983).
6. H. M. Clearfield, D. K. Shaffer and J. S. Ahearn, *Proc. 18th Natl. SAMPE Tech. Conf.*, Seattle, WA, U.S.A., 1986 (SAMPE, Azusa, CA, 1986), p. 921.
7. A. Matthews, *Am. Mineral.* **61**, 419 (1976).
8. Y. Moji and J. A. Marceau, U.S. Patent No. 3959091, assigned to the Boeing Company (1976).
9. P. A. Redhead, J. P. Hobson, and E. V. Kornelsen, *The Physical Basis of Ultrahigh Vacuum* (Chapman and Hall, London, 1968).
10. A. Desai, private communication.
11. A. Goldsmith, H. J. Hirschhorn, and T. E. Waterman, *Thermophysical Properties of Solid Materials*, Vol. II. WADC Tech. Rep. 58-476 (Wright Air Development Division, Dayton, OH, 1960).
12. H. M. Clearfield, C. P. Blankenship, D. K. Shaffer, and J. S. Ahearn, unpublished results.
13. L. S. Hsu, R. Rujkorakarn, J. R. Sites, and C. Y. She, *J. Appl. Phys.* **59**, 3475 (1986).

Cathodic Debonding of Neoprene from Steel†

F. J. BOERIO, S. J. HUDAK, M. A. MILLER and S. G. HONG

Department of Materials Science and Engineering, University of Cincinnati, Cincinnati, Ohio 45221, U.S.A.

(Received November 10, 1986)

X-ray photoelectron spectroscopy (XPS) has been used to determine the failure mechanisms in neoprene/steel adhesive bonds during cathodic delamination or during immersion in aqueous solutions of NaOH to simulate the effects of cathodic delamination at the bondline. Delamination of the rubber from substrates that had been pretreated by acid-etching began at the edges of the bonds and proceeded slowly inward. The centers of the bonds were always intact except for every long times when complete delamination of the rubber was observed. Failure was near the primer/oxide interface but with islands of rubber remaining on the substrate and islands of oxide remaining on the rubber. The failure mechanism was associated with degradation of the phenolic primer and with dehydrohalogenation of chlorinated rubber in the adhesive and primer. Dehydrohalogenation resulted in the formation of inorganic salts which could dissolve during exposure to water at high pH values, leading to large osmotic pressures at the interface. Debonding of rubber from polished substrates was much faster, leaving little rubber on the substrate failure surfaces and little oxide on the rubber failure surfaces, and indicating that mechanical interlocking of the rubber with the substrate has an important effect on the environmental stability of rubber-to-metal bonds.

KEY WORDS Cathodic delamination; chlorinated rubber adhesives; durability; phenolic primers; rubber-to-metal bonding; X-ray photoelectron spectroscopy.

I INTRODUCTION

The acoustical window on wet-end sonar transducers is usually prepared by curing a slab of neoprene in contact with a steel shroud

† Presented at the Tenth Annual Meeting of The Adhesion Society, Inc., Williamsburg, Virginia, U.S.A., February 22-27, 1987.

and an aluminum head mass that have been pretreated with adhesive systems consisting of metal primers and adhesives. The resulting adhesive bonds must withstand mechanical stresses, temperature extremes, and chemical attack by sea water. Debonding would lead to the entry of water and loss of function in the transducer.

Several investigations concerned with the environmental stability of rubber-to-metal bonds have been reported recently. Ting¹ used the conical button and 90° peel tests to evaluate seven commercial, proprietary adhesive systems for elastomer/metal bonding in transducers. Most of the adhesive systems provided adequate dry strength in the conical button test and failure was usually cohesive within the rubber. However, when 90° peel specimens were statically loaded and immersed in sea water, some attack of the bondline occurred, especially in the presence of oxygen, and failure of the bonds became more interfacial.

Ting² subsequently suggested that electrochemical reactions could affect the durability of rubber-to-metal bonds in sonar transducers. The steel shrouds of poorly insulated transducers could become cathodic with respect to sacrificial zinc anodes attached to the hull of a ship and hydroxyl ions generated by the reduction of oxygen at the steel surface could lead to debonding of the rubber. Ting² also suggested that chloride ions released during the degradation of adhesives or primers containing chlorinated rubber might lead to corrosion of the steel substrate and to debonding of the acoustical window.

Stevenson³ has also investigated the durability of rubber-to-steel bonds during immersion in sea water and found that the mechanical properties of most rubbers were not significantly degraded even when they absorbed large amounts of water and that most bonds were stable in electrochemically inert environments. However, when cathodic potentials were applied to the steel, rapid failure of the bonds occurred but without corrosion of the steel. Delamination always proceeded inward from an exposed edge and was not affected by the type of rubber or by the application of shear stresses to the rubber. Stevenson did not determine the failure mechanism for rubber-to-steel bonds undergoing cathodic delamination but speculated that hydroxyl ions resulting from the reduction of hydrogen ions or oxygen at the steel surface were involved.

Several research groups have investigated cathodic delamination of coatings and adhesives from steel and proposed mechanisms to explain their results. Dickie and coworkers^{4,6} immersed coated steel panels in 5% NaCl solutions at a potential of -1.05 volts *versus* SCE, measured the delamination of the coatings away from a scribe line as a function of time, and used X-ray photoelectron spectroscopy (XPS) to determine the composition of the "coating" and "substrate" failure surfaces. Derivatization and curve-fitting techniques were used to show that carboxylate groups, which were attributed to hydrolysis of ester groups, were present on the failure surfaces of epoxy-ester coatings and on the surfaces of neat coatings immersed in NaOH solutions but not on the surfaces of the neat coatings. Considering that polymer residues were also detected on the substrate failure surfaces, it was concluded that cathodic delamination involved degradation of the coatings very near the coating/oxide interface.⁴

Similar investigations were carried out for epoxy/amine and epoxy/urethane coatings.^{5,6} The failure surfaces of the epoxy/urethane coatings contained more oxygen and less nitrogen than the surface of the neat coating and more sodium than could be explained as NaCl. When the coating failure surface was rinsed with distilled water, the sodium and oxygen concentrations were greatly reduced. It was concluded that a water-soluble salt, sodium carbonate, had formed on the coating failure surface from the hydrolysis products of the urethane groups. Sodium carbonate and small amounts of the epoxy/urethane polymer were found on the substrate failure surface and it was again concluded that cathodic delamination was related to degradation of the coatings near the coating/oxide interface.

The epoxy/amine coatings were more resistant to cathodic delamination than the epoxy/urethane coatings but the failure mechanisms were similar. Sodium carbonate, formed from the hydrolysis products of urea groups in the crosslinking agent, was observed on the coating and substrate failure surfaces and some residual coating was found on the substrate. Once again delamination was attributed to degradation of the resin near the interface.

Watts and Castle^{7,8} conducted experiments on the cathodic delamination of polybutadiene and epoxy coatings from steel panels in 3% NaCl at a potential of -1.05 volts *versus* SCE. They

measured the delamination away from a circular defect at the center of the panels and used XPS to characterize the coating and substrate failure surfaces. Polybutadiene was a reducing agent when cured against steel.⁷ Fe^{+3} ions in the oxide were reduced to Fe^{+2} , providing an interphase with unique composition between the coating and the oxide. Two types of delamination were observed for the polybutadiene coating. Near the circular defect, the interphase itself was attacked and remained attached to the coating failure surface. However, a few millimeters away from the defect the polymer near the interphase was attacked and the interphase remained attached to the substrate.

Somewhat similar results were obtained in the case of epoxy coatings.⁸ Near the circular defect, the oxide was reduced and the coating was delaminated. Thereafter, the failure was associated with hydrolysis at the coating/oxide interface. Carbonates were detected on the failure surfaces using XPS but only after an induction time of several weeks. It was concluded that the carbonates were associated with carbon dioxide absorbed by the test solutions and not with degradation of the coatings. Watts and Castle⁸ also investigated the effects of substrate surface roughness on cathodic delamination and found that roughness affected the rate of debonding but not the mechanism.

The purpose of this paper is to describe the use of X-ray photoelectron spectroscopy to determine the failure mechanisms in neoprene/steel bonds undergoing cathodic delamination.

II EXPERIMENTAL

Adhesive joints were prepared by curing neoprene in contact with steel in the strip-blister configuration (see Figure 1). Steel coupons ($1 \times 6 \times 0.063$ ") were cut from large sheets of interstitial-free steel, cleaned in an aqueous solution of a commercial alkaline cleaner (Parko 338, Parker Chemical Co.) at approximately 60°C, rinsed in water, and cleaned again. After the second cleaning step, the coupons were rinsed and then etched in a solution containing 5% nitric acid, 30% phosphoric acid, and 65% distilled water by volume as described by Trawinski.⁹ Trawinski recommended that a small amount of fluorinated surfactant also be added to the etching

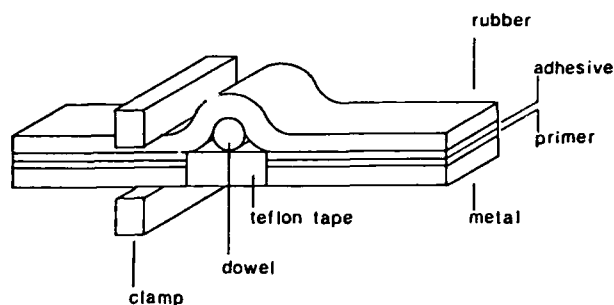


FIGURE 1 Diagram of the strip-blister specimen.

solution but that was omitted here. A metal primer and adhesive (Chemlok 205 and Chemlok 220, Lord Corporation) were applied to the cleaned, etched coupons by brushing and neoprene rubber was cured in contact with the steel by compression molding at 155°C for 45 minutes. The rubber composition is given in Table I.

A debonded region was provided near one end of the specimen by covering the substrate with fluorocarbon tape before the rubber was applied and cured. After curing, a fluorocarbon rod 0.375" in diameter was inserted between the rubber and the fluorocarbon tape to apply a load at the tip of the debonded region. A clamp was applied at one end of the debond to prevent crack propagation in that direction.

The strip-blister specimens were aged in several ways. In some cases, the steel substrates were connected directly to sacrificial zinc anodes in 3.5% aqueous solutions of NaCl. In other cases, the steel substrates were held at a potential of -1.05 volts *vs* SCE in 3.5% NaCl. However, in most cases, the strip-blister specimens

TABLE I

Composition of neoprene rubber	
Neoprene GRT	100.0 parts
Stearic acid	1.0
Carbon black	31.0
Red lead dispersion	15.0
Octylated diphenyl amine	2.0
MBTS	1.5
TE-70 processing aid	2.0

were simply immersed in 1N aqueous solutions of NaOH to simulate the conditions obtained at the bondline in the other two types of environments.

At appropriate intervals, specimens were removed from the test solutions and examined visually. It was usually observed that delamination progressed slowly inward from the initial debond and from exposed edges of the specimens and that the innermost portions of the bonds remained intact. Delamination was not observed in a few cases where the bondline was covered by rubber during the molding operation and not exposed directly to the test solution. The rate of delamination was decreased when pressure was applied to the faces of the specimens as by the clamps (see Figure 1).

The rubber was removed from the substrate to expose the "rubber" and "substrate" failure surfaces by cutting the intact bonds near the centers of the joints with a sharp blade. Samples for surface analysis were cut from both failure surfaces, rinsed in water, and dried. The rubber samples were usually outgassed at room temperature under vacuum in an oven or a desiccator for a few days before surface analysis.

XPS spectra of the failure surfaces were obtained using a Physical Electronics 5300 X-Ray Photoelectron Spectrometer and Mg K α radiation. Reference spectra were also obtained from the cured rubber and from films of the adhesive and primer that were cast onto steel substrates and then cured at elevated temperatures. All observed spectra were corrected for the effects of sample charging by referring the C(1s) binding energy for saturated hydrocarbons to a value of 284.6 eV.

III RESULTS AND DISCUSSION

The O(1s), C(1s), Cl(2p), and Pb(4f) spectra observed for the primer, adhesive, and rubber are shown in Figure 2 and summarized in Table II. The XPS results were consistent with results obtained from infrared spectroscopy¹⁰ which showed that the primer was mostly a phenolic polymer blended with a chlorinated rubber and that the adhesive was mostly a chlorinated rubber.

The Cl(2p) spectrum obtained from the adhesive consisted of a

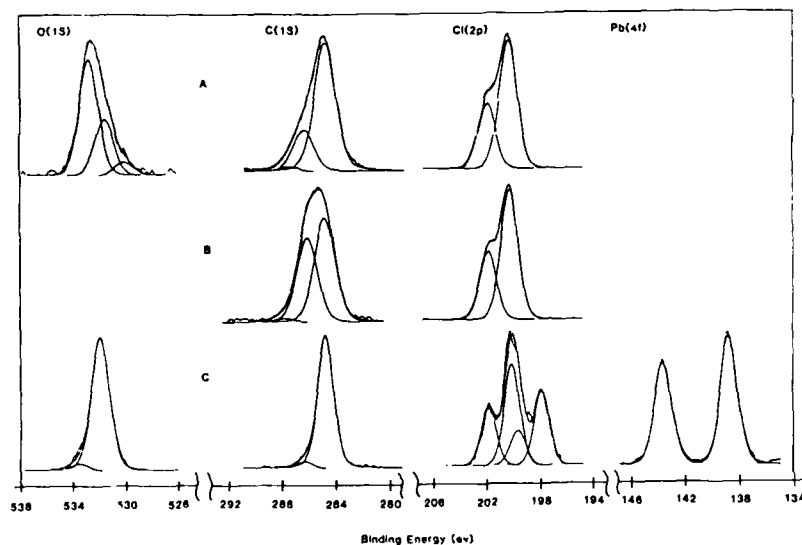


FIGURE 2 XPS spectra observed for (A)-primer, (B)-adhesive, and (C)-neoprene rubber.

doublet near 200.1 and 201.7 eV due to $2p_{1/2}$ and $2p_{3/2}$ electrons and the C(1s) spectrum was a doublet separated by about 1.3 eV due to the primary and secondary substituent effects of chlorine on carbon. Such spectra are very characteristic of chlorinated hydrocarbons.¹¹ The C(1s) spectrum of the primer consisted mostly of bands near

TABLE II
XPS spectra observed for primer, adhesive, and neoprene

	Pb(4f)	Cl(2p)	C(1s)	O(1s)
Primer		200.1	284.6	530.2
		201.7	286.2	531.7
			287.4	532.9
			291.3	
Adhesive		200.1	284.6	
		201.7	285.9	
Neoprene	138.6	197.8	284.6	531.6
	143.5	199.2		
		200.1		
		201.7		

284.6 and 286.2 eV that are typical of hydrocarbons containing hydroxyl groups¹¹ and the Cl(2p) spectrum was a doublet near 200.1 and 201.7 eV. O(1s) spectra of the primer consisted of three bands near 530.2, 531.7, and 532.9 eV. The band near 532.9 eV was related to phenolic oxygen while those near 530.2 and 531.7 eV were probably related to inorganic fillers such as TiO₂ and ZnO and aluminosilicates which are known to be present in the primer from infrared spectroscopy¹⁰ and from energy-dispersive X-ray analysis or EDAX.^{10,12}

Some interesting features were observed in the spectra of the rubber. A pair of lines related to Pb 4f_{7/2} and 4f_{5/2} electrons was observed near 138.6 and 143.5 eV. The Cl(2p) spectra consisted of two pairs of lines, attributed to 2p_{3/2} and 2p_{1/2} electrons from organic (200.1 and 201.7 eV) and inorganic (197.8 and 199.2 eV) chlorides. The inorganic chlorides were presumably lead chlorides formed by the reaction of the red lead (Pb₃O₄) curing agent with tertiary, allylic chlorides in neoprene during the curing reaction and the binding energies of Pb(4f_{7/2}) and Pb(4f_{5/2}) electrons in PbCl₂ were in fact observed near 138.5 and 143.4 eV. O(1s) spectra from the rubber consisted of a single band near 531.6 eV. The binding energies of oxygen atoms making one or two bonds with carbon are usually higher by at least 1.0 eV.¹¹ Therefore, the band near 531.6 eV in the O(1s) spectra of the rubber is probably related to unreacted Pb₃O₄ curing agent.

XPS spectra obtained from the "substrate" and "rubber" failure surfaces of a strip-blister specimen that was immersed in 1N NaOH for eight days are shown in Figure 3 and summarized in Table III. Iron was found on both surfaces, implying that the failure was near the interface but partly within the oxide and partly within the organic phase. The O(1s) spectra from the substrate failure surface were complex and contained four main bands, near 529.7, 531.0, 531.8, and 532.9 eV, and weak bands near 534.1 and 535.5 eV. The bands near 529.7 and 531.0 eV were characteristic of oxides and hydroxides on the surface of the substrate but the bands near 531.8 and 532.9 eV were typical of the primer, indicating that failure of the specimens was near the primer/oxide interface. The C(1s) spectrum of the substrate failure surface consisted of the band near 284.6 eV due to saturated hydrocarbons and additional bands that were shifted upwards in binding energy by about 1.6, 3.0, and

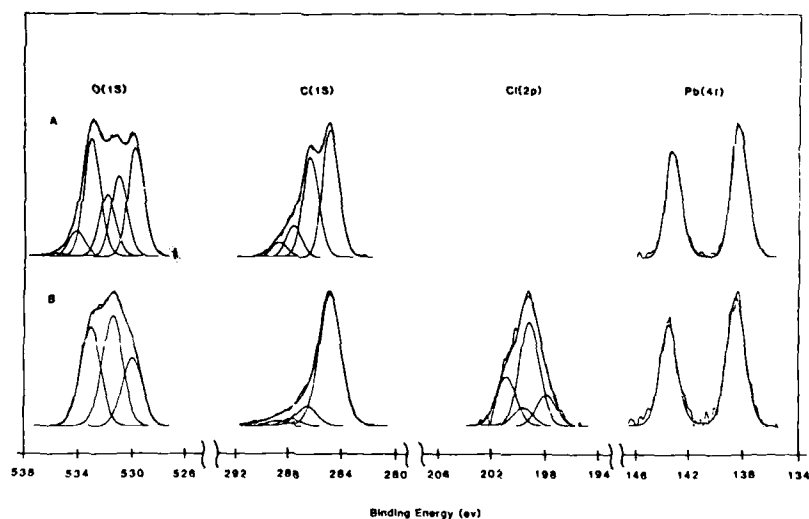


FIGURE 3 XPS spectra observed for (A)-substrate and (B)-rubber failure surfaces of strip-blister specimens prepared from acid-etched steel and then immersed in 1 N NaOH for eight days.

4.1 eV and assigned to carbon forming one, two, or three bonds with oxygen. As described above, carbon forming one bond with oxygen was found in the primer but more highly oxidized forms of carbon were not and it was concluded that carboxylate groups may have been formed in the primer during the debonding reaction.

TABLE III
XPS spectra observed for substrate and rubber failure surfaces of neoprene/steel strip-blister specimens prepared from acid-etched substrates

	Pb(4f)	Cl(2p)	C(1s)	O(1s)
Substrate	138.2		284.6	529.7
	143.0		286.2	531.0
			287.6	531.8
			288.7	532.9
				534.1
Rubber				535.5
	138.3	198.0	284.6	530.1
	143.2	199.1	286.1	531.5
		199.6	287.3	533.0
		200.7	288.7	

Lead was always observed on the substrate failure surfaces. Some of the lead may have come from the lead chlorides formed in the rubber during curing, indicating the presence of small islands of rubber remaining on the substrate failure surface or from diffusion of lead from the rubber into the interface during curing. However, small amounts of lead, which may have diffused to the interface during curing, have also been found in the adhesive.¹²

The O(1s) spectra of the rubber failure surface had bands near 533.0, 531.5, and 530.1 eV which were all typical of the primer. However, the intensity of the band near 531.5 eV was greater than expected for the primer, perhaps due to segregation at the interface of oxide fillers in the primer. Residual NaOH may also have contributed to the intensity of the band near 531.5 eV. C(1s) spectra of the rubber failure consisted of the usual strong band near 284.6 eV that is characteristic of hydrocarbons and weaker bands shifted toward higher energies by 1.5, 2.7, and 4.1 eV that were related to carbon forming one, two, or three bonds with oxygen.

An interesting result concerned the nature of the chlorine present on the rubber failure surfaces. As discussed above, the Cl 2p_{1/2} and 2p_{3/2} spectra of the primer were observed near 200.1 and 201.7 eV, as expected for chlorinated hydrocarbons. The Cl(2p) spectra obtained from the rubber failure surface contained additional bands near 198.0 and 199.1 eV, perhaps indicating some breakdown of the chlorinated rubber in the primer and the formation of metal chlorides. However, it was also possible that the inorganic chlorides on the rubber failure surfaces simply indicated that the locus of failure was at least partly within the rubber. As discussed above, the formation of a lead chloride during curing was expected and an inorganic chloride was in fact observed on the surface of neoprene that was cured but never exposed to NaOH (see Figure 2).

In order to determine the significance of the lead and the inorganic chlorides found on the rubber and substrate failure surfaces, several strip-blister specimens were prepared as described above except that the steel substrates were mechanically polished before the primer and adhesive were applied. These samples were immersed in 3.5% NaCl and held at a potential of -1.05 volts vs SCE. Debonding of the rubber from the polished steel was rapid and complete delamination was observed within a few days. By comparison, debonding from the etched steel substrates was rela-

tively slow and complete delamination sometimes required several months.

The large differences in the rate of delamination from etched and polished substrates may have been related to differences in surface composition or morphology of the substrates. Results obtained from XPS indicated that there were differences in surface composition. A small amount of phosphorous, presumably due to a phosphate, was found on substrates that were etched but not on those that were polished. However, the debonding of neoprene from grit-blasted substrates, with no phosphates present on the surface, was also very slow. Therefore, it seems likely that surface morphology, and not surface composition, was responsible for the difference in the rate at which neoprene debonded from etched and polished substrates and that mechanical interlocking between the rubber and asperities on the surface of the substrate contributed significantly to the bond strength. As described earlier, Watts and Castle⁸ reported similar results.

When XPS spectra were obtained from the failure surfaces of joints prepared from polished substrates, some interesting results were obtained (see Figure 4 and Table IV). There was very little

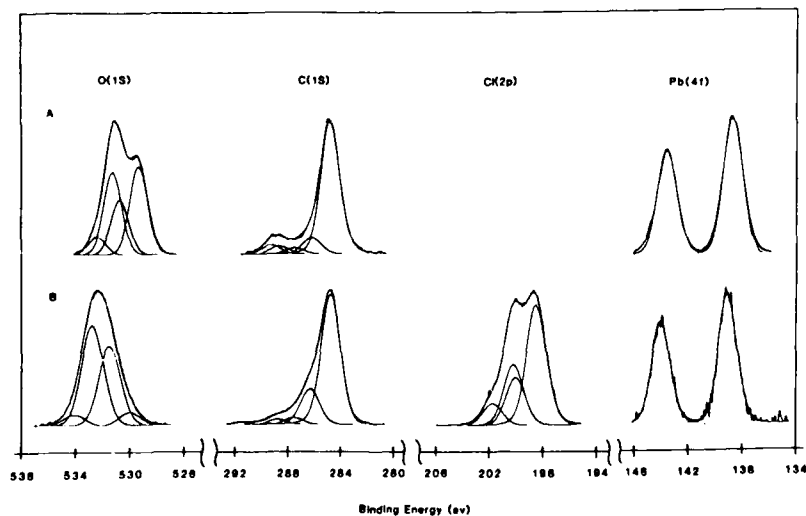


FIGURE 4 XPS spectra observed for (A)-substrate and (B)-rubber failure surfaces of strip-blister specimens prepared from mechanically polished steel and then immersed in 3.5% NaCl at a potential of -1.05 volts *vs* SCE.

TABLE IV
XPS spectra observed for substrate and rubber failure surfaces of
neoprene/steel strip-blister specimens prepared from polished
substrates

	Pb(4f)	Cl(2p)	C(1s)	O(1s)
Substrate	138.4		284.6	529.4
	143.2		286.1	530.8
			287.4	531.4
			288.6	532.6
			289.2	
Rubber	138.8	198.4	284.6	530.2
	143.6	200.0	286.2	531.7
		200.1	287.4	532.9
		201.7	288.6	534.3
			289.2	
			291.2	

iron on the rubber failure surface and the O(1s) spectra were similar to those of the primer. O(1s) spectra of the steel failure surface were characterized by bands near 531.4, 530.8, and 529.4 eV that were attributed to carbonates, hydroxides, and oxides on the substrate, respectively. Failure was evidently very near the primer/oxide interface and there was little evidence for primer left on the substrate. The Cl(2p) spectra obtained from the rubber failure surface had components near 198.4 and 200.1 eV due to inorganic chlorides and near 200.0 and 201.7 due to organic chlorides. Very similar spectra were obtained from the failure surface of the primer that had delaminated from *beneath* the fluorocarbon tape that was used to provide the initial debond (see Figure 1). Since there was no possibility of rubber remaining on that surface, it was concluded that the inorganic chlorides were formed by dehydrohalogenation of chlorinated rubber in the primer or adhesive and reaction of the chlorine with lead or zinc which are present in the adhesive and primer.

Several experiments were conducted to determine whether dehydrohalogenation occurred during exposure to water at high pH values or during curing. In one case, infrared spectroscopy was used to determine the stability of chlorinated rubber films as a function of immersion time in aqueous solutions of NaOH. Very little change was observed, even after immersion of the films in 2.8 N NaOH for several weeks, indicating that chlorinated rubbers.

such as are found in the primer and adhesive, are stable in water at high pH values.¹³ In another case, the Cl(2p) XPS spectra of neat films of the primer were examined before and after the surfaces of the films were etched by sputtering briefly with argon ions. Before sputtering only bands attributed to organic chlorides were observed. After sputtering lightly, the bands related to inorganic chlorides appeared, implying that the inorganic chlorides were formed during curing but were covered by a thin polymer layer on the surface of the primer film.

The C(1s) spectra of the substrate failure surface were characterized by the usual band near 284.6 eV but with a component shifted upward in binding energy by about 4.6 eV due to the surface carbonates.⁴ Bands characteristic of lead were observed near 138.4 and 143.2 eV, suggesting that the carbonates on the steel surface were lead carbonates. Reflection infrared spectra obtained from the steel failure surface confirmed the presence of lead carbonate.¹³ There was a considerable amount of lead on the rubber and steel failure surfaces except from beneath the fluorocarbon tape, implying that lead did diffuse from the rubber into the bondline during curing.

The results described above suggest two possible mechanisms for the debonding of neoprene rubber from steel during cathodic delamination or during exposure to environments, such as aqueous solutions of NaOH, meant to simulate conditions obtained at the bondline during cathodic delamination. They include degradation of the phenolic resin in the primer and the presence of large osmotic pressures at the interface.

Degradation of the primer could occur by oxidation of the methylene linkages between phenol residues to form carboxylic acids and quinones¹⁴ or by alkaline hydrolysis of the methylene linkages to form phenol and carbon dioxide.¹⁵ Some support for each mechanism has been obtained. As discussed above, carboxylate groups have been detected in XPS spectra obtained from the failure surfaces. Carbonates, perhaps formed by carbon dioxide resulting from alkaline hydrolysis, have also been detected. Preliminary results from infrared spectroscopy have verified that the methylene linkages between phenol residues are readily attacked when phenolic polymers are exposed to aqueous solutions of NaOH at room temperature.¹³

As described above, Watts⁸ observed carbonates on the failure surfaces of epoxy coatings on steel following cathodic delamination in 0.52 M NaCl for several weeks but attributed them to precipitation of carbon dioxide absorbed by the test solutions. Hammond⁶ also observed carbonates on the failure surfaces of epoxy/urethane and epoxy/amine coatings on steel following cathodic delamination for much shorter times. The carbonates were attributed to degradation of urethane and amine groups to form carbon dioxide which combined with metal ions to give carbonates which were detected by XPS. We detected carbonates on the failure surfaces of neoprene/steel strip-blister specimens prepared from polished substrates after cathodic delamination for only two days. Since the carbonates observed on the failure surfaces of the strip-blister specimens formed so quickly, they may have resulted from degradation of the primer.

Formation of salts that were soluble at neutral or high pH values could lead to large osmotic pressures at the interface and to delamination as observed by Ashbee¹⁶ in composites. Inorganic chlorides were found on the rubber failure surfaces of strip-blister specimens that delaminated in aqueous solutions of NaOH or in aqueous solutions of NaCl when the steel substrates were held at cathodic potentials. The chlorides may have formed during delamination or during curing but, as discussed above, present indications are that chlorinated rubbers do not undergo dehydrohalogenation during immersion in concentrated solutions of NaOH.

Delamination was not observed when strip-blister specimens were exposed to aqueous solutions of NaCl without an applied potential or when the bondline was covered by rubber and not exposed directly to the test solution. Thus, diffusion of water and soluble species directly through the rubber were not important. High pH values and, in the case of cathodic delamination, exposed steel where the cathodic reduction of oxygen to form hydroxyl ions could occur, were required for debonding.

The rate of delamination decreased when pressure was applied to the rubber by the clamps that were used to ensure that the starter crack propagated in only one direction. That may indicate that osmotic pressure is an important factor in the delamination process since pressure applied to the rubber would decrease the osmotic

pressure at the interface. However, pressure may also reduce the diffusion constant for water along the interface.

The failure mechanism for cathodic delamination of neoprene from steel involves degradation of the primer by hydroxyl ions and, perhaps, large osmotic pressures caused by the presence of lead chlorides at the interface which are soluble at high pH values. Additional work is in progress to determine which mechanism is most important.

IV CONCLUSIONS

Adhesive bonds between neoprene rubber and steel fail near the primer/oxide interface during cathodic delamination or during aging in aqueous solutions at high pH values to simulate the conditions obtained at the bondline during cathodic delamination. The failure mechanism involves dehydrohalogenation of chlorinated rubber in the adhesive and the primer and degradation of the phenolic resin found in the primer.

Degradation of the primer is sufficient to cause failure of the bonds. However, the presence of soluble metal chlorides at the bondline due to dehydrohalogenation could lead to large osmotic pressures at the interface during exposure of the bonds to water at high pH values and contribute to bond failure. Either failure mechanism is consistent with the previous suggestion that failure of rubber-to-metal bonds during cathodic delamination is not dependent on the nature of the rubber.

V Acknowledgements

This research was supported in part by a grant from the Office of Naval Research. The X-ray photoelectron spectrometer was obtained through grants from the Office of Naval Research, Armco, Inc., and Republic Steel Corp. Dr. Corley Thompson of the Office of Naval Research, Underwater Sound Reference Detachment, Orlando, Florida provided the neoprene and Kristen A. Boerio assisted in preparing the figures. Numerous helpful discussions with Dr. David A. Dillard and Ramzi Hamadeh of Virginia Polytechnic Institute and State University regarding the cathodic delamination of neoprene from steel are also acknowledged.

References

1. R. Y. Ting, in *Adhesive Joints: Formation, Characteristics, and Testing*, K. L. Mittal, Ed. (Plenum Press, New York, 1984).
2. R. Y. Ting, *Polymer News* **10**, 197 (1985).
3. A. Stevenson, *Int. J. Adhesion and Adhesives* **5**, 81 (1985).
4. J. W. Holubka, J. S. Hammond, J. E. DeVries, and R. A. Dickie, *J. Coatings Tech.* **52**, 63 (1980).
5. J. S. Hammond, J. W. Holubka, and R. A. Dickie, *J. Coatings Tech.* **51**, 45 (1979).
6. J. S. Hammond, J. W. Holubka, J. E. DeVries, and R. A. Dickie, *Corros. Sci.* **21**, 239 (1981).
7. J. F. Watts and J. E. Castle, *J. Matls. Sci.* **18**, 2987 (1983).
8. J. F. Watts and J. E. Castle, *J. Matls. Sci.* **19**, 2259 (1984).
9. D. L. Trawinski, *SAMPE Quarterly* **16**, 1 (1984).
10. M. A. Miller, M. S. Thesis, University of Cincinnati, 1985.
11. A. Dilks, in *Electron Spectroscopy: Theory, Techniques, and Applications*, Vol. 4, C. R. Brundle and A. D. Baker, Eds. (Academic Press, London, 1980), chap. 5.
12. E. Cutts, in *Developments in Adhesives*, Vol. 2, A. J. Kinloch, Ed. (Applied Science Publishers, London, 1981), chap. 10.
13. F. J. Boerio, S. J. Hudak, and S. G. Hong, to be published.
14. R. T. Conley, *J. Applied Polymer Sci.* **7**, 103 (1963).
15. R. M. Summers, *J. Polymer Sci., Polymer Chem. Ed.* **16**, 1669 (1978).
16. K. H. G. Ashbee, and N. R. Farrar, *J. Phys. D: Appl. Phys.* **11**, 1009 (1978).

New and Improved Tests for Adhesion†

A. N. GENT

Institute of Polymer Science, The University of Akron, Akron, Ohio 44325, U.S.A.

(Received August 29, 1986)

Three new methods are discussed for measuring the work G_a required to detach unit area of an adhering material from a substrate. The first is a simple modification of the Outwater double-torsion test for long rectangular plates, bonded together. This method is suitable for evaluating aluminum-epoxy bonds, for example, or the transverse strength of fibrous composites. The second is a pull-off test for long strips adhering to a rigid surface. It seems suitable for adhesive tapes and laminates. The third is a reconsideration of the "blister" test for films and coatings, in which a circular debond at the interface is made to grow by internal pressure. The relation obtained between pull-off force F for a strip, or blow-off pressure P for a layer, takes the unusual form:

$$F^4 \text{ (or } P^4) \propto KG_a^3$$

where K is the tensile stiffness of the detaching layer. This dependence arises from the non-linear (cubic) relation between load or pressure and deflection in these configurations. Nevertheless, the product $F\theta$, where θ is the angle of detachment of a strip, or Py , where y is the height of a "blister", give direct measures of the strength of adhesion G_a , independent of the stiffness of the adhering material and of the extent of detachment.

KEY WORDS Blister test; detachment; fracture mechanics; pull-off; test methods; torsion.

1 INTRODUCTION

Ideally, a test method for adhesion should have the following features. First, it should employ simple specimens. Secondly, the

† Presented at the Tenth Annual Meeting of The Adhesion Society, Inc., Williamsburg, Virginia, U.S.A., February 22-27, 1987.

failure force should remain constant, at least in principle, while the line of detachment is driven forwards over long distances, so that an average strength of adhesion can be readily determined. And, finally, the fracture energy G_a should be obtained directly in terms of the specimen dimensions, its stiffness during loading and the critical load at which the process of detachment takes place. No other measurements are needed then to determine the energy G_a of separation per unit of bonded area.

Three such test methods are reviewed here. The first is particularly suitable for relatively stiff adhesives and adherends while the other two can be used with materials having a wide range of stiffness.

2 THE OUTWATER TORSION TEST^{1,2}

A sketch of a suitable bonded specimen is given in Figure 1. It consists of two long rectangular plates, bonded together along one edge. An initial crack of length c_0 is made between them. The specimen is then clamped, as shown in Figure 2, and subjected to a steadily increasing angular rotation θ of one arm with respect to the other. The corresponding torque M is measured by means of a long rigid moment arm, as shown in Figure 2.

At a critical value of the applied torque, denoted M_c , the crack will advance. At this point elastic energy stored in the twisted arms of the specimen begins to be expended in fracture. Assuming that the arms are linearly-elastic in torsion and that the torsional stiffness M/θ is inversely proportional to the length c of the arms, we can deduce that the fracture energy G_a is given by¹

$$G_a = M_c^2 / 2kt \quad (1)$$

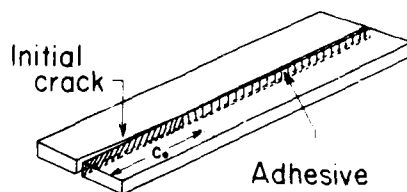


FIGURE 1 Sketch of specimen for double-torsion test.

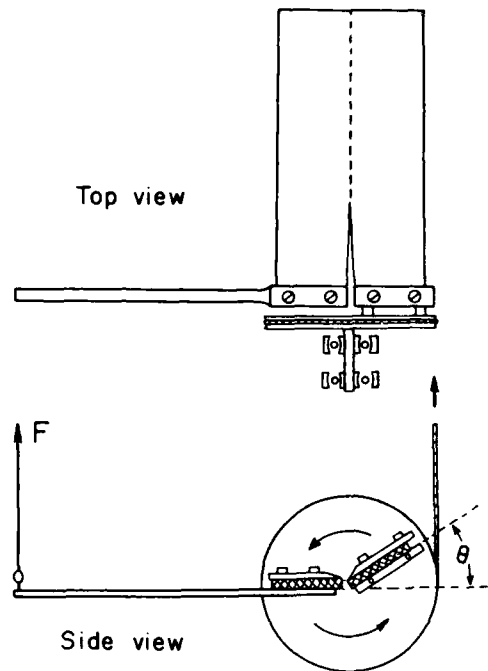


FIGURE 2 Method of applying large rotations θ and measuring the corresponding torque².

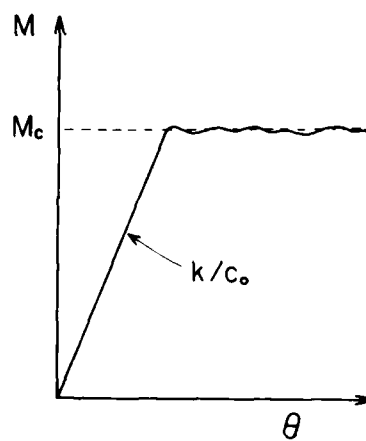


FIGURE 3 Relation between applied torque M and pulley rotation θ .

where

$$k = Mc/\theta. \quad (2)$$

k denotes the torsional stiffness of the specimen for a crack of unit length and t is the thickness of the specimen. The value of k can be obtained from the experimental relation between torque M and rotation θ up to the onset of fracture, Figure 3, and the mean value of M_c can be measured thereafter, over long distances for long test pieces. Thus, the mean fracture energy G_a can be measured with some confidence, using a single specimen of simple design.

3 PULL-OFF TEST FOR ADHERING STRIPS³

This simple test arrangement is shown in Figure 4. An adhesive strip of width w is pulled away from a rigid substrate at an angle θ by a force F . Work is done both in stretching the strip as it detaches and in fracturing the interfacial bond. Assuming that the strip is linearly-elastic and the angle θ is small, the relation between F and θ is as follows:

$$F = K\theta^3 \quad (3)$$

where K is the tensile stiffness coefficient of the strip (force per unit of tensile strain). In terms of the fracture energy G_a ,³

$$wG_a = (3/8)(F^4/K)^{1/3}. \quad (4)$$

Thus, if measurements of the pull-off force F only are made, an independent measurement of the stiffness of the strip is required in order to determine the strength of adhesion. However, a simple relation is obtained in terms of the product of the force F and detachment angle θ , both of which remain constant, at least in

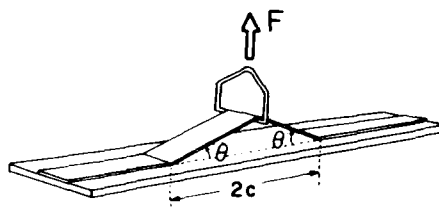


FIGURE 4 Pull-off test for an adhering strip³.

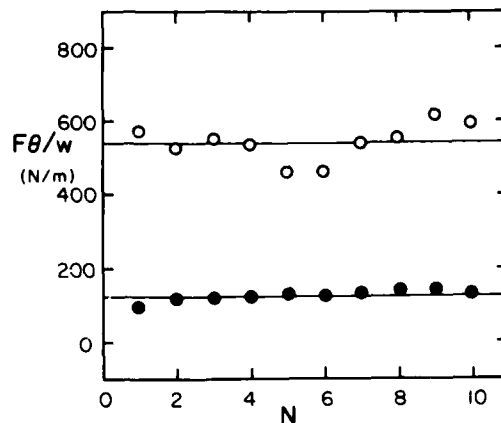


FIGURE 5 Product of pull-off force F and angle θ plotted against the number N of layers of an adhesive tape plied up and pulled off together. Open symbols, detaching from glass; filled symbols, detaching from Teflon³.

principle, during continued detachment:³

$$G_a = 3F\theta/8w \quad (5)$$

Thus, the mean value of the fracture energy can be obtained from simple measurements on a single specimen.

Values of the product $F\theta/w$ are shown in Figure 5 for an adhesive tape detaching from glass and Teflon substrates. A number N of layers were adhered one on top of another to give a composite tape having N times the stiffness of a single layer, but the same level of adhesion. Correspondingly, the pull-off force F was greater and the angle θ was smaller than for a single layer. But the product $F\theta$ was quite independent of N , as the theory predicts. It thus provides a measure of the strength of adhesion G_a , independent of the stiffness of the tape. (G_a is, of course, different for the different substrates, as would be expected.)

4 BLOW-OFF ("BLISTER") TEST FOR ADHERING LAYERS⁴⁻⁷

This test, shown schematically in Figure 6, was proposed by Dannenberg⁴ and applied by Williams⁵ and Andrews and Stevenson⁶ to the study of adhesion. But the latter authors focussed

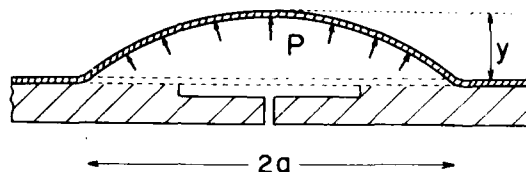


FIGURE 6 Blister test for an adhering layer.

on the bending deformation of a relatively thick layer, with a blister of relatively small radius a underneath it. When the blister is large in radius, and the layer is relatively thin, then the principal deformation is a biaxial stretching of the layer, rather than bending. In this case the relation between inflating pressure P and height y of the center of the blister is given by

$$P = 4.75K'y^3/a^4 \quad (6)$$

for small degrees of inflation of the layer, again assumed to be linearly-elastic, where K' denotes the tensile stiffness coefficient for a strip of unit width; $K' = Et$, where E is the effective tensile (Young's) modulus and t is the layer thickness.

At a critical pressure the blister will grow in size by further detachment. By considering an energy balance, in which the work of inflation is expended partly in stretching a larger portion of the layer and partly in detaching it, we deduce that⁷

$$G_a = 0.39(P^4 a^4 / K')^{1/3} \quad (7)$$

or

$$G_a = 0.65Py. \quad (8)$$

Although in this case the pressure required to cause detachment does not stay constant as the blister increases in radius, but decreases continuously, nevertheless the product of the momentary pressure P and corresponding blister height y gives a direct measure of the characteristic fracture energy G_a for the adhesive bond.

Measured values of P and y are shown in Figure 7 for a layer of a polypropylene-backed packing tape adhering to a Plexiglas substrate, with an initially debonded circular patch of radius $a = 25 \text{ mm}$. On inflation, the pressure increased in proportion to y^3 , in agreement with Eq. (6), until further debonding started at the edge

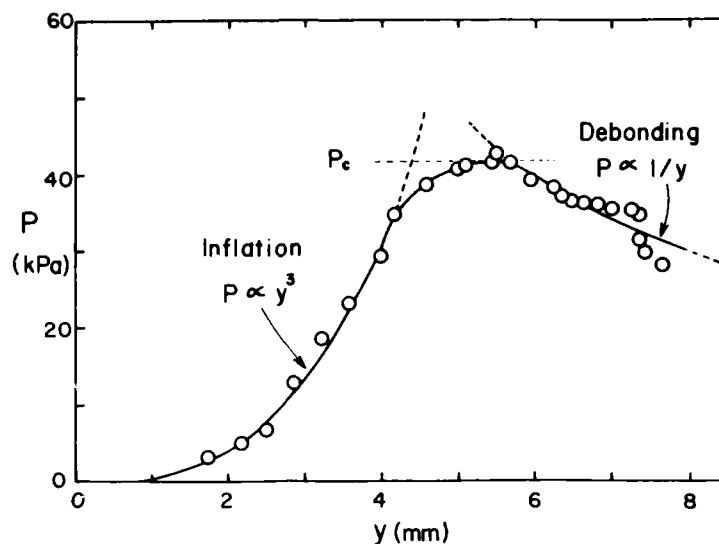


FIGURE 7 Blow-off pressure P plotted against the height y of the blister for a polypropylene-backed packing tape. P_c denotes the pressure at which further detachment started at the edge of the initial debond⁷.

of the initial circular debond. Thereafter, as the blister propagated, the pressure decreased in inverse proportion to the blister height y , in accordance with Eq. (8).

Thus, even though the blow-off pressure is not constant, it can be employed with the corresponding blister height to obtain mean values of the strength of adhesion over large areas of the interface. And no other parameters are required.

5 LIMITATIONS

The first method discussed above, involving the torsion of rectangular plates, is only applicable to materials which deform elastically up to the debonding stress. They must not undergo plastic yielding or flow. Also, they must not be so soft that the plates would twist through angles greater than 180° before detaching.

The other methods require, at least for the simple relations given in Eqs. 5 and 8 to hold, that the imposed deflections be small. In

practice, this restriction is not a severe one. Values of pull-off angle of up to 25° , and blister height approaching the magnitude of the blister radius, yield results in good agreement with the theoretical relations based on the assumption that the deflections are small.^{3,7} But, again, plastic yielding or flow of the adhering strip or layer would invalidate the analyses, which require linear relations to hold between stress and strain. Small departures from linearity seem to be acceptable, however, yielding results for G_a that are approximately correct. And it is noteworthy that reversibility of the stress-strain relations is not required at all, because the deformations remain constant or increase as debonding proceeds.

Acknowledgements

The work forms part of a program of adhesion research at The University of Akron supported by the Adhesive and Sealant Council. Additional support by the Office of Naval Research (Contract N00014-85-K-0222) is gratefully acknowledged.

References

1. J. O. Outwater and D. J. Gerry, *J. Adhesion* **1**, 290-295 (1969).
2. K. Cho and A. N. Gent, *Int. J. Fracture* **28**, 239-244 (1985).
3. A. N. Gent and S. Kaang, *J. Appl. Polym. Sci.* **32**, 4689-4700 (1986).
4. H. Dannenberg, *J. Appl. Polym. Sci.* **14**, 125-134 (1961).
5. M. L. Williams, *J. Appl. Polym. Sci.* 29-40 (1969).
6. E. H. Andrews and A. Stevenson, *J. Mater. Sci.* **13**, 1680-1688 (1978).
7. A. N. Gent and L. Lewandowski, *J. Appl. Polym. Sci.*, in press.

A Comparison Between Measurements and Finite Element Predictions of Crack Opening Displacements Near the Front of an Interface Crack[†]

K. M. LIECHTI,[‡] D. GINSBURG and E. C. HANSON

Department of Aerospace Engineering and Engineering Mechanics, The University of Texas at Austin, Austin, Texas 78712, U.S.A.

(Received November 7, 1986)

Crack opening displacements close to the front of an interface crack between glass and epoxy determined from measurements and finite-element solutions are compared. The measurements were made using optical interferometry, and the finite-element solutions were based on a linear material response and the displacements that were applied during crack initiation experiments using a blister test configuration. Various load levels, up to initiation, are considered, and the effect of fracture mode-mix examined by considering different initial crack diameters. The comparisons indicate that a relative increase in the mode II component gave rise to a significant increase in inelastic behavior near the crack front.

KEY WORDS Fracture mechanics; mixed-mode debonding; interface crack initiation; crack opening interferometry, finite-element analysis.

1 INTRODUCTION

Measurements of adhesive fracture energies or critical-strain energy release rates associated with mixed-mode adhesive crack growth

[†] Presented at the Tenth Annual Meeting of The Adhesion Society, Inc., Williamsburg, Virginia, U.S.A., February 22-27, 1987.

[‡] To whom correspondence regarding this paper should be addressed.

have indicated^{1,2} that these quantities increase with relative increases in the mode II component. However, if the adhesive fracture energy is thought of as an intrinsic material property that reflects the strength of bonds, then it should be a constant, independent of the fracture mode mixture. The reasons cited for the noted increases include the possibilities of non coplanar crack growth for more brittle materials^{1,3} and dissipative effects arising from inelastic material behavior near the crack front.² Thus, if the growth of macroscopically coplanar cracks under mixed-mode conditions is to be predicted in a rational manner, such localized phenomena must be accounted for. In view of the increasing use of tougher adhesives, the purpose of the present work is to examine the effect of inelastic material behavior on crack opening displacements close to the crack front through a comparison of direct measurements and linear elastic stress analyses.

Although near-tip singular behavior can be examined using the methods of photoelasticity⁴ and caustics,⁵ they both involve assumptions as to the constitutive behavior of the materials in the highly stressed crack front region. On the other hand, measurements of displacements are direct, requiring no such assumptions. Since the near-tip region is of interest, the displacements to be measured are small and therefore require the resolution of electron microscopic⁶ or optical interferometric techniques.⁷⁻¹⁰ Of the latter, crack opening interferometry^{9,10} was chosen for the present study because the crack front geometry can be examined. The price for this piece of information is that only the component of crack opening displacements normal to the plane of the crack can be measured. However, this was not felt to be unduly restrictive for the objectives of the present study.

Linear elastic, small deflection analyses of bimaterial bodies containing interface cracks have been conducted over the years for various simple geometries and loadings. The main contributions are summarized in the paper by Piva and Viola.¹¹ As is well known and discussed by now, all predict a complex singularity in crack front stresses which gives rise to rapid oscillations in the stresses and interpenetration of crack faces as the crack front is approached. If finite deformations are allowed,¹² the complex nature of the singularity has been found to disappear, indicating that the anomalous behavior is due to the linearization of the problem. More

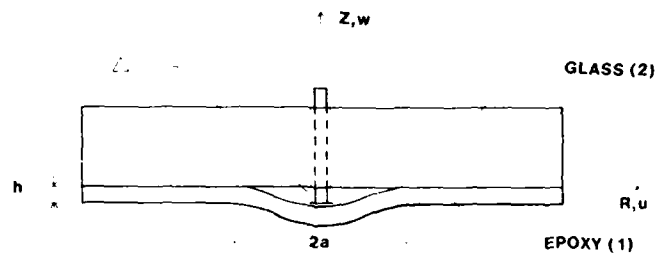
general geometries and loadings have been analyzed by numerical techniques such as boundary collocation¹³ and finite-element analysis with hybrid elements¹⁴ which retain the complex singularities. Fracture parameters for interface cracks have also been determined from finite-element analyses that do not make use of special interface crack elements.¹⁵⁻¹⁷ Such procedures can be justified by the small size of the region of interpenetration and the conclusions of Ref. 12. Furthermore, contour integral methods,^{15,17} which are relatively insensitive to the exact nature of the stress field at the crack front, are often used to extract stress intensity factors. The finite-element code VISTA¹⁸ was used for the linear elastic analyses in this study.

The details of the specimen geometry, loading and measurement and finite-element procedures are next described in section 2. Measurements of and finite-element solutions for crack opening displacements up to crack initiation and under a range of mixed-mode conditions are then compared in section 3. Conclusions are given in section 4.

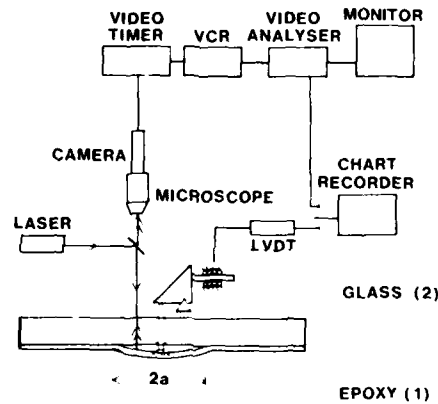
2 EXPERIMENTAL AND ANALYTICAL PROCEDURES

The plate blister test configuration was chosen for this study because it provides a range of mixed-mode conditions.^{19,1} Furthermore, crack growth for the glass epoxy bimaterial combination considered here was interfacial and axisymmetric in nature. The latter feature simplified the subsequent finite-element analysis because edge effects did not have to be considered. The specimen geometry is shown in Figure 1a where a modified bisphenol A epoxy, Araldite 502,[†] that had been mixed with a liquid amido-amine hardener, Araldite 955,[†] was cast directly to the glass. Initial debonds between the glass and Araldite were formed by a circular piece of Teflon tape that was stuck to a flattened screw head which formed the base of a punch. Driving the punch through applied displacements, Δ , produced circular debonds having a diameter, $2a$. The punch base was designed so that plastic deformations in the contact region were avoided. The thickness, h , of the Araldite

[†] Products of CIBA-Geigy, Inc.



a) SPECIMEN GEOMETRY



b) APPARATUS

FIGURE 1 Specimen geometry and apparatus.

varied from specimen to specimen but in all cases was uniform to within 0.127 mm. The details of the specimen fabrication and the compact blister loader are given in Ref. 20.

The stress-strain behavior of the epoxy was determined from uniaxial tension tests that were conducted on coupons that were obtained from the delaminated blister specimens. Elastic properties were determined from strain gage measurements of axial and transverse strain. The plastic response of the material was determined using an extensometer. The data were fit (Figure 2) to the Ramberg-Osgood relation.

$$\epsilon = \frac{\sigma}{E} \left[1 + \frac{3}{7} \left(\frac{\sigma}{\sigma_0} \right)^{n-1} \right] \quad (1)$$

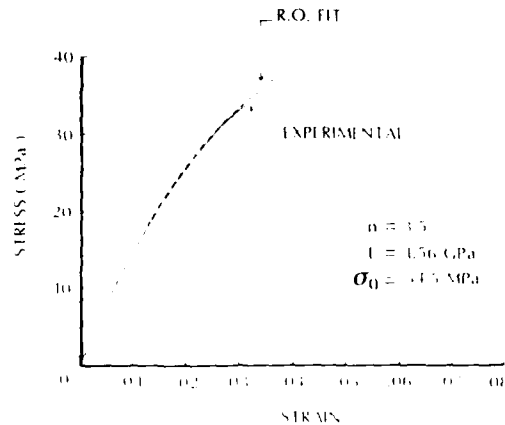


FIGURE 2 Stress strain behavior of Araldite 502.

where E is the Young's modulus of the material, σ_0 is the yield stress, and n is the hardening exponent.

For the values of the parameters noted in Table I, it can be seen that Eq. (1) fits the data well up to 3% strain, after which the material behaves in an essentially perfectly plastic manner. The manufacturer's values for the elastic properties of the glass and the punch base, which was actually embedded in the Araldite, are also listed in Table I.

TABLE I
Material properties

Material	Young's modulus E (GPa)	Poisson's ratio ν	Yield stress σ_0 (MPa)	Hardening exponent n
Araldite	1.56	0.36	3.45	3.5
Glass	68.95	0.20	—	—
Steel	206.85	0.30	—	—

Measurement of normal crack opening displacements

The normal crack opening displacements (NCOD) were measured using crack opening interferometry.^{2,10} A schematic of the apparatus that was used for this study is shown in Figure 1b. The coherent light of the laser is reflected by the crack faces to produce two beams which interfere with one another, giving rise to light and

dark interference fringes. The fringes are loci of constant NCOD, Δw , and are resolved by a microscope focussed on the crack plane. The changing fringe patterns, as the specimen is loaded, are recorded through a video system which consists of a camera, timer, cassette recorder, analyzer and monitor. The components are used to determine the NCOD at various applied displacement levels up to and including the instant of crack initiation. For the particular arrangement used here,²⁰ the NCOD are given by

$$\Delta w = m\lambda/2 \quad m = 0, 1, 2, \dots \quad (2)$$

where m is the order of the dark fringes and λ is the wavelength of the illuminating beam.

An Argon Ion laser, having a wavelength $\lambda = 0.5145 \mu\text{m}$, was used and thus provided a resolution of $0.2573 \mu\text{m}$ in NCOD. In regions of higher displacement gradients, resolution was easily increased to $0.1287 \mu\text{m}$ by considering bright fringes in addition to the dark ones. The fact that fringes were formed at all indicates that cracks were coplanar to at least the same ($0.1287 \mu\text{m}$) degree. The fringes could be located to within $5 \mu\text{m}$ over a $500 \mu\text{m}$ field of view, a somewhat closer view of the crack front region than is provided by a number of other techniques.

The measurements of NCOD up to and including initiation were made over a range of fracture mode mixtures by conducting a series of experiments at various crack diameters. The displacement-controlled tests provided stable crack growth so that cracks, once initiated, could be arrested, thus allowing several experiments to be conducted on the same specimen. Very circular debonds were produced and radial profiles of NCOD at various levels of applied displacement are shown in Figure 3 for an intermediate crack diameter. A reliable indication of crack initiation was provided by comparing a number of profiles around an approximate initiation time. The values of NCOD and applied displacements at initiation are denoted by Δw_i and Δ_i , respectively, and it can be seen that there is some crack blunting associated with initiation. In all experiments there was initially some non-zero value of NCOD due to residual stresses and a small preload which was applied to ensure that, at all times, the crack was fully open right up to its front.²⁰ These were lumped into an equivalent residual applied displacement, Δ_R , whose determination is now described.

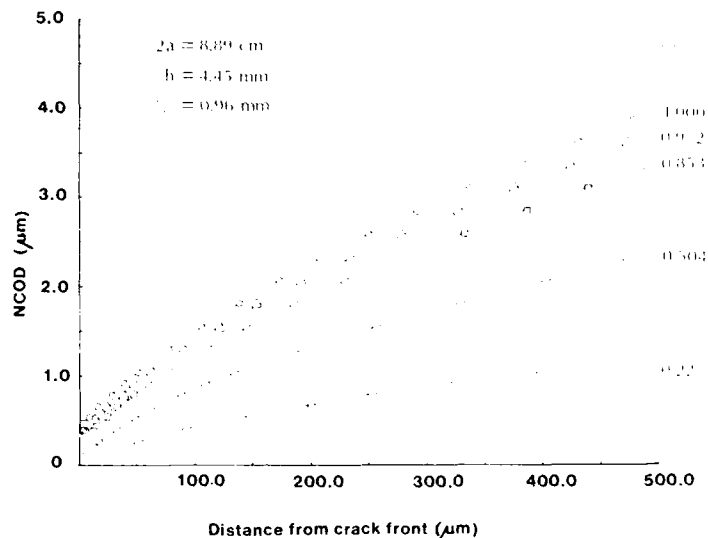


FIGURE 3 Radial profiles of NCOD at various levels of applied displacement.

The dependence of the NCOD on the applied displacements at various distances from the crack front can be examined by cross-plotting the data of Figure 3. The response determined in this way is shown in Figure 4 at 250, 150 and 25 μm from the crack front. As was indicated above, there was an initial crack opening for zero measured applied displacement. For relatively low levels of the applied displacement, the response is linear at all locations and can be extrapolated back to zero NCOD. Although the linear portions of the responses were chosen to pass through the same point at zero NCOD as they should, it can be seen that this was accomplished without unduly compromising the rest of the data. More weight was given to the response at 250 μm in selecting the point of intersection of the responses which was then considered to be the true zero state. A second abscissa originating from this point was then drawn to reflect the total applied displacements. All values of applied displacements quoted in the paper are referred to this measure. Thus, for example, the residual and critical values of applied displacement were, respectively, $\Delta_R = 0.25$ mm and $\Delta_c = 0.96$ mm. It can be seen that, as the applied displacements approach Δ_c , the

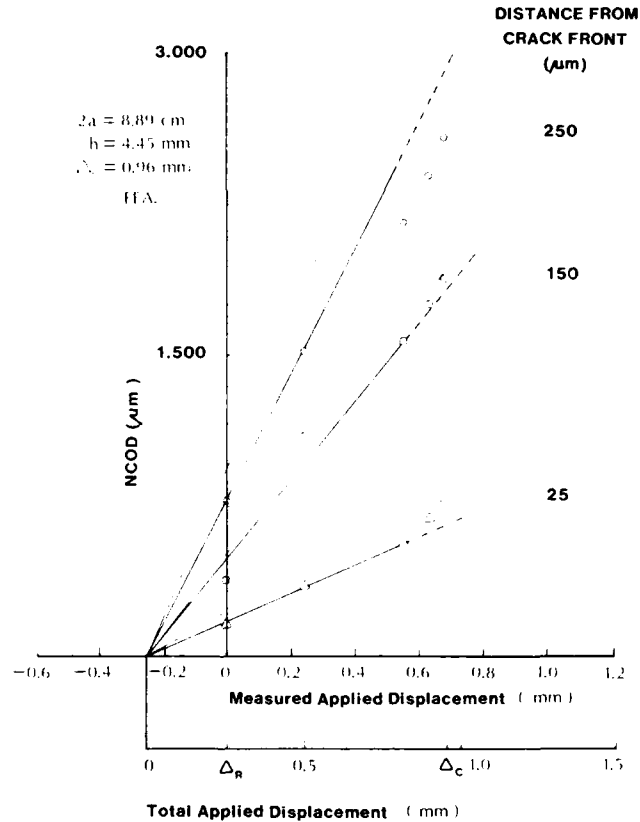
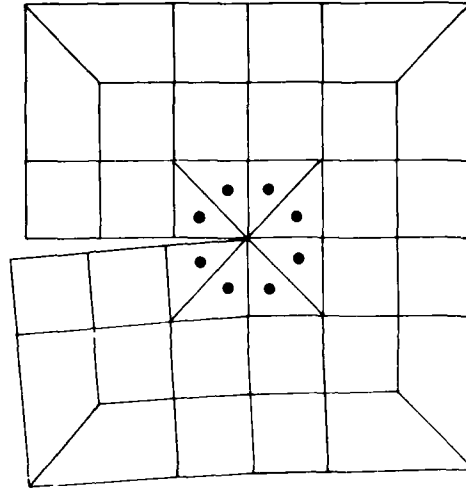


FIGURE 4 NCOD response at various locations from the crack front.

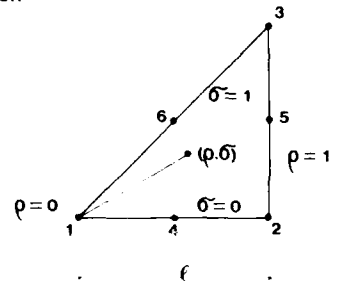
response departs from linearity with the extent of departure increasing with decreasing distance from the crack front.

Finite element analyses

Although it is clear from the results depicted in Figure 4 that non-linear effects are occurring close to the crack front, the analyses here were based, as a first step, on a linear material response using the finite-element code VISTA.¹⁸ Regions removed from the crack front were modelled using eight-node isoparametric quadratic quadrilaterals, while the crack front itself was surrounded (Figure 5)



(a) CRACK TIP MESH



(b) SINGULAR ELEMENT

FIGURE 5 Finite-element mesh close to the crack front.

by eight triangular elements of the variable singularity type.²¹ The element is conformable with isoparametric quadrilateral elements and also contains constant strain fields making it complete with respect to globally linear displacement fields. In the present study, the square-root singularity associated with cracks was selected so that the element captured the square root and linear terms in the expansions for displacements near the crack front. The degree of mesh refinement in the crack front region should, therefore, be chosen to reflect these effects and was thus the first consideration.

Mesh refinement studies were made for the 8.89 cm crack diameter considered in Figures 3 and 4. Axisymmetric analyses were conducted using the elastic properties listed in Table 1 for the Araldite layer, the glass substrate and the steel punch base. The total applied displacements, as derived from Figure 4, were considered to act uniformly over the steel punch. As can be seen from Figure 5, the off-hypotenuse sides of the singular elements were of the same length, l . The singular elements were surrounded by three rings of square quadrilateral elements with side lengths that were also equal to l . The element size outside this region was gradually increased. Four levels of mesh refinement were considered in which the side length, l , was a quarter, an eighth, a sixteenth and a thirty-second of the Araldite layer thickness, h . In some cases l was greater than the $500\text{ }\mu\text{m}$ field of view, and the NCOD, Δw , were derived from the shape functions, N_i , of the singular element and nodal point displacements, w_i , through the equation

$$\Delta w = \sum_{i=1}^6 N_i [w_i^{(2)} - w_i^{(1)}] \quad (3)$$

where the superscripts 1 and 2 refer to the Araldite and the glass, respectively. The shape functions are given in the Appendix and reflect a change in nodal numbering from the original.²¹

The NCOD near the crack front for the different levels of mesh refinement are compared with the measured values in Figure 6. The applied displacements that were required to produce these displacements were $\Delta = 0.227\Delta_c$, which were well within the region of linear response defined by Figure 4. It can be seen that, at larger distances from the crack front, the coarsest mesh gave rise to the largest crack opening displacements. The NCOD predicted by the two finest levels of mesh refinement were exactly the same, indicating that convergence was obtained for the mesh refinement level of at least $h/l = 16$. The measured NCOD are less than all solutions for distances from the crack front less than $100\text{ }\mu\text{m}$ and agree most closely with the mesh refinement level of $h/l = 8$ thereafter. A cross plot of the comparisons is shown in Figure 7 where the NCOD at 25, 100 and $250\text{ }\mu\text{m}$ are plotted against the applied displacements. The differences are small, but it is interesting to note that at $250\text{ }\mu\text{m}$ from the crack front the largest NCOD are predicted by the coarsest mesh, whereas the situation is reversed

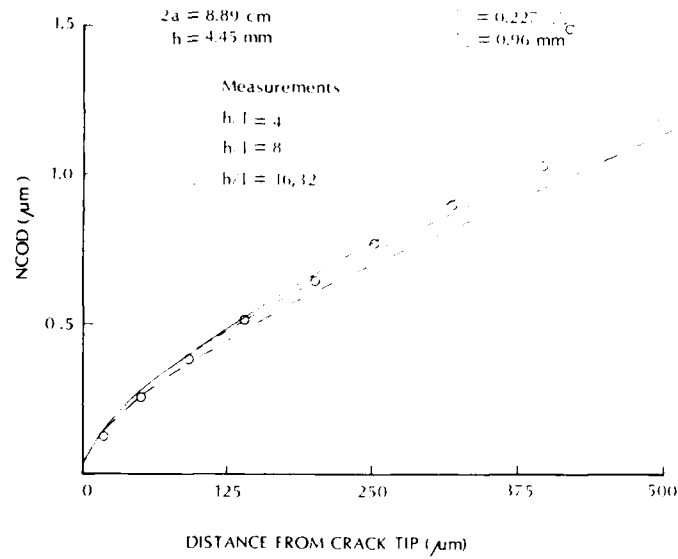


FIGURE 6 Effect of mesh refinement on predicted NCOD.

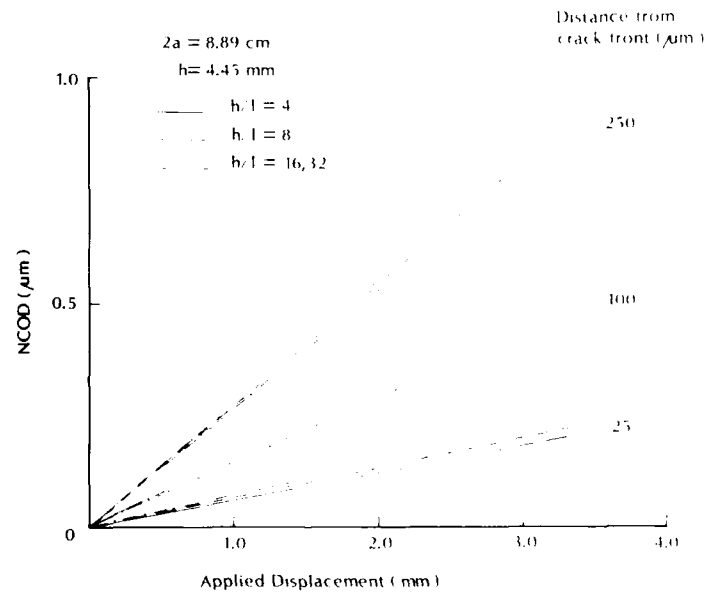


FIGURE 7 Effect of mesh refinement on compliance near the crack front.

at $25\text{ }\mu\text{m}$. The mesh refinement level in subsequent analyses was taken to be $h/l = 8$.

3 COMPARISON OF RESULTS

Crack initiation experiments were conducted over a range of crack diameters. For short cracks, there was little evidence of crack blunting at the instant of crack propagation. However, the extent of crack blunting did increase with increasing crack diameter and occurred at applied displacement levels that were lower than the critical value. In the region of blunting, double logarithmic plots of NCOD vs. distance from crack front²⁰ indicated a power law dependence with exponents that decreased from 0.5 as the crack diameter was increased. On the basis of elastic analyses, the increase in crack diameter is associated with a relative increase in mode II component. The following comparisons between measurements and finite-element solutions for NCOD were made for representative cases of short, intermediate and long crack diameters. The intermediate case is considered first since it has formed the basis of considerations so far.

A series of NCOD profiles are shown in Figure 8 for applied displacements ranging from the initial value up to the critical value. It can be seen that there is excellent agreement between measurements and predictions for applied displacements up to $0.5\Delta_c$. At higher applied displacements, the finite-element solutions predict larger values of NCOD far away from the crack front. However, very close to the crack front there is some evidence of crack blunting in the measured NCOD, making them larger than the finite-element predictions. When the results are compared in the cross plot (Figure 4) depicting NCOD as a function of applied displacements for various distances from the crack front, the slope of the fitted linear portion of the measured response is always less than the finite-element predictions. The cause of this difference could be due to errors in the measurement of crack diameter, NCOD and applied displacement, uncertainties in the modulus of the Araldite and assignment of Δ_R and, finally, the choice of mesh refinement level. Crack diameters were measured to within $25\text{ }\mu\text{m}$ and, during load application, changes of crack front location up to

$$2a = 8.89 \text{ cm} \quad , \quad h = 4.45 \text{ mm} \quad , \quad \Delta_c = 0.96 \text{ mm}$$

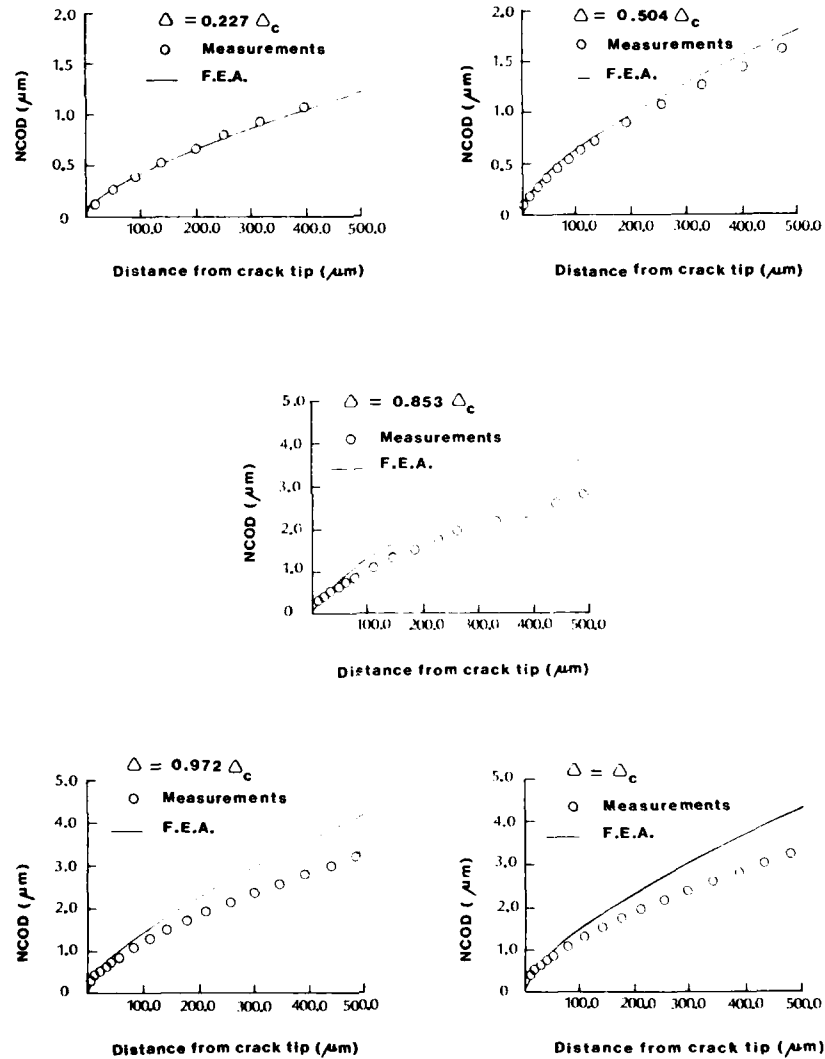


FIGURE 8 Comparison of measured and predicted values of NCOD for an intermediate crack diameter.

15 μm were sometimes observed. However, such variations did not change the predicted NCOD when accounted for in a check case. Uncertainties in NCOD are introduced in locating the fringes rather than through Eq. (2). However, the maximum possible error in fringe location is 1% which would not give rise to the noted differences. The measured value of the Araldite tensile modulus was 1.560 GPa. Some differences could arise from specimen to specimen. In order to obtain bounds on the effect of modulus, Araldite moduli of 0.693 and 6.93 GPa were considered. The effect on the response in the crack front region is shown in Figure 9 where it can be seen that the larger modulus gave rise to a larger slope. The factor of 10 difference in Araldite modulus produces similar differences in slope as were observed in Figure 4. However, it is unlikely that such variations in modulus would occur in practice.

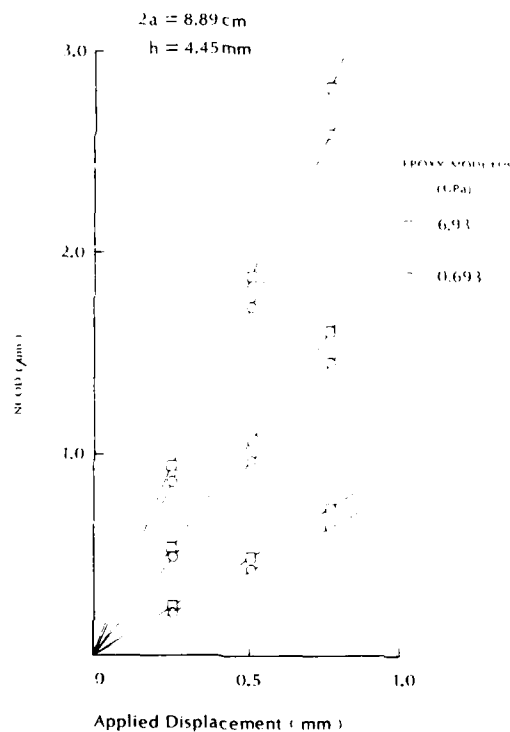


FIGURE 9 Effect of Araldite modulus on NCOD response.

The results of the mesh refinement study (Figure 7) indicate that the measurements and finite-element analyses would have been in slightly closer agreement had a mesh refinement level of $h/l = 16$ been used. The assignment of Δ_R in attempting to obtain the best linear fit to the measurements clearly affects the slopes of these lines. However, an assessment of the error in Δ_R is difficult to make because it was determined from a crossplot and therefore subject to a degree of arbitrariness. An attempt to remove arbitrariness was made by fitting lines having the slope given by the finite-element analysis to the measured values. Such a procedure did not give rise to a consistent value of Δ_R at the three locations from the crack front at which evaluations were made. However, the agreement between predicted and measured NCOD for $\Delta = \Delta_R$ (Figure 8) indicate that Δ_R was well chosen. The final possibility in accounting for the noted differences in slopes arises from the measurement of applied displacements. The resolution of the applied displacements was 0.1% of full scale which would not produce a notable difference. However, the increasing difference between predicted and measured NCOD with increasing applied displacement (Fig. 8) in regions far removed from the crack front leads us to suspect that the loading device was not sufficiently stiff. The suspicions are strengthened by later comparisons of the results from a short-diameter crack which presents the stiffest specimen to the loading device. A compliant loading device would give rise to measurement of applied displacements that were higher than those that were actually applied to the Araldite layer. Thus, since the predicted values of NCOD were obtained from the finite-element analyses based on the measured applied displacements, predicted NCOD would be higher than the measured NCOD. Thus, of the potential reasons for difference noted above, loading device compliance appears to be the most likely cause.

The slope differences are not the only differences in response that can be observed in Figure 4. There is some curvature to the measured response, indicating the presence of nonlinear effects. In this case, the departure from linearity starts at $0.85\Delta_c$ and is most apparent closer to the crack front. Nonetheless, when all effects are combined the comparisons in Figures 4 and 8 indicate a rather good (fortuitous) agreement between measured and predicted values of the critical NCOD up to $150 \mu\text{m}$ from the crack front.

Similar comparisons are made in Figures 10 and 11 for a short-diameter crack. NCOD profiles at various load levels are compared in Figure 10, where it can be seen that there is quite close agreement up to $0.62\Delta_c$. There is, however, a large difference between measurements and predictions of the critical NCOD. The reason for this difference can be seen more clearly when the results are cross-plotted in Figure 11. The departure of the measured NCOD from their linear fit initially follows the same pattern as before with an increase in slope. However, at initiation there is a

$$2a = 5.30 \text{ cm} , \quad h = 2.54 \text{ mm} , \quad \Delta_c = 1.39 \text{ mm}$$

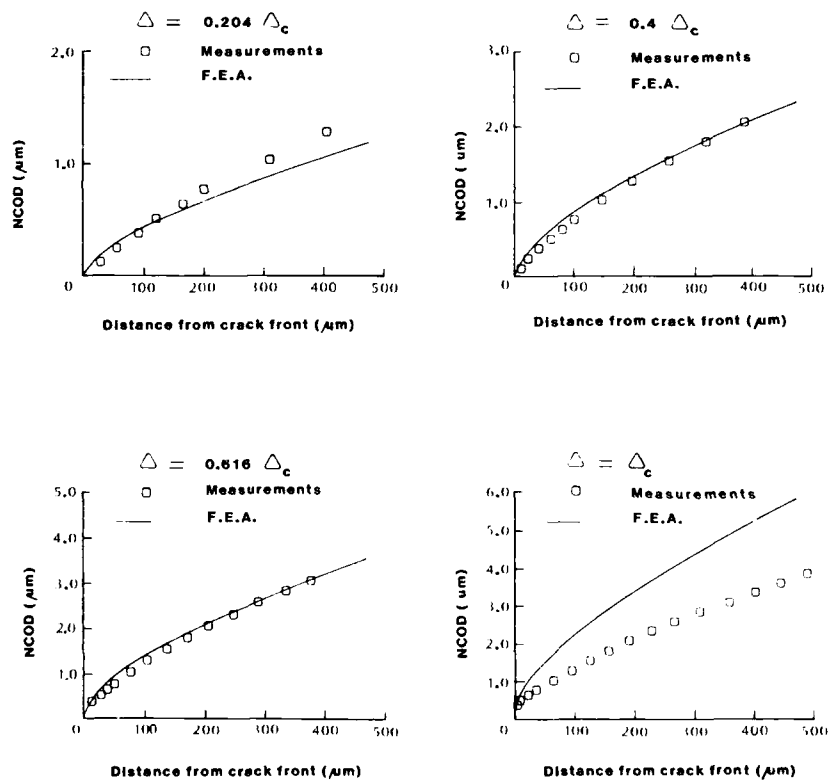


FIGURE 10 Comparison of measured and predicted NCOD profiles for a short crack diameter.

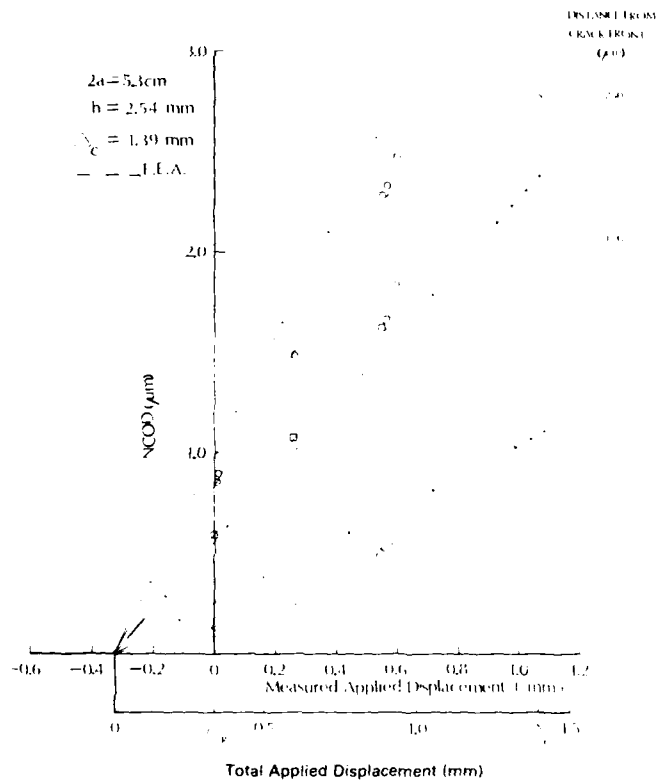


FIGURE 11 Comparisons of NCOD response for a short crack diameter.

large jump in applied displacement for a relatively small change in NCOD, so that the slope decreases. Since the shortest crack presents the stiffest specimen to the loading device, it is suspected that the large apparent applied displacement is due to insufficient stiffness in the loading device. The initial nonlinearity in the crack tip response was due to some highly localized crack blunting.

The scale of crack blunting was much larger for the large-diameter cracks as can be seen from the examples of NCOD profiles shown in Figure 12. In this case, for distances greater than about $35 \mu\text{m}$ from the crack front, the finite-element solutions for the NCOD were consistently higher than the measured values for all load cases. The foregoing was also true closer to the crack front

$$2a = 11.83 \text{ cm}, \quad h = 4.45 \text{ mm}, \quad \Delta_c = 1.90 \text{ mm}$$

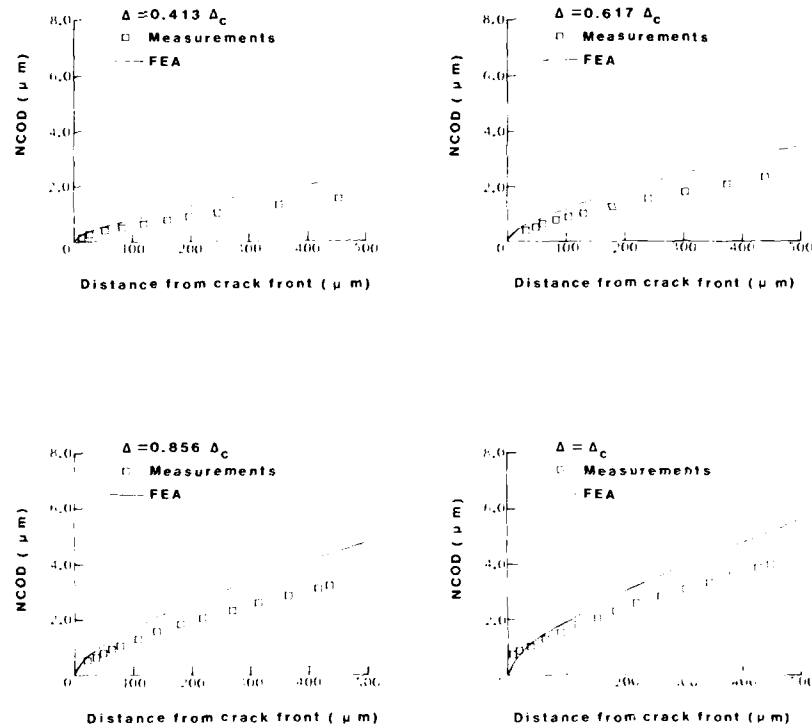


FIGURE 12 Comparison of measured and predicted NCOD profiles for a large crack diameter.

except at the critical load where the blunting at the crack front reversed the situation. In the cross plot of the data (Figure 13), the slopes of the predicted responses are higher than those of the linear fits to the measurements except at $25 \mu\text{m}$ from the crack front. The increased level of crack blunting is manifest in a higher degree of nonlinearity than was evident in the other two crack-diameter cases that were considered.

In all three cases, it can be concluded that, at load levels approaching the critical values, the finite-element solutions for the NCOD are higher than the measured values except in regions of crack blunting. The main reasons for this behavior are loading-

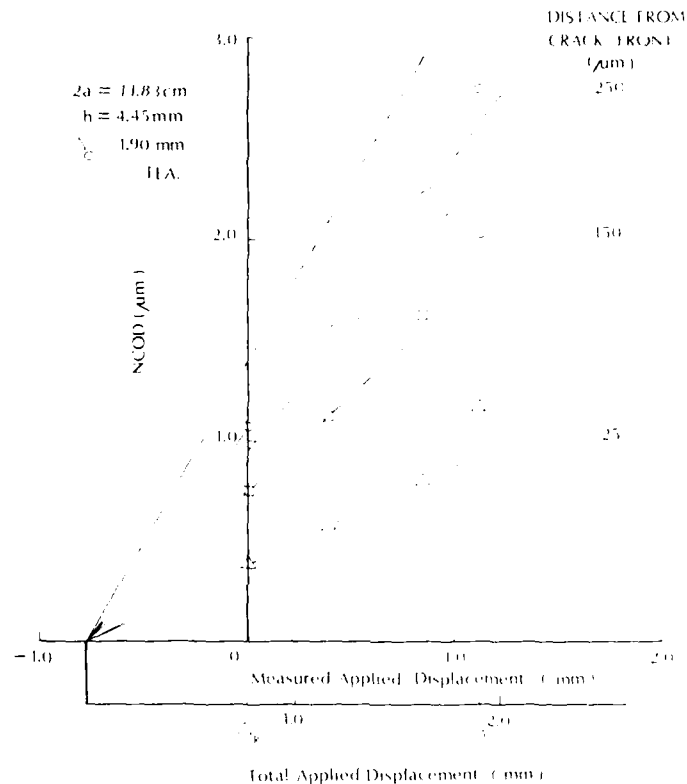


FIGURE 13 Comparisons of NCOD response for a large crack diameter.

device compliance and non-linear effects in the material behavior in the crack front region. In the first case, excessive loading-device compliance leads to measurements of applied displacement that are higher than those that are actually applied to the Araldite layer. Since these overestimates of actual applied displacement are then used as the boundary conditions in the finite-element analyses, the finite-element solutions for NCOD will be correspondingly higher than the measured NCOD. In the case of material non-linear behavior, a plastic zone is produced in the crack front region. In the simplest way of accounting for this, an effective crack is considered whose diameter is made up of the actual crack diameter plus the plastic zone length. The larger crack diameter results in a more

compliant layer which leads to measured NCOD and slopes that are larger than those obtained on the basis of linear analyses.

However, the higher loads are of most interest, particularly for examining mixed-mode fracture parameters and criteria for crack initiation. While the confidence in the measured NCOD is high, they do not, by themselves, provide enough information to determine mixed-mode fracture parameters. On the other hand, although the finite-element solutions provide not only the NCOD but also tangential crack opening displacements (TCOD), stresses and strains for the examination of any fracture parameter, they were based on overestimates of applied displacements and linear material behavior, and were not in agreement with measured NCOD at the critical load. Nonetheless, for purposes of examination of linear elastic fracture mechanics parameters, a hybrid approach is suggested wherein the NCOD from the finite-element solutions are matched with measurements of NCOD outside the plastic region through a simple scaling. The finite-element solutions thus scaled can then be used to examine any mixed-mode fracture parameter of interest.

In order to effect the scaling, the measurements of and finite-element solutions for the critical NCOD were fit to the relation

$$\Delta w_c = Ar^{1/2} + Br \quad (4)$$

through a least-squares procedure where the measurements were taken in the region $r > 25 \mu\text{m}$. The coefficients A and B thus determined are noted in Table II for the three crack diameters considered here. The correlation coefficients for the measured NCOD are also noted and indicate that Eq. (4) is a reasonable representation. The ratios of the coefficients of the square root and

TABLE II
Comparison of coefficients in near tip expansions for critical NCOD

Crack diameter (cm)	Measurement			Finite element		$\frac{A_F}{A_M}$	$\frac{B_F}{B_M}$	Scale factor
	A_M	B_M	r^a	A_F	B_F			
5.30	1.228 E-1	3.287 E-3	0.96	1.872 E-1	2.836 E-3	2.524	0.863	0.753
8.89	1.294 E-1	2.162 E-3	0.99	1.337 E-1	4.073 E-3	1.118	1.884	0.782
11.89	1.486 E-1	1.707 E-3	0.95	1.503 E-1	4.393 E-3	1.011	2.574	0.799

^a r is the correlation coefficient.

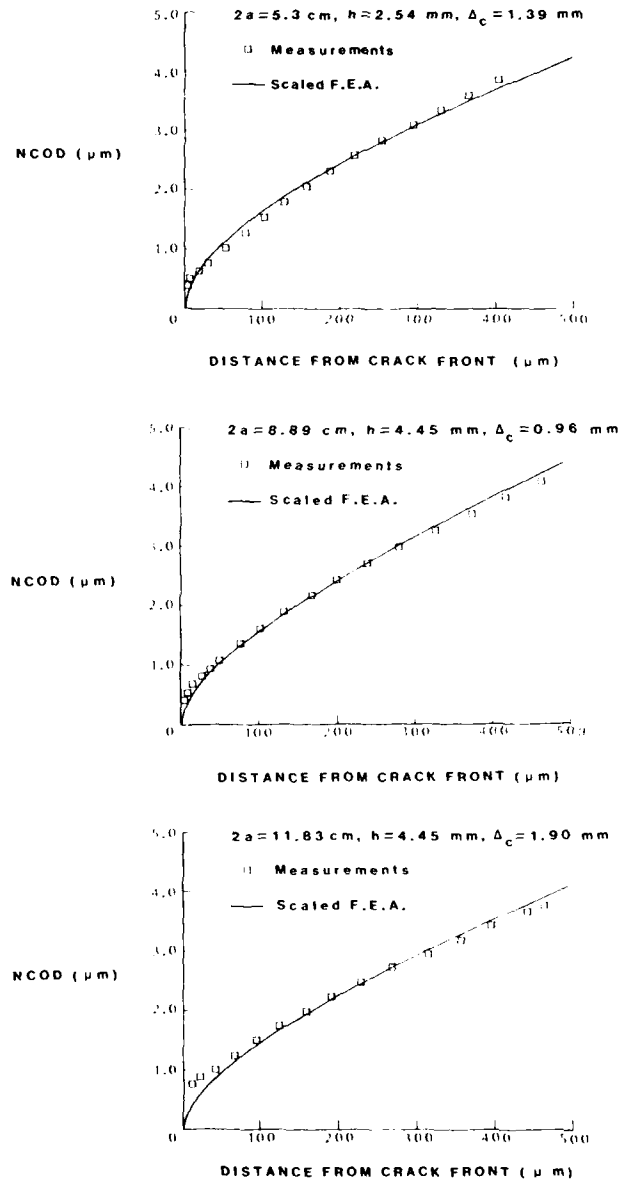


FIGURE 14 Comparison of scaled finite-element solutions and measurements of critical NCOD for three crack diameters.

linear terms based on the finite-element solution and the measurements are also noted in Table II. It can be seen that, as the crack diameter becomes larger, the agreement in the square root coefficient improves while the ratio B_F/B_M also becomes larger. The shapes of the NCOD profiles are therefore different. For distances from the crack front less than $5\text{ }\mu\text{m}$, the contribution to the NCOD from the linear term in (4) was less than 5% of the square root term in all cases. However, at $500\text{ }\mu\text{m}$, the contribution from the linear term was as high as 50%. Thus, a simple scaling of the finite-element solution by the ratio A_F/A_M , for example, would not produce a good match with the measured NCOD over the whole field of view. Since the NCOD response was linear for distances from the crack front greater than $250\text{ }\mu\text{m}$ (and linear elastic fracture parameters are often evaluated in this region using other methods), the NCOD were matched at this point. The scale factors that were applied to the finite-element solution in order to match the NCOD are noted in Table II. It can be inferred from the scale factors that the original finite-element solutions were 20–25% higher than the measured critical NCOD at this point. The matched finite-element solutions are compared with the measured critical NCOD in Figure 14 for the three crack diameters considered here. Based on the fit to the measurements, the scaled finite-element solutions are first lower and then higher than the measured NCOD for the intermediate and larger crack diameter. The situation is reversed for the short-diameter crack, but the difference in all cases was less than 8%. The difference between the scaled finite-element solution and the actual displacements in the blunting region is, of course, even greater.

4 CONCLUSIONS

The results of crack initiation experiments for mixed-mode interfacial crack growth that were reported in a previous paper²⁰ were compared with analyses that were made using the finite-element method. The circular cracks resulting from a point-loaded blister configuration allowed axisymmetric analyses to be conducted. The analyses were based on the measurements of applied displacements that were made during the crack initiation experiments. The stress-strain behavior of the epoxy layer was considered to be

linearly elastic, and singular elements were used around the crack front. The optimum size of the singular element and surrounding eight-node quadrilaterals was found to be one-sixteenth of the epoxy layer thickness.

The basis of comparison between the finite-element solutions and the experiments was the normal crack opening displacements (NCOD) near the crack front which had been measured using optical interferometry. The comparisons were made for three different crack diameters and at various applied displacement levels up to and including crack initiation. Short, intermediate and long crack diameters were chosen because increasing amounts of crack blunting had been associated with them during the experiments. The closest agreement between finite-element solutions and measurements was obtained at the lower levels of applied displacements. Various potential causes of the differences noted at higher load levels were considered. The most likely causes were found to be loading-device compliance and nonlinear material behavior in the crack front region. The feasibility of a matching procedure was explored that would allow the finite-element solutions to be used to examine mixed-mode fracture parameters and criteria.

Acknowledgements

This work was supported by the Solid Mechanics Division of the National Science Foundation (Grant MEA-8402064) and the Department of Aerospace Engineering and Engineering Mechanics, The University of Texas at Austin; the support is gratefully acknowledged. The accurate and timely typing of the manuscript by Lynn McKay is also greatly appreciated.

References

1. G. P. Anderson, K. L. DeVries and M. L. Williams, *Int. J. of Fracture* **10**, 565-583 (1974).
2. D. R. Mulville, D. L. Hunston and P. W. Mast, *J. Eng. Mat. Tech.* **100**, 25-31 (1978).
3. G. P. Anderson, K. L. DeVries and M. L. Williams, *J. Colloid and Int. Sci.* **47**, 600-609 (1974).
4. E. E. Gdoutos and G. Papakaliatakis, *Engineering Fracture Mechanics* **6**, 177-187 (1982).
5. P. S. Theocaris and C. A. Strassinakis, *Engineering Fracture Mechanics* **14**, 363-372 (1981).
6. D. L. Davidson, D. R. Williams and J. E. Buckingham, *Experimental Mechanics* **23**, 242-248 (1983).

7. D. Post, *Experimental Mechanics* **23**, 203-210 (1983).
8. M. E. Fournery, in *Speckle Metrology*, R. K. Erf, Ed. (Academic Press, New York, 1978).
9. E. Sommer, *Eng. Fract. Mech.* **1**, 705-718 (1970).
10. K. M. Liechti and W. G. Knauss, *Experimental Mechanics* **22**, 262-269 (1982).
11. A. Piva and E. Viola, *Engineering Fracture Mechanics* **13**, 143-174 (1980).
12. J. K. Knowles and E. Sternberg, *Int. J. Solids and Structures* **11**, 1173 (1975).
13. S. G. Sawyer and R. B. Anderson, *Eng. Fract. Mech.* **4**, 605-616 (1972).
14. K. Y. Lin and J. W. Mar, *Int. J. Fracture* **12**, 521-531 (1976).
15. C. C. Hong and M. Stern, *J. Elasticity* **8**, 21-34 (1978).
16. R. E. Smelser, *Int. J. Fracture* **15**, 135-143 (1979).
17. J. F. Yau and S. S. Wang, *Eng. Fracture Mechanics* **20**, 423-432 (1984).
18. E. B. Becker, *et al.*, "Viscoelastic Stress Analysis Including Moisture Diffusion for Adhesively Bonded Joint", Air Force, Wright Aeronautical Lab. Report #AFWAL-TR-84-4057 (1984).
19. F. Erdogan and K. Arin, *J. Eng. Sci.* **10**, 115-125 (1972).
20. K. M. Liechti and E. C. Hanson, "An Examination of Mixed-Mode Debonding in the Blister Test", to be published in *ASTM STP xxx* (1987), International Symposium on Adhesively Bonded Joints: Testing, Analysis and Design.
21. M. Stern, *Int. J. for Num. Meth. in Eng.* **14**, 409-421 (1979).

Appendix

INTERPOLATING SHAPE FUNCTIONS FOR SINGULAR ELEMENTS

For singularities of strength λ , the shape functions for the singular element are given by the equations below. The nodal numbering is shown in Figure 5.

$$N_1(\rho, \sigma) = 1 + \frac{2 - 2^{1-\lambda}}{2^{1-\lambda} - 1} \rho - \frac{1}{2^{1-\lambda} - 1} \rho^\lambda$$

$$N_2(\rho, \sigma) = \frac{2^{1-\lambda}}{2^{1-\lambda} - 1} (1 - \sigma)\rho - \left(\frac{1}{2^{1-\lambda} - 1} 2\sigma \right) (1 - \sigma)\rho^\lambda$$

$$N_3(\rho, \sigma) = \frac{2^{1-\lambda}}{2^{1-\lambda} - 1} \sigma\rho - \left(\frac{1}{2^{1-\lambda} - 1} + (1 - \sigma) \right) \sigma\rho^\lambda$$

$$N_4(\rho, \sigma) = \frac{-2}{2^{1-\lambda} - 1} (1 - \sigma)\rho + \frac{2}{2^{1-\lambda} - 1} (1 - \sigma)\rho^\lambda$$

$$N_5(\rho, \sigma) = 4\sigma(1 - \sigma)\rho^\lambda$$

$$N_6(\rho, \sigma) = \frac{-2}{2^{1-\lambda} - 1} \sigma\rho + \frac{2}{2^{1-\lambda} - 1} \sigma\rho^\lambda$$

SESSION OF THE
UNITED STATES. II

Anisotropic Wetting of Liquids on Finely Grooved Surfaces†

H. SCHONHORN‡

AT & T Bell Laboratories, Murray Hill, New Jersey 07974, U.S.A.

A photolithographically-prepared, parallel-grooved surface on silica has been employed as a model to study the influence of roughness on the spreading equilibrium of liquid drops. The equations generated by Oliver, Huh and Mason for cylindrically shaped drops were extended to account for wetting by liquid crystals. The observed drop shapes were dependent upon surface roughness. The equilibrium contact angles on a smooth surface can be calculated from the roughness, contact angles both parallel and perpendicular to the grooves, and the drop shape. Reasonably good agreement with experimental contact angles was obtained.

KEY WORDS Anisotropic wetting; contact angles; grooved surfaces; liquid crystals; periodic roughness; spreading equilibrium.

INTRODUCTION

Surfaces with periodic roughnesses and specific surface interactions appear to be able to orient and align liquid crystal molecules. Recently, Berreman¹ and Wolff, *et al.*,² have suggested that alignment of liquid crystal molecules on surfaces of microscopic parallel grooves is associated with an elastic distortion energy, which is a function of the surface contour and the average elastic modulus of the liquid crystal. Surfaces formed either by oblique evaporation of SiO_2 ³ or rubbing,⁴ are uncontrolled and difficult to reproduce or quantify. By using gratings with grooves of known dimension, which are fabricated using conventional photo-

† Presented at the Tenth Annual Meeting of the Adhesion Society, Inc., Williamsburg, Virginia, U.S.A., February 22-27, 1987.

‡ Present address: Kendall Company, 17 Hartwell Avenue, Lexington, MA 02173, U.S.A.

lithographic techniques, Flanders, Shavers and Smith⁵ have produced specific alignments of liquid crystals.

Although our primary reason for investigating grooved surfaces is their potential ability to orient liquid crystals, our initial effort is directed to understanding the wetting of these surfaces by liquid crystals. Perhaps the most careful and quantitative examination of the wetting by liquids on well-characterized roughened surfaces is due to Johnson and Dettre^{6,7,8} and more recently to Oliver, Huh and Mason (O, H and M).⁹ These authors (O, H and M) have utilized a mechanistic rather than a thermodynamic approach to discuss the wetting of parallel-grooved surfaces. Under certain conditions, liquid drops become distorted resulting in elongated shapes. For the almost spherical drop, on a parallel grooved surface, the equation of Cassie and Baxter¹⁰ appears valid. However, O, H and M find for other types of roughened surfaces the general applicability of the Cassie-Baxter equation is not warranted. From a balance of interfacial forces, O, H and M derive an expression for cylindrically shaped drops which relates θ_a , the contact angle parallel to the groove direction, to the surface roughness. Although O, H and M cite that their elongated drops are cylindrical, we have observed, for liquid crystal drops, that even for ratios of length to width of at least 5, the drops still appeared to have spherical caps when viewed parallel or perpendicular to the grooved surface. Consequently, we have modified the expressions derived by O, H and M to include both radii of curvature.

Mathematical analysis

O, H and M⁹ considered a balance of forces for spherical and cylindrical drops on parallel grooved surfaces across a plane bisecting the drops lengthwise (Figure 1). Acting across the whole cross sectional area A of the bisected drop, the capillary pressure ΔP is opposed by surface tension forces, γ , of the free liquid surface pulling over its circumference S normal to the cross-section. In addition, there will be a horizontal component of γ acting on the solid locally along the contact line, resulting in

$$\Delta PA - \gamma S - \gamma L_{LV} + \gamma L_{SL} \cos \theta_0 = 0 \quad (1)$$

where θ_0 is the equilibrium contact angle for a smooth surface and

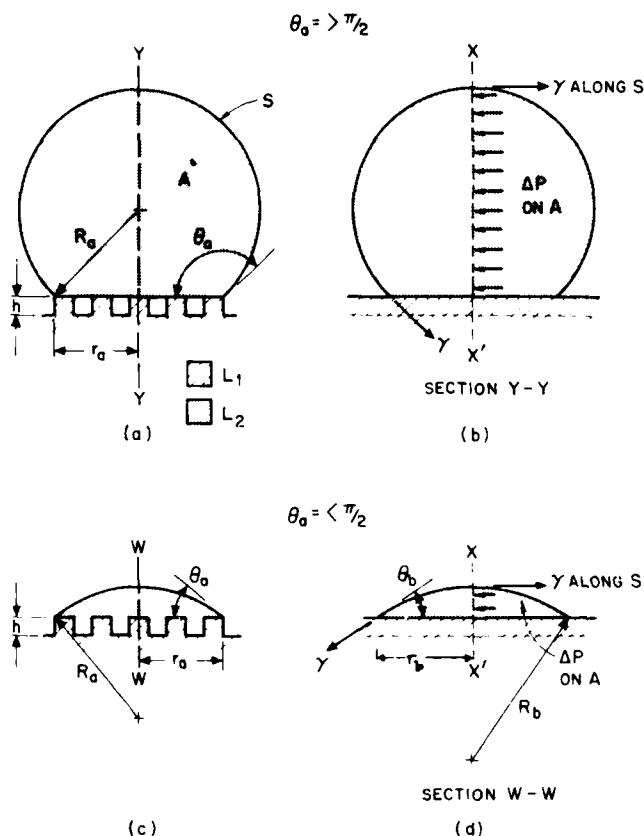


FIGURE 1 Equilibrium of liquid drops on parallel-grooved surfaces. (a) Cross-sectional view at the bisecting plane (shown by XX' in (b)) of a spherical drop. For low-wetting liquids ($\theta_0 > 90^\circ$), a composite surface is formed on the solid consisting of solid-liquid and liquid-void (dotted) interfaces. (b) Side view of the spherical drop. Broken lines indicate the contact line for the liquid-void interface and drop profile over the grooved area. (c) Cross-sectional view and (d) side view of a cylindrical drop. For high-wetting liquids ($\theta_0 < 90^\circ$) a non-composite surface is formed.

L_{LS} and L_{LV} are the respective cross-sectional arc lengths of solid-liquid and liquid-void interfaces at the bisecting plane. A similar argument, using a free energy approach, likewise yields Eq. 1.¹¹ Since we observed the drops to be approximately spherical caps both parallel and perpendicular to the grooved surface, the capillary

pressure to a first approximation may be written as

$$\Delta P = \gamma \left(\frac{1}{R_a} + \frac{1}{R_b} \right) \quad (2)$$

where R_a and R_b are the two radii of curvature, a denotes the direction parallel to the groove and b is perpendicular to the groove direction. A complete analysis of the surface contour of the drop is beyond the scope of the present study. From simple geometry, Figure 1, we obtain,

$$\begin{aligned} A &= R_a^2 [\theta_a - \sin \theta_a \cos \theta_a] \\ S &= 2R_a \theta_a \\ r_a &= R_a \sin \theta_a \\ r_b &= R_b \sin \theta_b \end{aligned} \quad (3)$$

where θ_a and θ_b are the contact angles parallel and perpendicular to the groove direction, respectively. Inserting Eqs. 2 and 3 into Eq. 1 yields

$$\begin{aligned} \left[\frac{L_{SL} \cos \theta_0}{2r_a} - \frac{L_{LV}}{2r_a} \right] &= \frac{1}{2} \left[\cos \theta_a + \frac{\theta_a}{\sin \theta_a} \right] \\ &+ \frac{1}{2} \left(\frac{r_a}{r_b} \right) \left(\frac{\sin \theta_b}{\sin \theta_a} \right) \left[\cos \theta_a - \frac{\theta_a}{\sin \theta_a} \right] \end{aligned} \quad (4)$$

which differs from the equation of O, H and M by the last term on the right hand side of Eq. 4. In the two limiting cases when $R_a = R_b$ and $R_b = \infty$, Eq. 4 yields the equations derived by O, H and M.⁹

Clearly, when $R_a = R_b$,

$$\frac{L_{SL} \cos \theta_0}{2r_a} - \frac{L_{LV}}{2r_a} = \cos \theta_a \quad (5)$$

Equation 5 is the Cassie and Baxter equation for composite surfaces. If there is no void space ($L_{LV} = 0$), $L_{SL}/2r_a$ becomes the conventional area ratio and Eq. 5 reduces to the Wenzel relation.¹² O, H and M state that the Cassie-Baxter equation is valid only for parallel grooves. The general application for Eq. 5 for other types of roughened surfaces is not warranted. If, as in the work of O, H

and M , R_b is considered infinite, the drop being truly cylindrical,

$$\frac{L_{SL} \cos \theta_0}{2r_a} - \frac{L_{LV}}{2r_a} = \frac{1}{2} \left[\cos \theta_a + \frac{\theta_a}{\sin \theta_a} \right] \quad (6)$$

we obtain Eq. 3 of O, H and M.⁹

In the experiments described below, we test the applicability of Eq. 4 for the wetting of modified silica surfaces by liquid crystals, glycerol, and mercury. In addition, we re-examine the earlier data of Good, *et al.*,¹³ and show how use of Eq. 4 may account for their observed anisotropic wetting behavior.

EXPERIMENTAL

(a) Surface preparation

Parallel-grooved surfaces were prepared on silica using conventional photolithographic techniques.¹⁴ Four distinct regions of varying groove separations were prepared on one piece of silica. Figure 2 is a composite showing the uniformity of the four regions. The array is a square grating with periodicity (ridges and valleys) varying from 2 to 5 μm and depth of 1 μm . Clearly, the photolithographic techniques used for forming these surfaces yield an array of parallel grooves. Since the liquid crystals and glycerol will spread on silica along the groove direction, not yielding discrete elongated drops, the silica surfaces were rendered oleophobic by depositing $\sim 40 \text{ \AA}$ of a fluoropolymer. The thickness of the fluoropolymer, which is formed by exposing C_2F_4 to a glow discharge,¹⁵ was monitored by the change in frequency of a quartz crystal.

(b) Drop formation

To ascertain the effect of the grooved surface on the shape of the sessile drop, glycerol, mercury and two liquid crystals were employed. Small drops were placed onto these surfaces from a hypodermic needle. The glycerol has a surface tension of 63.4 mJ/m^2 and a viscosity of 9.45 p at 23°C . P'-methoxybenzylidene-p-n-butylaniline (MBBA) has a surface tension of 30 mJ/m^2 and a viscosity of $\sim 1.0 \text{ p}$ at 23.5°C . Licristal-Nematic

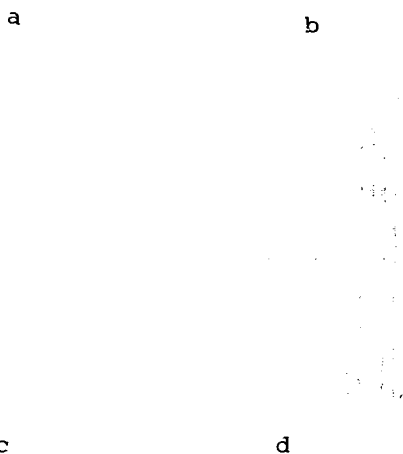


FIGURE 2 Parallel grooved square grating in silica. Four different surface roughnesses are represented. (a) $R = 1.20$, (b) $R = 1.25$, (c) $R \approx 1.33$, (d) $R = 1.50$. $R = 1 + h/L$.

Phase V is a mixture of liquid crystals having a surface tension of 30 mJ/m^2 and viscosity similar to MBBA. Mercury has a surface tension of 485 mJ/m^2 and a viscosity of $\sim 0.02p$ at 23°C . The surface tensions of the liquid crystals and glycerol were measured using a Du Nuoy tensionmeter. The surface tension of mercury was taken from the literature.

(c) Contact angle measurements and drop dimensions

Contact angles were measured parallel and perpendicular to the groove direction as well as on the smooth surface using a Rame-

Hart contact angle goniometer. The dimensions of the drops were measured from photographs taken at $10\times$ with a Polaroid camera. As in the study of O, H and M, drop sizes were sufficiently small such that gravitational effects were negligible and therefore excluded from consideration.

Contact angles were measured on both sides of the drop and the average values reported. The average deviation for the contact angle of liquids on the fluoropolymer modified silica is $\leq 2^\circ$.

RESULTS AND DISCUSSION

When silica surfaces were used without the deposited fluoropolymer, we noted, as did O, H and M, that tongues of liquid extended ahead of the drop in the groove (Figure 3). However, with the fluoropolymer coating, we observed no extension of liquid beyond the drop perimeter.

Figures 4-7 illustrate the effect of uniform surface roughness on the wetting of two liquid crystals, glycerol and mercury. For $\theta_0 < 90^\circ$, the greater the surface roughness, $(1 + h/L)$, the more

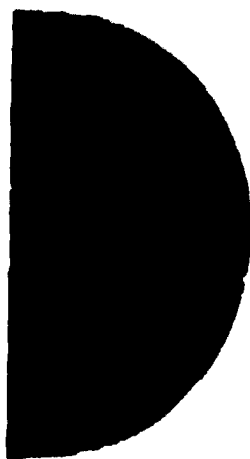


FIGURE 3 Tongues of liquid penetrating channels.

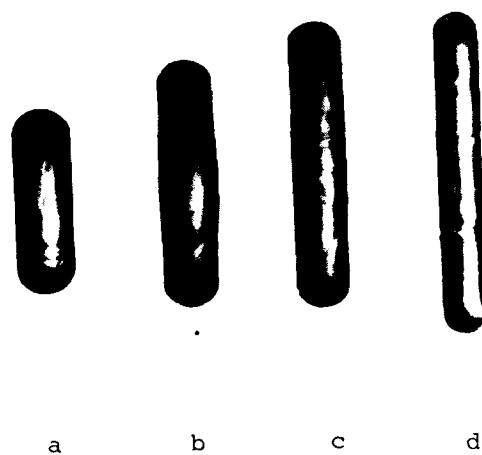


FIGURE 4 Wetting by MBBA on fluoropolymer coated silica. Surfaces are those represented in Figure 2.

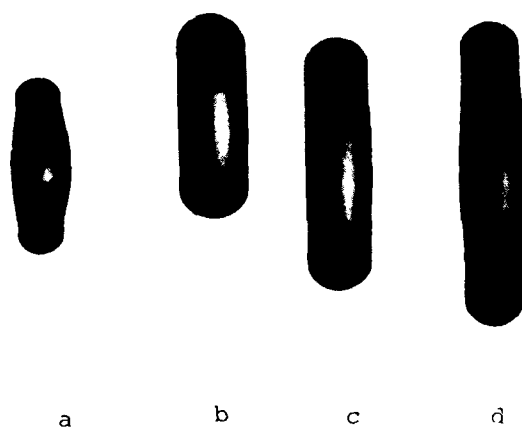


FIGURE 5 Wetting by Licristal-Nematic Phase V on fluoropolymer coated silica. Surfaces are those represented in Figure 2.

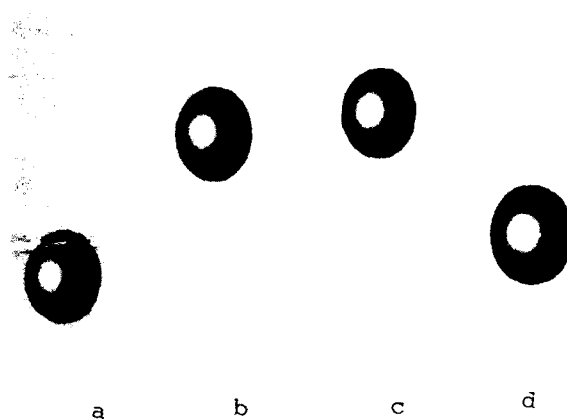


FIGURE 6 Wetting of Glycerol on Fluoropolymer coated silica. Surfaces are those represented in Figure 2.

pronounced the extent of drop elongation (see derivation in the appendix). Initially, we employed the analysis of O, H and M, but the computed θ_0 values were inconsistent. We were able to account for the discrepancy by including in the analysis the contact angle both parallel and perpendicular to the groove direction as well as the ratio of the drop diameters (Eq. 4). The data in Table I in

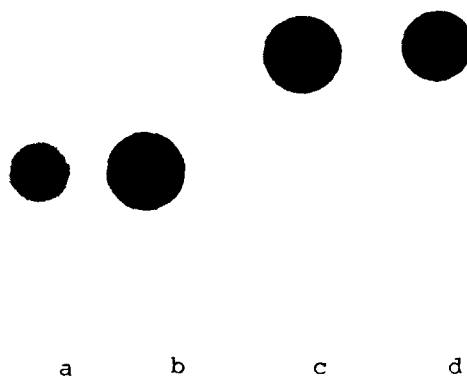


FIGURE 7 Wetting by mercury on fluoropolymer coated silica. Surfaces are those shown in Figure 2.

TABLE I
Wetting of anisotropic drops of liquids on a fluoropolymer coated square grating on silica

Liquid	L_1	L_2	h	R	$2r_a$	$2r_b$	θ_a	θ_b	θ_{calc}
	μm	μm	μm		mm	mm			
MBBA	5	5	1	1.20	0.95	3.05	110	47	62
	4	4	1	1.25	1.00	4.05	109	49	61
	3	3	1	1.33	0.90	4.70	120	43	63
	2	2	1	1.50	0.73	5.25	120	35	63
								$(\theta_0)_{exp}$	61
Licristal-Nematic Phase V	5	5	1	1.20	0.98	2.85	122	58	67
	4	4	1	1.25	1.15	3.35	120	55	67
	3	3	1	1.33	1.10	4.10	118	52	63
	2	2	1	1.50	1.10	4.95	117	48	64
								$(\theta_0)_{exp}$	62
Glycerol	5	5	1	1.20	1.23	1.48	125	105	95
	4	4	1	1.25	1.23	1.50	125	111	88
	3	3	1	1.33	1.20	1.45	125	112	87
	2	2	1	1.50	1.35	1.63	126	111	92
								$(\theta_0)_{exp}$	95

conjunction with Eq. 4 are used to compute the equilibrium contact angles for a smooth surface, θ_0 . The agreement is quite satisfactory when compared to the measured θ_0 .

When the data of Table I were included in Figure 8, (Figure 5 of Reference 9), we observed discrepancies for $\theta_a \sim 90^\circ$.

From Eq. 4, if $\theta_a = 90^\circ$,

$$\frac{L_{SL}}{2r_a} \cos \theta_0 - \frac{L_{LV}}{2r_a} = \frac{\pi}{4} \left[1 - \frac{r_a}{r_b} \sin \theta_b \right] \quad (7)$$

For a parallel grooved surface, when $\theta_a \sim 90^\circ$, we find that $\theta_b < \theta_a$ and $r_a < r_b$. Under these circumstances, Eq. (7) predicts

$$\frac{L_{SL}}{2r_a} \cos \theta_0 - \frac{L_{LV}}{2r_a} < \pi/4 \quad (8)$$

which is confirmed by plotting the data of Table I in Figure 8.

Equation (A.5) suggests that for spherical drops on parallel-grooved surfaces, where the number of grooves, $N \gg 1$, $L_{SL} = L_{LV}$ and $\theta_0 > 90$, the contact angle of a liquid on the roughened surface

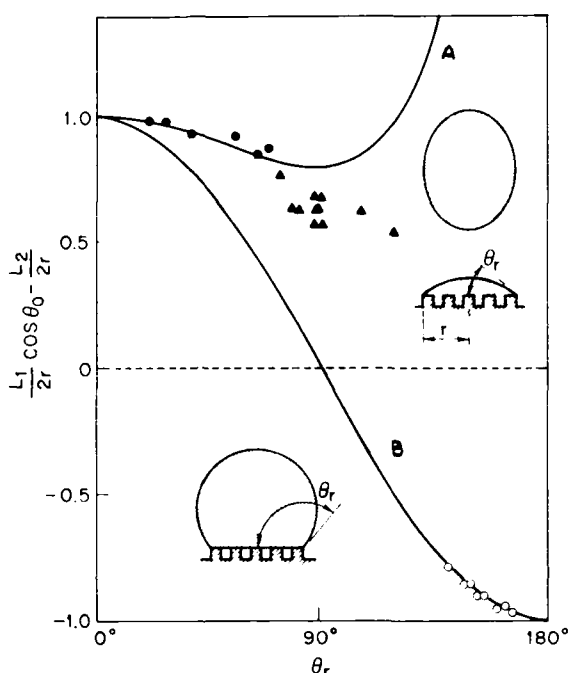


FIGURE 8 Measured values of the apparent advancing contact angle θ_a for approximately spherical drops of mercury (open points) and for nearly-cylindrical drops of PPE (closed points). The solid lines are calculated from Eq. (2) (curve A), and Eq. (3) (curve B), both of Ref. 9. Note for curve A, when $\theta_r < 90^\circ$, $L_{LV}/2r$ becomes zero and Eq. (2)⁹ reduces to Wenzel's equation. The triangles are from this study.

is independent of the roughness. To test this hypothesis, drops of mercury were placed on the roughened surfaces and the values of θ_a measured. The results in Table II lend credence to the analysis. Indeed, the values of θ_a are essentially independent of the surface roughness. When θ_0 is close to 90° , as in the case of glycerol, there is some deviation from being spherical the drop is slightly elliptical.

Since we observed that the drop is a spherical segment both parallel and perpendicular to the groove direction, it is clear from Figure 1 that

$$\frac{h_a}{r_a} = \frac{1 - \cos \theta_a}{\sin \theta_a}$$

TABLE II
The wetting of mercury on the square
array fluoropolymer modified silica surface

Roughness (1 + h/L)	r_a/r_b	θ_a	θ_b
1.00	1.0	130	130
1.20	1.0	141	124
1.25	1.0	142	125
1.33	1.0	145	130
1.50	1.0	148	137

and

$$\frac{h_b}{r_b} = \frac{1 - \cos \theta_b}{\sin \theta_b}$$

where h is the depth of the groove. Since $h_a = h_b$,

$$r_a \left[\frac{1 - \cos \theta_a}{\sin \theta_a} \right] = r_b \left[\frac{1 - \cos \theta_b}{\sin \theta_b} \right] \quad (9)$$

The data in Table III indicate the Eq. (9) holds reasonably well

TABLE III
Test for spherical segment of drop parallel and perpendicular to groove direction

MBBA						
R	r_o	θ_a	$r_o \left\{ \frac{1 - \cos \theta_a}{\sin \theta_a} \right\}$	r_b	θ_b	$r_b \left\{ \frac{1 - \cos \theta_b}{\sin \theta_b} \right\}$
	mm			mm		
1.20	0.48	110	0.69	1.53	47	0.67
1.25	0.50	109	0.70	2.03	49	0.93
1.33	0.45	120	0.86	2.35	43	0.93
1.50	0.37	120	0.71	2.63	35	0.83
Licristal Nematic Phase V						
1.20	0.49	122	0.88	1.43	58	0.79
1.25	0.58	120	1.00	1.68	55	0.87
1.33	0.55	118	0.92	2.05	52	1.00
1.50	0.55	117	0.90	2.48	48	1.10
Glycerol						
1.20	0.62	125	1.19	0.74	105	0.96
1.25	0.62	125	1.19	0.75	111	1.09
1.33	0.61	125	1.17	0.73	112	1.08
1.50	0.68	126	1.33	0.92	111	1.19

TABLE IV
Contact of *n*-hydrocarbons on stained (160%) teflon FEP*

Liquid	θ_a	θ_b	r_a/r_b	$(\theta_o)_{\text{meas}}$	$(\theta_o)_{\text{calc}}$ Eq. 4
<i>n</i> -hexadecane	60.0	49.0	0.78	55.0	54.0
<i>n</i> -tetradecane	57.6	45.9	0.78	51.8	52.0
<i>n</i> -dodecene	53.5	42.5	0.78	47.8	48.7
<i>n</i> -decane	48.9	39.1	0.78	43.6	45.8
<i>n</i> -octane	41.1	31.1	0.78	36.0	38.6
ethylene glycol	100.0	91.7	0.85	92.3	92.4

confirming the need to consider both radii of curvature in a complete analysis.

In an earlier study of the spreading of liquids on roughened polymer surfaces, Good, Kvikstad and Bailey¹³ rejected the concept of surface roughness as being responsible for elongated shapes of drops in favor of an anisotropic force field. Unfortunately, they presented no quantitative analysis since there is no orderly roughness as in the case studied by Flanders, *et al.*⁵

Unfortunately, Good, Kvitstad and Bailey report only the θ_a and θ_b values for *n*-hydrocarbons on the highly strained fluoropolymer. However, if we assume that Figure 1 of their paper represents the drop dimensions for all the hydrocarbons and that the surface has a roughness of 1.05, which is entirely reasonable from their photomicrographs, we can compute θ_o from Eq. (4). The results of these calculations are in Table IV. Clearly, the agreement is quite satisfactory. We include also the case of the more polar liquid ethylene glycol. Here, to get reasonable agreement the ratio r_a/r_b is taken to be about 0.85.

Although Good, Kvikstad and Bailey conclude that an anisotropic force field is responsible for the elongated drops, the introduction of a modest surface roughening can account for this deviation from circularity. We feel that the results of their study are better interpreted using roughness as the criterion for elongated drops rather than invoke a difficult-to-analyze anisotropic force field.

Acknowledgement

The author appreciates the assistance of G. D. Boyd and J. Cheng for the preparation of the grooved silica surfaces and for their enthusiasm to continue this

study. I should also like to thank M. Sammon and S. Meiboom for their fluoropolymer deposition and their valuable discussions.

References

1. D. W. Berreman, *Mol. Cryst. Liq. Cryst.*, **23**, 215 (1973).
2. V. Wolff, W. Greubel, H. Kruger, *ibid.* **23**, 187 (1973).
3. J. L. Janning, *Appl. Phys. Lett.* **21**, 173 (1972).
4. L. T. Creagh and A. R. Kmetz, *Mol. Cryst. Liq. Cryst.* **24**, 59 (1973).
5. D. C. Flanders, D. C. Shavers and H. I. Smith, *Appl. Phys. Lett.* **32**, 597 (1978).
6. R. E. Johnson, Jr., and R. H. Dettre, in *Contact Angle, Wettability and Adhesion*, Adv. Chem. Series. **43**, 112 (1964).
7. R. H. Dettre and R. E. Johnson, Jr., in *Wetting*, S.C.I. Monograph No. 25, 144 (1967).
8. R. E. Johnson, Jr. and R. H. Dettre, *Surf. Coll. Sci.* **2**, 85 (1969).
9. J. F. Oliver, C. Huh and S. G. Mason, *J. Adhesion* **8**, 223 (1977).
10. A. B. D. Cassie and S. Baxter, *Trans. Farad. Soc.* **40**, 545 (1944).
11. H. M. Princen, *J. Colloid Sci.* **30**, 69 (1969).
12. R. N. Wenzel, *Ind. Eng. Chem.* **28**, 988 (1936).
13. R. J. Good, J. A. Kvikstad and W. O. Bailey, *J. Colloid Inter. Sci.* **35**, 314, (1971).
14. J. Cheng and G. D. Boyd, *Appl. Phys. Letters* **35**, 444 (1979).
15. M. Sammon, private communication.

Appendix

SURFACE ROUGHNESS OF SQUARE ARRAY $\theta_0 < 90^\circ$

If n = number of grooves, then the solid-liquid contact area for a drop of $\theta_0 < 90^\circ$, covering n grooves (Figure 1A) in a square well

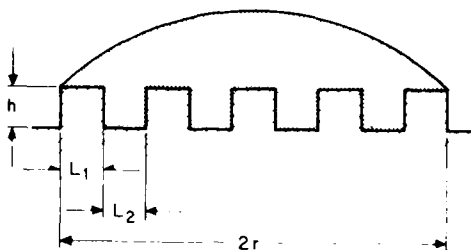


FIGURE 1A Schematic of sessile drop on a surface of n parallel grooves.

array is

$$(n+1)L_1 + nL_2 + 2nh = L_{SL}$$

where

$$2r = (n+1)L_1 + nL_2$$

In the above situation there is only solid-liquid interfacial contact and

$$\frac{L_{SL}}{2r_a} \cos \theta_0 = \left[1 + \frac{2nh}{[(n+1)L_1 + nL_2]} \right] \cos \theta_0 \quad (A1)$$

If $n \gg 1$ and $L_1 = L_2$,

$$\left(1 + \frac{h}{L} \right) \cos \theta_0 = \left(\frac{L_{SL}}{2r_a} \right) \cos \theta_0 \quad (A2)$$

where $(1 + h/L)$ is a measure of the surface roughness.

Surface roughness of square array $\theta_0 > 90^\circ$

For a composite interface where we have both solid-liquid and liquid-vapor interfaces,

$$\frac{L_{SL}}{2r_a} \cos \theta_0 - \frac{L_{LV}}{2r_a} = \frac{(n+1)L_1 \cos \theta_0 - nL_2}{(n+1)L_1 + nL_2} = \cos \theta_a \quad (A3)$$

If $n \gg 1$ and $L_1 = L_2$,

$$\frac{L_{SL}}{2r_a} \cos \theta_0 - \frac{L_{LV}}{2r_a} = \frac{\cos \theta_0 - 1}{2} = \cos \theta_a \quad (A4)$$

or

$$\cos \theta_0 = 2 \cos \theta_a + 1 \quad (A5)$$

Consequently, for a spherical drop ($\theta_0 > 90^\circ$) on a parallel square array where $L_1 = L_2$ and $n \gg 1$ the contact angle should be reasonably independent of surface roughness.

The Study of Reactive Functional Groups in Adhesive Bonding at the Aramid-Epoxy Interface†

L. S. PENN,‡ T. J. BYERLEY and T. K. LIAO

Midwest Research Institute, Kansas City, Missouri 64110, U.S.A.

(Received September 15, 1986)

In polymeric composites, reactive functional groups on the fiber surface are assumed to enhance the mechanical strength of the fiber-matrix interface greatly by forming covalent bonds with the matrix. To test this assumption, we sought to promote covalent bonding at the aramid fiber-epoxy matrix interface by attaching flexible reactive pendent groups to the fiber surface. Other factors that could affect interfacial adhesion were kept constant, *i.e.*, surface energy and surface topography. Quantitative analysis showed a pendent group attachment level of 1.5 to 4.5 groups per 100 Å² of fiber surface, a level that agrees well with the theoretical amount. Surprisingly, in adhesive performance tests, the presence of these reactive pendent groups did not improve the fiber-matrix interface strength. Specific chemical tests for covalent bond formation between the terminal amine of the pendent group and the epoxy molecule showed that covalent bonding did not occur, thus explaining the unexpected lack of improvement in adhesive performance.

KEY WORDS Chemical bonding at interface; quantitative analysis of surface; aramid fiber-epoxy adhesion; single filament pull-out test; functional groups on fiber surface; reactive pendent groups.

INTRODUCTION

In polymeric composites, the presence of reactive functional groups on the fiber surface is expected to enhance the mechanical strength

† Presented at the Tenth Annual Meeting of The Adhesion Society, Inc., Williamsburg, Virginia, U.S.A., February 22–27, 1987.

‡ To whom all correspondence should be addressed at Department of Chemical Engineering, Polytechnic University, Brooklyn, NY, 11201, U.S.A.

of the fiber-matrix interface greatly through a covalent bonding mechanism. The advent of sophisticated surface analysis techniques has permitted the identification of atoms and, in some cases, of specific functional groups on fiber surfaces. However, whether the functional groups actually form covalent bonds with a reactive matrix has not been clarified. The only exceptions to this are the investigations which addressed glass-reinforced composites, where in some cases silicate particles were used as high surface area models for glass fibers. In these, direct evidence was provided for covalent bond formation between the glass substrate and the silane coupling agents and also between amino silane coupling agents and epoxy resin.¹⁻²

Practical problems have hindered meaningful study of the role of covalent bonding at the interface. One major problem is that the interface represents a very small portion of the material in a bulk composite and is buried within the solid. This makes *in situ* spectroscopic investigations difficult even with modern instruments. Another severe problem is that the various factors that contribute to interface bonding are difficult to control and quantify. Experiments are needed where the functional group content, *i.e.*, the covalent bonding capability, of the fiber surface is used as a variable while the surface topography and the surface energy are held constant.

The aramid fiber, Kevlar 49® (poly-p-phenylene terephthalamide), appears to offer the opportunity for such controlled experiments. Although the fiber is chemically inert under normal conditions, reactive functional groups have been attached covalently to its surface by reactive gas plasma treatment. Such attached groups could serve as a basis for subsequent covalent bonding at the fiber-matrix interface. The high degree of crystallinity of the fiber suggests that under the proper experimental conditions, the gross smoothness of the surface topography can be retained.³ Furthermore, the organic nature of the fiber offers the possibility that attachment of organic functional groups to the surface can be accomplished without significant change in atomic composition, and therefore, that fiber surface energetics can be maintained constant. The latter can occur because a key determinant of surface energetics is atomic composition. For example, the surface energetics of polymers containing only C, H are similar to each other, whereas

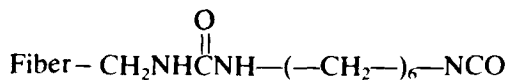
the surface energetics of polymers containing C, H, N, O are similar to each other but different from the C, H polymers. This concept has been demonstrated specifically for modified and unmodified aramid fiber surface.^{4,5}

In the work described in this paper, we sought to promote covalent bonding at the interface by attaching flexible reactive pendent groups to the fiber surface while keeping the fiber surface topography and surface energetics constant. In principle, holding these two factors constant should permit a clearer assessment of the role of fiber surface functional groups in fiber-matrix adhesion.

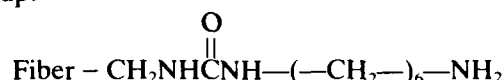
BACKGROUND

The first step in attaching pendent groups is to activate the relatively inert aramid fiber surface by plasma treatment. This affects only the surface and does not degrade the bulk properties of the fiber. Previous studies⁶⁻¹⁰ provide evidence that either the plasma treatment itself or the associated procedures (*e.g.*, vacuum) cause the fiber surface to form a better adhesive bond with the matrix in the fiber composite. Since these investigations have shown that chemical changes,⁶⁻⁸ surface etching,⁹ formation of persistent free radicals,⁹ and moisture desorption¹⁰ can all occur as a result of plasma treatment, it is difficult to determine the specific cause of the improved fiber-matrix interface. In our application of plasma treatment we wished to eliminate all the effects mentioned above except the surface chemical changes.

Monomethyl amine plasma has been reported to attach the aminomethyl group to the aromatic ring of the fiber polymer chain.^{7,8} One attached, each aminomethyl group can be extended by chemical reaction with an aliphatic diisocyanate. A heterogeneous chemical reaction between the aminomethyl group on the fiber surface and the isocyanate in the liquid phase will form, through a urea linkage, an extended pendent group terminating in an isocyanate group.



Exposure to moist air will convert the terminal isocyanate to a primary amine with liberation of carbon dioxide giving the desired pendent group.



Conversion of isocyanate groups on solid surfaces by moist air has been confirmed spectroscopically.¹¹

The aliphatic segment of the pendent group is intended to make the terminal primary amine much more accessible for reaction with the epoxy molecules when the fiber and matrix are joined to make the fiber composite. The effectiveness of six-carbon aliphatic segments in increasing the accessibility of terminal functional groups at solid-liquid interfaces has been demonstrated previously.^{12,13}

An attractive feature of the proposed pendent group is that it can be cleaved at the urea linkage for quantitative analysis of the cleavage product in solution. For small amounts of material, quantitative analysis is accomplished much more accurately by solution techniques than by solid phase surface analysis techniques. Another advantage of the proposed pendent group is that it would not be expected to alter significantly the fiber surface energetics since it, like the fiber, is composed of C, H, N, and O atoms.

Once the pendent groups have been added to the fiber surface, determination must be made of their surface concentration, permanence, configuration, and extent of chemical reaction with epoxide functional groups. In addition, the strength of the adhesive bond between the modified fiber and the epoxy matrix must be assessed and compared to that of the control fiber. The most direct method for measuring fiber-matrix adhesion is the single filament pull-out test. It is conceptually simple and provides a valid comparison of fiber-matrix systems when only the interface is modified but not the bulk fiber and matrix. A good correlation between interfacial adhesive strength and the fiber surface pendent group content would be strong evidence for the presence of covalent bonding at the interface.

The following section provides the experimental details of fiber treatment procedures, the analysis of the fiber surface, the test for reaction with epoxide groups, and the mechanical testing of the interfacial bond.

EXPERIMENTAL

Fiber cleaning: Unbound, absorbed matter was removed from the as-received aramid fiber, Kevlar 49, by a three-step procedure. A 24-hr washing in 0.2 M Na_2HPO_4 solution (pH 9.1) at reflux was followed by a thorough rinse in deionized water. The final step was a rinse in spectroscopic grade anhydrous acetone to remove excess water. The clean fiber was vacuum-dried at 80°C and stored in a dessicator in the dark. Vacuum drying the fiber at this stage greatly reduced the time required to achieve the high vacuum conditions necessary to begin the plasma treatment of the fiber in the next step. Dark storage was important at all times during the program to avoid possible sunlight damage to the fiber.

Plasma treatment: To attach aminomethyl groups, $-\text{CH}_2\text{NH}_2$, to the surface, fiber specimens were exposed to monomethyl amine plasma. The exposure times of 2, 5, and 15 minutes covered a range selected to achieve a measurable level of pendent group attachment without fiber strength degradation or surface etching. The minimum was selected using Allred's data⁷ while the maximum was determined by trial and error in our laboratory on the basis of fiber tensile strength. The plasma treatment was carried out in a tubular glass reactor containing a glass frame to support the fiber. The rf energy (27.1 MHz) was supplied by a Tomac Dithery unit, model 1565, with a power setting of 100 W and was inductively coupled with a 20-cm diameter two-turn coil perpendicular to the length of the reactor. Prior to each plasma treatment, the reactor containing the sample was evacuated until sample outgassing stopped and a stable low pressure less than 10^{-3} torr was reached. This ensured the removal of residual moisture and air from the fiber which could possibly interfere with the plasma treatment. A steady state flow of monomethyl amine gas from a reservoir was then established in the reactor. The gas pressure was maintained at 0.2 torr by a diffusion pump system while the rf field was on, creating the plasma. After treatment, the fiber was stored in the dark. Dry storage was not necessary at this point.

Post-plasma wash: To ensure the removal of any unbound, adsorbed material and to ensure decay of any persistent free radicals resulting from the plasma treatment, the fiber was washed, dried, and stored as described above. The functional groups

attached by the plasma to the fiber surface were extended chemically as described below. Dryness was very important at this point in order that the reaction below not be poisoned by moisture.

Extension of pendent group with 1,6-diisocyanatohexane: Degassed 1,6-diisocyanatohexane (NCO) in neat liquid form was exposed to plasma-treated fiber for 48 hr at room temperature in the presence of a catalytic amount (1 drop) of dibutyl tin dilaurate. Unreacted NCO was removed from the fiber by two separate Soxhlet extractions. Dry nonpolar methylene chloride or Skelly B was used first to remove the excess NCO without causing moisture-induced side reactions involving chemically-bound groups on the fiber surface. Acetone was used to remove any adsorbed polar species remaining. After exposure to moist air, the fiber surface was assumed to contain covalently attached pendent groups, each with a urea linkage, a six-carbon aliphatic segment, and a terminal primary amine. Once the pendent groups were attached, there was no reason to keep the fiber in a dessicator. The fiber is known to absorb moisture rapidly, making it difficult to keep moisture-free during ordinary laboratory operations and testing. Therefore, to ensure that all further testing be carried out on fiber having a stable moisture content, we allowed the NCO-treated fiber to equilibrate at ambient conditions. However, the specimens were still stored in the dark to avoid sunlight.

Surface topography evaluation: A JEOL 35 scanning electron microscope was used to monitor surface topography of the fiber at selected stages of treatment. Fibers exposed to the 2-min plasma treatment (without NCO) and to the 5-min plasma treatment (without NCO) were examined to determine if undesired plasma etching had occurred. Fibers subjected to 2-min plasma plus NCO were examined to determine if undesirable globules of polymer had been deposited as a result of NCO addition. All were compared to control fiber surface.

Surface energetics evaluation: The surface energetics of untreated (control) fiber and of one type of fully-treated fiber (2-min plasma plus NCO) were evaluated and compared by the Wilhelmy wetting force method from which contact angle cosines are computed.¹⁴ Water was used as the probe liquid since it is the most sensitive of all liquids to changes in surface polarity. Testing was carried out at ambient conditions.

Infrared analysis: A computerized Perkin-Elmer 283 spectrophotometer was used with an attenuated total reflectance attachment and KRS5 crystal to obtain spectra of control, 2-min plasma-treated, and fully-treated (2-min plasma plus NCO) fiber surfaces, all at ambient conditions. The signal-to-noise ratio was enhanced by averaging multiple scans.

X-ray photoelectron spectroscopy (XPS): Analysis of the atom content of fiber surfaces was carried out by Structure Probe, Inc., of Metuchen, New Jersey, on a Perkin-Elmer Model 549-XPS/AES/SAM. The specimens were in the form of woven swatches, mounted on aluminum specimen holders. They were placed in the sample chamber which was evacuated to 10^{-7} torr and areas 2 mm in diameter were sampled to a depth of 20 Å. Standard spectra for elements pertinent to this study were obtained from Handbook of X-Ray Photoelectron Spectroscopy.¹⁵ Empirically derived atomic sensitivity factors from the same handbook were used. Besides evaluating the control fiber and one of the fully-treated fiber types (2-min plasma plus NCO), we evaluated fiber with different plasma treatment times and no NCO to check for progressive plasma modification of the surface. Both survey spectra and high resolution spectra (C, N, O region) were obtained. High resolution XPS data were corrected for surface charge shift by referencing the C1s photoelectron line due to aromatic hydrocarbon species at 284.5 eV. A consequence of the high vacuum conditions of the XPS specimen chamber is that adsorbed or absorbed moisture is removed from the specimen just before the spectrum is taken.

Cleavage of pendent groups from the fibers: For quantitative analysis, the pendent groups were hydrolytically cleaved at the urea linkage by a high-pressure steam procedure that we developed. Each fiber specimen of nominal 2-g mass was vacuum-dried for accurate determination of the dry weight and subsequently placed in its own 32-ml cylindrical steel bomb along with 20 ml of deaerated, deionized water. The contents were blanketed with argon gas to displace all oxygen and the tightly sealed bomb was placed in hot oil at 200°C for 30-min (225 psi computed steam pressure). The sealed bomb was dropped into cold water to quench the reaction after which the liquid contents were transferred to a 100 ml volumetric flask. Some 0.2 M Na_2HPO_4 solution was used to rinse the fiber

specimen and this was also added to the volumetric. The contents were diluted to volume with 0.2 M Na_2HPO_4 , as required for the subsequent fluorescence assay conducted at pH 9.1. Fiber specimens were rinsed with acetone and vacuum-dried for accurate determination of the dry weight. After weighing, they were stored in the dark at ambient conditions.

Quantitative analysis of cleaved product: A fluorescence assay specific for primary amines was used to analyze the above 0.2 M Na_2HPO_4 solution for the cleavage product 1,6-diaminohexane.¹⁶ A Perkin-Elmer LS-5 luminescence spectrometer provided sensitive detection of the fluorescamine-amine fluorescent complex. Since, theoretically, cleavage of one pendent group simultaneously produces one molecule of 1,6-diaminohexane and one residual aminomethyl group on the fiber, we arbitrarily decided to convert the fluorescence assay result from a mass of diaminohexane to mass of aminomethyl group using the molecular weight ratio. Our results are tabulated as parts per million (micrograms of aminomethyl group per gram of fiber).

Reaction of pendent groups with epoxide groups: From a batch of ten fully-treated specimens (5-min plasma plus NCO) five specimens were selected for pendent group quantitative analysis by the hydrolytic cleavage and fluorescence assay procedures described above. The other five specimens were exposed individually to neat butyl glycidyl ether, a reactive epoxy, at room temperature for 24 hr. After Soxhlet extraction with Skelly B and then with acetone to remove excess unreacted epoxy, these fiber specimens were also subjected to hydrolytic cleavage and fluorescence assay.

Fiber-matrix interfacial bond strength: The adhesive bond strength at the interface was evaluated directly by a single filament pull-out test.¹⁷ To insure stable and realistic moisture content, the fibers used for this test were also allowed to equilibrate with ambient laboratory atmosphere. The matrix resin used was Ciba-Geigy's 6010 epoxy, cured with Ciba-Geigy's 956 triethylenetetramine. Curing was carried out at atmospheric pressure for 3 hr at 120°C. Single filament pull-out tests were conducted on specimens made from control (clean, untreated) fiber and from three fully-treated fiber types: 2-min plasma plus NCO, 5-min plasma plus NCO, and 15-min plasma plus NCO. Pulled-out filaments were checked microscopically to verify that the locus of failure was at the fiber-matrix interface.

RESULTS AND DISCUSSION

Surface topography: Scanning electron micrographs (Figure 1) of typical fibers at selected stages of treatment showed that the smooth surface topography of the control fiber (top) was retained as desired. The plasma treatment did not etch or pit the surface (middle) and the NCO addition to plasma-treated fiber left only small scale low profile deposits (bottom).

Surface energetics: The advancing and receding contact angle cosines, $\cos \theta_a$ and $\cos \theta_r$, obtained for control fiber and for fully-treated fiber, are shown in Table I.

For the two fiber types there is no difference between the $\cos \theta_r$ values but there is a statistically significant difference between the $\cos \theta_a$ values (Student *t*-test at $\alpha = 0.995$). The fact that the treatment lowered $\cos \theta_a$ but not $\cos \theta_r$ indicates that the treatment produced microscopic regions of reduced polarity on the fiber surface. We attribute the reduced polarity to the presence of the pendent groups' aliphatic six-carbon segments which are large nonpolar segments. A change in surface polarity of the modest magnitude detected here has been found to have no effect on fiber-matrix adhesion in similar situations.^{4,5} Because the wettability method tests a surface layer less than 5 Å deep, the results obtained on the fiber with the 2-min plasma plus NCO can be assumed to be representative of any fully-treated surface with similar pendent group concentration.

Infrared analysis: The attenuated total reflectance technique with its 10,000-Å sampling depth (10% of fiber diameter) is not as surface-sensitive as XPS or wettability analysis. The signals from the functional groups on the fiber surface are diluted by the signals from the large amount of bulk organic fiber present in the sampling volume. Dominated by the underlying bulk fiber, the spectra of treated and nontreated specimens were so similar that no distinct conclusions could be drawn from them regarding changes in the surface functional groups.

XPS: Since the XPS technique's sampling depth is 20 Å, the results presented in Table II represent surface plus some subsurface material. The estimated atom percent values shown in part A (top) cannot be taken as absolute because XPS does not analyze for hydrogen. Atom percents are computed only on the basis of analyzed elements and, therefore, can deviate substantially from the

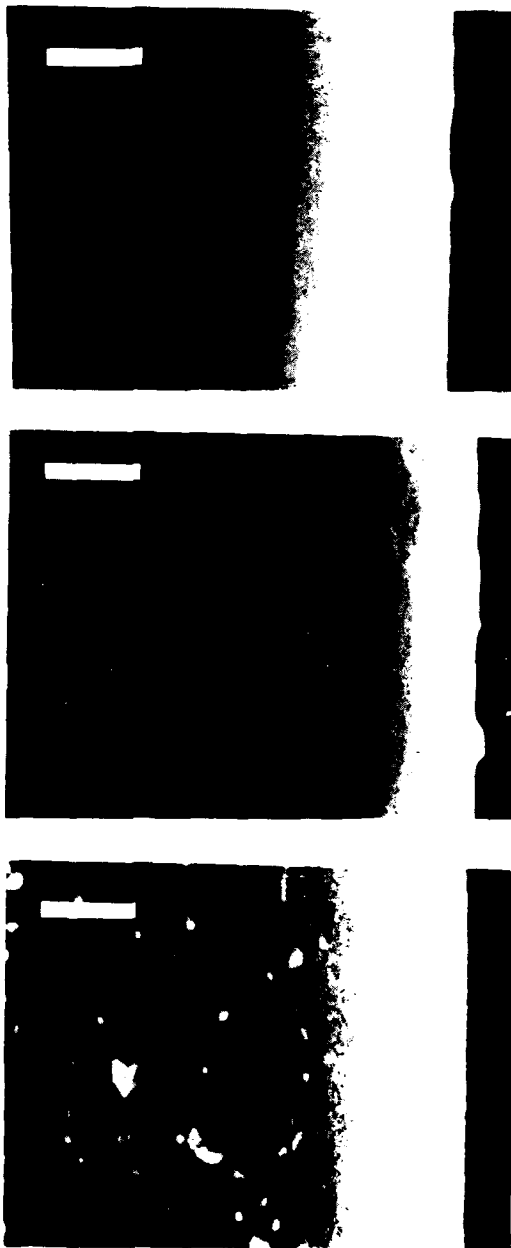


TABLE I
Contact angle cosines of water on control and treated fiber

Fiber	$\cos \theta_r$	$\cos \theta_a$	N
Control	0.822 ± 0.106	0.407 ± 0.136	15
2-min plasma plus NCO	0.744 ± 0.107	0.255 ± 0.114	13

TABLE II
XPS analysis of fiber surface

A. Estimated atomic compositions (%) within 20 Angstrom analyzed layer

Specimen	C	N	O	Si	P	S	Ca	Sn
Theoretical aramid polymer	78.0	11.0	11.0	0.0	0.0	0.0	0.0	0.0
Control	74.2	7.8	17.3	—	—	0.7?	—	—
2-min plasma	66.0	4.5	21.7	6.2	—	—	1.7	—
5-min plasma	63.1	4.6	22.9	6.9	—	—	2.5	—
15-min plasma	66.6	6.9	20.1	3.5	0.8	—	2.2	—
2-min plasma + NCO	67.9	10.3	18.4	1.5	0.7	—	1.0	0.3

B. Relative amounts of key surface atoms in analyzed layer

Specimen	N/C	O/C	N/O	O/N
Theoretical	0.143	0.143	1.000	1.000
Control	0.105	0.233	0.451	2.22
2-min plasma	0.068	0.329	0.207	4.82
5-min plasma	0.073	0.363	0.201	4.98
15-min plasma	0.104	0.302	0.343	2.91
2-min plasma + NCO	0.152	0.271	0.560	1.79

absolute atom percent when hydrogen is present. However, within a specimen, the relative accuracy is within 5%. The top portion (A) of Table II shows introduction of Si and Ca into the fiber surface at longer plasma treatment times, probably from the glass reactor walls. It is also evident that the post-plasma wash removed (or the NCO treatment buried) these species.

FIGURE 1 Scanning electron micrographs of aramid fiber showing that surface smoothness is retained after treatments. Top—control; middle—2-min plasma without NCO (5-min plasma treatment gave identical results); bottom—2-min plasma plus NCO. Original magnification— $18,000\times$. White bars each represent 1 micron.

For meaningful comparison of the changes in C, N, and O at the fiber surface, ratios of the atoms within a specimen were computed from part A and are shown in part B of Table II. The surface of the control fiber contained more than the theoretical oxygen atom content computed for the pure poly-p-phenylene terephthalamide polymer, an observation also made by others.^{7,18} This has been interpreted to mean that the fiber surface is somewhat oxidized by the manufacturing process. The plasma treatment oxidized the fiber surface even further, although the treatment was carried out on dry fiber in the absence of air. It is probable that this oxidation actually occurred when the fiber was removed from the plasma reactor and residual surface free radicals reacted with oxygen from the air.

The Table shows that when NCO was added to the plasma-treated fiber, the oxygen in the analyzed depth diminished relative to both C and N while the nitrogen increased relative to C and O, consistent with expected consequences of NCO treatment. It is not possible to draw additional conclusions from the atom content data because the treatments to which the fiber was subjected could have caused both addition and removal (by burial or ablation) of atoms from the 20-Å deep surface layer.

XPS has a limited ability to distinguish the functional group in which a given atom resides. When carried out at high resolution, XPS can distinguish oxidized from reduced atoms by means of their small binding energy shifts. The high resolution spectra, while not able to indicate specific functional groups, can yield helpful information, as discussed below.

The nitrogen spectrum for each and all specimens showed that the nitrogen atom was in reduced form (e.g., amide, amine). This means that the oxidation that occurred both during manufacture and as a result of plasma treatment did not involve the amide nitrogen of the fiber's polymer chains.

The high resolution carbon spectrum for each and all specimens showed a dominant species at 284.5 eV corresponding to the aromatic ring carbon (reduced). Two carbon species at higher binding energies (oxidized) were present, one of which was assumed to be the carbonyl carbon. Located as shoulders on the dominant peak, they grew with plasma treatment time (Figure 2). For the fully treated fiber, 2-min plasma plus NCO, the six aliphatic carbons (reduced) of the pendent group chemically attached to the surface

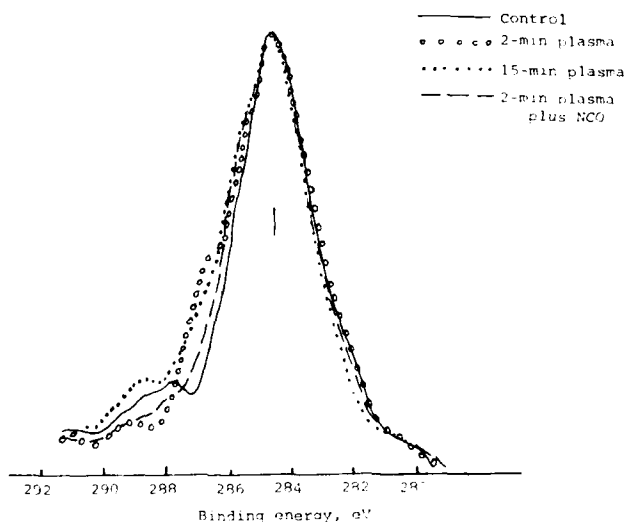


FIGURE 2 High resolution XPS spectrum for carbon atom. Spectra from four fiber specimens are superimposed to show differences. The dominant peak is aromatic ring carbon. Shoulders at higher binding energies are oxidized species. Note increases in oxidized species relative to ring carbons at longer plasma treatment times. Also note diminution in relative amount of oxidized carbon after pendent group attachment (2-min plasma plus NCO), as expected.

have almost exactly the same binding energy as the aromatic carbons.¹⁵ Therefore, their only effect on the spectrum would be to diminish the relative contribution of the oxidized carbons, as Figure 2 shows. The high resolution oxygen spectra for all specimens showed a dominant contribution from carbonyl oxygen at 531–532 eV,^{7,15} surrounded by contributions from species of both higher and lower binding energies. The NCO treatment, as might be expected, seemed to reduce the relative contributions of all oxygen species other than the carbonyl at 531.7 eV (Figure 3).

In sum, the high resolution XPS data shed some light on the nature of the surface oxidation and are consistent with attachment of the proposed pendent group.

Cleavage of pendent groups: It was important that the pendent group's urea linkage be cleaved without significant cleavage of the amide linkages in the fiber polymer itself. Even a limited release of

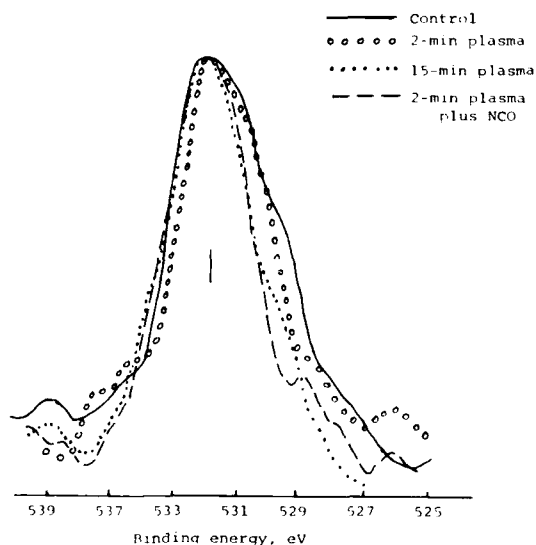


FIGURE 3 High resolution XPS spectrum for oxygen atom. Spectra from four fiber specimens are superimposed to show differences. The dominant peak is the carbonyl carbon of the amide linkage in the fiber polymer chain. Other oxygen species are present in all spectra. Note the diminution in relative amount of the other oxygen species after pendent group attachment (2-min plasma plus NCO), as expected.

primary amine cleavage product from the fiber polymer might be sufficient to interfere with the quantitative analysis of the pendent group. While acid¹⁹ or basic^{20,21} hydrolysis of the urea linkage is known, strong acid²² or base^{22,23} also have been found to cleave extensively the amide linkage of the aramid polymer. Seeking a compromise, we tested the ability of mild base (0.2 M Na_2HPO_4 , pH 9.1) at reflux to hydrolyze the fiber pendent groups. Known to be harmless to the fiber itself, the mild base was found by fluorescence assay also to be ineffective in cleaving pendent groups. Therefore, using a reference to steam hydrolysis of urea in waste water²⁴ as a starting point, we developed conditions for selective hydrolytic cleavage.

The effectiveness of the steam hydrolysis procedure in cleaving the urea linkage of the pendent group without cleaving the amide linkage of the fiber polymer was carefully checked on model

compounds bis(benzyl urea)hexane and N-phenylbenzamide. The cleavage conditions developed succeeded in hydrolyzing 95% of the urea model compound to primary amine while hydrolyzing less than 7% of the amide model compound. Survivability of primary amine under the cleavage conditions was also checked and found to be >80%.

Control fiber (no plasma, no NCO) specimens were subjected to the steam hydrolysis procedure to establish the background level of primary amine issuing from fiber with no pendent groups. From 23 replicates, this value was found to be 8.30 ± 3.48 ppm, a low level with small variation.

Analysis of pendent groups: Results of fluorescence analysis for fully-treated fiber types are presented in Figure 4, in three separate charts corresponding to the three different plasma treatment times before NCO addition. The charts display ppm $-\text{CH}_2\text{NH}_2$ group for each hydrolytic cleavage conducted on the fiber. The background level of 8.80 ± 3.48 ppm obtained for control fiber (no plasma, no NCO) is shown as a shaded band for comparison. Multiple additions of NCO were carried out, each addition followed by more than one cleavage procedure to determine completeness of pendent group removal. The second or third NCO additions were designed to test the ability of the fiber's cleaved surface to react with NCO again.

The quantitative analysis results show the presence of a substantial number of pendent groups on the fibers' surfaces. The analysis values are wide-ranging, as is often the case for sensitive quantitative analysis of surface species, but significantly above background. The source of variation is the fiber surface rather than the fluorescence assay technique, since replicate assays of the same specimen routinely gave <2% variation. In most cases, all or nearly all of the pendent groups were removed by the first hydrolytic cleavage, as indicated by the much lower values (close or equal to background) obtained in the second cleavage. We have no explanation for the behavior of one group of specimens with 2-min plasma plus NCO which showed continued release of pendent groups through several cleavage procedures.

The data also show that pendent groups can be reestablished on the hydrolytically-cleaved surface of the fiber by another addition of NCO (return to high ppm levels of 2nd and 3rd NCO). Through the

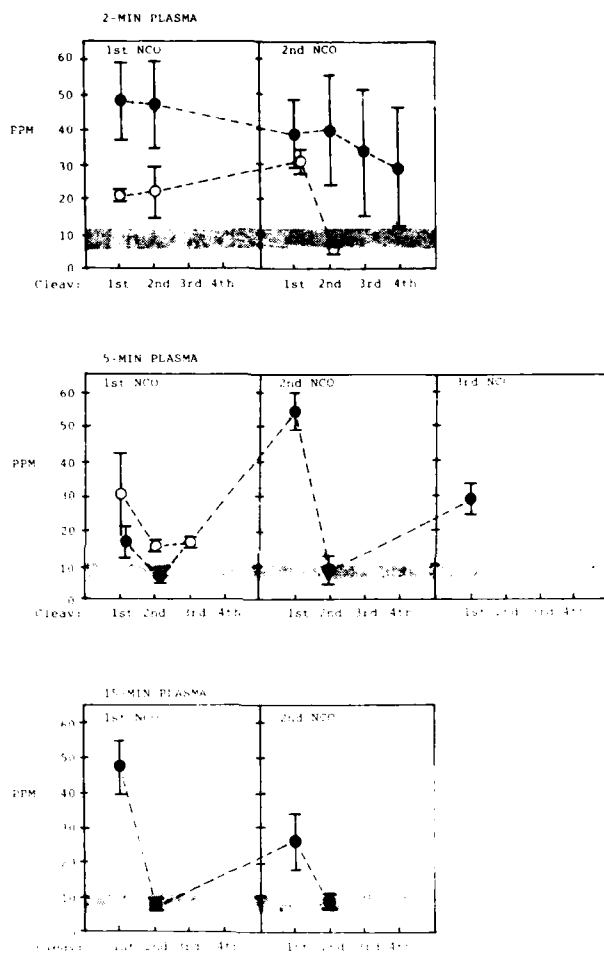


FIGURE 4 Fluorescence assay results for fiber surface pendent groups showing they can be cleaved and regenerated repeatedly. Data for fibers with different plasma treatment times are shown on separate charts. Open and closed circles are averages of groups of 5 to 10 fiber specimens (error bars: ± 1 S.D.). Background is shown as shaded horizontal band. A dotted line tracks each group of specimens through the cycles of cleavage and regeneration.

many cycles of pendent group addition and cleavage, the mass of the fiber remained unchanged within the 100 ppm sensitivity of the analytical balance. This sensitivity was insufficient to detect the 17–55 ppm increases due to pendent group addition but was sufficient to show that there was no gross mass loss or increase over many treatment cycles.

The final conclusion that can be drawn from Figure 4 is that there is no real difference between the three plasma treatment times used to activate the fiber surface initially. Addition of NCO to all three types of fibers produced surface pendent group concentrations in the same wide range of 17–55 ppm.

The meaning of these analysis values on a molecular scale can be visualized by converting micrograms of $-\text{CH}_2\text{NH}_2$ per gram of fiber to number of pendent groups per unit surface area. The mass of aminomethyl group is changed to number using group molecular weight and Avogadro's number. The surface area per gram of fiber is computed using known fiber density,¹⁸ diameter, and right cylinder geometry (computation shown in Appendix). The resultant factor of 0.0883 converts the values 17–55 ppm shown in Figure 2 to 1.5–4.5 pendent groups per 100 \AA^2 of fiber surface area. We can make an estimate of the reasonableness of these values. In each aromatic ring, if the poly-p-phenylene terephthalamide polymer is assumed to offer one site for pendent group attachment, the sites per unit fiber surface area can be computed from known crystal structure.²⁵ The result is that a maximum of 4 pendent groups can be attached per 100 \AA^2 of fiber surface. The experimentally obtained range of pendent group attachment agrees well with the theoretically predicted value of up to 4 pendent groups per 100 \AA^2 .

Other surface reactions: Several considerations suggested to us that another reaction might have taken place at the fiber surface besides the assumed coupling of NCO with aminomethyl groups. First, the high resolution XPS data indicated the presence of oxygens other than carbonyl oxygens on the surface of both untreated and plasma-treated fiber. This opens the possibility that some of the other oxygens are in the form of hydroxyl groups. The rapid reaction of NCO with the hydroxyl groups on a solid surface is a well-documented reaction.¹⁶ Second, it may be a misconception to regard the secondary amide group in the fiber polymer chain as a relatively non-reactive group. The reaction of such N-substituted

amides with isocyanates is documented in the literature.²⁶ Finally, and most importantly, as Figure 4 showed, there was no distinction in pendent group content between fibers with different plasma treatment times. All plasma-treated fibers behaved as though they offered the maximum of 4 attachment sites for NCO per 100 Å². Thus, we postulated that the active sites available on the untreated or plasma-treated fiber could include hydroxyl and secondary amide as well as aminomethyl. The urethane and substituted urea linkages formed by reaction of NCO with hydroxyl and secondary amide, respectively, should be stable to mild base but readily hydrolyzed by the steam hydrolysis procedure to produce diaminohexane.

To check for evidence of pendent group *via* an active site other than aminomethyl, we exposed control fiber (no plasma-treatment) to NCO as described for plasma-treated fiber. Fiber specimens treated in this way showed complete stability to mild base (0.2 M Na₂HPO₄) at reflux, releasing no primary amine. However, when NCO-treated fiber was subjected to the steam hydrolysis procedure, the fluorescence assay was positive. The results, shown in Figure 5, are similar in every way to those in Figure 4. This is conclusive evidence that there are covalently attached pendent groups formed by the reaction of NCO with existing reactive groups on the fiber surface. No efforts at specific identification of the reactive groups were made in this research program. Such identification is the subject of future research.

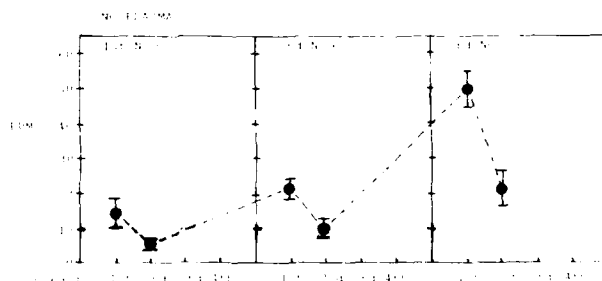


FIGURE 5 Fluorescence assay results for fiber surface pendent groups on fiber with no plasma treatment. Closed circles are averages of a group of five specimens (error bars: ± 1 S.D.). Background is shown as a shaded horizontal band. Data points show repeated cleavage and regeneration of pendent groups, similar to that of plasma-treated fibers.

For the plasma-treated fiber, the question of what portion, if any, of the pendent groups were formed from the reaction of NCO with aminomethyl group cannot be answered. The fluorescence assay we used detected only cleaved primary amine, and both types of pendent groups would give the same amine as hydrolytic-cleavage product.

Reaction with epoxy: The fluorescence assay results for ten fully-treated fiber specimens (5-min plasma plus NCO), five of which were exposed to reactive liquid epoxy, are shown in Table III. The epoxy, a monofunctional model of those used in matrix resins, was used without curing agent to eliminate competitive curing reaction. Occurrence of chemical reaction between the epoxide ring of the epoxy molecule and the terminal primary amine of the pendent group would transform the primary amine to secondary amine which cannot be detected by our fluorescence assay method. Therefore, a reduction in fluorescence assay values would signify that reaction has occurred.

The results from the two groups are identical (29.6 ± 4.67 ppm for unexposed, 29.0 ± 4.80 ppm for exposed) indicating that there was no reaction between the pendent groups and the epoxy. This unexpected result is one of the most important findings of this work.

As an explanation for the lack of reaction with epoxy, it is tempting to postulate that, in the establishment of the pendent

TABLE III
Fluorescence assay results
from two groups of fiber
specimens—unexposed
and exposed (*) to epoxy

Fiber specimen	ppm
1	29.8
2	23.6*
3	37.2
4	30.4*
5	28.9
6	33.6*
7	24.7
8	24.2*
9	27.4
10	33.1*

groups earlier, both ends of the NCO molecule covalently attached to the hydroxyl or aminomethyl groups on the fiber surface. However, because the configurational requirements are severe it is unlikely that this would have happened to any great extent, and yet the results in Table III indicate 100 percent unavailability of terminal amine. A more likely explanation is that the flexible pendent groups arranged themselves in a configuration to minimize the fiber surface energy and in doing so made the terminal amine groups inaccessible to epoxy. This type of behavior has been found in surface vibrational spectroscopy studies of fatty acids on metal surfaces.²⁷ Exactly what has happened to the surface pendent groups in the work presented here is a subject for future research.

Strength of the fiber-matrix interface: Before presenting the results, two important features of single filament testing must be mentioned. Firstly, large scatter (20–30%) is typical of results obtained in adhesive tests using single filaments.^{4,5,17,28–33} This is due to tremendous local variation in surface energetics possessed by all materials,³⁴ incapable of being averaged out as much in small diameter fibers. These local variations are manifested as large scatter in adhesive bond strength values when the volume of material being tested is small. Secondly, the interfacial bond strength values obtained in the single filament test are not independent of imbedment depth.^{35,36} Therefore, for strictly valid comparisons, only results from specimens with the same imbedment depth can be used. Because we could not control the imbedment depth, but could measure it after test, results from specimens with an imbedment depth of 0.25 mm were selected from a much larger pool of results. They are presented below in Table IV.

The Table shows that the adhesive bond strength at the fiber-matrix

TABLE IV
Interfacial bond strengths (Ave. \pm 1 S.D.) for control and fully-treated aramid fibers in epoxy matrix

Fiber treatment	Interfacial bond strength, psi	No. specimens, N
None (control)	4940 \pm 820	26
2-min plasma plus NCO	4960 \pm 1040	23
5-min plasma plus NCO	4650 \pm 1140	45
15-min plasma plus NCO	4520 \pm 1160	32

interface was not improved by the presence of the flexible reactive pendent groups. This is consistent with the negative chemical reaction results described above.

SUMMARY AND CONCLUSIONS

The key findings of this work are summarized briefly below.

- 1) Pendent groups, each containing a flexible six-carbon aliphatic segment and a terminal primary amine, were covalently attached to the aramid fiber surface.
- 2) The groups were chemically attached through a functional group found to be already present on the untreated fiber surface or through the aminomethyl groups placed on the surface by plasma activation or through both.
- 3) Quantitative analysis of pendent groups showed surface attachment levels of 1.5–4.5 groups/100 Å², agreeing with the theoretical maximum of 4 groups/100 Å².
- 4) Mechanical tests of the adhesive bond strength between fiber with pendent groups and epoxy matrix showed no improvement over the adhesive strength between control fiber and epoxy matrix.
- 5) Specific chemical tests for the reaction of pendent groups with epoxy molecules showed that no reaction took place.

The general conclusion to be drawn from these findings is that, contrary to common assumption, reactive functional groups on a fiber surface do not necessarily form covalent bonds with a reactive matrix. In the case reported here, the fact that there was no chemical reaction between the pendent groups and the epoxy molecule precluded the improvement of fiber-matrix adhesion by a covalent bonding mechanism. It is, of course, still reasonable to assume that if covalent bonding between the fiber and matrix could be achieved, adhesive bonding would be improved.

The question that remains from this work is why the particular pendent groups, designed to be accessible and reactive, did not react with the epoxy. As suggested earlier, a preferred conformation may have rendered the terminal amines inaccessible. This question is the subject of continuing research.

Acknowledgement

This work was supported in part by the Office of Naval Research. We thank Michelle Shelton, Randy Nelson, Rich Brown, and Gordon Shaw for technical assistance.

References

1. H. Ishida and J. L. Koenig, *J. Colloid Interface Sci.* **64**, 555 (1978).
2. S. R. Culler, H. Ishida, and J. L. Koenig, *ibid.* **109**, 1 (1986).
3. M. G. Northolt, *Polymer* **21**, 1199 (1980).
4. L. S. Penn, F. A. Bystry, and H. J. Marchionni, *Polymer Composites* **4**, 26 (1983).
5. L. S. Penn and T. K. Liao, *Composites Technol. Rev.* **6**, 133 (1984).
6. E. M. Petric and J. C. Chottiner, in *Proc. 40th Annual SPE Tech. Conf. and Exhib: ANTEC 1982*, (Soc. Plast. Engr., St. Louis, MO, U.S.A., May, 1982), p. 777.
7. R. E. Allred, "Surface Chemical Modification of Polyaramid Filaments", Dissertation for D.Sc., Massachusetts Institute of Technology, Cambridge, MA, U.S.A. (1983).
8. R. E. Allred, "XPS Analysis of Amine-Plasma Treated Polyaramid Filaments", *Abstracts of the Seventh Annual Meeting of the Adhesion Society* held in Jacksonville, FL, February 13-15, 1984.
9. M. R. Wertheimer and H. P. Schreiber, *J. Appl. Poly. Sci.* **26**, 2087 (1981).
10. R. Tira, "Continuous Plasma Treatment and Resin Impregnation of a High Strength Fiber Material", Bendix Report BDC-613-2983, Bendix Corp., Kansas City, MO, September, 1983.
11. D. Allara, Bell Communications Research, personal communication, 1986.
12. I. Parikh and P. Cuatrecasas, *Chem. Eng. News* August 26, 1985, p. 17.
13. A. S. Hoffman, G. Schmer, C. Harris, and W. G. Kraft, *Trans. Amer. Soc. Artif. Int. Organs* **18**, 10 (1972).
14. B. Miller, L. S. Penn, and S. Hedvat, *Colloids and Surfaces* **6**, 49 (1983).
15. C. D. Wagner, *et al.*, *Handbook of X-Ray Photoelectron Spectroscopy* (Perkin-Elmer Corp., Physical Electronics Division, Eden Prairie, MN, U.S.A., 1979).
16. S. V. Caro, Jr., C. S. Paik Sung, and E. W. Merrill, *J. Appl. Polym. Sci.* **20**, 3241 (1976).
17. L. S. Penn, and S. M. Lee, *Fibre Science Technol.* **17**, 91 (1982).
18. L. Penn and F. Larsen, *J. Appl. Polym. Sci.* **23**, 59 (1979).
19. D. W. Farlow and R. B. Moodie, *J. Chem. Soc. (B)*, 407 (1971).
20. R. W. Frei, J. F. Lawrence, and D. S. LeGay, *Analyst* **98**, 9 (1973).
21. C. J. Giffney and C. J. O'Connor, *J. C.S. Perkin II*, p. 362 (1975).
22. T. S. Keller, A. S. Hoffman, B. D. Ratner, and B. J. McElroy, *Proceedings of the International Symposium of Physicochemical Aspects of Polymer Surfaces*, Vol. 2, K. L. Mittal, Ed. (Plenum Press, New York, 1983), p. 861.
23. L. Penn, H. A. Newey, and T. T. Chiao, *J. Mat. Sci.* **11**, 190 (1976).
24. N. J. Landis, U.S. Patent 4,341,640, "Urea Hydrolysis," July 1982, to Standard Oil Co.
25. M. G. Northolt, *European Polym. J.* **10**, 799 (1974).
26. P. F. Wiley, *J. Amer. Chem. Soc.* **71**, 3746 (1949).
27. D. Allara, "Spectroscopic Characterization of Modified Surfaces," *Abstracts of the Eighth Annual Meeting of the Adhesion Society*, held in Savannah, GA, U.S.A., February 24-27, 1985.

28. J. P. Favre and M. C. Merienne, *Int. J. Adhesion and Adhesives* **1**, 311 (1981).
29. R. J. Gray, *ibid.*, **3**, 197 (1983).
30. P. S. Chua and M. R. Piggott, *Comp. Sci. Technol.* **22**, 33 (1985).
31. L. T. Drzal, M. J. Rich, J. D. Canning, and W. J. Park, in *Proceedings of the 35th Annual Technical Conference*, Reinforced Plastics/Composites Institute, The Society of the Plastics Industry, Inc., Section 20-C (1980).
32. S. J. DeTeresa, R. J. Farris, and R. S. Porter, "Fracture and Interface Studies of Aramid Reinforced Polyamide Composites: Compressive Effects and Critical Length Measurements", Office of Naval Research Report 18 on Contract No. N00014-75-C-0686, Project NR 356-584, October 20, 1981, available from DTIC as No. ADA109506.
33. A. T. DiBenedetto, "Evaluation of Fiber Adhesion in Composites," in *NATO Conference Series 6*, Vol. 3, 113 (1981).
34. L. S. Penn and B. Miller, *J. Colloid Interface Sci.* **78**, 238 (1980).
35. M. R. Piggott and P. S. Chua, *Ind. Eng. Chem., Prod. Res. Devel.*, in press (1987).
36. L. S. Penn and S. M. Lee, "Interpretation of Experimental Results in the Single Filament Pull-out Test Results", submitted to *Composites Technol. and Research*, 1987.

Appendix

The computation used to convert micrograms of $-\text{CH}_2\text{NH}_2$ groups per gram of bulk fiber (expressed in the text as ppm) to number of pendent groups per 100 \AA^2 of fiber surface area is shown below:

- Given: a) Specific surface area = $0.227 \text{ m}^2/\text{g}$
 from B.E.T. measurements (Ref. 7).
 b) Mol. wt. of $-\text{CH}_2\text{NH}_2$ group = 30.05 g/mole
 c) Avogadro's number = $6.023 \times 10^{23} \text{ groups/mole}$

Let Q = dimensionless numerical value of ppm.

To convert Q into number of groups/g fiber:

$$\frac{Q \times 10^{-6} \text{ g}}{1 \text{ g fiber}} \times \frac{(6.023 \times 10^{23} \text{ groups/mole})}{(30.05 \text{ g/mole})} = \frac{Q \times 0.200 \times 10^{17} \text{ groups}}{1 \text{ g fiber}}$$

To convert from groups/g to groups/ 100 \AA^2 :

$$\frac{Q \times 0.200 \times 10^{17} \text{ groups}}{1 \text{ g fiber}} \times \frac{100}{\left(\frac{0.227 \text{ m}^2}{1 \text{ g fiber}}\right) \left(\frac{10^{20} \text{ \AA}^2}{\text{m}^2}\right)} = \frac{Q \times 0.0883 \text{ groups}}{100 \text{ \AA}^2}$$

Poster Session

Thermodynamic Criteria for the Maximum and Minimum Strength of Fibre-Reinforced Composite Materials†

W. GUTOWSKI

CSIRO Division of Building Research,‡ Melbourne, Australia

(Received October 3, 1986)

The overall performance and reliability of composite materials are, in most cases, dependent upon the behaviour of the reinforcement-matrix interface, particularly upon its ability to transfer stress.

A theory for predicting thermodynamic conditions for the maximum and zero-adhesion at the reinforcement-matrix interface is tested in this paper, based on experimental data. Proposed is a model of the relationship between mechanical properties of composite materials (tensile strength, flexural strength, Young's modulus and impact resistance) and energetic properties of matrix and reinforcement expressed by the energy ratio $a = \gamma_1/\gamma_2$.

KEY WORDS Adhesion; Composite materials; Flexural strength; Impact strength; Interfacial energy; Work of adhesion.

INTRODUCTION

The use of composite materials in aerospace, automotive and construction industries, instead of traditionally-used monolithic materials, *e.g.* metals, ceramics and plastics, is rapidly increasing. The principles of designing with composites are based on a

† Presented as a Poster Paper at the Tenth Annual Meeting of The Adhesion Society, Inc., Williamsburg, Virginia, U.S.A., February 22–27, 1987.

‡ Postal address: PO Box 56, Highett, Victoria, 3190, Australia.

knowledge of mechanical properties of bulk materials, *e.g.* matrix and reinforcement under expected service conditions and their properties in a composite. However, the overall performance and reliability of composite materials are, in most cases, dependent upon the behaviour of the reinforcement-matrix interface, particularly upon its ability to transfer stress. Therefore, there is a need for an understanding of interactions in this particular region in order to predict (a) conditions for maximum strength, (b) conditions under which the bond at the reinforcement-matrix interface fails, and (c) possibilities of adjustment of surface properties of the reinforcement and/or matrix material to maximise the strength and durability of the composite.

This becomes possible if the bond at the matrix-reinforcement interface is considered as a thermodynamic system whose properties are described in terms of relevant thermodynamic parameters, *e.g.* surface energies, enthalpies or solubility parameters and wettability characteristics of the components.

This paper has two purposes: firstly, to outline the theory of thermodynamic criteria for the maximum and zero-strength of adhesion between matrix and reinforcement, and secondly, to analyse the experimental data regarding fibre-reinforced composite materials to justify the theory.

THEORY

A theory of thermodynamic criteria for the maximum and zero-strength of an adhesive bond has been presented elsewhere.¹ In this paper, this theory is applied for predicting the performance of composite materials, assuming that the terms adhesive and substrate used previously can equally be regarded as matrix and reinforcement in the present case.

Criteria for the maximum strength

In accordance with the second law of thermodynamics, the system exhibits a maximum stability when its free energy is minimum.

It has been shown elsewhere¹⁻⁵ that the minimum of the above free energy, considered as minimum interfacial energy, gives

conditions for a maximum adhesion between the substrate and adhesive, *e.g.* reinforcement and matrix.

From reference to the work,¹ interfacial free energy at the reinforcement-matrix interface can be estimated using the following expressions (see Nomenclature for explanations of the terms used):

$$\gamma_{12} = \begin{cases} \gamma_1 - \gamma_2(1 + m_1) + m_1 \frac{\gamma_2^2}{\gamma_{C(1)}} & \text{for } \gamma_2 \geq \gamma_{C(1)} \\ \gamma_1 - \gamma_2 & \text{for } \gamma_2 \leq \gamma_{C(1)}, \end{cases} \quad (1)$$

or alternatively

$$\frac{\gamma_{12}}{\gamma_1} = \begin{cases} 1 + \frac{m_1}{a^2 \Phi_{0(1)}^2} - \frac{(1 + m_1)}{a} & \text{for } 0 < a \leq a_s \\ 1 - \frac{1}{a} & \text{for } a \geq a_s, \end{cases} \quad (2)$$

where

$$\Phi_{0(1)} = [\gamma_{C(1)}/\gamma_1]^{1/2}, \quad (3)$$

and

$$a = \gamma_1/\gamma_2. \quad (4)$$

Accordingly, the minimum interfacial energy which corresponds to the conditions for the maximum strength is achieved at the energy ratio

$$a_{\text{MIN}} = \frac{2m_1}{(1 + m_1)\Phi_{0(1)}^2}. \quad (5)$$

Criteria for zero-strength

Conditions for zero-strength of adhesive bond at the reinforcement-matrix interface were found¹ from the analysis of expressions for thermodynamic work of adhesion, assuming that there is no net force across the interface when $W_A = 0$. It follows that the strength is zero for any energy ratio:

$$a \leq a_1^{\text{CRIT}} = \frac{m_1}{[2 + m_1 + (\pi_{e(1)}/\gamma_2)]\Phi_{0(1)}^2}. \quad (6)$$

It has been shown elsewhere¹ by the present author that apart from condition (8), there is another critical point at which $W_A = 0$ and

this relates to the complete thermodynamic wetting of the substrate (reinforcement) by matrix material. Accordingly, this is achieved for any energy ratio:

$$a \geq a_2^{\text{CRIT}} = \frac{[2 + m_2 + (\pi_{e(2)}/\gamma_1)]}{m_2} \cdot \Phi_{0(2)}^2 \quad (9)$$

in which

$$\Phi_{0(2)} = [\gamma_{C(2)}/\gamma_2^C]^{1/2} \quad (10)$$

Further, we provide experimental evidence of existence of a_1^{CRIT} and a_2^{CRIT} indicating conditions for zero-strength of adhesive bond.

EXPERIMENTAL CONFIRMATION OF THE THEORY

General

Theoretical criteria developed in paper¹ have been evaluated based on experimental data. Thermodynamic parameters necessary for analysis were calculated using the following equations: (a) interfacial energy: Eqs. (1) to (4), (b) specific bonding efficiency factor: Eqs. (5) and (10), and (c) critical energy ratios: Eqs. (8) and (9).

Basic experimental data for analysis include: (a) surface energies of the reinforcement material, γ_1 , and matrix in its cured state, *i.e.* γ_2^C , and (b) wettability characteristics of the reinforcement and matrix in terms of the parameters m and γ_C .

It is assumed as a first approximation that: (a) $m = 1$ and $\Phi_0 = 1$ when the wettability characteristics are unknown, and (b) equilibrium spreading pressure is negligible, *i.e.* $\pi_e \approx 0$.

Fibre reinforced composites

Polyester matrix. Evaluation of the theoretical criteria has been carried out using strength data from Yip and Shorthall⁶ on fibre-reinforced composites as well as the author's data on surface energies of *E*-glass fibres surface-modified with the same type of polymers as used by these authors. Fibres ($d_{50} \approx 30 \mu\text{m}$) were heat cleaned and water sprayed, followed by treatment with selected chemicals prior to fabrication of composites.

TABLE I
Data for construction of strength characteristic of polyester-glass fibre system

No.	Treatment of E-glass	γ_1 (mJ/m ²)	a^a	γ_{12}/γ_1	Interfacial shear strength ^b (MPa)
1	heat + rinsed in H ₂ O	63.0	1.56	0.36	34.5
2	0.3% silane A-174	42.9	1.06	0.06	52.3
3	0.3% silane A-153	33.2	0.82	0.05	22.2
4	silicone resin	15.8	0.39	2.45	0
5	5% PVA resin	35.1	0.87	0.02	37.1

^a calculated using $\gamma_2^C = 40.4$ mJ/m².

^b strength data from Ref. 6 for single fibre pull-out tests.

Relevant data on strength and surface energies, listed in Table I, were used for calculation of interfacial energies; the strength characteristic diagram of the series of composites was constructed in coordinates; strength *v.* γ_{12}/γ_1 and is given in Figure 1a.

Figure 1a shows that the maximum strength is achieved when the surface energy of modified fibre (as achieved by treatment with silane A-174, Union Carbide) is closest to the surface energy of the

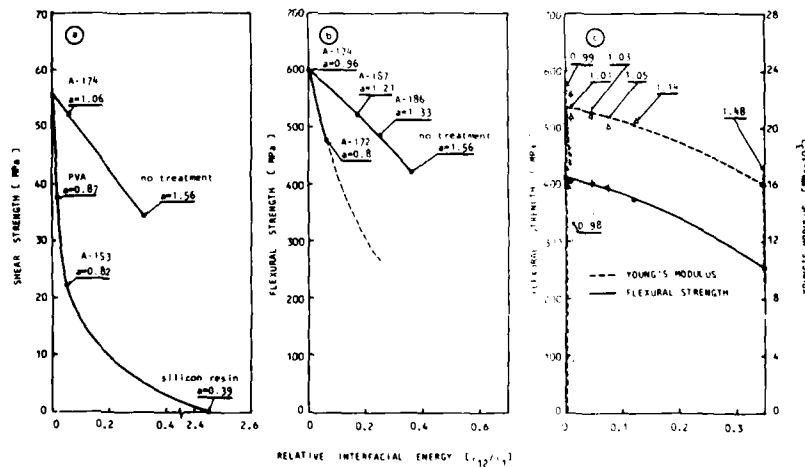


FIGURE 1 Relationship between strength and relative interfacial energy for E-glass/polyester composite material (a) single fibre pull-out, (b) laminate, and (c) dependence of the Young's modulus and flexural strength upon relative interfacial energy.

TABLE II
Data for construction of strength characteristic of polyester-glass cloth composite

No.	Treatment of E-glass	γ_1 (mJ/m ²)	a^a	γ_{12}/γ_1	Flexural strength ^b (MPa)
1	No treatment	63.0	1.56	0.36	420.6
2	Silane A-172	32.3	0.80	0.06	475.7
3	Silane A-174	38.7	0.96	0.002	599.8
4	Silane A-187	48.8	1.21	0.17	524.0
5	Silane A-186	53.7	1.33	0.25	489.5

^a calculated using $\gamma_2^C = 40.4$ mJ/m².

^b strength data from Ref. 7.

cured matrix material. Treatment with another silane (A-153, Union Carbide) provides lower fibre surface energy than treatment with PVA, resulting in correspondingly lower strength. Treatment with the silicone resin leads to the energy ratio $a \approx 0.39$, which is close to $a_1^{CRIT} \approx 0.333$ corresponding to zero-strength.

A similar strength characteristic diagram has been drawn from reinterpreted data of Broutman⁷ who investigated composite materials of cloth treated with different silanes and a polyester matrix. Surface energies of cloth treated with silanes used in the experiment and the calculated resultant interfacial energies have been determined (see Table II) in order to construct the strength characteristic diagram illustrated in Figure 1b.

Again, the maximum strength is achieved when the energy ratio is close to $a_{MIN} = 1.0$, as obtained after treatment with methacrylate-silane A-174. It can be argued at this stage that the organofunctionality of the A-174 silane, as being designed for polyester-based composites, is responsible for the maximum strength of this system. However, we provide further data which support an hypothesis that the minimum interfacial energy, resulting from equilibrium of energies of substrate and matrix, plays a primary role in enhancement of adhesion. It is the author's opinion that organofunctionality of the adhesion promoter (in this case the silane) plays only a secondary role.

It becomes apparent from Figures 1a and 1b that there are two branches on the strength characteristic diagram: strength *vs.* γ_{12}/γ_1 : (a) a lower, steep branch for energy ratios $a \leq a_s$, and (b) an upper,

TABLE III
Data for construction of strength characteristic of polyester-glass cloth composite

No.	Concentration (%) of γ -MPS	γ_1 (mJ/m ²)	a^a	γ_{12}/γ_1	Young's modulus ^b (MPa $\times 10^3$)	Flexural strength ^b (MPa)
1	0	63.0	1.56	0.36	16.0	252
2	0.1	46.0	1.14	0.12	20.35	375
3	0.3	42.3	1.05	0.048	20.85	404
4	0.5	40.8	1.01	0.0099	21.20	406
5	0.8	39.5	0.98	0.0004	20.40	396
6	1.1	40.0	0.99	0.0001	20.50	412
7	1.5	40.8	1.01	0.0099	21.60	409
8	2.0	43.7	1.03	0.0750	20.05	396

^a calculated using $\gamma_2^C = 40.4 \text{ mJ/m}^2$

^b calculated as average from data in Ref. 8.

shallow branch for $a \geq a_s$, which is relevant to thermodynamic wetting of a filament by matrix material.

An interesting study has been presented by Graf, Koenig and Ishida⁸ who investigated the influence of γ -methacryloxypropyltrimethoxy (γ -MPS) silane on the structure of adsorbed silane layers and the flexural strength and the Young's modulus of *E*-glass-polyester composite materials. Our data on surface energies of γ -MPS modified *E*-glass, resultant interfacial energies and the strength data of Graf *et al.*,⁸ are presented in Table III. It is necessary to note that we have calculated the flexural strength and Young's modulus (see Table III) as an average from Graf's dry and wet conditioning data because, in our view, 80°C water immersion for 40 hours (considered as wet conditioning⁸) is not sufficient to hydrolyse Si—O—Si bonds to Si—OH.

The strength characteristic diagram in Figure 1c indicates an excellent agreement with our previous approach^{1,5} emphasising the role of energy equilibrium at the interface on adhesion enhancement. Modulus of elasticity of the composites investigated (see Figure 1c), depends upon interfacial energy in the same manner as strength, as expected.

Epoxy matrix Adhesion of *E*-glass fibres to epoxy resin was investigated by Berger and Eckstein.^{9,10} Glass fibres were treated with A-1100 and A-174 silanes diluted in water to the required concentrations. Epoxy resin DER 331 (Dow Chemical) was used as

TABLE IV
Data for construction of strength characteristic of epoxy-glass fibre system

No.	Treatment of E-glass	γ_1 (mJ/m ²)	a^a	γ_{12}/γ_1	Flexural strength ^b (MPa)
1	No treatment	35.4	0.90	0.012	9.1
2	A-1100 0.2	31.35	0.80	0.062	6.8
3	0.5	34.63	0.88	0.018	7.1
4	1.0	36.19	0.92	0.008	8.7
5	2.5	44.07	1.12	0.107	5.4
6	A-174 0.2	40.31	1.02	0.024	12.2
7	1.0	42.1	1.07	0.065	8.2
8	2.5	41.0	1.04	0.038	7.1

^a calculated using $\gamma_2^C = 39.33 \text{ mJ/m}^2$ (data from Ref. 9)

^b single fibre pull-out test; data from Refs. 9, 10.

a matrix. Data necessary for calculation of interfacial energies and strength of the systems investigated are listed in Table IV, as given by the original authors. The pattern of the relationship: strength *vs.* γ_{12}/γ_1 , as Figure 2a shows, confirms the earlier approach.

It is apparent from data presented that the maximum strength (at the energy ratio $a \approx 1.0$), is achieved by treatment with a 0.2% solution of γ -MPS silane, which theoretically should give a lower strength than the amino-silane A-1100. However, the amino-silane, designed to provide more favourable conditions for chemical interaction with the epoxy resin matrix, has not been used at the optimum concentration to yield the energy ratio close to a_{MIN} .

It is seen that the surface energy of the substrate (treated by a silane) is crucial in regard to maximum adhesion. A similar conclusion can be drawn from analysis of the strength characteristic in Figure 2b, constructed from Plueddemann's data.¹¹ Also in this case, the glass fibre-epoxy composites were fabricated using fabric pretreated with different silanes, as described in Figure 2b. It is apparent that the maximum strength is achieved with the silane providing the energy ratio close to 1.0, *i.e.* styrylamine silane Z-6032 (Dow Corning).

Epoxy silane (Z-6040) yields the same strength of the composite as chloroalkyl-(Z-6076) and mercapto- (Z-6062) functional silanes, all Dow Corning materials, whilst theoretically the optimal (within the scope of the experiment) diamino-silane (Z-6020) results in even lower strength.

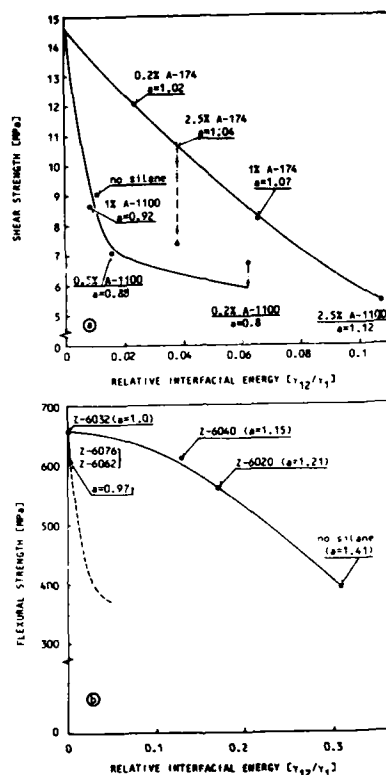


FIGURE 2 Relationship between strength and relative interfacial energy for E-glass/epoxy composite material (a) single fibre pull-out, and (b) laminate.

EXPERIMENTAL EVIDENCE OF THE EXISTENCE OF TWO CRITICAL REGIONS FOR ZERO-INTERFACIAL SHEAR STRENGTH IN COMPOSITES

As noted earlier, there are two theoretical boundaries relevant to zero-interfacial shear strength, as given by Eqs. (8) and (9). To a first approximation, these can be simplified to

$$a_1^{\text{CRIT}} \cong 0.333, \text{ and} \quad (8)$$

$$a_2^{\text{CRIT}} \cong 3.0. \quad (9)$$

In order to observe the trends in the relationship between the strength and the energy ratio of the system, we have analysed literature data on the strength of adhesive bonds (lap-shear specimens)^{1-4,12,13}. These have been reinterpreted to give graphs of strength *vs.* *a*, illustrated in Figure 3a. The pattern of this relationship is the same for all the systems analysed, despite the type of substrates and adhesives.

It is apparent from the graphs that apart from the maximum at $a \cong 1.0$, there is a significant decrease in bond strength which can be deduced to approach a minimum at two different regions, *e.g.* for $a = 0.3$ to 0.5 and $a > 1.8$. (for non-metallic substrates this minimum corresponds to zero-strength, whilst for metals there is some

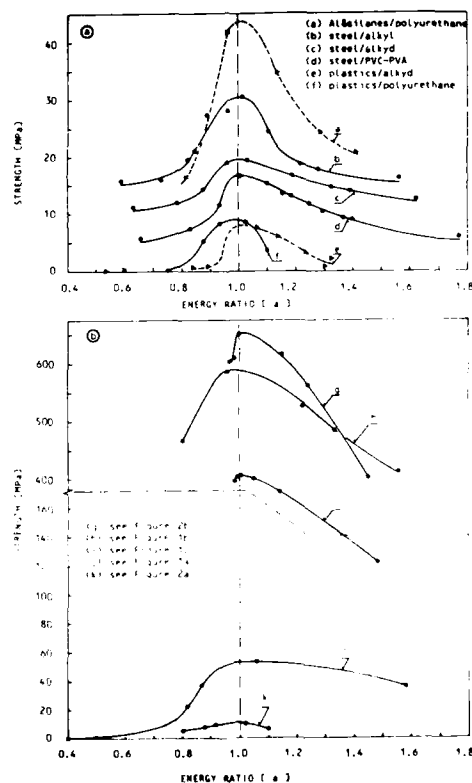


FIGURE 3 Experimental data on the relationship between strength and energy ratio (a) lap-shear adhesive joints, and (b) composite materials.

residual strength). In Figure 3b we have plotted a similar graph for the fibre-reinforced plastics analysed in this paper. The pattern of the relationship is similar to that exhibited by the lap-shear adhesive bonds. However, to apply the approach to composite materials we have to distinguish a substantial difference between the load-bearing capacity of classic adhesive bonds and composite materials, arising from the critical criteria of Eqs. (8) and (9), namely:

a) When the properties of the materials yield an energy ratio relevant to conditions (8) and (9) then, for an adhesive bond either the existing bond fails catastrophically, or attempts to produce an adhesive bond, using the given substrates and adhesive cannot be successful. In both cases the overall load-bearing capacity of the system is zero.

b) When conditions (8) and (9) are applicable in a fibre-reinforced composite, then similarly, there is no net attractive force across the interface (*i.e.* no adhesion between phases). However, the matrix itself provides inherent load-bearing capacity. This is further increased by a contribution from a friction bond created by

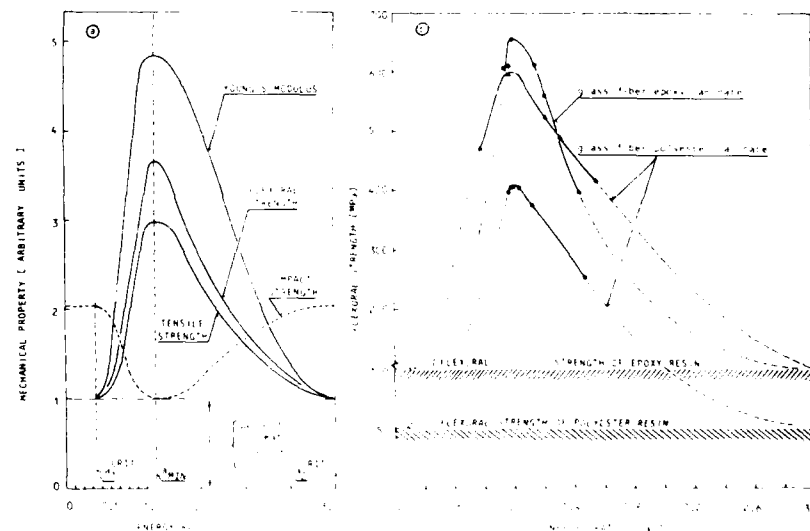


FIGURE 4 The model of the relationship between mechanical properties of composite materials (flexural strength, tensile strength, impact strength) and energy ratio in composite materials (a) proposed model, and (b) experimental evidence for polyester- and epoxy-based composites.

a radial compressive stress resulting from matrix shrinkage during cure. We propose that the critical criteria (8) and (9) applied to composite materials can be interpreted as Figure 4a illustrates.

Experimental points relating flexural strength and the energy ratio for polyester- and epoxy-based composite materials, as analysed in this paper, are shown in Figure 4b, as well as the average value of the flexural strength of neat polyester and epoxy resins.


If the model proposed in Figure 4a is followed (based on data from Figure 3) then we can deduce that it can be applied to composite materials. However, further experimental evidence must be given to locate strength *vs. a* graphs for those energy moduli which have not yet been fully investigated (*e.g.* 'a' ranges from 1.5 to 3.0 and 0.4 to 0.6).

NOMENCLATURE

γ_1, γ_2	total surface energy of phase 1 or 2
γ_c	critical surface tension for wetting
γ_{12}	interfacial energy
W_A	thermodynamic work of adhesion
m	parameter dependent upon the slope of the wettability characteristic
γ_{12}/γ_2	relative interfacial energy
$a = \gamma_1/\gamma_2$	energy ratio of the system
$a_s = 1/\Phi_0^2$	threshold energy ratio for self-spreading
a^{CRIT}	critical energy ratio for $W_A = 0$, corresponding to zero-strength
a_{MIN}	optimum energy ratio for γ_{12}^{MIN} and $[\gamma_{12}/\gamma_1]_{MIN}$, corresponding to the maximum strength
Φ_0	specific bonding efficiency factor

References

1. W. Gutowski, "Thermodynamic model of the adhesive bond". Submitted for publication in *Journal of Adhesion*.
2. M. Levine, G. Ilkka and P. Weiss, *Polym. Lett.* **2**, 915 (1964).
3. G. A. Dyckerhoff and P. J. Sell, *Angew. Macromol. Chem.* **21**, 169 (1972).

4. *Polymer Science and Technology*, Vol. 9A, K. L. Mittal, Ed. (Plenum Press, New York, 1975), p. 129.
 5. W. Gutowski, "Pattern of the Relationship Between the Strength of Adhesive Bond and Thermodynamic Properties of Bond Components" (In press).
 6. H. W. C. Yip and J. B. Shorthall, *J. Adhesion* **8**, 155 (1976).
 7. L. J. Broutman, *ibid.* **2**, 147 (1970).
 8. R. T. Graf, J. L. Koenig and H. Ishida, *ibid.* **16**, 97 (1983).
 9. E. Berger and Y. Eckstein, in *Adhesive Joints: Formation, Characteristics, and Testing* K. L. Mittal, Ed., (Plenum Press, New York and London, 1984).
 10. Y. Eckstein and E. Berger, in *Adhesive Chemistry: Developments and Trends* L. H. Lee, Ed., (Plenum Press, New York and London, 1985), p. 139.
 11. E. P. Plueddemann, *Silane Coupling Agents* (Plenum Press, New York and London, 1982), pp. 141-154.
 12. P. Walkner, *J. Coat. Technol.* **52**, 49 (1980).
 13. O. Oldfield and T. E. F. Symes, *J. Adhesion* **16**, 77 (1983).
- 

A Study on the Properties and Structure of Polyether-Sulfone-Modified Epoxy Adhesives†

WANG ZHI-LU, CHEN DAO-YI and LIU XIAO-HUI

Petrochemical Institute of Heilongjiang Academy, Harbin, China

Properties and morphology of PES-modified epoxy adhesives were studied in this paper. These systems have excellent mechanical properties and can be used as heat-resistant adhesives. SEM and EDX observations showed that the system has a two-phase structure. At lower PES content, there is a PES dispersed phase and a epoxy continuous phase. At higher PES content, there are two continuous phases. From these results, the relationship between structure and properties of this system were discussed.

KEY WORDS Epoxy adhesive; mechanical properties; morphology; phase separation; polyethersulfone (PES), structure.

INTRODUCTION

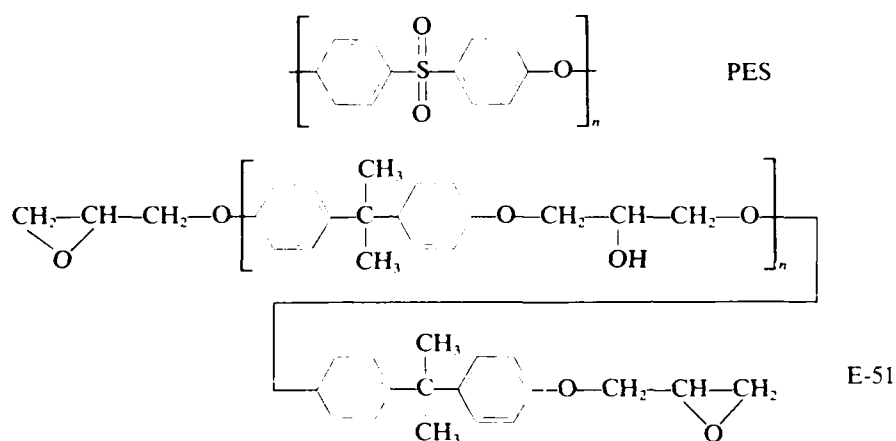
Polysulfones are a class of high-temperature-resistant thermoplastic materials, which have excellent mechanical properties and thermal stability. Adding polysulfones to epoxy resins, high mechanical strength could be obtained. Such systems have, therefore, found wide application in the fields of adhesives, coatings and composites.^{1,2} This paper describes the properties and morphology of polyethersulfone (PES)-modified epoxy resins and discusses the relationship between structure and properties.

† Presented as a Poster Paper at the Tenth Annual Meeting of The Adhesion Society, Inc., Williamsburg, Virginia, U.S.A., February 22-27, 1987.

EXPERIMENTAL

1 Raw material

The chemical structures of the two resins used in the study are shown below. E-51 (Epon 828) epoxy has a viscosity of 2500 cp at 40°C, an epoxy equivalent weight of 196 g mol⁻¹, and a molecular weight of ~392. The PES has a molecular weight of ~25000. The hardener was dicyandiamide [DICY].



2 Experimental methods

(i) *Measurements of mechanical properties* Adhesives were prepared by mixing E-51 epoxy with PES previously dissolved in DMF and adding the hardener DICY. The adherends were LY 12 CZ aluminum alloy sheets.

The surface preparation of adherends was accomplished by degreasing, sanding and acid chemical etching, washing in running water and drying at 60°C.

The surface-prepared adherends were coated with the adhesives, dried at 110°C, and cured at 180°C for 3 hrs under 1 kg/sq cm pressure.

The shear strength, peel strength and non-uniform tear strength were measured according to GOST.

(ii) *SEM analysis of the fracture surface.* Adhesive solutions were

heated to drive off the solvent, and cured at 180°C for 3 hrs, to produce samples. These samples were fractured at room temperature, coated with a thin layer of Au and examined by scanning electron microscope (SEM). Other samples were coated with carbon and subjected to energy dispersive X-ray (EDX) microanalysis for sulfur using SEM.

RESULTS AND DISCUSSION

Figure 1 and Figure 2 show the correlation between bond strength and concentration of PES. Epoxy adhesive containing 40–50 wt. % of PES has maximum bond strength, the maximum lap shear strength being 380 and 310 kg/sq cm, respectively, at 25°C and 150°C. The 90° peel strength is 7 kg/cm and the non-uniform tear strength is 66 kg/cm. In this system the two resins behave synergistically.

Table I shows the resistance of PES modified epoxy adhesives to liquid media compared to a polysulfone (P1700)-modified material. This system displays better solvent resistance, oil resistance and boiling water resistance than the general polysulfone [P1700] modified epoxy adhesive.

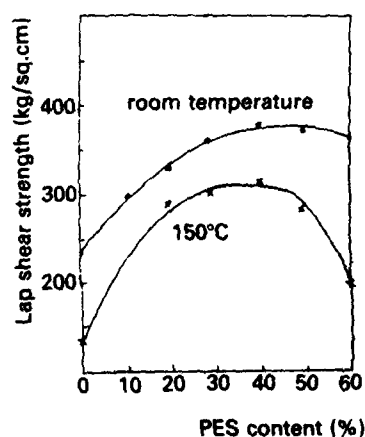


FIGURE 1 Lap shear strength vs PES content.

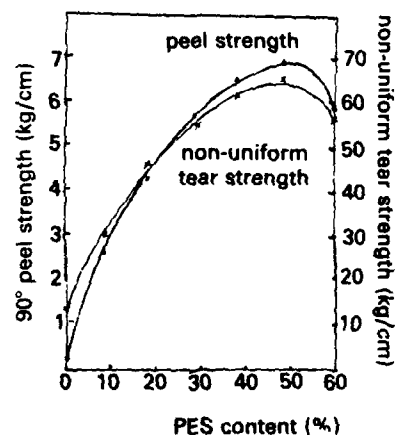


FIGURE 2 90° peel, non-uniform tear strength vs PES content.

TABLE I
Effect of liquid media on bond strength

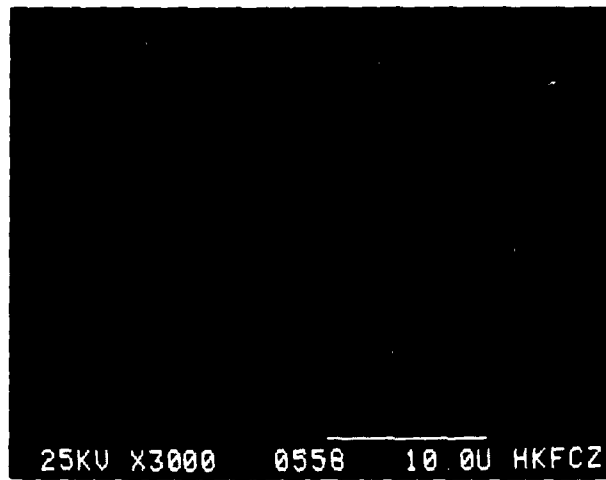
Media	Immersion time (days)	Average lap shear strength (kg/sq cm)	Lap shear strength retention (%)	Polysulfone (P1700) E-51 adhesives retention (%)
Ethyl acetate	30(R.T.)	357	98.0	81.6
Kerosene	30(R.T.)	362	99.5	71.5
Alcohol (95%)	30(R.T.)	347	95.0	88.2
	2 hrs	362	99.4	79.3
	6 hrs	353	97.0	75.0
Boiling water	48 hrs	335	92.0	55.0
	168 hrs	295	81.0	—

Figure 3 shows the morphology of the fracture surface of PES-modified epoxy resin samples. At lower PES content (Figure 3a) the system contains a dispersed phase appearing as globules. In order to identify the PES rich phase, EDX microanalysis was used to determine the distribution of sulfur in the fracture surface of the samples. These globules show a significantly higher concentration of sulfur than the surrounding matrix (Figure 3a₀). It is clear that these globules also contain cross-linked epoxy resin. At 20% PES content



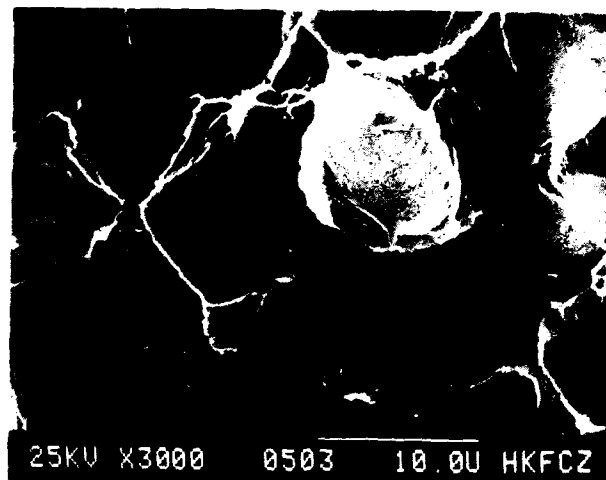
(a)

FIGURE 3 Morphology vs PES contents.



(a)

FIGURE 3 (contd)



(b)

FIGURE 3 (contd)

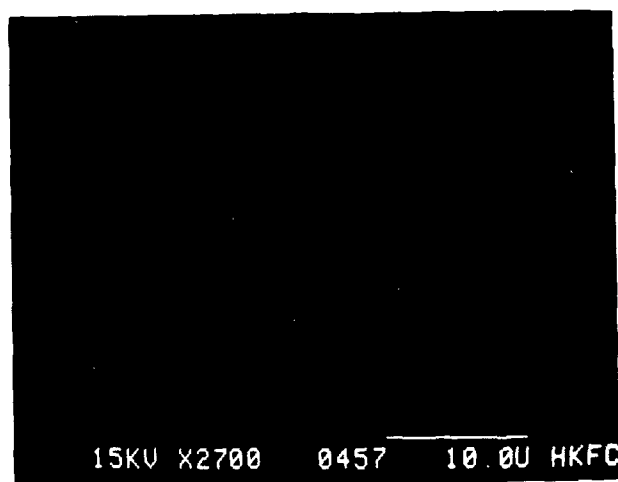
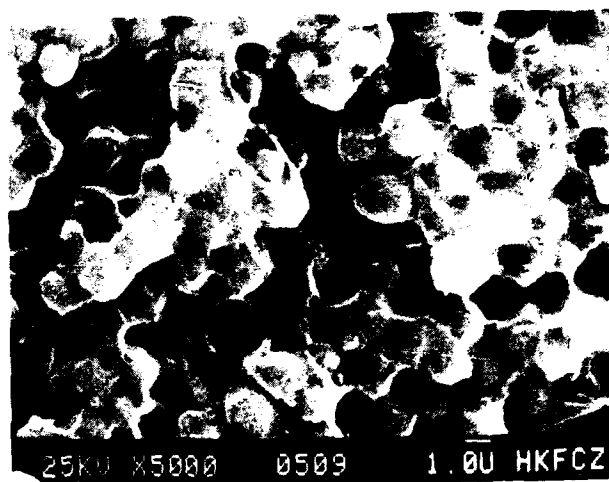
(b₀)

FIGURE 3 (contd)



(c)

FIGURE 3 (contd)

(Figure 3b), the globules disappear and the system exhibits a new morphology of two continuous phases (Figure 3b₀). PES forms the more continuous phase and the epoxy forms a cellular structure. With increasing PES contents, the sizes of the epoxy cellular structure decrease rapidly, with the cellular structure disappearing at 60% PES content (see Table II).

TABLE II
Relationship between morphology and PES content

PES content wt. %	Morphology	Average domain diameter (μm)
0	a homogeneous phase	
10	a dispersed PES phase	2
20	two continuous phases	8
30	two continuous phases	2
40	two continuous phases	1
50	two continuous phases	0.5
60	a homogeneous phase	0

It has been noted that some cracks appear around the globules (Figure 3a). These cracks are similar to those in some CTBN-modified epoxy resins. In this respect, the PES globules probably act in a similar way as the rubber globules in CTBN-modified resins, in as much as the presence of the globules appears to benefit the bond strength of PES-modified epoxy adhesives.

At higher PES content (Figure 3b, Figure 3c), the phase boundary is not clear. This means that the compatibility of the two resins in phase boundary is much better. PES is a linear thermoplastic polymer, whereas the cured epoxy resin is a network polymer. On the basis of the morphology and the composition, it is suggested that a snake-cage structure was formed, the cured epoxy resin forming cages and PES forming snakes. From the difference of the solubility parameters ($\Delta\delta = 3.3(\text{cal}/\text{cm}^3)^{1/2}$), PES and epoxy resin are chemically incompatible polymers, phase separation taking place in the curing reaction. But the snake cage structure can limit phase separation^{3,4} and improve the bond strength.

CONCLUSIONS

1. PES-modified epoxy adhesives have high bond strength at room and high temperature, and excellent resistance to liquid media.

2. At lower PES content ($<20\%$) the system contains a PES dispersed phase, which acts in a similar way as the rubber globules in CTBN-modified epoxy resins.

3. At higher PES content (≥ 20 wt.%), the system exhibits a morphology of two continuous phases. PES forms the more continuous phase, epoxy resin forms a cellular structure. The size of the cellular structure depends on the compositions, and a snake-cage structure was probably formed.

References

1. K. Terence, Ger. Offen. 2, 130, 407 23 Dec 1971.
2. Toho Beslon, Jpn. Kokai Tokkyo Koho JP 58, 134, 126 10 Aug 1983
3. A. A. Donatelli, *et al.*, *Macromolecules* **9**(4), 671 (1976).
4. R. Jerome *et al.*, *J. Applied Polym. Sci.* **26**(6), 1741 (1981).

SESSION OF THE
UNITED STATES. III

Effect of Adhesive Ductility on Cyclic Debond Mechanism in Composite-to-Composite Bonded Joints †

S. MALL

*Department of Aeronautics and Astronautics, Air Force Institute of Technology,
Wright-Patterson Air Force Base, OH 45433-6583, U.S.A.*

K. T. YUN

*Department of Aerospace Engineering and Engineering Mechanics, University
of Texas, Austin TX 78712, U.S.A.*

(Received June 6, 1986)

An investigation of an adhesively bonded composite joint with a brittle adhesive was conducted to characterize both the static and fatigue debond growth mechanism under mode *I* and mixed mode *I-II* loadings. The bonded system consisted of graphite/epoxy adherends bonded with FM-400 adhesive. Two specimen types were tested: (1) a double-cantilever-beam specimen for mode *I* loading and (2) a cracked-lap-shear specimen for mixed mode *I-II* loading. In all specimens tested, failure occurred in the form of debond growth either in a cohesive or adhesive manner. The total strain-energy-release rate is not the criterion for cohesive debond growth under static and fatigue loading in the brittle adhesive as observed in previous studies with the ductile adhesives. Furthermore, the relative fatigue resistance and threshold value of cyclic debond growth in terms of its static fracture strength is higher in the brittle adhesive than its counterpart in the ductile adhesive.

KEY WORDS Adhesive bonding; composite materials; debond propagation; strain-energy-release rates; fracture mechanics; fatigue.

† Presented at the Tenth Annual Meeting of The Adhesion Society, Inc., Williamsburg, Virginia, U.S.A., February 22-27, 1987.

INTRODUCTION

Adhesive bonds have several major advantages relative to mechanical fastenings, including potential savings in weight and in manufacturing costs. It has a special attraction in joining of fiber reinforced composite structural components since it eliminates the cutting of fibers as well as holes and stress concentration associated with them. Thus, substantial weight savings can be realized which is a major reason for selecting composite materials for structural components. If the advantages of adhesively bonded joints, as compared to mechanically fastened joints, are to be fully exploited, a thorough understanding is required of failure mechanism in terms of service environmental regimes, including cyclic mechanical load, both load and application time, temperature and humidity. In this paper, attention will be focused on fatigue load environment.

One of first tasks in an effective study of the fatigue of any structure is to define the possible modes of damage propagation. In joints with mechanical fasteners, the growth of a crack from a fastener is the principal mode of damage. When an adhesively bonded joint is subjected to fatigue loading, one of the possible damage modes that can occur, is called cyclic debond—progressive separation of the adherends by failure of the adhesive bond under cyclic load. Roderick, *et al.*¹ and Mostovoy and Ripling² were the first to study cycling debonding in bonded joints. Roderick, *et al.* studied the cyclic debond phenomenon in composite-to-metal joints under in-plane, mixed-mode constant amplitude loading, while Mostovoy and Ripling investigated the cyclic debonding under opening mode alternating loads. These early studies showed that the correlations between cyclic debond growth rate and corresponding strain-energy-release rate resulted in the same sigmoidal shapes that had been previously observed in studies of fatigue crack propagation in metals.

Later on, Marceau, *et al.*³ found that the cyclic debond growth rate is influenced by temperature and moisture, and Jablonski⁴ investigated the crack closure effects on fatigue crack growth in a bondline under mode I condition. Brussat, *et al.*⁵ developed the crack-lap-shear specimen to study the effect of mixed-mode loading on adhesive joints. Romanko, *et al.*⁶ extended these fracture

mechanics concepts to investigate the fatigue failure of adhesive joints under various environmental condition involving temperature, moisture, etc. However, the correlations between debond growth rates and fracture mechanics parameters from this study⁶ were completed by Lin and Liechti.⁷ To assess the repeatability of debond growth rates in adhesively bonded joints subjected to constant-amplitude cyclic loading, a study was recently undertaken by Everett and Johnson.⁸ Everett has also investigated the role of peel stresses in cyclic debonding.⁹

Besides, the above mentioned studies, the first author and his colleagues have conducted several studies involving the fatigue failure behavior of adhesive bonds between composite adherends.¹⁰⁻¹² In these studies, cyclic debonding was investigated under opening mode *I* and in-plane mixed-mode *I-II* loading. For this purpose, graphite/epoxy double-cantilever-beam (DCB) and cracked-lap-shear (CLS) specimens were tested under constant-amplitude cyclic loading in an ambient laboratory environment. These studies showed that the relations G_I versus da/dN from the DCB specimens and G_T versus da/dN from the CLS specimens agreed with each other, where G_I is the total (and also opening mode *I*) strain-energy-release rate for DCB specimens, and G_T is the total strain-energy-release rate for CLS specimens. The relation G_I versus da/dN from the CLS specimen under mixed-mode loading did not, however, agree with the relation G_I versus da/dN from the DCB specimen under the opening mode *I* loading. The results of these studies, thus, showed that the cyclic debond failure in the adhesively bonded composite joints is governed by the total strain-energy-release rate.

In these studies¹⁰⁻¹² two adhesives were used: EC 3445 (3M) and FM-300 (Bloomindale Div., American Cyanamid). Both these adhesives are rubber toughened epoxy structural adhesives, and are ductile adhesives. These studies were extended to investigate the effect of adhesive properties (*i.e.*, brittle versus ductile adhesives) on the cyclic debond mechanism. This was the objective of the present study. For this purpose, graphite/epoxy double-cantilever-beam and cracked-lap-shear specimens were tested using FM-400 (American Cyanamid) which is a relatively more brittle adhesive. This investigation focused on the correlation of the measured cyclic

debond growth rate with the corresponding strain-energy-release rate. The present study as well as previous studies, thus, provided the data to evaluate the effect of adhesive ductility on the cyclic debond mechanism.

SPECIMEN FABRICATION AND CONFIGURATION

Two specimen types were fabricated: DCB and CLS specimens, as shown in Figures 1 and 2. The DCB and CLS specimens were used to characterize debond growth under opening mode I loading and mixed-mode loading, respectively. The DCB and CLS specimen

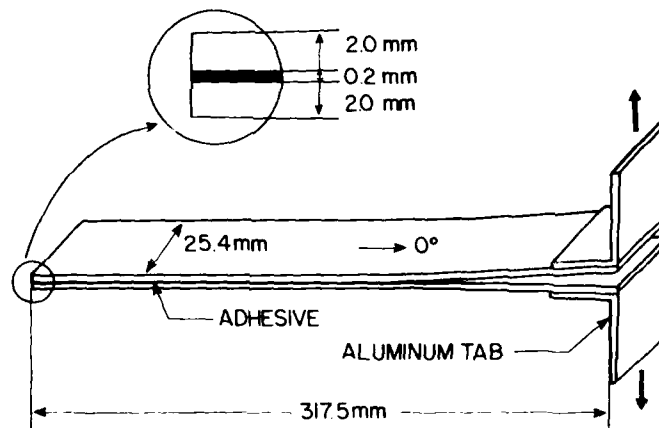


FIGURE 1 Double-cantilever-beam specimen.

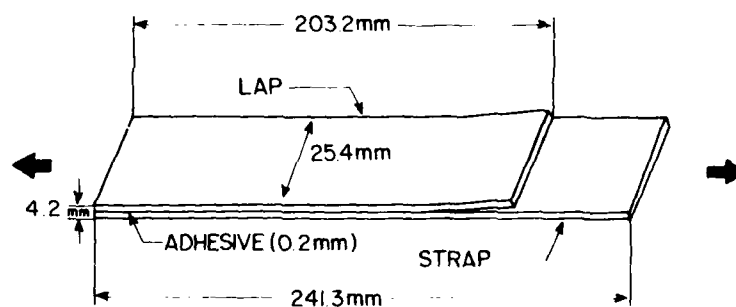


FIGURE 2 Cracked-lap-shear specimen.

consisted of two bonded graphite/epoxy (T300/5208; NARMCO Corp.) adherends, each having 15 unidirectional plies with an initial debond length of 38 mm. This debond was introduced by a Teflon film equal to the adhesive bondline. Two 0.5 mm thick aluminum ends tabs were bonded to the DCB specimen. The peeling load was applied through these tabs. The bonding was done as per manufacturers' recommended procedure. The nominal adhesive thickness was 0.2 mm.

EXPERIMENTS

The experimental program included the static and fatigue tests for both DCB and CLS specimens. The purpose of this program was to measure the critical strain-energy-release rate under the static loading, and to measure the debond growth rate under the cyclic loading. These are already described in details in Ref. 11, where a similar study was carried on with EC 3445 and FM-300 adhesives as mentioned earlier. A brief description of the experimental program is given in the following for the sake of completeness.

DCB specimen

Both static and fatigue tests of the DCB specimen were conducted in the displacement test mode. Prior to testing, either for static or fatigue loading, these specimens were fatigued to create a debond of at least 6 mm beyond the end of Teflon film. The static tests involved the application of displacement at a slow crosshead speed (1.0 cm/min). The critical load corresponding to onset of debond growth was measured carefully. The debond occurred in the stable manner which resulted in the deviation from linearity in the measured load *versus* cross-head displacement relation. This was also verified by a clip-gage near the debond front. After each static test, the specimen was fatigued until the debond grew at least 6 mm further, thus forming a sharp crack for the next static test. A series of static tests were performed on each specimen, which provided the averaged value of G_{IC} for each specimen as per the procedure described in Ref. 11.

The fatigue tests of DCB specimens were performed at a cyclic

frequency of 2 Hz and a stress ratio of 0.1 under constant amplitude cyclic displacement. During fatigue tests debond lengths, fatigue cycles, applied loads, and displacements were monitored continuously. The measured relation between the debond length and fatigue cycle provided the debond growth rate, da/dN . The strain-energy-release rate G_I associated with the cyclic debonding was computed as per the procedure described in Ref. 11.

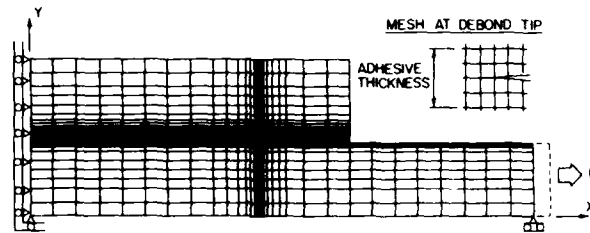
CLS specimen

Static tests of CLS specimen were conducted in the displacement test mode. Prior to testing, the specimen was fatigued to create an initial sharp debond. The critical load corresponding to unstable debond growth was measured from the recorded load-displacement curve. The debond growth resulted in the deviation in the load-displacement curve. The displacement was measured with two displacement transducers attached on the opposite side of the specimen. Only one measurement could be obtained from each specimen, since the debond grew into the composite strap adherend.

Fatigue tests of CLS specimens were conducted under constant amplitude cyclic load at 2 Hz frequency and stress ratio, $R = 0.1$. Debond lengths and fatigue cycles were monitored continuously throughout the test. The measured relation between the debond length and fatigue cycles provided the debond growth rate, da/dN . Tests were conducted at two or more constant amplitude stress levels to get several values of debond growth rates from each specimen. The tested CLS specimens were analyzed with the finite element program to compute strain-energy-release rates for both static and fatigue loading, as explained in the following section.

FINITE ELEMENT ANALYSIS

A geometric nonlinear finite element program, GAMNAS,¹³ was used to analyze the tested CLS specimens in order to account for the nonlinearity associated with the large rotations in the unsymmetric CLS specimen. A typical finite-element model (FEM) of a cracked-lap-shear specimen is shown in Figure 3. This FEM mesh

FIGURE 3 Finite element mesh (Y Coordinates are magnified $20 \times$).

consisted of about 1200 isoparametric 4-node elements and had about 2400 degrees of freedom. A multipoint constraint was applied to the loaded end of the model to prevent rotation (*i.e.*, all of the axial displacements along the ends are equal to simulate actual grip loading of the specimen). Plane-strain condition was assumed in the analysis. The material properties of composite adherend and adhesive are listed in Tables I and II. The strain-energy-release rate was computed using a virtual crack-closure technique.¹⁴

TABLE I
Graphite/epoxy^a adherend material properties^b

Modulus, ^c GPa			Poisson's ratio ^c	
E_{11}	E_{22}	G_{12}	ν_{12}	ν_{23}
131.0	13.0	6.4	0.34	0.35

^a T300/5208, fiber volume fraction = 0.63

^b $E_{33} = E_{22}$, $\nu_{13} = \nu_{12}$, $G_{13} = G_{12}$

^c The subscripts 1, 2 and 3 correspond to the longitudinal, transverse and thickness directions, respectively, of an unidirectional ply.

The previous study¹⁰ indicated that at least 12 elements were required through the adhesive thickness to reach convergence on G_I and G_{II} calculations. However, the calculation of G_T was not affected by the number of elements through the adhesive thickness.

TABLE II
Adhesive material properties

Adhesive	Modulus, GPa		Poisson's ratio
	E	G	ν
FM-400	4.83	1.72	0.4

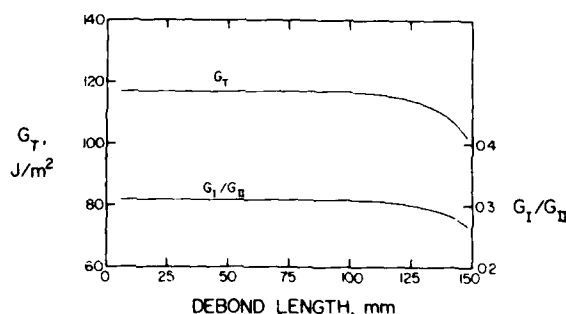


FIGURE 4 Variation of strain-energy-release rates with debond length for the applied stress of 175 MPa.

Further, it was found that G_T was not affected by the location of debond through the adhesive thickness, *i.e.*, whether it was cohesive or adhesive failure. On the other hand, G_I/G_{II} varied slightly with the location of the debond through the adhesive thickness. The focus of the present study was not to investigate the interaction of mixed mode loading on cycling debonding like the previous studies¹⁰⁻¹² but to study the effect of adhesive ductility on cyclic debond behavior. For this purpose, four elements through the adhesive thickness were considered sufficient to calculate the strain-energy-release rates for the tested CLS specimens. The debond was modeled at the middle of the adhesive thickness. Figure 4 shows the variation of the computed strain-energy-release rates G_T and G_I/G_{II} with the debond length.

ADHESIVE DETAILS

This section will present the background information regarding the adhesive FM-400 used in the present study as well as of FM-300 and EC 3445 adhesives used in the previous studies,¹⁰⁻¹² in order to discuss the results of the present study as well as previous studies in this context.

FM-400 is a modified epoxy adhesive film with an aluminum filler and a light weight nylon carrier. On the other hand, FM-300 and EC 3445 are rubber-modified, epoxy structural adhesives. FM-300 is a mat-reinforced film adhesive, while EC 3445 is a one-part paste.

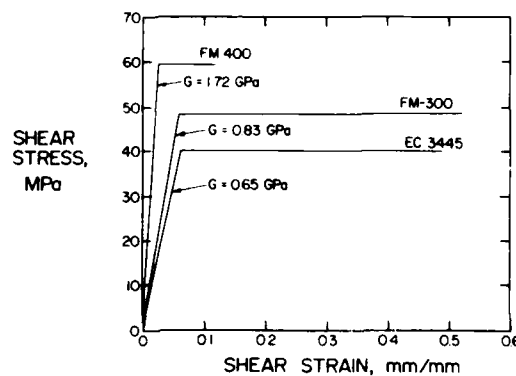


FIGURE 5 Comparison of shear stress-strain response of three adhesives.

All three adhesives are currently being used in the aerospace industry. Due to differences in chemistry and reinforcement (rigid *versus* flexible), FM-400 has a higher strength and modulus than compared to FM-300 and EC 3445. Further, FM-400 is of a comparatively more brittle type than FM-300 and EC 3445 which are more ductile. Hence, FM-400 adhesive will be referred as a brittle adhesive, while FM-300 and EC 3445 will be referred as ductile adhesives. These characteristics are depicted in terms of bondline shear stress and shear strain relations in Figure 5. These stress-strain relations were measured with a thick adherend specimen and were obtained from the manufacturers of these adhesives. These are the average representation of adhesives bondline behavior at room temperature, and not the exact behavior. Therefore, they are represented as an elastic-perfectly plastic material instead of having the usual nonlinear behavior, as commonly observed.

RESULTS AND DISCUSSIONS

Debond locations

All DCB and CLS specimens tested in the present study with FM-400 failed by debond propagation during both static and fatigue tests. The debond grew either in a cohesive manner (*i.e.*, within adhesive) or adhesive manner (*i.e.*, at, or near, the adherend-

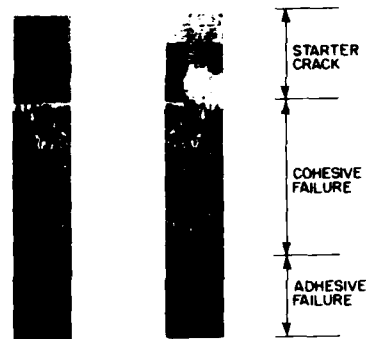


FIGURE 6 Debonded surfaces of double-cantilever-beam specimen.

adhesive interface). There was no consistent pattern for this behavior. In both specimens, it was observed that once debond growth occurred in the adhesive manner, it continued in that manner. However, if it grew in the cohesive manner, it continued in that manner or sometimes it changed to the adhesive type of failure. Typical debond surfaces with these failure details are shown in Figures 6 and 7. The sudden transition from cohesive to adhesive failure in the adhesive bondline with scrim cloth can be probably attributed to weak bonds between the mat carrier and the adhesive (either poorly bonded or not chemically bonded) which provided the crack growth path toward the interface. And, once debond growth occurred in adhesive manner, it continued in that manner since it is the weakest link in the tested bonded system.

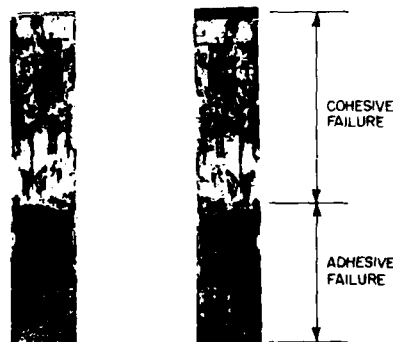


FIGURE 7 Debonded surfaces of cracked-lap-shear specimen.

Thus, the presence of scrim or mat carrier may weaken a bonded joint. This effect has been investigated in a thick adherend model joint, in a qualitative way, in a previous study.¹⁵

The above mentioned debond growth characteristic was also observed in the DCB specimen with FM-300 where the debond propagated in an irregular manner during both static and fatigue tests involving cohesive, adhesive, or mixed cohesive-adhesive debonding. However, CLS specimens with FM-300 debonded in a cohesive manner only during static and fatigue tests. On the other hand, with adhesive EC 3445 (without any carrier cloth), the debond propagated in a cohesive manner for both specimens (DCB and CLS) and loadings (static and fatigue).¹⁰⁻¹¹ Further, in CLS specimens with FM-400 in the present study, as well as with FM-300 and EC 3445 adhesives in the previous study,¹⁰ the debond was always closer to the strap than the lap adherend. A possible explanation for this debond characteristic has been investigated with the finite element analysis in the previous study.¹⁰

Static debonding behavior

Table III presents the critical strain-energy-release rates G_{IC} and $G_{(I-II)C}$ for both cohesive and adhesive failures obtained from static tests of DCB and CLS specimens with FM-400 adhesive, respectively. Also, the corresponding values for FM-300 and EC 3445 adhesives from previous studies¹¹ are provided for comparison purposes. This shows that the static fracture strength of a bonded joint with the brittle adhesive under the mixed mode I-II condition is about 20 percent less than its counterpart under mode I for

TABLE III
Fracture energies of three adhesives

Adhesive	Avg. G_{IC} J/m ²		Avg. $G_{(I-II)C}$ J/m ²	
	Cohesive failure	Adhesive failure	Cohesive failure	Adhesive failure
FM-400	603	306	474	245
FM-300	933	551	991	—
EC 3445	888	—	848	—

cohesive failure. On the other hand, both of these are equal in the case of a bonded joint with the ductile adhesives. Further, the static fracture strengths of these bonded joints in the case of adhesive failure are considerably lower than their counterparts with cohesive failure.

Cyclic debonding behavior

The measured debond growth rate data for FM-400 adhesive were correlated with the corresponding strain-energy-release rates as shown in Figure 8. These obeyed a relationship of the form

$$\frac{da}{dN} = c(G_I \text{ or } G_T)^n \quad (1)$$

where c and n are constants dependent on the material and test environment. The solid lines in Figure 8 showing these relations were fitted to the data by using a least-squares regression analysis. The value of c and n thus obtained from the least-squares fit are given in Table IV along with their counterparts for EC 3445 and

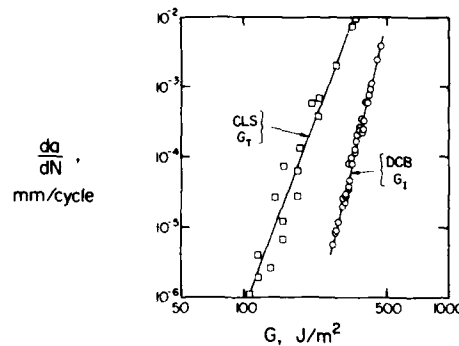


FIGURE 8 Relations between strain-energy-release rates and debond growth rate from two specimens.

TABLE IV
Constants c and n of Eq. (1)

Adhesive	Mode I		Mixed mode I-II	
	c	n	c	n
FM-400	1.91E-35	12.09	2.24E-22	7.74
FM-300	1.52E-15	4.55	1.52E-15	4.55
EC 3445	1.81E-14	4.34	1.81E-14	4.34

FM-300 adhesives obtained from the previous studies.^{10,11} As mentioned earlier, the relationship between strain-energy-release rate and cyclic debond growth rate in ductile adhesives remains unchanged from mixed mode *I-II* to opening-mode *I*. However, this is not the case with the brittle adhesive. This comparison clearly shows that the total strain-energy-release is not the criterion for cyclic debond growth in brittle adhesive as was observed in the ductile adhesive. The primary contribution of mixed mode fatigue loading in the brittle adhesive was the reduction in the debond growth resistance and the exponent, n , as shown in Figure 8 and Table IV. This, thus, leads to the considerable decrease in fatigue threshold value, G_{th} (defined here arbitrarily the strain-energy-release rate corresponding to $da/dN = 10^{-6}$ mm/cycle) under mixed mode loading when compared with opening mode loading in the case of the brittle adhesive.

The energy absorbed per cycle was more under mixed mode loading than opening mode in the brittle adhesive. Hence, the micro-mechanical damage mechanisms which control debond growth are more degrading when the brittle adhesive is subjected to mixed mode loading. This can be attributed to the type of reinforcement used (rigid particulate, *i.e.*, aluminium filler) in the brittle adhesive to increase its strength. On the other hand, in the ductile adhesives, the reinforcement was a flexible particulate, *i.e.* rubber. This flexible particulate permitted an equal amount of energy absorption per fatigue cycle under both mixed mode *I-II* and mode *I* loadings, which resulted in the same value for fatigue threshold value and debond growth exponent, n .

Further, the comparison of cyclic debond behavior between softer but more ductile *versus* harder but more brittle adhesives shows that the former will experience more hysteresis per cycle (more energy absorbed), and hence more micro-damage at the crack tip is likely. This phenomenon thus reduces the fatigue resistance of the softer but ductile adhesive in comparison to the harder but brittle adhesive. This feature is shown in Figure 9 where debond growth resistance is replotted in terms of the corresponding static fracture strength, G_{IC} or $G_{(I-II)C}$. This comparison clearly shows that the relative fatigue resistance and threshold value for cyclic debonding in terms of its original static strength is higher in the brittle adhesive than in the ductile adhesive. Thus, increase in ductility of adhesive may not be beneficial in this context, in spite of its effect in

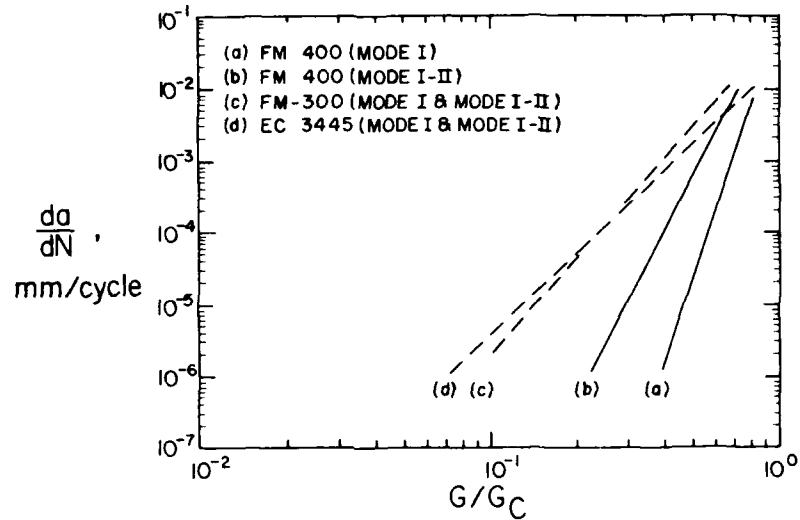


FIGURE 9 Relations between normalized strain-energy-release rate and debond growth rate of different adhesives.

improving the fracture strength, *i.e.* G_{IC} or $G_{(I-II)C}$, under static loading. However, this should be verified for various other brittle and ductile adhesives.

The previous discussion was for the situation when debond growth occurred in the cohesive manner. As mentioned earlier, the debond grew either in a cohesive manner or adhesive manner. Figure 10

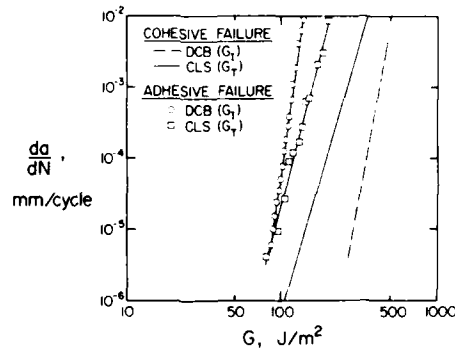


FIGURE 10 Comparison between cohesive and adhesive debond growth rates.

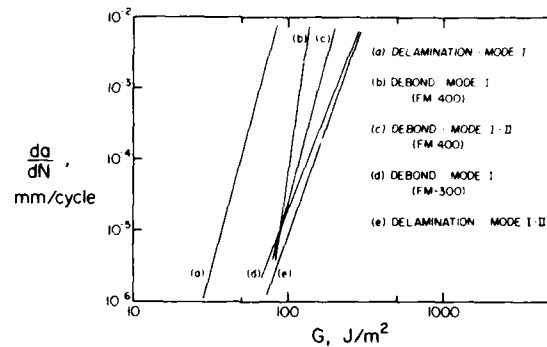


FIGURE 11 Comparison between adhesive debond growth rates and delamination growth rates.

shows the relationships between the measured debond growth rate and strain-energy-release rate from the present DCB and CLS specimens (with FM-400 adhesive) from adhesive failure. Also, the corresponding relationships for cohesive failure are shown in this figure. When these debond growth relations for interfacial failure are compared with their counterparts for cohesive failure, it can be observed that there is a shift in these relations. This shift is towards the left which physically means that there is a several-fold reduction in the fatigue resistance of the bonded joint in case failure occurs in the adhesive manner. Figure 11 shows cyclic delamination growth relationships of the composite adherends used in the tested specimens, *i.e.* graphite/epoxy (T300/5200) for mode *I* and mixed-mode *I-II* from a previous study¹⁶ along with adhesive debond growth relations from the present study. Also, the corresponding relationship for adhesive failure with FM-300 adhesive from the previous study¹¹ is shown in this figure. This comparison clearly shows that fatigue strength of interfacial failure in these bonded joints is about of the same order as that of cyclic delamination growth of adherend composite under mixed-mode *I-II* loading especially at low debond growth rates.

CONCLUDING REMARKS

A study of composite-to-composite bonded joints with a brittle adhesive was conducted to characterize the debond growth mechan-

ism under mode *I* and mixed mode *I-II* static and fatigue loadings. The bonded system consisted of graphite/epoxy adherends (T300/5208) bonded with FM-400 adhesive. Two specimen types were tested: (1) a double-cantilever-beam specimen for mode *I* loading and (2) a cracked-lap-shear specimen for mixed mode *I-II* loading. The following conclusions were obtained from this study:

1) The total strain-energy-release rate is not the criterion for cohesive debond growth under static and fatigue loading in the brittle adhesive as observed in the ductile adhesive.

2) There is a considerable reduction in the cyclic debond growth resistance in mixed mode fatigue loading in comparison to opening mode fatigue loading in the case of the brittle adhesive.

3) The relative fatigue resistance and threshold value of cyclic debond growth in terms of its static fracture strength is higher in the brittle adhesive than its counterpart in the ductile adhesive.

Acknowledgement

The work reported was performed at University of Missouri-Rolla under the sponsorship of NASA Langley Research Center, Hampton, Virginia. The authors wish to acknowledge the support and encouragement of Dr. W. S. Johnson, NASA Langley Research Center, during the course of this investigation.

References

1. G. L. Roderick, R. A. Everett, Jr., and J. H. Crews, Jr., in *Fatigue of Composite Materials*, ASTM STP 569 (Am. Socy. for Testing and Materials, Philadelphia, 1975), pp. 295-306.
2. S. Mostovoy and E. J. Ripling, in *Adhesion Science and Technology*, 9B (Plenum Press, N.Y., 1975), pp. 513-562.
3. J. A. Marceau, J. C. McMillan and W. M. Scardino, *Proc. of 22nd Nat. SAMPE Symp. and Exhibition*, 22, 64-80 (1977).
4. D. A. Jablonski, *J. Adhesion* 12, 125-143 (1980).
5. T. R. Brussat and S. T. Chiu, *J. Eng. Materials and Technology* 100, 39-45 (1978).
6. J. Romanko, K. M. Liechti and W. G. Knauss, *AFWAL-TR-82-4139*, Air Force Wright Aeronautical Laboratories, November 1982.
7. C. Lin and K. M. Liechti, *Engineering Mechanics Research Laboratory Report NO. 85/6*, The University of Texas at Austin, August 1985.
8. R. A. Everett, Jr. and W. S. Johnson, in *Delamination and Debonding of Materials*, ASTM STP 876 (Amer. Soc. for Testing and Materials, Philadelphia, 1985), pp. 267-281.
9. R. A. Everett, Jr., *Adhesives Age* 26(5), 24-29 (1983).
10. S. Mall, W. S. Johnson and R. A. Everett, Jr., in *Adhesive Joints: Their*

- Formation, Characteristics, and Testing* (Plenum Press, New York, 1984), pp. 639-658.
11. S. Mall and W. S. Johnson, in *Composite Materials: Testing and Design (Seventh Conference)*, ASTM STP 893 (Amer. Soc. for Testing and Materials, Philadelphia, 1986), pp. 322-334.
 12. S. Mall, M. A. Rezaizadeh and G. Ramamurthy, *J. Eng. Materials and Technology* **109**, 17-21 (1987).
 13. J. D. Whitcomb and B. Dattaguru, *NASA TM 85734*, Jan. 1984.
 14. E. F. Rybicki and M. F. Kanninen, *Eng. Fracture Mechanics* **9**, 931-938 (1977).
 15. E. C. Francis and D. Gutierrez-Lemini, in *Adhesive Joints: Their Formation, Characteristics, and Testing* (Plenum Press, New York, 1984), pp. 639-658.
 16. R. L. Ramkumar and J. D. Whitcomb, in *Delamination and Debonding of Materials*, ASTM STP 876 (Amer. Soc. for Testing and Materials, Philadelphia, 1985), pp. 315-335.

Elastoplastic Fracture Behavior of Structural Adhesives Under Monotonic Loading†

EROL SANCAKTAR, HOOSHANG JOZAVI, JOSEPH BALDWIN and JING TANG

Department of Mechanical and Industrial Engineering, Clarkson University, Potsdam, New York 13676, U.S.A.

Elastic-plastic fracture behavior of a structural adhesive in the bulk and bonded forms is discussed. The model adhesive chosen, Metlbond 1113 (with scrim carrier cloth) and 1113-2 (neat resin) solid film adhesives exhibit a relatively brittle material behavior to justify the use of LEFM methods.

The solid film adhesives are first cast in the form of tensile coupons to determine the bulk fracture properties with the use of single-edge-cracked specimen geometry. K_{IC} evaluation is done using the procedure suggested by the ASTM standard. A K -calibration method based on application of boundary collocation procedure to the William's stress function is utilized to relate the measured critical loads to the K_{IC} values. The yield stresses and elastic moduli values in the bulk tensile mode are also evaluated. The availability of K_{IC} , σ_y , E and ν (Poisson's ratio) values makes the calculation of crack tip plastic zone radii (r_{pc}) and fracture energy (G_{IC}) values possible on the basis of Irwin's theory. The bulk casting procedure is done under different cure (temperature, time and cool-down) conditions to determine optimum properties.

The fracture behavior of the same adhesives in the bonded form is studied with the use of Independently Loaded Mixed Mode Specimen (ILMMS) geometry. This specimen allows independent measurement of P_I and P_{II} (and consequently G_I and G_{II}) values. Since the fracture energy values are affected by the thickness of the adherend and the bondline, an experimental program is executed first by varying these geometrical parameters to determine the plane strain conditions. The relationship between the bondline thickness and the crack tip plastic zone radius values calculated earlier is also studied. Expressions developed on the basis of LEFM assumptions are utilized to calculate G_{IC} and G_{IIc} values in the bonded form. The G_{IC} values obtained in this manner are compared to the bulk G_{IC} values obtained earlier.

† Presented at the Tenth Annual Meeting of the Adhesion Society, Inc., Williamsburg, Virginia, U.S.A., February 22-27, 1987.

With the availability of P_I and P_{II} (G_I and G_{II}) values that result in failure in the bonded form, the fracture condition (i.e. the fracture failure criterion) in mixed mode (modes *I* and *II*) loading is determined for adhesively bonded joints. The use of both 1113 and 1113-2 adhesives also reveals the effects of the carrier cloth on the mechanical phenomena cited above.

KEY WORDS Elastoplastic bulk and bonded adhesive fracture; energy balance criterion; maximum principal stress criterion; independently loaded mixed mode adhesive fracture specimen; plastic deformation zone-adhesive thickness interdependence; compliance calibration.

INTRODUCTION

Adhesively bonded joint failures are usually results of catastrophic crack propagations (brittle fracture) originating from inherent flaws (voids or trapped air bubbles) and impurities.¹ These flaws are mainly formed in the bulk of the adhesive material during the curing process if ideal bonding and surface preparation of adherends prevail. Hence, a complete characterization of adhesives requires investigation of flaw-related material properties as well as bulk tensile properties as functions of cure and other service parameters. Since inherent flaws usually cause structural adhesives to fail in a brittle manner, the use of an LEFM (Linear Elastic Fracture Mechanics) method can be considered appropriate for characterizing their fracture behavior.

This paper presents data using model thermosetting adhesives Metlbond 1113 and 1113-2 which are commercially available from Narmco Materials, Inc. (Costa Mesa, California) in 0.25 mm and 0.13 mm (respectively) thick solid film rolls. Metlbond 1113 is a 100% solids, modified nitrile epoxy film with a synthetic carrier cloth. Metlbond 1113-2 is identical to 1113 matrix without the carrier cloth.

Brinson *et al.*² determined that the mechanical behavior of bulk Metlbond 1113 and 1113-2 adhesives is affected by the rate of straining. They showed that the constant strain rate stress-strain behavior of the adhesives approaches a perfectly elastic-plastic behavior as the magnitude of strain rate is increased. This mechanical behavior was described with the use of a modified Bingham viscoelastic-plastic model.

Since the stresses at a crack tip reach high values upon loading,

yielding occurs in a zone called the "crack tip plastic zone." If this zone is small compared to crack length, it will not greatly disturb the elastic stress field around it. Consequently, the extent of the plastic zone can be defined by the elastic stresses. Apparently, the use of an elastic-plastic material assumption in stress analysis problems greatly facilitates the solution.

The elastic-plastic material behavior assumption has been widely used for adhesive materials by a number of investigators such as Bascom³ and Hart-Smith.⁴ Bascom used a crack tip plane-strain assumption to relate the adhesive tensile yield stress, elastic modulus and the crack tip critical plastic zone radius to the fracture energy (G_{IC}). He calculated the critical plastic zone radius (r_{yc}) by using experimentally measured values of G_{IC} , σ_y and E .³

In order to be able to interpret the bulk data to design bonded joints, however, one needs to understand the constraint mechanism imposed on the adhesive material in the bonded form. Bascom³ reports that the maximum fracture energy for an adhesive in the bonded form was obtained when the bond thickness was approximately equal to the critical plastic zone diameter ($2r_{yc}$). His investigations also revealed that this maximum G_{IC} value was equal to that obtained with the bulk form of the adhesive.

In adhesively bonded joints crack propagation is constrained within the adhesive layer regardless of the loading orientation. Because of this condition one needs to consider mixed mode fracture. The majority of practical adhesive applications involve only G_I and G_{II} due to the peel and in-plane-shear stresses that arise in the use of lap joint geometries. In such geometries, adhesive cracks are exposed to both tension and shear resulting in mixed mode cracking.

The Independently Loaded Mixed Mode Specimen (ILMMS) geometry is used during the current investigation for mixed mode testing of adhesives in the bonded form. This geometry was originally proposed by Ripling *et al.*⁵ It allows simultaneous but physically separate application of cleavage and shear loads. Monotonic loading of the specimens with different P_I to P_{II} ratios enables us to determine the failure criterion for fracture of adhesively bonded specimens.

In order to determine the fracture toughness (K_{IC}) of bulk adhesives, the single-edge-cracked specimen geometry shown in

Figure 1 was chosen. The pertinent dimensions of plate specimens for K_{IC} testing are the crack length, thickness and the ligament (uncracked) length. According to ASTM standards,⁶ for a K_{IC} test to be valid, these dimensions should exceed a certain multiple of the quantity $(K_{IC}/\sigma_y)^2$. This quantity has been shown⁶ to be directly proportional to the radius of the crack tip critical plastic zone. Based on the elastic-plastic material assumption, the LEFM solutions are valid beyond the plastically deformed zone around the crack tip, if the size of this zone is small.

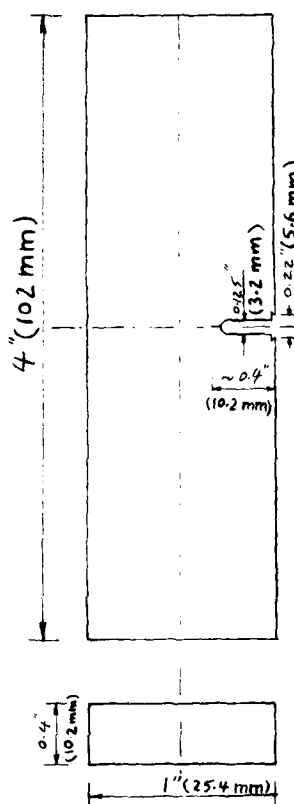


FIGURE 1 Single-edge-cracked specimen geometry used for fracture toughness (K_{IC}) measurements.

Based on the above considerations, this paper presents elastoplastic fracture behavior of a model solid film epoxy adhesive (Metlbond) with (1113) and without (1113-2) carrier cloth using bulk and bonded specimens. The bulk specimens are tested under monotonic loading using single-edge-crack specimen geometry. The Independently Loaded Mixed Mode specimen (ILMMS) geometry is used for mixed mode testing in the bonded form. In both cases, a high rate of monotonic loading is used to achieve an approximate elastic-plastic material behavior since the mechanical behaviors of the model adhesives were shown to approach elastic-plastic behavior at high strain rates.²

The solid film adhesives are first cast in the form of tensile coupons to determine the bulk fracture properties under monotonic loading with the use of single-edge-crack specimen geometry. K_{IC} evaluation is done using the procedure suggested by the ASTM standard. A K -calibration method based on application of boundary collocation procedure to the William's stress function is utilized to relate the measured critical loads to the K_{IC} values. The yield stresses and elastic moduli values for the model adhesives in the bulk tensile mode have already been evaluated by Sancaktar *et al.* and reported in the literature.⁷ The availability of K_{IC} , σ_y , E and ν (Poisson's ratio) values makes the calculation of crack tip critical plastic zone radii (r_{yc}) and fracture energy (G_{IC}) values possible on the basis of Irwin's theory.⁸ The effects of cure time, temperature and cool-down conditions on r_{yc} and G_{IC} are also illustrated and the (optimum) cure conditions resulting in the maximum r_{yc} and G_{IC} values are evaluated. These cure conditions are used in curing of bonded samples.

The fracture behavior of the model adhesives in the bonded form is studied with the use of Independently Loaded Mixed Mode Specimen (ILMMS) geometry. Since the fracture energy values are affected by the thickness of the adherend and the bondline, an experimental program is executed first by varying these geometrical parameters to determine the plane strain conditions. The relationship between the bondline thickness and the crack tip plastic zone radius values calculated earlier with the use of bulk data is also studied. Expressions developed on the basis of LEFM assumptions are utilized to calculate G_{IC} and G_{IIC} values in the bonded form. The G_{IC} values obtained in this manner are compared to the bulk G_{IC} values obtained earlier.

With the availability of P_I and P_{II} (G_I and G_{II}) values that result in failure in the bonded form, the fracture condition (*i.e.*, the fracture failure criterion) in mixed mode (modes *I* and *II*) loading is determined for adhesively bonded joints. For this purpose, energy balance and maximum principal stress criteria are used.

The use of model adhesives Metlbond 1113 (with carrier cloth) and 1113-2 (neat resin) also reveals the effects of the carrier cloth on the mechanical phenomena cited above.

ANALYTICAL CONSIDERATIONS

Irwin⁸ showed that for an isotropic material in the bulk form and crack tip plane strain conditions, the stress intensity factor can be expressed as

$$K_I = (G_I E / (1 - \nu^2))^{1/2} \quad (1)$$

where ν is the Poisson's ratio.

For ductile materials the crack propagation process involves mainly plastic energy due to crack tip plastic deformation. Furthermore, the mathematical formulation of the stress field based on perfectly elastic material behavior suffers from singularity at the crack tip. In order to resolve this problem, Irwin assumed elastic-plastic material behavior and stated that the failure stress at the crack tip is equal to the uniaxial yield stress acting over a region called the plastic zone. Beyond this zone the elastic stress distribution remains undisturbed. Irwin⁸ calculated the size (diameter) of the plastic deformation zone by considering an infinite plate containing a single crack under the action of tensile in-plane loading perpendicular to the crack. The diameter of the plastic (deformation) zone was thus shown to be

$$r_p = K_{IC}^2 / \pi \sigma_y^2 \quad (2)$$

Based on Eqs. (2) and (1), the "corrected" critical strain energy release rate could then be written as

$$G_{IC} = \pi \sigma_y^2 r_p (1 - \nu^2) / E \quad (3)$$

Irwin showed that the plane-strain elastic constraint will increase the tensile yield stress for plastic yielding and thus affect the size of

the plastic zone. Such an increase in the yield strength was estimated to be by a factor of approximately the square root of 3.^{8,9} The critical radius of the crack tip deformation zone can, therefore, be written as

$$2r_{yc} = (1/\pi)\{K_{IC}/(3)^{1/2}\sigma_y\}^2 \quad (4)$$

for plane-strain conditions. Substitution into Eq. (1) results in

$$G_{IC} \approx 6\pi\sigma_y^2 r_{yc}(1 - \nu^2)/E. \quad (5)$$

For an elastic cracked structure subjected to some mode I load (P_I), the rate of strain energy release (G_I) has been related to the material and geometrical properties and applied load⁹ with the equation

$$G_I = (P_I^2/2b)(\partial c/\partial a) \quad (6)$$

where b = material thickness in the vicinity of crack ($b = 10.2$ mm in Figure 1), $\partial c/\partial a$ = change in compliance (c) with crack length (a), ($a = 10.2$ mm in Figure 1).

The load level at which spontaneous crack growth occurs is called the critical load (P_c) and the corresponding energy release rate is called the fracture energy (G_c).

In order to utilize Eq. (6) one needs to determine the variation of compliance (ratio of displacement to the applied load) for different crack lengths of a given specimen geometry.

Determination of fracture energy in bonded and bulk samples

A. Bonded samples

There are three basic specimen geometries for mixed mode testing of adhesives in the bonded form. They are cracked lap-shear,¹⁰ scarf joint¹¹ and the Independently Loaded Mixed Mode Specimen (ILMMS) geometries. Among these, the only specimen geometry which allows independent measurement of P_I and P_{II} (and consequently G_I and G_{II}) is the ILMMS. The other two require finite element analysis to calculate G_I and G_{II} values from a load applied in only one direction. In order to avoid any inaccuracies which may be involved in the calculation of G_I and G_{II} values with the use of a

finite element program and due to its practicality in load measurement, the ILMMS geometry is used during the current investigation. In order to test different P_I to P_{II} ratios, a hydraulic actuator force is applied statically in mode *II* and the specimen is loaded monotonically in mode *I* until failure. Subsequently, the static force is applied in mode *I* while the specimen is loaded monotonically in mode *II* until failure.

Examination of the literature and our experience show that the strain energy values are affected by the thickness of the adherend and the bondline. For this reason it is necessary first to determine, experimentally, the adhesive and adherend thickness values that result in plane strain conditions. The following methods are used for this purpose:

As mentioned earlier, Bascom³ reports that the maximum fracture energy for an adhesive in the bonded form is obtained when the bond thickness is approximately equal to the critical plastic zone diameter ($2r_{yc}$). His investigations also reveal that this maximum G_{IC} value is equal to that obtained with the bulk form of the adhesive.

Limited information is available in the literature regarding the effects of adherend thickness (b) (or crack front length) on G_{IC} . Kinloch *et al.* report that the stress condition at the crack tip of an adhesive bond varies from one of plane stress for short crack fronts (thin bonds) and at the edges of thicker bonds, to one of plane strain near the center of thick bonds. The increased constraint present in plane strain conditions results in a smaller zone of plastic deformation.¹² This indicates that as the adherend thickness increases, thereby increasing constraint on material deformation, the fracture energy will decrease.

The advantage in using the ILMM specimens is the option of not having to calculate G_I or G_{II} values in order to determine the fracture criterion. The availability of separate P_I and P_{II} values is sufficient to obtain such a criterion. However, calculation of G_I and G_{II} values is helpful in accounting for geometrical effects (when different geometries are used) and for comparison purposes.

Our experiments showed that P_{IIC} is a (linear) function of the bond length (L), ($L = 12.7$ cm in Figures 2 and 3) and therefore necessary terms must be included in any G_{IIC} relation to render this material constant (G_{IIC}) independent of geometrical effects. For this

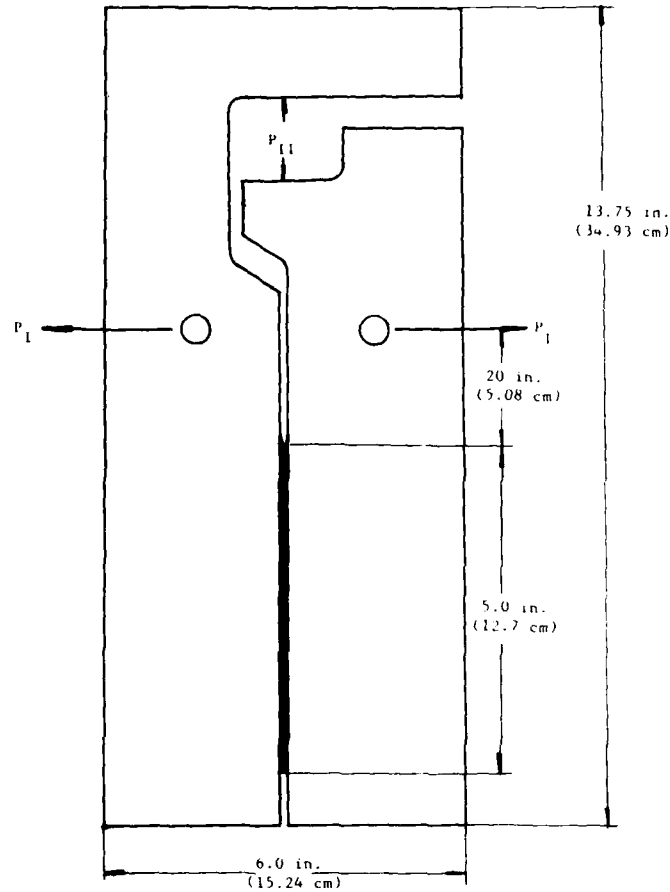


FIGURE 2 ILMM specimen geometry A for monotonic opening, static in-plane shear loading.

purpose, the following simplified approach is used: If we assume that in an ILMM specimen the axial load varies linearly along the overlap direction¹³ then the total elastic energy (W_T) stored in the adhesive and the adherends can be written as

$$W_T = \int_0^L \int_0^h \int_0^b (P_{II}^2/E_s h^2 b^2)(1 - y/L)^2 dx dy dz + (nbL)(\tau_{avg}^2/2G_A) \quad (7)$$

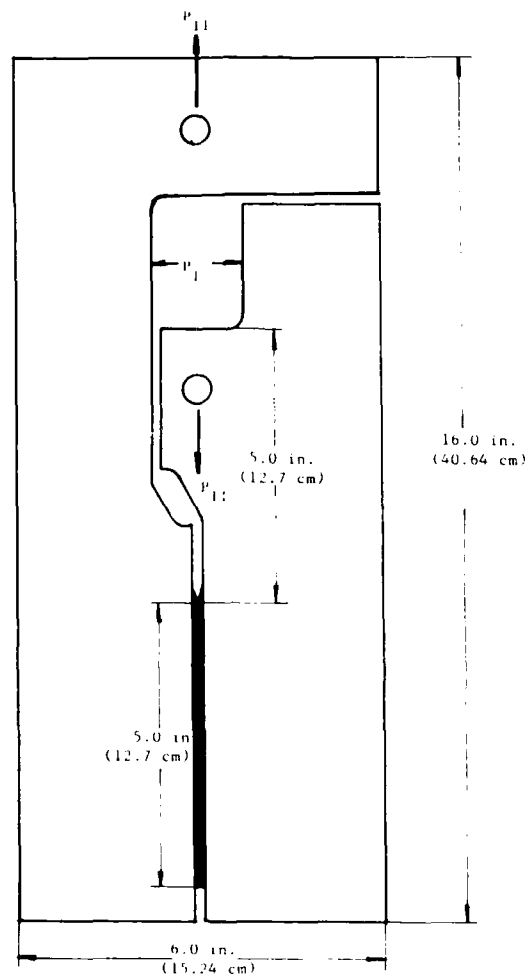


FIGURE 3 ILMM specimen geometry *B* for monotonic in-plane shear static opening loading.

where, h = adherend beam height ($2h = 15.24$ cm in Figures 2 and 3), E_{st} = Young's modulus for the steel adherends, n = adhesive thickness, G_A = elastic shear modulus for the adhesive, and $\tau_{avg} = P_{II}/Lb$ = average shear stress in the adhesive layer. Solution of Eq. (7) with the assumption

$$G_{II} = W_T/2Lb \quad (8)$$

yields

$$G_{II} = (P_{II}^2/2b^2)(1/3hE + n/2L^2G_A). \quad (9)$$

Note that Eq. (9) accommodates the linear increase of P_{II} with L .

A widely accepted relation for G_I in (bonded) double cantilever beam specimens is

$$G_{IC} = 4P_{IC}^2(3(a + a_0)^2 + h^2)/b^2h^3E. \quad (10)$$

Experimentation shows that in addition to bending and shear deflections, there exists additional deflection due to rotation at the assumed "built in" end of the beam. It is assumed that this rotation can be treated as an increase in crack length and hence it is accounted for with the use of the empirical rotation factor a_0 in Eq. (10). The value of a_0 , however, must be determined experimentally when the geometrical parameters are varied. This is accomplished by means of experimental compliance calibration.

B. Bulk samples

For the single-edge-crack geometry used for bulk samples, Gross *et al.*¹⁴ applied a boundary collocation procedure to the William's stress function to determine the elastic stress distribution at the tip of an edge crack in a finite-width specimen subjected to uniform tensile loading. The K -calibration for the single-edge-crack geometry is given by:

$$K_{IC}bw/P_Ca^{1/2} \approx 1.99 - 0.41(a/w) + 18.7(a/w)^2 - 38.48(a/w)^3 + 53.85(a/w)^4 \quad (11)$$

where w is the specimen width. Examination of the literature⁶ reveals that in single-edge-crack samples a plane strain condition is ensured when the minimum values for specimen thickness (b) and crack length (a) are given by:

$$a, b \geq 2.5(K_{IC}/\sigma_y)^2. \quad (12)$$

Determination of failure criterion

With the application of the energy balance criterion we get:

$$K_I^2 + K_{II}^2 = \text{constant} \quad (13)$$

where the locus of failure is a quarter circle. However, previous

experimentation by other researchers¹⁵ showed that an elliptical condition is more realistic, *i.e.*

$$(P_I/P_{IC})^2 + (P_{II}/P_{IIC})^2 = 1. \quad (14)$$

A second criterion that must be considered involves the possibility of failure in mode *I* under the action of the maximum principal stress since a biaxial state of stress is applied globally. It should be noted that the mode *I* in such cases will be at angle to the applied P_I load, with this angle being determined by the applied P_I to P_{II} ratio. Obviously, such an inclined crack will have to connect with similar ones or simply continue propagating in the P_{II} direction (possibly close to or at the interface) to result in catastrophic failure. The likelihood of this type of failure is high, especially for brittle adhesives.

We propose the following simplified approach to describe this type of failure: If one takes a biaxial stress element well ahead of the crack tip where the stresses are defined and uniform, then the elementary theory defines the maximum principal stress as:

$$(\sigma/2) + [(\sigma^2/4) + \tau^2]^{1/2} = \text{constant} \quad (15)$$

Assuming that loads and stresses are linearly related, substitution into Eq. (15) yields:

$$CAP_I + B^2P_{II}^2 = C^2. \quad (16)$$

Note that Eq. (16) describes a parabolic failure condition while Eq. (14) described an elliptical one. Obviously Eq. (16) should contain at least an additional P_I^2 term resulting from the contribution of shear loading to the opening direction. However, this contribution is neglected, as it is assumed to be small.

It should also be noted that Eq. (16) can be rewritten in terms of the stress intensity factors as:

$$(K_I/K_{IC}) + (K_{II}/K_{IIC})^2 = 1 \quad (17)$$

EXPERIMENTAL PROCEDURES

Bulk samples¹⁶

Metlbond 1113 and 1113-2 adhesive rolls were stored in a freezer at -1°C and 0% RH. First, the adhesive roll was taken out of the

freezer and allowed to thaw in the ambient temperature until it was flexible enough to work with. It was determined that for Metlbond 1113 (with carrier cloth) 45 layers and for Meltbond 1113-2 (without carrier cloth) 78 layers were needed to make thickness of 10.16 mm of cured material. Each layer was cut to 38 mm \times 330 mm size. Two aluminum plates with 5 mm \times 38 mm \times 330 mm grooves were sprayed with Teflon[®] and were used to cast the multilayered adhesive. For this purpose, the adhesive layers were carefully laid on one grooved plate and smoothened. The second plate was then placed on top of the first one and the two plates were tightly and uniformly clamped together. The assembly was subsequently placed in the oven for curing.

At the end of the cure cycle, the assembly was cooled either quickly or slowly to simulate the fast and slow cool-down conditions.

For each cure condition three specimens were manufactured. In order to facilitate the machining of the specimens, the cured adhesive plate was taped to a metal specimen template using two-sided tape. A vertical contour saw was used to remove most of the excess adhesive along the template border. The final contour shaping was done by using a carbide-bit router as the template slid along a guide pin to ensure a uniform specimen shape. Finally, the surfaces of the specimen were smoothened with a fine grade sanding block. The starter crack was produced subsequently by tapping a sharp knife at the base of the machined notch. The knife-edge at the mouth of the machined notch (Figure 1) was made to facilitate mounting of a Crack Opening Displacement (C.O.D.) gage which was used in determining the K_{IC} values. The final specimen dimensions are shown in Figure 1.

Several measurements had to be made before testing a specimen. The width and thickness were accurately measured using a micrometer. The total crack length (including the depth of machined notch and starter crack) was measured using a light reflective microscope at a magnification of 10 \times . This was done on both sides of the specimen and an average crack length value was calculated.

Bonded samples

The original dimensions and geometry proposed by Ripling and Mostovoy were altered substantially, on the basis of our experimen-

tal stress analysis through the use of reflection and transmission photoelasticity in order to minimize any interference between the two modes (*i.e.*, cleavage loads resulting from shear loads, etc.) and to reduce the effects of stress discontinuities. This new geometry allows the use of a small hydraulic actuator inside the specimen. The geometries developed are shown in Figures 2 and 3. Since the width of the actuator used is larger than its height, it was necessary to develop two different specimen geometries with geometry *A* (Figure 2) being used for static loading in mode *II* and geometry *B* used for static loading in mode *I*. Examination of Figures 2 and 3 reveals the presence of frictional resistance affecting the loads applied orthogonal to the static loads. These frictional loads were measured experimentally and subtracted from the applied (monotonic) loads. Even though the frictional resistance existed only in the sliding mode during all our experiments, the validity of the subtraction procedure based on static equilibrium was checked with the use of rolling friction. For this purpose steel pins were placed in between the actuator face and the specimen. In both sliding and rolling friction cases the same G_I and G_{II} ratios were obtained corresponding to the same crack opening displacements and also at failure.

Bonded specimen preparation

There are three major steps to bonded specimen preparation. They are:

A. Pre-etch preparation

Original specimens are cut from cold rolled 1095 steel flat stock. Specimens are reused by grinding off the old adhesive with a belt sander. With the use of 1095 grade steel, any permanent deformation of the adherends is avoided. The difference in surface roughness provided by belt sanding and milling is found to have no measurable effect on bond strength. Specimen dimensions and bond line alignment should be checked prior to the etching procedure since, after etching, handling must be kept to a minimum. Bonding surfaces should align squarely.

It is very important for the specimens to be thoroughly degreased

prior to etching. Any cutting oils left on the specimen when it is inserted into the acid bath will linger as a film on the surface of the bath and redeposit itself on the specimen as it is removed from the bath. Acetone and trichloroethane are both effective degreasing agents. A simple check to determine whether a specimen has any residual grease or oils on it is to dip it into water. If the entire surface wets, that is if a thin film of water remains on the specimen when it is taken out of the water, then it has been thoroughly degreased. However, if dry areas break out on the specimen, this indicates an oil residue and the specimen should be degreased.

B. Acid bath etching

The standard etching procedure for steel, provided by Narmco Corporation, is employed. The acid bath consists of:

150 ml sulfuric acid	7.5% by volume
300 ml nitric acid (70)	15% by volume
25-50 ml powdered sodium dichromate	5% by volume
1500 ml tap water	72.5% by volume.

The above solution is combined in a Pyrex baking dish large enough to hold both halves of a specimen. The specimens are etched one at a time at room temperature for about 2 minutes. This work must be done under a hood because of the noxious fumes given off by the reaction. Acid resistant gloves are used to handle the specimens while they are in the acid. At the end of the etching period, the specimen is removed from the bath and placed in a bucket of tap water until it can be rinsed under running water. The water rinse is needed to remove the significant oxidation layer that is formed on the specimen while in the acid bath. In fact, in order to get the specimen really clean, a Scotchbrite® pad is used and the specimen is scrubbed rigorously under running water. Care is taken to insure that no soap residue is introduced during this scrubbing.

Finally, the specimens are wiped dry with clean paper towels and baked in a 49°C oven for 15 minutes to drive off any surface moisture. If the specimens are allowed to air dry as recommended by Narmco, a thin oxidation film results. At this point, the specimens are placed in a protective enclosure (a steel tool box) for transportation and storage until they can be bonded. Bonding

should proceed as soon after etching as possible, certainly within 24 hours.

C. Bonding

It was observed that the bonding procedure was the most sensitive, and therefore the most difficult, to accomplish successfully when compared with the other steps in specimen preparation. Temperature, humidity, cleanliness, and clamping pressure are all important parameters.

To begin with, the working area must be uncluttered and dust free. It is recommended that surgical gloves be worn to eliminate the transfer of any oils or moisture from the skin to the bonding surface.

The ambient temperature of the bonding area should be high enough to soften the adhesive, making it somewhat tacky. A temperature between 21°C and 29°C allows the adhesive to be applied with a minimum of difficulty and without air inclusions. The specimens should not be cooler than the bonding environment. If cooler specimens are introduced to the bonding environment surface condensation of moisture could result.

Although 6 layers of Metlbond 1113-2 adhesive should have been enough to provide 0.64 mm bondline thickness used, it was soon discovered that double that amount of adhesive was needed to provide enough pressure to ensure a good bond. The majority of Metlbond 1113-2 tests were done with 13 layers of adhesive. For bonding with the Metlbond 1113 adhesive, 7 layers were sufficient due to the presence of the carrier cloth. The reason for the use of 0.64 mm bondline thickness will be explained later.

After the adhesive had been applied on one side of the specimen the two halves are joined and placed in a bonding jig. Teflon coated steel spacing shims are placed at either end of the bond and clamping pressure is applied.

All four specimens are then placed in an oven set at 149°C for 30 minutes. The specimens are allowed to cool slowly (usually overnight) by turning off the oven and leaving the door closed.

Once cool, excess adhesive is filed off the sides of the specimens and bondline measurements are taken. The specimens are then ready for testing.

Both bulk and bonded specimens were tested under monotonic tension with a constant crosshead rate of 50.8 mm/min. Such a fast head rate was used to minimize the viscoelastic effects.

RESULTS AND DISCUSSIONS

Bulk samples

As mentioned earlier, information on the size of the crack tip critical plastic zone radius makes it possible to relate the bulk properties to fracture properties in the form of fracture toughness and fracture energy. Such a relation is possible on the basis of a "small scale" yielding assumption¹¹ and Eqs. (5) and (1). Figures 4 and 5 show the effects of cure conditions on the (calculated) critical plastic zone radius of Metlbond 1113 and 1113-2, respectively. Examination of these figures reveals that r_{yc} values corresponding to optimum K_{IC} 's for the fast or slow cool-down conditions are relatively constant. Therefore, it seems possible that one can use some average r_{yc} values (based on optimum K_{IC} 's) to represent the

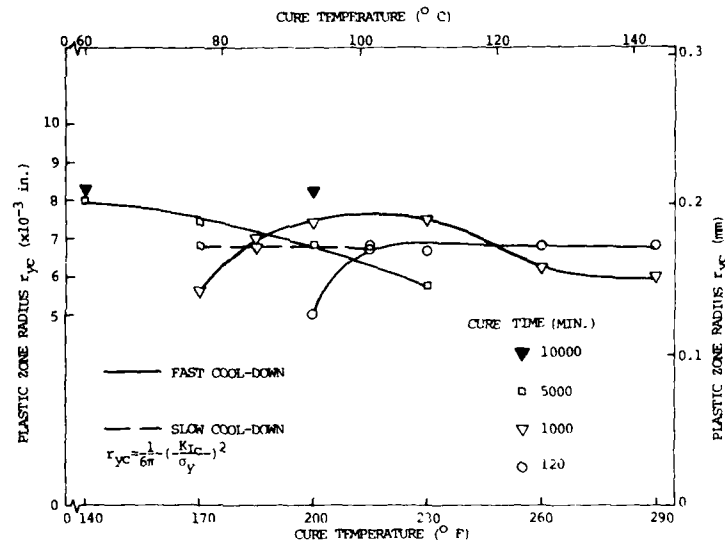


FIGURE 4 Effect of cure conditions on the plastic zone radius based on bulk tensile and fracture toughness data of Metlbond 1113.

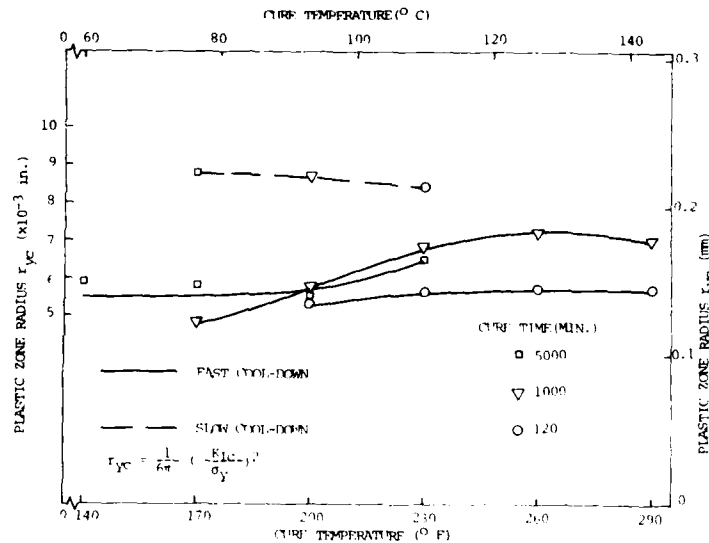


FIGURE 5 Effect of cure conditions on the plastic zone radius based on bulk tensile and fracture toughness data of Metlbond 1113-2.

typical critical plastic zone radii sizes for either material subjected to the fast or slow cool-down conditions. Using this concept, it can be seen in Figure 5 that the average critical plastic zone radius for Metlbond 1113-2 with the slow cool-down condition is higher than that for the fast cool-down condition. As expected, this implies that the slow cool-down condition results in a tougher adhesive matrix material, as the availability of a larger plastic zone size at the crack tip enables relieving of higher stress levels at that location thus resulting in higher crack growth resistance. It is not possible to offer a similar argument for the adhesive with the carrier cloth as the values obtained with slow and fast cool-down conditions are about the same (Figure 4). This result, however, is also expected since it is already known that the effect of cool-down conditions on Metlbond 1113 fracture toughness is minimal as attributed to the presence of the carrier cloth.¹⁶

The availability of these average r_{yc} values along with previously measured σ_y and E data made the calculations of G_{IC} values possible based on Eq. (5). These calculated values could also be

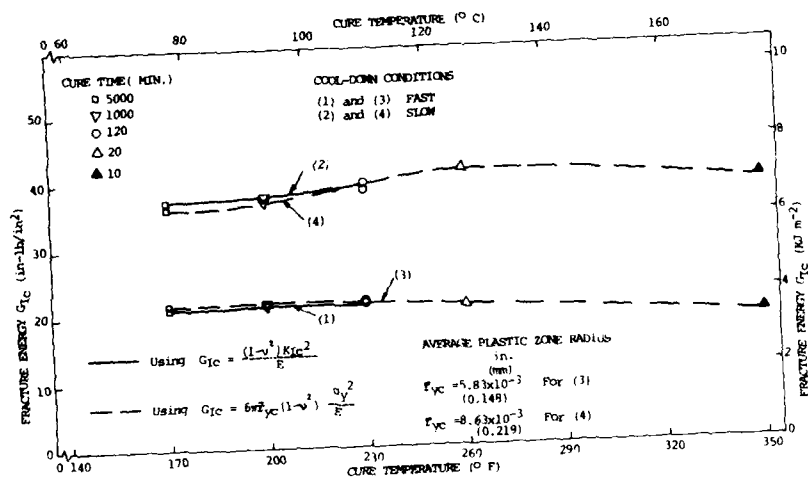


FIGURE 6 Metlbond 1113-2, slow and fast cool-down fracture energy-cure optimization curves calculated based on bulk tensile and fracture toughness data.

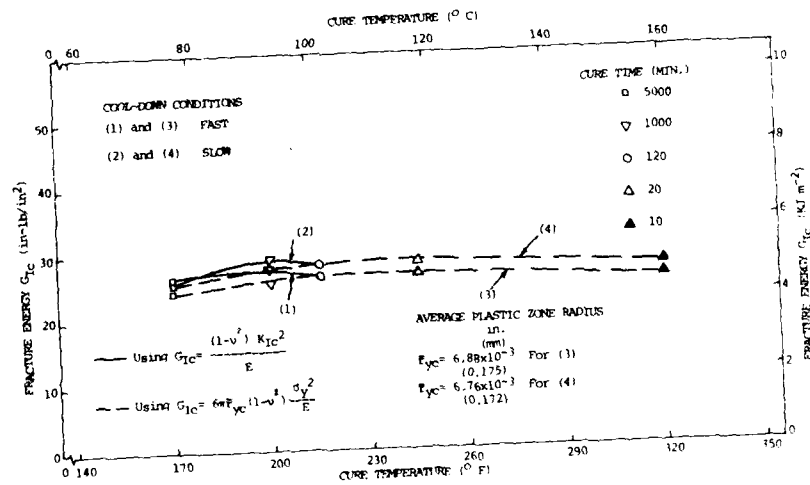


FIGURE 7 Metlbond 1113, slow and fast cool-down, fracture energy-cure optimization curves based on bulk tensile and fracture toughness data.

compared with the G_{IC} values which were obtained on the basis of measured K_{IC} values and Eq. (1) to verify the validity of using an average r_{yc} value in Eq. (5). In calculating fracture energies the value of Poisson's ratio (ν) was assumed to be the constant value of 0.374 for both materials.² Figures 6 and 7 show the effects of cure conditions on the fracture energy of Metlbond 1113-2 and 1113, respectively. Comparison of Figures 6 and 7 confirms that: i) With the fast cool-down condition Metlbond 1113 yields higher G_{IC} values than Metlbond 1113-2; ii) With the slow cool-down condition the optimum G_{IC} values are significantly higher using Metlbond 1113-2 as compared with Metlbond 1113; iii) Cure temperature and time do not seem to have a significant effect on fracture energy for either material.

Bonded samples

Experimental results indicate that for the adhesive without the carrier cloth the G_{IC} values are maximum when the adherend thickness (b) is equal to 6.35 mm. A plane strain condition is attained when $b = 1.27$ cm (Figure 8). For the adhesive with the carrier cloth (1113) the G_{IC} value is maximum when $b = 3.18$ mm

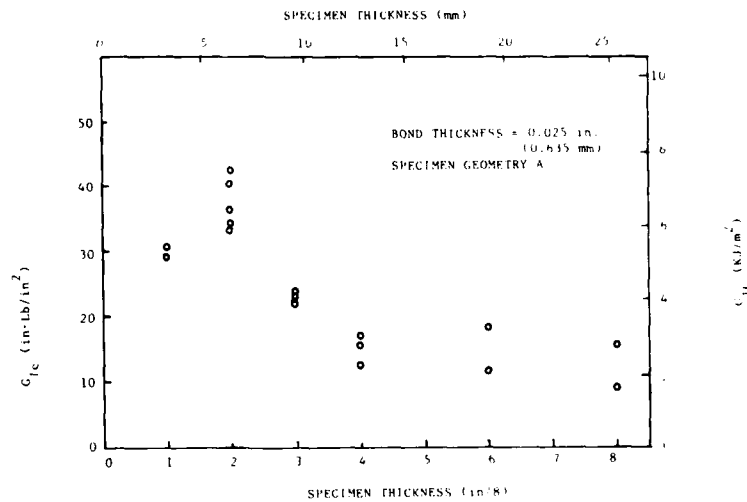


FIGURE 8 Variation of G_{IC} with specimen thickness for 1113-2 adhesive.

and the plane strain condition is attained when $b = 9.53$ mm (Figure 9). For both adhesives $b = 1.27$ cm is used for the plane strain condition. It should be noted that the maximum G_{IC} values obtained with 1113-2 and 1113 adhesives are close to the G_{IC} values previously measured by us¹⁶ using bulk edge-crack compact tension specimens and the values measured by O'Conner¹⁷ using bonded Tapered Double Cantilever Beam (TDCB) specimens.

As mentioned earlier, Bascom³ reports that the G_{IC} values in the bonded form are maximum and equal to bulk G_{IC} values when the bond thicknesses (n) are equal to $2r_{yc}$. Our experimental results showed further confirmation of this assertion. For 1113-2 samples with $b = 6.35$ mm and $b = 1.27$ cm adherend thicknesses, G_{IC} is maximized and remains constant when the plane strain condition is attained slightly above the $n = 0.508$ mm value (Figures 10, 11). The adhesive thickness corresponding to the onset of the plane strain condition is close to the $2r_{yc}$ value calculated by us based on our previous bulk fracture tests¹⁶ (Figure 5). For the adhesive with the carrier cloth the plane strain condition is achieved slightly above $n = 0.254$ mm. This value is very close to our previously calculated $2r_{yc}$ value for the 1113 adhesive¹⁶ (Figure 4). These results also reveal the stabilizing effect of the carrier cloth on G_{IC} values.

In order to be able to use Eq. (10) in determining G_{IC} values, it is

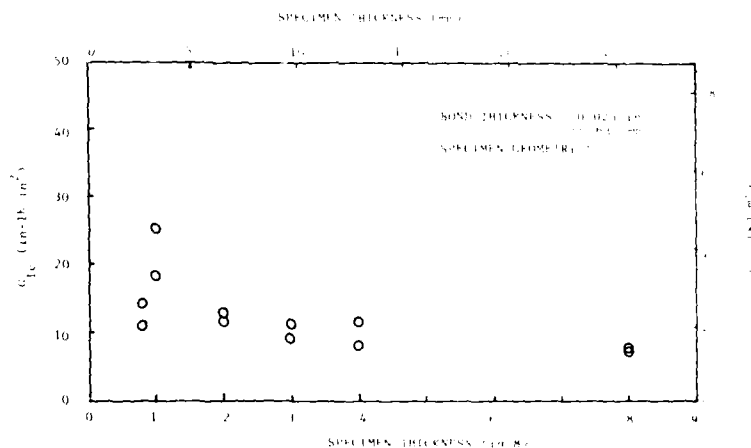


FIGURE 9 Variation of G_{IC} with specimen thickness for 1113 adhesive.

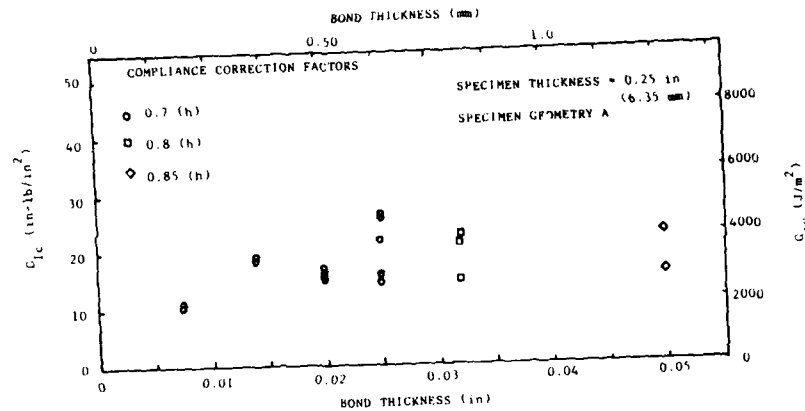


FIGURE 10 Variation of G_{IC} with bond thickness for 1113-2 adhesive.

necessary to evaluate first the rotation factor a_0 experimentally. This is done by means of compliance calibration: The specimen compliance (c) is defined as

$$c = \delta / P \quad (18)$$

where δ = crack opening displacement and P = applied opening load. Apparently, if δ vs. P values are determined for different

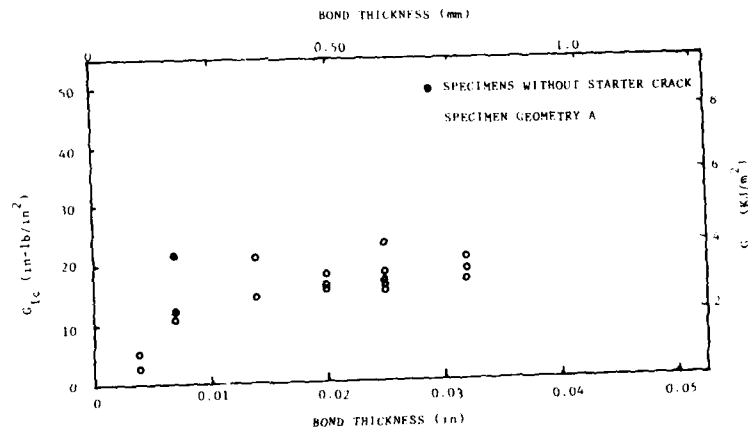


FIGURE 11 Variation of G_{IC} with adhesive thickness for 0.5 in (12.7 mm) thick specimens bonded with 1113-2 adhesive.

crack lengths then the compliance equation

$$C = (2/3EI)[(a + a_0)^3 + h^2a] \quad (19)$$

can be fitted to these data by using the appropriate a_0 value. Figure 12 shows such compliance calibration curves for different adherend thicknesses of specimen geometry A bonded with 0.635 mm thick Metlbond 1113-2 adhesive. Obviously, for geometry A with $6.35 \text{ mm} \leq b \leq 12.7 \text{ mm}$, the correction factor a_0 is $(0.7)h$ where h is the beam height. Other rotation factor (a_0) values were obtained by means of compliance calibration for different adherend thicknesses, adhesive thicknesses, specimen geometries (A or B) and adhesive types (with or without carrier cloth) as shown below:

- 1) For the adhesive without the carrier cloth (1113-2):
 - i) For geometry A with $6.35 \text{ mm} \leq b \leq 12.7 \text{ mm}$ (adherend thickness) and $0.178 \text{ mm} \leq n \leq 0.635 \text{ mm}$ (adhesive thickness): $a_0 = (0.7)h$.
 - ii) Same as in 1-i except $n = 1.27 \text{ mm}$: $a_0 = (0.85)h$.
 - iii) For geometry b with $6.35 \text{ mm} \leq b \leq 12.7 \text{ mm}$ with $n = 0.635 \text{ mm}$: $a_0 = (0.6)h$.

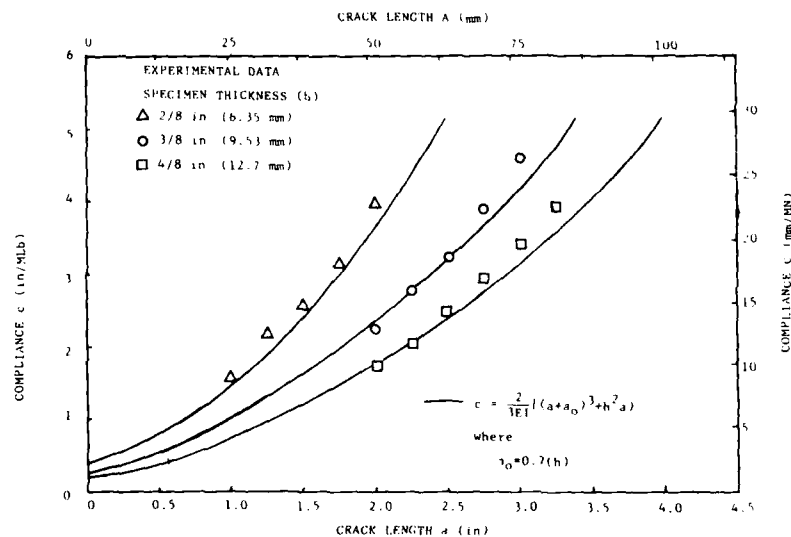


FIGURE 12 Compliance calibration for different thicknesses of geometry A bonded with 0.025 in (0.635 mm) thick 1113-2 adhesive.

2) For the adhesive with the carrier cloth (1113):

- i) For geometry *A* with $b = 6.35$ mm and $n = 0.63$ mm: $a_0 = (0.6)h$.
- ii) Same as in 2-i except $b = 12.7$ mm: $a_0 = (0.8)h$.
- iii) For geometry *B* with $b = 12.7$ mm and $n = 0.635$ mm: $a_0 = (0.8)h$.

It should be noted that some of the a_0 values reported above may be in error by as much as 25% due to experimental difficulties and functional dependence of a_0 on crack length.

Another geometrical consideration in fracture energy calculations involves the effect of bondline length on G_{II} values. Our experiments with double cantilever beams revealed that the mode II breaking force (P_{IIC}) increases with increasing bond length. This behavior was observed with two different beam thicknesses ($b = 6.35$ mm and 12.7 mm) and appeared to be a linear function between the P_{IIC} and the bond length (L) (Figure 13).

Failure criteria data and curves showing P_I vs. P_{II} for 1113-2 and 1113 adhesives are depicted in Figures 14 through 16. Results obtained using geometry *A* (monotonic in opening, static in shear) and *B* (monotonic in shear and static in opening) are combined in these figures. Since the two geometries have different crack lengths (5.08 cm for geometry *A* and 15.24 cm for geometry *B*), opening

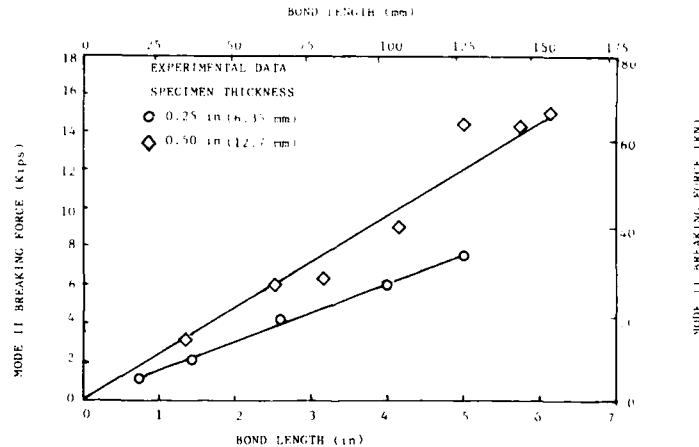


FIGURE 13 Variation of mode II breaking force with bond length.

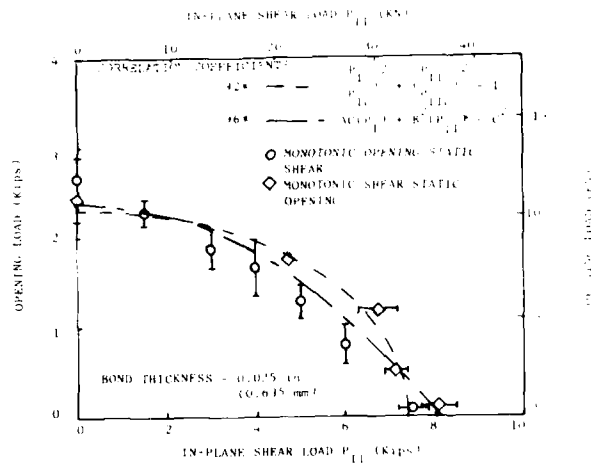


FIGURE 14 Opening load vs. in-plane shear load for 0.25 in (6.35 mm) thick 1113-2 ILMM specimens and comparison with theory.

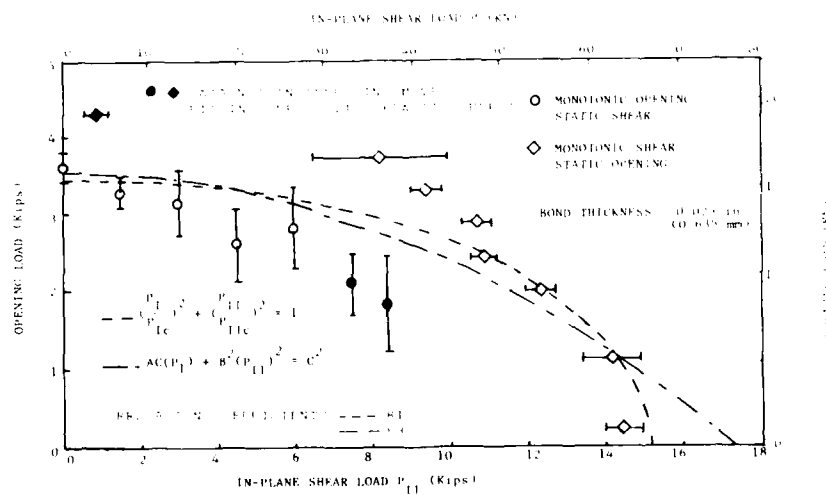


FIGURE 15 Opening load vs. in-plane shear load for 0.5 in (12.7 mm) thick 1113-2 ILMM specimens and comparison with theory.

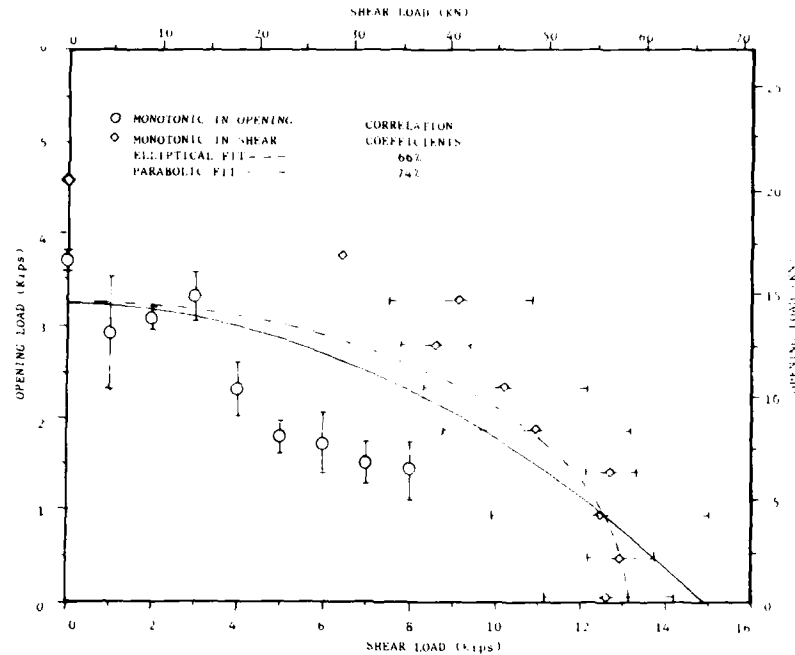


FIGURE 16 Opening load vs. in-plane shear load at fracture for 0.5 in (12.7 mm) thick 1113 ILMM specimens and comparison with theory. The adhesive bond thickness is 0.025 in (0.635 mm).

mode loads for geometry *B* were normalized with respect to those obtained with geometry *A*. This was done with the application of the G_I relation (Eq. (10)). The data shown in Figures 14 and 15 were obtained with the adhesive without the carrier cloth using specimens with 6.35 mm and 12.7 mm thick adherends respectively. The data for the adhesive with the carrier cloth is shown in Figure 16 for the adherend thickness of 12.7 mm. Included in these figures are also correlation coefficients to indicate the goodness of fit for elliptical (Eq. (14)) and parabolic (Eq. (16)) functions based on energy balance and principal stress criteria respectively.

Comparison of Figures 15 and 16 reveal that larger P_I and/or P_{II} loads (and consequently the corresponding fracture energy values) are required for the failure of ILMM specimens bonded with the adhesive without the carrier cloth (Metlbond 1113-2) in comparison

to the samples bonded using the adhesive with the carrier cloth (Metlbond 1113). This result is in agreement with the results of our bulk fracture experiments where higher G_{IC} values were obtained for Metlbond 1113-2 in comparison to Metlbond 1113. Note that this comparison between the bulk and bonded samples is made only for the samples that have matching cure conditions with the slow cool-down condition being the most important.

The experimental results also reveal more randomness and hence more data scatter in the bonded fracture behavior of the adhesive with the carrier cloth in comparison to the fracture behavior of the neat resin.

Examination of Figures 14 through 16 also reveal two important points common to all of them:

- 1) The presence of viscoelastic effects is observed in the application of the static load. In other words, relaxation processes take place prior to failure. These effects are especially severe when the static load is applied in mode *I*. The presence of delayed failure in mode *I* at high loads is an indication of this behavior. It is, therefore, assumed that some relaxation takes place at the crack tip, rendering the actual static loads somewhat less than shown. This is

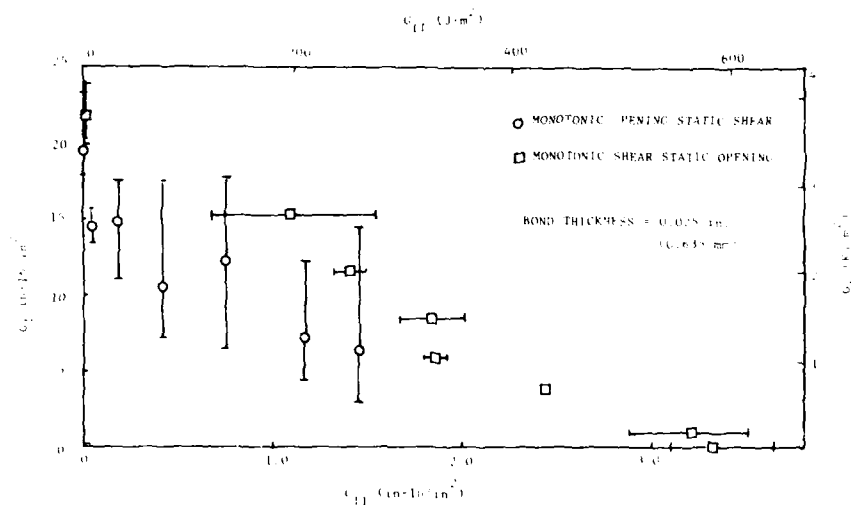


FIGURE 17 G_I vs. G_{II} behavior of 0.5 in (12.7 mm) thick specimens bonded with 1113-2 adhesive.

why the data obtained using geometry *B* lie above those obtained using geometry *A* when the P_{II} values are the same in magnitude (note that their mode of application is different). The use of data from both geometries *A* and *B* in determining the failure criteria is thought to have some averaging effect on this behavior.

2) The parabolic (principal stress) criterion defined by Eq. (16) consistently provides a better fit to the experimental data in comparison to the elliptical criterion given by Eq. (14).

The G_I vs. G_{II} behavior for the Metlbond 1113-2 adhesive is shown in Figure 17.

CONCLUSIONS

The application of the elastoplastic fracture behavior assumption proved adequate and useful for the model adhesives under study. Excellent correlation was obtained between the properties measured using bulk and bonded specimens. The concept of a plastic deformation zone proves especially useful in determining the optimum adhesive thickness in bonded samples.

The results presented in this paper reveal that when the energy balance criterion is used, the mixed *I-II* mode fracture energy (total energy) values of failure for combined cleavage and shear loading are lower than mode *I* (pure cleavage) fracture energy values at failure. Consequently, G_{IC} is not a sufficient criterion for the failure analysis of adhesively bonded joints. This finding corroborates similar conclusions reported earlier by Bascom *et al.*¹⁸

Another important conclusion that can be drawn from the data presented is the necessity for considering a maximum principal stress criterion for "brittle" adhesives such as Metlbond. Obviously, the data could be correlated better with the use of a principal stress criterion in comparison to an energy balance criterion. The applicability of a principal stress criterion to ductile adhesives or to glassy polymers subjected to high temperatures, however, is still not known.

The experimental data reveal that the fracture resistance of the model adhesive without the carrier cloth is higher than the fracture resistance of the same adhesive with the carrier cloth in both bonded (mixed mode) and bulk (cleavage only) modes.

The successful application of ILMMS geometry in testing large number of samples should be considered the most important contribution of this work. The physical separation of opening and in-plane shear loads while they are being applied simultaneously allows determination of a failure criterion on the basis of applied loads. Consequently, it becomes possible to compare the failure behavior of different adhesives under similar conditions or to assess the failure behavior of an adhesive under different environmental conditions without calculating any strain energy release rate or stress intensity values.

Acknowledgments

The material covered in this paper is based upon work supported by the National Science Foundation under grants No. CME-8007251 and CEE-8317428. Mr. J. Baldwin's first place award for his work based on this project, earned in the American Institute of Aeronautics 1986 National Graduate Student Competition, is also acknowledged.

References

1. D. W. Dwight, E. Sancaktar and H. F. Brinson, in *Adhesion and Adsorption of Polymers* (Plenum Press, New York, 1980), pp. 141-164.
2. H. F. Brinson, M. P. Renieri and C. T. Herakovich, *ASTM STP* 593, 177 (1975).
3. W. D. Bascom, R. L. Cottingham and C. D. Timmons, *J. Appl. Polym. Sci.* **32**, 165 (1977).
4. L. J. Hart-Smith, *Design and Analysis of Adhesive Bonded Joints*, McDonnell-Douglas Co. Report No. 6059A (1972).
5. E. J. Ripling, S. Mostovoy and R. L. Patrick, *ASTM STP* **360**, 5 (1963).
6. *Annual Book of ASTM Standards* (ASTM, Philadelphia, 1984), Vol. 03.01, Designation: E 399-83, pp. 519-554.
7. E. Sancaktar, H. Jozavi and R. M. Klein, *J. Adhesion* **15**, 241 (1983).
8. G. R. Irwin, *Proc. 7th Sagamore Conf.*, pp. IV, 63-173 (1960).
9. D. Broek, *Elementary Engineering Fracture Mechanics*, 3rd. ed. (Noordhoff International Publishing, Leyden, Netherlands, 1974), Chap. 5, p. 116.
10. S. Mall, W. S. Johnson and R. A. Everett, *Cyclic Debonding of Adhesively Bonded Composites*, NASA Tech. Memo. 84577, Nov. 1982.
11. A. J. Kinloch, *Developments in Adhesives-2* (Applied Science Publishers, London, 1981), Chap. 3, pp. 83-124.
12. A. J. Kinloch and S. J. Shaw, *J. Adhesion* **12**, 59 (1981).
13. F. Szczepe, *Proc. 2nd SESI Int. Congress on Exp. Mech.*, pp. 478-484 (1965).
14. B. Gross, J. E. Srawley and W. F. Brown Jr., *Stress Intensity Factors for a Single-Edge-Notched Tension Specimen by Boundary Collocation of a Stress Function*, NASA Tech. Note D-2395, Aug. 1964.

15. W. S. Johnson and P. D. Mangalgiri, *Influence of the Resin on Interlaminar Mixed-Mode Fracture*, NASA Tech. Memo. 87571, July 1985.
16. H. Jozavi and E. Sancaktar, *J. Adhesion* **18**, 25 (1985).
17. D. G. O'Conner, *Factors Affecting the Fracture Energy for a Structural Adhesive*, M.S. Thesis, V.P.I. and S.U. Blacksburg, Virginia, Aug. 1979.
18. W. D. Bascom, R. L. Jones and C. O. Timmons, in *Adhesion Sci. and Tech.*, Vol. 9B (Plenum Press, New York, 1975), pp. 501-511.

Effect of Adherend Thickness and Mixed Mode Loading on Debond Growth in Adhesively Bonded Composite Joints†

P. D. MANGALGIRI, W. S. JOHNSON and R. A. EVERETT, JR.

NASA Langley Research Center, Hampton, Virginia

(Received October 20, 1986)

Symmetric and unsymmetric double cantilever beam (DCB) specimens were tested and analyzed to assess the effect of (1) adherend thickness and (2) a predominantly mode I mixed mode loading on cyclic debond growth and static fracture toughness. The specimens were made of unidirectional composite (T300/5208) adherends bonded together with EC3445 structural adhesive. The thickness was 8, 16 or 24 plies. The experimental results indicated that the static fracture toughness increases and the cyclic debond growth rate decreases with increasing adherend thickness. This behavior was related to the length of the plastic zone ahead of the debond tip. For the symmetric DCB specimens, it was further found that displacement control tests resulted in higher debond growth rates than did load control tests. While the symmetric DCB tests always resulted in cohesive failures in the bondline, the unsymmetric DCB tests resulted in the debond growing into the thinner adherend and the damage progressing as delamination in that adherend. This behavior resulted in much lower fracture toughness and damage growth rates than found in the symmetric DCB tests.

KEY WORDS Adhesive joints; composites; double cantilever beam; fatigue; fracture toughness; mixed mode.

1 INTRODUCTION

Fiber reinforced composite materials offer significant advantages in terms of strength-to-weight and stiffness-to-weight ratios in con-

† Presented at the Tenth Annual Meeting of The Adhesion Society, Inc., Williamsburg, Virginia, U.S.A., February 22-27, 1987.

structing aerospace structures. However, their effective use may be limited by the efficiency and reliability of the joining methods used in the construction. Mechanical fastener holes weaken the composites significantly, and some of the advantage in weight saving may be lost in strengthening these holes. Adhesive bonding offers a viable alternative with a number of potential advantages such as (1) higher joint efficiency, (2) no strength degradation of basic composite, (3) less expensive and simpler fabrication techniques, and (4) lower part count and maintenance cost. Currently, most aerospace industries are hesitant to use adhesive bonding in joining primary structures. This is due partly to the lack of understanding of adhesive bond behavior, particularly under conditions of repeated loading over an extended period of time. The objective of the present paper is to contribute toward a better understanding of the adhesive debond growth behavior by using fracture mechanics concepts.

Earlier, the fracture mechanics concept of strain energy release rate was used to model the debond growth under cyclic loading by Roderick, Everett and Crews¹ while studying composite-to-metal joints. The rate of debond growth was correlated to the total strain energy release rate. The total strain energy release rate, G_T , in adhesive debonding may be composed of three components: opening mode G_I , sliding mode G_{II} , and tearing mode G_{III} . However, in most cases of practical adhesive joints, the strain energy release rate is composed of only G_I and G_{II} . Two types of specimens have been commonly used in the past for debond studies: (1) Double Cantilever Beam (DCB) specimen to study pure mode I behavior and (2) Cracked Lap Shear (CLS) specimen to study mixed mode I and II behavior with G_I/G_{II} in the range of 0.25–0.5.^{2–6} Various investigators of the debond behavior have used different kinds of adherend and adhesive thicknesses in DCB specimens in their studies. Whereas considerable attention has been devoted in the past to the influence of the bondline thickness, little information exists on the influence of adherend thickness. A change in adherend thickness would result in change of stress state ahead of the debond tip, and it is of interest to examine how this would influence the debond growth behavior and static fracture toughness.

Mall, Johnson, and Everett² studied the debond growth in CLS specimens with quasi-isotropic graphite-epoxy adherends and two

adhesives. They found that even though the debond grew in mixed mode ($0.25 < G_I/G_{II} < 0.38$), the debond growth rate correlated better with the total strain energy release rate than with either G_I or G_{II} alone. Mall and Johnson³ further examined this correlation with experiments on DCB (mode I) specimens and found that the correlation of debond growth rate with $G_I = G_T$ in DCB specimens agreed with that of G_T in CLS specimens. These experiments lead to an hypothesis that the total strain energy release rate is the governing parameter for the debond growth in adhesive joints. The practical significance of such a finding is that it will simplify design and analysis procedures, since total strain energy release rate is much easier to determine than the individual components. These studies on the mixed mode behavior than the individual components. These studies on the mixed mode behavior have demonstrated the validity of the hypothesis under predominantly mode II conditions existing in CLS specimens ($G_I/G_{II} < 0.38$) and the pure mode I conditions in the DCB specimen. It needs to be verified in other cases of mixed mode loading.

The purpose of this paper is twofold: (1) to investigate the influence of adherend thickness on debond growth under static and fatigue loading and (2) to study debond growth in mixed mode under a predominantly mode I loading ($G_I/G_{II} > 5.6$). Experiments were conducted on DCB specimens of various thicknesses. Mixed mode was introduced by making the two adherends of different thicknesses thus making the specimen unsymmetric. The influence of various parameters is ascertained by measuring fracture toughness (critical strain energy release rate) in static loading and cyclic debond growth rates in fatigue loading. Analysis by the Finite Element Method (FEM) was used to determine individual components of strain energy release rate and to interpret other results.

2 EXPERIMENTS

2.1 Specimen, materials and preparation

The double cantilever beam specimen as shown in Figure 1 was used in the present study. When the two adherends are of equal thickness the specimen is "symmetric" and has pure mode I

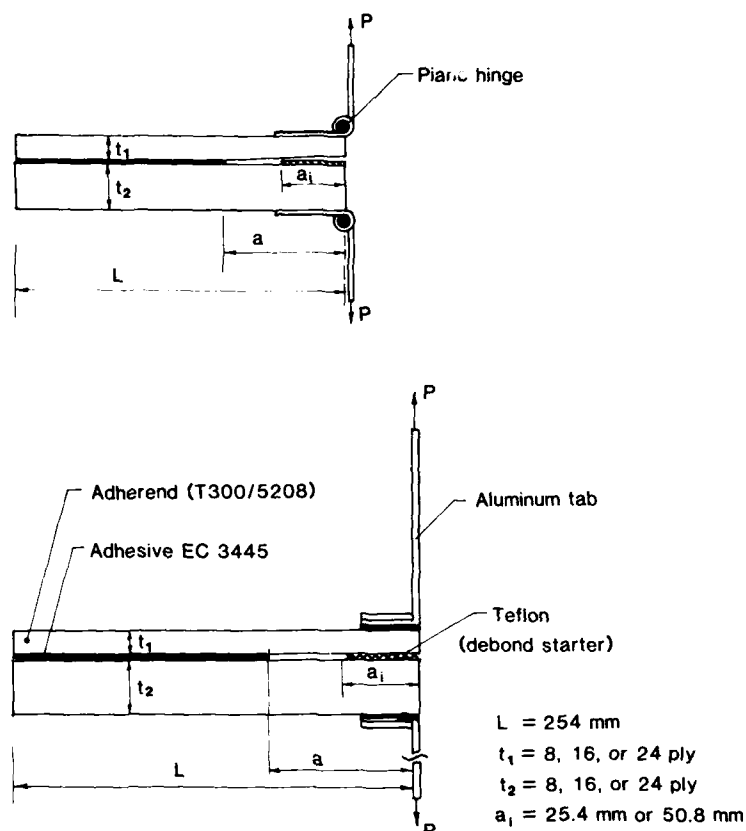


FIGURE 1 Specimen geometry and nomenclature.

behavior under the loads shown in the figure. By making one adherend thicker than the other, the specimen can be made "unsymmetric" introducing a mixed mode behavior under the same loading conditions while maintaining a predominantly mode I situation. For the present work, adherends were made of unidirectional graphite-epoxy (T300/5208)[†] composite and the adhesive used was EC3445,[‡] a thermosetting paste adhesive with a cure temperature of 121°C. The material properties of the unidirectional

[†] T300/5208 supplied by Hexcel Corp., California, USA.

[‡] EC3445 is manufactured by 3-M Corp., Minnesota, USA.

graphite-epoxy adherends were obtained from Ref. 7. These are presented in Table I. The EC3445 adhesive is the paste version of the AF-55 adhesive film; therefore, the Young's modulus of EC3445 was calculated from the data on AF-55 by assuming the adhesive to be an isotropic material with Poisson's ratio of 0.4. These properties taken from Ref. 2 are also presented in Table I.

Three panels, one each of 8, 16, and 24 plies thickness, of unidirectional graphite-epoxy (T300/5208) were first fabricated. Strips of width 25.4 mm (1.0 in) and length 254 mm (10.0 in) were cut from these panels. Symmetric (8-ply to 8-ply, 16-ply to 16-ply, 24-ply to 24-ply) and unsymmetric (8-ply to 16-ply, 8-ply to 24-ply, 16-ply to 24-ply) DCB specimens were fabricated by bonding two of these strips together with EC3445 adhesive using a conventional secondary bonding procedure. Nominal adhesive thickness was maintained at 0.10 mm (0.004 in) by random sprinkling of a small volume fraction (less than 0.1%) of glass beads of 0.10 mm diameter. An initial debond was introduced by inserting a Teflon[®] film 0.0125 mm (0.0005 in) thick during the bonding procedure. The length of this initial debond was kept 25.4 mm (1.0 in) for thinner specimens and 50.8 mm (2.0 in) for thicker specimens to allow similar loading ranges. Initially, two aluminum tabs 0.5 mm thick were bonded at the ends of DCB specimens (see Figure 1a) to facilitate application of load. A room temperature cure adhesive was used for bonding these tabs. These tabs debonded in certain cases and also introduced additional constraints at the ends. Subsequently, steel hinges were employed instead of the aluminum tabs (see Figure 1b) which led to a very satisfactory performance.

TABLE I
Elastic properties of adherend and adhesive materials

	E_1 (GPa)	E_2 (GPa)	G_{12} (GPa)	ν_{12}
1. Adherend T300/5208 Undirectional	131.0	13.0	6.4	0.34
2. Adhesive EC3445	1.81	1.81	0.65	0.40

Virtually all the results reported herein are from specimens using the steel hinges.

2.2 Testing procedure

The objective of the test program was to determine two characteristics: (1) the critical strain energy release rate in static loading and (2) the debond growth rate under cyclic fatigue loading. Both the static and fatigue tests were carried out in the same set-up as described below.

All specimens were tested in a closed-loop electro-hydraulic test machine specially equipped to measure and control small testing loads (less than 225 N or 50 lbs). All static tests and most fatigue tests were performed in the displacement control mode. For fatigue tests, cyclic loads were applied in both load and displacement control mode to ascertain the difference in the two procedures. In such tests, it was found convenient to apply load control at smaller crack-lengths (when loads are comparatively large and displacements small) and displacement control at larger crack-lengths (when loads are comparatively small and displacements large). Both edges of the specimen were coated with white brittle fluid (in this case typewriter correction fluid) to aid in visually locating the debond tip. Fine visible scale marks were put on the edges of the specimen to aid in the measurement. The debond tip was observed through microscopes having a magnification factor of 20. The magnification and the fine scale helped to locate the debond tip within 0.25 mm (0.01 in) accuracy. The debond length was observed on both sides of the specimen. The mean difference in readings on the two sides was less than 5%, and the maximum difference was 15% of the debond length (12 mm over a width of 25.4 mm). The debond length was taken as the average of readings on both sides of the specimen.

During the static fracture toughness tests the crosshead speeds were adjusted to obtain strain rates normal to the crack surface in the adhesive 0.1 mm ahead of the crack tip in the range of 0.001–0.0025 per minute for each test. Since the stresses at the crack tip in a DCB specimen are inversely proportional to the square of the length, the crosshead speeds were increased as the

square of the debond length to achieve nearly the same crack tip strain rate for all tests. As the displacement was applied, the onset of growth resulted in a deviation from linearity in the load-displacement curve. After the onset of growth was observed, the specimen was unloaded at the same crosshead speeds.

For fatigue tests, cyclic loads were applied at a frequency of 3 Hz. This frequency was chosen to facilitate comparison with the earlier data.^{2,3} Constant amplitude cyclic loading was applied with the ratio of minimum to maximum load (or displacement) of 0.1. In the load control mode (constant load amplitude), the debond growth rate increases as the debond grows whereas in the displacement control mode (constant displacement amplitude) the growth rate decreases with the growth of the debond. Therefore, in the load control mode cyclic load amplitude was chosen to give very slow growth rates (1-5 nm/cycle) to start with and maintained until the debond growth rates were too fast to be accurately measured or controlled (approximately 0.05 mm/cycle). The load amplitude was then reduced for a further increment of the debond growth starting with the slow growth rate. On the other hand, in the displacement control mode cyclic displacement amplitude was chosen to give high but controllable and measurable debond growth rate (approximately 0.05 mm/cycle) to start with and was maintained until the growth rate became very slow (1-5 nm/cycle). The displacement amplitude was then increased for a further increment of the debond growth starting with the high growth rate. Static tests were usually conducted at the changeover from one amplitude to the other. This also provided the required sharp crack for the static tests. Debond length (a), number of load cycles (N), and the applied load (P) or displacement (v) were monitored throughout the tests. The crack growth data taken immediately after a static fracture test was not used in the calculation of the crack growth rate. Load-displacement records were taken at suitable intervals of debond length.

The values of the strain energy release rates were calculated from the recorded load displacement relationship and the applied loads. The record of debond lengths at various numbers of cycles provided data for the calculation of the debond growth rate da/dN . The details of the computational procedures are given in the next section.

3 ANALYSIS

As reported in the earlier section, load-displacement records were obtained at several debond lengths. To obtain the strain energy release rate, the compliance of the specimen was calculated at each debond length from the load-displacement record. The total strain energy release rate (G_T) is related to the compliance (C) by the relation

$$G_T = 0.5(P^2/b) dC/da \quad (1)$$

A simple strength of materials analysis derived from linear beam theory for the symmetric DCB specimen^{3,9} gives the compliance as

$$C = 8a^3/bEt^3 \quad (2)$$

for plane stress conditions where E is taken as the longitudinal modulus.⁸ This expression is valid as long as the modulus is taken as the apparent modulus as discussed by Ashizawa.¹⁰ Ashizawa has also presented correction factors for the flexural modulus. The unsymmetric DCB specimen can also be analyzed in a similar fashion by treating each half as a cantilever beam having different flexural stiffnesses. Since the specimen is unsymmetric, it will tend to rotate somewhat under load (*i.e.*, the bondline will not remain perfectly horizontal). As long as this rotation is rather small, the compliance C is then given by

$$C = 4(a^3/bE)(1/t_1^3 + 1/t_2^3). \quad (3)$$

The compliance given by Eq. (3) is in good agreement with finite element analysis of the specimen. As seen from the Eqs. (2, 3), the value of C is very sensitive to the measurements of thickness and crack length. Moreover, correction factors need to be applied to the modulus E as shown by Ashizawa.¹⁰ Hence, these equations cannot be directly used to analyze experimental data. Since, in general, the compliance is proportional to the cube of the crack length a , a relation of

$$C = A(a)^3 \quad (4)$$

was fitted through the experimental data points by the method of least squares. The total strain energy release rate is then calculated using Eq. (1).

A finite element analysis using GAMNAS, a program developed at NASA,¹¹ was also conducted for comparison with the beam theory and to calculate the stress state ahead of the debond tip. The virtual crack closure technique was used to calculate the strain energy release rates. Plane strain conditions were assumed to exist in the bondline. The finite element mesh was refined to the extent that further refinement resulted in essentially the same results. The GAMNAS program was also used to assess the effect of the adhesive bondline plasticity on the specimen load-displacement behavior. The adhesive was modeled as a bi-linear elastic-plastic material with a yield strength of 32 MPa. The elastic modulus was 1.81 GPa and the plastic modulus was taken as 0.40 GPa. Only the 24- to 24-ply specimen was analyzed because it showed the greatest effect of loading mode on resulting debond growth rate.

4 RESULTS AND DISCUSSION

In this section the data obtained in the static and fatigue tests are analyzed and the results are discussed. First, the determination of basic parameters, namely compliance, strain energy release rate, and debond growth rates, is discussed. These and other data are then used to discuss various aspects such as the influence of load or displacement control mode, the influence of adherend thickness, and the influence of mixed mode on static and fatigue debond growth.

4.1 Determination of basic parameters

The static tests yielded the compliance data and the critical loads. The relation of Eq. (4) was found to fit very well with the experimental data as shown in Figure 2. Data points are shown for a symmetric 24-ply to 24-ply and unsymmetric 24-ply to 8-ply specimens. Values obtained by FEM analysis are also shown in the figure. Although the FEM values show the cubic variation, they differ from the experimental values by as much as 12%. As noted earlier in the section on analysis, the compliance values are very sensitive to the measurement of thickness and debond length. In practice, the thickness of the specimen was not uniform. Other

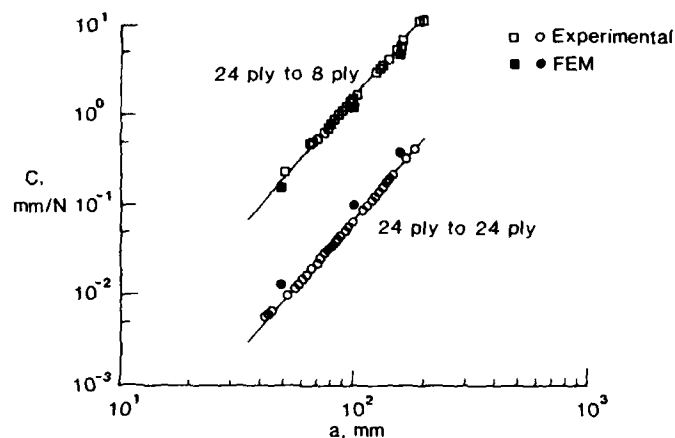


FIGURE 2 Relation between compliance C and debond length a , for symmetric and unsymmetric DCB specimens.

factors such as experimental errors in load control and compliance measurements could also contribute to this rather small difference between the analysis and experiment.

Linear FEM analysis with the debond placed in the middle of the adhesive yielded compliance values which showed the cubic variation with respect to a . Further, the geometric nonlinear analysis did not indicate any significant difference in either the compliance or the computed G values from the linear analysis. The maximum difference in G_T was less than 3% for a debond length of 100 mm under maximum experimental load. A significant outcome of the FEM analysis was the individual values of G_I and G_{II} for the unsymmetric DCB. Maximum G_{II} contribution was in the most

TABLE II
Mixed mode ratios for the unsymmetric DCB specimens

Configuration	G_I/G_{II}	G_I/G_T
8-ply to 24-ply	5.67	0.85
8-ply to 16-ply	11.50	0.92
16-ply to 24-ply	24.00	0.96
Symmetric	—	1.00

unsymmetric case (24-ply to 8-ply) and was about 15% of G_T . The G_I/G_{II} ratios for the unsymmetric DCB specimens are shown in Table II. The analyses did not show any significant variation in G_I/G_{II} with either the load or the debond length.

The fatigue tests yielded the debond growth data. The values of the operating strain energy release rate (G_T) at the center of the debond increment were calculated from the compliance relationship, Eq. (4), obtained by a least squares fit of the compliance data. Plots of da/dN vs. G_T were made and a least squares fit was used to obtain the constants c and n in the relationship

$$da/dN = cG_T^n \quad (5)$$

This equation was found to fit well for all data sets. Table III gives the values of parameters c and n obtained for the various cases. The results obtained are discussed below.

TABLE III
Crack growth rate parameters c and n in the relation $da/dN = c(G_T)^n$ m/cycle with DG in J/m²

Configuration		Control mode			No. of data points
t_1 Plies	t_2 Plies				
8	8	Load	3.381E-19	4.801	36
		Disp	6.124E-20	5.083	36
		Both	2.658E-19	4.831	72
16	16	Load	3.528E-19	4.980	32
		Disp	3.207E-23	6.282	42
		Both	5.080E-24	6.495	74
24	24	Load	1.368E-21	5.598	19
		Disp	1.737E-24	7.165	36
		Both	8.009E-20	5.157	55
8	16 ^a	Disp	4.076E-21	6.178	70
8	24 ^b	Disp	8.601E-38	13.815	62

^a Failure at the interface/Delamination in the adherend.

^b Delamination in the adherend.

4.2 Influence of load/displacement control mode

Figures 3a, 3b, and 3c show the debond growth rate with the cyclic G values for symmetric DCB specimens with 8-, 16- and 24-ply adherends, respectively. The filled symbols and the solid lines refer to the data obtained in the displacement control mode whereas the open symbols and the broken lines refer to those in load control mode. If apparent threshold data were present (this applies to the data at growth rates below 10^{-10} m/cycle that tend toward a vertical line), the threshold related data points were not used in the determination of best fit line to the debond growth rate data. For example, the seven open symbols below the growth rate of 10^{-10} in Figure 3a were not used to determine the best fit line. The control mode had little if any effect on the cyclic debond growth behavior in the case of the thin (8-ply) adherends, Figure 3a, but the effect became more significant as the adherends became thicker as shown by the data for the 16-ply and 24-ply cases in Figure 3b and 3c, respectively. Where the effect was significant, the displacement control mode resulted in a higher debond growth rate for the same

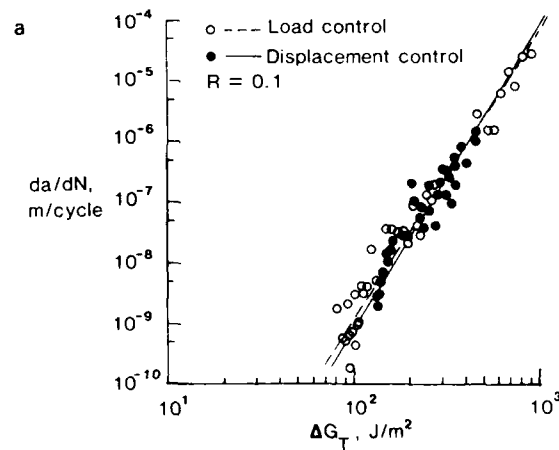


FIGURE 3 (a) Effect of load/displacement control mode on debond growth rate in symmetric DCB specimens (8-ply to 8-ply). (b) Effect of load/displacement control mode on debond growth rate in symmetric DCB specimens (16-ply to 16-ply). (c) Effect of load/displacement control mode on debond growth rate in symmetric DCB specimens (24-ply to 24-ply).

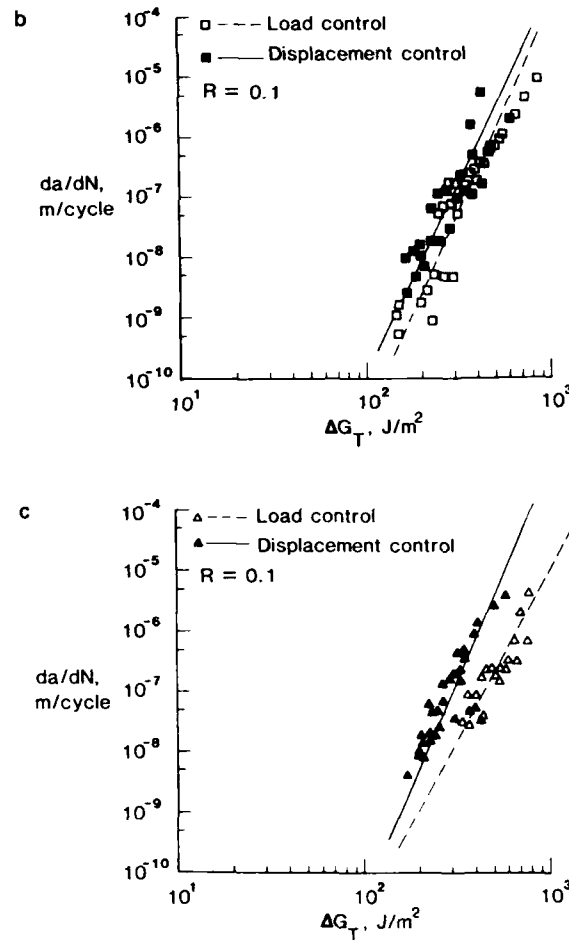


FIGURE 3 (continued)

operating strain energy release rate. This is consistent with the observation made earlier by Mall and Johnson.³

The G_I values are calculated based on elastic material response; however, structural adhesives are both elastic-plastic and viscoelastic. In the displacement control mode the amount of debond tip opening and the resulting stress distribution ahead of the debond are rather constant for a given applied displacement because the

displacements are controlled by the adherends. However, for the load control mode the debond tip may open further than calculated elastically due to either a plastic or viscoelastic deformation of the adhesive. Therefore, the stress distribution ahead of the debond may increase, resulting in a larger plastic zone. Perhaps this contributes in some way to the reason why the load control tests result in slower crack growth rates.

The finite element analysis of the 24- to 24-ply DCB specimen supported the fact that the specimen would open more under load control with the elastic-plastic adhesive properties than with the purely elastic adhesive properties. The analysis also showed that the displacement controlled tests with the elastic-plastic adhesive required less reactive load than a specimen with an elastic adhesive. However, at an applied G_I level of 480 J/m^2 , the differences in the elastic and the elastic-plastic results were far less than one percent. This difference is too small to account for the observed behavior of the adherend in controlling the load-displacement response of the specimen. The plasticity at the crack tip has little influence on the over all specimen stiffness response.

The 24-ply debond growth rate is as much as an order of magnitude less for the load controlled data than for the displacement controlled; or at a given debond growth rate, tests in load control require up to twice the G level. There is at the moment no explanation for this behavior using linear elastic fracture mechanics.

4.3 Influence of adherend thickness

The higher flexural rigidity of the thicker adherends affects the stress distribution ahead of the debond tip. It is of interest to investigate whether this would affect the fracture toughness and debond growth rates.

Figure 4 shows the results obtained in static fracture toughness tests with various symmetric DCB specimens. Two specimens of each type were tested at several debond lengths. The average toughness values and the range of scatter are shown in the figure. The numerals in the parentheses indicate the number of data points. It is observed from the figure that there is an increase in the average value of G_{Ic} as the adherends become thicker. The change in G_{Ic} is more significant from 8-ply to 16-ply than from 16-ply to 24-ply.

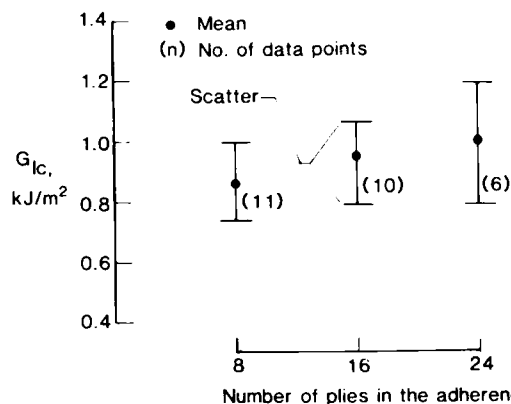


FIGURE 4 Influence of adherend thickness on fracture toughness in symmetric DCB specimens.

However, the change in average G_{Ic} with adherend thickness is of the same order as the scatter in the data, therefore, more information is needed to confirm this trend. Devitt, Schapery, and Bradley¹² have shown a similar thickness-dependent interlaminar fracture toughness in glass/epoxy composites. They tested 8-, 12-, and 16-ply specimens and found the average toughness from five tests to be 831, 873, and 904 J/m², respectively. Their data trend is similar to that reported herein.

To study the influence of the adhered thickness on the cyclic debond growth, the data obtained in the fatigue tests are replotted in Figures 5a and 5b. Figure 5a shows the results for the load control mode and Figure 5b for the displacement control mode. The influence of adherend thickness is much less in the displacement control mode than in the load control mode. Further, it appears that the thicker adherends resulted in slower growth rates, particularly for low growth rates. Also, considering the scatter in the individual data sets (Figures 3a, 3b and 3c), it may be observed that the change of the adherend thickness from 16- to 8-ply affected the growth rates more significantly than the change from 24- to 16-ply. Thus, the influence may be more significant for thinner specimens.

In Figure 5b the present results are compared with the results obtained by Mall and Johnson³ from cracked lap shear and DCB specimens made with the same adhesive and adherend materials.

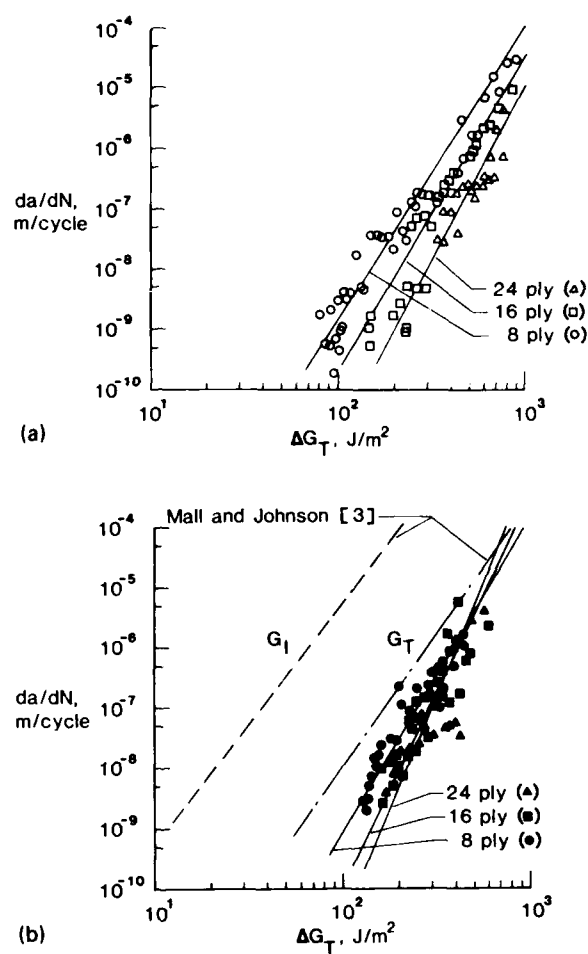


FIGURE 5 (a) Influence of adherend thickness on cyclic debond growth of EC3445 adhesive in symmetric DCB specimens under load control mode. The lines are fitted to the data above 10^{-8} m/cycle. Below 10^{-8} m/cycle debond growth is in the threshold range. (b) Influence of adherend thickness on cyclic debond growth rate in symmetric DCB specimens tested under displacement control mode.

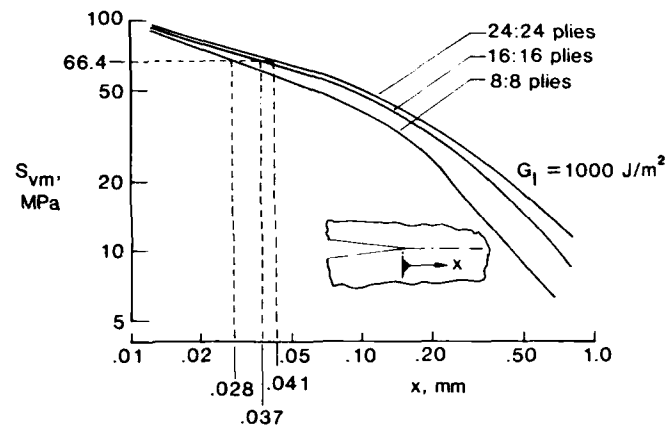


FIGURE 6 Variation of von Mises stress ahead of crack tip for symmetric DCB specimens with various adherend thicknesses and a debond length of 100 mm.

The present data correlate well with the G_T data line but not to the G_I . This supports the previous observations³ that the debond growth rate of these types of structural adhesives is a function of the total strain energy release rate and not just the mode I component.

An attempt was made to interpret these results in terms of the stress distribution ahead of the crack tip. To facilitate a comparison of the amount of plastic deformation ahead of the crack tip at the same value of the strain energy release rate (irrespective of the loads) in the different specimens, the von Mises's stress is plotted *versus* the distance ahead of the crack tip. The von Mises' stress is defined as

$$S_{vm} = (s_x^2 + s_y^2 + s_z^2 + s_x * s_y + s_y * s_z + s_z * s_x)^{0.5}. \quad (7)$$

Figure 6 shows the variation of S_{vm} ahead of the crack tip of a 100 mm long debond for the three adherend thicknesses tested. Each specimen is loaded so that G is equal to a G_{Ic} of 1000 J/m^2 . These data are useful for comparing the relative approximate length of the yield zone at fracture by assuming a value for the adhesive yield stress. The yield shear stress for EC3445 is about 33.2 MPa (4820 psi)[†] which gives the normal yield stress of 66.4 MPa

[†] A. V. Pocius, Private Communication, 3M Company, St. Paul, Minnesota 55144-1000, U.S.A.

(9640 psi). Assuming that the distance ahead of the crack tip at which S_{vm} decays to the yield stress is a reasonable approximation of the plastic zone ahead of the crack tip, we observe that the plastic zone size increases with the adherend thickness for the same applied elastic strain energy release rate. The rate of increase in the plastic zone size decreases as the thickness increases (*i.e.*, the change from 24-ply to 16-ply is less than that from 16-ply to 8-ply).

It may be speculated that more energy is dissipated by the plastic deformation of the adhesive as the debond grows in the thicker adherend case than the thinner one. Since the total strain energy release rates are the same for each case, the remaining energy available for crack extension (that is, the total energy minus the energy used for plastic deformation associated with the debond growth) is decreasing with increasing adherend thickness. This leads us to expect that the actual fracture toughness of the thicker adherend may be more than that of the thinner adherend. It also follows that the thicker adherend specimens would show a slower debond growth rate for a given applied G . This agrees with trends of the experimental results in Figures 4 and 5.

Figure 7 shows the normal stress component ahead of the debond tip for each specimen type. These stresses are also from the GAMNAS finite element analysis. Each specimen is loaded such that G_I is equal to 39 J/m^2 . The stresses are the same at the debond tip, as expected; however, the stresses are higher over a longer length for the thicker adherend specimen.

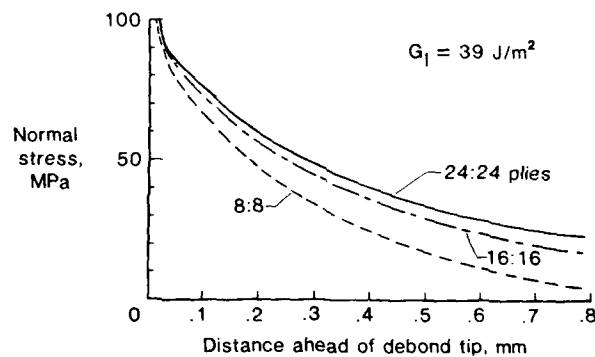


FIGURE 7 Normal stress distribution ahead of debond front.

Figure 5 indicates that the thinner specimens would have lower values of threshold G for cyclic debonding. Since the design of bonded joints may be based on threshold values because of the large values of the exponent n ,¹³ this effect may become important for thin adherends. An important implication of this result is that a choice of too thick a specimen for measurement of fatigue characteristics may overestimate the threshold G and fatigue life. However, the shift in debond growth rate due to adherend thicknesses is almost within the scatter band of the data.

Shivakumar and Crews¹⁴ have stated that the height of the plastic zone, not the area, is what influences the relative toughness. If this is true, perhaps a thicker adherend may cause high enough stresses to yield the composite matrix material above and below the bondline to a greater extent than a thinner adherend. This possibility was not explored in this study.

The examination of the fracture surfaces of the symmetric DCB specimen (see Figure 8) revealed that the fracture remained mainly in the adhesive showing a cohesive failure of the adhesive material as in Figure 8a. Occasionally, a few fibers were pulled from one surface to the other, particularly, at larger crack lengths (see Figure 8b), but the failure was predominantly in the adhesive.

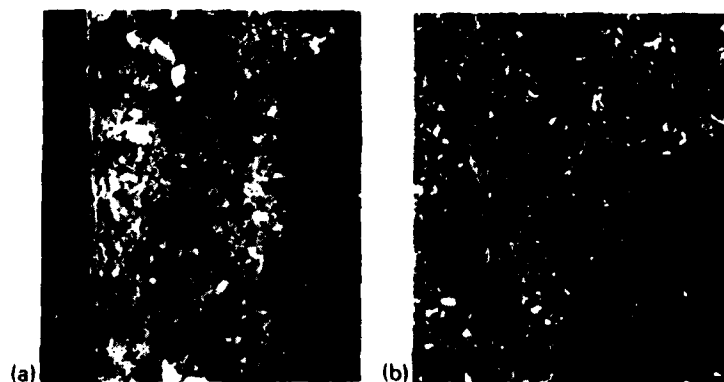


FIGURE 8 Typical failure surfaces of symmetric DCB specimen. (a) Debond surface near the Teflon starter. (b) Debond surface 50 mm away from the Teflon starter. Failure is through the adhesive.

4.4 Influence of the mixed mode

The influence of the mixed mode in a predominantly mode I situation was studied using unsymmetric DCB specimens. Both static fracture toughness and fatigue debond growth rate tests were conducted on 8-ply to 16-ply and 8-ply to 24-ply specimens. These tests showed unexpectedly low fracture toughness values (see Figure 9) and high debond growth rates (see Figure 10a, b). On examination of the fracture surfaces, it was found that the debond in the adhesive quickly migrated to the thinner adherend and propagated as an interfacial failure and further on as delamination in the composite adherend for both the static and fatigue loading. These results are discussed below.

The static fracture toughness values obtained as the debond migrated from the center of the adhesive layer to the interface and further into the adherend as a delamination are shown in Figure 9. There is a continuous reduction in the fracture toughness as the migration of the debond proceeds. The zone in which the failure was fully in the adhesive was very small and at the beginning of the test (near the Teflon starter, see Figure 11a). The transition zone can be seen in Figure 11a only a little distance away from the crack starter. The delamination failure as shown in Figure 11b was seen everywhere else. The low toughness values corresponding to the delamination are somewhat higher than the delamination toughness

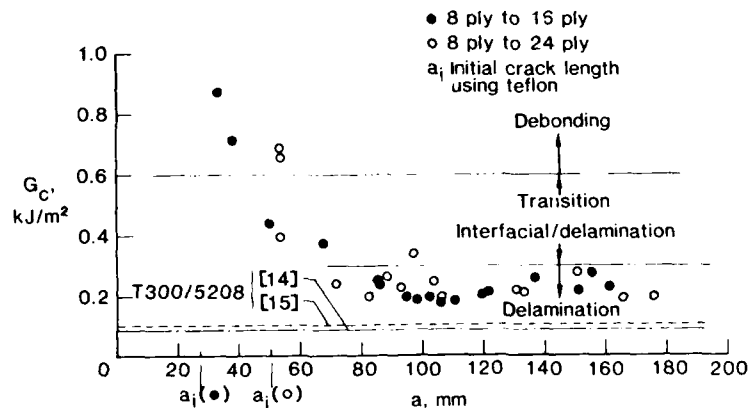


FIGURE 9 Decrease in the fracture toughness with change of failure mode as debond grows in unsymmetric DCB specimen.

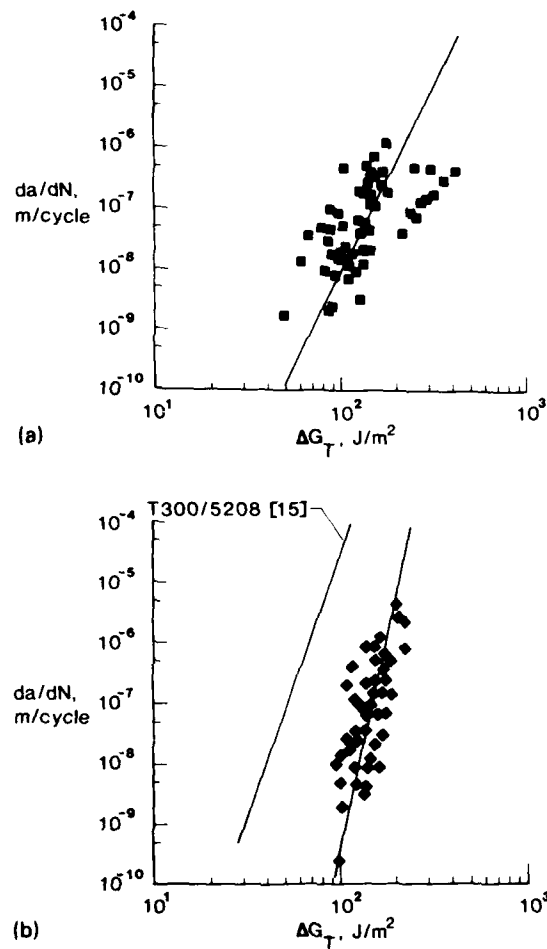


FIGURE 10 (a) Cyclic debond growth in unsymmetric 8-ply to 16-ply DCB specimen. (b) Cyclic debond growth in unsymmetric 8-ply to 24-ply DCB specimen.

values obtained in DCB tests on T300/5208 composites by earlier investigators.^{15,16} However, as discussed in Ref. 13, even a small amount of mixed mode is expected to increase the total critical strain energy release rate by a significant amount for a brittle resin like 5208. This is reflected in the higher values of the delamination toughness in the present tests.

High rates of crack growth were obtained in the fatigue tests on the unsymmetric specimens, as seen from Figures 10a,b. Figure 10a shows the cyclic crack growth data for the 8-ply to 16-ply case, and Figure 10b shows the same for the more unsymmetric 8-ply to 24-ply case. It is seen that the more unsymmetric case led to a steeper slope of the best fit line. Figure 10b also shows an earlier result on delamination of T300/5208 unidirectional composite from Ref. 14. Note that the slope of the line in the present case is comparable to the one corresponding to the delamination. The examination of the failure surfaces revealed that in the 8-ply to 24-ply case, the debond migrated to the adherend almost immediately after the start of the test and propagated as delamination (a typical failure surface is shown in Fig. 11b); whereas, in the 8-ply to 16-ply case, the transition to delamination was somewhat more gradual (failure surface as in Figure 11a). Because the debond growth rate data consists of both debonding of EC3445 adhesive and delamination growth in the adherend matrix material 5208, the scatter in the 8-ply to 16-ply data is greater than that in the 8-ply to 24-ply data (see Figures 10a,b). Thus, it is observed that the introduction of asymmetry and mixed mode has caused the debond

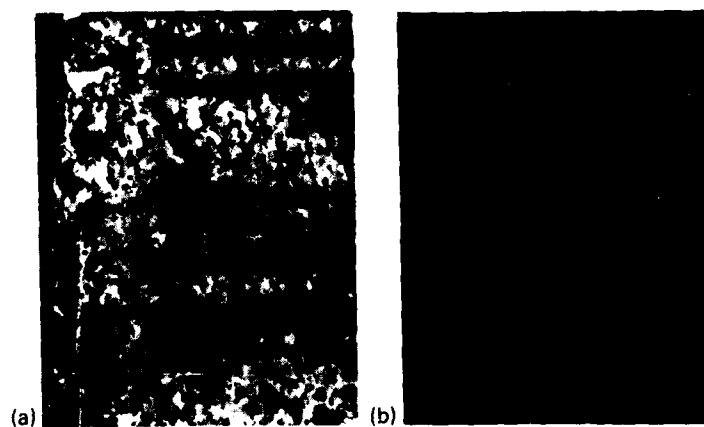


FIGURE 11 Typical failure surfaces of unsymmetric DCB specimens. (a) Fracture surface near the Teflon starter. Failure is primarily in the adhesive layer. (b) Fracture surface 10 mm away from the Teflon starter. Failure is through the graphite-epoxy adherend.

to be pushed to the thinner adherend interface and even inside the composite adherend. This resulted in an undesirable combination of high fatigue growth rates, low fatigue threshold, and low fracture toughness.

It may be noted here that the earlier experiments on the CLS specimens^{2,17} of the same adhesive-adherend system with 0-degree plies next to the adhesive showed cohesive failures in the bondline. These CLS specimens also had different adherend thicknesses which resulted in various mixed mode loadings. In the case of CLS specimens, G_I/G_{II} ratios were in the range 0.25–0.31 compared to 5–24 for the unsymmetric DCB specimens. As previously discussed, the symmetric DCB specimens also did not result in delamination of the adherend. The authors cannot explain at this time why a small amount of mode II in the unsymmetric DCB case would cause the debond to wander into the adherend. However, it appears that in the unsymmetric DCB case, the thinner adherend experienced higher bending stresses in the ply next to the adhesive than the thicker adherend; hence, it is more apt to experience fiber failure. The finite element analysis results indicate that the strain in the fiber next to the adhesive approaches 0.01 as the G_I approaches the G_{Ic} of the EC3445 adhesive (850 J/m²). This, coupled with high interlaminar shear stresses due to the bending, makes the damage more prone to progress into the thinner adherend.

Since the debond wandered into the thinner adherend and continued to grow as a delamination, the debonding behavior of the adhesive under the predominately mode I mixed mode loading could not be evaluated with the present set of specimens.

5 CONCLUSIONS

Symmetric and unsymmetric double cantilever beam (DCB) specimens were tested to investigate the effects of adherend thickness and mixed mode on debond growth in adhesively bonded composite joints in predominantly mode I situations. The tests were conducted under both load and displacement control. The adherends were 8-, 16- and 24-ply thick and made from unidirectional graphite-epoxy (T300/5208) composite. The adhesive was EC3445. Static and fatigue tests were conducted to obtain fracture toughness and

fatigue debond growth rates. The following conclusions were drawn from the present study:

(i) The thickness of the adherend in double cantilever beam specimens influences the measured static fracture toughness of the adhesive. The thicker the adherend the higher the static toughness. The rate of increase in toughness decreases with increasing adherend thickness. The increase in average toughness was less than 20% between 8-ply and 24-ply thick adherends.

(ii) Cyclic debond growth rates are influenced by the adherend thickness. Thicker adherends produce slower debond growth rates. The thickness effects are greatest at low values of strain energy release rate. Thicker adherends result in higher threshold strain energy release rates. The observed adherend thickness effect is much greater for specimens tested in load control than it is in those tested in displacement control.

(iii) The influence of thicker adherends in increasing fracture toughness and lowering crack growth rates appears to be related to the size of the plastic zone (stress distribution) ahead of the debond tip. The plastic zone is longer for thicker adherends. The thicker adherend specimens use a larger percent of the available energy to create the associated larger plastic zone, thereby leaving less energy to propagate the damage. This conclusion is only speculative because there are several unresolved issues.

(iv) Load controlled double cantilever beam tests produced slower debond growth rate data than did the displacement controlled tests. A definite reason for this behavior could not be found. However, it too may be related to the stress distribution ahead of the debond.

(v) The symmetric double cantilever beam specimens produced cohesive debond failures. The unsymmetric double cantilever beam specimens produced debonds that quickly grew to the adhesive/adherend interface then became a delamination in the thinner adherend. Since the 5208 matrix material has lower fracture toughness and higher delamination growth rate than the EC3445 adhesive, this damage migration markedly decreases the damage tolerance of the joint.

(vi) The cyclic debond growth rates data from the symmetric double cantilever beam specimens and cracked lap shear specimens correlated better with G_T than with G_I , supporting the hypothesis

that total strain energy release rate is the governing factor for cyclic debond growth in tough adhesives. The hypothesis could not be tested for the mixed mode unsymmetric double cantilever beam specimen because of the wandering of the damage into the adherend.

Acknowledgement

The first author, P. D. Mangalgi (National Research Council Resident Research Associate), gratefully acknowledges the support extended by the National Research Council, Washington D.C., through their Associateships Program.

References

1. G. L. Roderick, R. A. Everett Jr. and J. H. Crews, Jr., "Debond Propagation in Composite-Reinforced Metals", *Fatigue of Composite Materials*, ASTM STP 569 (American Society for Testing and Materials, Philadelphia, 1975), pp. 295-306.
2. S. Mall, W. S. Johnson and R. A. Everett, Jr., "Cyclic Debonding of Adhesively Bonded Composites", in *Adhesive Joints*, K. L. Mittal, Ed. (Plenum Press, New York, 1982), pp. 639-658.
3. S. Mall and W. S. Johnson, "Characterisation of Mode I and Mixed Mode Failure of Adhesive Bonds between Composite Adherends", *Composite Materials Testing and Design (Seventh Conference)*, ASTM STP 893, J. M. Whitney Ed. (American Society for Testing and Materials, Philadelphia, 1986), pp. 322-334.
4. T. R. Brussat, S. T. Chiu and S. Mostovoy, "Fracture Mechanics for Structural Adhesive Bonds", *AFML-TR-77-163*, Air Force Materials Laboratory, Wright-Patterson AFB, Ohio, U.S.A., 1977.
5. J. Romanko and W. G. Knauss, "Fatigue Behaviour of Adhesively Bonded Joints", *AFWAL-TR-80-4037*, Vol. 1, Air Force Wright Aeronautical Laboratories (Materials Laboratory), Wright-Patterson Air Force Base, Ohio, U.S.A., Apr. 1980.
6. R. A. Everett, Jr., "The Role of Peel Stresses in Cyclic Debonding", *Adhesives Age*, **26**, (5), 24-29 (1983).
7. K. N. Shivakumar and J. H. Crews, Jr., "Bolt Clamp-up Relaxation in a Graphite/Epoxy Laminate", *Long Term Behaviour of Composites*, ASTM STP 813, T. K. O'Brien, Ed. (American Society for Testing and Materials, Philadelphia, 1983), pp. 5-22.
8. G. R. Irwin, "Fracture Mechanics", in *Structural Mechanics*, Goodier and Hoff Eds. (Pergamon Press, New York, 1960), p. 557.
9. D. J. Wilkins, et al., "Characterising Delamination Growth in Graphite-Epoxy", *Damage in Composite Materials: Basic Mechanisms, Accumulation, Tolerance and Characterization*, ASTM STP 775, K. L. Reifsnider Ed. (American Society for Testing and Materials, Philadelphia, 1981), pp. 168-183.
10. M. Ashizawa, "Improving Damage Tolerance of Laminated Composites Through the Use of New Tough Resins", *Proc. Sixth Conf. on Fibrous Composites in Structural Design*, New Orleans, Jan. 1983.

11. B. Dattaguru, R. A. Everett, Jr., J. Whitcomb and W. S. Johnson, *J. Engng. Maths. and Technology*, ASME, **106**, 59-65 (1984).
12. D. F. Devitt, R. A. Schapery and W. L. Bradley, *J. Composite Maths.* **14**, 270 (1980).
13. W. S. Johnson and S. Mall, "A Fracture Mechanics Approach for Designing Adhesively Bonded Joints", in *Delamination and Debonding of Materials*, ASTM STP 876, W. S. Johnson Ed. (American Society for Testing and Materials, Philadelphia, 1985), pp. 189-199.
14. K. N. Shivakumar and J. H. Crews, Jr., "Energy Dissipation Associated with Crack Extension in an Elastic-Plastic Material", *NASA Tsr 89032*, National Aeronautics and Space Administration, Washington DC, October 1986.
15. W. S. Johnson and P. D. Mangalgiri, "Influence of the Resin on Interlaminar Mixed Mode Fracture", in *Toughened Composites*, ASTM STP 937, N. J. Johnston, Ed. (American Society of Testing and Materials, Philadelphia, 1987), pp. 295-315.
16. R. L. Ramkumar and J. D. Whitcomb, "Characterisation of Mode I and Mixed Mode Delamination Growth in T300/S208 Graphite/Epoxy", in *Delamination and Debonding of Materials*, ASTM STP 876, W. S. Johnson Ed. (American Society for Testing and Materials, Philadelphia, 1985), pp. 315-335.
17. W. S. Johnson and S. Mall, *J. Composites Technology and Research*, ASTM, **8**, 3-7 (1986).

Predicting Bond Strength†

G. P. ANDERSON

Morton Thiokol, Inc., Brigham City, Utah 84302, U.S.A.

K. L. DEVRIES

University of Utah, Salt Lake City, Utah 84112, U.S.A.

(Received August 21, 1986)

Methods are presented for predicting the load carrying capability of a bonded joint using relatively simple laboratory test samples. It is first shown that using an average stress criterion can lead to errors of an order of magnitude in predicted load carrying capability. A fracture mechanics approach is then shown to predict failure load accurately in a joint bonded with either a polyurethane or a relatively brittle epoxy when proper consideration is given to loading mode, temperature, and load rate. The principal contribution of this paper is in extending fracture mechanics theory to regions where classical singular points do not exist. Analyses are combined with test data to deduce an "inherent" flaw size.

KEY WORDS Adhesives; structural analysis; fracture mechanics; testing; bond strength; prediction of failure load.

INTRODUCTION

One factor retarding the use of adhesives is our inability to predict the strength of a bonded joint using our present standard laboratory tests and our standard method of interpreting the output from such tests.

An engineer is often required to obtain bond strength data from laboratory-size samples and infer the strength of a given bonded

† Presented at the Tenth Annual Meeting of The Adhesion Society, Inc., Williamsburg, Virginia, U.S.A., February 22-27, 1987.

joint from these data. A straightforward approach would be to prepare and test several standard laboratory specimens using the adhesive type and surface preparation technique to be evaluated. The strength of these standard bond tests is usually reported as an average failure stress, which is defined as the breaking load per unit of bond area. This stress is then compared with the average stress that exists in the joint being evaluated when its maximum load is applied. However, if the joint geometry, loading time, and other conditions are not identical to that of the laboratory test conditions, the direct comparison can lead to unsafe joint designs.

The reason that the direct comparison of average stress values is not valid is that average stresses do not account for variations in stress within the bonded joint. Other factors must also be accounted for including loading mode (direction of load application with respect to a crack or debond termination line), loading rate, joint temperature, adhesive thickness, joint geometry, residual stresses, moisture content and moisture distribution within the adhesive, adherend stiffness, and adhesive stiffness and compressibility (Poisson's ratio). Each one of these factors can change the load carrying capability of a joint by more than a factor of two. Improper testing and data interpretation can, therefore, lead to predictions of load carrying capability of a given bonded joint that are in error in excess of an order of magnitude.

Since the average stress in a bondline is generally not a reliable tool for predicting failure in a bonded joint, an alternative approach is required. If it is hypothesized that failure of a bonded joint occurs when the stress (or some functional of the stresses) reaches a critical value, one might evaluate the stress at each point in a test specimen bondline. The value of the maximum stress(es) at which the bond broke would be termed the bond stress capability. The next step would be to evaluate the stresses at each point in the joint bond when it is subjected to its maximum expected load. The highest resulting stress (or stress functional) at any location in the bond would then be termed the joint requirements. The amount by which the bond capability exceeded the joint requirement would provide the margin of safety of the joint.

This procedure has been very useful in homogeneous materials except when a notch or crack (360-degree notch) is present in the material. In such cases, the stresses are not defined at the notch tip

when linear elastic analyses are employed; *i.e.*, the notch tip is a point of stress singularity. One normally relies on a fracture mechanics analysis to predict load carrying capability for such geometries.

Notches in an adhesive and initial debonds are obvious points of bondline stress singularity. In addition, many bond termination geometries are points of singular stress.^{1,2,3,4} Thus, for debonds initiating at bond edges, even in the absence of voids or initial debonds, both the joint requirement and bond capability must be quantified in terms of fracture mechanics parameters. Bond failure does not always initiate at a point of apparent stress singularity. Thus a failure criterion which is applicable to both singular and nonsingular points is highly desirable. Our approach is to determine an "inherent" flaw size from which energy release rates can be calculated, whether failure initiates within a bonded joint or at the bond edge. These inherent flaws may be related to those that exist naturally in all bonds due to such things as air bubbles, local surface discontinuities, etc.

The applicability of a fracture mechanics approach to bondline strength prediction can be validated by determining fracture mechanics parameters such as critical energy release rate (G_c) and inherent flaw size (a_0) from laboratory tests and using these values to predict the load carrying capability of other bonded joints. Agreement of predicted and measured values from a wide variety of geometries would build confidence in the approach.

Our efforts in validating a bond strength prediction technique were initiated using relatively simple materials and are progressing to more complex materials as described below.

VERIFICATION FOR LINEAR ELASTIC MATERIAL

A polyurethane (Solithane 113 Morton Thiokol, Inc.) to polymethylmethacrylate (PMMA) joint was selected for the initial study. Solithane 113 is a nearly incompressible linear elastic material for temperatures above 70°F and load times longer than 0.005 seconds. The Solithane to PMMA bond strength is low enough to allow "adhesive" failure.

Testing was completed using this bond system in test specimens with the various geometries depicted in Figure 1. A small amount of

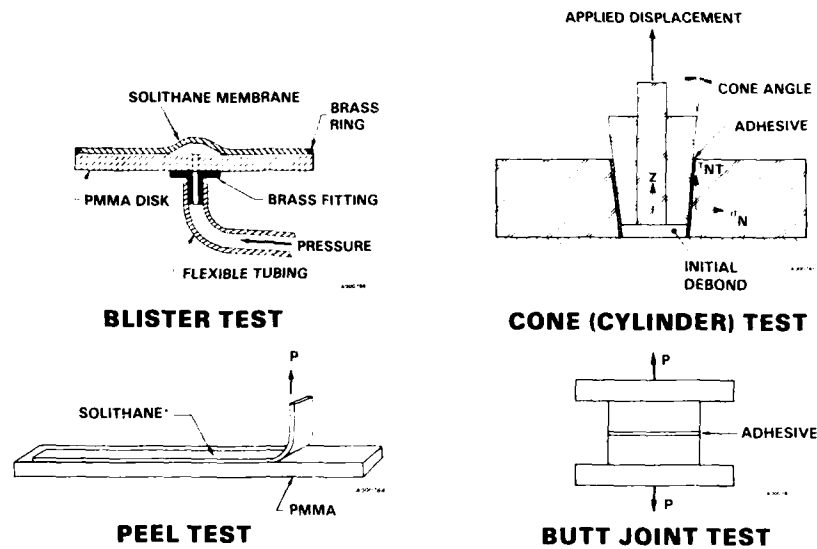


FIGURE 1 Adhesive testing configurations.

debond was initiated in each specimen prior to loading. The load rate was adjusted such that debond propagated in each specimen in 35 ± 10 seconds. The resulting critical energy release rates are dependent on loading mode^{4,5} as shown below (this phenomenon has also been reported by Trantina⁶ and Johnson⁷):

Dominant Mode	Test	G_c , J/m^2 (in.-lb/in. ²)
I	90° Peel	31 (0.18)
	Thick Blister	30 (0.17)
	Butt Joint in Tension	23 (0.13)
II	Thin Blister	72 (0.41)
	Cylinder Pull-Out	60 (0.34)
III	Butt Joint in Torsion	102 (0.58)

As explained in References 4, 5, and 8, the specimens are not purely Mode I, II, and III as depicted in the above table. There is, in reality, a fairly significant Mode II component in both the

90-degree peel and thick blister (19 percent Mode II) specimens while the butt joint in tension has less than 2 percent Mode II loading. This may be one reason for the relatively low critical energy release rate for the butt joint in tension. In addition, since failure loads are proportional to the square root of critical energy release rate, failure load predictions would differ by only 14 percent when 23 is used in place of 31 for the critical energy release rate.

The fairly close agreement in critical energy release rates for the tests dominated by Mode I loads, supports the use of a fracture mechanics approach for these materials and loading mode when an initial debond is present. However, most bonded joints do not have a known initial debond. One approach to bond strength prediction is to assume the bondline has an inherent flaw of size, a_0 , and base the failure theory on the energy release rate for the inherent flaw. The applicability of this approach is illustrated below.

Three sets of five Solithane/PMMA buttons were tested using the test fixture of Figure 2. The following average failure loads, P_{cr} ,

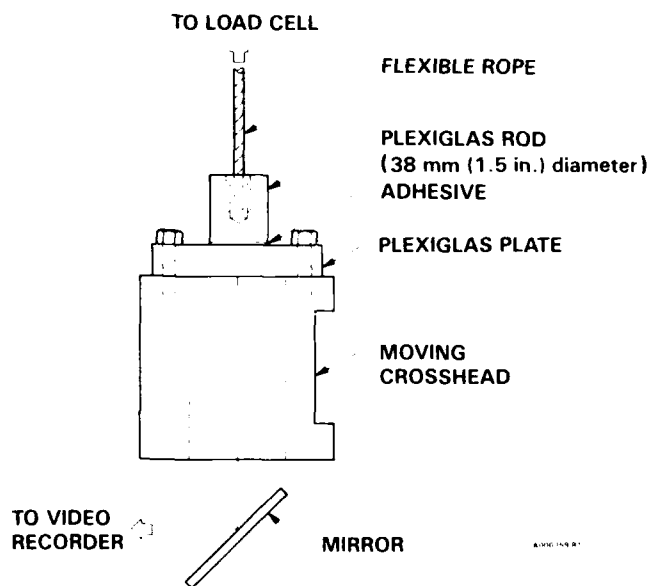


FIGURE 2 Transparent tensile test apparatus.

were obtained:

Adhesive Thickness,		Initial Debond,		P_{cr}	
mm	(in.)	mm	(in.)	N	(lb)
6.38	(0.251)	3.30	(0.130)	286	(64)
6.17	(0.243)	6.45	(0.254)	138	(31)
0.71	(0.028)	a_0		1430	(322)

The average critical energy release rate from the first test set was 23 J/m^2 ($0.13 \text{ in.-lb/in.}^2$). With this value of G_c , the failure load for the 6.45 mm (0.254 in.) flaw was predicted to be 146 N (35 lb). This value compares closely to the measured 138 N (31 lb) load.

The inherent flaw size, a_0 , is defined as the amount of debond necessary to produce the proper critical energy release rate, 23 J/m^2 ($0.13 \text{ in.-lb/in.}^2$), at the measured peak load, 1430 N (322 lb), in specimens with no initial debond. For the Solithane to PMMA bond, the inherent flaw size was determined to be 0.076 mm (0.003 in.).

Once G_c and a_0 are known, the load capability of other bonded joints can be predicted. This is demonstrated by predicting the change in bond strength with adhesive thickness in butt joint tests (Figure 2). Adhesive thicknesses between 0.15 mm and 25 mm (0.006 in. and 1.0 in.) produced failure loads ranging from 1900 N (430 lb) for thin bonds, to 180 N (40 lb) for thick bonds (Figure 3). Adhesive failure initiated at the bond edges for joints thicker than 2.5 mm (0.1 in.) and near the centerline for joints thinner than 2.5 mm (0.1 in.). Both the failure loads and debond initiation points were predicted using fracture mechanics theory as illustrated by the solid curve in Figure 3.

The analytical prediction was made by assuming that an inherent flaw of 0.076 mm (0.003 in.) existed at the bond edge and extended around the periphery of the specimen (axisymmetric flaw). With this flaw, an energy release rate was found for each adhesive thickness. A second analysis was then completed by assuming the inherent flaw existed at the specimen center and again evaluating energy release rate as a function of adhesive thickness. The data from the two resulting analyses are plotted as the square root of energy release rate per unit load versus bond thickness in Figure 4.

For thin bonds, the energy release rate is greater for a center flaw

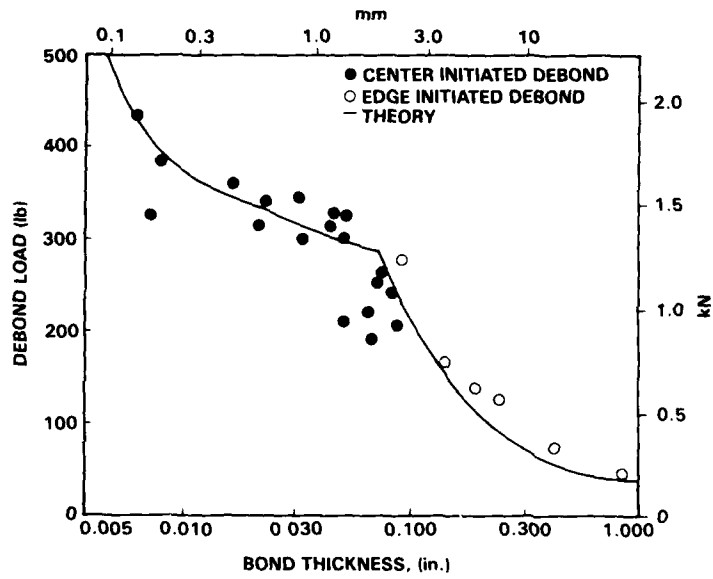


FIGURE 3 Effect of adhesive thickness on debond load—polyurethane.

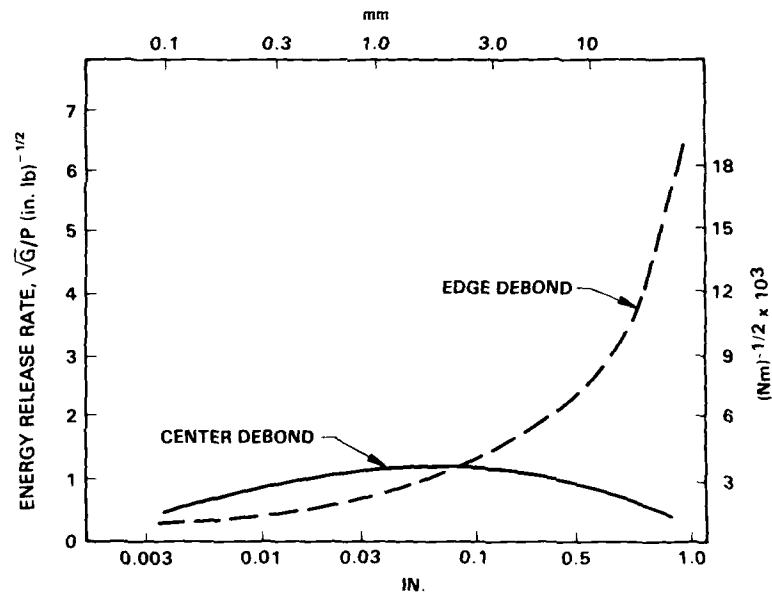


FIGURE 4 Energy release rate for 0.076 mm (0.003 in.) debond.

than for edge flaws, therefore debond is predicted to initiate at the specimen radial center. The energy release rate increases with bond thickness (strength drops) until the bond thickness is 2.3 mm (0.09 in.). When the adhesive thickness exceeds 2.3 mm (0.09 in.) the energy release rate for edge debonds exceeds that for center debonds. Thus the transition from center to edge debonds is properly predicted from the analysis.

The use of an inherent flaw size in conjunction with the energy release rate approach to failure was felt to be necessary because of the discontinuity in energy release rate as the debond size approaches zero and to allow a common failure criterion to be used for edge-initiated debonds (singular point) and internally-initiated debonds.

VERIFICATION FOR BRITTLE EPOXY

The fracture mechanics approach was also evaluated with a nearly linear elastic brittle epoxy (Figure 5a). A critical energy release rate of 32 J/m^2 ($0.18 \text{ in.-lb/in.}^2$) was obtained for 29 mm (1.13 in.) diameter tensile buttons with an initial debond of 2.5 mm (0.1 in.) and a failure load of 7.1 kN (1600 lb) (average for 10 tests). The critical load of 4.2 kN (954 lb) was then predicted for buttons with 5.1 mm (0.2 in.) initial flaws. This prediction was within one percent of the test results.

A series of 10 specimens with no initial debonds was then tested. These specimens had an adhesive thickness of 1.7 mm (0.068 in.) and

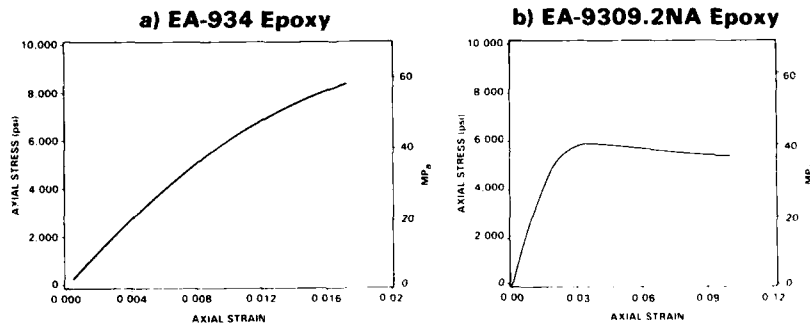


FIGURE 5 Stress-strain curves for two epoxy systems.

failed at an average of 21 kN (4760 lb). These data are summarized in the following table:

Initial Debond		Failure Load		Result
mm	(in.)	kN	(lb)	
2.5	(0.1)	7.1	(1600)	$G_c = 32 \text{ J/m}^2$ (0.18 in.-lb/in. ²)
5.1	(0.2)	4.3	(967)	1% prediction error
a_0		21	(4760)	$a_0 = 0.025 \text{ mm}$ (0.001 in.)

To obtain the inherent flaw size, the energy release rate was calculated using finite element techniques, (Figure 6) as a function of debond length for small initial debonds at the specimen outer diameter. A failure load of 21 kN (4760 lb) was used in computing the energy release rate. Since this was the failure load obtained from the test data, the ordinate in Figure 6 is the critical energy release rate. However, the critical energy release rate was determined to be 32 J/m^2 (0.18 in.-lb./in.²) from the first set of tests (initial debond 2.5 mm, 0.1 in.). Thus, it can be determined from the Figure 6 plot that the bond system has inherent flaws of 0.25 mm (0.001 in.). The two parameters—critical energy release

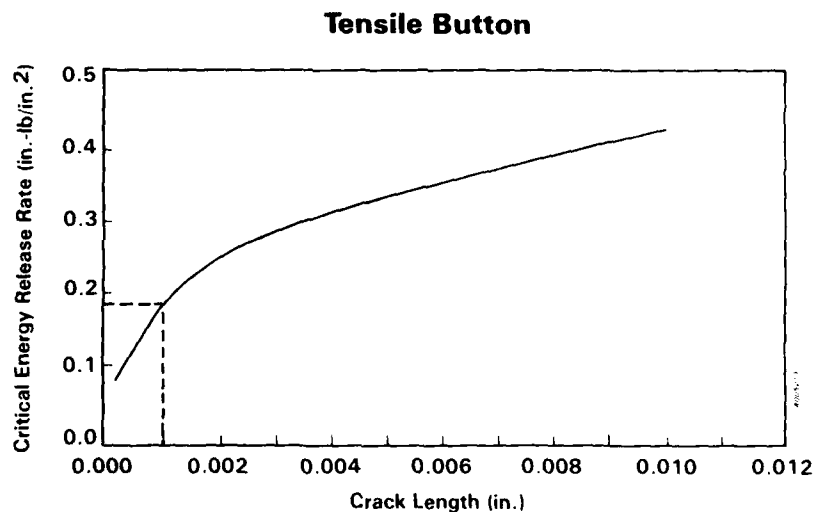


FIGURE 6 Critical energy release rate for EA-934 tensile buttons.

rate and inherent flaw size—are then felt to characterize the bond capability.

A series of tensile button tests was then completed where adhesive thickness ranged from 0.127 mm to 13.3 mm (0.005 in. to 0.525 in.). Average values (10 replications) from these tests are presented in Table I. An attempt was made to adjust the load rate to obtain a constant load time to failure. However, the resulting load times were not constant. Thus, additional testing was completed to allow an empirical correction of the first data set.

Three sets of 0.27 mm (0.060 in.) bondline tensile adhesion buttons were tested at different displacement rates to assess the effects of strain rate on tensile strength. The three displacement rates used were 0.022 mm/min (0.005 in./min), 0.22 mm/min (0.050 in./min), and 2.2 mm/min (0.500 in./min). Ten buttons were tested at each rate. The resulting data from these tests were empirically fit by the following equation:

$$P_{cr} = a \left(\frac{\dot{u}}{h} \right)^n$$

where P_{cr} is the failure force and \dot{u} is the displacement rate. Therefore, the ratio of critical loads P_{cr1}/P_{cr2} for different rates and thicknesses may be expressed:

$$\frac{P_{cr1}}{P_{cr2}} = \left(\frac{\dot{u}_1 h_2}{\dot{u}_2 h_1} \right)^n$$

The test data were then adjusted as shown in Table I. These

TABLE I
Tensile adhesion tests with EA-934 epoxy adhesive^a

Adhesive thickness, mm (in).	Load rate, mm/min (in./min)	Failure load, kN (lb)		
		Measured	Adjusted	Predicted
0.13 (0.005)	1.27 (0.050)	30.1 (6770)	32.2 (7230)	34.8 (7820)
0.58 (0.023)	1.27 (0.050)	24.8 (5570)	25.4 (5720)	26.2 (5900)
1.73 (0.068)	1.27 (0.050)	21.1 (4770)	21.2 (4760)	21.0 (4710)
3.30 (0.130)	1.91 (0.075)	16.2 (3650)	16.1 (3620)	14.6 (3280)
13.30 (0.525)	2.54 (0.100)	10.6 (2380)	10.1 (2280)	9.4 (2120)

^a Hysol Division, Dexter Corp.

adjusted data are plotted as a function of bond thickness in Figure 7. Using the critical energy release rate of 32 J/m^2 ($0.18 \text{ in.-lb/in.}^2$), the inherent flaw size of 0.025 mm (0.001 in.) and a curve of energy release rate as a function of bond thickness (Figure 8), the effect of adhesive thickness on bond strength was predicted. The predicted values presented in Table I and Figure 7 show very close agreement with measured results. Thus, we feel that the reason for adhesive strength changes corresponding to adhesive thickness (at least for polyurethane and brittle epoxies) is completely accounted for by changes in energy release rate.

For all tensile button tests with epoxy, edge-initiated failures are predicted since the energy release rate for an inherent flaw size of 0.025 mm (0.001 in.) is greater for an edge-initiated failure than for failures initiated internally. There was no direct experimental verification of the failure initiation point, since opaque adherends and adhesives were used. The observed failures were primarily cohesive within the adhesive layer. However, in most cases a small area of adhesive failure existed near the bond edge. Our hypothesis is that failure initiated at the adhesive/adherend interface adjacent to the bond edge. Failure then propagated into the adhesive to the

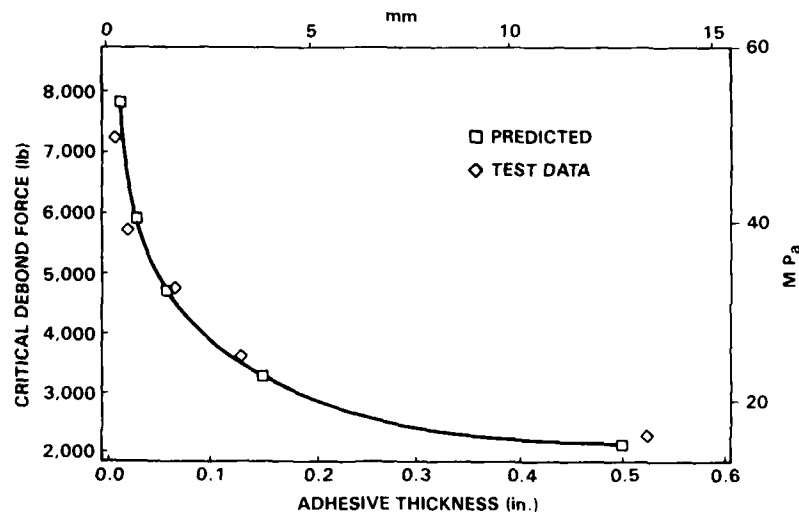


FIGURE 7 Effect of adhesive thickness on debond load—EA-934 epoxy.

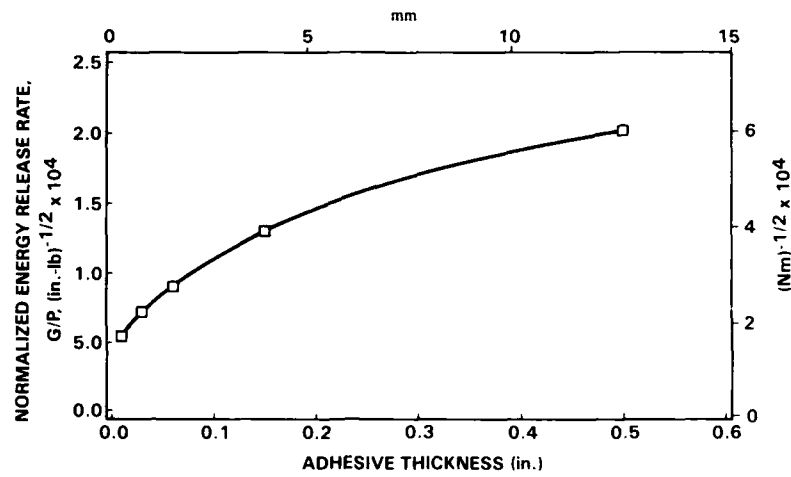


FIGURE 8 Energy release rate versus adhesive thickness, Poisson's ratio = 0.34, $a_0 = 0.025 \text{ mm}$ (0.001 in.).

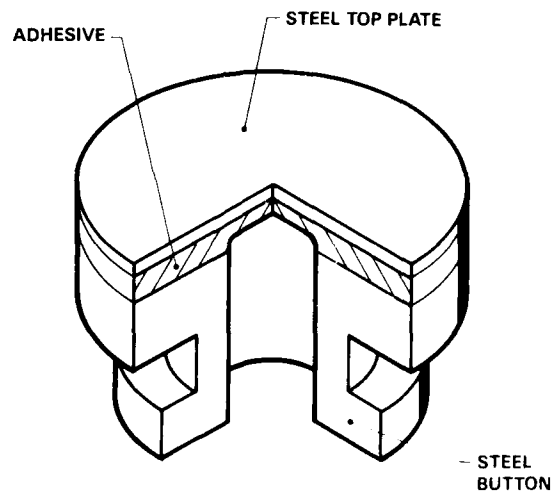


FIGURE 9 Blister test specimens.

bond axial center, then continued through the center of the adhesive layer.

The calculated values of critical energy release rate and inherent flaw size were then successfully used to predict failure in the modified blister test illustrated in Figure 9. A failure pressure of 2360 was calculated. This was within five percent of the average test value from 11 test specimens.

The fracture mechanics approach has shown very promising results for a linear epoxy loaded in Mode I. Further work is in progress to extend the theory to Mode II loads, to nonlinear adhesives, and to show the effects of temperature and load rate on the failure criterion.

CONCLUSIONS

It is concluded that average stress determined from bond tests is a very poor predictor of failure in bonded joints. Furthermore, other stress failure criteria have serious deficiencies due to stress singularities which exist at notches, debonds, and bond termination points. Fracture mechanics theory has shown very promising results in Mode I loading of both a polyurethane and a linear epoxy. Further work is progressing to extend the theory to include nonlinear adhesives. The effect of load rate and temperature also need to be studied. For some test specimens, such as peel geometries, large deformations and rotations complicate analysis. Further work needs to be completed to reconcile these effects.

References

1. M. L. Williams, *Bulletin of the Seismological Society of America* **49**, No. 2, p. 199 (1959).
2. V. L. Hein and F. Erdogan, *Int. J. of Fracture Mechanics*, **7**, pp. 317-330 (1971).
3. E. H. Dill, A. L. Deak and W. F. Schmidt, *Handbook for Engineering Structural Analysis of Solid Propellants*, CPIA Publication 214 (1971), Chapter 5.
4. G. P. Anderson, S. J. Bennett and K. L. DeVries, *Analysis and Testing of Adhesive Bonds* (Academic Press, New York, 1977).
5. G. P. Anderson, K. L. DeVries and M. L. Williams, *Journal of Colloid and Interface Science* **47**, p. 600 (1972).
6. G. C. Trantina, *Journal of Composite Materials* **6**, p. 371 (1972).

7. W. S. Johnson and P. D. Mangaliri, *NASA Technical Memorandum 87571*, (July 1985).
8. G. P. Anderson, K. L. DeVries and G. Sharon, *American Society for Testing and Materials, ASTM STP 876* (Philadelphia, 1985), pp. 115-134.
9. G. P. Anderson and K. L. DeVries, to appear in *Adhesion and Adhesives* **6** (1986).

9

AUTHOR INDEX

ABSOLOM, D. R., 441
 ADAMS, R. D., 103
 AHEARN, J. S., 551
 ALLEN, K. W., 85
 ALON, E., 323
 AMANO, S., 19
 ANDERSON, G. P., 751
 ANNIGHOFER, F., 225
 ARNOLD, C. A., 535

BALDWIN, J., 695
 BAZINET, R., 425
 BERCHTEN, A. R., 241
 BOERIO, F. J., 567
 BOIZIAU, C., 489
 BOTT, R. H., 535
 BOWDITCH, M. R., 153
 BREWIS, D. M., 127
 BRIGGS, D., 167
 BROCKMANN, H., 187
 BYERLEY, T. J., 631

CAWLEY, P., 103
 CHARBONNIER, M., 469
 CHEN, DAO-YI, 669
 CHERRY, B. W., 283
 CLEARFIELD, H. M., 551
 COGNARD, J., 213
 COMYN, J., 127

DEVRIES, K. L., 751
 DODIUK, H., 339

EVELY, P. B., 283

EVERETT, R. A., JR., 725

FRISCH, B., 197

GAILLARD, F., 469
 GENT, A. N., 583
 GINSBURG, D., 591
 GUTOWSKI, W. S., 295, 655
 GUYOTT, C. C. H., 103

HANSON, E. C., 591
 HATA, T., 1
 HATANO, Y., 75
 HENNEMANN, O.-D., 183
 HIRAYAMA, N., 53
 HONG, S. G., 567
 HUDAK, S. J., 567

IKEGAMI, K., 35

JOHNSON, W. S., 725
 JOZAVI, H., 695

KATZ, D., 323
 KENIG, S., 339
 KINLOCH, A. J., 115
 KITAZAKI, Y., 1
 KREIBICH, U. T., 269

LAVIELLE, L., 513
 LE GRESSUS, C., 489
 LECAYON, G., 489
 LEROY, S., 489

- LIAO, T. K., 631
LIECHTI, K. M., 591
LIRAN, I., 339
LIU, XIAO-HUI, 669
- MALL, S., 677
MANGALGIRI, P. D., 725
MARCANTONIO, A. F., 269
MARTIN, C., 513
MATSUMOTO, T., 53
MATZ, C. W., 177
MAUGIS, D., 529
MCGRATH, J. E., 535
MCIVER, D. J. L., 365
MILLER, M. A., 567
MIYAGI, Z., 67
MIZUMACHI, H., 75
MORRIS, C. E. M., 309
MURRAY, D. G., 403
- NAKAMAE, K., 53
NEUMANN, A. W., 441
- PEARCE, P. J., 309
PENN, L. S., 631
PHANOPOULOS, C., 127
PONCE, S., 425
- REYNAUD, C., 489
ROCHE, A., 469
ROMAND, M., 469
ROULIN-MOLONEY, A. C., 241
RUSE, N. D., 403
- SAITO, T., 1
- SANCAKTAR, E., 695
SATO, S., 19
SCHMIDT, H., 193
SCHONHORN, H., 615
SCHREIBER, H. P., 425
SCHULTZ, J., 513
SCHURCH, S., 365
SHAFFER, D. K., 551
SMITH, D. C., 403
STANNARD, K. J., 153
STEVENSON, A., 137
SUGIBAYASHI, T., 35
SUMMERS, J. D., 535
- TAIG, C. M., 115
TANG, J., 695
TANIGAWA, S., 53
TAYLOR, L. T., 535
THIEDMAN, W., 309
THIELE, W. R., 197
TOLAN, F. C., 309
- VENABLES, J. D., 551
VIEL, P., 489
VOGT, J., 255
- WANG, ZHI-LU, 669
WARD, T. C., 535
- YAMAGUCHI, K., 53
YAMAGUCHI, Y., 19
YAMAMOTO, K., 67
YUN, K. T., 677
- ZUCCOLIN, J. D., 403

SUBJECT INDEX

- Acid-base interactions, in carbon fibre-epoxy composites, 513
- Acid-base, interactions, 425
- Acrylic ester-acrylic acid copolymer, dispersion of gamma-ferric oxide in, 53
- Acrylonitrile, interaction of, with nickel, with iron, with stainless steel, with aluminum, 489
- Adherence, of elastomers, fracture mechanics aspects of, 529
- Adherend thickness, effect of, on debond growth in adhesively bonded composite joints, 725
 - effect of, on fracture toughness of adhesively bonded composite joints, 725
- Adherends, Ti-6Al-4V, oxide morphology of, 551
- Adhesion effects, of intermediate layers on the densification of ceramic powders, 197
- Adhesion promoters, for glass, 193
 - silane coupling agents as, for aerospace structural film adhesives, 309
- Adhesion studies, application of SIMS to, 167
- Adhesion, between metals and polymers, as a three-dimensional system, 183
 - between metals and polymers, chemical aspects of, 187
 - blister test for, 583
 - cell, measurement of, 365
 - double-torsion test for, 583
 - epoxide/polyethylene, application of SIMS to study of, 167
 - kinetics of, 441
 - mechanism of, of cells to cells and non-cellular surfaces, 365
 - new and improved tests for, 583
 - of erythrocytes to polymer substrates in *aqueous media*, 441
 - of hydrophilic particles to polymer substrates in *aqueous media*, 441
 - of matrix and filler, in polyurethane elastomer, effect of water on, 153
 - of polymer to gamma-ferric oxide, 53
 - of rubber to metal, effect of electrochemical potentials on, 137
 - of rubber to metal, effect of sea water on, 137
 - particle, thermodynamic model for, 441
 - review of theories of, 85
 - role of ionic strength in, 441
 - role of pH in, 441
 - role of surface tension in, 441
 - thermodynamics of, 655
 - time dependence of, 425
 - to glass, 193
 - work of, 283, 655
- Adhesive bond, durability of, 295
- Adhesive bonded joints, of metals, method for estimating strength of, 35
- Adhesive bonding, at the aramid-epoxy interface, 631

- of Ti-6Al-4V adherends, 551
- of thermoplastic composites, 115
- spectroscopic characterization of modified surfaces for, 469
- to hydroxyapatite, 365
- to wood, durability of, 127
- Adhesive bond, thermodynamic model of, 295
- Adhesive ductility, effect of, on cyclic debond mechanism in composite-to-composite bonded joints, 677
- Adhesive joint strength, and interaction parameter, 283
- and work of adhesion, 283
- Adhesive joint, fracture energy of, measured by the wedge test, 213
- Adhesive properties, effect on, of siloxane modification of polyimides, 535
- Adhesive strength, of lap joints, methods for estimating, 35
- Adhesive, cured, wettability characteristic of, 295
- Adhesively bonded composite joints, effect of adherend thickness and mixed mode loading on debond growth in, 725
- Adhesively bonded joints, non-destructive inspection of, 103*
- Adhesives, crack tip plastic deformation zone in, 695
- epoxy, room temperature curing, for elevated temperature service, 339
- of organically modified silicates, for bonding siliceous surfaces, 193
- polyether-sulfone-modified epoxy, structure and properties of, 669
- reactive hot melt, from polyester and polyamide, 225
- structural, elastoplastic behavior of, under monotonic loading, 695
- structural, for the automotive industry, new developments in, 269
- thermoset, by imidazole-catalyzed curing of epoxide resins, 255
- Adsorbed polymer, conformation of, on gamma-ferric oxide, 53
- Aerospace structural film adhesives, silane coupling agents as adhesion promoters for, 309
- Analysis, of crack opening displacements near front of interface crack, 591
- quantitative, of functional groups at an aramid surface, 631
- Anisotropic wetting, of liquids on finely grooved surfaces, 615
- Aramid-epoxy interface, reactive functional groups in adhesive bonding at, 631
- Atomic oxygen resistance, of siloxane-modified polyimides, 535
- Automotive industry, structural adhesives for, new developments in, 269
- Bending moment, reinforcement of T-type adhesive joint against, 19
- Bioadhesion, 365
- Blister test, for adhesion, 583
- for determination of fracture surface energy of adhesive joints, 283
- Bond strength, prediction of, 751
- Bonded joints, composite-to-composite, effect of adhesive ductility on debond mechanism in, 677
- mechanical testing of, 469
- methods for prediction of strength of, 751
- non-destructive inspection of, 103
- Bonding, adhesive, at the aramid-epoxy interface, 631
- adhesive, of thermoplastic composites, 115
- adhesive, spectroscopic characterization of modified surfaces for, 469
- rubber-to-metal, 567
- Bone, adhesion to, 365
- Boundary layers, between metals and polymers, 183
- Boundary slippage, in shear adhesion test for pressure-sensitive adhesive tape, 67
- Boundary zone, in bonded carbon fibre reinforced plastics, 177
- Carbon fibre, as reinforcement in thermoplastic composites, 115
- Carbon fibre reinforced plastics, adhesion to, 177
- Carbon fibre-epoxy composites, role of interface in, 513
- Carbon fibres, surface properties of, 513
- Catalysts, imidazoles, for curing of epoxy resins, 255
- Cathodic debonding, of neoprene from steel, 567
- Cell adhesion, 441

- measurement of, 365
- Cell/surface interactions, 441
- Ceramic powders, densification of, by adhesion effects of intermediate layers, 197
- Characterization, of siloxane-modified copolymers, 535
 - spectroscopic, of modified surfaces, for adhesive bonding or painting, 469
- Chemical aspects, of adhesion between metals and polymers, 187
- Chromatography, inverse gas, in the study of acid-base interactions in carbon fibre-epoxy composites, 513
- Chromic acid anodized Ti-6Al-4V adherends, oxide morphology of, 551
- Cohesive properties, poor, location of, by ultrasonic inspection, 103
- Cohesive slippage, in shear adhesion test for pressure-sensitive adhesive tape, 67
- Coin tap test, in non-destructive inspection of adhesively bonded joints, 103
- Composite joints, adhesively bonded, effect of adherend thickness and mixed mode loading on debond growth in, 725
- Composite materials, fibre-reinforced, thermodynamic criteria for maximum and minimum strength of, 655
- Composite-to-composite bonded joints, effect of adhesive ductility on debond mechanism in, 677
- Composites, carbon fibre-epoxy, role of interface in, 513
 - thermoplastic, adhesive bonding of, 115
- Concrete structures, repair of, by injection with epoxide resin, 241
- Conformation, of adsorbed polymer, on gamma-ferric oxide, 53
- Contact angle methods, for estimating the surface energy of polymer solids, 1
- Contact angles, of liquid drops on finely grooved surfaces, 615
- Copolymers, segmented, synthesis of, 535
- Correlation, between total morphology of an epoxy system and some of its properties, 323
- Coupling agents, silane, as adhesion promoters for aerospace structural film adhesives, 309
 - silane, effect of, on hydrolytic stability of filled polyurethane elastomer, 153
- Crack opening displacements, near front of interface crack, 591
- Crack opening interferometry, for glass-epoxy joints, 591
- Cracked concrete structure, repair of, by injection with epoxide resin, 241
- Cracked lap shear specimen, for study of effect of adhesive ductility on debond mechanism in composite-to-composite bonded joints, 677
- Crack, interface, displacements near front of, 591
- Criteria, for maximum strength of fibre-reinforced composite materials, 655
- Critical energy release rate, in adhesives, 751
- Critical surface tension, relationship of, to surface tension of a polymer solid, 1
- Crosslinking hot melt adhesives, from polyester and polyamide, 225
- Crosslinking, rate of, as affected by fillers, 425
- Curing, of epoxy resins, imidazole catalysts for, 255
- Cyclic debonding behavior, of double cantilever and cracked lap shear specimen, 677
- Dam, repair of, by injection of epoxide resin, 241
- Debond growth, effect of adherend thickness and mixed mode loading on, in adhesively bonded composite joints, 725
- Debond mechanism, in composite-to-composite bonded joints, effect of adhesive ductility on, 677
- Debonding, cathodic, of neoprene from steel, 567
- Defects, in non-destructive inspection of adhesively bonded joints, 103
- Delamination, cathodic, of neoprene from steel, 567
 - interfacial, 655
 - thermodynamic conditions for, 295
- Densification, of ceramic powders, by adhesion effects of intermediate layers, 197
- Diffusion mechanisms, in adhesion, 85
- Dispersibility, of gamma-ferric oxide in a polymer, 53

- Double cantilever beam specimen, for study of effect of adhesive ductility on debond mechanism in composite-to-composite bonded joints, 677
 unsymmetric, use of, to study the effect of mixed mode loading on debond growth in adhesively bonded composite joints, 725
- Double-torsion test, for adhesion, 583
- Ductility, adhesive, effect of, on debond mechanism in composite-to-composite bonded joints, 677
- Durability, environmental, of new structural adhesives for the automotive industry, 269
 moisture, of siloxane-modified polyimides, 535
 of adhesive bonds to wood, 127
 of adhesive joint, measured by the wedge test, 213
 of carbon fibre reinforced plastics, 177
 of joints to aluminium with aerospace structural film adhesives, using silane coupling agents as adhesion promoters, 309
 of neoprene/steel adhesive joints, 567
 of rubber/metal bonds in sea water, 137
- Durapatite, 365
- Elastomer, polyurethane, effect of water on matrix/filler adhesion in, 153
- Elastomers, fracture mechanics aspects of adherence of, 529
- Elastoplastic fracture behavior, of structural adhesives under monotonic loading, 695
- Electrochemical potentials, effect of, on durability of rubber/metal bonds in sea water, 137
- Electrostatic interactions, in adhesion, 85
- Elementary mechanisms, in the interaction of organic molecules with mineral surfaces, 489
- Elevated temperature service, room temperature curing epoxy adhesives for, 339
- Energy of fracture, of adhesive joint, quantitative measurement of, using the wedge test, 213
- Environmental durability, of new structural adhesives for the automotive industry, 269
- Epoxide resin, for repair of concrete structures, 241
- Epoxide/polyethylene adhesion, application of SIMS to study of, 167
- Epoxy adhesive, brittle, prediction of failure load in bonded joint made with, 751
- Epoxy adhesives, polyether-sulfone-modified, structure and properties of, 669
 room temperature curing, for elevated temperature service, 339
- Epoxy paste adhesives, new structural, for the automotive industry, 269
- Epoxy resins, curing of, by imidazole catalysts, 255
- Epoxy system, microheterogeneities in, 323
 physical aging of, 323
 total morphology of, and correlation with some of its properties, 323
- Epoxy-aramid interface, functional groups in adhesive bonding at, 631
- Epoxy-carbon fibre composites, role of interface in, 513
- Estimation, of surface energy of polymer solids, 1
- Failure mechanisms, of neoprene/steel adhesive bonds during cathodic delamination, 567
- Failure mode, in adhesively-bonded Ti-6Al-4V adherends treated with CAA, 551
- Failure, locus of, in epoxide/polyethylene joints, as studied by SIMS, 167
- Ferric oxide powder, gamma, adhesion of polymer to, 53
- Fiber-matrix interface, strength of, 631
- Fibre-reinforced composite materials, thermodynamic criteria for maximum and minimum strength of, 655
- Field repair, of cracked concrete structure, by injection of epoxide resin, 241
- Filled epoxy systems, component interaction and properties of, 425
- Filler/matrix adhesion, in polyurethane elastomer, effect of water on, 153
- Film adhesives, aerospace structural, silane coupling agents as adhesion promoters for, 309
- Film tape adhesives, new structural, for the automotive industry, 269

- Finite element analysis, of cracked lap shear specimen, 677
- Finite element predictions, of crack opening displacements near front of interface crack, 591
- Fluid interfaces, and cell adhesion, 365
- Fokker bond tester, in non-destructive inspection of adhesively bonded joints, 103
- Fractography, of adhesively bonded thermoplastic composites, 115
- Fracture behavior, elastoplastic, of structural adhesives under monotonic loading, 695
- Fracture energy, quantitative measurement of, for an adhesive joint, using the wedge test, 213
- Fracture mechanics aspects, of adherence of elastomers, 529
- Fracture mechanics, use of, to predict failure load of adhesively bonded joints, 751
- Fracture surface energy, of adhesive joints, determination of by blister test technique, 283
- Fracture, of adhesively bonded thermoplastic composites, 115
- Functional groups, reactive, study of, in adhesive bonding at the aramid-epoxy interface, 631
- Glass-epoxy joints, crack opening interferometry of, 591
- Glass, adhesion promoters for, 193
- Honeycomb structures, non-destructive inspection of, 103
- Hot melt adhesives, reactive, from polyester and polyamide, 225
- reactive, new structural, for the automotive industry, 269
- Humidity, effect of, on fracture energy of an adhesive joint, 213
- Hydrophilic particles, adhesion of, to polymer substrates in aqueous media, 441
- Hydroxyapatite, surface characteristics of, and adhesive bonding, 403
- surface preparation of, for adhesive bonding, 365
- synthetic, 365
- Imidazoles, as catalysts for curing of epoxy resins, 255
- Improved tests, for adhesion, 583
- Inspection, non-destructive, of adhesively bonded joints, 103
- Interaction parameter, and the strength of adhesive joints, 283
- Interaction, of organic molecules with mineral surfaces, 489
- Interactions, acid-base, 425
- Interface crack, displacements near front of, 591
- Interface, aramid-epoxy, functional groups in adhesive bonding at, 631
- role of, in carbon fibre-epoxy composites, 513
- Interferometry, crack opening, for glass-epoxy joints, 591
- Intermediate layers, effects of adhesion in, on densification of ceramic powders, 197
- Interphases, between metals and polymers, 183
- Inverse gas chromatography, for measurement of acid-base interaction parameters, 425
- in the study of acid-base interactions in carbon fibre-epoxy composites, 513
- Isocyanates, blocked, use of, in reactive hot melt adhesives, 225
- Joints, adhesive, of metals, method for estimating strength of, 35
- adhesively bonded, non-destructive inspection of, 103
- Lap joints, of metals, method for estimating strength of, 35
- Liquid crystals, on finely grooved surfaces, anisotropic wetting by, 615
- Liquids, anisotropic wetting of, on finely grooved surfaces, 615
- Loading, mixed mode, effect of, on debond growth in adhesively bonded composite joints, 725
- monotonic, effect of, on elastoplastic behavior of structural adhesives, 695
- Locus of failure, in epoxide/polyethylene joints, as studied by SIMS, 167
- Low-energy electron-induced X-ray spectroscopy (LEEIXS), use of, to study near-surface chemistry of metallic substrates, 469

- Magnetic paint, of gamma-ferric oxide dispersed in acrylic ester-acrylic acid copolymer, 53
- Mass spectrometry, secondary ion, application of, to adhesion studies, 167
- Matrix/filler adhesion, effect of water on, 153
- Maximum strength, of fibre-reinforced composite materials, thermodynamic criteria for, 655
thermodynamic conditions for, 295
- Mean pore size, effect of, on densification of ceramic powders, 197
- Measurement, of cell adhesion, 365
of crack opening displacements near front of interface crack, 591
- Mechanical interlocking, in adhesion, 85
- Mechanical properties, of epoxy resins cured by catalysis with imidazoles, 255
of filled polyurethane elastomer, effect of water on, 153
of new structural adhesives for the automotive industry, 269
of polyether-sulfone-modified epoxy adhesives, 669
of room temperature curing epoxy adhesives for high temperature service, 339
- Mechanics, fracture, and the adherence of elastomers, 529
- Mechanisms, elementary, in the interaction of organic molecules with mineral surfaces, 489
- Mercury, on finely grooved surfaces, anisotropic wetting by, 615
- Metal/polymer adhesion, chemical aspects of, 187
- Metal/rubber bonds, durability of, in sea water, 137
- Metals, adhesive joints of, method for estimating strength of, 35
- Method, for estimating the strength of adhesive bonded joints of metals, 35
- Methods, for estimating surface energy of polymer solids, 1
- Microheterogeneities, in an epoxy system, 323
- Microstructure, of room temperature curing epoxy adhesives for high temperature service, 339
- Mineral surfaces, interaction of organic molecules with, 489
- Mixed mode loading, effect of, on debond growth in adhesively bonded composite joints, 725
- Mixed-mode debonding, of glass-epoxy joint, 591
- Modelling, of cell adhesion, 365
- Model, of interaction of acrylonitrile with negatively-polarized surface, 489
to study influence of roughness on spreading equilibrium of liquid drops, 615
- Modified surfaces, spectroscopic characterization of, for adhesive bonding or painting, 469
- Moisture durability, of siloxane-modified polyimides, 535
- Morphology, of hydroxyapatite, as a result of various treatments, 365
of polyether-sulfone-modified epoxy adhesives, 669
of room temperature curing epoxy adhesives for high temperature service, 339
oxide, of chromic acid anodized Ti-6Al-4V adherends, 551
total, correlation of, with some properties of an epoxy system, 323
- Near-surface chemistry, of metallic substrates, as studied by LEEIXS, 469
- Neoprene, cathodic debonding of, from steel, 567
- New tests, for adhesion, 583
- Optical interferometry, for measurement of crack opening displacements near front of interface crack, 591
- Organic molecules, interaction of, with mineral surfaces, 489
- Organically modified silicates, as adhesives for siliceous surfaces, 187
- Oxide layers, in joints between metals and polymers, 183
- Oxide morphology, of chromic acid anodized Ti-6Al-4V adherends, 551
- Oxide stability, of CAA-treated Ti-6Al-4V adherends, 551
- Painting, spectroscopic characterization of modified surfaces for, 469
- Particles, hydrophilic, adhesion of, to polymer substrates in aqueous media, 441

- Phase separation, in polyether-sulfone-modified epoxy adhesives, 669
- Phenolic primers, use of, in neoprene/steel adhesive bonds, 567
- Pigmented epoxy systems, component interaction and properties of, 425
- Plasma cleaning, of hydroxyapatite, 365
- Poly(imide siloxanes), synthesis and characterization of, 535
- Polyamide, as basis for reactive hot melt adhesives, 225
- Polyester, as basis for reactive hot melt adhesives, 225
- Polyether-sulfone-modified epoxy adhesives, structure and properties of, 669
- Polyethylene/epoxide adhesion, application of SIMS to study of, 167
- Polyimides, siloxane-modified, synthesis of, 535
- Polymer mixing, and cell adhesion, 365
- Polymer solids, estimation of surface energy of, 1
- Polymer solutions, mixing of, and thermodynamics of cell adhesion at fluid interfaces, 365
- Polymer substrates, adhesion of hydrophilic particles to, in aqueous media, 441
- Polyurethane adhesive, prediction of failure load in bonded joint made with, 751
- Polyurethane adhesives, new structural, for the automotive industry, 269
- Polyurethane elastomer, effect of water on matrix/filler adhesion in, 153
- Powder, of gamma-ferric oxide, adhesion of, to polymer, 53
- Pre-bond treatments, of metallic adherends, as studied by LEEIXS, 469
- Prebonding treatments, for carbon fibre reinforced plastic, 177
- Prediction, of bond strength, 751
- Pressure-sensitive adhesive tape, viscoelastic analysis of shear test for adhesion of, 67
- Pressure-sensitive adhesives, rheological study of tack of, 75
- Primers, phenolic, use of, in neoprene/steel adhesive bonds, 567
- Properties, and structure, of polyether-sulfone-modified epoxy adhesives, 669
- of an epoxy system, correlation of, with its total morphology, 323
- of pigmented epoxy systems, 425
- Pull-off test, for adhering strips, 583
- Pulling cylinder test, for measuring tack of pressure-sensitive adhesives, 75
- Reaction processes, effect on, of fillers, 425
- Reactive functional groups, study of, in adhesive bonding at the aramid-epoxy interface, 631
- Reactive hot melt adhesives, from polyester and polyamide, 225
- Red blood cells, 441
- Reinforcement, of T-type adhesive joint against bending moment, 19
- Repair, of concrete structures by injection with epoxide resin, 241
- Review, of theories of adhesion, 85
- Rheological study, of tack of pressure-sensitive adhesives, 75
- Rigid adherends, stress distribution in T-type adhesive joint made with, 19
- Rolling ball test, for measuring tack of pressure-sensitive adhesives, 75
- Rolling friction coefficient, of ball on pressure-sensitive adhesives, 75
- Room temperature curing epoxy adhesives, for elevated temperature service, 339
- Rubber-to-metal bonding, 567
- Rubber/metal bonds, durability of, in sea water, 137
- SIMS, application of, to adhesion studies, 167
- Sea water, durability of rubber/metal bonds in, 137
- Secondary ion mass spectrometry, application of, to adhesion studies, 167
- Segmented copolymers, synthesis of, 535
- Shear adhesion test, viscoelastic analysis of, for pressure-sensitive adhesive tape, 67
- Side chain length, of polymer, effect of, on adhesion and dispersibility of gamma-ferric oxide, 53
- Silane coupling agents, as adhesion promoters for aerospace structural film adhesives, 309
- effect of, on hydrolytic stability of filled polyurethane elastomer, 153

- Silicates, organically modified, as adhesives for siliceous surfaces, 187
- Siliceous surfaces, bonded by organically modified silicates, 193
- Siloxane incorporation, into polyimides, effect of, on adhesive properties, 535
- Siloxane-modified polyimides, synthesis and characterization of, 535
- Solution properties, of the cell surface, 365
- Sonic vibrations, in non-destructive inspection of adhesively bonded joints, 103
- Sorption, selective, by fillers, 425
- Spectrometry, secondary ion mass, application of, to adhesion studies, 167
- Spectroscopic characterization, of modified surfaces, for adhesive bonding or painting, 469
- Spreading equilibrium, of liquid drops on finely grooved surfaces, 615
- Static debonding behavior, of double cantilever and cracked lap shear specimen, 677
- Steel, cathodic debonding of neoprene from, 567
- Steels, near-surface chemistry of, as studied by LEEIXS, 469
- Strain energy release rate, total, and cyclic debond growth in adhesively bonded composite joints, 725
- Strength law, adhesive, for lap joints of metals, 35
- Strength, and surface tension, 441
- bond, prediction of, 751
- of T-type adhesive joint with reinforcement, 19
- of adhesive bonded joints of metals, method of estimating strength of, 35
- of fiber-matrix interface, 631
- Stress analysis, of adhesively bonded thermoplastic composites, 115
- Stress distribution, in T-type adhesive joint with reinforcement, 19
- Structural adhesives, elastoplastic fracture behavior of, under monotonic loading, 695
- for the automotive industry, new developments in, 269
- thermoset, by imidazole-catalyzed curing of epoxide resins, 255
- Structural analysis, of adhesive bonds, 751
- Structure/property relationships, in epoxy systems, 323
- Structure, and properties, of polyether-sulfone-modified epoxy adhesives, 669
- Surface analysis, of CAA-treated Ti-6Al-4V adherends, 551
- Surface analytical studies, of adhesive bonding to wood, 127
- Surface characteristics, of hydroxyapatite, and adhesive bonding, 403
- Surface characterization, of hydroxyapatite, 365
- Surface chemistry, near, of metallic substrates, study of, by low-energy electron-induced spectroscopy (LEEIXS), 469
- Surface energy, estimation of, for polymer solids, 1
- of adhesive and substrate, 295
- Surface modification, of polyimides, by siloxane incorporation, 535
- Surface properties, of carbon fibres, 513
- Surface segregation, in siloxane-modified polyimides, 535
- Surface spectroscopy, of hydroxyapatite subjected to various treatments, 365
- Surface thermodynamics, of cell adhesion, 365
- Surface treatment, of thermoplastic composites, for adhesive bonding, 115
- Surface, of true mineral solids, 489
- Surfaces, characterization of, by LEEIXS, 469
- finely grooved, anisotropic wetting of liquids on, 615
- mineral, interaction of organic molecules with, 489
- modified, spectroscopic characterization of, for adhesive bonding or painting, 469
- Surfactants, effect of, on densification of ceramic powders, 197
- Synthesis, of siloxane-modified polyimides, 535
- T-type adhesive joint, reinforcement of, against bending moment, 19
- Tack, of pressure-sensitive adhesives, rheological study of, 75
- Tape, pressure-sensitive adhesive, viscoelastic analysis of shear test for adhesion of, 67
- Teeth, adhesion to, 365
- Test apparatus, for measuring adhesion in shear of pressure-sensitive adhesive tape, 67

- Testing, non-destructive, of adhesively bonded joints, 103
- Test, shear adhesion, viscoelastic analysis of, for pressure-sensitive adhesive tape, 67
- Tests, new and improved, for adhesion, 583
- Theories of adhesion, review of, 85
- Thermal properties, of room temperature curing epoxy adhesives for high temperature service, 339
- Thermal resistance, of reactive hot melt adhesives based on polyester and polyamide, 225
- Thermodynamic equilibrium diagrams, 295
- Thermodynamic model, for particle adhesion, 441
 - of the adhesive bond, 295
- Thermoplastic composites, adhesive bonding of, 115
- Thermoset matrices, for structural adhesives, by imidazole catalyzed curing of epoxide resins, 255
- Thickness, adherend, effect of, on debond growth in adhesively bonded composite joints, 725
 - of adhesive, effect of, on bond strength, 751
- Ti-6Al-4V, near-surface chemistry of, as studied by LEEIXS, 469
- Torsion test, double, for adhesion, 583
- Toughening, with ATBN, of room temperature curing epoxy adhesives for high temperature service, 339
- Two-liquid method, for estimating the surface energy of polymer solids, 1
- Ultrasonics, in non-destructive inspection of adhesively bonded joints, 103
- Viscoelastic analysis, of shear adhesion test for pressure-sensitive adhesive tape, 67
- Viscoelastic properties, of pressure-sensitive adhesives, measured by rolling ball and pulling cylinder test, 75
- Voight model, for analysis of shear adhesion test for pressure-sensitive adhesive tape, 67
- Water absorption, effect of, on matrix/filler adhesion in polyurethane elastomer, 153
- Water, sea, durability of rubber/metal bonds in, 137
- Wedge test, as measure of durability of joints to aluminium made with aerospace structural film adhesives, 309
 - for quantitative measurement of energy of fracture of an adhesive joint, 213
- Wettability characteristic, of cured adhesive and substrate, 295
- Wetting, anisotropic, of liquids on finely grooved surfaces, 615
 - by liquids, 365
- Wood, durability of adhesive bonds to, 127
 - surface analytical studies of adhesive bonding to, 127
- Work of adhesion methods, for estimating the surface energy of polymer solids, 1
- Work of adhesion, 295
 - of aqueous polymer solutions to cell surfaces, 365
- X-ray photoelectron spectroscopy, use of, to study cathodic delamination of neoprene/steel adhesive bonds, 567
- X-ray spectroscopy, low-energy electron-induced, use of, to study near-surface chemistry of metallic substrates, 469
- XPS, use of, to study cathodic delamination of neoprene/steel adhesive bonds, 567